Tribological analysis of White Etching Crack (WEC) failures in rolling element bearings

Arnaud Ruellan Du Créhu

N° d'ordre 2014ISAL0116 Année 2014

Thèse

Tribological analysis of White Etching Crack (WEC) failures in Rolling Element Bearings

Présentée devant

L'Institut National des Sciences Appliquées de Lyon

Ecole doctorale des Sciences pour l'Ingénieur de Lyon:
Mécanique, Energétique, Génie Civil, Acoustique (MEGA)
Spécialité : Mécanique

Pour obtenir

Le grade de docteur

Par

Arnaud RUELLAN Du CREHU
Ingénieur INSA Lyon

Thèse soutenue le 05 Décembre 2014 devant la commission d'examen composée de :

Pr. Michel FILLON	Université de Poitiers (France) - Institut Pprime	Président du jury
Pr. Motohiro KANETA	Université de Brno (République Tchèque)	Membre invité
Pr. Xavier KLEBER	INSA Lyon (France) - MATEIS	Directeur de thèse
M. Bernard LIATARD	NTN-SNR – Annecy (France)	Encadrant industriel
Pr. Gerhard POLL	Université de Hannovre (Germany) - IMKT	Rapporteur
Pr. Jorge SEABRA	Université de Porto (Portugal) - INEGI	Rapporteur
Pr. Fabrice VILLE	INSA Lyon (France) - LaMCoS	Directeur de thèse

Cette thèse a été préparée au Laboratoire de Mécanique des Contacts et des Structures (**LaMCoS**) et au laboratoire Matériau Ingénierie et Sciences (**MATEIS**) de l'INSA de Lyon, en collaboration avec l'entreprise **NTN-SNR.**

INSA Direction de la Recherche - Ecoles Doctorales – Quinquennal 2011-2015

SIGLE	ECOLE DOCTORALE	NOM ET COORDONNEES DU RESPONSABLE
CHIMIE	**CHIMIE DE LYON** http://www.edchimie-lyon.fr Sec : Renée EL MELHEM Bat Blaise Pascal 3e etage 04 72 43 80 46 Insa : R. GOURDON	M. Jean Marc LANCELIN Université de Lyon – Collège Doctoral Bât ESCPE 43 bd du 11 novembre 1918 69622 VILLEURBANNE Cedex Tél : 04.72.43 13 95 directeur@edchimie-lyon.fr
E.E.A.	**ELECTRONIQUE, ELECTROTECHNIQUE, AUTOMATIQUE** http://edeea.ec-lyon.fr Sec : M.C. HAVGOUDOUKIAN eea@ec-lyon.fr	M. Gérard SCORLETTI Ecole Centrale de Lyon 36 avenue Guy de Collongue 69134 ECULLY Tél : 04.72.18 60.97 Fax : 04 78 43 37 17 Gerard.scorletti@ec-lyon.fr
E2M2	**EVOLUTION, ECOSYSTEME, MICROBIOLOGIE, MODELISATION** http://e2m2.universite-lyon.fr Sec : Safia AIT CHALAL Bat Darwin - UCB Lyon 1 04.72.43.28.91 Insa : H. CHARLES	Mme Gudrun BORNETTE CNRS UMR 5023 LEHNA Université Claude Bernard Lyon 1 Bât Forel 43 bd du 11 novembre 1918 69622 VILLEURBANNE Cédex Tél : 06.07.53.89.13 e2m2@ univ-lyon1.fr
EDISS	**INTERDISCIPLINAIRE SCIENCES-SANTE** http://www.ediss-lyon.fr Sec : Safia AIT CHALAL Hôpital Louis Pradel - Bron 04 72 68 49 09 Insa : M. LAGARDE Safia.ait-chalal@univ-lyon1.fr	Mme Emmanuelle CANET-SOULAS INSERM U1060, CarMeN lab, Univ. Lyon 1 Bâtiment IMBL 11 avenue Jean Capelle INSA de Lyon 696621 Villeurbanne Tél : 04.72.68.49.09 Fax :04 72 68 49 16 Emmanuelle.canet@univ-lyon1.fr
INFOMATHS	**INFORMATIQUE ET MATHEMATIQUES** http://infomaths.univ-lyon1.fr Sec :Renée EL MELHEM Bat Blaise Pascal 3e etage infomaths@univ-lyon1.fr	Mme Sylvie CALABRETTO LIRIS – INSA de Lyon Bat Blaise Pascal 7 avenue Jean Capelle 69622 VILLEURBANNE Cedex Tél : 04.72. 43. 80. 46 Fax 04 72 43 16 87 Sylvie.calabretto@insa-lyon.fr
Matériaux	**MATERIAUX DE LYON** http://ed34.universite-lyon.fr Sec : M. LABOUNE PM : 71.70 –Fax : 87.12 Bat. Saint Exupéry Ed.materiaux@insa-lyon.fr	M. Jean-Yves BUFFIERE INSA de Lyon MATEIS Bâtiment Saint Exupéry 7 avenue Jean Capelle 69621 VILLEURBANNE Cedex Tél : 04.72.43 83 18 Fax 04 72 43 85 28 Jean-yves.buffiere@insa-lyon.fr
MEGA	**MECANIQUE, ENERGETIQUE, GENIE CIVIL, ACOUSTIQUE** http://mega.universite-lyon.fr Sec : M. LABOUNE PM : 71.70 –Fax : 87.12 Bat. Saint Exupéry mega@insa-lyon.fr	M. Philippe BOISSE INSA de Lyon Laboratoire LAMCOS Bâtiment Jacquard 25 bis avenue Jean Capelle 69621 VILLEURBANNE Cedex Tél :04.72 .43.71.70 Fax : 04 72 43 72 37 Philippe.boisse@insa-lyon.fr
ScSo	**ScSo*** http://recherche.univ-lyon2.fr/scso/ Sec : Viviane POLSINELLI Brigitte DUBOIS Insa : J.Y. TOUSSAINT	Mme Isabelle VON BUELTZINGLOEWEN Université Lyon 2 86 rue Pasteur 69365 LYON Cedex 07 Tél : 04.78.77.23.86 Fax : 04.37.28.04.48 viviane.polsinelli@univ-lyon2.fr

*ScSo : Histoire, Géographie, Aménagement, Urbanisme, Archéologie, Science politique, Sociologie, Anthropologie

Il est souvent nécessaire d'entreprendre pour espérer et de persévérer pour réussir.
Gilbert Cesbron

&

Perseverance is not a long race, it is many short races one after the other.
Walter Elliot

Foreword

The work results from a close collaboration between the laboratory of Contact and Structure Mechanics (LaMCoS) of INSA Lyon (France), the laboratory MATEriaux: Ingénierie et Sciences (MATEIS) of INSA Lyon (France), and the bearing company NTN-SNR.

The PhD took place in the doctoral school MEGA (Mechanics, Energetics, Civil Engineering, Acoustics), and has been funded by the National Agency for Research and Technology (ANRT) through an Industrial Research Convention (CIFRE) grant number 2011/1336.

PhD supervisors	LaMCoS MATEIS	*Fabrice VILLE* *Xavier XLEBER*
Member of the jury	University of Poitiers (France) University of Brno (Czech Republic)	*Michel FILLON* *Motohiro KANETA*
Reviewers	University of Hannover (Germany) University of Porto (Portugal)	*Gerhard POLL* *Jorge SEABRA*
LaMCoS	Director Head of the SMC* team	*David DUREISSEIX* *Philippe VELEX*
MATEIS	Director Head of the Metal team	*Jérôme CHEVALIER* *Eric MAIRE*
INSA Lyon	Director Director of Research	*Eric MAURINCOMME* *Jean-François GERARD*
MEGA doctoral school	Director	*Philippe BOISSE*
NTN-SNR	Chairman of the Managing Board Director of Industry Business Unit Head of Technologies & Innovation	*Didier SEPULCHRE DE CONDE* *Hervé BRELAUD* *Bernard LIATARD*

** Contacts and Mechanical Systems*

Acknowledgements

As this research project results from a rich collaboration between the different aforementioned industrial and academic partners, I would like to express my profound gratitude to all the aforementioned directors and heads of division of each entity for giving me the opportunity to lead such an interesting project in two internationally reputed laboratories, LaMCoS and MATEIS, with the full support of the bearing manufacturer NTN-SNR. I also would like to acknowledge and sincerely thank all participants that have steered and contributed to this research project.

Members of the jury

- Pr. Michel Fillon (for accepting to be president of the jury);
- Pr. Gerhard Poll and Pr. Jorge Seabra (for reviewing thoroughly this thesis and for all the interesting discussion we have had on the topic);
- Pr. Motohiro Kaneta (for his interest in the presented work, for his advice and for accepting to be member of the jury);
- Pr. Fabrice Ville and Pr. Xavier Kleber (for their scientific and human incommensurable and generous support as PhD supervisors as well as for the autonomy and opportunities they have trustfully given me).
- Bernard Liatard (for his constant support to this research project at NTN-SNR as well as for all the opportunities he has given me);

LaMCoS and MATEIS

- Pr. Beneybka Bou-Saïd (for all the opportunities suggesting me to go on with a PhD);
- Jérôme Cavoret (for all the measurements and discussions on many various topics);
- Vincent Baudin (for all the help on the Twin-Disc Machine);
- Dr. Aurélien Saulot (for the access to the LaMCoS SEM);
- Dr. Claude Duret (for the hydrogen charging protocol and chemistry teaching);
- Sophie De Oliveira (for all the support regarding conferences and trips to Annecy);
- All PhD students and co-workers for all their help, for all the great time spent together, for all the extras after work and smiles: Pierre R., Marion L., Mathieu C., Jérôme D., Charlotte M., Guillaume C., Jérôme R., Rudy C., Nina S., Vincent S., Jean-David W., Nicolas W., Marine M., Davide T., Jacopo B, Sandrine L., Jean-Philippe N., Serge P., Komla K., Eymard K., Grégoire I., etc.

NTN-SNR

- Aurélien Arnaudon (for the supervision and help during the first half of the project);
- Cédric Burnet (for the supervision and help during the second half of the project);
- Dr. Daniel Girodin (for his expertise, his advice and all the interesting discussions);
- Frédéric Gelloz (for the openings on the wind turbine market)
- Christine Sidoroff (for all the help on metallographic and material aspects)
- Renaud Moreau (for Sharclab® and all the extras);
- Elodie Lefort (for all the interesting topics we've discussed together);

– Jean-Marc Favre (for his expertise on bearing failures);
– Audrey Bornes (for chemical analyses on lubricants)
– Frederic Chappeluz and Gilles Saccani (for the help on NTN-SNR test rigs)

And finally, thank you, reader, for the time spent reading, discussing, contesting and or continuing this study; or in other words, thank you for making this thesis lively and worth to be written.

To Pépère,

To my friends, you all know who you are,

To my family, Maman, Papa, Nicolas and Thomas,

And to my beloved wife Florence.

Abstract

Tribological analysis of White Etching Crack (WEC) failures in Rolling Element Bearings

Despite constant expansion and engineering progress, wind turbines still present unexpected failures of heavy duty mechanical components drastically affecting the cost of energy. Among the most prevalent tribological failures in wind turbine rolling element bearings, a peculiar rolling contact fatigue mode has been associated to broad subsurface three-dimensional branching crack networks bordered by white etching microstructure, and thus named White Etching Cracks (WEC).

Compared to conventional microstructural alterations, WECs tend to develop at moderate loads and cycles eventually leading to premature failures that remain unpredictable using fatigue life estimations. Far from being generic to specific manufacturers, WECs occur in various industrial applications, for various bearing types, components, lubricants, steels grades and heat treatments. As WEC occurrences present no common evident denominator, they remain delicate to reproduce on laboratory test rigs without prior artificial hydrogen charging, so that no consensus on WEC formation mechanisms have been confirmed yet.

In this study, a thorough tribological analysis of WEC formation mechanisms has been led. Expertise protocols have been established to best reveal and observe WECs that commonly develop at unconventional locations versus the contact area. First analysis of WEC reproductions on standard rolling element bearings either hydrogen precharged or kept neutral have signified that artificial hydrogen charging, commonly employed to apprehend the failure mode, results in similar WEC morphologies but tends to alter WEC tribological initiation.

In consequence, WEC reproductions in remarkably different configurations but without hydrogen charging have been compared in order to propose a better understanding of WEC surface-affected formation mechanisms: first, initiation via tribochemical hydrogen permeation at nascent steel surfaces formed either directly at the raceway or at surface microcracks flanks and second, propagation by local hydrogen embrittlement at crack tips function of the stress state.

An extensive root cause analysis have then been led suggesting that WEC may be associated to various combinations of macroscopic operating conditions that often interact and come down to similar tribological parameters including high sliding energy thresholds, specific lubricant formulations and tribochemical drivers such as water contamination and/or electrical potentials. Further investigations on a minimalist twin-disc fatigue tribometer have provided additional evidence that WEC influent drivers are non-self-sufficient, supporting that WEC formation mechanisms rely on a subtle equilibrium between tribo-material, tribo-mechanical and tribo-chemical drivers that all should be mastered to design efficient and durable countermeasures.

Keywords: Wind turbines, Rolling Element Bearings, Rolling Contact Fatigue, White Etching Cracks, Tribochemical drivers, Root cause analysis, Hydrogen embrittlement, Twin-Disc Machine

Résumé

Analyse tribologique des défaillances de roulements par fatigue de contact de type White Etching Cracks (WEC)

Malgré les innovations technologiques et une expansion fulgurante, le marché de l'énergie éolienne reste sujet à des défaillances prématurées de composants mécaniques imposants, ayant alors des conséquences considérables sur le coût de l'énergie. Parmi les défaillances tribologiques majeures au sein des roulements d'éoliennes, un mode de fatigue de contact atypique se caractérise par de vastes réseaux de fissures ramifiées avec des phases microstructurales adjacentes d'apparence blanche à l'origine de la dénomination White Etching Cracks (WEC).

Contrairement à la fatigue de contact classique, les WEC apparaissent pour un nombre de cycles et des charges relativement faibles, menant à une défaillance du composant imprévisible selon les modèles de durée de vie actuels. Les WEC ont été observés chez tous les roulementiers, dans diverses applications industrielles et pour différents types de roulements, éléments, lubrifiants, aciers et traitements thermiques. Ce manque de dénominateur commun rend les WEC difficilement reproductibles sur bancs d'essais sans avoir recours au chargement artificiel en hydrogène de l'acier. Ainsi, pour le moment, la formation des WEC ne fait pas l'objet d'un consensus.

Une analyse approfondie des reproductions de WEC a alors été menée afin d'en comprendre les mécanismes tribologiques. Des protocoles expérimentaux ont été établis pour révéler les WEC, souvent situés à des positions inhabituelles par rapport au contact. Leur reproduction sur des roulements standards, chargés ou non en hydrogène, a permis de démontrer que le chargement artificiel en hydrogène, jusque-là couramment employé pour étudier la défaillance, reproduit des faciès identiques mais semble modifier l'initiation des WEC.

Par conséquent, des reproductions de WEC sans chargement en hydrogène et dans des configurations différentes ont été comparées afin d'appréhender les phénomènes tribologiques à l'origine des WEC. Les résultats suggèrent que l'initiation est principalement déclenchée par des phénomènes de surfaces avec l'absorption tribochimique d'hydrogène au niveau des surfaces métalliques fraîches sur la piste de roulement ou au niveau des flancs de microfissures superficielles. La propagation est ensuite assistée chimiquement par l'hydrogène concentré en pointe de fissure.

Un arbre des causes étendu construit progressivement révèle que les WEC peuvent être associées à de multiples combinaisons de conditions opératoires qui semblent cependant conduire à des paramètres tribologiques similaires à l'échelle du contact avec, notamment, de fortes cinématiques de glissement, des formulations de lubrifiants spécifiques et des paramètres tribochimiques catalyseurs comme la présence d'eau et/ou d'électricité. Une vaste campagne d'essai a alors été conduite sur un tribomètre bi-disques afin de simuler la fatigue de contact. Les résultats confirment que les facteurs influents identifiés ne sont pas pour autant auto-suffisants. La formation des WEC repose sur un équilibre instable entre aspects matériaux, mécaniques et tribochimiques, à maitriser pour concevoir des solutions industrielles efficaces et durables.

Mots clé: Eolienne, Roulements, Fatigue de contact, White Etching Cracks, Analyse de défaillance, Tribochimie, Fragilisation par hydrogène, Machine Bi-Disques

Table of content

List of figures

List of tables

Notations

General

μ	Global friction coefficient, μ=T/N	[.]
μ_x	Local friction coefficient in the OD, $\mu_x=\tau_{xy}/\sigma_z$	[.]
a	Minor semi-axis of the contact ellipse	[m]
b	Major semi-axis of the contact ellipse	[m]
D	Diameter	[m]
D_m	Pitch diameter, $D_m \approx 1/2$(bore diameter + outer diameter)	[m]
E	Material elastic Young's modulus	[Pa]
E*	Material equivalent Young's modulus	[Pa]
F	Osculation, $f_{ir}=r_{ir}/D_b$	[.]
F_a	Axial load of the bearing	[N]
F_r	Radial load of the bearing	[N]
G*	Material parameter *(Appendix A. Contact theory)*	[.]
h	Asperity heights	[m]
H*	Dimensionless film thickness *(Appendix A. Contact theory)*	[.]
H_1	Maximum Hertzian pressure with no plastic deformation	[MPa]
h_c	Central film thickness	[m]
k	Ellipse ratio, k=b/a *(Appendix A. Contact theory)*	[.]
C	Basic dynamic capacity of a REB	[N]
l	Line contact length	[m]
L_{10}	Expected life of 90% of similar bearings under similar conditions	[.]
n	Rotational speed	[min^{-1}]
N	Normal contact load	[N]
N_c	Number of cycles	[.]
P	Local contact pressure along the major contact axis	[Pa]
P_H	Maximum Hertzian pressure *(Appendix A. Contact theory)*	[Pa]
r	Radius of curvature of a raceway	[m]
Q	Equivalent REB load	[N]
R	Radius	[m]
R*	Equivalent radius of curvature *(section 1.2.1.1)*	[m]
R'	Relative radius of curvature *(section 1.2.1.1)*	[m]
R_a	Arithmetic average of the roughness profile	[m]
R_q	Root mean square roughness	[m]
SRR	Slide to roll ratio: SRR=($\Delta U/U_r$)	[.]
T	Tangential contact load	[N]
U	Linear velocity of the components at contact	[$m.s^{-1}$]
U*	Speed parameter *(Appendix A. Contact theory)*	[.]
U_r	Lubricant entrainment speed or Rolling velocity, $U_r=(U_1+U_2)/2$	[$m.s^{-1}$]
V	Linear velocity of the components	[$m.s^{-1}$]
W*	Load parameter *(Appendix A. Contact theory)*	[.]
wt.%	Percentage in weight	[.]
wt.ppm	Part per million in weight	[.]

z	Depth below he contact surface	[m]
α	Angle of contact	[°]
α*	Piezoviscosity coefficient	[Pa^{-1}]
δ	Maximum Hertzian deformation *(Appendix A. Contact theory)*	[m]
ΔU	Sliding velocity at contact	[$m.s^{-1}$]
ε	Strain	[.]
η	Lubricant dynamic viscosity at contact inlet	[$Pa.s^{-1}$]
η_{100}	Lubricant dynamic viscosity at 100°C	[$Pa.s^{-1}$]
η_{40}	Lubricant dynamic viscosity at 40°C	[$Pa.s^{-1}$]
θ	Temperature	[°C]
λ	Film thickness ratio, $\lambda=h_c/(R_{q,1}^2+R_{q,2}^2)^{0.5}$	[.]
μ	Friction coefficient	[.]
ν	Material Poisons coefficient	[.]
ϱ	Lubricant density	[.]
σ	Normal stress	[MPa]
σ_{oct}	Octahedral equivalent stress	[MPa]
$\sigma_{p0.002}$	Tensile micro-yield strength limit	[MPa]
$\sigma_{p0.2}$	Tensile yield strength limit	[MPa]
σ_{VM}	Equivalent Von Mises stress	[MPa]
σ_{VM}	Von Mises equivalent stress	[MPa]
τ	Shear stress	[MPa]
τ_0	Maximum alternative orthogonal shear stress	[MPa]
τ_{max}	Maximum shear stress or Tresca shear stress	[MPa]
$\tau_{p0.002}$	Micro-yield shear strength limit	[MPa]
Ω	Angular velocity, $\Omega=n\pi/30$	[rad/s^{-1}]

Subscripts

1	Relative to body 1 in contact
2	Relative to body 2 in contact
b	Relative to the ball
ir	Relative to the inner ring
max	Maximum
or	Relative to the outer ring
rk	Relative to the roller
x,y,z	x,y,z respective direction

Coordinates

x	Over-rolling direction
z	Subsurface depth direction
y	Corresponding axial direction

Abbreviations

General

3D	Three dimensional
AW	Anti-wear additives
CaS	Calcium Sulfonates
CoE	Cost of Energy
DLC	Diamond Like Coatings
EDTA	Ethylenediaminetetraacetic acid
EDX	Energy dispersive X-ray spectroscopy
EHD	ElastoHydroDynamic
EP	Extreme pressure additives
FM	Friction modifiers
H	Hydrogen
HD	Hydrodynamic
ISO	International Organization for Standardization
LOM	Light Optical Microscopy
NDT	Non Destructive Technique
O&M	Operations and Maintenance
OD	Over-rolling direction
PAG	Polyalkylene glycol oil
PAO	Polyalphaolefin synthetic oil
SEM	Scanning electron microscope (for this study: FEI Quanta 600 coupled with an Oxford Instruments EDX probe controlled by INCA software)
TDA	Thermal Desorption analysis
TDM	Twin-Disc machine
VI	Viscosity index
XRD	X-Ray Diffraction
ZDDP	Zinc Diakyldithiophospohates
ZnDTP	Zinc Dithiophosphates

Bearings

ACBB	Angular contact ball bearing
AISI	American Iron and Steel Institute
CRTB	Cylindrical roller thrust bearing
DER	Dark etching region
DGBB	Deep groove ball bearing
IR	Inner ring
OD	Over-rolling direction
OR	Outer ring
RCF	Rolling contact fatigue
REB	Rolling element bearing
REB	Rolling Element Bearings

SABB	Self-aligning ball bearing
SRB	Spherical roller bearing
TRB	Tapered roller bearing
WEA	White etching area
WEB	White etching bands
WEC	White Etching Cracks
WEL	White etching layer
WSF	White structure flaking

Tribological analysis of White Etching Crack (WEC) failures in Rolling Element Bearing

General introduction

The wind turbine market expansion

Have you ever imagined our world without electricity? No more light, no more transportation means, no more industries, no more computers, reduced food production... Electricity is everywhere and human nature is obviously becoming more and more fundamentally dependent on it. To fulfill a growing reliance of an expanding worldwide population, the electricity generation is constantly increasing (**Figure 1**), especially in developing countries where both modern technologies and populations present the greatest expansion rates. For the moment, the main sources of electricity are non-renewable energies as fossil fuels and nuclear plants.

However, in recent years, the influence of human exponential need of energy has become a major concern considering both environmental issues and the depletion of the earth's non-renewable resources. Therefore, broad renewable energy projects, derived from natural processes that are replenished constantly by nature like sunlight, wind, tides, plant growth and geothermal heat, are developed and are projected to grow strongly in the coming decades, by enjoying a wide public acceptance (**Figure 2**) and significant governmental financial support. In 2011, according from the U.S. Energy Information Administration, about 17% of global final electrical consumption was supplied by renewables resources (**Figure 1**). After biomass and hydroelectricity, wind power presently accounts for 2.5% of the electricity generation. It is, however, currently growing at the greatest rate of all, reaching around 25% annually (**Figure 3** and **Figure 5**).

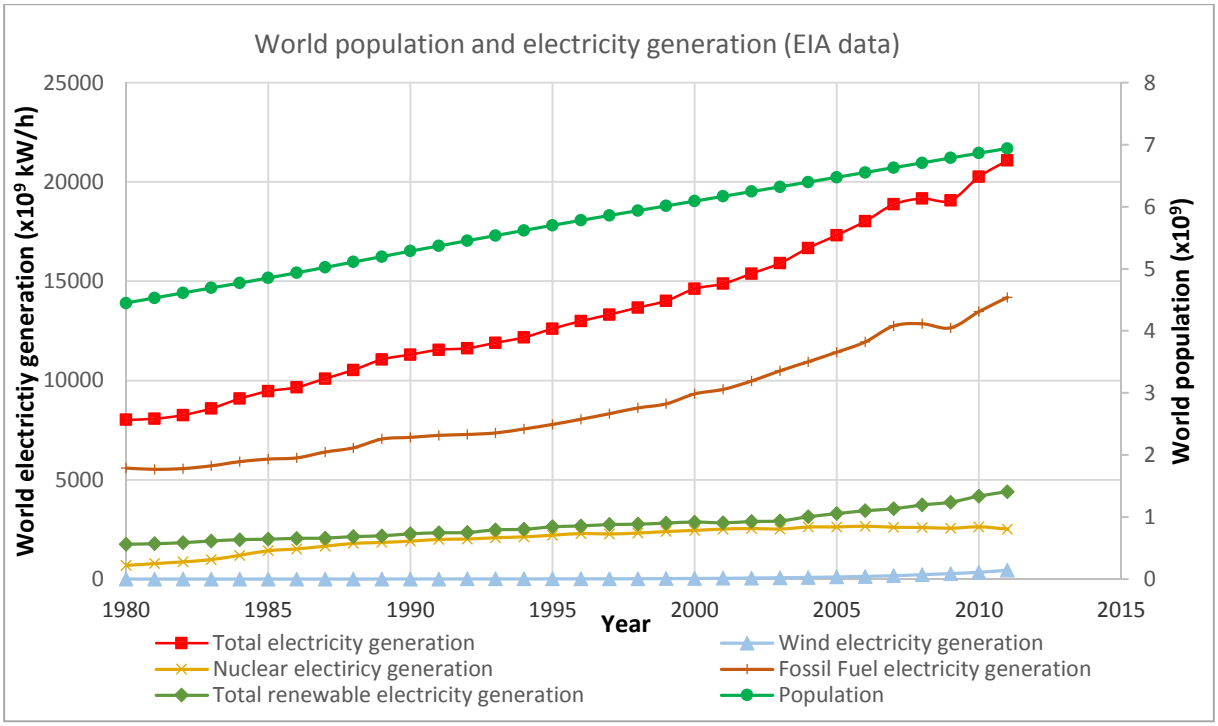

Figure 1: Worldwide population and electricity generation, highlighting the limited but developing wind energy (numerical data from [1]).

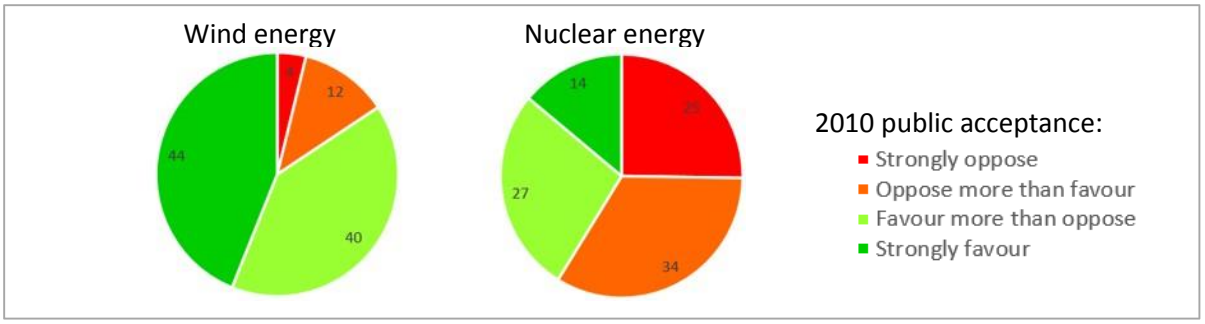

Figure 2: Public acceptance of wind and nuclear energy (poll from 2010 on 6255 adults aged 16-64 equally distributed among the U.S.A, U.K, France, Spain, Italy and Germany [2]).

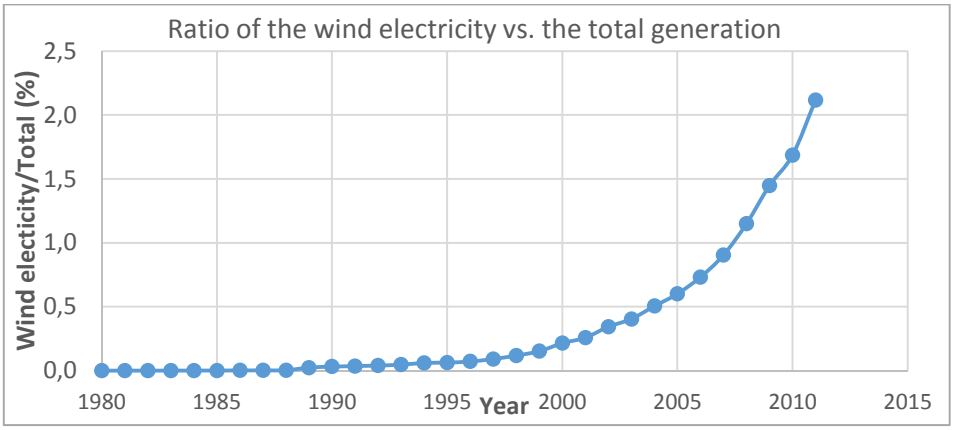

Figure 3: Zoom on the worldwide ratio of wind turbine electricity generation versus total generation from **Figure 1** (numerical data from [1]).

Wind energy is converted in electrical power by means of wind turbines that basically employ the wind kinetic energy continuously acting on blades to rotate a shaft that is itself connected to an AC/DC electrical generator via a multiplicative gearbox (**Figure 4**) to accommodate the main shaft and generator rotational speeds. If some wind turbines rotate along a vertical axis, the most common and developed models are horizontal axis wind turbines composed of three blades connected via a hub to the main shaft and the nacelle at the top of the tower (**Figure 4**). According to Betz' law, only 59% of the total kinetic energy of the air flow can be captured by the rotor and due to different efficiency losses, 75% of this energy finally transformed in electrical power.

Forming a new and worldwide rapidly growing industrial branch, wind turbines have tremendously increased in size and in number of installations in the past decades (**Figure 5** and **Figure 6**), and are now commonly displayed in arrays of 10 to hundreds of turbines, known as wind farms, in order to collect the produced electrical power via an electrical grid. In the past five years, at least approximately 40 GW of wind turbine nominal power has been installed annually leading to a cumulative power of more than 300 GW in 2013 (**Figure 5**). For the moment, the onshore Gansu Wind Farm in China is the biggest wind farm, with near 8GW of installed wind power and a maximum planned of 20GW by 2020, erecting 36 wind turbine every day. As a comparison, common nuclear plants deliver between 0.8 to 2.6 GW of nominal power.

As of today, half of the wind turbines installed have a nominal power between 2 and 3 MW with an increasing share of larger wind turbines of 3 to 7.5 MW. A typical example being currently deployed is Areva Multibrid M5000 5 MW offshore wind turbine that has been prized several times for its "lightweight" design (**Figure 4**). Some specifications are listed below [3]:

- Tripod foundation structures: 45 m high and 710 tons
- Tower: 90 m high and 350 tons
- Rotor diameter 116 m (2009) and 135 m (mid 2014)
- Swept area: 10500 m² and 14300 m² (two times a football field)
- Nacelle and rotor assembly: 349 tons placed at the top of the tower (equipped with a helicopter landing pad)
- Cost: example of Global Tech North Sea Wind Park €800 million contract with AREVA for 80 M5000 (2012)

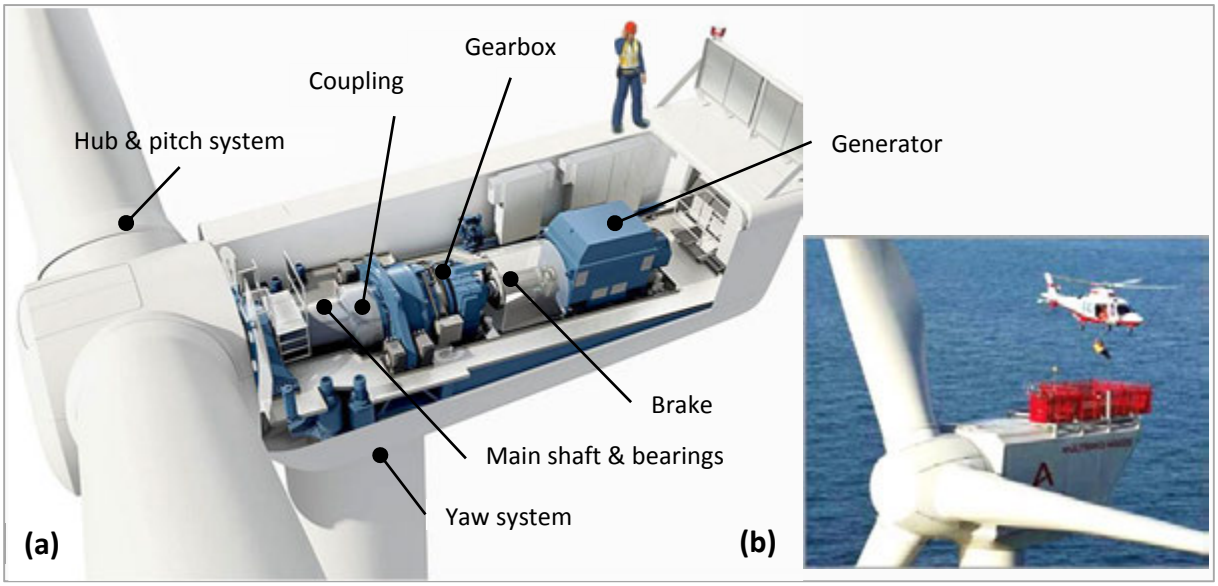

Figure 4: Typical horizontal axis MW wind turbine structure at the top of the tower (courtesy of ZF transmission, www.zf.com); (b) AREVA M5000 5 MW wind turbine maintenance [3].

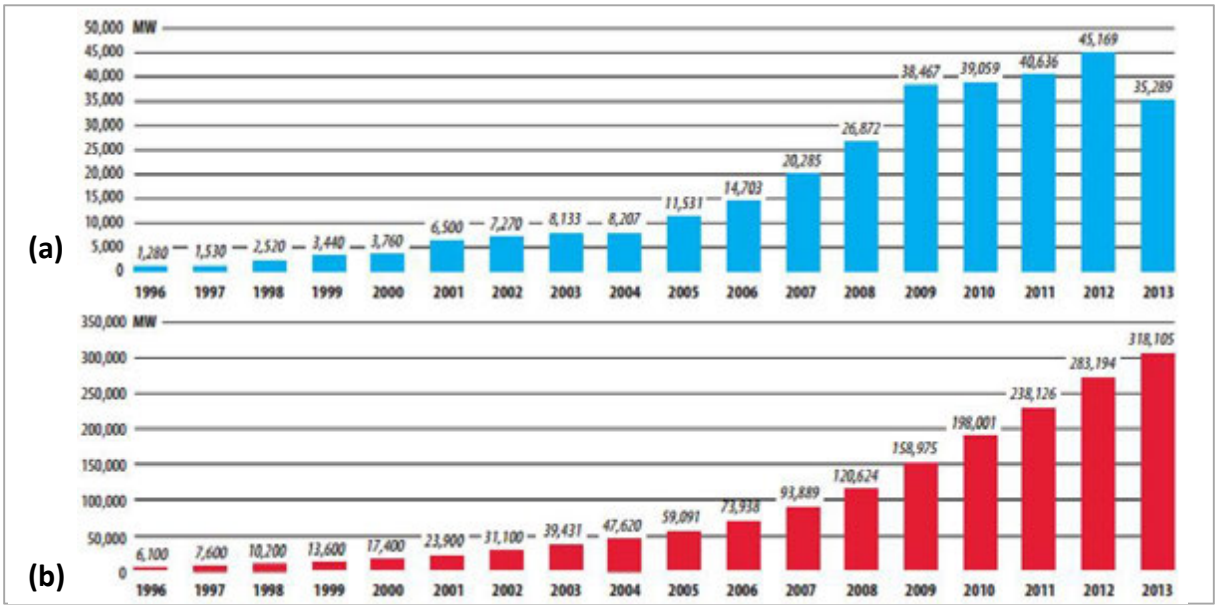

Figure 5: Wind turbine (a) annual and (b) cumulative worldwide nominal power installed power in MW [4].

One main limitation in wind turbine dimensions is that blade tip velocities have to be kept below the velocity of sound in air. Hence, the main-shaft rotational speeds are limited to

approximately 10 to 35 rpm depending on the rotor diameter and, high quality multi-stage gearboxes of important ratio are most often required to multiply the main shaft rotational speed in order to comply with the nominal rotational speed of the generator being either 1500 rpm (Europe) or 1800 rpm (U.S.A) function of the local electrical grid 50 or 60 Hz respective configuration [5].

Considering that firstly, 45 GW has been installed in 2012 deploying mainly 2 MW wind turbines [5] with a 90 m rotor diameter and that, secondly, the spacing between two wind turbines is commonly 10 times the rotor diameter (even though recent results recommend 15 times for larger turbines and optimal economic outcomes), it can be estimated that over a year 22500 wind turbines have been deployed mobilizing an approximate area of 100000 km² worldwide, representing a fifth of France's metropolitan area (550000 km²)! This, in addition to the potential noise and visual disturbances wind turbines can induce, clearly supports massive development of offshore wind turbine technology [5].

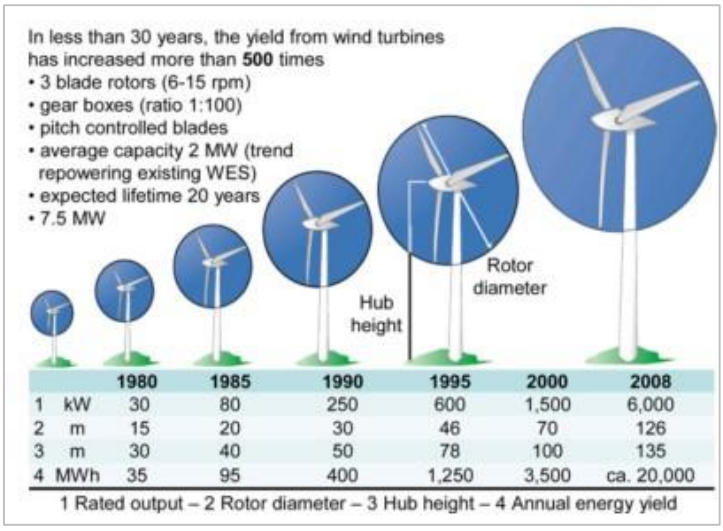

		1980	1985	1990	1995	2000	2008
1	kW	30	80	250	600	1,500	6,000
2	m	15	20	30	46	70	126
3	m	30	40	50	78	100	135
4	MWh	35	95	400	1,250	3,500	ca. 20,000

1 Rated output – 2 Rotor diameter – 3 Hub height – 4 Annual energy yield

Figure 6: Summary of the wind turbines' expansion in the past decades [5].

The wind turbine cost of energy affected by unexpected failures

Contrasting to this prospering development, wind turbine industry faces some major challenges to reduce the Cost of Energy (CoE) in order to manage competitiveness with non-renewable energy sources. Apparently more significant than pure efficiency, the reliability and Operation and Maintenance (O&M) costs due to unscheduled failures have a direct impact on the CoE, notably for offshore wind farms. O&M costs represent up to 20% of the CoE in the U.S.A. [6]. Even though main mechanical components including the rotor blades, the generator and the gearbox present a relatively low failure rate compared to electrical components, they represent up to 75% (**Figure 7**) [5] of the O&M costs due to expensive spare components, consequential maintenance operations and excessive downtime, especially for offshore wind turbines. Indeed replacing an unexpected gearbox or generator failure in an offshore turbine require mobilizing and routing rapidly specialized vessels and cranes and then waiting for suitable weather for intervention.

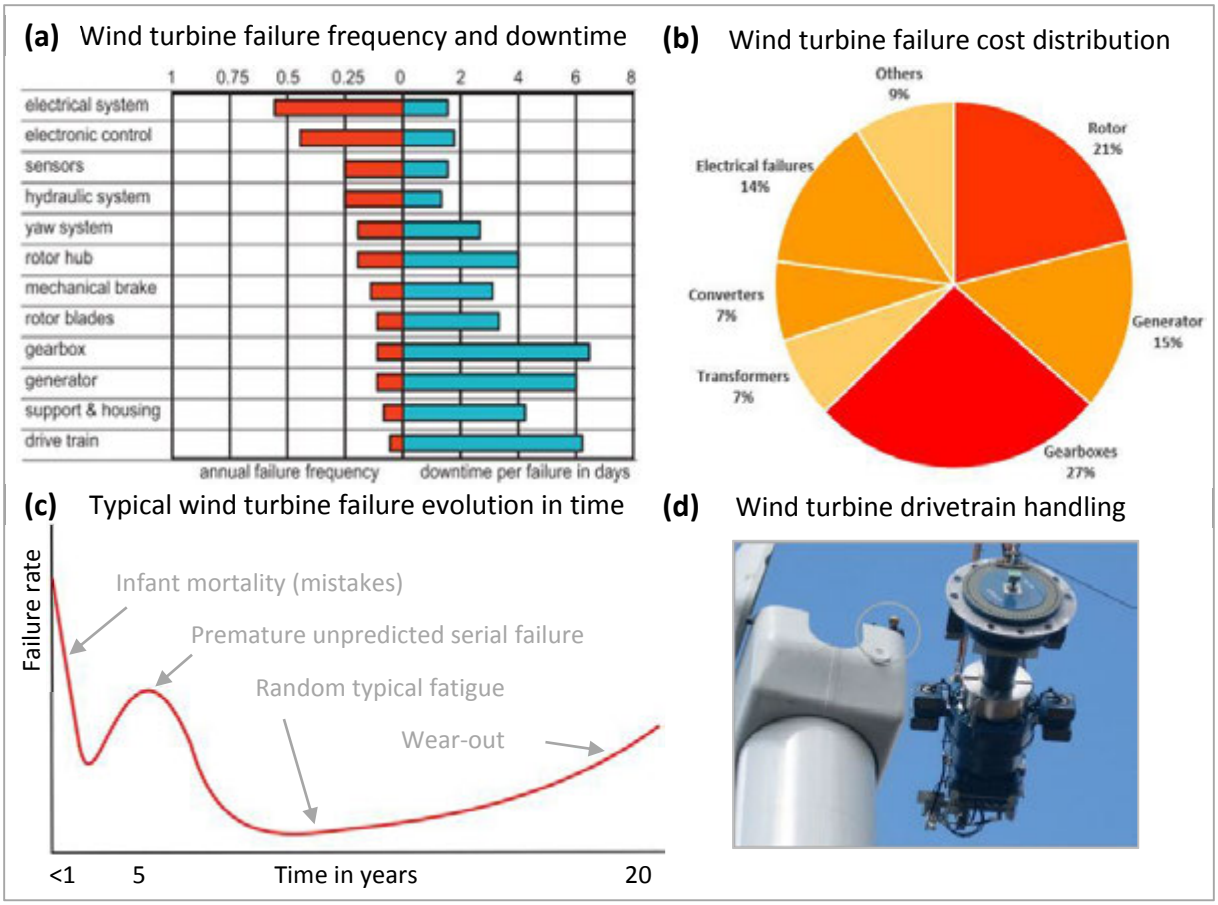

Figure 7: (a) (b) Wind turbine failures distribution in 2009 and the impact on the O&M costs [5]; (c) typical wind turbine failure rate evolution in time with premature failures; (d) wind turbine drivetrain handling.

Despite maintenance and engineering efforts following the international standard IEC 61400 guidelines, only few wind turbines reach the desired lifetime of 20 years without one or more major mechanical component failures (**Figure 7**(c)) [7,8]. One of the main issue remains the gearbox that has to evolve with increasing nominal powers and that, even though designed to operate for 20 years under International Standard Office ISO 81400-4:2005, is actually failing prematurely in the five first years of operation representing between 27% [5] and 38% [8] of the O&M costs (**Figure 7** (a)(b)). Those massive gearboxes (**Figure 8**) often have to comply with thrust loads equivalent to a GE90 aircraft engine and with an estimate of 15000 overloads per year [9]. They weigh about 10 tons per MW and have often more than 15 rolling element bearings (REB).

One explanation for unexpected failures could be that, unlike other energy generating machines mainly operating at a nominal power, wind turbines have operate under a spectrum of power levels and transient loadings that must be absorbed within the gearbox due to ever fluctuating wind gusts and to main shaft cyclic bending relative to the 3 blade design [10]. This causes severe misalignments and transient loadings in gearboxes that also have to keep up with a downsizing trend to reduce O&M costs and inertial power losses.

Within the gearbox, thanks to adapted lubricant formulation and enhanced gear microgeometry, gear failures tend to disappear in newer turbines therefore now revealing drastic bearing failures [7]. It has been mentioned that 80% of the gearbox failures are related to REB [11] and that 15% of the gearbox REB fail before 5 years of service [12]. It has been also specified that

wind turbine REB failures seem to be generic and widespread, not being limited to a bearing design, manufacturer or gearbox model [7,8,13].

Moreover, wind turbine bearing failures are not limited to the gearbox and affect also the main shaft support REB, the generator REB, and the pitch and yaw systems REB [5,7,10]. The large majority of REB failures are tribological failures, i.e. related to contacts between components in relative motion involving friction, wear and lubrication. Pitch and yaw bearing failures have mainly been attributed to small oscillatory movements around their nominal position chasing the lubricant out of the contact and leading to false brinelling (section 1.3).

For main shaft, generator and gearbox bearings, the main failures modes are smearing and premature rolling contact fatigue induced cracking [6,7] (section 1.3). While smearing failures are currently being mastered by changing the bearing design to limit slippage and unsufficient lubrication [7], the secondly mentioned failure corresponds to an unconventional fatigue failure mode called White Etching Cracks (WEC) (**Figure 8**) that is often qualified as the least understood failure mode experienced in wind turbines and as the most critical since it remains unpredictable using bearing models and condition monitoring. While not unique to the wind industry, it is found to be much more prevalent than in other applications, namely in terms of frequency and impact on O&M costs.

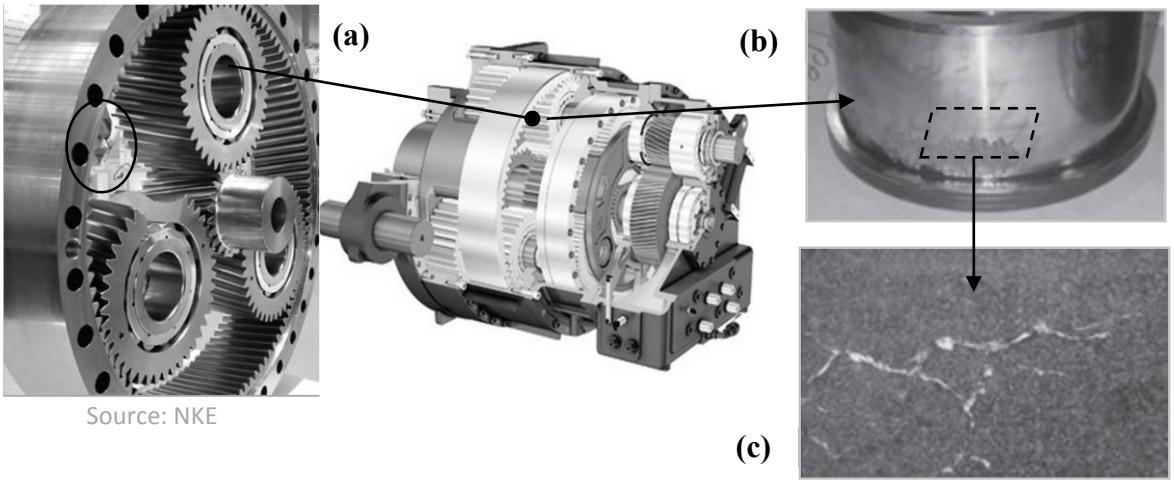

Figure 8: (a) Multi-MW wind turbine gearbox layout and size compared to a human head; (b) Example of wind turbine REB fatigue failure [7] associated to (c) the formation of White Etching Cracks (WEC) [7].

Aims and outline of the present work

To take benefits the wind industry market expansion, bearing manufacturers have to propose robust and durable bearing designs. In order to do so, a thorough tribological analysis of the failure modes has to be led in order to propose efficient and durable countermeasures, notably concerning the unconventional and costly WEC related failures. This corresponds to the context of the research work presented in this thesis entitled *Tribological analysis of the White Etching Crack failures in rolling element bearings*. This title has been chosen in order to enlighten that the present study does not detail specific investigations on the material and physical microstructural understanding of the WEC formation mechanisms, as it has been proposed recently by others [14–16], but details *experimental investigations* that have been led on the *full tribological system involved in WEC formation*

mechanisms comprising mechanical, material, chemical and thermal aspects acting both at macroscopic and tribological scales.

In this context, the **main objectives** of the present work are specified in the graph (**Figure 9**):

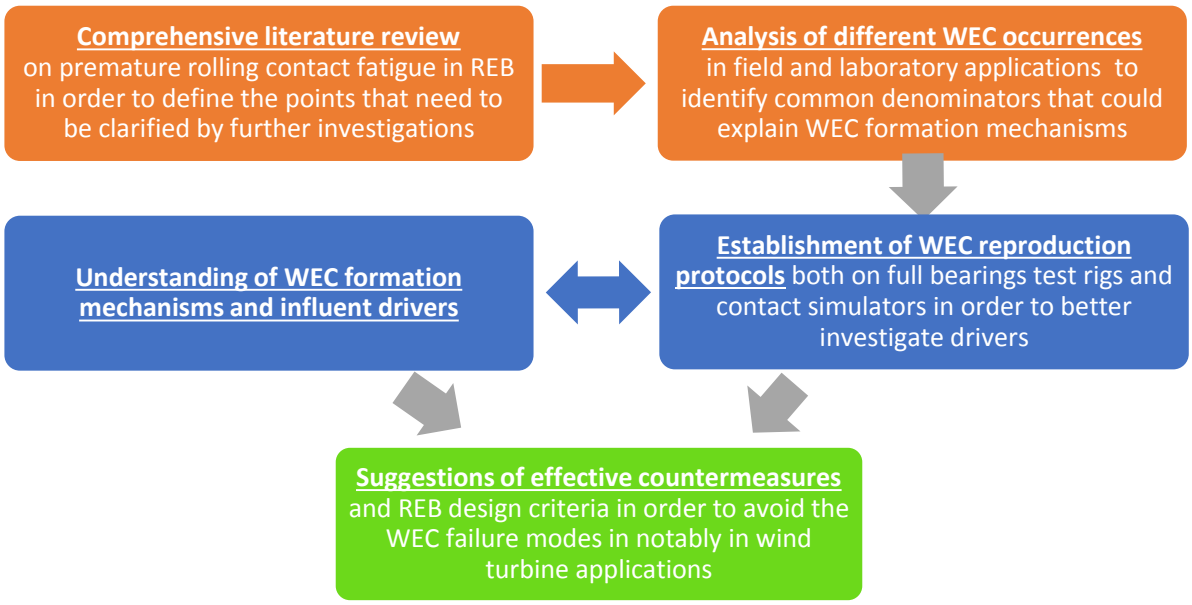

Figure 9: Main objective layout of the project.

In order to best relate the **experimental investigations and findings**, the present thesis will follow the following outline:

Chapter 1 first overviews the fundamentals in bearing technology and tribology and then details the relevant rolling contact fatigue failure modes, making regular focuses on the wind turbine application. Finally the WEC failure mode is defined characterized from a tribological point of view insisting on the fact it differs significantly from previously described failures modes.

Chapter 2 presents the overall methodology and main experimental procedures used in this study for WEC tribological analysis, with first, full bearing RCF testing on a NTN-SNR standard ball bearing test rig, second, the tribological transposition on the LaMCoS Twin-Disc machine, and finally the different characterization techniques and methods revealing WEC networks.

Chapter 3 provides results of WEC reproduction on neutral and hydrogen precharged specimens in order to demonstrate that first WEC networks appear in specific locations and then that if WEC most certainly propagate by local hydrogen embrittlement, artificial hydrogen charging seems to modify WEC initiation mechanisms, making this method irrelevant to design effective countermeasures.

Chapter 4 first consists of a thorough tribological comparison of WEC reproduction on two radically different bearing configurations in order to identify the respective main tribological parameters influencing WEC formation. Then, WEC surface affected initiation and tribochemical propagation mechanisms will be proposed suggesting that they could slightly differ depending on the application even though they come down to similar phenomena at tribological scales.

Chapter 5 finally focuses on an exhaustive characterization of the various WEC formation influent drivers from the macroscopic scale down to the tribological scale based on WEC field occurrences and previously described test results. The identified drivers will be transposed one by one on the LaMCoS Twin-Disc Machine and various tests will be conducted in order to qualify their influence on WEC initiation and propagation mechanisms with an enhanced control of the tribological conditions.

Thesis flow chart

As each fore detailed chapter of the thesis do not correspond to each defined objective of the study (**Figure 9**) a thesis flow chart is proposed below (**Figure 10**) and recalled at the beginning of each chapter highlighting the addressed objectives, the concerned steps of WEC tribological analysis and the employed test rigs and characterization techniques. As schemed (**Figure 10**), the different objectives can hardly be treated independently one after the other since they often interact and increment each other, e.g. WEC reproduction rely on WEC understanding and vice versa. This is why, for sake of clarity, instead of corresponding to each objective, the chapters of this thesis mainly correspond to the three main contributions of this study proposing novel elements to the WEC tribological analysis. In addition, as this thesis relates a progressive reasoning in understanding WEC formation mechanisms, the main steps, facts and conjectures will be highlighted throughout the text by light grey individual wrap-ups.

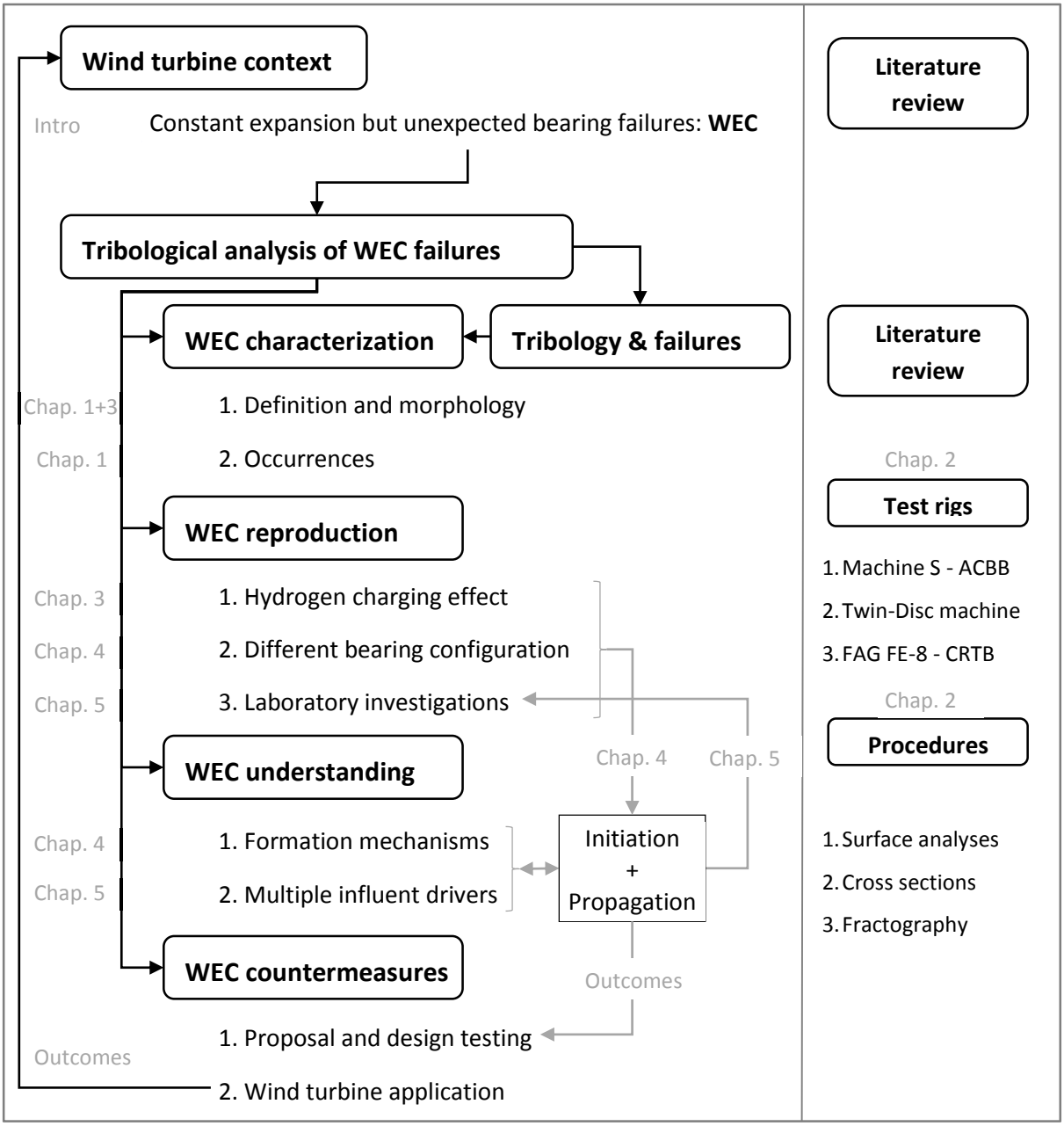

Figure 10: General thesis flow chart.

Tribological analysis of White Etching Crack (WEC) failures in Rolling Element Bearing

Chapter 1:

White Etching Cracks characterization as fatigue in rolling element bearings

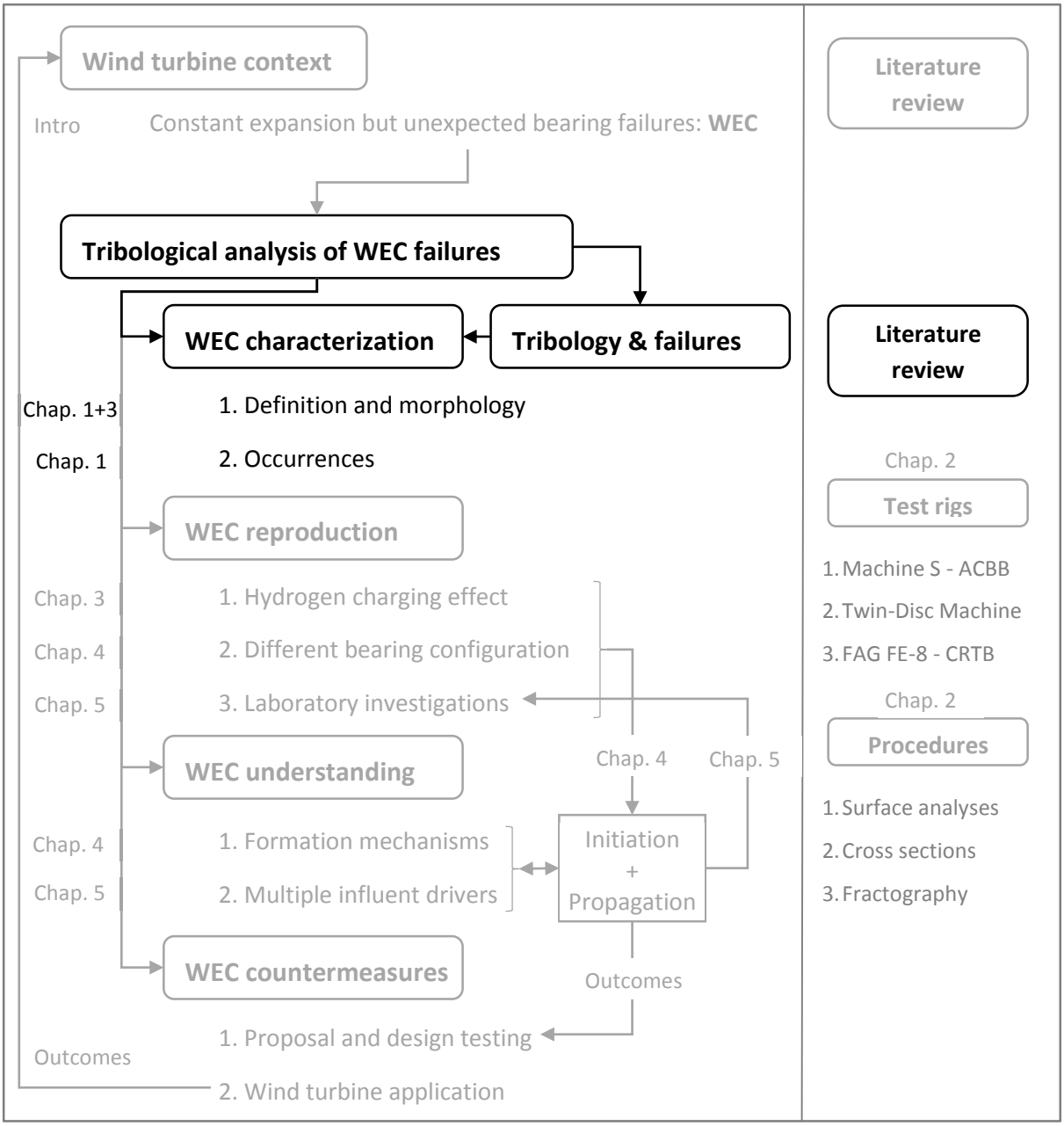

The first chapter of this work introduces the reader to the fundamentals of bearing technology and to the White Etching Crack phenomena. Rolling element bearing designs, tribology, and relevant failure modes relevant are first described through a literature review and engineering aspects. At the end of each part, a brief focus is made on the wind turbine bearing designs, operating conditions and failures. As a closure, White Etching Cracks are introduced and characterized as an unconventional rolling contact fatigue failure mode to provide the reader with the overall background of the following chapters.

1.1 Rolling element bearing fundamentals

1.1.1 What are rolling element bearings?

1.1.1.1 Definition and functions

The Oxford English Dictionary defines a bearing as "part of a machine that allows one part to rotate or move in contact with another part with as little friction as possible". Additional functions can be added to this definition such as the transmission of loads and the accurate positioning of components in the mechanical system.

A Rolling Element Bearing (REB), often simply called "bearing" as to its tremendous use in worldwide machinery, is a bearing that encloses rolling elements, as ball or rollers, between two concentric rings, allowing the rings to rotate relatively with minimal frictional resistance whilst supporting applied thrust and radial loads (**Fig. 1.1**). This concept may seem simple but the operation of rolling element bearings is very complex due to numerous contacts, high surface and subsurface stresses, transient loadings, complex lubrication regimes, local temperature rises, possible contaminations, etc. Extensive details to this complexity have been and are still the focus of reference work in the domain [17,18]. REB are composed of an inner ring (IR), an outer ring (OR), various number of rolling elements (REs), a cage used to separate the REs and possible seals to avoid lubricant leaks or exterior contamination (**Fig. 1.1**).

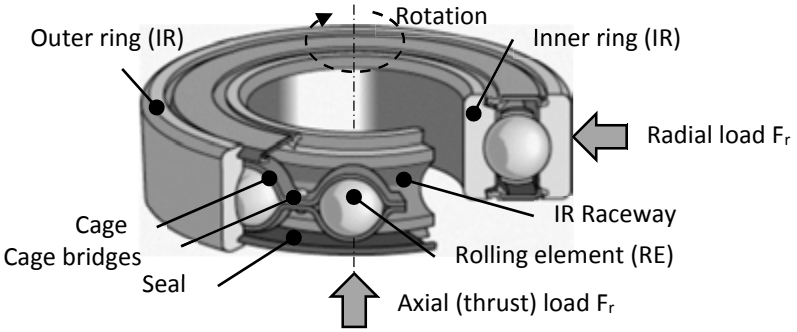

Fig. 1.1: Rolling Element Bearing (REB) typical structure, components and speeds (courtesy of SKF).

1.1.1.2 Bearing types

With centuries of existence serving various industries in wide range of operating conditions, REB designs have evolved into numerous bearing types displaying geometrical characteristics that make them more or less appropriate depending on the application (**Fig. 1.2**). Bearing types and sizes are often selected based on compromises considering [17]:

- Overall bearing arrangements in the mechanical system and possible combinations
- Magnitudes and directions of the applied loads
- Desired rotational speeds
- Desired lifetime based on static and dynamic load capacities
- Available space and acceptable weight
- Mounting and dismounting constraints

- Stiffness, accuracy, internal clearance and misalignment constraints
- Overall environment, lubrication, temperature and possible contamination
- Costs

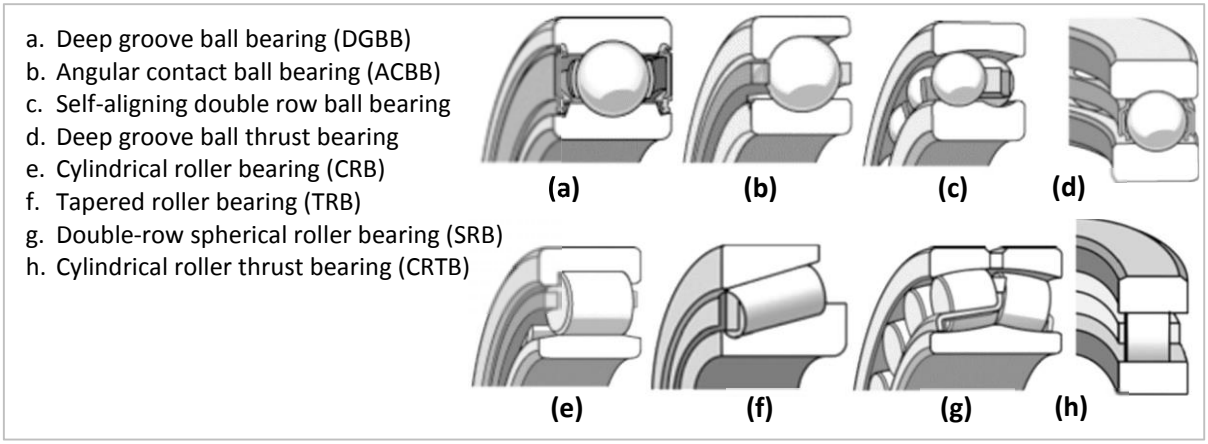

Fig. 1.2: Typical examples of REB types (courtesy of SKF).

1.1.1.3 Bearing hardened steels

Given their designs, REBs have to sustain severe static and cyclic loadings while operating in various environments. Therefore, the vast majority of REB rings and rolling elements are made of steels that have to contend possibly contradictory material properties to achieve high resistance to fatigue and to avoid excessive deformations despite severe loads, the overall within moderate costs (**Fig. 1.3**). If some specific REBs can totally or partially be made of ceramics such as silicon nitride, to achieve high performances at lowered weight, in 2001, it was estimated that 300 tons of steel per day was produced for REB manufacturing. In this section, the most common bearing steels and properties will be detailed as they are mentioned in following chapters. Further details regarding manufacturing techniques employed to reach high quality standards and specific steels can be found in [17,19,20].

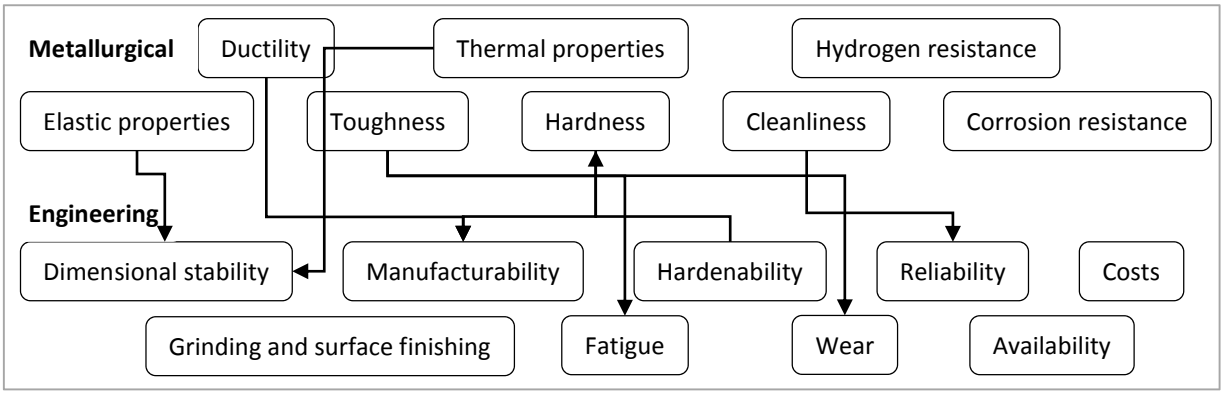

Fig. 1.3: Typical metallurgical and engineering properties required for bearing steels and examples of interdependencies

a. Through-hardened bearing steels

The largest tonnage of bearing steels produced corresponds to through-hardened bearing steels, namely high carbon chromium steel like 100Cr6 (AISI 52100, JIS-SUJ2) due to its relative low cost and high hardenability [17]. Through-hardening steels are classified as hypereutectoid

steels containing more than 0.85 wt.% of carbon and less than 5 wt.% of total alloying elements. They are most frequently made martensitic by quenching in oil or salt after austenization and then tempered in order to balance conflicting properties that can arise [19]. They can also be made bainitic for lower austenite content and greater dimensional stability [21]. In the end, the microstructure is very complex. It can contain martensite, retained austenite, ferrite, cementite, and undissolved carbides from austenitization in different proportions [17,22]. Even for steels of the same grade, the microstructure can differ depending on the manufacturing processes and heat treatments [23,24]. In this study high quality NTN-SNR 100Cr6 steel has been used with two different available heat treatments referenced D2 and S9 (**Table 1-1**) [25]. Typical hardness of through-hardened bearing steels are comprised between 750 (60) and 800 (63) Hv (HRC). For large size REBs, additional silicon, manganese and molybdenum are incorporated in the alloys to enhance hardenability when the ring sections are thicker. **Table 1-1** provides the chemical composition of through hardened-bearing steels commonly used.

Table 1-1 : Typical through hardened bearing steel chemical composition (wt.%) limits (ISO 683-17:1999 standard on bearing steels) and precise chemical composition of the 100Cr6 steel used in this study.

Ref.	C	Cr	Mn	Si	Ni	S	P	Mo
100Cr6	0.93-1.05	1.35-1.60	0.25-0.45	0.15-0.35	-	<0.015	<0.025	<0.10
100CrMo7-3	0.93-1.05	1.65-1.95	0.60-0.80	0.15-0.35	-	<0.015	<0.025	0.20-0.35
100Cr6 used for study[1,2]	1.00	1.54	0.32	0.23	0.14	0.009	0.012	0.04

[1] Martensitic: *austenization 10 min at 850°C, quenching in oil at 40°C* [25]
[2] Tempering: D2 (*60 min at 170°C*) - S9 (*120 min at 240°C for a lower retained austenite content*) [25]

b. Case-hardened bearing steels

As REBs grow larger, the steel cannot become martensitic throughout the whole ring section by satisfactory through-hardening processes, even when adding alloy elements. Hence, case-hardened steels are often employed. These steels are classified as hypoeutectoid containing less than 0.85 wt.% of carbon and consequently alloyed with larger amounts of nickel, chromium, molybdenum, vanadium and manganese to increase hardenability (**Table 1-2**).

Table 1-2 : Example of case-hardened bearing steel chemical composition (wt.%) (ISO 683-17:1999).

Ref.	C	Cr	Mn	Si	Ni	S	P	Mo
20NiCrMo7	0.17-0.23	0.35-0.65	0.40-0.70	<0.40	1.60-2.00	<0.015	<0.025	0.20-0.30
16NiCRMo16	0.14-0.18	1.00-1.40	0.25-0.55	<0.40	3.80-4.30	<0.010	<0.025	0.20-0.30
32CrMoV13*	0.29-0.36	2.80-3.30	0.40-0.70	0.10-0.40	-	<0.010	<0.025	4.00-4.50

* *Nitrided* [26]

Additional carbon and/or nitrogen are diffused into the surface during the heat treatment to form hard martensite and reach the required surface properties that of 100Cr6. If they remain more expensive, case-carburized, nitrided and carbo-nitrided rings, for example, combine hard wear-resistant top case and a tougher core than through hardened steels. This toughness relates to the lower carbon content and to the compressive residual stresses induced by the heat treatment [26]. The main point affecting endurance of case-hardened steels is that the case depth has to be

sufficient to go beyond the depths concerned by contact mechanical stresses. In case of surface initiated fatigue, case-hardened or through-hardened REBs show similar limitations.

c. Mechanical properties

Among prevalent material properties, steel mechanical properties are required to design REBs satisfying lifetime estimations and high dimensional stability under severe contact and structural stresses. The elastic limit, also known as yield strength, corresponds to the stress at which the material begins to deform plastically and is commonly assimilated to the 0.2% proof strength $\sigma_{p0.2}$ measured at 0.2% of permanent plastic strain. It corresponds to a limit where all types of dislocations are activated in the matrix.

In recent years, some authors have considered that the first dislocation bond is activated as soon as 0.002% of at plastic strain [27,28]. The stress to reach this strain is commonly called the micro-yield strength limit $\sigma_{p0.002}$ and can be measured by nano-indentation techniques [28]. The corresponding micro-yield shear stress limit $\tau_{p0.002}$ can be used to establish a physical criteria corresponding to an endurance limit in terms of rolling contact fatigue. Indeed, the maximum contact pressure H_1 that does induce not any plastic deformation in the steel matrix can then be computed based on $\tau_{p0.002}$ [27]. However, dislocation movements are highly dependent of the overall stress state and homogeneity of the steel matrix. Therefore, this endurance limit H_1 highly depends on the operating conditions and types of inhomogeneities present in the steel. This is why H_1 has also been considered for the fragile inclusion – steel interface [25,27].

Table 1-3 : 100Cr6 D2 bearing steel mechanical properties at room temperature (data from NTN-SNR also available in [25] and in good agreement with [29]).

Young's modulus (MPa)	Poisson's coefficient	Hardness (Hv)	$\sigma_{p0.2}$ (MPa)	$\sigma_{p0.002}$ (MPa)	H_1 (MPa) steel matrix	H_1 (MPa) inclusions interface
210000	0.29	750-800	1500* 2500**	1350*-1830**[1] 1020* (100°C)	2200 1700 (100°C)	1580 1200 (100°C)

* measured in traction
** measured in compression
[1] data from [27]

d. Steel cleanliness

The contribution of mechanical properties to REB life and failures is considerably affected by the presence of inhomogeneity, such as inclusions, carbides and voids present in the bulk steel. Their incoherent interface with the matrix are preferential sites for crack nucleation. Non-metallic inclusions correspond to inevitable contamination and chemical reactions during steel casting, melting and segregation processes. There are different types of non-metallic inclusions that can vary in size, distribution and orientation depending on the steel manufacturing processes [19,23,30]. The international standard ISO 4967:2013 proposes an assessment method for inclusion cleanliness considering five groups of commonly observed inclusions with their respective morphologies and possible duplex (e.g. B+D for Al_2O_3):

- A: Globular to elongated soft-edged *sulfides* (e.g. manganese and calcium sulfides)
- B: Small sharp-angled *aluminates* (silicate aluminates)
- C: Cubic to rectangular sharp-angled *silicates*

- D: Globular or sharp-angled *oxides* (e.g. aluminate oxide aggregates)
- Ds: Unique circular particle (e.g. chromium and titanium carbides, calcium aluminates)
- Nitrides: often additionally included in cleanliness assessment of carbonitrited steels

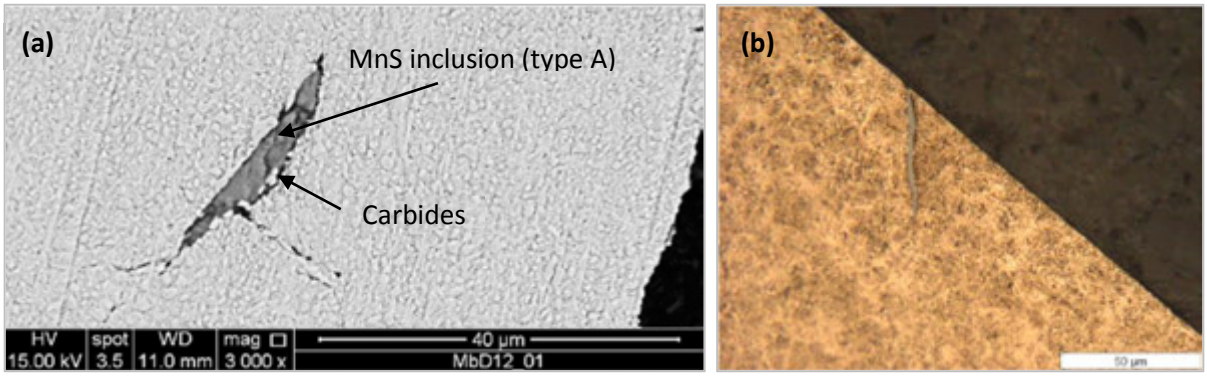

Fig. 1.4: (a) SEM image of a manganese sulfide (MnS) inclusion and (b) optical micrograph of another MnS emerging inclusions both found in a 100Cr6 D2 specimen.

All those inclusions do not have the same effect on the steel resistance to rolling contact fatigue. According to Harris et al. [17], inclusions less than 500 µm in length are considered as micro-inclusions. However, the first rating indexes established by ISO 4967:2013 correspond to inclusions limited to 20 to 40 µm in length depending on the inclusion type. In the past decades, particularly with the vacuum degassing and arc remelting processes, steel cleanliness has been significantly improved. For example, oxygen and hydrogen contents have been lowered to ~10 wt.ppm and ~1-2 wt.ppm respectively [19], below the ISO 683-17:1999 limits. Nowadays even rolling contact fatigue tests have been considered unsufficient for steel quality discrimination due to the fact steels have reached high levels of cleanliness [23]. As steels get cleaner, the inclusion density and distribution appear to be more influential than the size. This point has been addressed by the ASTM E2283-03 standard.

1.1.1.4 Bearing manufacturing process

The three steps manufacturing process of REB ring is briefly presented in **Fig. 1.5** as for example, turning or forging the ring influences microstructural grain flow and inclusion orientations, thus affecting the overall resistance to rolling contact fatigue. The rolling element manufacturing processes are not detailed as they are most often identical from a bearing to another.

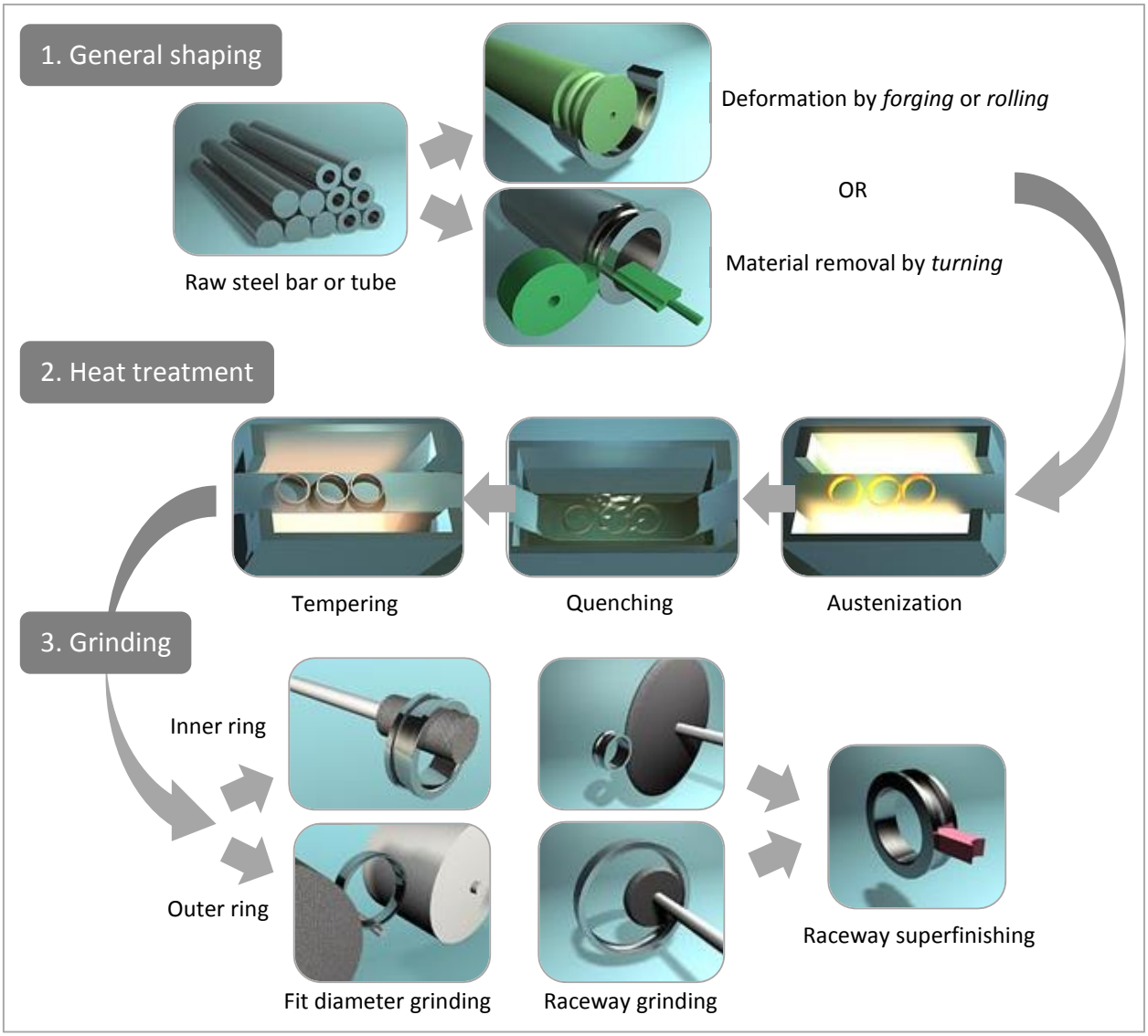

Fig. 1.5: Main steps of the REB ring manufacturing process (courtesy of NTN-SNR).

1.1.2 Wind turbine bearings beyond historical know-hows

As mentioned in the general introduction, wind turbines operate through a number of rotational movements, namely the main rotor as well as the pitch and yaw systems that are all contented by REBs in order to minimize friction losses (**Fig. 1.6**). The REB types and arrangements evolve with the products proposed by bearing manufacturers and depend on the overall drivetrain layout. In **Fig. 1.6** for example, the main shaft is supported by two REBs. Some compact wind turbine designs exist with only one main shaft REB, the second one being directly incorporated in the gearbox.

To keep up with the wind turbine market expansion, bearing manufacturers have had to achieve for the first time mass production of meter-scale bearings guarantying a 20 year lifetime. Indeed, while production of large size bearing requires dedicated tools and transportation means, heat treating, grinding, finishing, fitting and aligning meter-scale REBs with a precision of 10 µm is far from evident. In addition specific steels have to be used to ensure satisfying material properties. It is indeed extremely complex to obtain low and equally distributed fitting hoop

stresses and/or homogenous surface treatments since induction heating, for example, requires specific set-ups for such large perimeters [31]. In addition, the tribological scale-up issue is also non-negligible as REB designs and life models are mainly based on comparatively small automotive bearings. Serial testing as it has been done for automotive REBs is indeed unconceivable for large-size REBs. Hence, most of the feedback comes directly from the field and condition monitoring.

As bearing manufacturers are not part of wind turbine operating staff, they most often do not have full information regarding the complex loadings REBs have to endure, notably with unpredictable transient loadings. One of the main conclusion of the wind turbine business meeting held at the 2014 STLE 69th Annual Meeting and Exhibition [32], is that a better collaboration between bearing manufacturers, gearbox manufacturers, wind turbine manufacturers and wind turbines exploiters is required to help design REBs that can survive the intended 20 year lifetime. Therefore, collaborative projects as the Wind Turbine Seminar and Gearbox Reliability Collaborative organized by the National Renewable Energy Lab (NREL) in the U.S.A. are starting to gather more and more data on the topic [13,33,34].

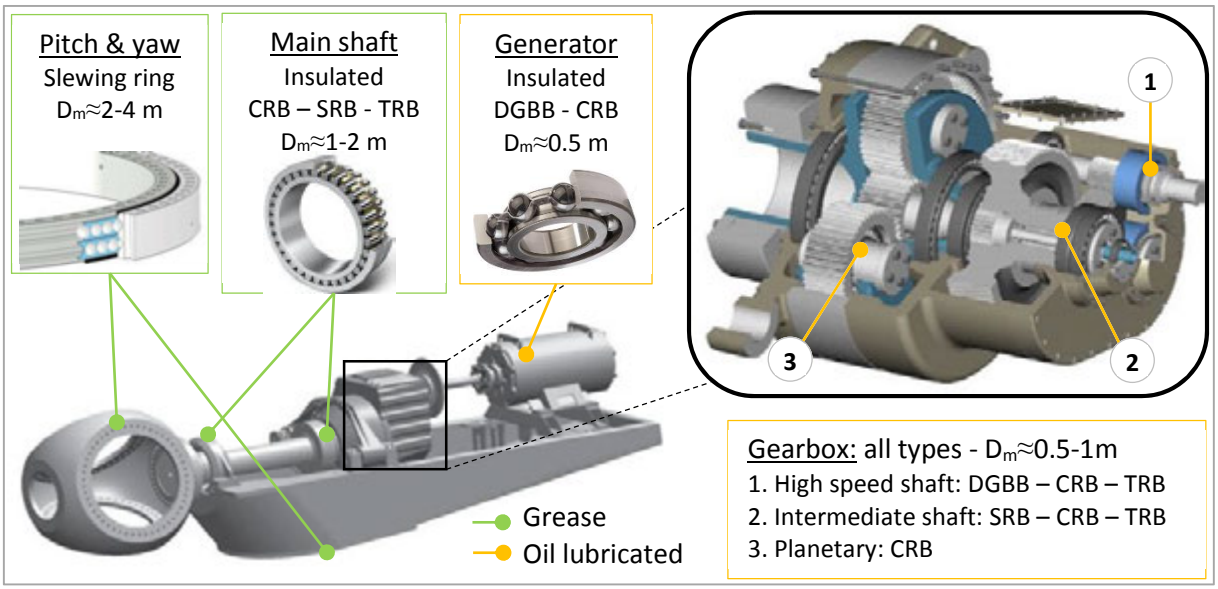

Fig. 1.6: Overview of REB arrangements in a typical MW wind turbine.

1.2 Rolling element bearing tribology

The word *tribology* comes from the Greek words τρβειν (friction) and λογος (study). The Oxford English Dictionary defines tribology as the study of *friction*, *wear*, and *lubrication* or in other words the science of interacting surfaces in relative motion. As suggested by Tichy [35], "*Tri*-bology" could also be a reminder of the fundamental tripod to tribology, friction, wear and lubrication. Tribology is everywhere in everyday life, form the bone cartilages to the satellite deployment. It therefore corresponds to the complex encounters of contact mechanics, fluid mechanics, chemistry and material properties as suggested by Dowson in his book on the history of tribology [36]. According to a recent study of the French Technical Centre for Mechanical Industries (CETIM) [37], 80% of failures in mechanical components start at tribological interfaces, which remain extremely complex to study as one cannot observe a contact without modifying its state prior observation.

Therefore, as contacts are inherent to REB design, a brief overview of REB tribology fundamentals is proposed in this section in order to define the general *multiscale* background of the experimental work detailed in the following chapters. Loads acting on REBs are transmitted via very small contact area between the non-conformal geometries of the rolling elements and the ring raceway, thus inducing high cyclic over-rolling contact stresses (**Fig. 1.7**). As contact stresses are limited to the first hundreds of microns near the surface, most REB failures are initiated in this region and are therefore associated to *multiple tribological phenomena* mentioned in **Fig. 1.7** different than usual structural fatigue [18]. Consequently, this section will mainly focus on the respective contact stresses, kinematics, lubrication and friction.

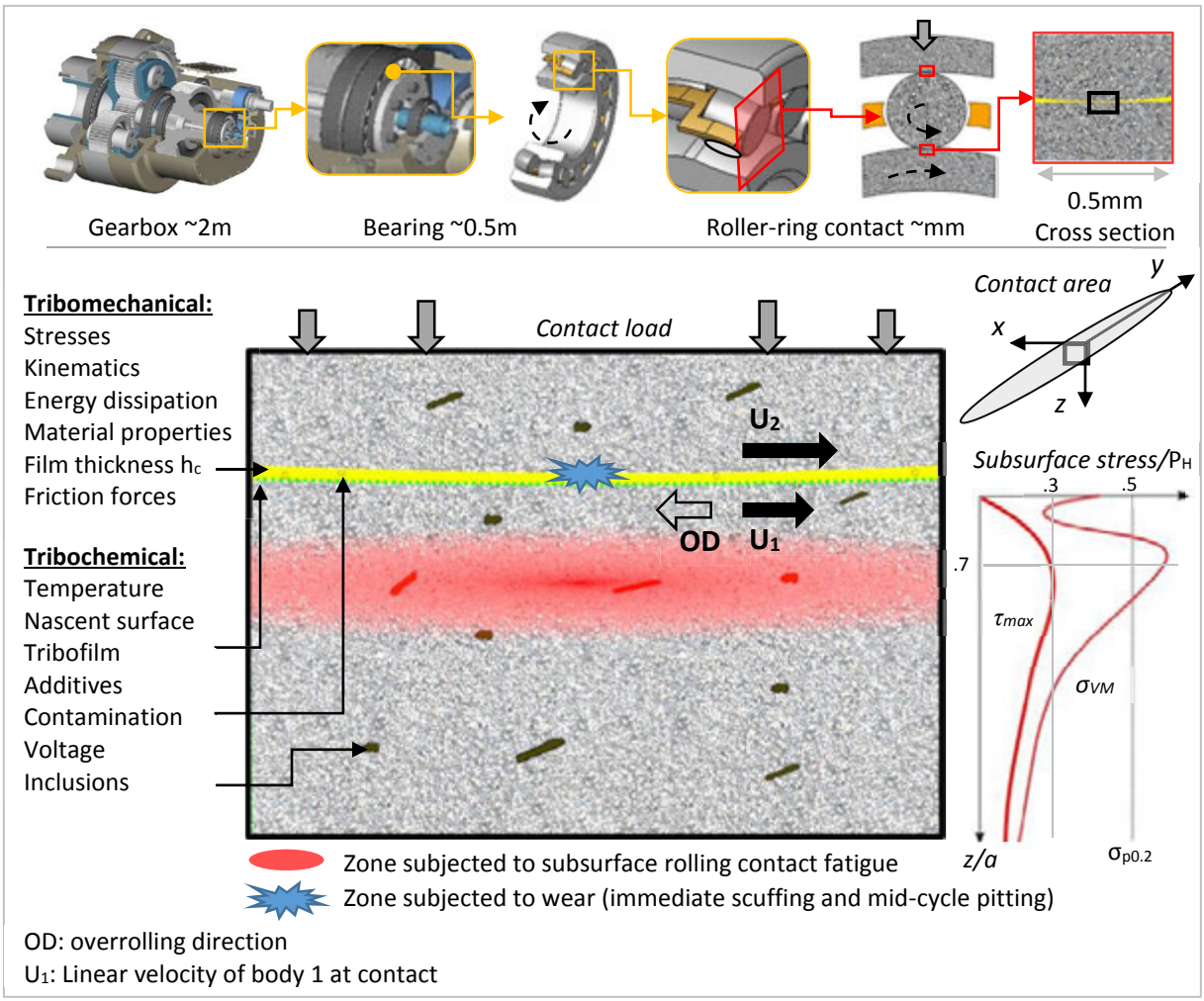

Fig. 1.7: Schematic overview of a tribological contact in a REB considering both tribomechanical and tribochemical parameters affecting the life time before surface or subsurface failure.

1.2.1 Contact stresses

To avoid any further confusion, *contact pressure* refers to the pressure at the contact surface, i.e. the normal stress corresponding to the ratio of the normal load by the contact area. *Contact stresses* to the subsurface stresses that can be considered at different locations and depths, as normal stresses σ, shear stresses τ, and the equivalent Von Mises stress σ_{VM} [17,18,38].

1.2.1.1 Hertz contact theory

a. Contact geometry

In general the contact geometries in REBs are rather complex with different curvature ratio depending on the axial or circumferential cross sections. As the contact area is small compared to the overall dimensions of the bodies, it is possible to approximate the majority of REB contact geometries by the equivalent geometry of a barrel on a plane contact. The following equations are employed to obtain the relative curvature radii (**Fig. 1.8**). In case of roller REBs, the contact is simplified as a line contact extruding the scheme corresponding to the non-conformal contact of the length of l in the y direction, and considering R'_y as infinite.

Relative radius for non-conformal contacts:

$$\frac{1}{R'_x} = \frac{1}{R_{x1}} + \frac{1}{R_{x2}}$$

Relative radius for conformal contacts:

$$\frac{1}{R'_y} = \left| \frac{1}{R_{y1}} - \frac{1}{R_{y2}} \right|$$

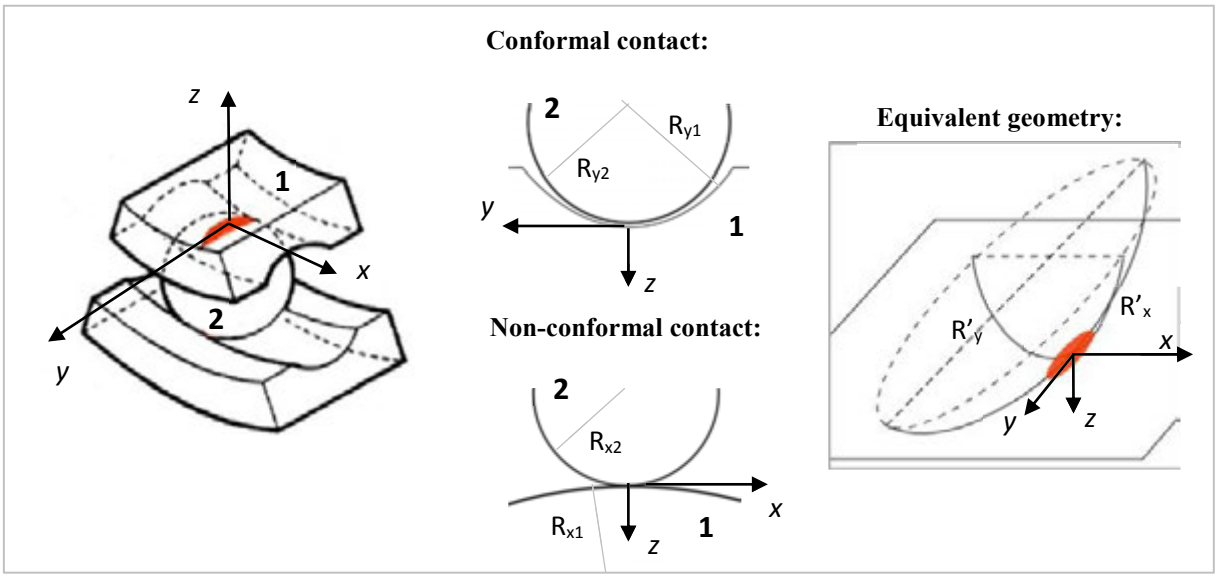

Fig. 1.8: Typical equivalent contact geometry of a raceway (1) – ball (2) elliptical contact.

b. Hertz contact area and pressure

Considering perfectly rigid and smooth counter parts, the normal static loading of a surface onto another will result in a point or line contact depending on the conformity. In reality however, the surfaces will deform elastically to form a contact area, generating a contact pressure at the interface. Hertz was the first to propose a solution for the equivalent barrel on plane contact deformation and pressure [39]. The equations used to compute all contact parameters of the following chapters have been developed in Appendix A. Those contacts are commonly referred to "Hertzian contacts and are considered as the basics of contact mechanics and tribology.

1.2.1.2 Subsurface stresses

When a smooth surface is subjected to cycling rolling contact, the highest shear stress exists in the subsurface and not at the extreme surface (**Fig. 1.9**). Substantial proof to this fact are the subsurface residual stress build-up and microstructural alterations [40–42]. The understanding of subsurface stresses proposed in this section is inspired from the references [17,38,43,44].

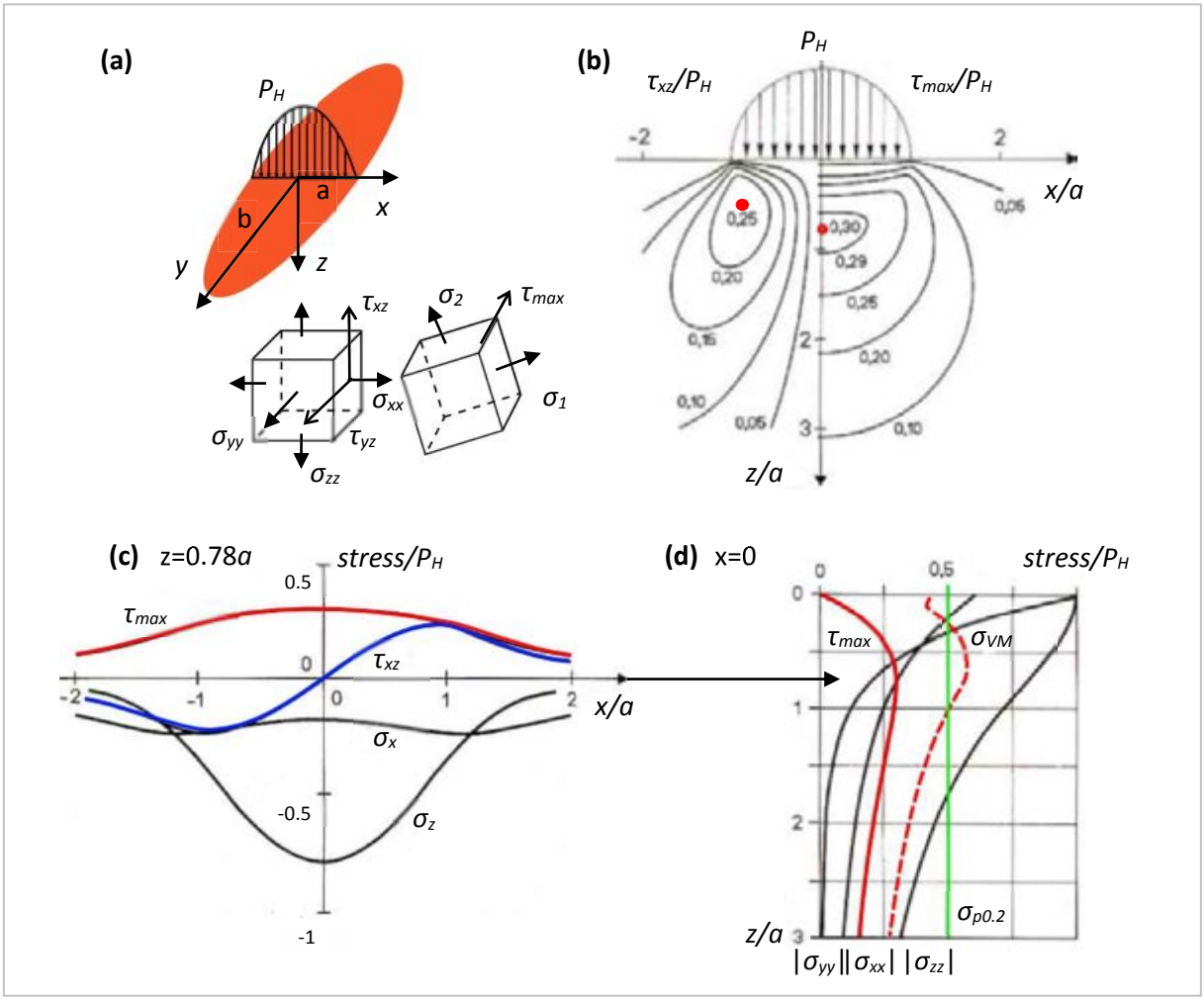

Fig. 1.9: (a) Infinitesimal orthogonal stresses and principal stresses beneath a hertzian contact; (b) Contours of the orthogonal shear stress τ_{xz} and Tresca shear stress τ_{max} for a line contact, highlighting their respective maximum locations; (c) Evolution of τ_{max}, τ_{xz}, and principal compressive normal stresses along the x direction at the depth of maximum shear stress z=0.78a; (d) Evolution of the absolute values of the principal normal stresses, τ_{max}, and Von Mises equivalent stress σ_{VM} along the z direction for x=0 (plots adapted from [45]).

a. Subsurface stresses in theoretical hertzian contacts

For a Hertzian contact, the orthogonal normal stresses σ_{xx}, σ_{yy}, σ_{zz}, and shear stresses as τ_{xy} can be computed for each subsurface infinitesimal element (x,y,z) (**Fig. 1.9**) [38]. In contact mechanics normal stresses are compressive in nature (**Fig. 1.9** (c)), and thus shear stresses are most often considered for fatigue criteria. Referring to Mohr's circle, it is possible to determine the principal stresses σ_1, σ_2, σ_3, and the maximum shear stress τ_{max} also referred to as the Tresca shear stress (**Fig. 1.9**).

$$\tau_{max} = \frac{1}{2}\max(|\sigma_1 - \sigma_2|, |\sigma_3 - \sigma_2|, |\sigma_1 - \sigma_3|)$$

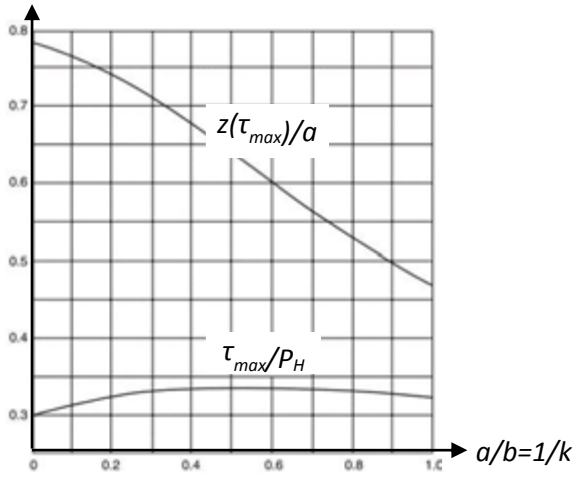

Fig. 1.10: Tresca shear stress τ_{max} and respective depth $z(\tau_{max})$ at x=0 function ratio of the degree of ellipticity: case of a line contact for a/b=0 with τ_{max}=0.3P_H at z=0.78a; case of a circular contact for a/b=1 with τ_{max}=0.31P_H at z=0.48a (plot adapted from [17]).

As highly loaded contacts in REBs typically present an elongated ellipse ratio k>10, the subsurface stresses are often approximated by line contact [46] rather than by a circular contact (**Fig. 1.10**). This is why **Fig. 1.9** and the following plots of shear stresses and Von Mises equivalent stress are given for a line contact.

The first empirical models in predicting subsurface fatigue were based on the maximum alternative orthogonal shear stress $\tau_0=\tau_{xy,max}$ as its amplitude over an over-rolling cycle is greater than the amplitude of the Tresca shear stress (**Fig. 1.9** (c)). Indeed, it presents a maximum amplitude of ±0.25P_H (thus 0.5P_H peak to peak) at x=±0.85a and z=0.50a.

However it has been demonstrated that most microstructural alterations associated to subsurface fatigue appears at depths around z=0.75a in REB highly elliptical or linear contacts. This supports the frequent use of the Tresca shear stress criteria in physical models for subsurface initiated fatigue. The Tresca shear stress τ_{max}, also referred to as τ_{45}, reaches a maximum of 0.30P_H at x=0 and z=0.78a. This maximum shear stress is often considered as the most relevant regarding physical subsurface microstructural stresses and dislocation bonds.

Moreover, the Von Mises stress σ_{VM} based on the distortion energy is also frequently used in contact fatigue models since it is usually easier to implement in numerical calculations [47] and since it can be directly compared to the yield strength of the material $\sigma_{p0.2}$ (**Fig. 1.9**). Some researchers also work with the proportional octahedral shear stress σ_{oct} [48]. They are expressed by the following equations:

$$\sigma_{VM}(x,y,z) = \sqrt{\frac{1}{2}[(\sigma_x - \sigma_y)^2 + (\sigma_y - \sigma_z)^2 + +(\sigma_z - \sigma_x)^2 + +6(\tau_{xy}^2 + \tau_{yz}^2 + \tau_{zx}^2)]}$$

$$\sigma_{oct} = \frac{\sqrt{2}}{3}\sigma_{VM}$$

The Von Mises stress, accounting for normal and shear stresses, reaches a maximum of $0.56P_H$ at x=0 and at depths z between $0.71a$ and $0.8a$ (**Fig. 1.9** (d)). Compared to the Tresca shear stress, the Von Mises equivalent stress also accounts for high principal stresses at the surface. Another equivalent stress is used by researchers applying the Dang Van multiaxial criteria [49].

To summarize, as a first approximation, in REB contacts it can be considered that:

- Typical hertzian pressures P_H are comprised between 1.5-2.5 GPa for roller bearings and 2.5-3.5 for ball bearing
- The maximum Tresca shear stress of $0.3P_H$ and the maximum Von Mises equivalent stress of $0.5P_H$ are located at depths of around $0.75a$ (a being the minor semi-axis)
- Contact subsurface stresses are considered as nil at depths below $4a$ (extension of zone 4 in **Fig. 1.12**). Only structural stresses like mounting hoop stress remain.

b. Effect of surface asperities on subsurface stress field

The previous subsurface stresses computations have been led under the hypothesis of a Hertzian, i.e. with ideally smooth contact surfaces. In reality, surfaces often present defects as they are (1) inevitably textured by the machining and polishing processes, thus considered as *rough* (**Fig. 1.11**) and (2) commonly *dented* by hard particles in case of contamination.

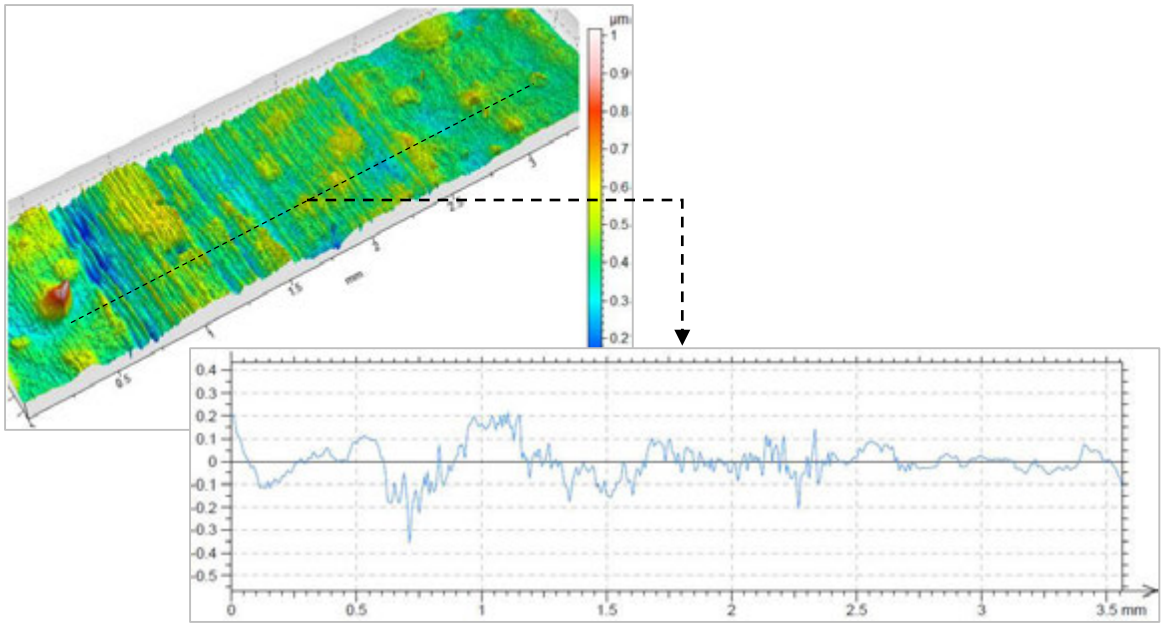

Fig. 1.11: Typical surface roughness and profile of a 100Cr6 roller after cycling on the Twin-Disc machine measured by SENSOFAR PLu neox optical profilometer (Appendix H Ref TDM08_01).

First, surface roughness is typically considered as the short wave-length surface asperity height fluctuations around the mean surface geometrical profile. They can be measured by contact or optical profilometers. Surface or profile roughness of contact surfaces are commonly expressed by R_a, being the arithmetic average of asperity heights, and by R_q, being the root mean square average of asperity heights. Considering common REB grinding methods, it is often estimated that $R_q \approx 1.25R_a$ [17]. The following basic equations express the profile roughness parameters:

$$R_a = \frac{1}{n}\sum_{i=1}^{n}|z_i| \text{ and } R_q = \sqrt{\frac{1}{n}\sum_{i=1}^{n}|z_i^2|} \text{ and } R_a \sim 1.25\, R_q$$

Analytical methods have been developed to compute the effect of surface roughness on the Hertzian pressure and subsurface stresses [48,50–52]. As illustrated in **Fig. 1.12**, surface asperities generate local pressure spikes. This greatly affects the subsurface equivalent stress field in the near surface region (zone 1) but does not modify significantly the Hertzian zone (zone 3). Therefore, surface roughness, especially in the case of poor lubrication enhances the probability of surface initiated failures. However, for sake of simplicity, if the lubrication is sufficient and the contact roughness within the REB standards, it is commonly considered that the Hertzian contact theory gives a good approximation to the subsurface stress field in REBs.

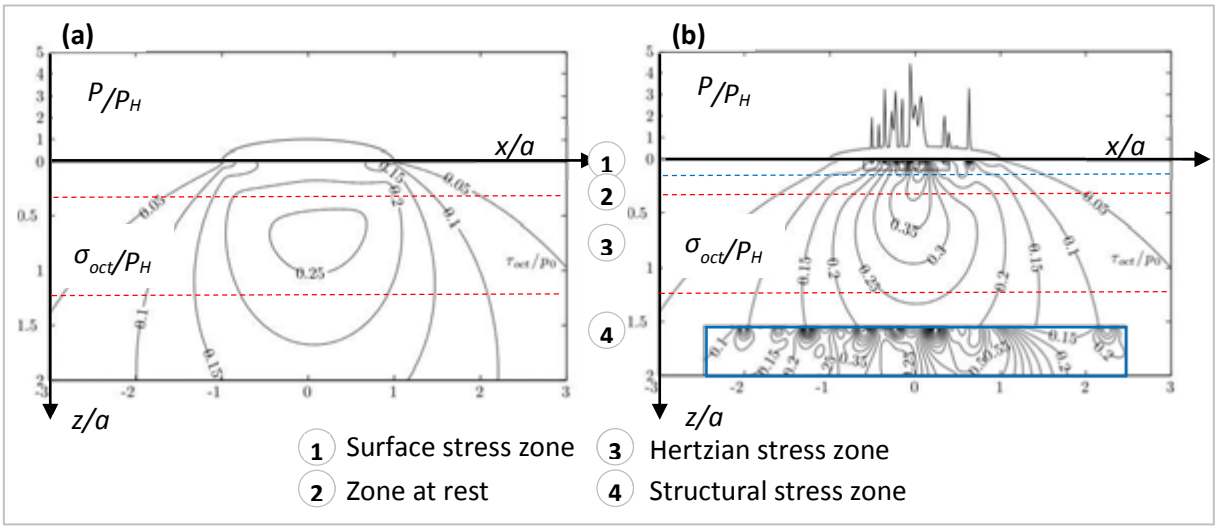

Fig. 1.12: (a) Octahedral stress contours and pressure distribution of a Hertzian line contact with a typical friction coefficient μ=0.05; (b) identical as (a) but contacting typical rough surfaces acting as stress raisers (surface zoom) (adapted from [48]).

Second, surface dents are observed on RE and ring raceways when the entrained lubricant is contaminated by wear debris or particles from the environment that either have managed to pass the various protective filters or that have remained trapped inside the contact (**Fig. 1.13**). Numerical and experimental studies based on predetermined contamination or artificial dents have been led in order to better understand the influence of surface dents on surface distress and on subsurface stresses [53–57]. An example is given in **Fig. 1.14**. It depicts that dent shoulders, also called ridges, act as important stress raisers in the near surface region without affecting the Hertzian zone, similarly to the effect of surface roughness [50].

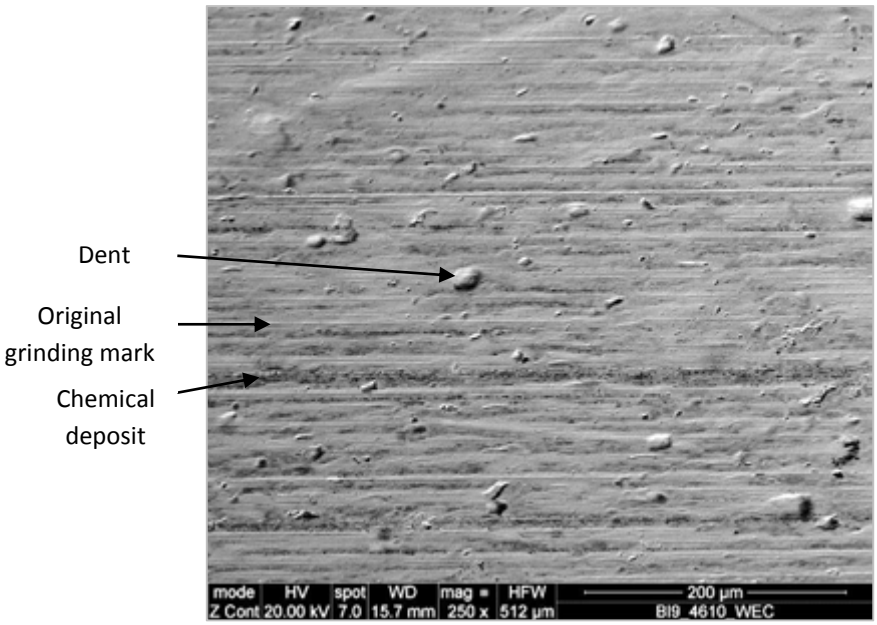

Fig. 1.13: Typical SEM analysis of an ACBB IR raceway revealing dents after 1265 h of service (#9 Appendix D).

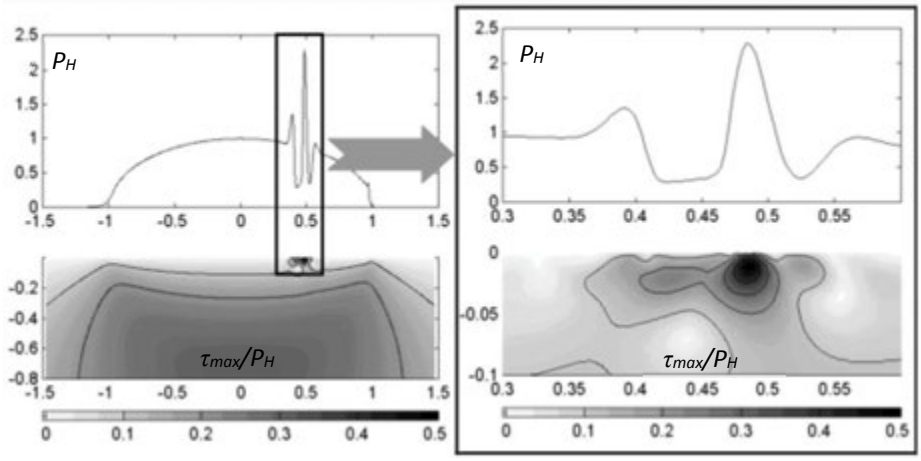

Fig. 1.14: Typical effect of a dent on the contact pressure and subsurface shear stress field of a Hertzian contact (from [54]).

c. Effect of friction on subsurface stress fields

Motion is inherent to REB contacts combining both rolling and sliding kinematics. As sliding occurs, a frictional tangential force T is exerted at the contact surface by principally due to lubricant shear. Hence, the driver surface tends to be decelerated by the follower and the follower accelerated by the driver. The mean tangential force over the contact area is proportional to the normal load N and function of the friction coefficient μ:

$$T = \mu N$$

When combining frictional tangential load to the normal load of a Hertzian contact, the maximum Tresca shear stress τ_{max} slightly increases and is more or less raised towards the surface depending on the friction coefficient μ (**Fig. 1.15**). As typical friction coefficients in fully lubricated REB contacts are globally as low as $\mu \approx 0.01\text{-}0.05$, it is commonly considered that the frictionless

Hertzian contact theory still gives a good approximation to the subsurface stress field (**Fig. 1.12** (a)). However, the friction coefficient might be significantly increased in case of unsufficient lubrication and high surface roughness, thus enhancing the risk of near surface initiated failures.

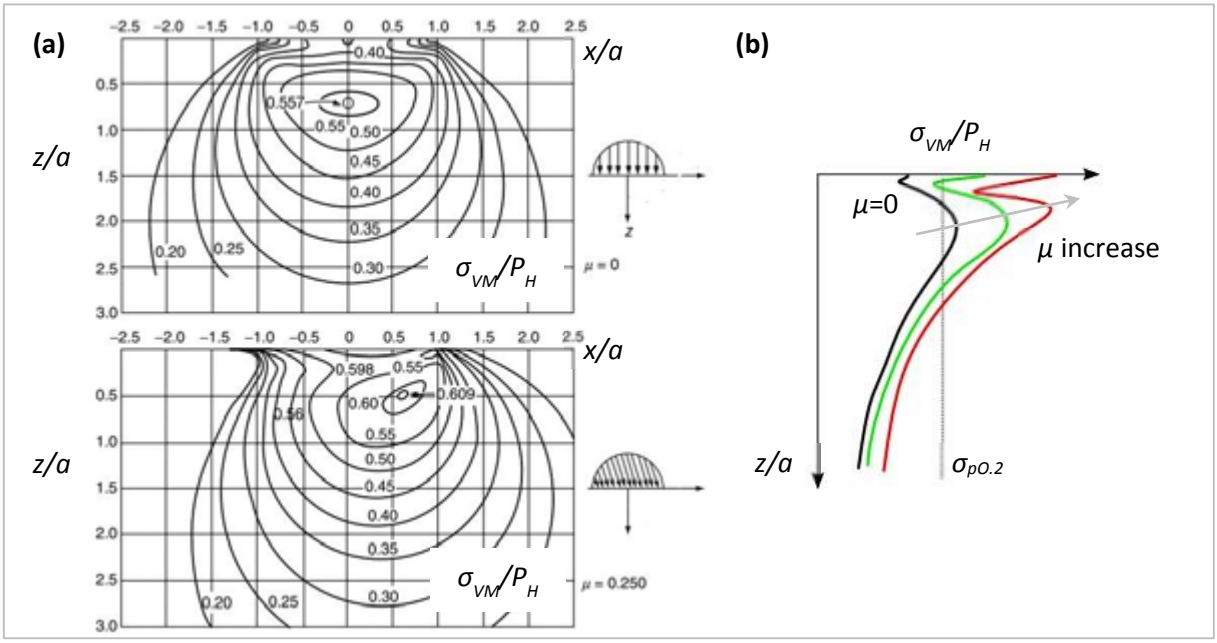

Fig. 1.15: (a) Comparison of the contours of Von Mises stress for frictionless hertzian contact and for a friction coefficient μ=0.25 (adapted from [17]) with the same normal load;
(b) Typical Von Mises stress profile modification as the friction coefficient increases.

To summarize, both surface roughness and contact friction increase the stress rate of the near surface, thus competing with hertzian subsurface stresses regarding the material yield strength to initiate surface or subsurface failures [58].

1.2.2 Contact kinematics

Despite their name, motions occurring in REBs are not restricted to pure rolling movements. REB kinematics highly depend on the applied loads affecting on the positioning and deformation of the REB components. For example, in the ACBB depicted in **Fig. 1.16**, while the IR rotates at a steady angular velocity $\Omega_{ir,y}$, the ball orbits around the same axis at the angular velocity of the cage $\Omega_{cage,y}$ both rolling on the same axis at $\Omega_{b,y}$ and spinning on its own spin axis at $\Omega_{b,spin}$ depending on the contact angle and hence the load.

Hence, considering the analytical developments in [17,18] and the multiple computer models developed to assess the bearing kinematics and dynamics such as A.D.O.R.E by P.K. Gupta (http://www.pradeepkguptainc.com), the relative motions of REs and raceways of ball bearings are somewhat more complex than those in roller bearings. Indeed, the latter is often similar to the specific case of a fixed contact angle ball bearings [44]. This section will not insist on the complex REB kinematic equations but on the main sliding motions commonly occurring in REBs.

1.2.2.1 Rolling kinematics

For bearings operating at moderate and steady rotational speeds, the internal speeds can be accurately predicted under the conjunctions that the rolling elements rolls on the raceway *without sliding* and that inertial forces can be neglected.

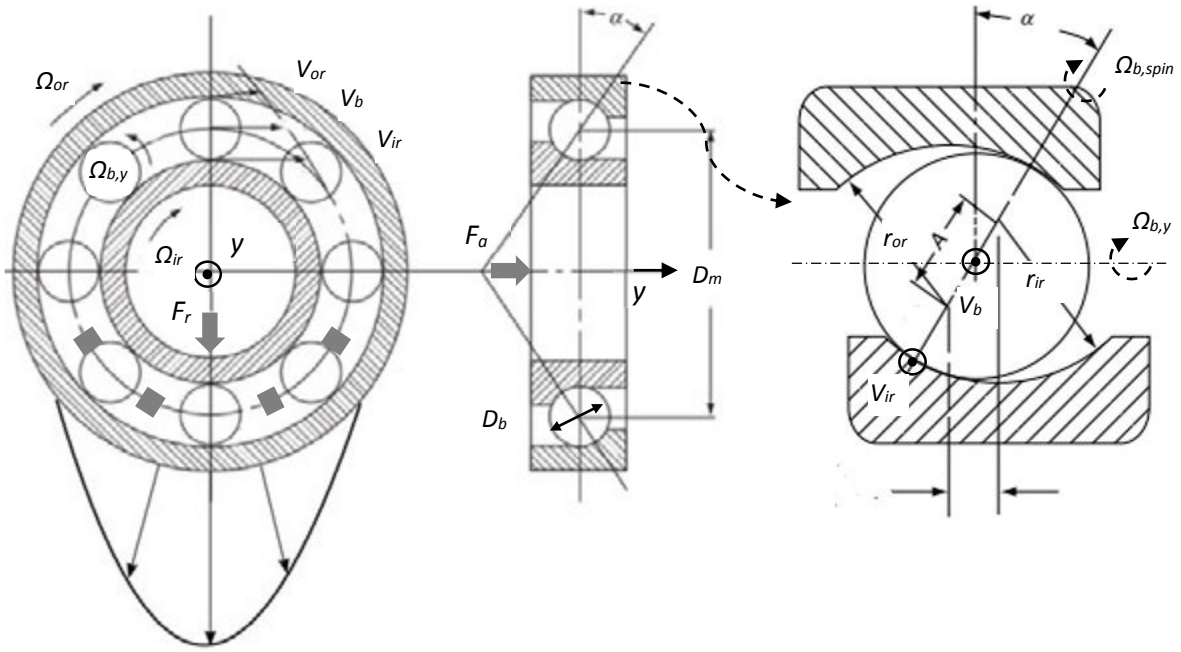

Fig. 1.16: Basic rolling kinematics of an angular contact ball bearing under a typical load illustrating the different velocities, contact angle, osculation and dynamic effects of the cage (adapted from [17]).

As it applies for the further described bearing tests, it will be assumed that the IR and OR have a common contact angle α as illustrated in **Fig. 1.16**. Hence, for a steady IR rotation on its axis *y* the linear velocity at center of contact V_{ir} is:

$$V_{ir} = \frac{1}{2}\Omega_{ir}(D_m - D_b\cos(\alpha))$$

If there is no gross sliding at the ball-raceway contact, the linear velocity of the ball at point of contact U_b and the linear velocity of the ball at the pitch diameter V_b (corresponding to the linear velocity of the cage) are:

$$U_b = V_{ir} \text{ and } V_b = \frac{1}{2}(V_{ir} - V_{or})$$

Moreover, in application, REBs often operate with either fixed outer rings or fixed inner rings. As it applies for the bearing tests used in this study, the outer ring will be considered as fixed in the housing. Hence,

$$V_b = \frac{1}{2}V_{ir}$$

$$\Omega_{b,y} = \frac{D_m}{2D_b}\left(1 - \left(\frac{D_b}{D_m}\cos\alpha\right)^2\right)$$

These equations have been used in this study to estimate the number of cycles and to approximate velocities in the ACBB described thereafter. However, the actual motions of the contacting elements on the raceways is much more complex than pure rolling, which is one of the main source of energy dissipation and failures in REBs.

1.2.2.2 Sliding due to rolling motion

In a REB operating at steady state and its respective undeformed or deformed contact curvatures at the IR and OR, Heathcote has demonstrated that sliding is inherent to the over-rolling motion and that pure rolling only takes place in two lines [59]. Considering a contact angle of 0° and no other ball motion than that of its rotation versus the *y* axis, the two lines of pure rolling are positioned symmetrically versus the contact center, at a distance that is function of the contact osculation and on the ratio of the distance of the contact points to their respective axis of rotation (**Fig. 1.17**). This type of conforming contact curvature occurs mainly due to geometrical considerations of the raceway, but also possibly due to very local contact deformation. However, the Hertzian deformation is often negligible versus the geometric osculation. Moreover, there have been considerable work on what is called *microslip* associated to the surface deflection in the rolling direction. Yet, microslip is mainly related to dry and high friction contacts as the wheel-railway contact, and therefore supposed not to take place in lubricated bearing contacts.

The geometrical osculation of a contact corresponds to the ratio of the radius of curvature of the rolling element to that of the raceway in a direction transverse to the over-rolling direction:

$$f_{ir} = \frac{r_{ir}}{D_b} \text{ and } f_{or} = \frac{r_{or}}{D_b}$$

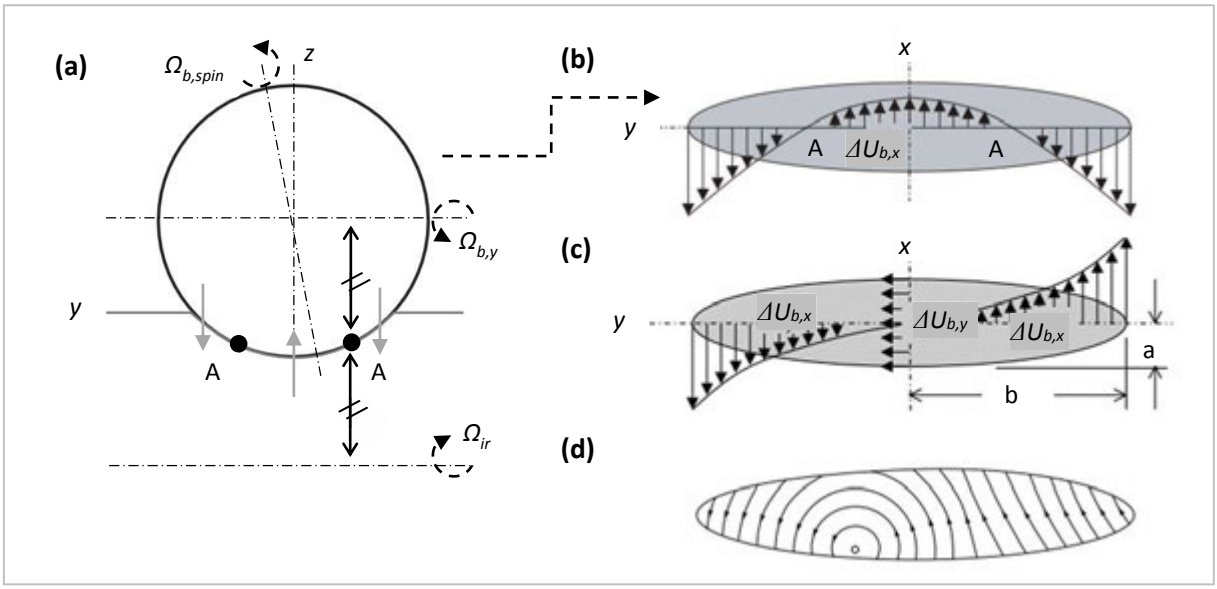

Fig. 1.17: (a) Heathcote conforming osculation with two lines of pure rolling in A; (b) ball contact sliding velocities in a radial loaded DGBB representing Heathcote slip; (c) ball contact sliding velocities in an ACBB accounting for transverse spinning motions; (d) overall sliding velocity lines in an ACBB without considering skidding (b, c, and d adapted from [17]).

1.2.2.3 Sliding due to spinning motion

In addition to the steady rolling motion around the bearing axial axis, ACBB and thrust loaded DGBB present an angle of contact that depends on the ratio of the thrust axial load F_a versus the

normal load F_r., on the bearing functional clearance and on the IR-OR respective curvatures. The contact angle α is formed by the line passing through the respective points of contact and a plane perpendicular to the bearing axis of rotation (**Fig. 1.16**). Considering an unloaded ACBB, the purely geometrical angle of contact is given by:

$$\cos\alpha = 1 - \left(\frac{C_d}{2BD_b}\right) \text{ where } B = f_{OR} + f_{IR} - 1$$

A small axial thrust load applied on 0° contact angle DGBBs can be magnified due to the induced contact angle and lead to premature failure of the bearing. Therefore the loading of an ACBB can greatly affect the ball and cage speeds. For TRBs, the contact angle is kept constant whatever the load, but the axial load will increase the risk of skidding as described thereafter.

1.2.2.4 Skidding

Skidding, also referred to as gross sliding, corresponds to undesired sliding motions that can occur in REBs for different reasons beyond the sliding induced by rolling motion. These sliding motions are generally more important than those relative to geometrical consideration. Therefore, there is no more point of pure rolling throughout the whole contact area. For usual REBs operating at steady-state in the correct position, skidding should not occur, but there are numerous drivers for skidding that are complex to consider in elemental kinematics analysis:

- Misalignment of the rolling elements versus the raceway due to:
  - Shaft bending or housing deformation that misposition the rings (**Fig. 1.18**);
  - Important ring deflection in case of highly loaded large size bearings ;
  - Roller skewing induced by friction between roller ends and ring flanges in case of CRB or TRB axially loaded.
- Dynamic aspects due to:
  - Entry and exit of loaded zone in radially loaded bearings (represented in **Fig. 1.16**) where REs are relatively free of motion in the unloaded zone then forced into the loaded zone by the cage and finally held back by the cage when expulsed from the loaded zone;
  - Overall transient acceleration or deceleration of the bearing in service.

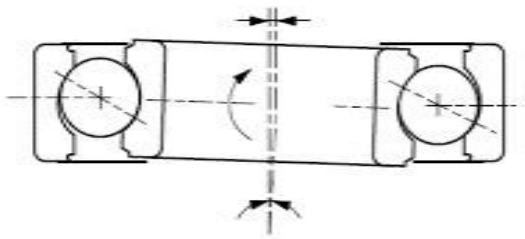

Fig. 1.18: Typical misalignment of a DGBB affecting contact kinematics (adapted from [17]).

1.2.3 Contact lubrication

As described previously, REB tribological contacts are subjected to severe contact pressures and important rolling-sliding velocities, which would lead to catastrophic power losses and scuffing failures if the steel surfaces were to come in full metal to metal contact. Lubrication of REB

contacts is thus recognized as a key parameter in REB efficiency and durability. In the present section, the different lubricants, lubrication regimes and tribochemical aspects will be briefly presented as they greatly influence White Etching Crack failure modes.

1.2.3.1 Multiple roles of lubrication

REB lubrication consists in introducing a lubricating fluid film between the contacting surfaces. The main roles of lubrication, all essential to REB efficiency and durability are the following:

- At the contact scale:
  - Separating the contacting surfaces in order to avoid friction and wear due to metal to metal contact
  - Accommodating the surface sliding velocities
  - Transmitting the normal damping vibrations and transient pressure spikes
- At the mechanical system scale:
  - Dissipating and evacuating frictional heat out of the contact
  - Evacuating contamination particles and wear debris out of the contact

Considering a full mechanical system, like wind turbine gearboxes, comprising both gears and bearings of different types, the lubricant choice is often delicate and critical as it has to comply with a large variety of tribological conditions (kinematics, stresses, bulk material, roughness, etc.) in order to satisfy a maximum of the fore listed roles.

1.2.3.2 Types of lubricant and formulation

Lubrication can be considered of three types: *liquid* (mainly mineral and synthetic oils), *semi-solid* (grease, paraffin, wax, etc.), and *solid* (surface coatings as oxides, soft metals, etc.). The most widespread are *liquid* lubricants, notably in mechanical systems as gearbox where a single lubricant is used for gear and bearing lubrication [18,60]. Relatively robust engineering tools have been developed to predict the capacity of *liquid* lubricants to separate contacting surfaces for given tribological conditions. Lubrication of bearings by *liquid* lubricants is commonly achieved by splash lubrication or circulating and jet lubrication.

As *semi-solid* lubricants, greases are commonly used in isolated, sealed and slow rotating bearings. Greases consist of oil that is physically retained in a thickener, similarly to water in a sponge. The thickener is generally soap which is capable of bleeding oil to meet the demands of the bearing contacts similarly to if they were lubricated by *liquid* lubricants, even though some rheological parameters may be affected by the grease formulation [61]. Nevertheless oil retained in grease thickeners can often be considered as similar to the liquid lubricants further described.

Current commercial *liquid* lubricants used in engines and gearboxes are mostly made of a *base stock oil*, either natural or synthetic, that represents around 75% to 95% in mass of the lubricant [60]. Base stock oils can be divided in three categories: vegetable, mineral, and synthetic oils [18,60,62], detailed in Appendix B. As of today, the use of synthetic and semi-synthetic (mixtures of synthetic and mineral) has become nearly systematic in most industries including wind turbines. However, this base oil alone however rarely meets all the requirements of the lubricant.

Therefore artificial *additives* of many types are blended into base oils in order to improve chemical and mechanical performance complying with the specifications in terms of viscosity,

friction, ageing, oxidation, corrosion, etc. [18,60]. For example (more details in Appendix B):

- *Boundary lubrication additives* have been designed for the most severe lubrication regimes, when surface separation is near non-existent in order to tribochemically react with the surfaces to form what has been called protective *tribofilms*. They are often mentioned as *Extreme Pressure (EP)* and *Anti-Wear (AW)* additives, one of the most being zinc dialkyldithiophosphates (ZnDTP), which also acts as an oxidation inhibitor thanks to its tribofilm forming capacity [63–65].
- *Detergents* are often employed in an over-based formulation (*over-based calcium sulfonates (CaS)*) both for their detergence and dispersive properties preventing undesired deposits from adhering to surfaces and for their corrosion inhibiting properties [64].
- *Emulsifiers* are also commonly added to stabilize water-in-oil emulsions, e.g. in wind turbines. The chemical solubility of water in oil, also called *hygroscopy,* as opposed to mechanical emulsion, is sometimes desired in order to prevent the formation of micro-bubbles of water that would collapse in the REB contacts inevitably leading to metal to metal contact and wear. During this study a protocol has been developed to confirm indeed that oil hygroscopy could vary significantly from a formulated oil to another.

To summarize, elaborating a lubricant formulation to meet given specifications consists in finding the balance between one or several base oils and the right additives, which is thus very complex considering all the different tribological conditions that can arise in a contact and the potential tribochemical interactions between additives themselves and with the steel substrate.

1.2.3.3 Lubrication regimes in bearings

The entrapment of the liquid lubricant in the converging gap of a tribological contact creates a hydrodynamic pressure enabling surface separation. The ratio between the film thickness and the combined surface roughness, referred to as the film thickness ratio λ, is commonly used to give an indication on the surface separation and thus on the severity of the lubrication regime [51,62,66]. Different definitions of λ are used throughout the literature. Surface roughness can be either the arithmetic roughness parameter R_a, or the root mean square R_q. The film thickness is approximated to the film thickness computed considering smooth surface, e.g. either the central film thickness h_c [51,66], or the minimum film thickness h_{min} [62]. As the λ ratio is commonly used to qualify the overall lubrication regime affecting the overall contact, the following expression has been chosen (*1* and *2* standing for the two contacting bodies):

$$\lambda = \frac{h_c}{\sqrt{R_{q1}^2 + R_{q2}^2}}$$

Depending on the λ ratio, tribological contacts are said to operate in one or several lubrication regimes. These are best depicted by the Stribeck curve (**Fig. 1.19**), which plots the friction coefficient as a function of a dimensionless number sometimes referred to as the Hersey number [62,67]. This number is function of the temperature-dependent lubricant viscosity, the contact rolling velocity and the contact pressure. Indeed, as these parameters vary, they affect the film thickness and thus the λ ratio. With the fore detailed definition of the λ ratio, the following main lubrication regimes are generally considered [51,66] (**Fig. 1.19**):

- *HydroDynamic (HD) lubrication.* ($\boldsymbol{\lambda \geq 3}$). For high lubricant viscosities, high rolling velocities entraining the lubricant inside the contact and/or low contact pressures, the oil film is thick enough to fully separate the rough contacting surfaces and therefore supports all the load. As there are no asperity contacts in this lubrication regime, friction only comes from lubricant shear and will therefore start to increase with more viscous fluids and thicker film thicknesses.
- *ElastoHydroDynamic (EHD) lubrication* ($\boldsymbol{\lambda \sim 3}$). This lubrication regime is a particular case of highly loaded non conformal contacts in thin film HD regime which takes into account the elastic deformation of contacting bodies as it is much larger than the film thickness itself. The full separation of the surfaces, combined with the low amount of fluid subjected to shearing, results in the minimum friction point. Most bearings are design to operate under the corresponding Hersey number and λ ratio often being the best compromise between efficiency and surface durability. The term "*full-film lubrication*" is also often used to designate both HD and EHD contacts. The latest is also referred to as EHL (L for lubrication). The term *micro-EHD* refers to the fact that in case of rough contacting surfaces, the elastic deformation of asperities inside the contact improves the λ ratio [66].
- *Mixed lubrication* ($\boldsymbol{1 \leq \lambda \leq 3}$). This lubrication regime constitutes the transition between the HD and boundary regimes. It is characterized by increasing friction for lower viscosities, lower velocities and/or higher contact pressures, reducing the film thickness that drops below the height of the deformed surface roughness. As the λ ratio gets lower than 3, an increasing number of direct contact occurs between both surfaces and the load is then supported by both the fluid and the surface asperities, increasing both the friction coefficient and surface distress.
- *Boundary lubrication* ($\boldsymbol{\lambda \leq 1}$). For low lubricant viscosities, low velocities and/or high contact pressures, the film thickness is quasi-inexistent: no surface separation occurs. This is the most severe lubrication regime, characterized by high friction and wear. The presence of the lubricant however remains vital as it provides the contact with friction and wear-reducing additives that can be tribochemically activated to form protective tribofilms.

To conclude, if in *HD* and *EHD* lubrication the lubricant viscosity plays an essential role on contact power losses and durability, in *boundary* and *mixed* lubrication, as high tribological energy is released by asperity metal to metal contacts, the lubricant formulation, and notably EP/AW and detergent additives, are the most influential on power losses, operating temperature and durability [61,62]. Due to the complexity of tribochemical reaction in *boundary* and *mixed lubrication*, most of the scientific unknowns lie in those severe lubrication regimes.

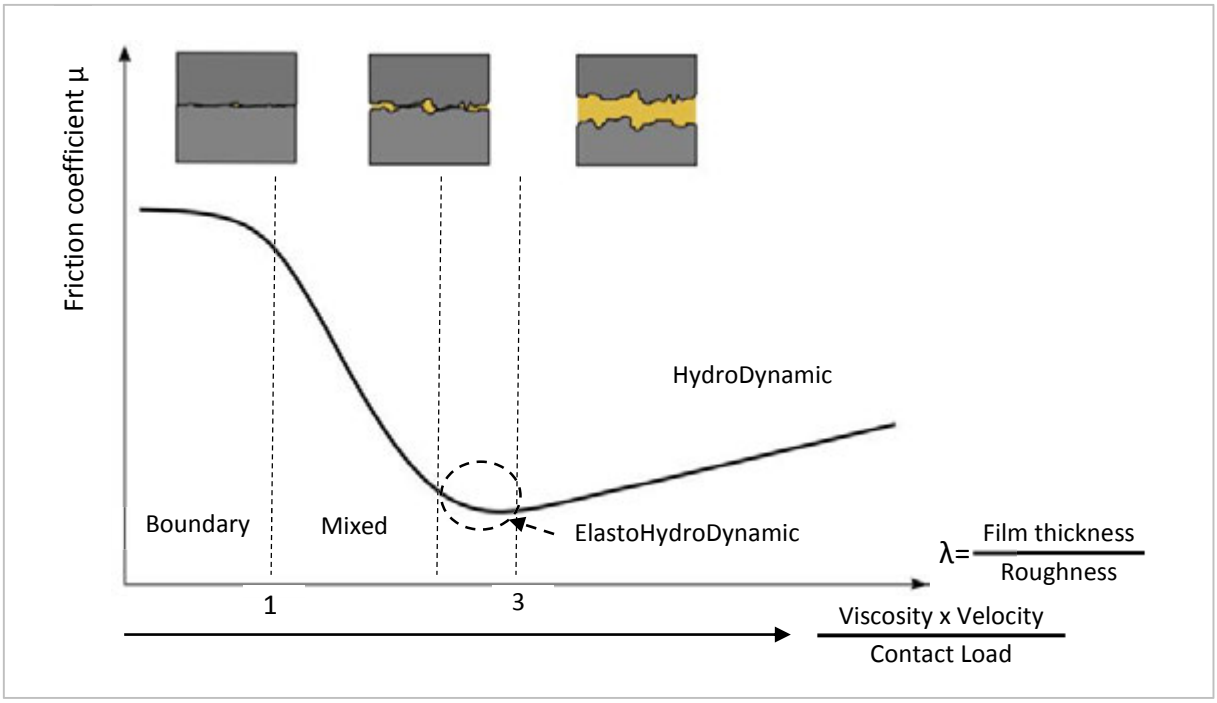

Fig. 1.19: Typical Stribeck curve representing the evolution the friction coefficient depending on the Hersey number or the λ film thickness ratio for the different lubrication regimes.

1.2.3.4 Lubricant film thickness calculations

As developed in Appendix A, the film thickness depends on the equivalent contact geometry R^*, the equivalent material properties E^*, the normal load N, the lubricant entrainment speed U_r, which actually corresponds to the mean rolling velocity, and the lubricant dynamic viscosity η. At ambient pressure, the lubricant viscosity is function of the bulk lubricant temperature (cf. Reynolds, Arrhenius or Williams-Landel-Ferry viscosity-temperature relationships). Inside EHD contacts, important piezo-viscous effects occur leaving the lubricant in a quasi-solid state as the viscosity increases exponentially with the contact pressure (cf. Barus or Roelands viscosity-pressure relationship). Hence, in the central zone of the contact, the lubricant film thickness h_c is quasi-constant. The pressure distribution it thus close to that of the Hertzian dry contact, despite a characteristic pressure spike relative to film thickness constriction at the contact outlet due to the sudden pressure drop but constant mass flow [68] (**Fig. 1.20**).

Hamrock and Dowson, have been the first, in the mid-seventies, to propose accurate models in predicting film thicknesses for elliptical isothermal tribological contacts operating under EHL [62,66,68–72]. As any EHL contact can be approximated by an ellipsoid on flat contact (section 1.2.1), these models are still currently used in engineering models for REB efficiency and durability. The expressions of the minimum and central film thickness (h_{min} and h_c) are detailed in Appendix A, considering an isothermal EHL contact under specific assumptions. Based on these equations, it has been demonstrated and verified by experimental results that the oil film thickness highly depends on the entrainment speed and lubricant viscosity (thus, on the inlet temperature) and only slightly on the load and material properties of the contacting bodies.

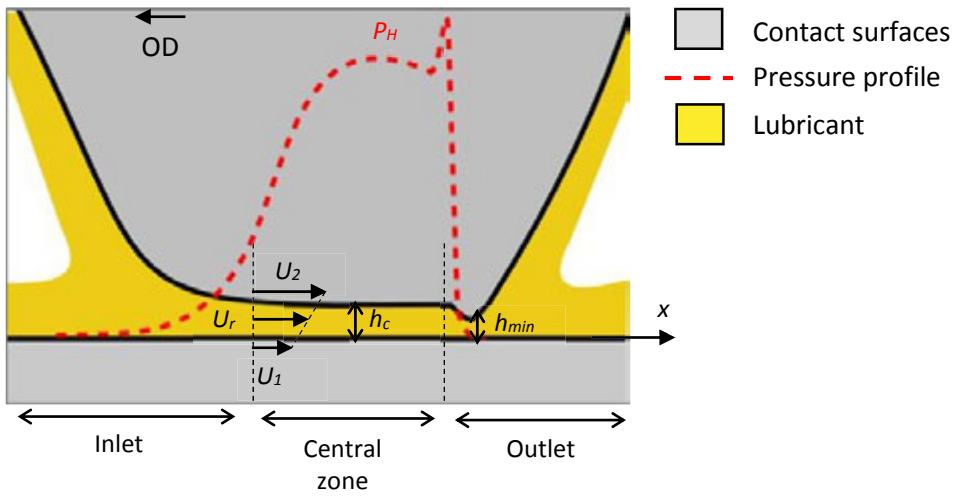

Fig. 1.20: Cross section of a typical EHL contact along the OD direction illustrating the contact pressure distribution and the film thickness profile (adapted from [66]).

1.2.3.5 Lubrication tribochemistry

Tribochemistry can be defined as the set of chemical reactions between contacting surfaces and the lubricant molecules that is triggered tribological energy. Tribochemistry thus affects the surface durability and integrity. Depending on the lubricant formulation and on the tribological conditions, numerous tribochemical reactions can occur in rolling/sliding contacts: oxidation, hydrolysis, thermal decomposition, polymerization, thermo-oxidative degradation, etc. A short literature review [65,73–82] reveals the complexity of tribochemical reactions, all hardly quantifiable but enhanced by:

- High contact pressures that enhance polymerization rather than decomposition
- High lubricant molecules shear due to sliding kinematics
- High local flash temperatures due to asperity contact and lubricant shear (up to 250°C)
- Formation of highly reactive and catalytic nascent steel surfaces by local welding or abrasive wear of the asperities
- Local tribo-electrical potentials and current depending on the lubricant conductivity (mainly function of the additive formulation and water content in the lubricant)
- Lubricant contamination (e.g. water ingress mainly function of the base oil and additive content)

The reaction products of the tribochemical reactions are nevertheless designed to best form thin protective film on the surface (from 1 to 100 nm), often referred to as *tribolayer* or *tribofilm*. In this study, on one hand, the term *tribolayer* will be employed for any chemical deposit at the surface that is easily cleaned off by solvent rinsing. On the other hand, *tribofilm* will be employed for any extreme surface chemical layer that presents strong adhesive and cohesive strengths despite its small thickness. Hence tribofilms corresponds to what remains after tissue and ultrasound rinsing using three solvents (ethanol, isopropanol, and heptane), but that can still be removed using ethylenediaminetetraacetic (EDTA) acid [80].

For durable surface protection despite severe lubrication regimes, the protective film formation rate should be equal or greater than the film removal rate. It has been demonstrated that

successful tribofilms typically consist of a mixture of wear particles, high molecular mass polymeric products and elements such as zinc, phosphorus, sulfur from additives [73,74,79,81–83]. Tribofilms considerably affect friction in boundary and mixed lubrication regimes [84] and are known to enhance REB fatigue life. Nevertheless, depending on the bulk material, lubricant formulation and tribological conditions, the tribofilm chemical composition and structure can vary significantly [65,74,83]. In most cases, tribofilms are usually far from being completely homogenous and impermeable to chemical diffusion (**Fig. 1.21**). For instance, it has been illustrated several times in the literature that typical ZDDP tribofilms present a heterogonous and spotted layout on the surface (**Fig. 1.21** (a)) [76,78,85,86].

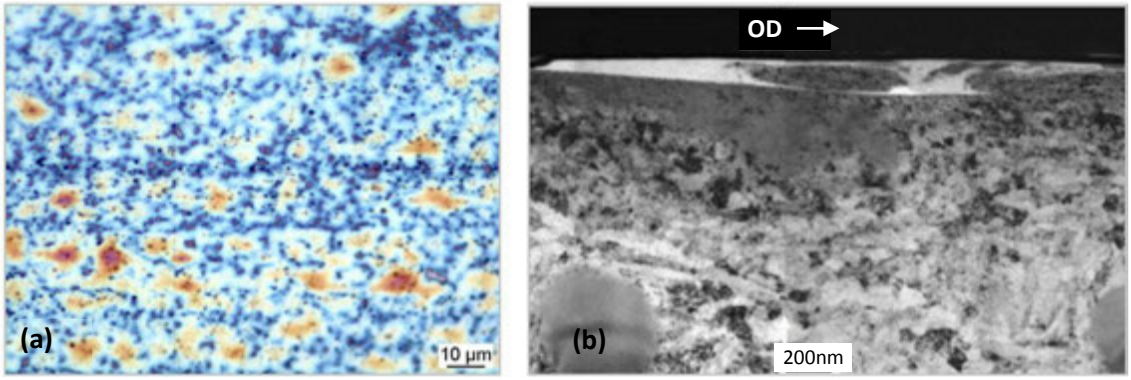

Fig. 1.21: (a) Optical image of a typical spotted ZDDP tribofilm (from [85]); (b) Typical cross section of a wear track revealing the heterogeneous structure of a MoS_2 based tribofilm (from [83]).

Consequently, lubricant additive tribochemical reactions also greatly affects rolling contact fatigue of REBs [87–90]. Indeed, there is a general trend to use less viscous lubricants to reduce gear and REB power losses. Therefore, tribological contacts often operate under severe lubrication regimes. Hence, more and more *boundary lubrication additives* are blended into commercial lubricants in order to favor the formation of protective tribofilms. In order to ensure that these additives will stay in suspension and reach the steel substrate in tribological contacts, excessive amounts of *detergents and dispersants* are also blended in the lubricants [64,77]. In particular, over-based CaS detergents, for example, tend to be widely used as they also act as *corrosion inhibitors* and *demulsifier*s [63,64,79,91]. However, *detergents and dispersants,* being strongly polar additives, have led to detrimental results altering the formation of tribofilms on the steel substrate [64,77,79,90] and chemically assisting crack propagation as they penetrate into surface initiated micro-cracks [87–90]. Therefore, nowadays tribochemistry has a major impact on REBs life, promoting the formation of protective tribofilms, but also chemically assisting rolling contact fatigue.

1.2.4 Contact friction

Even if REB were historically called *antifriction* because of their low friction properties, the rolling contact implies inevitable sliding (section 1.2.2). The sliding velocities of two contacting surfaces are accommodated by the contact interface, which introduces a resistance to motion, i.e. friction. As best depicted by the Stribeck curve (**Fig. 1.19**), friction in rolling/sliding contacts is intimately linked to the lubrication regime.

1.2.4.1 Boundary and mixed lubrication

As the lubrication regimes tend to *boundary and mixed lubrication*, asperities come in contact significantly increasing the resistance to motion partly represented by the friction coefficient. Even though this phenomena might eventually be counterbalanced by significant tribochemistry, it is extremely delicate to quantify. The coefficient of friction has been estimated to 0.1 in boundary lubricated REB contacts [18].

1.2.4.2 Full-film regime

In *full-film regimes*, since surfaces are fully separated by the lubricant film, friction solely comes from lubricant shear when accommodating the surface sliding velocities $\Delta U=U_1-U_2$ (**Fig. 1.20**). As depicted by the Stribeck curves, under full film lubrication, the friction coefficient increases as the film thickness increases due to fluid shearing. Moreover, as Stribeck curves are plotted for a given slide to roll ratio $SRR=\Delta U/U_r$, contact friction in full-film regimes is also widely studied using *traction curves*. The latest plot the friction coefficient μ function of the SRR for a specific lubricant-bulk material combination and for discrete combinations of contact pressure, entrainment speed and lubricant temperature (respectively P_H, U_r, θ). Extensive work is currently being led to be able to predict the friction coefficient for all (P_H, θ, V_r) combinations based on empirical models, including both full-film regimes and mixed lubrication [92,93].

1.2.4.3 Coefficient of friction measurement

As detailed in section 1.2.2, there are numerous sources of sliding in REBs all being source of friction. Yet, friction due to rolling of surface over each other is considerably lower than that encountered by spinning or skidding of the same surface over each other. Rolling/sliding contact friction coefficient is complex to quantify on a REB test rig as friction losses measured generally also comprise drag losses, cage friction, etc. Therefore, several tribometer as the commercial PCS Instruments Mini Traction Machine (MTM) [84] or various twin-disc machines [93,94] have been designed to simulate individual REB contacts in order to measure precisely the contact friction coefficient and plot Stribeck and/or traction curves.

In order to characterize lubricants used in this study, the LaMCoS two-disc machine described in [92,94] was used in order to plot traction curves for various combinations of (P_H, θ, V_r) corresponding to typical REB contacts and gather sufficient experimental data to feed the empirical model proposed by Diab et al. [92]. The traction curves obtained (**Fig. 1.22**) are in agreement with previous studies [93] as they also reveal three different rheological behaviors of the sheared lubricant as the SRR increases: (a) the lubricant behaves as a Newtonian fluid, i.e. the friction coefficient is proportional to the SRR-imposed shear; (b) the lubricant reaches its limiting shear stress; (c) excessive lubricant shear generates high contact flash temperatures that lower the viscosity and thus the friction coefficient. The plots from **Fig. 1.22** illustrate that: (a) the Newtonian behavior is quasi-independent of the pressure, the entrainment velocity and the temperature as the slope is mainly related to the piezoviscosity of the lubricant; (b) the limiting shear stress is greatly affected by the pressure and the inlet temperature; (c) the thermal region is mainly dependent of the entrainment velocity as it enhances significantly heat generation way above the inlet temperature.

To conclude, contact friction highly depends on the contact kinematics and lubrication regime. Moreover, Stribeck and traction curves are commonly obtained for ideal contacts. Therefore, the measured friction coefficient corresponds to the mean contact friction coefficient. In reality, the sliding kinematics most often vary along the contact ellipse, thus affecting the local friction coefficient and hence the subsurface stress field (section 1.2.1.2).

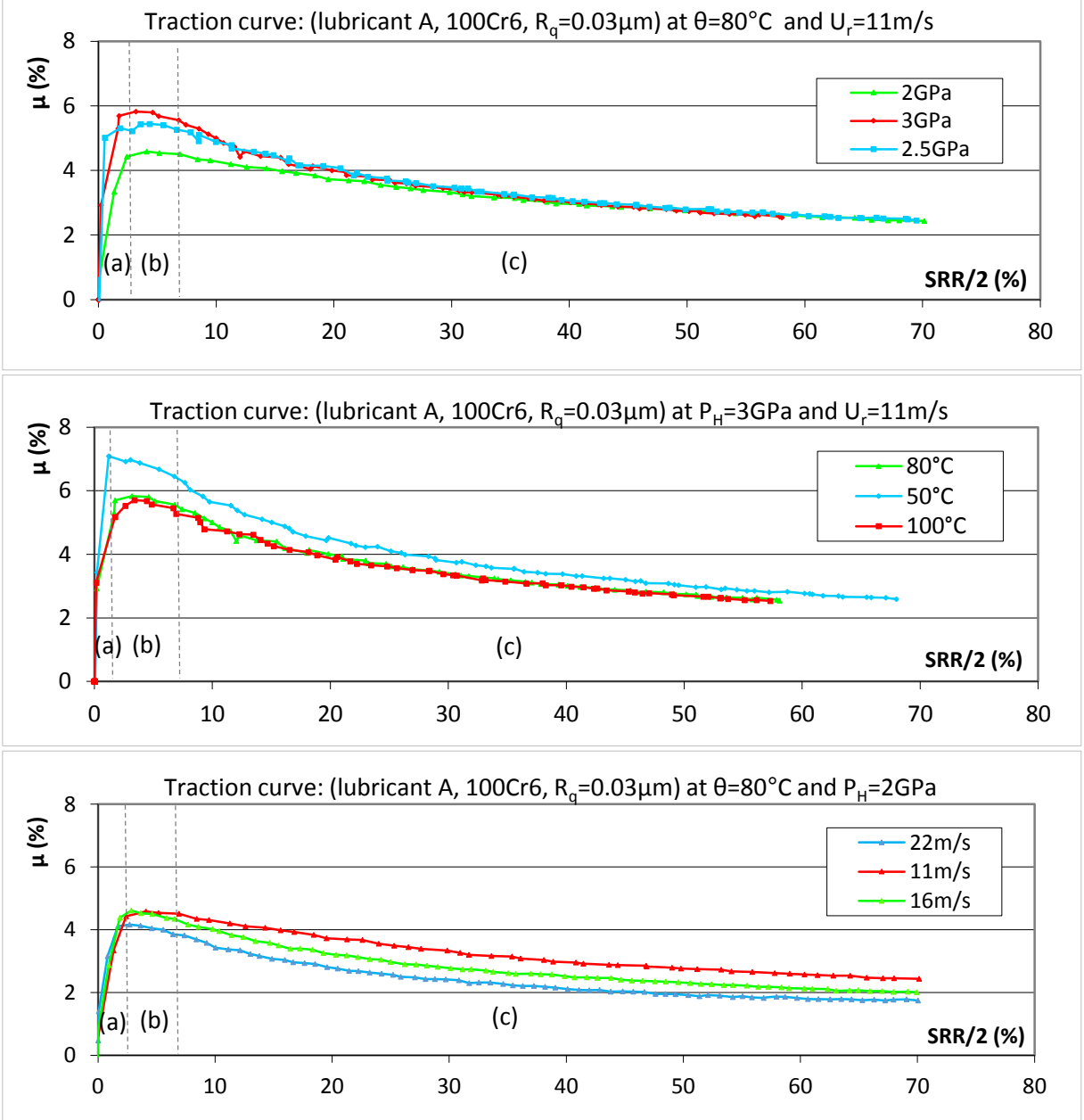

Fig. 1.22: Typical traction curves obtained on the LaMCoS two-disc machine for different conditions revealing: (a) the Newtonian domain, (b) the limiting shear stress domain and (c) the thermal affected domain.

1.2.5 Wind turbine bearings tribology

As described in section 1.1.2, large size wind turbine bearings have been designed beyond historical know-hows. Due to unexpected failure rates and high impact on the O&M costs, numerous studies have been conducted in recent years to better understand the tribological

behavior of such large size bearings operating under specific conditions that lead to severe tribological contact conditions, notably in terms of sliding kinematics and lubrication regimes.

1.2.5.1 Transient loadings and high sliding kinematics

Due to the excessive O&M costs associated to bearing failures in wind turbines, there seems to be a general precautious trend to over-size wind turbines REBs relative to the standard IEC 61400-4. In addition, while waiting for the connection to the electrical grid, it is not uncommon for REB to operate under low loads but nominal speed. In this situation, as the nD_m factor (rotational speed by the mean diameter in mm) may approach $2x10^6$ [22], the massive unloaded REs are subjected to significant inertial forces inducing high sliding and unexpected kinematics.

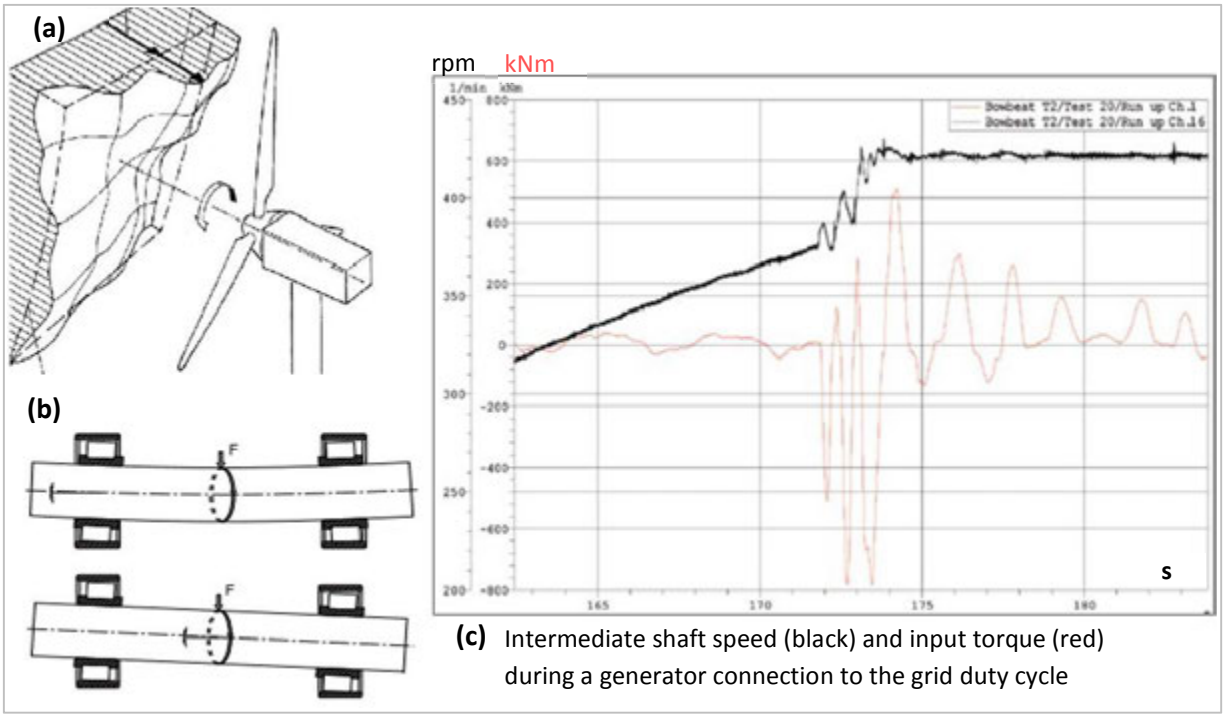

Fig. 1.23: Examples of wind turbine loadings affecting the REB tribological contacts: (a) wind fluctuations; (b) REB misalignments due shaft displacement (bottom) or bending (top); typical transient events in wind turbine gearboxes (from [9]).

Moreover, whereas REBs in the automotive or aerospace industries are usually designed to operate at nominal speeds and powers, wind turbine REBs are subjected to ever fluctuating torques due to uneven wind distribution versus three-blade design and to transient duty cycles like emergency stops and generator connections to the electrical grid (**Fig. 1.23**). Therefore, condition monitoring of a wind turbine gearbox has revealed that the intermediate shaft could live up to 3000 grid connections every year, each time inducing ~5 brutal torque reversals relative to inertial effects (-800 kNm to +430 kNm in less than 1 s) (**Fig. 1.23**). This results in ~15000 transient overloads pear year [9]. Consequently, considerable intermediate shaft displacements have been measured inside the relatively flexible housing (200 µm lateral movement and 550 µm vertical downward movement [9]). These displacements are often beyond the maximum radial clearance usually specified by the bearing manufacturer (~120 µm). Therefore, important REB misalignments frequently occur and lead to up to 200 µm of skew at the roller ends [9]. As a consequence of long periods at low loads and severe component mispositioning in the nacelle, wind turbine REB contacts are subjected to *high sliding kinematics*.

1.2.5.2 Severe lubrication regimes

Moreover, even though sophisticated oil circuits have been developed, wind turbine REBs are extremely complex to lubricate due to their large size and to the wide operating temperature ranges. With wind turbines expansion, the *main shaft* REB rotational speeds have been limited from ~25 to ~15 rpm so that the blade tip velocities do not exceed the speed of sound in air. Therefore those REBs are most commonly grease lubricated. In the *gearbox*, a unique oil is employed to lubricate a large variety of gear and REB contacts with shafts rotating from ~15 to ~1500 rpm. In order to ensure sufficient film thicknesses despite low rotational speeds, these oils commonly present high viscosities at ambient temperature (~320 mm^2/s at 40°C). Consequently, filter bypasses are often required during cold start to avoid starvation [10]. This increases the risk of particle contamination. In addition, it is not uncommon that wind turbines have to last long stand-still periods waiting for their connection to the electrical grid during which small oscillatory movements and vibrations tend to chase the lubricant out of the contact, especially for grease lubricated REBs. Therefore, wind turbine REBs often operate under *boundary or mixed lubrication regime* [5,7,95,96].

1.2.5.3 Multiple tribochemical drivers

To account for the severe lubrication regimes wind turbine REBs have to endure, wind turbine oils and greases are often based on semi-synthetic or synthetic base oils (PAO and PAG) that are highly additivated. This affects numerous tribochemical parameters. Wind turbine oils, for example, often contain high concentrations of *detergents* and *dispersants* to avoid additives fall-out [97] (section 1.2.3.2). However, these additives are usually commonly designed based on automotive industry feedbacks. Therefore, they might precautiously be blended in excess for wind turbine applications leading to unexpected detrimental effects (section 1.2.3.5). Moreover, the additive contents not only seem to enhance tribochemical cracking, but also affect considerably the lubricant *capacity to ingress water* [97] and its *electrical properties* [98].

Indeed, wind turbines often operate in humid environments near or on seas as well as in geographical deserts with wide day-night temperature gap. Hence, wind turbine nacelles are subjected to significant condensation. Function of their formulation, the lubricants are going to chemically ingress more or less water. Most lubricants have been provided additive packages to avoid the formation of micro-bubbles, which would deteriorate the lubricant film. In those cases, lubricants may be capable of ingressing up to 2000 wt.ppm of water content according to Karl Fisher analyses [97]. The water saturation limit is clearly increased by the presence of polar compounds such as blended esters, detergents, dispersants, and emulsifiers (Appendix B).

Finally, wind turbines REBs are often subjected to electrical potentials and/or currents [96,99]. Not only multiple types of electrical currents can occur [99] but electro-static charging may also occur due to the rotor frictional tribo-charging sites [98,100] and to lubricant tribo-charging as it goes through numerous filters [101]. Depending on the film thickness and lubricant dielectrical properties (themselves mainly function of the additive formulation and water content), electrical charges either accumulate, eventually leading to brutal arcing discharges with local welding, or induce an insidious electrical current enhancing lubricant decomposition and thus affecting local tribochemical reactions between the lubricant and the contacting surfaces [98].

In a wrap-up, wind turbine REBs are commonly affected by severe transient tribological conditions with important sliding kinematics, severe lubrication and significant tribochemical

aspects. As they are not yet fully mastered wind turbine REBs are hardly designed to sustain them for the moment.

1.3 Rolling element bearing failures

Although REB appear to be relatively simple mechanisms, their internal operating conditions, especially at tribological scales, are relatively complex. In service, REB failures may occur by different mechanisms as thoroughly referenced by Tallian [58]. REB failures commonly manifest themselves as a brutal increase in deflection, vibrational level, operating temperature or component seizure [18], each of them eventually leading to the others. Failures unrelated to rolling/sliding contacts, such as cage damage, fretting corrosion at shaft and housing fits, machining or mounting defects, seal swell, etc. might occur disparately. But the majority REB failures are inherently related to the RE - raceway tribological contact and are therefore the topic of the present section.

As schemed in **Fig. 1.24**, tribological failures in REB can be categorized in two types: *wea*r and *Rolling Contact Fatigue (RCF)*. *Wear* is generally defined as the removal of component surface material in the form of loose particles during service [58]. As a surface failure, *wear* most often leads to surface deterioration with an increase of vibrational levels and operating temperature. *RCF* corresponds to surface or subsurface initiated cracking of the material due to the repeated cyclic rolling contact stresses in the component. It most often leads to brutal and deep surface removals, named spalls, or component seizure. "*Surface*" is understood as the layer from the extreme surface of the material down to ~10 μm below. *Wear* and *RCF* are widely considered as two competing mechanisms that highly depend on the tribological factors such as the surface and material quality, contact stresses, kinematics, lubrication, contamination, and environmental parameters [40,67,102,103]. On one hand, *wear* usually appears gradually as soon as severe tribological conditions are met. It can therefore be considered as low to mid-cycle fatigue. On the other hand, *RCF* tends to manifest itself brutally after a long steady state incubation period associated to material shakedown and microstructural alterations. It can thus be assimilated to high-cycle fatigue. At any time, both phenomena can be excessively enhanced by tribochemical drivers, thus reducing drastically the service life.

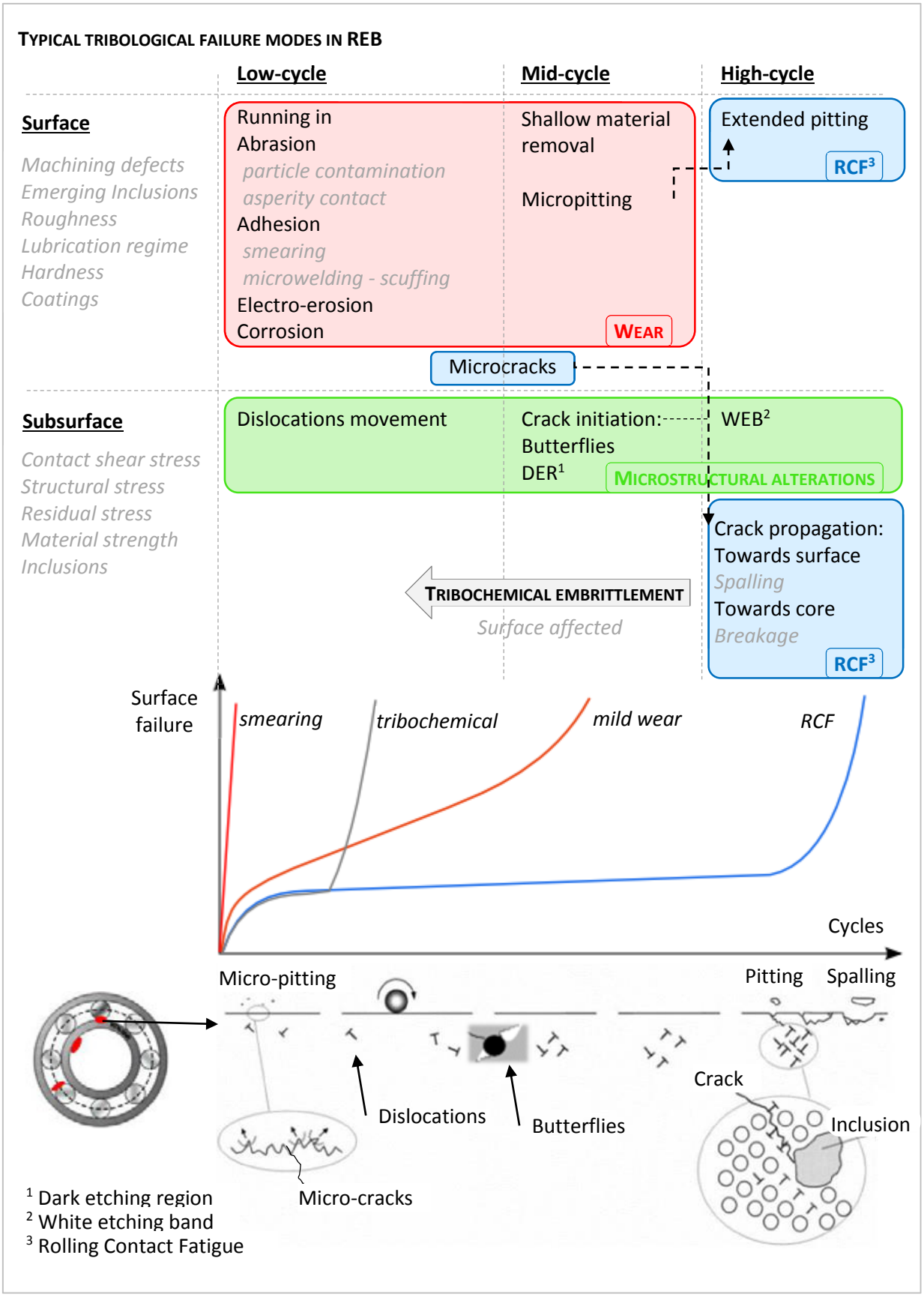

Fig. 1.24: Overview of the different tribological wear and RCF associated failure modes and microstructural evolutions in REB contacts function of service life (bottom image adapted from [67]).

1.3.1 Surface distress and wear

1.3.1.1 Microstructural surface distress

Prior to surface material removal, *surface distress* usually occurs at microstructural scales which is not considered as a fatigue phenomenon. Tallian narrowly defines *surface distress* as the plastic flow of surface material due to the application of high normal forces in asperity dimensions [58] and proposes that *glazing* corresponds to incipient surface distress [96]. In a way, this definition could be generalized to all microstructural surface damages that tend to initiate *wear*. If surface distress is not usually considered as related to Hertzian stress and material properties, there are many tribological mechanisms which result in this kind of damage [19]:

- Plastic flow due to surface asperities acting as local stress raisers in the vicinity of the surface layer, especially in case of partial breakdown of the lubricant film (section 1.2.1.2) where micro-welding can occur at metal to metal contacts at asperities.
- Plastic flow due to excessive friction in severe lubrication regimes (section 1.2.1.2).
- Plastic flow due to particle contaminated lubricants or high static loads that can cause raceway indentations [54,67,104–107] (**Fig. 1.13**) and *true brinelling* respectively. Particles can come from the environment or from wear debris.
- Plastic flow due to pulsating or oscillating *false brinelling* (also referred to as fretting) resulting in raceway marks acting as stress raisers and fresh surface available for tribochemical reactions.
- Formation of pits and excessive surface embrittlement due to electric arcs, electrochemical reactions, emerging inclusion chemical dissolution and corrosion (**Fig. 1.25**)[29,108,109]

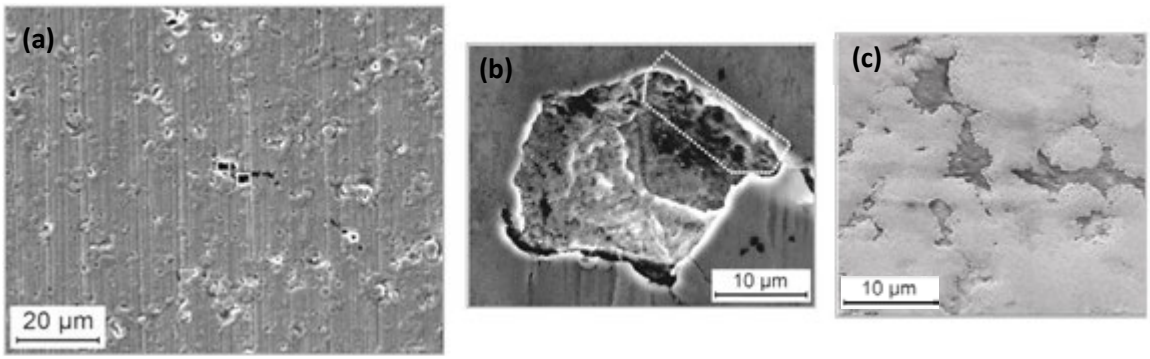

Fig. 1.25: Typical SEM analyses of tribochemically induced micropits on a IR raceway ((a-b) from [29]); Tribochemical surface distress of the tribofilm due to water contamination of the lubricant (from [109]).

It is necessary to keep in mind that REBs are subjected to numerous internal contacts (red dots in the REB illustrated in **Fig. 1.24**). Each of them can therefore be a source of wear debris that may affect the whole mechanical system via the circulating lubricant. Moreover, surface distress is often considered as a self-propagating phenomena eventually leading to wear as the surface roughnesses are gradually increased.

1.3.1.2 Typical macroscopic damages

In REB several wear mechanisms can thus be activated as microscopic *surface distress* develops and accumulates [45,58,67,104].

a. Mild Wear

For severe lubrication regimes, as asperities come in contact, surface distress usually leads to consequent surface material removal, named *mild wear,* dominated by mechanical and tribochemical events (**Fig. 1.26**). If contact stresses are high enough, permanent deformation and fracture of asperities are inevitable. In that case lubrication has little impact even when enhancing tribofilm formation [75]. If contact stresses are somewhat lower and if the lubricant is well formulated, a protective tribofilm is gradually formed limiting mild wear [75]. Tallian indicates that the worn surface to the naked eye appears "featureless, matte, and nondirectional" and that surface characteristic grinding marks are worn away [58]. Mild wear can be of three types [58,67]:

- *Adhesive*: under poor lubrication and sliding kinematics, metal to metal asperity contact can lead to micro-welding and local adhesion between the contacting surfaces
- *Abrasive* :high roughness or presence of hard particles in the lubricant can act as stress raisers and cause micro-abrasion in case of sliding kinematics
- *Tribochemical* :corrosive, electro-chemical or purely chemical reactions embrittle the surface leading to easy but very shallow material removal

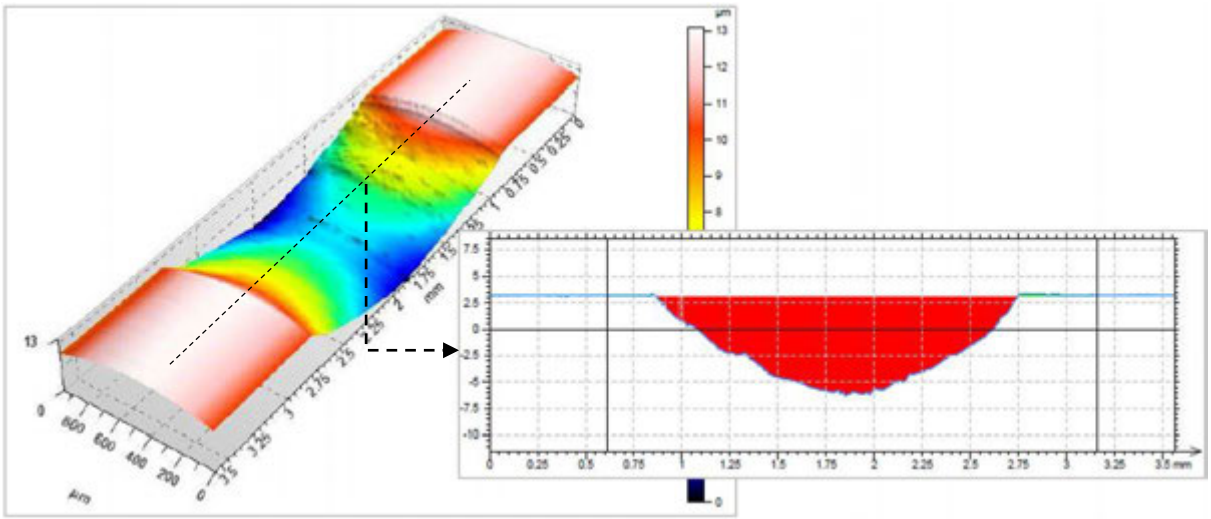

Fig. 1.26: Significant mild wear profile of a 100Cr6 driver roller after 10^6 cycles with important material removal measured by SENSOFAR PLu neox optical profilometer (Appendix H ref TDM09_04).

Mild wear is often associated to the *running-in* period and is considered as a benign form of wear. Indeed, depending on the rolling conditions and the initial surface roughness during this critical *running-in* period (**Fig. 1.24**), the surface roughnesses can either be enhanced or decreased by mild wear, leading either to severe deterioration and advanced wear (commonly shorten to *wear*) or to a stable incubation period of crack nucleation (**Fig. 1.24**). It should also be noted that mild wear can actually be beneficial to prevent the propagation of surface microcracks [103,110].

b. Smearing

Smearing corresponds to a consequent increase of adhesive mild wear affecting both contacting surfaces due to excessive skidding that eventually lead to irreversible premature failure [18,111]. In case of *smearing,* adhesive mild wear gradually increases surface roughness. Hence, lubrication is more and more severe and high flash temperatures occur in the contact, thus reducing the lubricant viscosity. Therefore partial or complete breakdown of the lubricant film occurs leading to micro-welding of the asperities in a couple of cycles (**Fig. 1.27**). When the temperature increases brutally and consequent material transfer occurs smearing is more commonly referred to as *scuffing* or scoring, which end in complete and sudden failure of the REB.

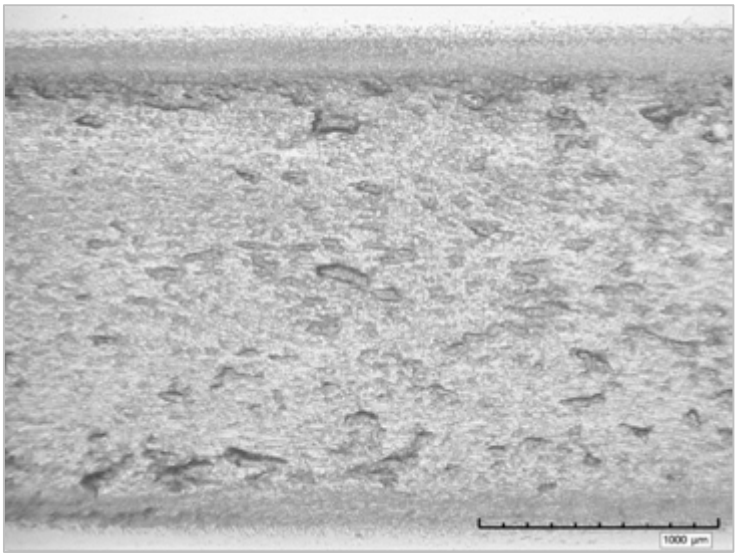

Fig. 1.27: Optical image of advanced smearing on a 100Cr6 driver roller (Appendix H ref TDM03).

c. Fretting

Fretting corresponds to an adhesive wear mechanism caused by vibrational oscillatory movements of a few microns applied to a loaded REB. They progressively squeeze the lubricant out of the contacts. In this case, the relative motion of the contacting surfaces is unsufficient for lubricant replenishment as the movement amplitude is significantly smaller than the contact width. *Fretting* starts by a short incubation period where preexistent protective oxide layer is progressively worn out, leading to mild adhesion. This phenomena is often referred to as *false brinelling* in comparison to the dented scar left by *true brinelling* in static and highly loaded REB [112]. False brinelling can occur either due to high frequency and small amplitudes of pulsating loads and/or oscillatory motion. Tallian also defines *false brinelling* as *fretting wear* in Hertzian contacts as opposed to common *fretting* in conformal contacts [96]. As *fretting* progresses, it is often associated to a mixt of adhesive and abrasive wear due to the accumulation of debris that inhibits the contact lubrication, which eventually leads to the formation of side surface cracks at the border of contact [113]. Moreover, as *fretting* develops, wear rate increases drastically leaving highly reactive fresh surface and steel debris continuously available for tribochemical reaction such as corrosion. At this stage, fretting is often called by extension *fretting corrosion* due to the reddish deposits visible at the surface or on the shafts.

d. Surface microcracks

Incipient *surface microcracks* can be initiated in the surface top layer (**Fig. 1.28**) when the surface normal and/or shear stresses overcome the crack nucleation threshold. This occurs notably at preferential sites such as asperities, transverse grinding marks, dent ridges or emerging microstructural inhomogeneities (**Fig. 1.4** (b))[114,115]. This is specifically the case of hardened steels as their poor ductility does not allow them to accommodate microstructural plastic flow at the surface due to stress concentrators as dents [55–57,105–107] or due to high surface traction [110,115]. Studies have demonstrated that incipient surface microcracks are initiated very early in service life, as soon as 10^5 cycles [110,114]. Sliding kinematics have a great influence on microcrack initiation and orientation as they affect surface tensile stress field [114–116] (**Fig. 1.28**). It has been observed that incipient microcracks often present an angle 15° to 40° versus the surface depending on the friction force. Propagation is favored on the follower surface where friction and over-rolling are opposite, thus allowing cycles of crack opening, oil seepage and oil entrapment in the cracks as the contact moves along (**Fig. 1.28** (a)) [57,116]. Anyhow, surface microcrack formation is inherently in competition with wear mechanisms since the latest could continuously wear away the microcracks.

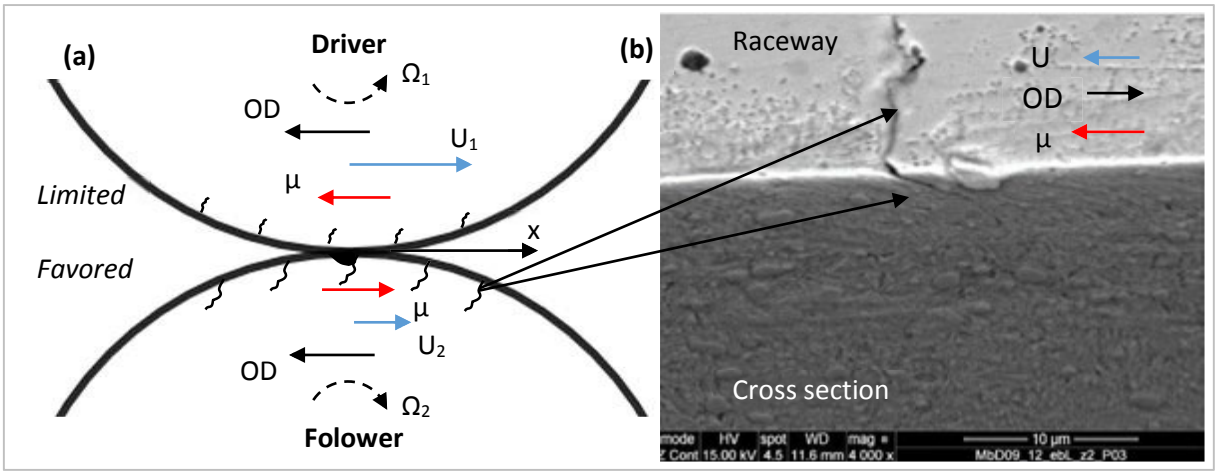

Fig. 1.28: (a) Scheme of microcrack development function of the contact kinematics and friction forces illustrating that surface microcrack propagation is favored on the follower surface; (b) SEM analysis of a 100Cr6 follower roller revealing a typical incipient surface microcrack (Appendix H ref TDM09_12).

e. Micropitting

Once surface microcracks are initiated, several parameters influence surface crack behavior: the material properties (hardness, toughness, cleanliness, and residual stresses) but also the tribological conditions (lubrication regime, contact stresses, friction, temperature, and tribochemical assisted cracking) (**Fig. 1.28** (a)) [110]. Indeed, all these parameters influence surface microcrack propagation into either surface limited *micropitting* or deep fatigue propagation leading to surface initiated spalls (**Fig. 1.24**). *Micropitting* refers to the shallow craters ($10<\zeta<50$ µm, scale of surface defects) that develop at asperity scales due to microcracks coalescence in the top layer of the surface [48,103,117]. *Micropitting* is considered as mid-cycle fatigue. It eventually leads to *flaking* (extended shallow micro-pits) or *peeling* (extended very-shallow micro-pits with a brittle aspect).

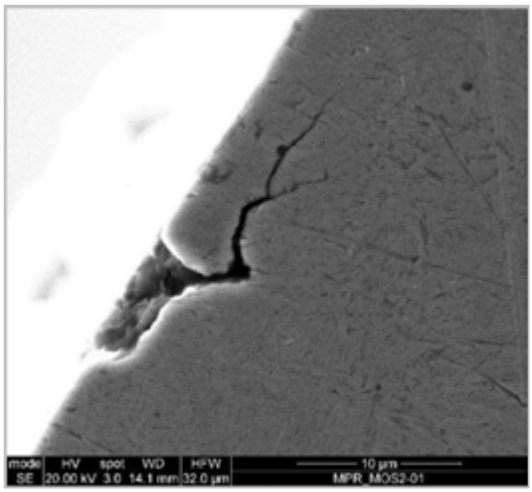

Fig. 1.29: SEM analysis of a typical incipient micropit obtained on a 100Cr6 roller.

1.3.2 Rolling contact fatigue

A REB with smooth contacting surfaces operating under full-film lubrication regimes in a neutral environment should not be subjected to *surface distress* and *wear*. However, even under those idealistic contact conditions, repeated loading of the contacting surfaces over a certain material threshold previously defined as H_1, inevitably leads to surface and subsurface microstructural damage accumulation, referred to as *rolling contact fatigue (RCF)*. As opposed to classical structural fatigue or wear, RCF occurs in a relatively small volume of stressed material with highly localized pressures of a few GPa and high hydrostatic stress component. RCF thus corresponds to a high cycle cracking phenomenon [102] triggered by repeated contact stresses that vary for each point of the material as the contact goes along. For example, in REB contacts, the principal stress axes constantly change during a stress cycle so that the direction of maximum shear stress also keep changing as opposed to structural mechanicals [118]. Even though some high cycle surface initiated failures can be associated to RCF, the latest is most often associated to subsurface crack initiation and propagation (**Fig. 1.24**). Indeed, RCF develops with the accumulation of subsurface microstructural alterations, ending either by the sudden and unstable formation of deep spalls at the raceway, or either by full component seizure depending on the structural stress state (**Fig. 1.24**).

1.3.2.1 Three-stage rolling contact fatigue

It has been experimentally observed that the subsurface microstructural changes in the Hertzian region undergoing RCF can be partitioned into *three stages* referred to as *shakedown, steady state and instable RCF* (**Fig. 1.24**)[40]. *Shakedown* covers the running-in response of the material during the first ~10^3 cycles where limited plastic micro-straining occurs, thus conditioning the material to the contact stresses (**Fig. 1.30**). During the *steady state* period, as the material is preconditioned, further plastic deformation is less easy and an elastic response to contact stresses is assumed. The *steady state* duration, from ~10^6 to ~10^9 cycles, highly depends on the operating conditions. Nevertheless, during this long incubation period, microstructural decay progressively accumulates and the material gradually loses its elastic properties. Therefore, plastic deformation, yield strength decrease and instable crack nucleation start to occur, corresponding to the beginning of *instable RCF stage*. This three-stage to crack nucleation accounting for microstructural damage

accumulation and instable propagation is in agreement with the RCF evolution curve depicted in **Fig. 1.24**.

During RCF development, because of the subsurface micro-plastic flow, for example due to retained austenite decay, the local variation in material volume leads to subsurface *residual stresses buildup*, usually compressive in nature. This phenomena is assumed to occur mainly in through-hardened components devoid of initial protective compressive stresses found in case-hardened components. Indeed, X-ray diffraction (XRD) analyses on 100Cr6 REB rings, after RCF testing with Hertzian pressures above 2.5 GPa, have revealed a gradual compressive hydrostatic residual stress buildup (**Fig. 1.30** (1)) [40,119–121]. The residual stress profiles may be used to estimate the maximum Hertzian pressure by locating the maximum residual stress depth at the center of contact [119,120]. Additionally, depending on the shape of the residual stress profile, it is possible identify whether the REB was operating under RCF or surface distress conditions (**Fig. 1.30** (2) (3)). More details about XRD analysis and residual stress assessment in case of though-hardened bearing steels are available in [29].

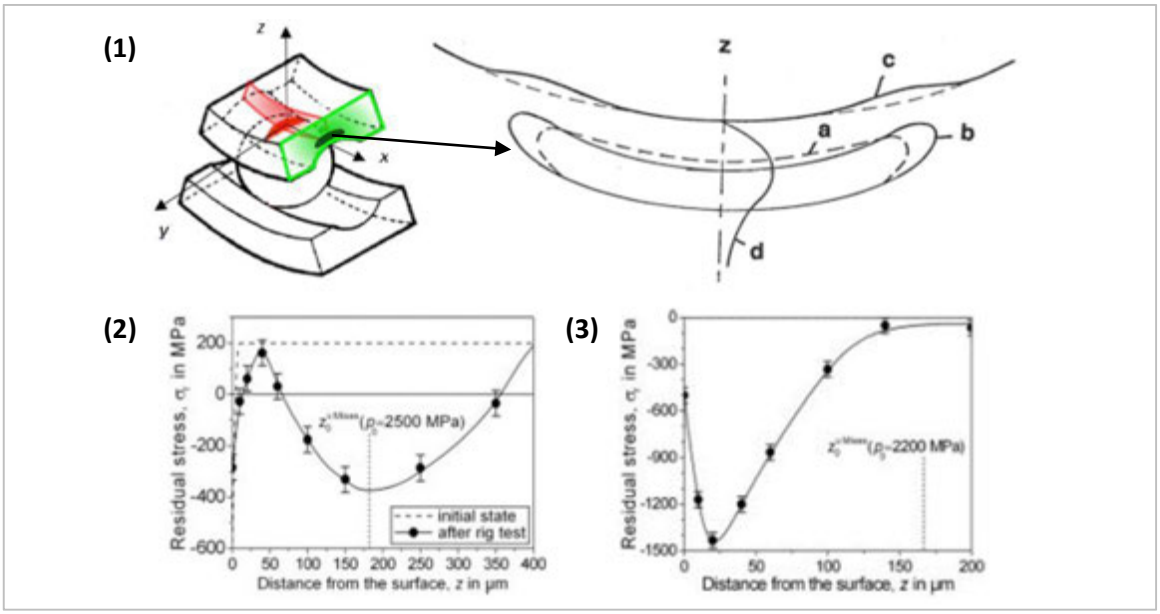

Fig. 1.30: (1) Schematic illustration of the micro-plastic flow in the Hertzian region beneath the rolling contact surface: the initial volume stressed above the yield limit (a) changes its form (b) causing an elevation of the rolling track (c) and residual stresses build-up exhibiting a profile (d) [40]; depth profile of residual stress measured by XRD analysis on: (2) a martensically hardened 100Cr6 TRB before and after rolling contact fatigue, (3) a DGBB operating under a similar contact pressure but with a heavily contaminated lubricant inducing high surface distress [120].

1.3.2.2 Conventional microstructural alterations

As the material endures high cycle fatigue, contact stresses gradually provokes dislocation movements in the lattice, thus leading to micro-plastic strain and microstructural alterations for loads above a certain threshold associated to H_1 (~2.5 GPa for 100Cr6 through hardened steels) (section 1.1.1.3)[25,27]. This is in agreement with the asymptote of the dashed line on the Schlicht diagram (**Fig. 1.31**) [122–124]. This diagram depicts the gradual alterations of the hardened steel matrix function of the number of cycles and maximum Hertzian pressure. It suggests that dark etching regions (DER) alterations are precursor of subsequently occurring white etching bands (WEB) [122,123]. Aside to these homogenous microstructural changes, discrete microstructures

(referred to as *butterflies* as to their specific morphology) tend to develop progressively at the highly stressed interface between the steel matrix and material inhomogeneities. All those microstructural changes are revealed by metallographic cross sections etched with Nital (2% of nitric acid in ethanol) commonly observed by reflected light optical microscopy (LOM) and/or SEM analyses. Etching corresponds to the corrosive attack of material. It reveals steel microstructure by contrasting the presence of material defects and phases. For example, refined grained phases will resist to etching and thus appear white under reflected light, contrarily to altered microstructures that will diffuse reflection as they are roughened by etching and appear dark.

Graphical identification adopted for the entirety of the thesis:

- Axial cross section bordered in green
- Circumferential cross sections bordered in red
- Zooms bordered with dashed lines

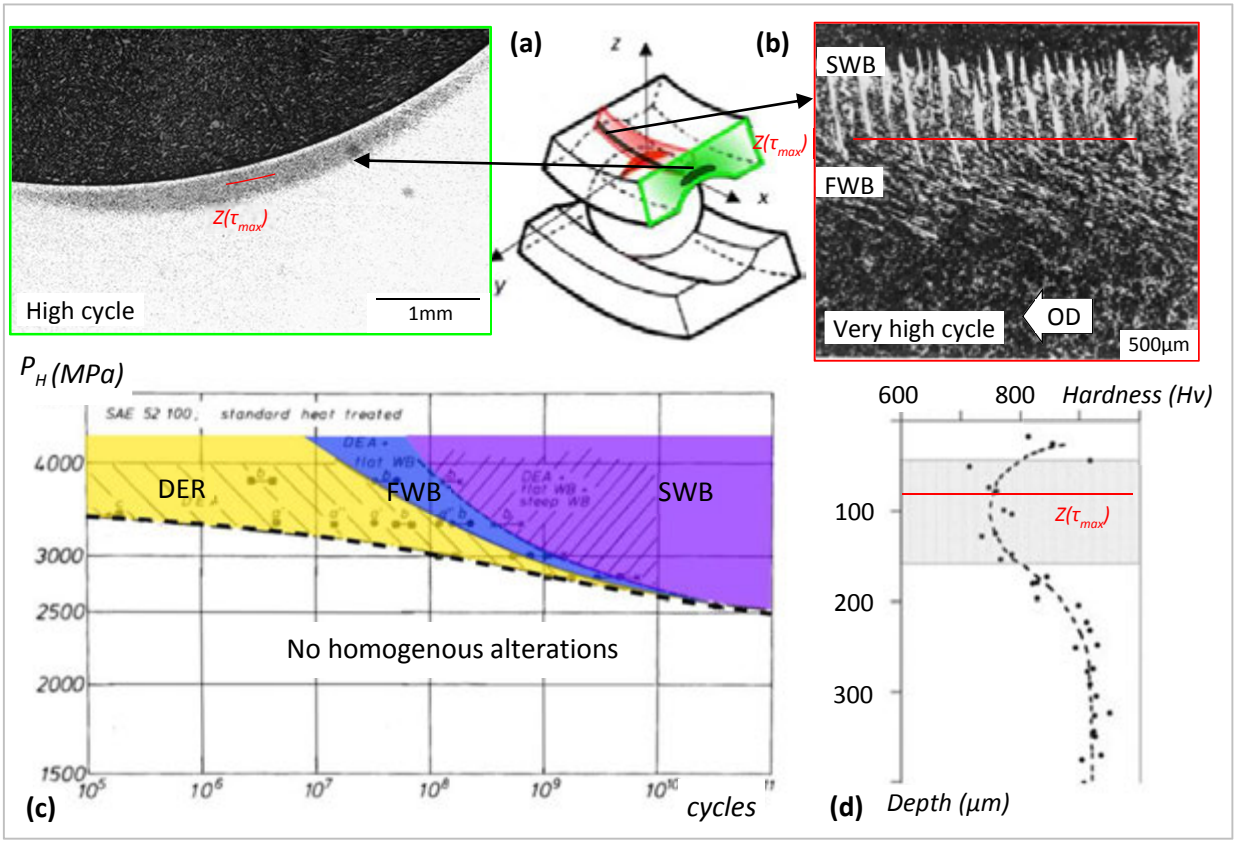

Fig. 1.31: (a) Etched axial cross section LOM of an ACBB IR after $4x10^7$ cycles at 3.5 GPa revealing the formation of DER at depths coherent with the maximum shear stress depth; (b) Etched circumferential cross section LOM of an IR revealing flat (30°) and steep (80°) WEBs in the maximum shear stress region [122]; (c) Schlicht diagram repositioning the microstructural changes versus the contact pressure and the number of cycles (adapted from [122]); (d) Microhardness profile of a through-hardened 100Cr6 subjected to high cycle RCF with the presence of DER and WEBs in the shaded band (adapted from [19]).

a. DER

Dark etching regions have been named so as they appear dark when observed under LOM after Nital etching. They are considered to be the first microstructural alterations occurring in the

Hertzian zone during RCF [122]. *DER* consist of dark microbands that do not possess any preferential orientation versus the raceway and that gradually appear around the depth of maximum shear stress with a well delimited upper boundary at ~0.25*a* from the surface and a more diffused lower boundary relative to the shear stress profile asymptote at ~2.5*a* (section 1.2.1.2) (**Fig. 1.31** (a)) [19]. *DER* have been characterized as mechanically tempered martensite due to carbon migration towards dislocated regions induced by microplastic straining. This alteration process results in material softening (~550-600 Hv) compared to the bulk structure, similarly to an over-tempering heat treatment [19,118,124].

b. WEB

White Etching Bands have been named after their remarkable directionality, when observed on a circumferential point of view, and after their white appearance under LOM due to their refined structure that present a high resistance to etching (**Fig. 1.31** (b)) [19,122,125–127]. *WEBs* appear at very high cycle or highly loaded RCF. They develop at depth of maximum shear stress, within pre-existent DER ((**Fig. 1.31** (b-c)). If the WEB microstructure is fairly well characterized as carbon-depleted refined ferrite phase, regularly separated by formation of induced plate-like carbides, it is not yet clear why deformation localizes and results in patterns [19,124,127]. The first WEBs to occur present an angle of ~30° versus the surface and are often named *Flat White Bands (FWB)*. FWB further develop in much thicker and noticeably longer *Steep White Bands (SWB)*, with an angle of ~80° versus the surface (**Fig. 1.31** (b)). It has been observed in several studies that the WEB region below the surface, similarly to DER, presents a lower hardness than the bulk material.

As *WEBs* are relatively soft and not associated to cracks, it is important to distinguish them from the carbon-saturated and hard *white etching microstructure* that form when either internally fractured surfaces, e.g. in the vicinity of inclusions as described thereafter [19], or unconnected surfaces rub energetically against each other, e.g. *white etching layers (WEL)* in the wheel-railway contact [128–130] or in high speed machining [131,132]. WEB formation mechanisms are reported in [40,124,127]. Nowadays, WEBs tend to be less commonly observed in REB expertise thanks to progress in REB designs to avoid prolonged and highly loaded RCF.

c. Butterflies

Aside the gradual development of homogenous and continuous microstructural alterations, the presence of inhomogeneities in the steel matrix act as local stress raisers that ease localized microstructural alterations and crack initiation during RCF. Inclusions, for example, depending on their differences in elastic modulus and/or coefficient of thermal expansion, often present a weak interfacial energy with the steel matrix that act as preferential sites for the development of *butterflies*. These alterations have been named after the two *White Etching Area* (WEA) "wings" that develop at ~45° of the surface along the OD bordering microcracks usually initiated at the inclusion-matrix interface (**Fig. 1.32**) [19,27,30,114,125,133,134]. Given their orientation and depth below the raceway, the development of *butterflies* have mainly been associated to the maximum shear stress τ_{max}. A threshold contact pressure H_1 of ~1.5 GPa has been proposed to prevent any plastic micro-strain and micro-crack nucleation at inclusion – matrix interfaces (section 1.1.1.3) [27], which is in agreement with the maximum shear stress threshold for butterfly formation of 400 MPa proposed in [30].

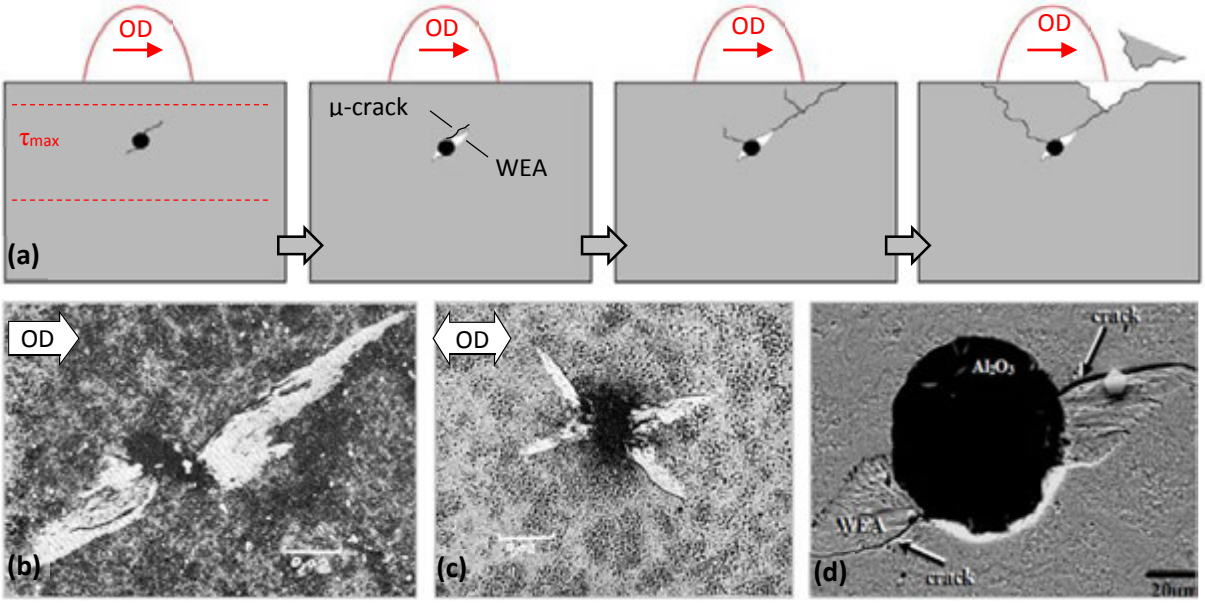

Fig. 1.32: (a) Development of a butterfly in the Hertzian shear stress zone leading to subsurface initiated spalling; (b) Typical development of the butterfly wings at ~45° versus the surface in the direction of OD [125]; (c) Double-winged butterfly in case of alternating OD [125]; (d) Typical SEM analysis of an incipient butterfly composed of lateral micro-cracks and WEA (from [124]).

The *butterfly wing WEA* has been characterized as nano-grained ferrite supersaturated in carbon product of a mechanical carbide dissolution. They present a micro-hardness 30-50% higher than the matrix (~1000-1300 Hv), similarly to WEL and contrarily to WEB [19,133,134]. TEM analyses have revealed the presence of smaller grains (10 – 50 nm) close to the main micro-crack and larger grains (50 – 100 nm) close to the opposite butterfly boundary [133,134]. This suggests that microcracks develops first, eventually leading to WEA formation by high local shearing and crack rubbing in a process similar to WEL. This conjecture is however still discussed [15,19,133,134]. As globular oxides found in oxide mono-inclusions or sulfide-oxide duplex are very hard and present a weak interface with the matrix comprising numerous micro-voids, they are often associated to *butterflies* while other inclusion types such as manganese sulfides (MnS) seldom initiate fatigue cracks under usual RCF conditions (section 1.1.1.3 for different inclusion types) [19,135].

While *butterfly* initiation seems to be perceptible at as soon as 10^5 cycles for contact stresses above 3 GPa [19], *butterfly* propagation has been observed to be relatively slow [19], in correlation with the incubation period of RCF development (**Fig. 1.24**). Nevertheless, this statement highly depends on what is called initiation and propagation… Does imitation correspond to the first incipient persistent slip band (PSB) at crystallographic scales, to first subsurface crack at the grain scale or to the first visible surface crack at the asperity scale? In this thesis, it is understood that initiation corresponds to the *first subsurface crack detectable by SEM analysis* and that propagation corresponds to subsurface cracking progressively reaching the raceway. In case of highly loaded RCF and poor steel cleanliness, *butterflies* might eventually lead to subsurface initiated deep spalling of the contacting surfaces and complete REB failure (**Fig. 1.32** (a)). However, unfailed bearings may contained high densities of butterflies and fore-described homogenous microstructural alterations (DER, WEB) within their stressed volume.

1.3.2.3 Typical macroscopic damages

REB failure is often detected by a sudden increase in vibrational level or in operating temperature synonymous of a sudden surface material removal or, worse, full component seizure. In case of RCF, REB macroscopic damages occur after a long incubation period (**Fig. 1.24**) and can be either surface initiated by microcracks (section 1.3.1) or subsurface initiated by gradual microstructural alteration and butterflies (section 1.3.2.2) [45,58,103,114].

a. Surface initiated

Surface initiated fatigue failures, mainly due to faulty operating conditions inducing important surface distress (section 1.3.1), can be associated to *RCF* in case of high cycle *macro-pitting* and development of *surface micro-crack* towards the core of the component eventually leading to deep *spalling*. *Macro-pitting* corresponds to a high-cycle progressive extension of micro-pitting leading to extended surface *flaking* with shallow craters also referred to as *spalling* since the surface is so deteriorated that it is hard to distinguish them from deeps spalls [103]. *Surface initiated RCF* also occurs for example with the typical *V-shaped spalls* that initiate on a surface dent in case of highly contaminated lubricant, and propagate below the raceway with an angle of ~30° leading to *shallow spalls*. These shallow spalls might also eventually propagate deeply down to the maximum shear stress region where compressive residual stress and inclusion interactions make them branch back to the surface to form *deeper spalls* (**Fig. 1.33**) [53–57].

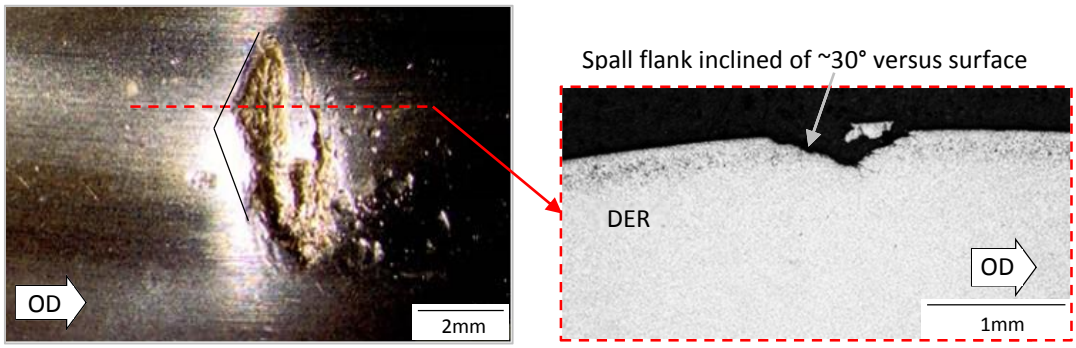

Fig. 1.33: Topview and corresponding circumferential metallographic cross section of a surface initiated spall on an ACBB IR during after ~50x10⁶ cycles of in-house testing: the V-shape indicates the position of the initial detrimental dent.

b. Subsurface initiated

During high cycle RCF, subsurface microcracks nucleate at material inhomogeneity interfaces or within the fore-described microstructural alterations and might propagate progressively towards the surface, leading to sudden surface material removal called *spalls* [58] (last step of **Fig. 1.32** (a)). As opposed to surface initiated spalls (**Fig. 1.33**), *subsurface initiated spalls* present an *oval shape* and are most often *deep*, as they initiate around the maximum shear stress depth $z(\tau_{max})$ (**Fig. 1.34**). Moreover, when observed on a circumferential cross section they present steep angled edges and a flat bottom mostly parallel to the surface (**Fig. 1.34** (c)). Subsurface initiated spalls tend to propagate in the direction of OD as secondary cracks preferentially develop on the down-line spall edge (**Fig. 1.34**) [136] and eventually lead to complete deterioration of the REB with increased vibrational levels and temperatures (**Fig. 1.34** (b)).

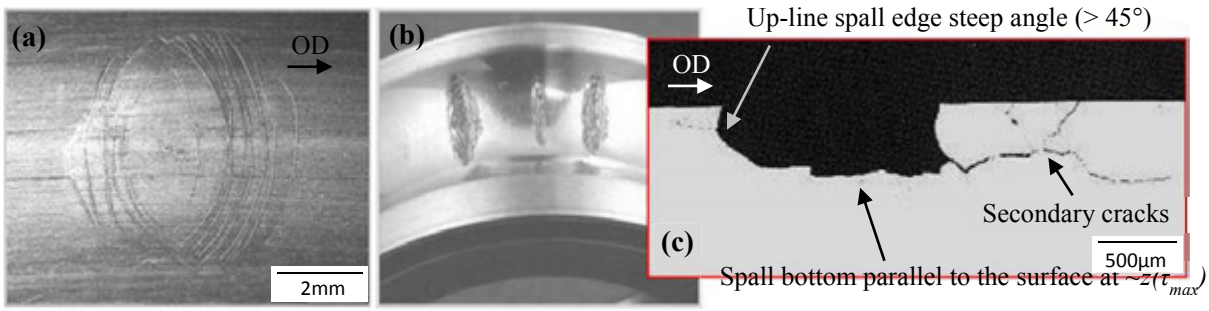

Fig. 1.34: (a) Top-view of a developing subsurface initiated spall presenting a typical oval form with more incipient cracks developing on the down-line edge; (b) Propagated subsurface initiated spalls on a DGBB IR; (c) Circumferential cross section revealing the typical morphology of a subsurface initiated spall.

1.3.3 Bearing life assessment

Tribological contacts of REBs in service are often subjected to a variety of operating conditions and an inevitable scatter in material and lubrication properties, that both significantly affect the REB failure mode and life. On one hand, *surface distress* and *wear* failure modes are mainly attributed to faulty operating conditions that have to be identified and mastered to ensure a robust REB design, e.g. boundary lubrication for which predictive tools have been established (section 1.2.3.3). On the other hand, considering the fore-described *surface and subsurface RCF* failures modes, statistical and physical models have been established to help engineers predict REB fatigue life and design long lasting REB for the stated operating conditions.

1.3.3.1 Competition between surface distress and RCF

As tribology is inherent to REBs, the main macroscopic failure modes could be roughly categorized in either surface distress or RCF, which are both greatly affected by many influent "*tribo*-drivers", so that REB life is dependent of:

- *Tribo-* mechanics: kinematics, stresses and material strengths, particle contamination, vibrations, etc.
- *Tribo-* physics: thermal and electrical properties of the media, surface roughness and reactivity, lubricant rheology, etc.
- *Tribo*-material: chemical composition and diffusion properties, heat treatment, cleanliness, voids, etc.
- *Tribo*-chemical: environmental acid or water contamination, lubricant additives, tribofilm formation, diffusivity of chemical elements in material, etc.

Depending on these "*tribo*-drivers", the tribological failure mode of REBs can vary significantly. Nowadays, as (1) steels are getting cleaner, (2) improved tools lead to better REB designs, and (3) lower viscosity and highly additivated lubricants are employed to lower power losses, up to 70% of operational failures are attributed to surface distress while only 10% REBs fail due to sub-surface initiated fatigue [19]. Surface distress and RCF are thus two competing failure modes as they do not occur in the same location and at the same time during REB service life (**Fig. 1.35**).

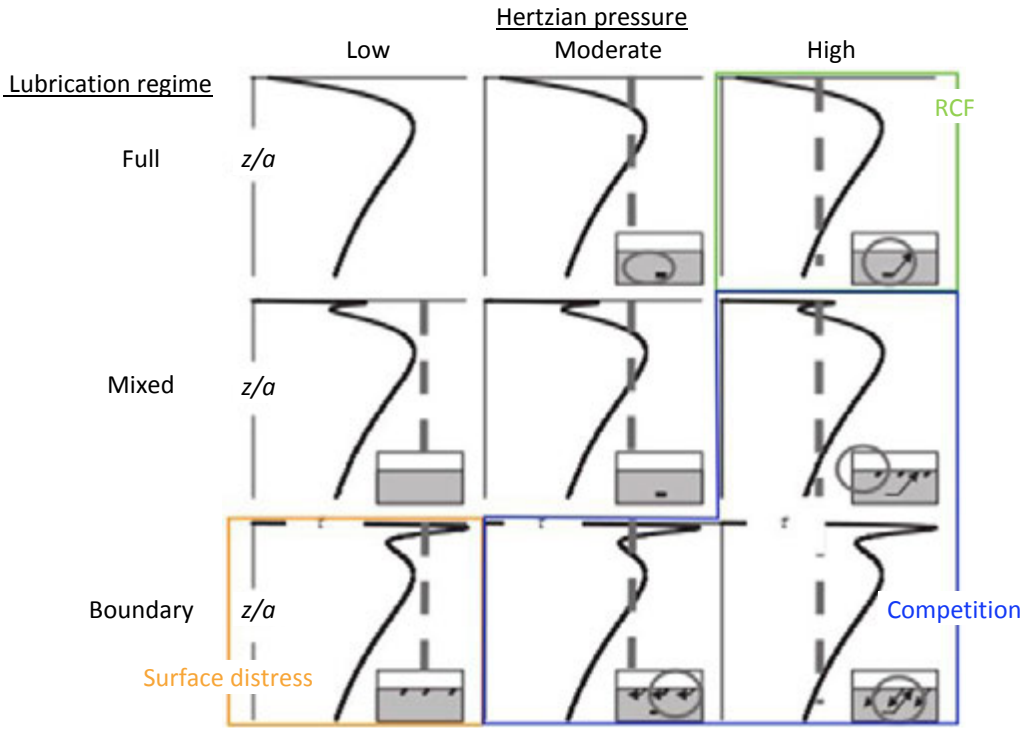

Fig. 1.35: Competition between surface distress and RCF failures modes of REBs depending on the tribological operating conditions and induced subsurface shear stress (adapted from [114]).

In REBs, surface distress does not correspond to a fatigue mechanism and is often considered as preventable by ensuring high quality finishing, proper lubrication, prevention of contaminants and a wholesome environment. Therefore, models have been and are being developed mainly focusing on RCF failure modes to better understand and estimate REB life. Indeed, assessing REB life versus RCF remains complex as it is determined by the damage accumulation mechanism that will prevail depending on the operating conditions and material properties. In addition, even if the latest were supposedly set constant, there would still be a lifetime distribution as to the random aspect of crack propagation and heterogeneous material microstructure that is best described by the probabilistic and physical approaches of RCF predictive models that have been developed over the years.

1.3.3.2 Probabilistic engineering models

REB *service life* or *fatigue life* can often be defined as the number of revolutions before raceway irreversible failure due to high-cycle fatigue as depict by the blue curve in **Fig. 1.24**. Due to the specific nature of RCF compared to structural fatigue, most work in determining REB life has been based on empirical results of extensive RCF testing led in the past century mainly for the automotive industry. If a population of apparently identical REB is tested under identical load, speed, lubrication and environmental conditions, the REB lifetime is statistically dispersed according to a Weibull distribution due to inevitable scatter in aforementioned tribological parameters. For example, there are inevitable material variations within the same steel batch, between different batches from the same manufacturer and between steels within the same specification range but supplied from different sources [19,23].

Lundberg and Palmgren [137] provided the first theoretical basis for REB life probabilistic models under the assumption of ideal operating conditions so that the contact stresses are well

approximated by Hertz' theory and that cracks are supposed to solely initiate due to fatigue in the subsurface zone of maximum alternating orthogonal shear stress τ (section 1.2.1.2). They applied the Weibull statistical fatigue distribution to the Hertzian stressed volume, *V,* to express the REB probability of survival to subsurface initiated fatigue, *S,* to a certain number of stress cycles *N*, as follows,

$$\ln\left(\frac{1}{S}\right) = A\frac{\tau^c N\, V}{z^h}$$

- *A being the material constant;*
- *c and h being Lundberg and Palmgren empirical coefficients.*

This formulation accounts for the fact that a probability of survival of 100% is nil and that the probability of finding weaker points is enhanced in large bearings as the stressed volume is larger. Lundberg and Palmgren [137] additionally simplified the previous equation by substituting τ, $z(\tau_{max})$ and V in terms of Hertzian parameters (section 1.2.1.1). Therefore, the L_{10} fatigue life of a REB, being the number of loading cycles in millions to which 90% of the REBs are predicted to survive for a given load condition (i.e. the REB probability of survival with a 90% reliability), could be expressed to an exponent of the REB loading. Extensive details of the developments are available in [17,18]. Hence,

$$L_{10} = \left(\frac{C}{Q}\right)^p$$

- *C being the dynamic load capacity of the REB, i.e. the load on the bearing that results in an estimated lifetime L_{10} of 10^6 cycles (available in catalogues);*
- *Q being the equivalent radial load applied on the REB: $Q=XF_a+YF_r$ (X and Y are constants recommended by tables provided by the American National Standard Institute (ANSI) commonly available in REB catalogs);*
- *p being an exponent that varies according to the bearing geometry* [17]
  - *p=3 for ball REBs*
  - *p=10/3 for roller REBs.*

In later years, this original formulation was found to underestimate REB fatigue life as it did not account for the progress in technologies affecting REB design, material, lubrication, machining, surface treatment, etc. It was indeed based on old empirical data achieved on basic through-hardened air-melt 100Cr6 bearings. Therefore it has been progressively modified considering generalization work provided by Ioannides, Harris, Zaretstky among others [17,138–143]. For example, empirical coefficients have been added to account for the degree of reliability, steel cleanliness, lubrication regimes, speeds, etc. Also, other critical stresses than the maximum orthogonal shear stress have been employed, like the Tresca shear stress or the equivalent Von Mises stress (section 1.2.1.2). It is indeed discussed in the literature which material stress criteria is most representative in predicting RCF life: orthogonal shear stress used in the Lundberg and Palmgren approach or the equivalent Von Mises stress. There is indeed quite a paradox as, (1) XRD analysis commonly reveal that residual stress build-up conforms to the depth of the maximum Von Mises stresses [29], whereas (2) RCF microstructural alterations occur mainly at the depth of the alternating orthogonal shear stress (section 1.3.2). Recent studies have also proposed an endurance limit for which infinite life could be achieved as suggested by the Schlicht diagram (**Fig. 1.31**),

based on thresholds similar to H_1 and crack arrest models [144,145]. A thorough review of these models is provided by [118].

The fore-detailed Lundberg-Palmgren equation and additional empirical developments of corrective coefficients are the basis of the bearing life standard ISO 281:1989 (reviewed in 2007) [17,18], which is still extensively used as the reference engineering probabilistic model for REB RCF. It expresses the REB fatigue life L_n in million cycles for a reliability of 100-n % as:

$$L_n = a_1 a_{ISO} \left(\frac{C}{Q}\right)^p \approx a_1 a_2 a_3 \dots a_i \left(\frac{C}{Q}\right)^p$$

- *a_1 being the reliability constant depending on n (e.g. a_1=1 for n=10)* [17]
- *a_2 being the constant for material properties depending on the steel grade, heat treatment and cleanliness (e.g. a_2 commonly fixed to 3 for vacuum arc remelted 100Cr6)* [17]
- *a_3 being the lubrication constant depending on the λ ratio (e.g. a_3>1.5 for λ>3), the contamination levels fixed by ISO 4406:1999, and sometimes on the lubricant formulation* [17–19]
- *a_i being possible in house coefficients for misalignment, press-fitting, water contamination, etc.*
- *Extensive details for corrective coefficients and about the a_{ISO} formulation available in* [18].

This rating standard is used to evaluate the fatigue performance of bearings in the majority of applications, if they operate in the following conditions [17]:

- Relatively slow rotational speed and moderate masses such that RE inertial and centrifugal forces are not significant compared to the applied forces
- Bearing rings accurately mounted on rigid shaft and housing
- Sufficient lubrication to prevent overheating and surface distress
- Bearing subjected to simple combination of constant axial or radial loadings
- Bearings kept free of abrasion, moisture, corrosion, electrical potential, etc.

Despite the corrective coefficient, the updated and standardized Lundberg-Palmgren REB RCF life models present several limitations that are nowadays becoming of major importance. Indeed, this model is based entirely on subsurface initiated fatigue even though more and more failure are attributed to surface initiated fatigue. For example, Lundberg-Palmgren based models do not account for surface traction even though sliding commonly occurs in REBs (section 1.2.2), nor do they account for surface roughness and tribochemical aspects. In addition, with improvements of steelmaking processes and inclusions ratings, overall amounts and size of non-metallic inclusions have been significantly reduced to a point where usual RCF benchmarking is often unsufficient to discriminate high quality bearing steels [146], so that subsurface initiated failures now represent a small proportion of REB failures. Therefore, these probabilistic models based on subsurface fatigue are nowadays more and more discussed and deterministic models are being developed to better feed engineering fatigue life assessment.

1.3.3.3 Physical and deterministic research models

Considering the aforementioned limitations of probabilistic models, deterministic research theoretical models are currently being developed as tools to study the influence of various tribological parameters on REB fatigue life focusing either on *crack initiation* or *propagation*, which is

far from being evident as the understanding of *initiation* may vary significantly from an author to another.

a. Analytical models for crack propagation

In the nineties, numerous *analytical developments* have been led to apply fracture mechanics to RCF based on cyclic Hertzian stress fields applied to geometries comprising a pre-existent surface or subsurface crack (**Fig. 1.36**) in order to (1) study the influence of tribological parameters such as surface traction, oil seepage, and/or inclusion density on crack propagation [110,116,147–149], (2) to identify potential thresholds to prevent crack propagation [150,151], and (3) to propose damage accumulation laws for RCF life prediction models [152–154].

Those models have allowed to establish for example oil seepage in surface cracks directly depends on the magnitude and direction of surface traction [116]. Therefore, high surface traction does not only affect RCF by shifting the maximum shear stresses towards the surface but also by enhancing crack propagation on the follower surface due to internal hydraulic pressure and reduced friction at rubbing crack flanks [116]. Another result of analytical models is that fatigue life could be considered as proportional to the square root of the area of the inclusions in the steel [155]. These results could thus help improving standards and coefficients used in engineering probabilistic tools.

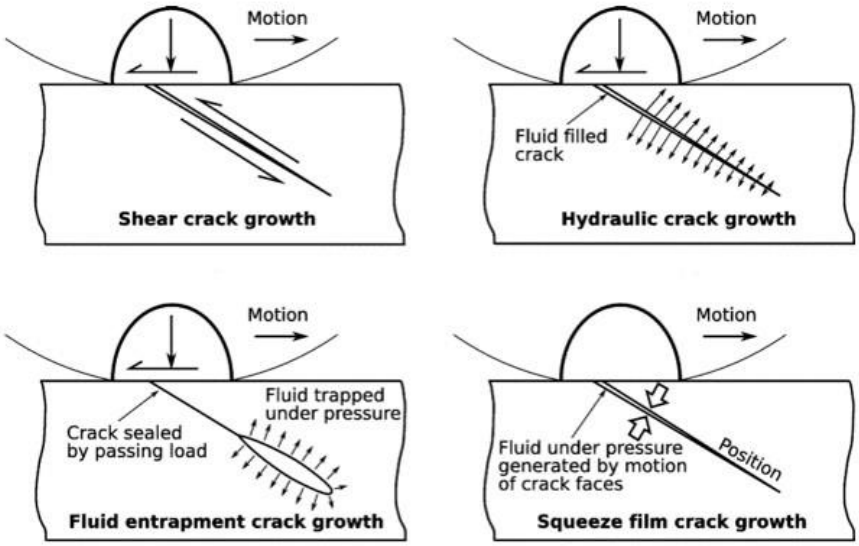

Fig. 1.36: Scheme of surface crack propagation modes studied by analytical models applying fracture mechanics to RCF [149].

b. Cohesive finite element models to simulate RCF

The fore-described analytical models have mainly been developed to study crack propagation under RCF conditions as they consider pre-existent cracks that often have dimensions of the magnitude of the contact minor semi-axis. Recent progress in computer capacity have allowed the development of finite element modeling applied to contact mechanics. In particular, extended finite element method (X-FEM) has been applied to RCF to simulate crack propagation without constant remeshing [113,156–158]. Moreover, Voronoi elements are currently being used in several studies to build cohesive finite element models capable simulating damage accumulation at grain boundaries in order to study crack initiation under RCF conditions (**Fig. 1.37**) [123,159,160]. For

the moment, these models are still under development and limited by computational times and lack of fundamental input knowledge when, for example, heterogeneous and anisotropic microstructural material properties need to be taken into account.

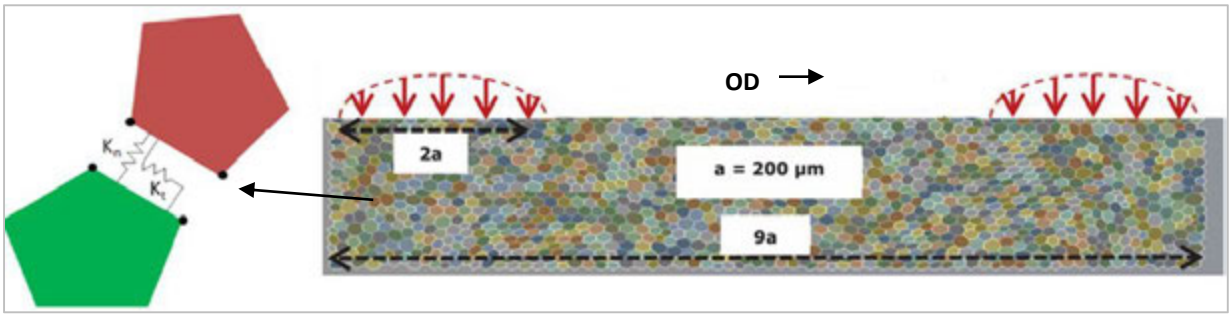

Fig. 1.37: Example of a cohesive finite element model simulating damage accumulation at grain boundaries to predict crack initiation in RCF conditions (from [161]).

1.3.4 Wind turbine bearing unexpected failures

1.3.4.1 Wind turbine bearing main failures

As detailed in the general introduction of this manuscript, up to 60% of the gearbox maintenance costs in the wind industry are attributed to REBs [7,33]. As a complement to his reference failure atlas [58], Tallian has referenced extensive REB failure data retrieved from wind turbines field reports [96]. In this dedicated failure atlas, ~65% of the plates concern *gearbox* CRB or SRB inner ring failures (mainly attributed to surface distress and/or spalling associated to axial cracking of the raceways), ~30% the *generators* DGBB balls or rings (mainly attributed to denting and electro-corrosion) and some concern the *main shaft* bearings (mainly attributed to faulty lubrication).

a. Main shaft bearings

A thorough review of the main cause for bearing failures [7], stipulates that *main shaft* REBs mainly suffer from faulty lubrication and poor heat evacuation affected by low rotational speed (~15-20 rpm) and grease lubrication (most common). This favors low-cycle wear and micropitting of the raceways. In cases of SRB configurations, the osculation adds geometrical sliding gradients to the overall skidding associated to the moderate and yet transient loadings (start & stops). This leads to premature and irreversible *smearing* failures (also occurring in SRBs for gearboxes) [7]. Efficient countermeasures have been introduced to limit sliding kinematics with SRBs replacement by TRBs [7] and by providing superfinished surfaces combined with a protective surface treatment such as tungsten carbide/amorphous hydrocarbon WC/aC-H coatings (proved to be more durable and efficient that black oxide treatments) [7,111].

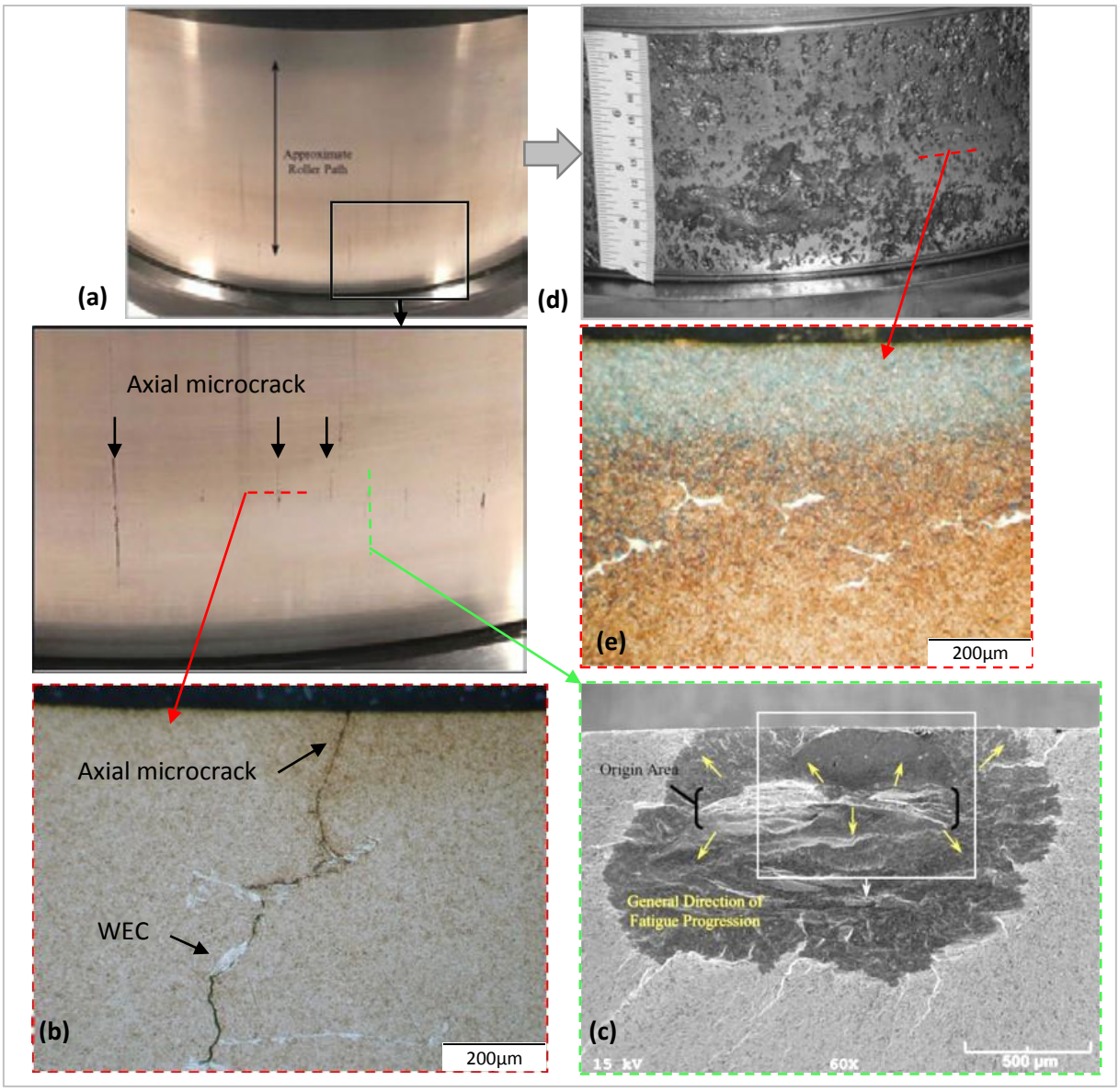

Fig. 1.38: Examples of wind turbine REB failure modes (all images from [162]): (a) premature radial cracking of a gearbox intermediate shaft 100Cr6 through-hardened CRB IR after $1.4x10^8$ cycles (~15% L_{10}); (b) circumferential metallographic cross section revealing White Etching Cracks (WEC) associated to the surface radial cracks; (c) axial fractograph opening deep radial crack networks in the IR; (d) extended macro-pitting of a main shaft case carburized CRB IR after $1.8x10^7$ cycles (~18% L_{10}); (e) circumferential metallographic cross section revealing WEC below the raceway of IR illustrated in (d).

b. Gearbox bearings

The main failure modes for wind turbine *gearbox REBs* are *smearing*, *fretting corrosion* and an unconventional premature cracking failure mode leading to deep *spalling* or *full component seizure* [7,13]. On one hand, important sliding due to geometrical considerations and transient loadings is responsible for *smearing* and part of *fretting corrosion*. Changing the REB design and adding durable protective surface treatments can significantly reduce those wear modes so that many bearing manufacturers now propose updated products to increase the REB life. On the other hand, the root causes for deep *spalling* (also called *flaking*) and component seizure due to *premature radial cracking* (**Fig. 1.38** (a)) are less understood. They correspond to the far most common wind turbine REB failure since they represent up to ~70-90% of the wind turbine gearbox failures nowadays

[6,162–164]! Metallographic cross sections and fractographs of those wind turbine REBs, revealed broad branching crack networks border by white etching microstructures (similar to butterfly wings), thus giving them the name *White Etching Cracks (WEC)* (**Fig. 1.38** (b-c))[6,29,96,162,165]. It has been demonstrated that radial cracking is significantly enhanced in large roller bearings due to inhomogeneous heat treatment and fitting induced hoop stresses [31]. Tallian also often suggests that surface axial cracks can be initiated by false brinelling during long stand still and vibrations during service [96]. These drivers thus may explain why wind turbine bearing life are so frequently reduced due to WEC-associated *premature radial cracking*.

Not only *WEC premature failures* are the most common in wind turbine gearboxes, they are also considered as the most costly and vicious failures. Indeed, they occur as soon as 2-20% of the L_{10} and remain undetectable by condition monitoring of the turbines before a sudden and catastrophic spalling or seizure of a REB component [6,162–165]. In wind turbines, WECs mainly occur on IRs of CRBs, TRBs, SRBs and DGBBs. They can be found at different locations in the gearbox (low speed shaft, intermediate shaft, high speed shaft, planet bearing and planet carrier), but also sometimes on *main shaft* and *generator* REBs (**Fig. 1.38** (d-e))[6,7,19,29,33,34,95,96,162–167]. Most *premature radial cracking* in wind turbine gearbox REBs are generic in nature and *not specific to a single manufacturer, turbine model or bearing reference*. Moreover, WECs are presumably *not due to conventional RCF subsurface initiated fatigue* as high dynamic capacity REBs with high estimated L_{10} are also massively affected.

c. Generator bearings

Generator bearing failures have been reported numerous times by Tallian [96] and have most often been attributed to *surface distress* due to electro-corrosion of the contacting surfaces and to *premature radial cracking* associated to *WECs*. High frequency currents from a faulty insulation of the bearing or from magnetic induced shaft currents are supposed to play a significant tribochemical role in both failure modes [98–100,108,168]. Many bearing manufacturers now propose insulated REBs using notably ceramic rolling elements to avoid such detrimental currents.

1.3.4.2 Wind turbine limited life prediction

Wind turbine bearings are commonly designed to achieve a lifetime of 20 years under nominal operating conditions according to the standard IEC 61400-4 based on the ISO 281:2007 Lundberg and Palmgren fatigue life prediction models. However the transition to large size REBs operating under unconventional tribological conditions (section 1.2.5), does not seem to be limited to a simple extrapolation of the historical know-hows on smaller REBs. Oversizing them with multiple security factors accounting for the increased probability of finding inclusions in larger stressed volumes and for the increasing risk of fracture with the increasing mean diameter (e.g. bearings with 400 mm pitch diameter would require 20% reduction of the fatigue limit) does not seem sufficient to avoid premature failures [144,169].

Indeed, even if those conventional subsurface RCF based standards are used to guaranty 20-year lifetimes, they yet do not consider the fore-described prevalent and premature failures modes mainly affected by *surface* and *tribochemical parameters* such as electro-corrosion, for example. A typical example has been underlined in [7]. The immediate reaction to reduce excessive *smearing* failures has been to use wider SRBs to increase the dynamic capacity of the REBs and thus their ability to withstand RCF. This was however not considering that wider contacts would also significantly

increase sliding and thus *smearing* risk. Another drastic example results from 6-year field investigations of over 500 turbines of the same type (**Fig. 1.38**) [162]. First, gearbox intermediate shaft through hardened 100Cr6 CRBs have presented a failure rate of 16% with a mean time for failure of 27200 hours (~15% of L_{10} according to ISO 281:2007). Second, main shaft case-carburized CRBs of a specific manufacturer have presented a failure rate of 17% with a mean time for failure of 26700 hours (~22% of L_{10} according to ISO 281:2007). Investigations on failed bearings have revealed wide WEC networks in both cases despite the large estimated lifetimes based on ISO 281:2007 standard (**Fig. 1.38**).

Therefore, nowadays, REB standards seem to be outdated for wind turbine applications and there seems to be *a severe lack of engineering tool and criterion* to design wind turbine REBs withstanding not only RCF but also surface initiated failures. This point is even more critical as the extraordinary dimensions and ever-fluctuating loads of wind turbine bearings make extensive fatigue benchmarking, as it was done in the past century for the automotive industry, unconceivable to validate reliability models. In this context, it is required to better understand the premature and yet unpredictable *WEC failure modes* in order to be able to take into account the influent drivers when designing wind turbine REBs, and finally to propose efficient countermeasures.

1.4 White Etching Cracks (WEC)

1.4.1 WEC definition

Terminology. To the authors' knowledge, *White Etching Cracks* (WEC) have first been revealed at the beginning of the eighties by metallographic cross sections of a TRB, based on which they were characterized as a peculiar cracking with adjacent white microstructural alteration [170]. WECs have then been the focus of several Japanese studies in the nineties after repeated occurrences on an automotive alternator DGBB, and were at the time first referred to as *brittle flaking* [171,172]. The apparently rare WEC failure modes have then not been of major interest until the expansion of the wind turbine market, for which WECs have been identified as the most costly and least understood REB failure mode in the past decade. Since then, WECs have been widely reported in the literature being both characterized on a material point of view and studied from a tribological point of view in order to understand the formation mechanisms [7,12,29,30,115,168,172–185]. WECs have at this occasion been named: *brittle flaking, white structure flaking (WSF), irregular white etching area (irWEA), peculiar white structure, white etching constituent, or hydrogen embrittlement*. The terminology *White Etching Cracks* has been more or less adopted by a consensus between the following authors [6,162,163,186] during the dedicated panel discussion held at the 2013 STLE 68th Annual Meeting and Exhibition [187], based on two main thorough reviews of the failure mode available at the time [29,163].

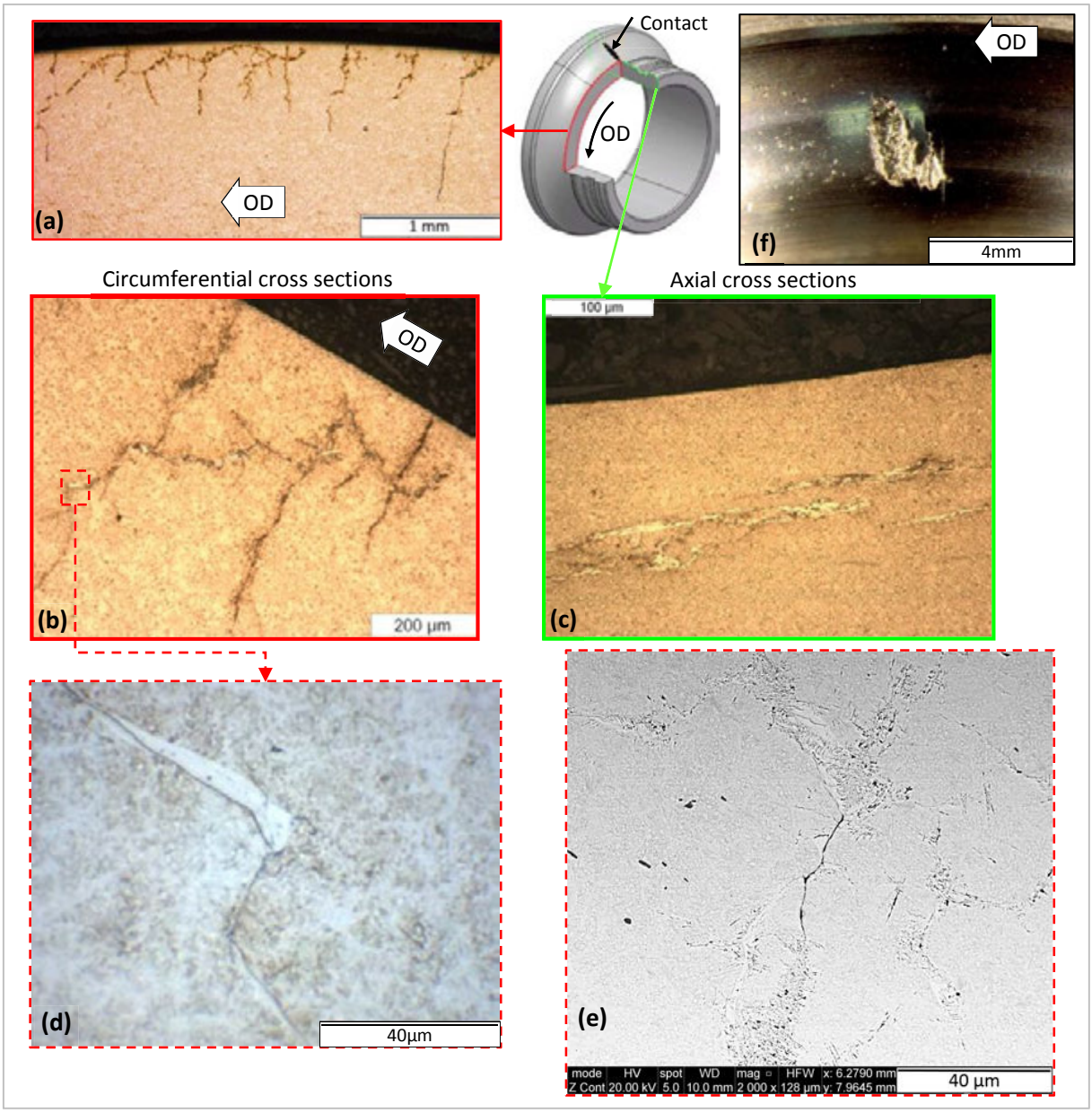

Fig. 1.39: Typical WEC networks revealed on an ACBB IR from further described NTN-SNR RCF test rig: (a) LOM revealing discrete WEC networks; (b) LOM revealing WEC vertical links to surface and an apparent stair-like top-down growth in the direction of OD; (c) LOM revealing WEC layout parallel to the surface from an axial point of view in accordance with the respective stair-like steps; (d) LOM zoom on the refined white etching microstructure; (e) SEM analysis revealing ultra-thin secondary cracks; (f) Raceway topview of a WEC-initiated spall presenting typical axial cracks.

Definition of White Etching Cracks (WEC) based on experimental observations (**Fig. 1.39**)*:*

- WEC correspond to broad but discrete peculiar three-dimensional (3D) and *multi-branching crack networks with a brittle aspect.*
- WEC mainly propagate *subsurface* and are often *punctually linked to the surface.*
- WEC consist of very *thin cracks* (<1 µm) bordered by *white etching microstructure* when etched with Nital on a metallographic cross section.
- WEC eventually lead to *radial cracking* or *flaking* depending on the structural stress state.

1.4.2 WEC characterization

As WECs present a peculiar and atypical morphology compared to conventional RCF microstructural alterations (section 1.3.2.2), several studies in recent years have been led to characterize their microstructure and macroscopic morphology in order to propose an understanding to this "novel" failure mode.

1.4.2.1 WEC microstructure

Under LOM after Nital etching, WECs appear to be similar to extended butterfly wings consisting in very thin cracks bordered by W*hite Etching Areas* (WEA) (Fig. 1.39 (d)). Cracks are best discerned prior to Nital etching which tend to emphasize drastically crack width. In doing so, WEC cracks appear to be *very thin* (~1 µm for primary cracks and significantly thinner for secondary cracks) even if they may reach hundreds of microns in cumulative length ((Fig. 1.39 (a)). After Nital etching, it can been perceived that WEAs tend to develop mainly along WEC fragments being somewhat parallel or low-angled versus the surface (Fig. 1.39 (b) and **Fig. 1.38** (b)). This may coincide with the fact these crack fragments propagate mainly under shear stress [116]. In consequence axial cross sections seem to contain more WEAs (Fig. 1.39 (c)). In WEC networks, WEAs have always been observed bordering cracks whereas cracks have been observed without WEA (vertical sections in Fig. 1.39 (d-e) and **Fig. 1.38** (b)). This suggests that *cracks tend to pre-exist WEAs*, similarly to butterfly wing formation [14,29]. This point may however still be contested by some authors. Nevertheless it is supported by the fact WEAs strictly follow the cracks paths (**Fig. 1.40**) [14,29] and that WEAs present a linear structure quite parallel to the cracks under sufficient magnification (**Fig. 1.41**) [6,14,29]. Moreover, LOM close-ups revealed that WEAs tend to develop preferentially on one side of the crack flanks, even though it is not clear yet if there is a unique predominant side. Finally, the volume of adjacent WEAs in WEC networks seem to vary significantly from an application to another thus changing considerably the macroscopic aspect of the WECs (**Fig. 1.44**). This may depend, for example, on the steel grade and heat treatment.

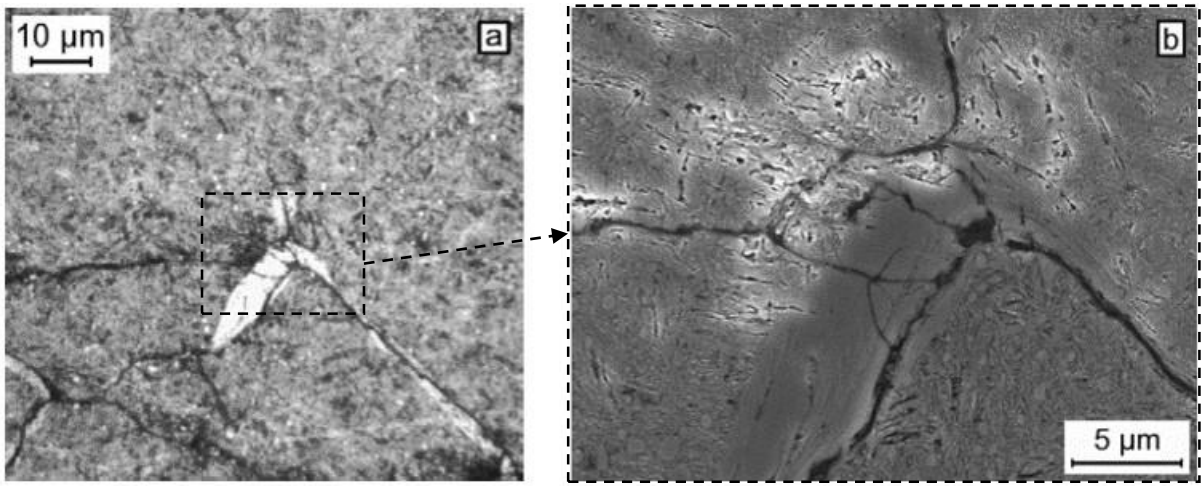

Fig. 1.40: Typical WEA bordering cracks of a multi-branching WEC network in (a) a LOM and (b) SEM micrographs of an etched cross section of a gearbox TRB IR (from [29]).

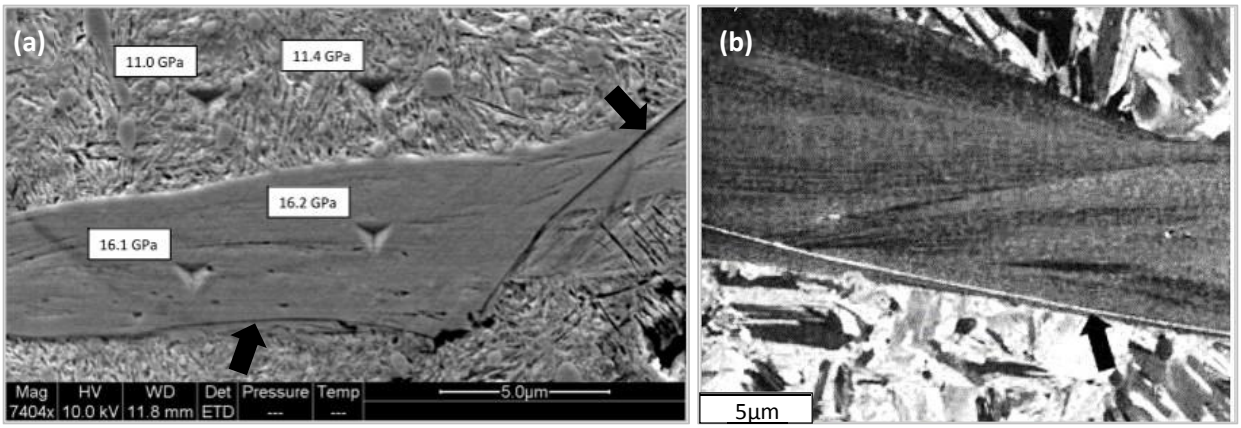

Fig. 1.41: (a) WEC close-up using SEM analysis with corresponding nanohardness indentations in the bulk matrix and the WEA (from [6]); (b) WEC close-up using ion channeling contrast to reveal linear feature inside WEAs developed mainly on the upper bound of the cracks (black arrow) but also incipiently on the lower bound, as in (a) (from [14]).

Further analyses based on nanohardness indentations have revealed that WEAs in WEC networks present a *hardness 30 - 50% higher than the bulk matrix* (**Fig. 1.41** (a)) [6,167,188], similarly to butterfly associated WEAs [15,134,170] and WELs found in hard turning and railway applications [128–130] (section 1.3.2.2). This increased hardness corresponds to the microstructural composition of the WEAs observed in WEC networks. Indeed, WEAs have been characterized as progressive refinement from martensitic breakdown and carbide dissolution into *nanocrystalline ferrite structure supersaturated with dissolved carbon*, thus very hard and resistant to etching [6,14,29,167,188]. This trend has been macroscopically confirmed by LOM of cross sections etched with Murakami reagent (10 mg $K_3Fe(CN)_6$ and 10 mg KOH in 100 ml H_2O at 55 °C) revealing that no carbides remain in adjacent WEAs (**Fig. 1.42**)[14].

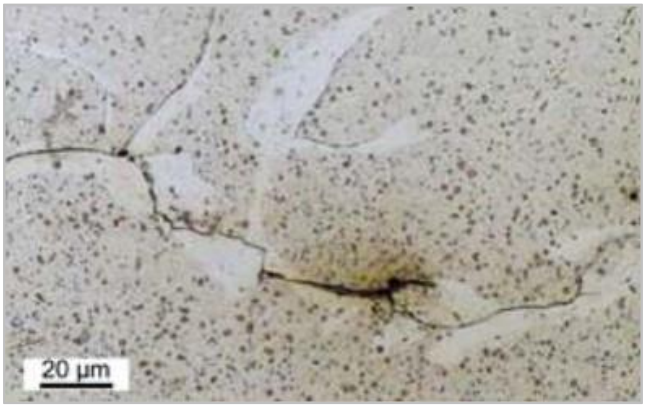

Fig. 1.42: Circumferential LOM of a WEC network after etching with Murakami reagent revealing carbides in the bulk matrix and confirming carbide dissolution in WEA bordering multi-branching cracks.

1.4.2.2 WEC macroscopic layout

From a macroscopic point of view, WECs present broad 3D subsurface layouts supported by the different morphological aspects on circumferential and axial cross sections of the same WEC-affected ACBB IR (**Fig. 1.39** (b-c)). This has been confirmed in numerous studies, notably by the high resolution manual *serial-sectioning* and 3D reconstruction of WEC networks proposed by Evans et al. [188] (**Fig. 1.43**). If there seems to be a common microstructure to all WEC occurrences and a general trend for a stair-like top-down growth in the direction of OD (**Fig. 1.39** and **Fig. 1.43**),

the overall morphological aspect seems to vary significantly from an application to another, both in terms of layout and WEA thickness function of the steel grade and stress state (**Fig. 1.44**).

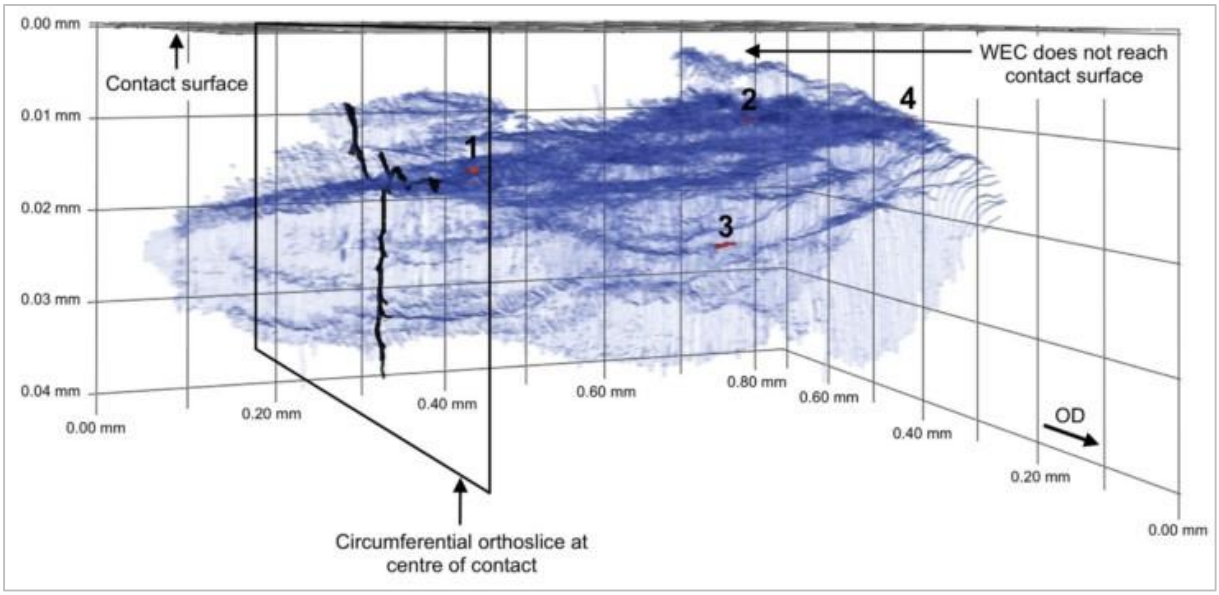

Fig. 1.43: 3D mapping of a WEC network reconstructed by manual serial-sectioning and segmentation techniques (in red, inclusion interacting with the cracks) [188].

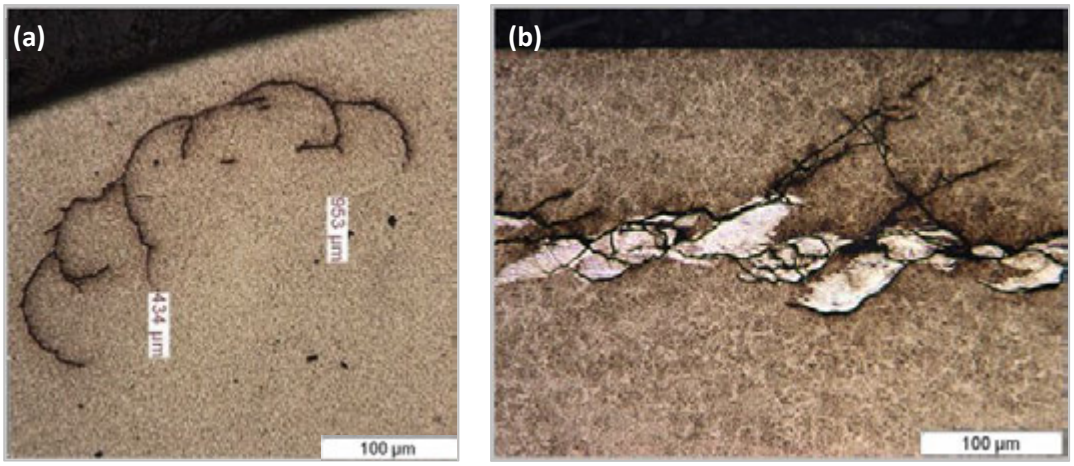

Fig. 1.44: (a) LOM of an automotive wheel ACBB through-hardened 100Cr6 ball; (b) LOM of a wind turbine case-hardened TRB IR (courtesy of NTN-SNR)

1.4.3 WEC occurrences

Literature reviews and technical reports point out that WEC occurrences present no evident common denominator as they occur in different industrial *application*, for different *bearing* types and components, for different *steels* and for different *lubricants*. This statement can also be supported by various but sporadic WEC failures experienced at NTN-SNR that have been synthetized at the beginning of this study in order to have an overview of all the potential influent drivers. The literature stipulates that WECs have led to REB premature failure as soon as 1% of L_{10} [185] and most generally at 5 – 20% of L_{10} [6,162–165,172,176,189]. The following list is most certainly not exhaustive as numerous REB failure expertise made in the past years may have missed WEC networks due to the fact that (1) manufacturers were not looking for them, (2) WEC failures might

have been masked by predominant gear failures or bearing steel cleanliness issues, and that (3) metallographic cross sections were far from systematic and probably done at the wrong location compared to the WEC specific location versus the contact area (detailed thereafter).

a. Application

WECs have not only been witnessed in aforementioned wind turbine REB applications, but also in other various industrial applications of different REB manufacturers and customers:

- Automotive gearbox, camshaft, wheel hubs and peripheral auxiliaries such as the alternator [29,167,168,172,174]
- Naval industry pod drives [29,190]
- Railway axels and hubs (sporadic cases at NTN-SNR)
- Compressors and air conditioning systems [190]
- Continuous variable transmissions [176]
- *Others:* paper machinery [167,190], cement mills [167,175,190–192], washing machine [192], hydrogen fuel cell systems [181], electrical applications [193], etc.

WECs have also been sporadically observed in automotive case-carburized gears and in steam turbine transmission gear teeth [191]. Nevertheless, WEC failure modes seem to be more frequent and critical in the wind turbine industry (section 1.3.4.1) than in the fore-listed applications.

b. Bearing types and components

In the literature, and as confirmed by some WEC observations at NTN-SNR, WECs have been observed in different REB types and on all types of bearing components, which are IR, OR, washers, rollers and balls [167,190,192] in:

- Radial bearings:
  - Ball bearings: DGBBs, ACBBs, Double row ball bearings, etc.
  - Roller bearings: CRBs, TRBs, SRBs, Double row SRBs, etc.
- Thrust bearings: roller and ball configurations

However there seems to be some predominant configurations. For example, (1) in wind turbine CRBs and SRBs, WECs are most often found on the IRs; (2) in automotive wheel hub ACBBs, WECs are commonly observed on balls, and (3) in railway axel REBs with fixed IRs, WEC commonly occur on the ORs.

c. Steel grades and heat treatments

WECs have been most commonly observed in martensically through hardened bearing steels [134,170,172,173,176,180,181,194,195], but also in different steel grades and heat treatments such as in bainitic steels [14,29,30,163,167,190] and in case-hardened steels [6,162,167,174,191]. NTN-SNR has reproduced WEC failures for example on C56 bearing steel as well as on carbo-nitrided 100Cr6 variant, but with a low reproducibility rate. This is in agreement with some beneficial treatments that have been mentioned in the literature: high chromium and/or vanadium contents [196,197], high retained austenite content [162], and surface treatments such as black oxides [165]. Nevertheless, these beneficial treatments only seem to delay WEC formation.

WECs have been observed in ultra-clean steels, so that some authors consider the WEC and butterflies to be mutually independent [29,190,192]. This point is however contested by other authors suggesting that WEC initiate at inclusions based on the fact they observe a certain amount of WEC interactions with inclusions, even very small in size [188,198–200] (**Fig. 1.43**).

d. Lubricants: oil and grease

Finally, WECs have been revealed in applications operating with very different lubricants, both oils and greases with various base oils and additive formulations and various levels of contamination, for example by water ingress [97,168,172,176,189,192,195]. The influence of water ingress as well as of the lubricant formulation on WEC occurrences has been confirmed in some NTN-SNR automotive REB field return and in-house testing.

1.5 Closure to the state of art

As a closure to the first chapter, after having introduced the fundamentals of REB designs (section 1.1), tribology (section 1.2) and relevant conventional failures mode (section 1.3), all prerequisites for the following chapters, the WEC failure mode has been defined based on a metallographic characterization and literature state of art as well as on a synthesis of WEC occurrences in application (section 1.4). In doing so, it appears that (1) WECs seem to be atypical and unconventional compared to the fore-described conventional RCF failure modes and that (2), even if WEC have been precisely characterized from a microstructural point of view, the formation mechanisms are not yet fully understood due to the lack of common denominator to all WEC occurrences without going down to tribological scales.

1.5.1 WEC: unconventional fatigue failure mode

Compared to conventional RCF continuous microstructural alterations limited to the subsurface Hertzian stress zone (section 1.3.2.2), WECs present a discrete and atypical morphology that can propagate beyond contact mechanical stresses (**Fig. 1.39** (a)). Moreover, WECs appear prematurely according to the RCF microstructural alterations diagram proposed in **Fig. 1.31**, as they can develop for Hertzian pressures as low as 1.9 GPa [79,188,192,201,202]. Consequently, only very limited material response is detected by XRD residual stress analyses on WEC-affected components [29,178]. On a DGBB endurance test from the literature [180], it has been noticed that lowering the contact curvatures, thus *lowering the contact stresses*, actually *decreased fatigue life* due to WEC associated failures. This observation is strictly opposite to conventional RCF predictions (section 1.3.3). In some applications, WECs may occur at a fairly high number of cycles compared to the L_{10} but the Weibull slope is always significantly steep [180,192].

Compared to conventional RCF butterflies, WECs present very similar microstructure with WEA adjacent to incipient subsurface cracks. However WECs propagate far beyond the maximum shear stress zone where butterflies usually develop. Moreover, WECs often present a preferential top-growth in the direction of OD (**Fig. 1.39**), which is in fact opposite to butterfly wing development (**Fig. 1.32**). This supports the fact that WECs and butterflies are mutually independent. Yet, butterflies most probably act as stress raisers and "WEC propagators", explaining why inclusions are often found in the vicinity of WEC networks [29,190,192]. Therefore, even though WECs

mainly propagate subsurface under repeated cycles as conventional RCF failures modes, they appear to be a *highly unconventional fatigue failure mode*.

1.5.2 WEC: an apparent chemical embrittlement not yet fully understood

The WEC occurrence synthesis has shown that WEC may appear in properly designed, manufactured, selected, mounted and lubricated bearings for which the potential *risk of surface or subsurface initiated fatigue is virtually nil*. In those cases, WECs appear prematurely compared to the high estimated L_{10}. Nevertheless, WECs still correspond to *a fatigue failure mode* as the crack networks often require *several million cycles* to develop before leading to irreversible REB deterioration. Despite the low contact stresses, the multi-branching and brittle aspect of WEC networks indicates that cracking seems to be strongly assisted by chemical embrittlement, as observed for example in cases of stress-corrosion induced cracking in pipelines subjected to hydrogen di-sulfide embrittlement [203]. As it has been proposed in the nineties [58,171,172] and more recently [18,96,163,174,176,182,194,199,204], WEC formation seems to be more specifically associated to *hydrogen embrittlement*, which will be confirmed and discussed in **Chapter 3**.

Nevertheless, as WEC occurrences present *no common macroscopic evident denominator,* given their diversity (section 1.4.3), WEC formation mechanisms, even if related to hydrogen embrittlement, are *not yet fully understood*. Failures, notably in the wind turbine industry, remain *unsolved*. It is indeed still highly contested whether WEC are surface or subsurface initiated. Moreover, WEC networks are so multi-branching and atypical versus conventional RCF crack propagation models [110,116,147–149], that it is not currently possible to predict surface damage or component seizure associated to WEC propagation by analytical or finite element modelling.

1.5.3 Objectives of the following chapters

In this context, as WECs have previously been subjected to highly precise microstructural characterization (section 1.4.2.1), the purpose of this study is to propose a full **tribological analysis of the WEC failure mode** based on laboratory WEC reproduction and analysis protocols described in **Chapter 2**. The effect of hydrogen on WEC formation mechanisms will then be studied in **Chapter 3** in order to confirm the hydrogen embrittlement hypothesis proposed in the literature. Then, comparing several laboratory WEC reproduction on radically different test rigs, WEC formation conjectures will be formulated in **Chapter 4**. Finally, laboratory twin-disc tests will be led in **Chapter. 5** to validate and explore various identified influent drivers on WEC initiation and propagation. As WECs are currently one of the main focus in wind turbine tribology, *specific literature review will be further addressed* in each chapter to discuss and/or support the tribological analysis here-proposed.

Tribological analysis of White Etching Crack (WEC) failures in Rolling Element Bearing

Chapter 2:

Methodology and experimental procedures to study White Etching Crack

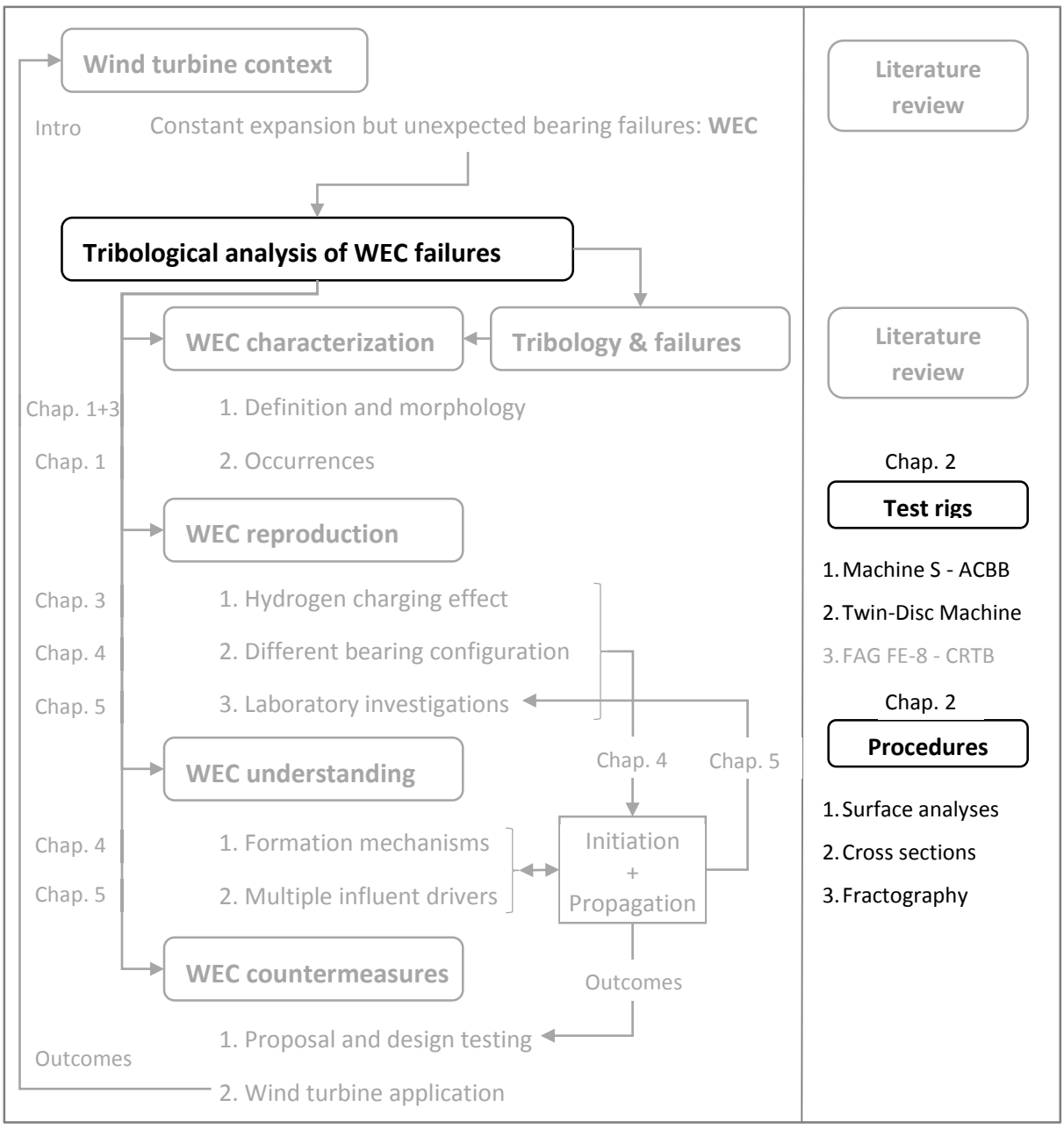

The second chapter of this thesis introduces the overall methodology and main experimental procedures used throughout this work to study WEC tribological formation mechanisms. Focus is first made on full bearing fatigue tests performed on an NTN-SNR standard endurance test rig on which WECs have been reproduced successfully. Then, the contact parameters will be transposed on the LaMCoS Twin-Disc Machine that has been extensively used to simulate rolling contact fatigue and to explore a wide range of WEC influent drivers with an efficient control of the tribological parameters. In the end, the different methods applied to reveal WEC networks and complementary tribological characterization employed in this study will be presented.

2.1 Overall methodology

The aim of the present work is to achieve a better understanding of WEC formation mechanisms and influent drivers, and to propose efficient countermeasures, based on a comprehensive literature review and specific experimental procedures. As depicted in the general introduction (**Figure 9**) and in the thesis flow chart (**Figure 10**), the understanding of this unusual tribological failure mode highly depends on the establishment of *experimental procedures to reproduce it* in order to characterize the influent and responsible tribological parameters.

Therefore, the overall methodology of this study consists in performing RCF tests in order to reproduce and better characterize WEC networks both on *full bearing Machine S endurance test* rigs available at NTN-SNR and on the *Twin-Disc Machine (TDM) tribological RCF simulator* available at the LaMCoS. Taking also into account other WEC reproductions from the literature, the full bearing contact conditions reproducing WECs have been transposed step by step on the TDM in order to ensure a better control of each individual tribological parameter and to be able to better qualify their influence on WEC formation mechanisms (**Fig. 2.1**). Complementary full bearing test were also led to confirm some hypotheses and to feed new TDM RCF simulations.

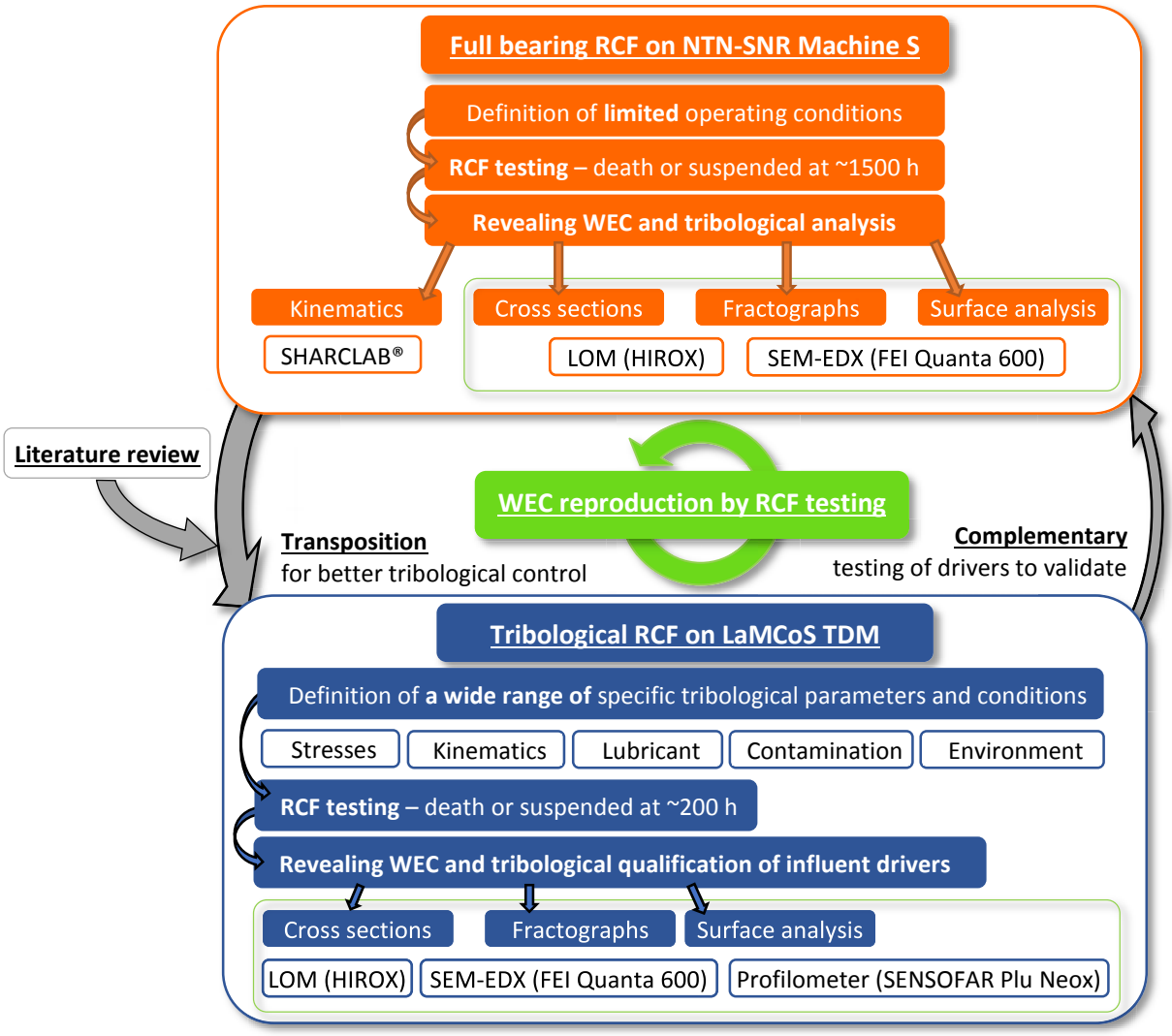

Fig. 2.1: Overall methodology and experimental procedures led for a tribological analysis of WECs.

As the contact pressures associated to WECs are relatively low, WECs tend to develop for a significant number of cycles even though they may be premature compared to the L_{10}. As the only available techniques to reveal WECs are destructive, the mean test duration were most often prolonged to 100 - 200 hours for the TDM tests and over 1000 - 1500 hours for the Machine S in order to reduce the risk of stopping the tests prematurely versus. Then, several additional days were required after each test to run the different analysis procedures and define the next test configuration. This time-consuming testing procedure thus *limited the number of tests* throughout the study.

2.2 Full bearing RCF testing on a Machine S endurance bench

2.2.1 Machine S operating conditions

The *NTN-SNR Machine S* is a minimalist endurance test bench to assess RCF of REBs. Several rows of Machine S are deployed at the NTN-SNR test center. Each Machine S comprises two posts (**Fig. 2.2** (a)) on which REBs are mounted by pairs (**Fig. 2.2** (b)) on a shaft supported by oversized CRBs and driven at a constant rotational speed Ω by a rubber-metal coupling with a pulley, itself connected to an electric motor by a poly-V belt. The constant radial and axial loads F_r and F_a are applied by constraint springs (**Fig. 2.2** (a)). Lubrication is most often achieved by a standard commercial ISO VG46 mineral gearbox oil (lubricant A detailed in section 2.3.3) at ambient temperature with a flow rate of ~0.5 L/min through jets positioned at the top of each tested REBs after being filtered at a level of 20 µm. The tested REB mounting illustrated in **Fig. 2.2** (b) is inserted inside the bronze housing visible in **Fig. 2.2** (a), the load being then applied by the springs. The Machine S presents a *narrow range of operating conditions* considering a given REB design, as only the constant loadings and rotational speed can be modified, the lubricant and temperature being imposed (**Table 2-1**).

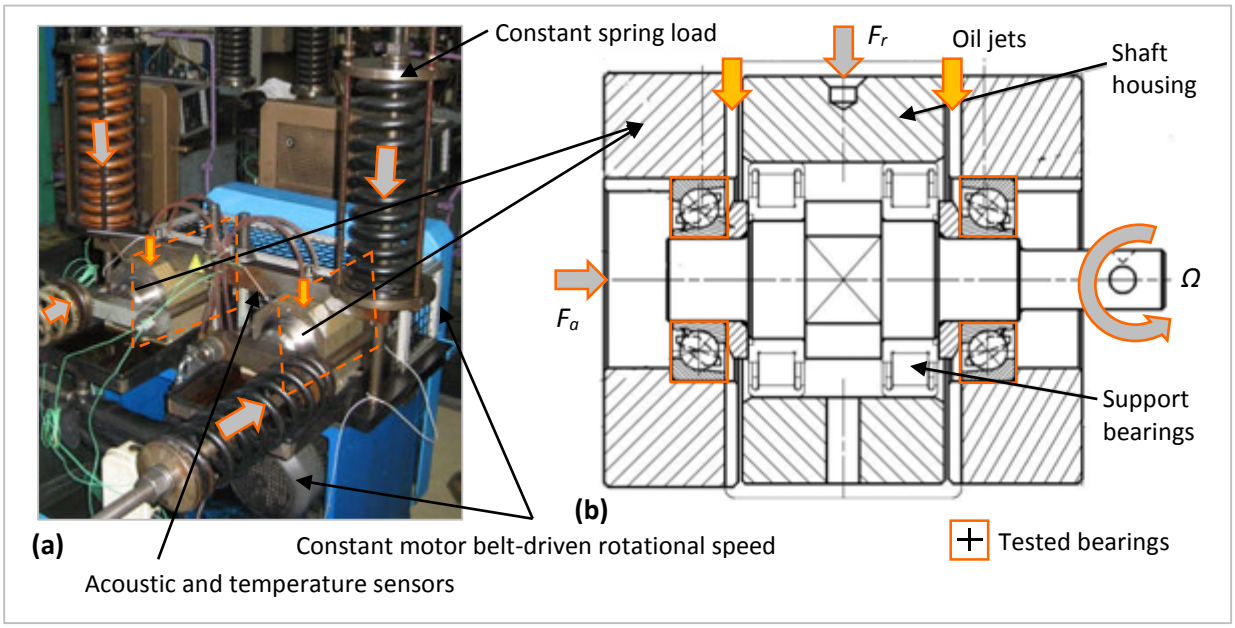

Fig. 2.2: (a) NTN-SNR Machine S endurance test rig;
(b) Cross section of the ACBB mounting used in this study for WEC reproduction.

Table 2-1: NTN-SNR Machine S endurance test rig operating conditions for the ACBB tests.

	Parameter	Technical solution	Operating conditions
Applied	*Radial and axial loads*	Constraint springs	**(1)** Fa=6.5 - Fr=9.5 kN **(2)** Fa=13.0 - Fr=9.5 kN **(3)** Fa=2.5 - Fr=8.0 kN **(4)** Fa=10.0 - Fr=3.5 kN **(5)** Fa=13.0 - Fr=2.5 kN
	Lubrication	Oil jets Filters	- ISO VG46 mineral gearbox oil (lub A Table 2-4) - ambient temperature - flow rate: ~0.5 L/min - filters: 20 µm + magnetic
	Rotational speed	Electric motor + belt entrainment	Constant: 2250 rpm
Measured	*Vibrational level*	Acoustic sensor	Threshold for test immediate stop
	OR temperature	Temperature probe	Typical stabilization ~40 - 50 °C Threshold for test immediate stop
	Duration	-	Test suspension at 1500 h

2.2.2 ACBB tested bearings

2.2.2.1 Standard NTN-SNR ACBBs

During this study, RCF tests have been performed on *Machine S* using NTN-SNR ACBB of mean diameter D_m=43.5mm (close to the universal reference 7305 BECBP) (**Fig. 2.3**). The ACBBs are composed of 10 balls and a polyamide cage. Given the ball diameter and the IR radius of curvature, the IR osculation ratio f_{ir} is ~0.516. The ACBB surfaces are super-finished, thus achieving a ball and IR mean surface roughnesses of respectively 0.02 and 0.06 µm (**Table 2-2**). The IRs are press-fitted on the shaft with a fit tolerance of $15<\delta<34$ µm to avoid micro-displacements and fretting corrosion, thus introducing an estimated *hoop stress* comprised between $90<\sigma_{hoop}<220$ MPa at the depth of further interest (details in Appendix C), which is representative of the hoop stress experienced by large wind turbine bearings leading to axial cracking [31].

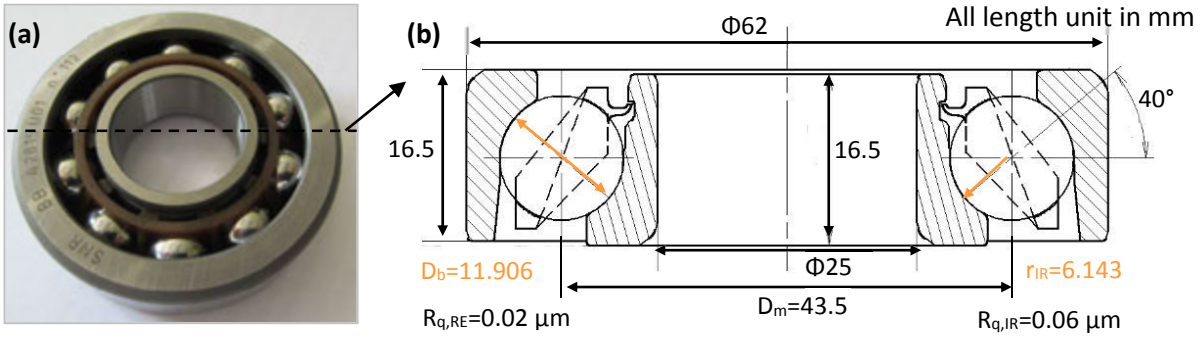

Fig. 2.3: (a) NTN-SNR ACBB with 10 balls and a polyamide cage used in this study; (b) Cross section of the ACBB with the mean diameter D_m, the ball diameter D_b and the IR curvature r_{IR}

The ACBBs were tested by pairs under *constant moderate* rotational speed and different *constant load cases* leading to a common maximum Hertzian pressure of 3.4 GPa for the most loaded ball/IR contact. **Table 2-2** provides a glimpse to the contact theoretical parameters and lubrication parameters computed for each load case using both the NTN-SNR software SHARCLAB® and

the Hamrock and Dowson film thickness equations (**Fig. 2.4**) (section 1.2.3.4). The bearings were tested under *full jet lubrication* and in a *neutral environment* (no oil contamination, no electrical current, no corrosion, no transient loadings, no vibrations, etc.). The L_{10} was theoretically under-estimated to 200 h. Based on NTN-SNR experience on RCF testing of similar bearings on Machine S, it has indeed been estimated that these ACBB should last more than 1000 h, if they were to fail. Therefore, the tests were either (1) suspended at 1500h, corresponding to ~$125x10^6$ cycles of the most loaded ball/IR contact (ball 6 in **Fig. 2.4** (a)) or (2) stopped prematurely after a significant increase in the vibration level, synonymous of surface damage of one of the bearings, the other one being therefore suspended. A total of *68 ACBBs* have been tested for this study in different load conditions influencing both kinematics and lubrication parameters as depicted (**Fig. 2.4** (c-d)) and detailed in **Table 2-2**. Specificities of each test are provided in Appendix D.

Table 2-2: ACBB load cases and tribological parameters at the most loaded ball/IR contact oil lubricated with ISO VG46 mineral oil at 40°C (position 6 in **Fig. 2.4** (a)).

Load case	F_a (kN)	F_r (kN)	b (mm)	P_H (GPa)	τ_{max} (MPa)	h_c (µm)	$z(\tau_{max})$ (µm)	λ	SRR_{max} (%)	α (°)
(1)*	6.5	9.5	2.88	3.40	1060	0.33	204	4.2	22	30.7
(2)*	13.0	9.5	2.79	3.21	1060	0.34	203	4.3	21	40.2
(3)	2.5	8.0	2.84	3.36	1040	0.33	199	4.2	19	17
(4)	10.0	3.5	2.20	2.56	820	0.35	158	4.4	13	42
(5)	13.0	2.5	2.26	2.70	840	0.33	160	4.2	14	44

** WEC reproduction*

*h_c computed for oil ISO VG 46 at **40°C***

λ computed for $R_{q,ball}$=0.025 µm and $R_{q,IR}$=0.075 µm

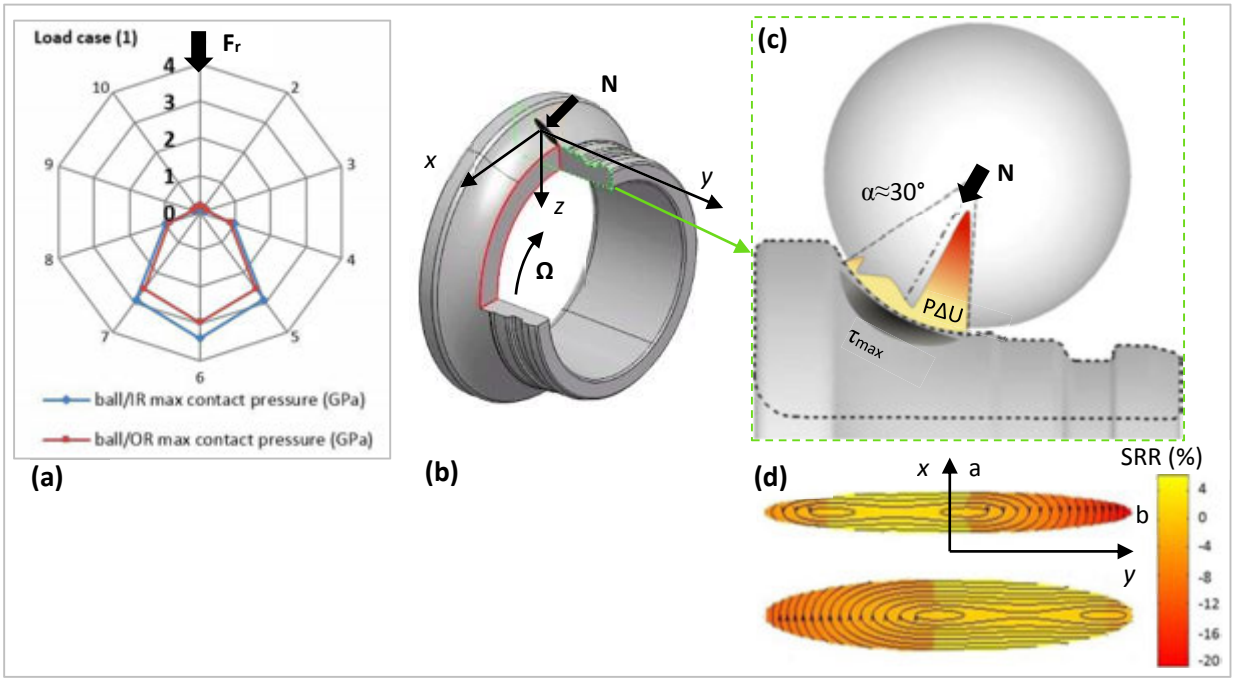

Fig. 2.4: (a) Contact pressure distribution in the ACBB; (b) Scheme of a cross sectioned IR of the tested ACBB; Schemes of the tribological parameters for the most loaded ball/IR contact in load case (1) with (b) illustrating the effective contact angle, subsurface shear stress and PΔU sliding energy criterion, and (c) the SRR lines in the IR and OR respective contact ellipsoid.

Given the geometrical constraints of ACBBs, they are designed to operate under a theoretical angle of contact, which in this case is of 40° (**Fig. 2.3** (b)). Function of the ratio of the axial load on the radial load F_a/F_r, this angle of contact varies significantly adapting the REB operation to the load (**Table 2-2**). As described in section 1.2.2, as the angle of contact increases so does spinning and therefore sliding at the contact edges, thus increasing the dissipated sliding energy represented by the criteria $P.\Delta U$ along the contact major axis (P and ΔU being respectively the local pressure and sliding velocity) (**Fig. 2.4** (c-d)), which will be of significant interest thereafter.

2.2.2.2 NTN-SNR ultra–clean bearing steel

The tested ACBBs are made of NTN-SNR 100Cr6 (AISI52100) through hardened and D2 tempered bearing steel whose composition and mechanical properties are detailed in **Table 1-1** and **Table 1-3**, respectively. As specified in Appendix D, the first sets of ACBB tested were made of *turned IR* and the others of *forged IR from a different steel batch*. If this does not affect the superfinishing process, it greatly affects the grain flow and the inhomogeneity preferential orientation when emerging at the raceway. In addition to roughness verifications (specified in **Table 2-2**), surface residual stresses have been measured using an X-Ray difractometer ELPHYSE Set X revealing a similar compressive machining residual stress field of ~500 MPa on the surface of both types of IRs (details in Appendix E).

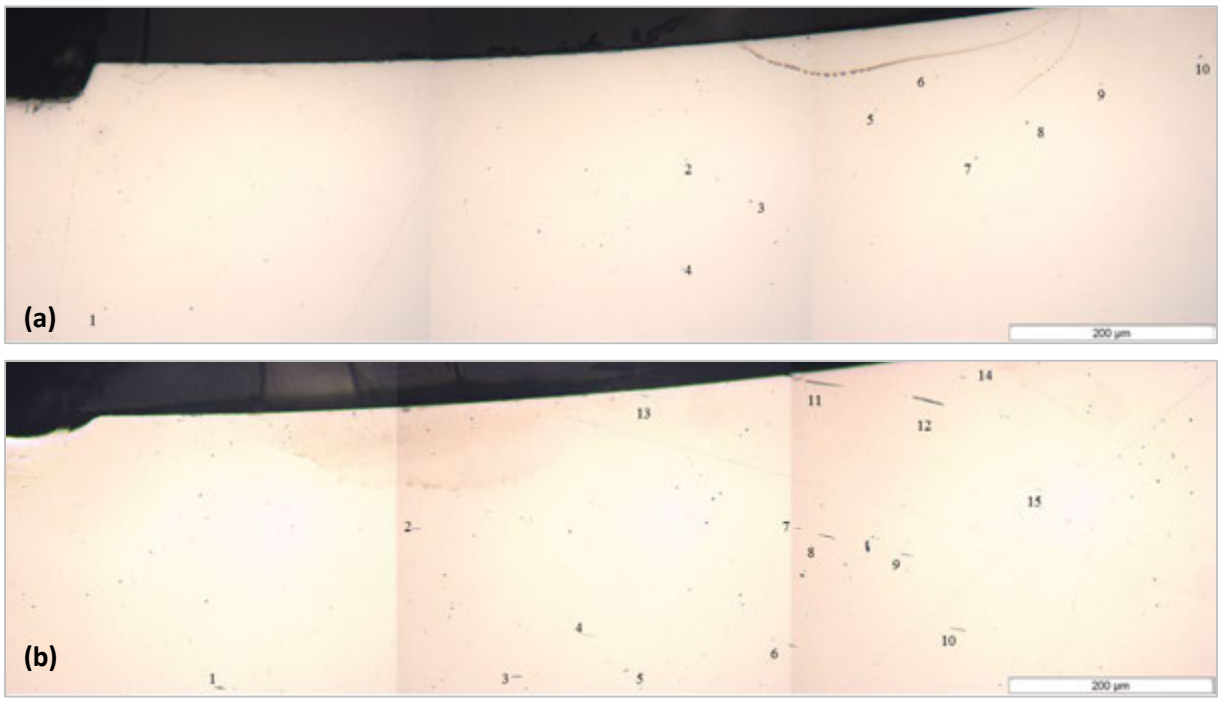

Fig. 2.5: Axial LOM prior to Nital etching revealing type A inclusions (MnS) of different morphologies and orientations vs. the raceway in forged (a) and turned (b) IRs coming from two different steel batches.

The steels used to manufacture the IRs have been attributed the automotive *top quality* grade defined at NTN-SNR which combines (1) the ISO 4967 Method A standard based on the worst field for each inclusion type, (2) the DIN 50602 standard for inclusion density, (3) the extreme value analysis method based on ASTM E 2282-3, (4) ultrasound detection of very large inclusions, and (5) RCF benchmarking on NTN-SNR FB2 test rigs as described in [146]. Therefore, to the exception of stringer MnS inclusions (type A) relevant in the turned IRs, the ACBB presented few amounts of inclusions of relatively small size as confirmed by the ratings provided in Appendix F.

As the influence of inclusions on WEC initiation is highly discussed in the literature, additional assessments have been led to evaluate the size and orientation of type A inclusions for both sets of IRs in the zone of interest. As depicted in **Fig. 2.5**, the turned IRs present long stringer MnS inclusions that emerge at the raceway with a preferential angle of ~20° whereas the forged IRs present only globular MnS that go along with the deformed grain flow mostly parallel to the raceway (details on the numbered inclusions in Appendix F).

2.3 Tribological RCF testing on a Twin-Disc Machine (TDM)

2.3.1 Machine and typical operating conditions

Further RCF experiments have been performed on the *Twin-Disc Machine (TDM)* available at the LaMCoS for an enhanced control of the tribological parameters [205]. This high-cycle *RCF tribological simulator* has been chosen for its minimalist and robust design compared to other simulators such as the Four-Ball RCF test or the PCS Instruments Micro-Pitting Rig (MPR). Previous RCF protocols designed for the TDM have shown to be very repeatable [55,90,205].

The TDM simulates the high-cycle fatigue of a Hertzian contact between two *discs*, also referred to as *rollers* or *specimens*, one being crowned and the counter one cylindrical (**Fig. 2.6**). The respective radii are chosen as a function of the desired contact pressure and ellipsoid ratio. The load is applied by a pneumatic jack controlled by a manometer. The rollers are driven by a single motor, a bevel gearbox and various combinations of pulleys and cranked belts in order to impose the desired *constant SRR* between the two rollers (**Fig. 2.6** (a)). The contact is lubricated by an *oil jet* fed by a pump connected to a ~5 L thermostatic oil container. The oil *temperature* is controlled by a probe inside the oil jet near the contact inlet. Each test is either interrupted willingly or stopped automatically when a defect is detected by the *electromagnetic sensors* at the proximity of each disc. Several specific installations, detailed afterwards, have been added to the TDM for this study.

Table 2-3: LaMCoS TDM RCF test rig operating condition ranges explored in this study

	Parameter	Technical solution	Operating conditions
Applied	*Normal load*	pneumatic jack	1000 – 7000 N
	Lubrication	oil jet thermostatic bath filters	- Oils *A, B, C, D* and H_2O contamination - maximum flow rate: Q_{pump}≈2 L/min for ISO VG 46 oil at 80°C - filter: magnetic
	Oil temperature	thermostatic bath	40-120°C
	SRR	pulley ratio	0 - 60%
	Rotational speed	speed regulator electric motor bevel gearbox	nominal speed regulated at:1500-3000 rpm
	Contact parameters	Disc geometry	Pressure $1 \leq P_H \leq 3.5$ GPa - ellipse ratio $1 \leq k < 5$
Measured	*Defect*	Magnetic sensor	Threshold for test immediate stop
	Oil inlet temperature	Temperature probe	40 - 80°C
	Duration	-	Test suspension at ~220 h

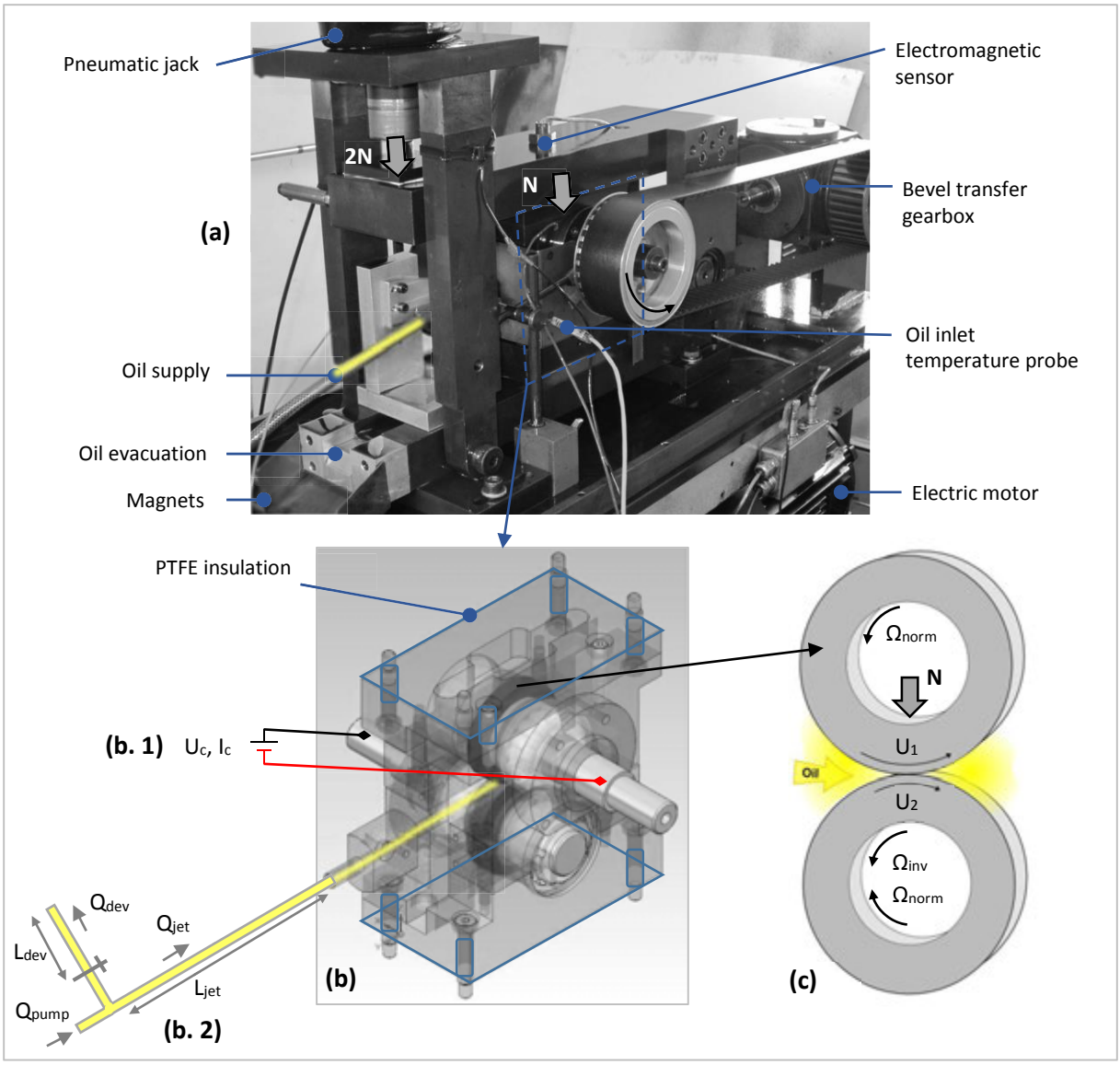

Fig. 2.6: LaMCoS TDM RCF test rig: (a) Main operational components and sensors; (b) Scheme of the roller mounting and optional specific installations to (1) impose an electric potential or current through the contact and to (2) regulate the jet oil flow Q_{jet} by varying the relative pipe losses of an opened deviation; (c) Scheme of the twin-disc tribological contact parameters.

The TDM is not equipped to measure the friction coefficient, contrarily to the specific *LaMCoS two-disc machine* mentioned in section 1.2.4.3. However, several traction curves have been plotted using the latest machine on which were mounted *standard TDM rollers* described hereunder. The friction coefficient has thus been plotted function of the SRR for several TDM test configurations, with lubricant A, for ranges of temperatures of 50 – 80 – 100 °C, of contact pressures of P_H=2 – 2.5 – 3 GPa, and of entrainment speed of U_r=11 – 16 – 22 m/s (**Fig. 1.22**). For several of these traction curves, the SRR was brought up to the scuffing point in order to identify an approximate $\mu.P_H.\Delta U$ *threshold for scuffing* (μ being the coefficient of friction) to avoid this irreversible deterioration during TDM RCF testing (**Fig. 2.7**). Scuffing has been defined has the point where the friction coefficient brutally increases, coinciding with the moment consequent smoke arises from the contact.

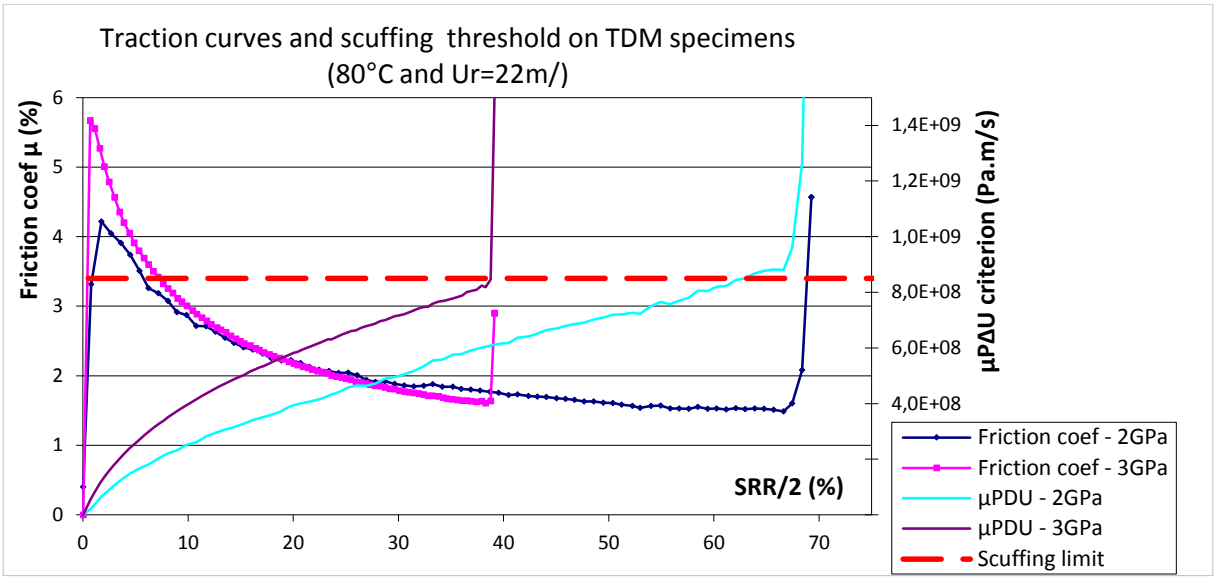

Fig. 2.7: Traction curves performed on the LaMCoS two-disc machine suggesting a μPΔU threshold to establish a scuffing limit for future TDM RCF tests.

2.3.2 Tested specimens

The tested specimens were made of the same *100Cr6* steel batch as the turned ACBB IRs and have been provided the same through hardening and *D2 tempering heat treatment* leading to a mean hardness of 780 Hv (63 HRc). Surface residual stresses have been measured using the X-Ray difractometer, giving compressive machining residual stress fields of ~150 MPa (Appendix E). All the rollers, crowned and cylindrical, have a fixed outer diameter of 70 mm. Rollers have been mounted on the shaft with a loose fit, being maintained in position by a screw *lateral fit* (**Fig. 2.8** (b)). In addition to the standard roller geometries dedicated to the TDM, specific rollers have been manufactured to modify the roller profiles, roughnesses, stress state and inclusions orientations in order to multiply the RCF testing configurations.

Crowning. The standard geometrical configuration to obtain a circular Hertzian contact area consists in a cylindrical roller on a crowned one with a crown radius of *17.5 mm* (**Fig. 2.8** (a)). In order to simulate elliptical contacts closer to the ones found in the ACBBs fore described, crowned discs with a crown radius of *200 mm* were also used in this study; the limitation being the significant decrease in maximum Hertzian pressure imposed by the limit of the pneumatic jack.

Roughness. The discs were commonly superfinished to a mean roughness R_q of *~0.02-0.03 μm* with circumferential machining (as for REB raceways). In addition, discs with an increased roughness of 0.15 μm have also been used to run RCF tests under *mixed lubrication regimes* (**Fig. 2.8** (a)).

Addition of structural stresses. In addition to the standard, specific specimens have been designed to study the influence of the superposition of diverse structural stresses, notably fitting hoop stresses, onto contact stresses (**Fig. 2.8** (c-d)). Hoop stress calculations are detailed in Appendix C. In addition, in certain rollers, holes of various diameters have been manufactured throughout the circumference in order to modify the stress field near the contact by different magnitudes.

Inclusions orientation. Rollers are commonly manufactured perpendicularly to the respective cylindrical steel rod for evident practical reasons. The type A inclusions being elongated in the principal direction of the steel rod, they thus lie parallel to the raceway in standard rollers. In order to evaluate the influence of the inclusion orientation versus the raceway, specific discs have been manufactured horizontally versus the steel rod (**Fig. 2.8** (e)), thus presenting a complete range of emerging inclusion angle along their circumferences (**Fig. 1.4** (b)). A mark was left in order to locate the principal steel rod dimension where MnS inclusions emerge vertically versus the raceway.

Tapered discs. In order to simulate a sliding velocity gradient along the contact axis transverse to rolling motion, specific tapered discs with raceways inclined by 10° have been manufactured. These rollers are then mounted with a crowned one of radius 17.5 mm to avoid any edge effect. It can thus be determined that this profile will induce a ±3.5% SRR difference at the respective contact edges, partially representative of sliding gradients occurring in cylindrical thrust REBs for example.

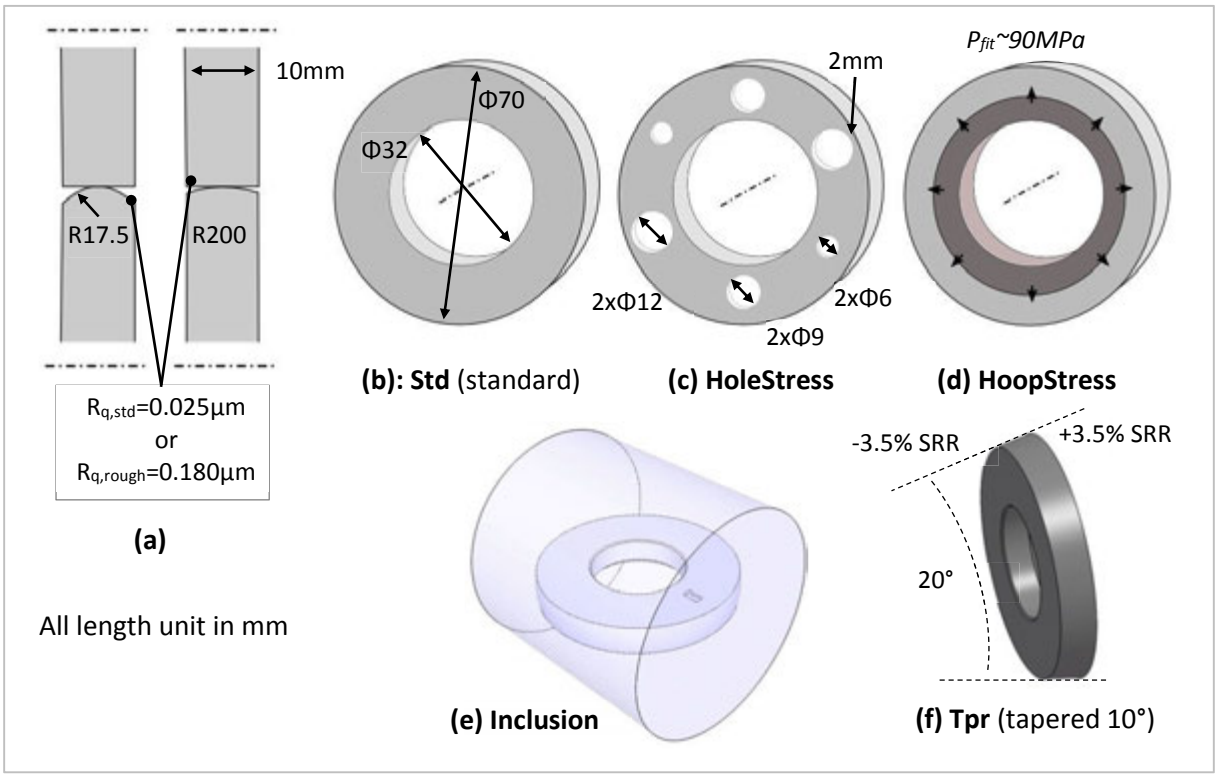

Fig. 2.8: Schemes of the different rollers used in this study and corresponding nomenclature used for Appendix H: (a) Cylindrical and crowned roller profiles and roughness configurations; (b) Standard roller geometry (c) Structural stress modifications using holes; (d) Press fitted IR inducing an estimated 90 MPa hoop stress into the tested cylindrical disc; (e) Disc manufactured horizontally versus the steel rod; (f) Tapered disc with a 10° raceway inclination inducing a ±3.5 % SRR linear gradient along the contact width.

2.3.3 Lubricants

In order to study WEC formation mechanisms on the TDM, the contact parameters of the Machine S ACBB have been transposed step by step on the TDM. Therefore the large majority of the tests have been performed with the same standard commercial ISO VG46 mineral gearbox oil (*lubricant A*). Additional TDM tests have been conducted with two similar ISO VG46 and ISO

VG35 gearbox mineral and semi-synthetic oils containing higher amounts of additives, notably sulfur/phosphorus EP/AW and detergent additives (*lubricant B and C*). A few tests have also been done with a known low reference PAO-based and highly additivated ISO VG320 wind turbine oil (*lubricant D*) but were limited as the high viscosity often implied higher film thicknesses than desired. Lubricant rheological properties and infrared emission spectrometry for chemical content indications (AFNOR standard NFT60-106 or ASTM D5185) are detailed respectively in **Table 2-4** and **Table 2-5**.

Table 2-4: Rheological properties of the lubricants (lubricant A for Machine S ACBB and TDM tests).

Ref	Density at 15°C	Viscosity at 40°C (mm²/s)	Viscosity at 100°C (mm²/s)
A	0.86	44.5	6.9
B	0.89	45.4	8.6
C	0.86	35.8	7.5
D	0.87	305	30.5

Table 2-5: Infrared emission spectrometry for lubricant chemical content in ppm (ASTM D5185).

Ref	P	Zn	Ca	Mg	Mo	Na	B	Ba	K	S
A	125	75	0	0	0	0	0	0	0	1582
B	485	261	468	6	49	31	2386	0	2591	9066
C	402	215	395	0	41	30	2374	0	2589	6165
D	1500	1900	0	1896	1283	4	34	0	8	6900

2.3.4 Specific procedures

Throughout this study, *extensive RCF testing has been led on the TDM* machine under many different conventional RCF tribological conditions, varying the operating conditions (section 2.3.1), the lubricant (section 2.3.2) and the specimen type (section 2.3.3). Nevertheless, as WECs seem to rely also on other unconventional drivers*, specific procedures* have been added in order to qualify their influence on WEC formation. All the TDM RCF tests specifications and results are available in Appendix H, resulting in more than 7500 hours of TDM service. The tests have been referenced TDMXX_YY, XX referencing the main configuration set and YY the number of the test.

2.3.4.1 Artificial dents

In order to accelerate the RCF tests and generate artificial surface microcracks, a standard protocol developed at the LaMCoS consists in performing artificial dents on one of the rollers, acting as stress raisers that accelerate surface initiated cracks on the counter roller (**Fig. 2.9**)[55,56,90]. In this study this protocol was employed to pre-initiate surface microcracks (all tests referenced TDM07_YY in Appendix H) in order to further study the influence of several tribological drivers on their propagation and on the formation of white etching microstructure at the crack flanks under RCF testing. All the artificial dents in this study were done using a 50 Kg Rockwell indenter, and thus had a ~250 µm diameter, in accordance with the 100Cr6 D2 hardness (**Fig. 2.9** (a) and exact profile detailed **Fig. 2.10** (b-c)). The dents were positioned equidistantly on the disc circumference, either aligned or spaced with an off-set depending on the disc geometry and on the desired microcrack opening location (**Fig. 2.10** (a)).

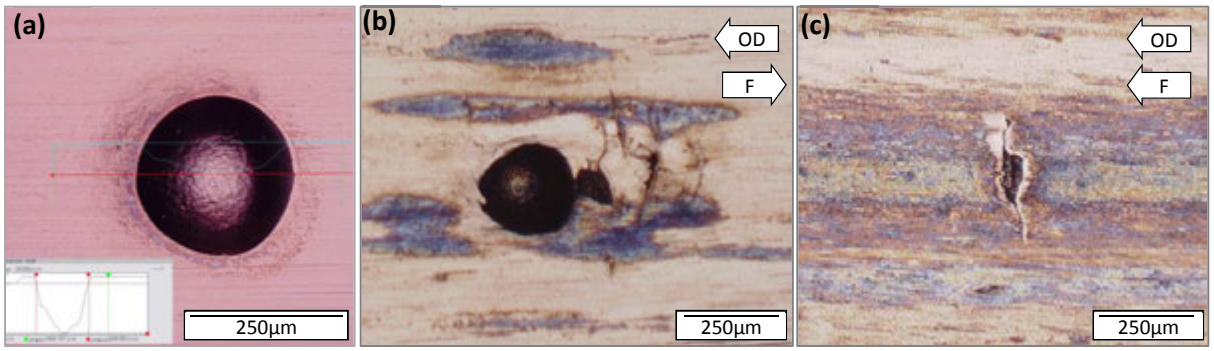

Fig. 2.9: LOM topview of disc raceways: (a) Artificial dent (50 Kg Rockwell indenter prior to testing); (b) Dent evolution after RCF testing on the follower surface (Appendix H ref TDM07_07) (c) Typical surface initiated crack at the raceway border on the counter driver roller (Appendix H ref TDM07_02_I_b).

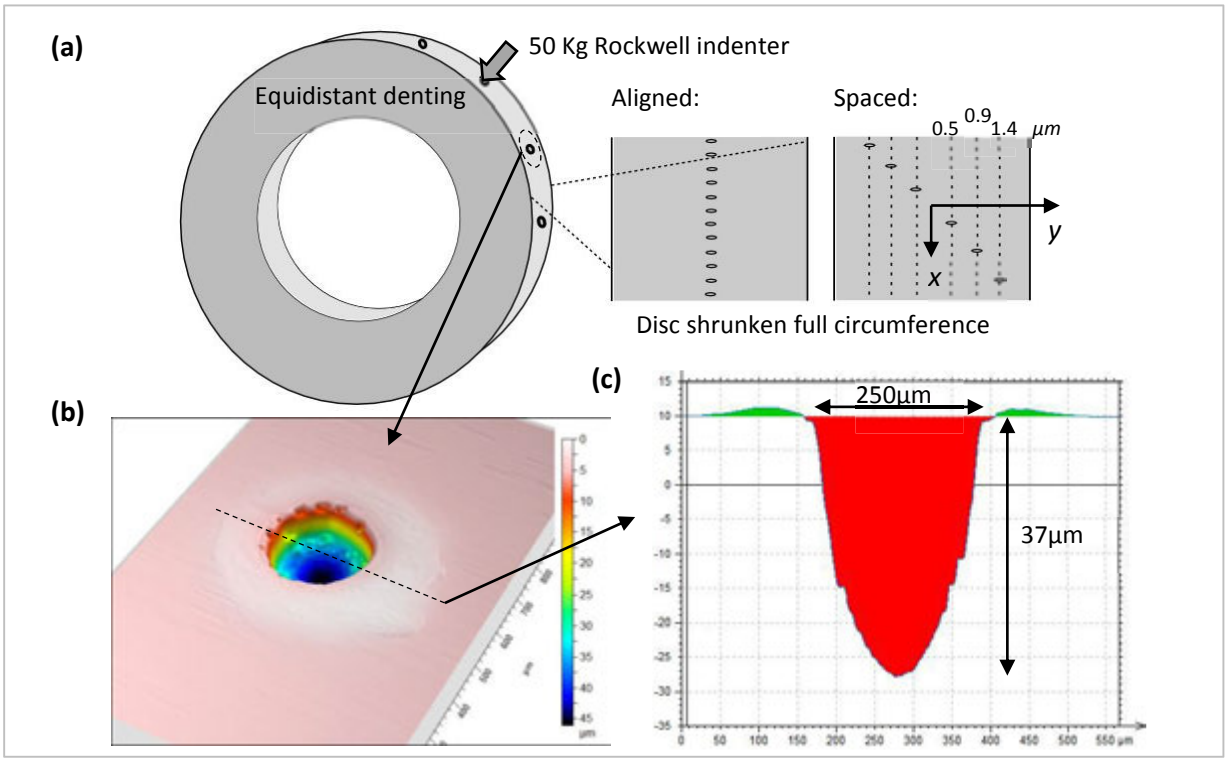

Fig. 2.10: Artificial dent analysis prior to RCF testing: (a) schemes of different dent positionings on the disc circumferences; (b) 3D dent topography and (c) profile measured with SENSOFAR PLu neox.

2.3.4.2 Oil flow rate reduction

In order to be able to perform TDM RCF tests under starved and mixed lubrication the oil circuit has been modified to reduce the oil flow rate at the contact inlet Q_{jet} as schemed in (**Fig. 2.6** (b. 2))[205]. As Q_{pump} cannot be set to less than ~2 L/min for lubricant A at 80°C, a deviation was installed to flush the unwanted oil directly back to the thermostatic bath at a flow rate of Q_{dev}. The ratio between Q_{jet} and Q_{dev} was set by adjusting the pipe lengths, thus losses, from the deviation to the jet L_{jet} and the oil bath L_{dev} respectively. The pipe lengths were first estimated using the conservative flow law and then precisely adjusted by dichotomy on Q_{jet} measured by timing the filling of a 500 mL container. This procedure allowed to reduce Q_{jet} down to $0.13L/min$, threshold for which *scuffing* risk is high considering the given operating conditions. Indeed, close to this threshold, the flow rate is not sufficient to evacuate the heat generated at the contact so that the

lubricant film collapses as the oil viscosity falls, which entrains a vicious circle leading to *scuffing* (section 1.2.3). As this scuffing flow rate threshold is highly dependent on the operating conditions and requires a precise adjustment of the pipes, this protocol has been used only in one particular set of TDM tests operating under the same conditions (load, speed, SRR, lubricant, etc.) (TDM09_YY in Appendix H).

2.3.4.3 Imposed electrical currents

Electrical currents have been mentioned to be influent on WEC formation mechanism [168,192,193] and are a probable tribological issue in various WEC-affected applications such as wind turbines [99], automotive alternators [172], and trains axels (required to transmit the signal of train presence on the tracks). In this context, the TDM housings of the respective top and bottom shaft – specimen assemblies have been insulated using PTFE (**Fig. 2.6** (b)). An electrical circuit has then been installed to impose an *electric potential* U_C or a contact *current* I_C through the contact lubricant film. In order to comply with *high variations in contact resistivity* function of the imposed current and/or the operating conditions (**Fig. 2.12**), as confirmed by [98,193], and in order to be able to impose insidious currents of the magnitude of 0.1 mA, a variable resistor R_V has been added in the circuit (**Fig. 2.11**). The electrical contact between the rotating discs has been performed by stripped copper wires brushing directly on the respective shafts (**Fig. 2.6** (b. 1)), the positive pole being the top shaft (**Fig. 2.11**). Experimental tests have been performed prior to RCF testing in order to adjust the electric potential or current. In doing so, it has been noticed that the contact resistivity, depending both on the asperity contact ratio and the lubricant natural resistivity, was highly dependent of the input current *Ic* (**Fig. 2.12**).

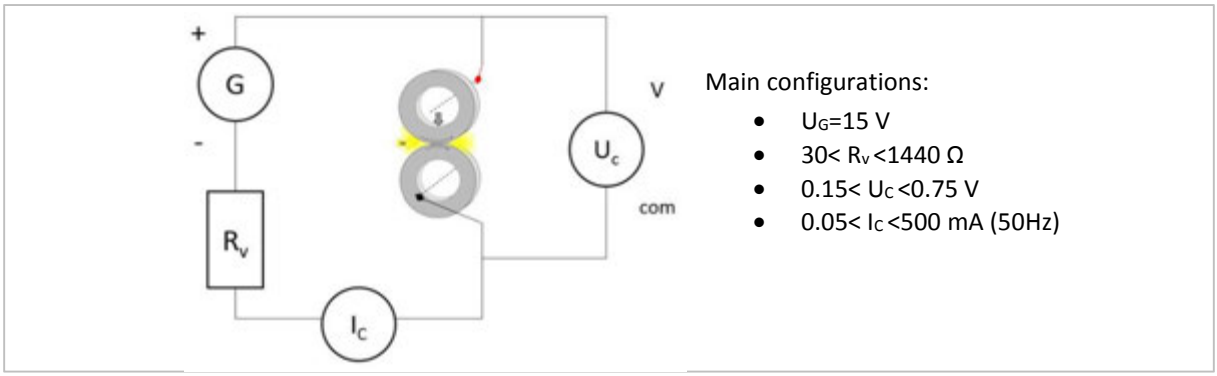

Fig. 2.11: Scheme of the electrical circuit deployed on the TDM.

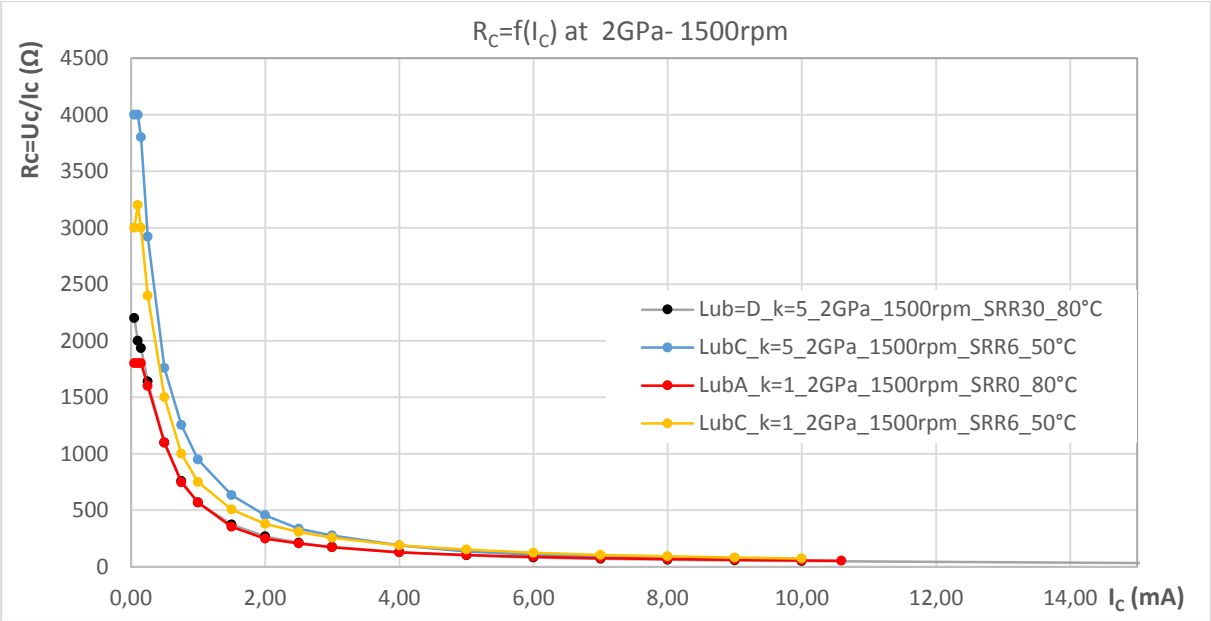

Fig. 2.12: Evolution of the contact resistance R_C as a function of the input current I_C for different TDM contacts at P_H=2 GPa, U_r=11 m/s for varying lubricant, temperature, SRR and ellipsoid ratio *k*.

2.3.4.4 Water ingress protocol

Oil water contamination has often been associated to accelerated RCF [109,195,206–211], even when water is present in incipient concentrations as low as tens of ppm corresponding to water ingress inside the oil chemistry, also referred to as *hygroscopy*. First, water is naturally present in lubricants in incipient concentrations. As illustrated by **Table 2-6**, this natural hygroscopy highly depends on the *lubricant formulation*, and notably on the presence of hygroscopic polar blends, (e.g. *PAG* and *esters*), and/or polar additives such as *detergents* and *emulsifiers* (section 1.2.3.2) [97,211]. Water ingress can be enhanced naturally by lubricant ageing as H_2O molecules are one of the products of the thermal-oxidation (combustion) of lubricant molecules inside the contact due to high contact pressures and flash temperatures [211–213]. Water ingress can also come from external contamination associated to seal leakage and condensation issues that are all commonly found in WEC related applications such as wind turbines subjected to wide day-night cycling temperature ranges [97,211], automotive wheel bearings (experienced at NTN-SNR), washing machines, air conditioners, fans, etc. It is worth mentioning that of the seven oils that have been associated to WEC failures at NTN-SNR, four contained over 500 wt.ppm of ingressed water (*F1, F2, F3, F4*), the other ones being lubricants *A, B, C* (**Table 2-6**).

In this context, a protocol has been established to ingress water into various lubricants (*A, B, C, D* and another commercial wind turbine oil referenced *E*) in order to evaluate the capacity of each lubricant to ingress water depending on its formulation. After visual control of the lubricant samples getting blurry after artificial water ingress (**Fig. 2.13**), the respective water content measurements have been made using the *Karl Fisher* titration method at NTN-SNR (NF T 60-154/ISO6296/ASTM D 1744) (**Table 2-7**). As the idea was to then use this water ingress protocol in TDM RCF tests, it was therefore achieved *without mechanical emulsion* by inserting the lubricant in a *hot and humid environment,* as suggested by [211], for a given time and at a given temperature (**Table 2-7**), protecting the lubricant container from potential condensation droplets that could form bubbles in the lubricant. This protocol thus prevented the formation of *micro-bubbles* in the

lubricant, which would modify its rheology and increase the risk of lubricant film breakdown inside the contact, leading to excessive and undesired surface distress. This issue probably occurs in specific water contamination studies in the literature where water is stirred inside the lubricant with excessive concentrations of up to ~5 - 40 wt. % [206,208,209,211,214]. The preliminary results in **Table 2-7** tend to confirm that (1) a lubricant hygroscopy is highly dependent of its formulation (as in **Table 2-6**) and that (2) the hotter the environment, the higher the water ingress even though a saturation level seems to be reached after a given time [211].

Table 2-6: Water content in wt. ppm determined by the Karl Fisher titration method applied to different lubricants either new or aged in application (in wt. ppm).

State/Oil	A*	B*	C*	D	E	F1*	F2*	F3*	F4*
New	50	250	180	430	90	450	930	920	820
Application	50 (2)	-	-	1000 (1)	162 (1)	-	-	-	-

In wt. ppm with ~10% uncertainty for each measure
(1): Wind turbine gearbox lubricants from field after >10000 hours of service
(2): NTN-SNR Machine S extensive service lubricant
** : WEC related lubricant, the others being also possibly WEC related but with no confirmation form experience or literature*

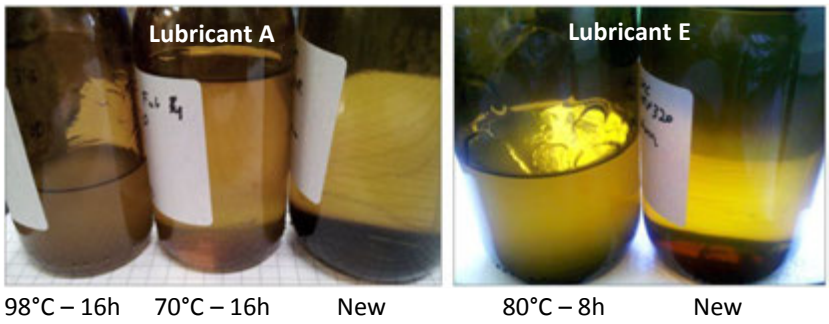

Fig. 2.13: Visual aspect of lubricant samples after environmental artificial water ingress.

Table 2-7: Water content determined by the Karl Fisher titration method applied to lubricants after different environmental artificial water ingress for a given time at a given temperature (wt. ppm).

Oil	New	16h at 70°C	16h at 98°C
A	50	220	540
Oil	**New**	**8h at 80°C**	**24h at 80°C**
D	430	1700	1700
E	90	650	660

In wt. ppm with ~10% uncertainty for each measure

For some of the *environmental* artificial water ingress performed in this study, *viscosity measurements* have been performed to verify that water contamination did not modify the basic rheological properties of the lubricant (**Table 2-8**). Additional tribological tests have been performed before the TDM tests using the PCS instruments High Frequency Reciprocating Rig (HFRR) in order to verify that water ingress does not modify the *tribo-mechanical behavior* of the lubricant. The HFRR tests have been performed by applying 5 gradual temperature steps from 40 to 120°C. The friction coefficient and estimated film thickness by capacitance measurements have first been plotted for the neutral and water ingressed lubricants (**Fig. 2.14**). Then wear scar topographical analyses have been performed using an optical profilometer (**Fig. 2.14**). The results

demonstrate that, in conditions of pure reciprocating sliding, the tribo-rheological behavior of the lubricant is not modified by the artificial water ingress protocol developed in this study. Indeed friction coefficient and wear remain quasi-identical at all temperature steps, thus supporting the absence of micro-bubbles (**Fig. 2.14**).

Table 2-8: Viscosity of the new and water contaminated lubricants (mm^2/s)

Oil	New	16h at 70°C	16h at 98°C	8h at 80°C
A	44.2	44.1	44.2	-
E	326	-	-	325

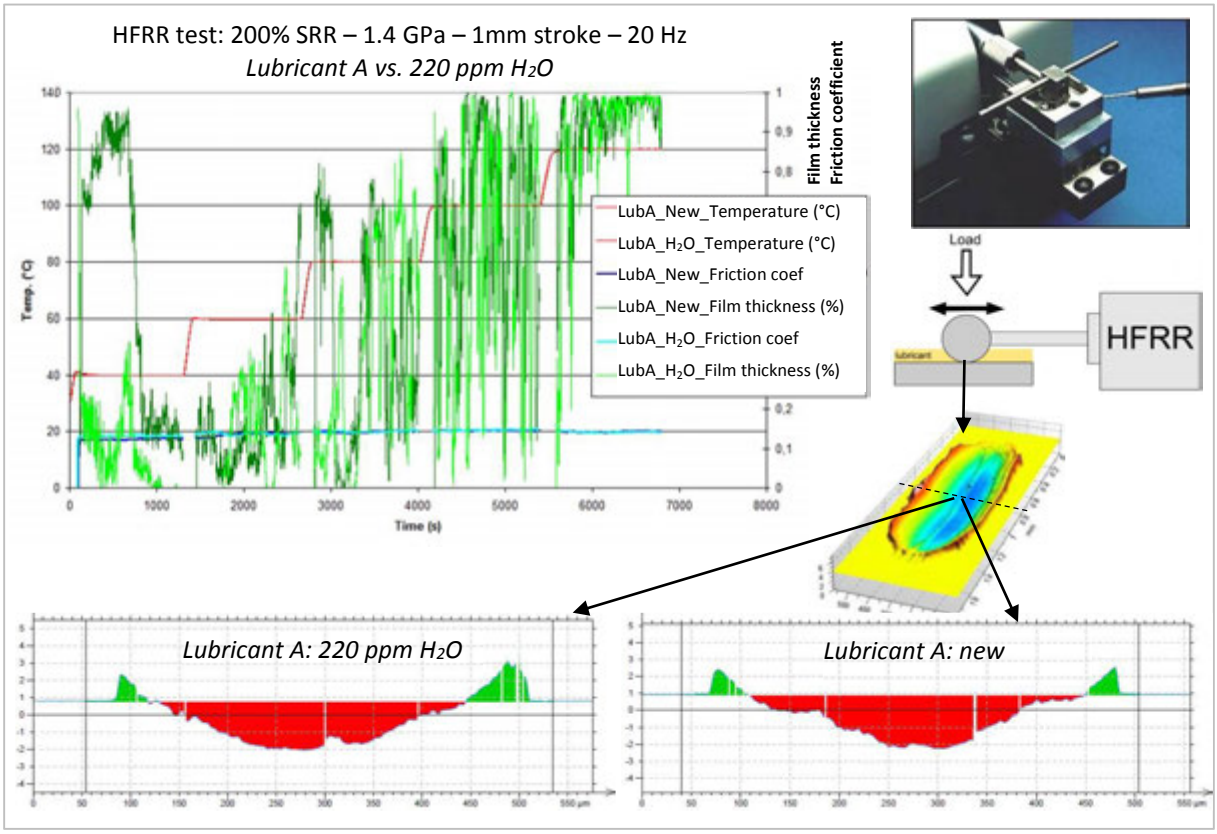

Fig. 2.14: Typical HFRR test result and wear scar profile by SENSOFAR PLu neox revealing respectively similar friction coefficient evolutions with the temperature and similar wear scars for lubricant A at neutral state and with 220 wt. ppm of artificially ingressed water.

2.4 Analysis and characterization protocols

Throughout this study, several analyses and characterization methods have been employed in addition to systematic LOM observations with the HIROX digital microscope KH-7700 comprising a wide choice of lenses and a useful adjustment of the lightning angle. On one hand, surface analyses such as *raceway profiles* and complementary *SEM-EDX analyses* have been performed to assess respectively the wear rate and the tribofilm aspect in order to better understand the tribological conditions affecting WEC formation mechanisms in the Machine S ACBB and TDM RCF test rigs (**Fig. 2.1** and **Fig. 2.15**). On the other hand, metallographic *serial sectioning* and *fractography* have been performed to reveal and analyze the subsurface WEC networks (**Fig. 2.1**).

2.4.1 Surface analysis

Surface analyses have most often been achieved by combining topographical assessments and microstructure observations, both detailed in the sub-sections thereafter (**Fig. 2.15**).

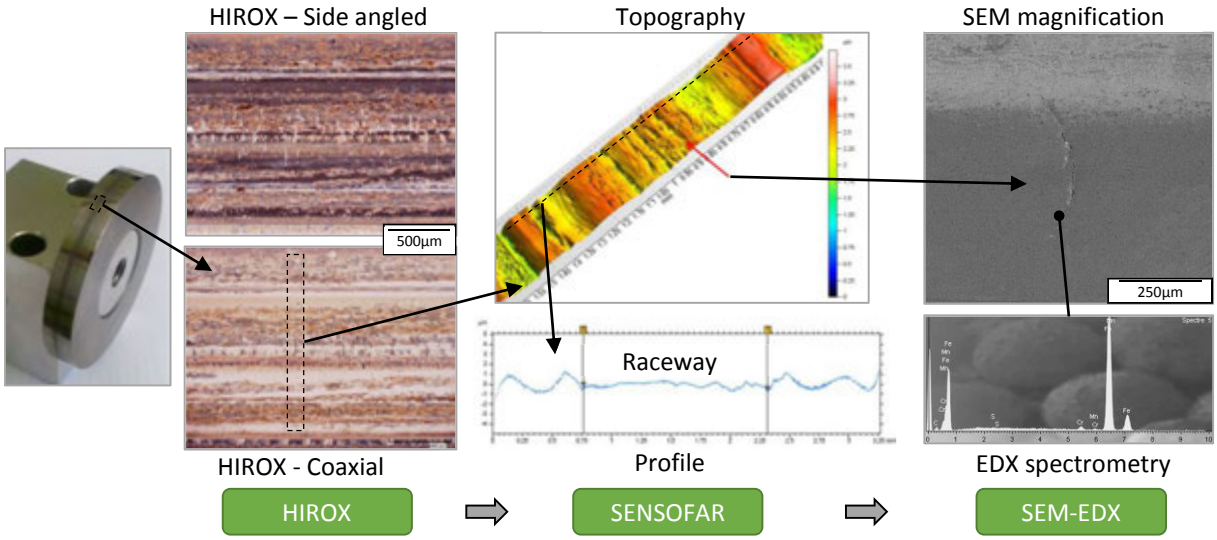

Fig. 2.15: Typical surface analyses of a TDM specimen: (1) HIROX LOM, (2) SENSOFAR raceway 3D topography and axial profile and (3) SEM-EDX and chemical spectroscopy in the vicinity of a microcrack.

2.4.1.1 Raceway profiles for roughness and wear

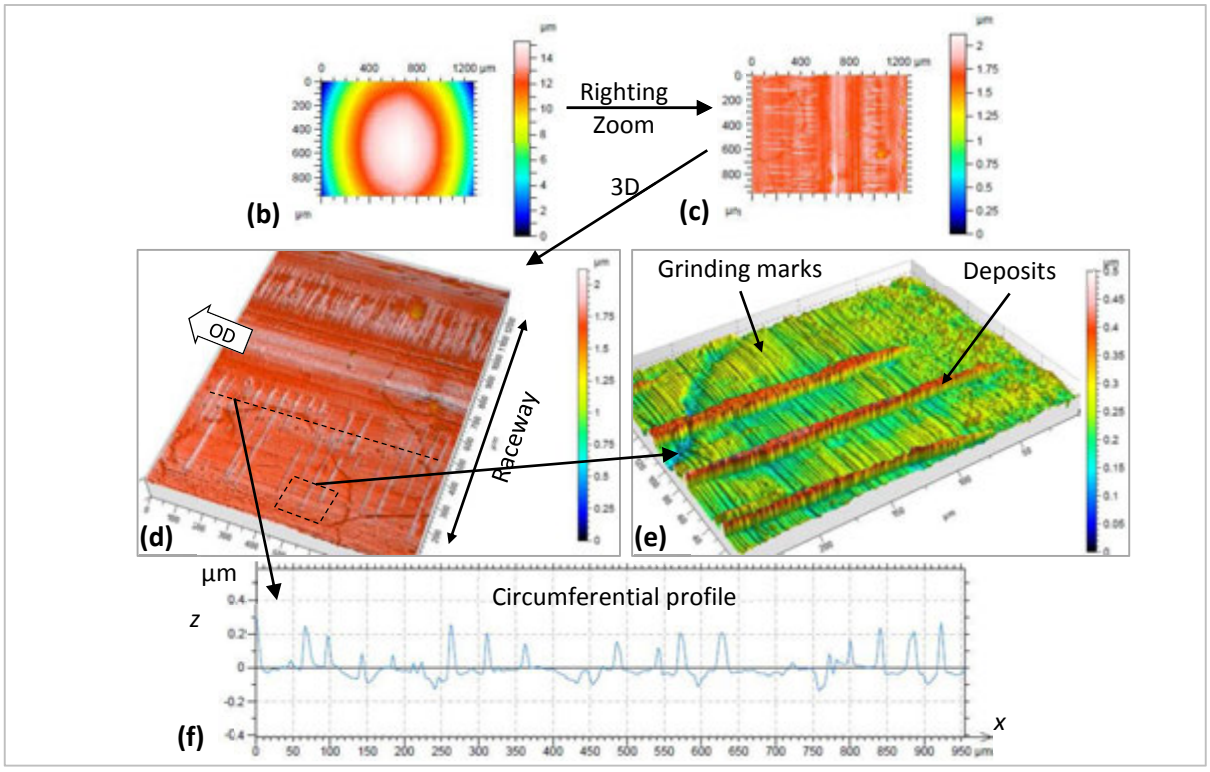

Fig. 2.16: Example of topography measurement by SENSOFAR PLu neox post-treated with MountainsMap (Appendix H ref TDM12_02): (a) raw measurement of a crown disc; (b) zoom at the raceway after righting; (c) 3D visual; (d) Close-up on features perpendicular to the circumferential grinding marks; (e) circumferential profile confirming regular transverse stripes of material deposit.

The topography of various raceways were acquired using the optical 3D profilometer SENSOFAR PLu neox, which combines confocal and interferometry acquisitions thanks to a z-axis step-motor with a piezoelectric actuator for nano-displacements. The resulting measurements were post-treated with the Digital Surf MountainsMap Topography XT 6 software in order to (1) fill-in the non-measured points by interpolation of the surrounding points, (2) suppress the surface macroscopic geometry, (3) generate 3D visuals, (4) edit profiles to identify wear and deposits along theraceways (**Fig. 2.16**). These topography analyses were achieved for most TDM RCF tests to acquire wear profiles and to analyse specific surface distress topographies (**Fig. 2.16**). However they remain much more delicate to acquire on ACBB rings due to their curvature.

2.4.1.2 Tribofilm characterization by SEM-EDX analysis and EDTA rinsing

As a complement to LOM and topography assessments, *Scanning Electron Microscopy (SEM)* combined with *Energy Dispersive X-Ray spectroscopy (EDX)* was regularly performed on REB rings as well as on TDM specimen raceways in order to achieve higher magnifications of surface features such as *microcracks* and to have an overview of the surface chemical compositions, for example in case of tribofilm formation. The SEM used during this study was a FEI Quanta 600 and both Secondary Electrons (SE) and Backscattered Electrons (BSE) detection have been employed as they often result in complementary images (**Fig. 2.17**). The Oxford Instruments x-sight EDX probe and the spectroscopy analysis were led by the Oxford Instruments INCA software.

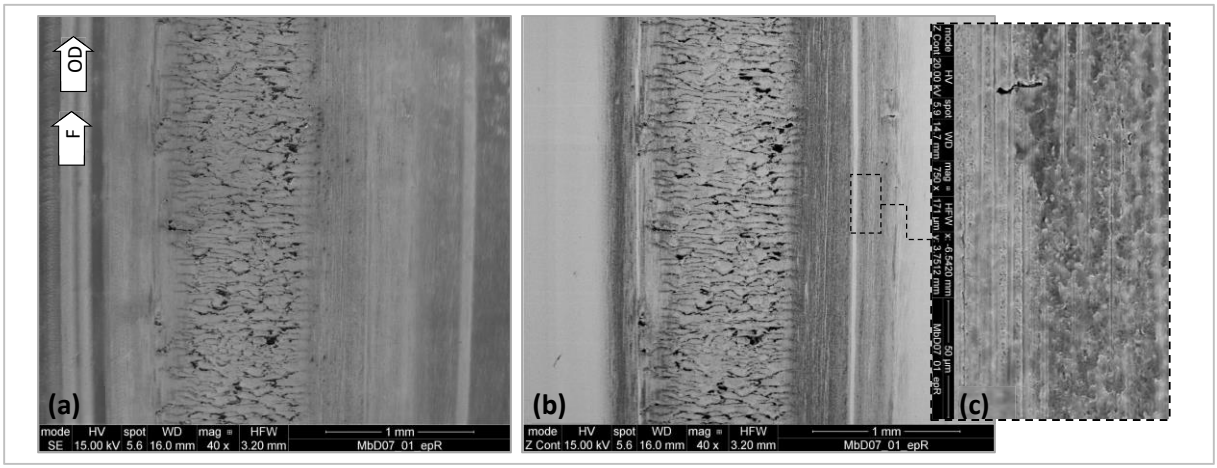

Fig. 2.17: SEM-EDX analysis led on a TDM specimen subjected to high surface distress and tribofilm deposit (Appendix H ref TDM07_01_II): (a) SE imaging; (b) BSE imaging revealing chemical deposits; (c) magnification of tribofilm deposit further confirmed by EDX analysis.

Prior to SEM-EDX analysis, all samples were rinsed with an ultrasound bath cleaning procedure based on three different solvents: *ethyl acetate, ethanol and heptane*. The chemical residue, usually appearing darker in BSE imaging and confirmed by EDX analysis, is then defined as unremoved tribolayer, i.e. *tribofilm*. However, one *main limitation* encountered in SEM analysis was that the disc specimens had to be sectioned to fit in the SEM chamber thus making it quite complex to follow surface tribofilm formation and/or distress during RCF testing. In order to be able to detect the presence of tribofilm directly using the HIROX, EDTA tissue cleaning was commonly led after the conventional three-solvent rinsing on part of the raceway as it is known to remove tribofilms, at least partially (section 1.2.3.5) [80]. This process is best depicted by co-axial and side-angled LOM and SEM-EDX observations (**Fig. 2.18**).

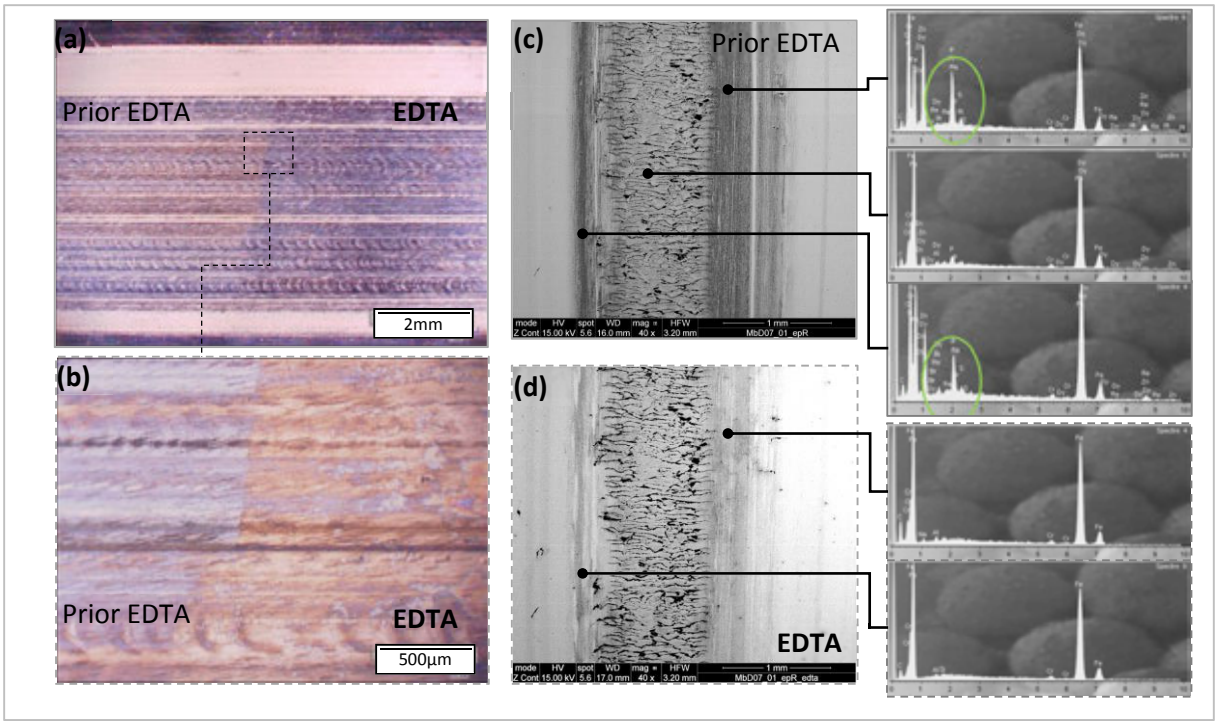

Fig. 2.18: Efficiency of EDTA to remove tribofilm deposits (1) illustrated by the clear frontier between the untouched left side and the EDTA tissue-cleaned right side of a TDM raceway observed on (a) side-angled LOM and (b) co-axial LOM close-up (Appendix H ref TDM12_07) and (2) confirmed by SEM-EDX analysis on a different TDM raceway (Appendix H ref TDM07_01_II) (c) prior and (d) after EDTA ultrasound bath rising where no more traces of sulfur and phosphorus remain.

2.4.2 Procedures to reveal White Etching Cracks

Considering the thinness of the cracks in WEC networks, especially that of secondary cracks (**Fig. 1.39** (e)), *no Non-Destructive Techniques (NDT)* were efficient in revealing the WECs entirety due to poor contrast with the bulk matrix considering both chemical composition (X-ray tomography) and mechanical properties (ultrasound probing). In case of ultrasound probing (even if the cracks were thick enough), all predominant vertical cracks, for example revealed in WEC networks of **Fig. 1.39**, would not reflect significantly the acoustic waves and therefore not be mapped. Therefore, two *destructive* techniques have been employed to reveal and study WEC subsurface features: *metallographic cross sections* and *fractographs*. The complementarity of these two techniques allows to obtain a representative 3D overview of WECs in REBs from RCF tests (**Fig. 2.19**) or from field applications such as wind turbines, as also employed by [34,162].

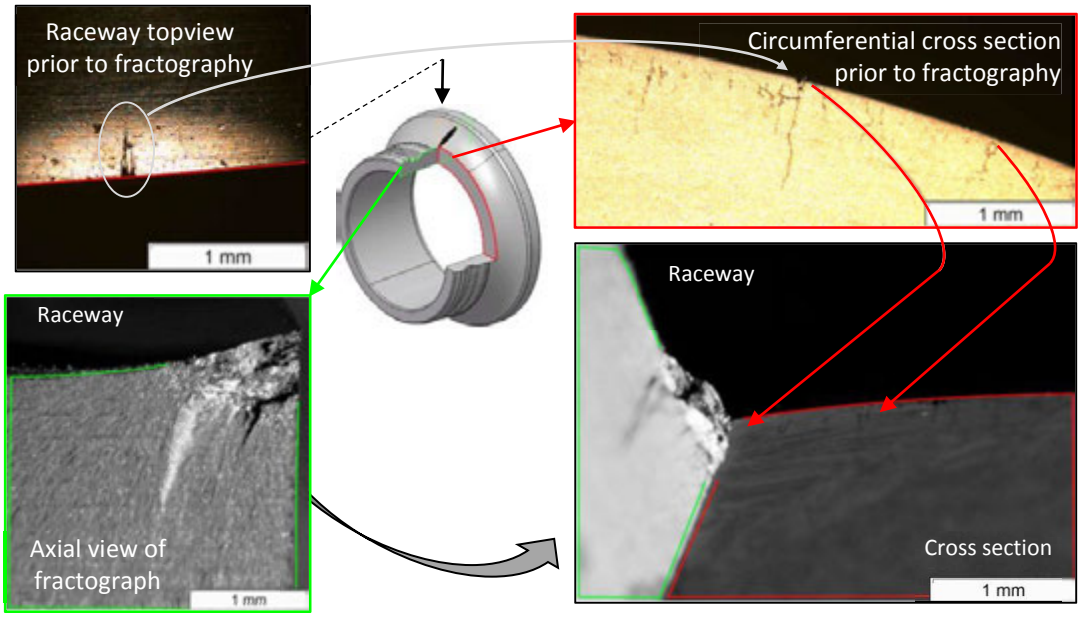

Fig. 2.19: Complementarity between metallographic cross sections and fractography to obtain a representative overview of WEC networks.

2.4.2.1 Metallographic sectioning and polishing

In order to observe subsurface microstructural alterations and crack networks, *metallographic cross sectioning* is probably the most employed technique (section 1.3.2). Whatever the component, either the ACBB IRs or the TDM specimens, the protocol is basically the same (**Fig. 2.20**):

1. Identify the location and orientation (*axial* or *circumferential*) of the plane of interest;
2. *Section* the component in order to best approach the plane of interest;
3. *Hot-mount* the specimen in resin for practical reasons, the plane of interest facing the exterior of the mount to be polished;
4. *Polish* progressively using the adequate polishing sheets (commonly from P320 down to 1 µm cloth);
5. *Etch* the polished surface to reveal the microstructure (usually with Nital 2%);
6. *Analyze* the specimen (LOM or SEM-EDX);
7. Back to step 4 if *serial sectioning* required;
8. *Break* the mount if required to verify the precise location of the plane of observation.

It should be emphasized that darker areas around the cracks may occur due to staining (etchant entrapment inside the cracks), thus possibly altering the interpretation of a LOM (**Fig. 2.20** and **Fig. 1.39**). The main advantages of *metallographic cross sectioning* are that it permits (1) to observe WEC networks with a low risk of modify them thanks to a progressive approach, and (2) to compare WEC related microstructural alterations with conventional RCF ones (section 1.3.2)(**Fig. 2.20**). Moreover, this protocol may be repeated at regular intervals of a few µm in order to map WECs entirety in 3D by superimposing the successive planes of observation using a segmentation software as Image J or Amira (**Fig. 1.43**) [188,200]. However, metallographic cross sectioning presents three main draw-backs. *First*, it is destructive. *Second,* it is time consuming. *Third,* it is a 2D technique (without considering serial sectioning) and thus presents a high risk of missing the WEC network if not well positioned. This last case is highly probable if (1) a circumferential cross section

is not at the WEC corresponding location versus the contact ellipsoid (discussed in **Chapter 3**); or if (2) an axial cross section misses a probable WEC network due to their discrete layout on a circumferential point of view (green line in **Fig. 2.20**). This third point is a real issue in WECs revealing as they present *no* or often *undetectable* incipient links to the surface that could help locate them prior to sectioning if the component has not spalled yet (discussed in **Chapter 3**).

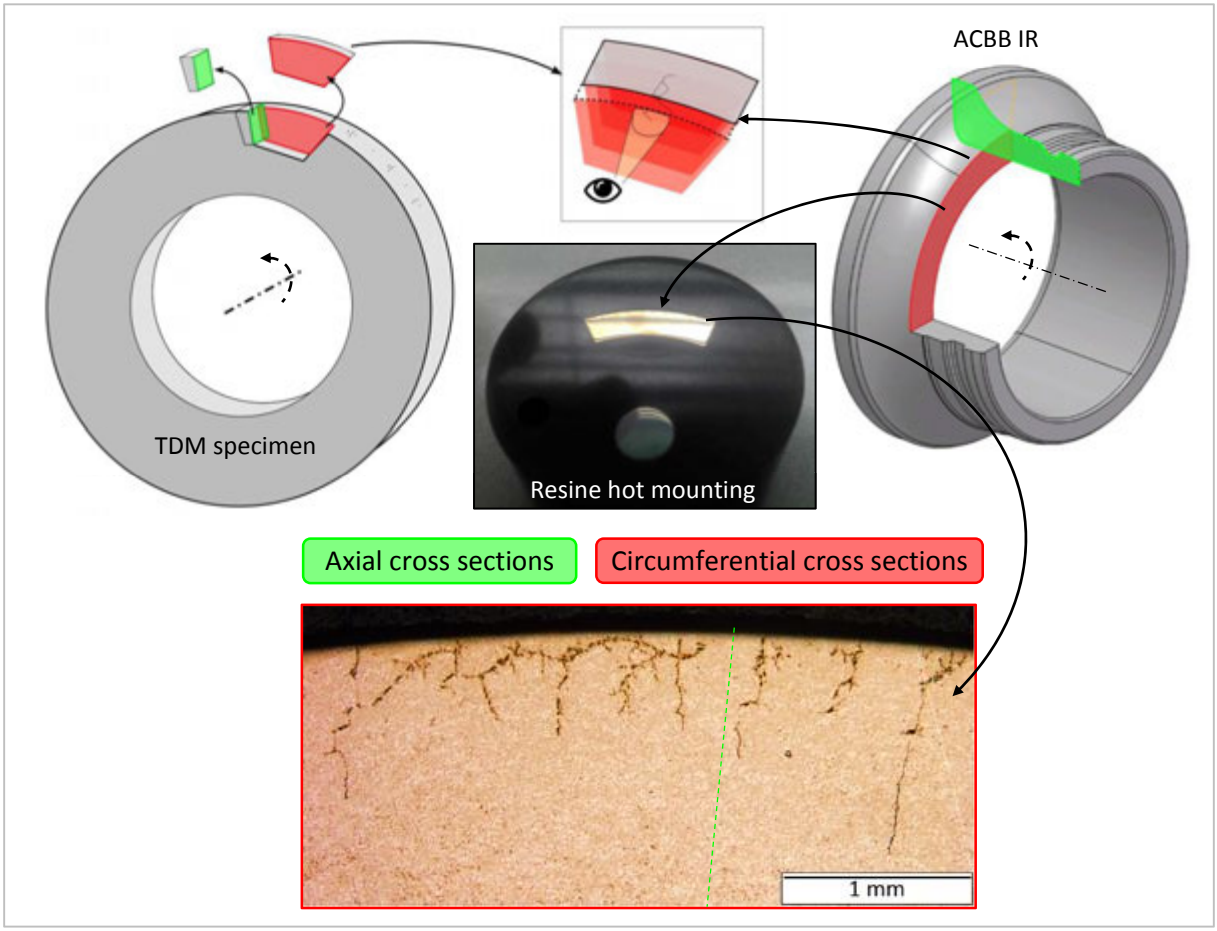

Fig. 2.20: TDM and ACBB IR axial and circumferential cross sections polished after hot mounting into resin in order to reveal potential WEC networks by Nital 2% etching.

2.4.2.2 Fractography

In order to deal with the *second and third* metallographic sectioning drawbacks, *fractography* has been performed on REB rings and TDM specimens to force open the WECs considering that the latest are, *if present*, pre-existent cracks that will act as a weak point thus initiating the bulk fracture. Fractographs are performed by circumferential three-point bending of specimens that may be pre-sectioned in order to ease the bulk fracture (especially for TDM specimens presenting thick cross sections) (**Fig. 2.21**). The load F is applied step by step until reaching fracture of the specimen thus opening the pre-existent WECs.

For REBs, specific positioning tools have been designed in order to maintain the portion of the IRs in place while applying the load (**Fig. 2.21** (a-b)). By additionally monitoring the applied load on a known WEC-free IR, it has been possible to establish a *load threshold* (F=35 kN) above which IRs are most probably WEC-free (or solely affected by incipient WEC that remain undetectable both by metallographic cross sectioning and fractography) (**Fig. 2.21** (d)). Above this

threshold, specimens mainly fracture brutally due to the worst defect whatsoever. On the contrary, when specimens are WEC-affected they most often fracture for loads three times lower than the threshold (usually for 12.5<F<14 kN) (**Fig. 2.21** (d)). WEC networks are then clearly visible with the naked eye as they present a brighter aspect than the bulk fracture (**Fig. 2.21** (e)). Further analysis using the HIROX digital microscope and/or the SEM-EDX confirms the pre-existent ground WEC crack flanks compared to the fresh bulk fracture (**Fig. 2.21** (f)) [6,29,162,164]. Metallographic serial sections have also been performed on a WEC fractograph in order to verify that the specific bright features were well associated to what has been defined as WEC (**Fig. 2.22**), in agreement with [6].

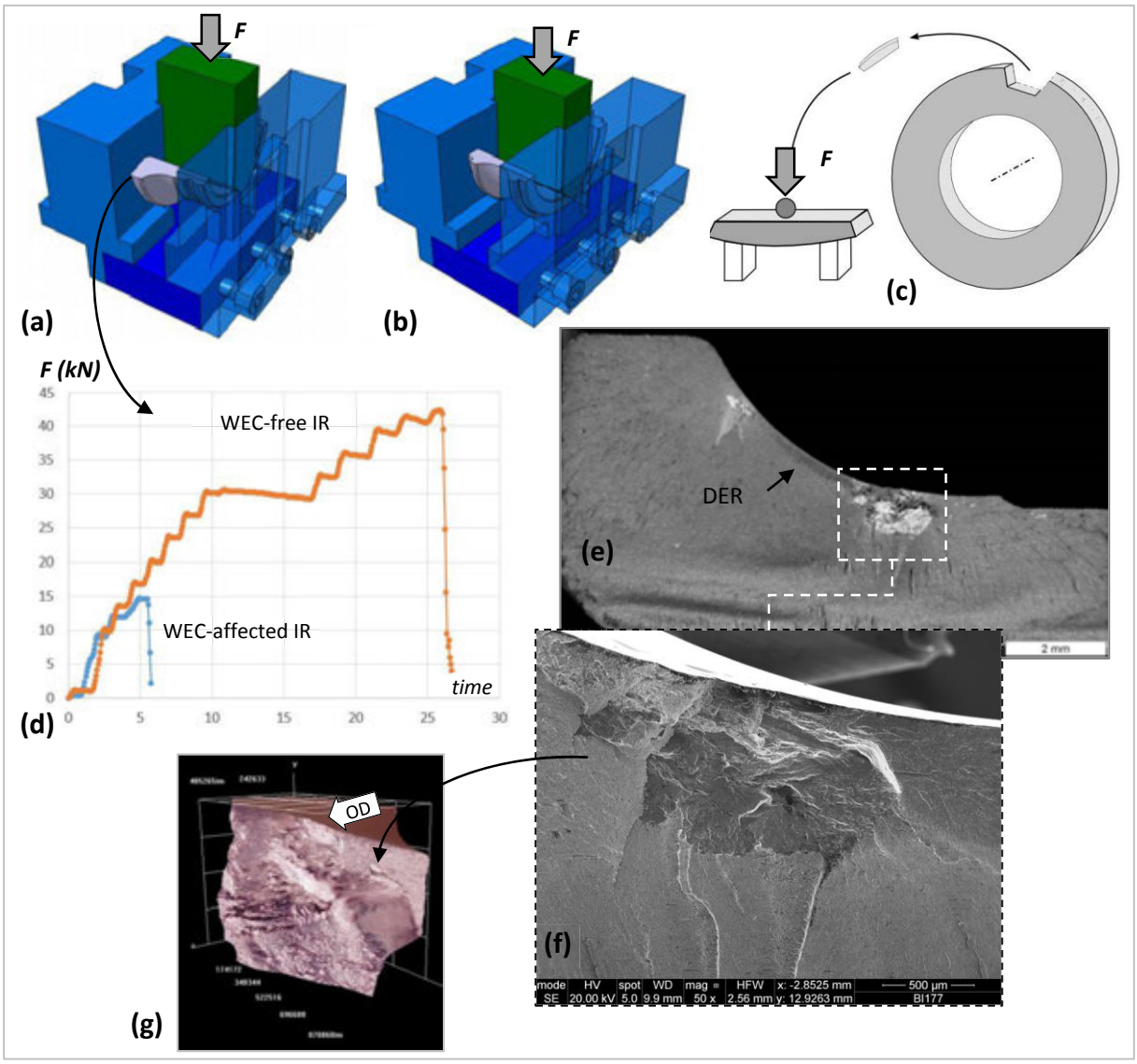

Fig. 2.21: Fractography protocol established to force open and reveal WECs: examples of specifically designed tools for ACBB IRs (a) and DGBB IRs (b); pre-sectioning and three-point bending for TDM raceway fractographs; (d) fractography load monitoring; (e) binocular microscopy of an ACBB IR fractograph revealing wide WEC networks; (f) SEM analysis close-up on the WEC network in (e); (g) WEC fractograph 3D assessment on HIROX KH-7700.

The fore established fractography protocol presents three main advantages. *First*, it allows to detect rapidly and at moderate costs WEC-affected components, especially when a load threshold may be established. *Second*, depending on the three point bending spacing and on the component

geometry, the stress field may be broad enough to seek a given circumferential portion of the component, thus enhancing the probability of detecting WECs compared to metallographic cross sectioning, supposing there are no other defects that could prevail versus the WEC (**Fig. 2.21** (e-f)). *Third,* fractography usually opens the main crack of the WEC networks, thus often revealing the WECs maximum dimensions and 3D stair-like propagation (**Fig. 2.21** (g)), contrarily to metallographic cross sectioning. Nevertheless, as best depicted in (**Fig. 2.23**), fractography presents one main drawback in addition to being destructive. Being performed such that tensile stresses are exerted only in axial directions, the fractograph naturally opens through the weakest plane, thus sometimes failing to reveal a pre-existent WEC link to the surface.

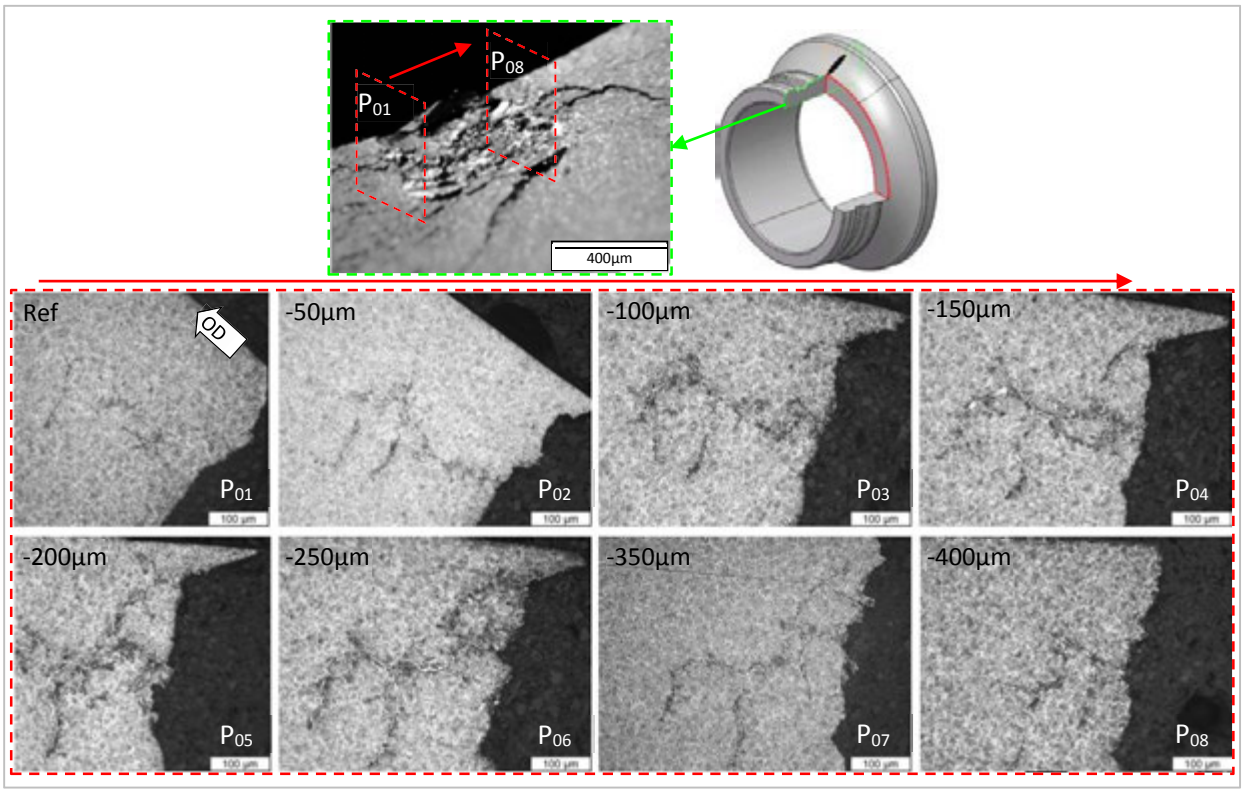

Fig. 2.22: Serial cross sections of a WEC fractographs to confirm the pre-existent feature in the fracture corresponds to part of a WEC network.

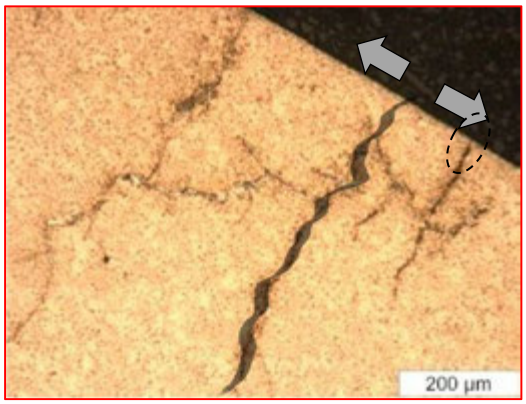

Fig. 2.23: Circumferential cross sections of a WEC suggesting a preferential plane of fracture under three point bending tensile induced stress which would not reveal the circled WEC link to surface (original figure available in **Fig. 1.39** (b)).

2.5 Closure

As a closure to this second chapter, the overall methodology and principal experimental procedures required for WEC tribological analysis have been presented. Two main RCF test rigs will be used throughout this study: one simulating full REB endurance under specific operating conditions, the other simulating RCF from a tribological point of view with specific specimens and protocols developed to address the various tribological drivers of WEC formation mechanisms. After each test, various analyses will be performed to better understand what has happen from a tribological point of view. As WECs appear to be delicate to observe, the protocols used to reveal them throughout this study has been presented.

Tribological analysis of White Etching Crack (WEC) failures in Rolling Element Bearings

Chapter 3:

The effect of artificial hydrogen charging on White Etching Crack reproduction

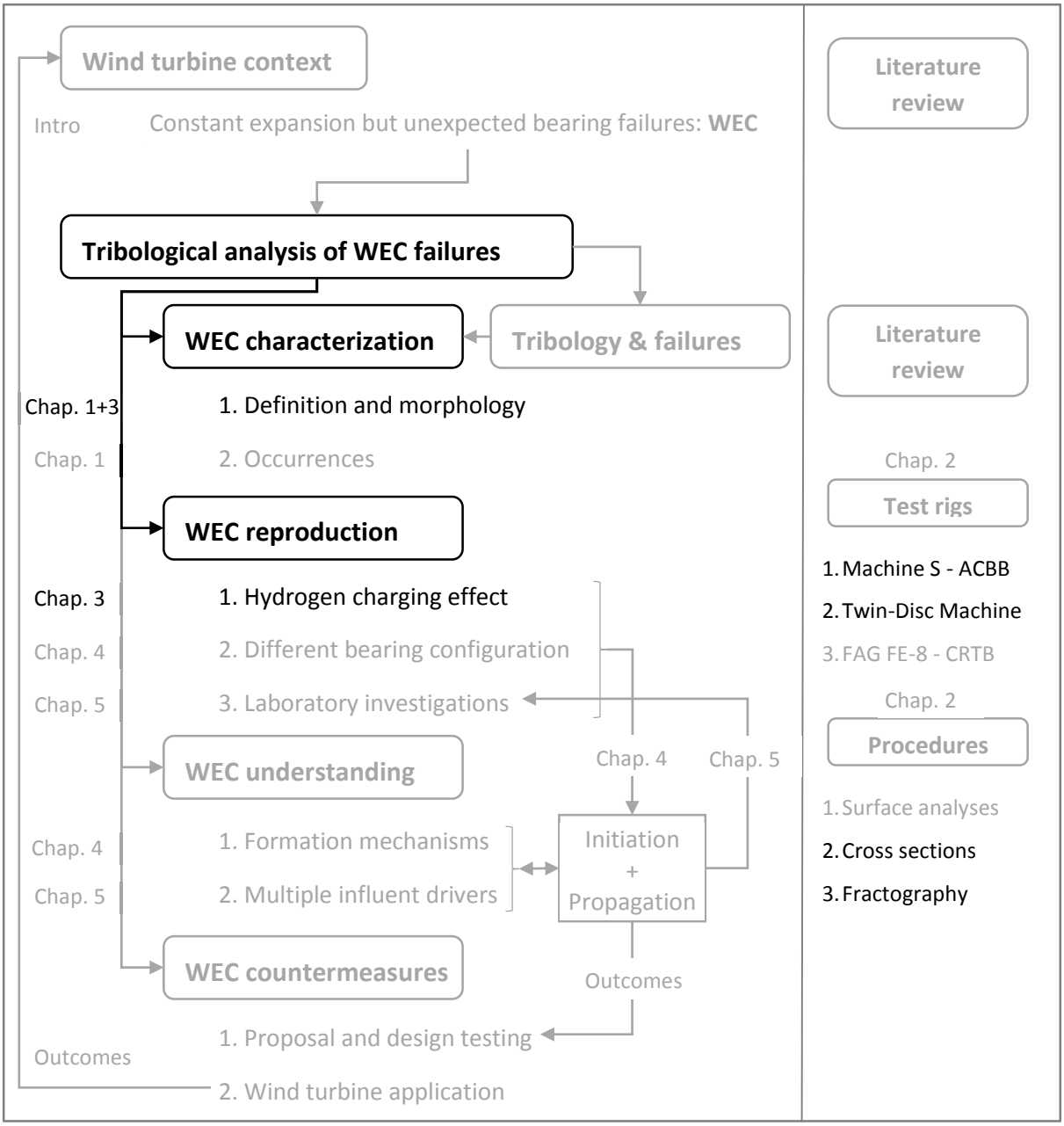

The third chapter of this thesis provides details of WEC reproduction on neutral and artificially hydrogen precharged specimens on both RCF test rigs described in the previous chapter. Focus will be made on WEC networks macroscopic and microstructural morphology as well as location versus the contact area in order to better understand the effect of hydrogen on WEC formation mechanisms. It will then be demonstrated that artificial hydrogen charging seems to modify WEC initiation mechanisms on both test rigs and that WEC in neutral specimens, as in application, can be delicate to reproduce observe as they often develop for specific tribological conditions at unconventional locations and leaving& quasi-undetectable features on the raceway.

3.1 WEC reproduction on neutral and hydrogenated specimens

The large majority of the literature dealing with WECs mention hydrogen embrittlement as a major root cause for the failure mode [6,17,19,29,58,96,164,171,172,174,177,179,180]. Several of authors have managed WEC reproduction on various RCF test rigs, quasi-regardless the contact conditions, using either artificially hydrogen precharged specimens [172,174,177,181,204] or gaseous hydrogen environments [194]. Those specific WEC reproductions are coherent with the fact that hydrogen contents above natural contents have been detected by performing Thermal Desorption Analysis (TDA) on non-hydrogen precharged but WEC-affected specimens from the field or various test rigs [16,115,172,174,178,183,189,195,201]. The role of hydrogen had been anticipated by a paper published in 1973 stipulating that significant quantities of hydrogen can be generated by lubricant decomposition and that hydrogen embrittlement should be considered when analyzing surface affected REB failure modes [215]. However, WECs remain very delicate to reproduce on test rigs without artificial hydrogen charging. Therefore, no study has proposed yet a *comparison of WEC networks* reproduced under the same test rig and operating conditions on *neutral* and *hydrogen pre-charged RCF specimens*. In this study, RCF tests have been performed both on the Machine S ACBB and on the TDM using neutral and hydrogen pre-charged specimens in order to clarify this point.

3.1.1 Artificial hydrogen charging

3.1.1.1 Hydrogen charging protocol

Artificial hydrogen charging of both ACBB IR and TDM rollers has been performed by placing the respective specimens in a *cathodic aqueous solution of sulfuric acid* H_2SO_4 (0.1mol/L) and potassium thiocyanate KSCN (1g/L) with an imposed current density of 8 mA/cm² during 2 hours at 21°C, close to the procedure proposed by [177,196,204,215–219]. This relatively short electro-cathodic procedure has been preferentially chosen instead of prolonged immersion in NH_4SCN acid for 24 – 48 hours [181,188,199,220]. This allowed to reduce the immersion time and provide cathodic protection to the immersed steel surfaces, thus limiting the risk of surface corrosion. It has indeed been noticed that prolonged immersion in aqueous acids tends to corrode and modify the surface roughnesses prior to RCF testing [181,199]. Hydrogen adsorption and absorption reactions mainly depends on [221–225]:

- Electrolysis current intensity
- Steel composition and microstructure
- Surface topography and discontinuities
- Acidity and chemical composition of the solution
- Presence or not of catalyzers also referred to as hydrogen poisons
- Bulk steel temperature
- Structural stress rate such as surface machining compressive residual stresses

More precisely, for a given steel and a given electrolytic solution, the intensity of the current will affect *hydrogen concentration* at the steel surface and thus the quantity of hydrogen absorbed into the steel. Then, according to the second law of Fick, the *depth of hydrogen permeation* will solely be

proportional to the square root of the product of the duration of the electrolysis and the respective hydrogen diffusion coefficient in the steel. This coefficient is function of the steel crystallography and bulk temperature. It has been estimated to $3.8x10^{-11}$ m^2/s in 100Cr6 bearing steel at room temperature.

Considering the artificial hydrogen charging protocols available in the literature (**Table 3-1**), *firstly*, the electric current applied in this study was fixed to ~*8 mA/cm²* of immersed steel surface (**Fig. 3.1**) in order to maximize the hydrogen concentration, and thus the WEC reproduction probability, without taking the risk of chemically deteriorating the surface as it has been observed for currents ~12 mA/cm² [217]. *Secondly*, the electrolytic charging duration was set to *2 hours* leaving sufficient time for hydrogen to diffuse in the first ~500 µm, thus beyond the Hertzian depths, as roughly estimated by using the second Fick law.

Table 3-1: Artificial hydrogen charging protocols available in the literature.

Authors	Current intensity (mA/cm²)	Duration	Solution
	Electrolytic hydrogen charging		
Ciruna et al. [215]	10	1-10 h	H_2SO_4 + CS_2
Fontana et al. [217]	12	-	H_2SO_4 + various poisons
Ray et al. [219]	1	20 min	H_2SO_4
Lunarska et al. [218]	5	2 h	H_2SO_4 + As_2O_3 (5 mg/L)
Hamada et al. [204]	0.1-0.5	20 h	H_2SO_4 + CH_4N_2S (1.4 g/L)
Kanezaki et al. [216]	2.7	672 h	H_2SO_4
Vegter et la. [177]	10	24	NaOH + CH_4N_2S
Szost et al. [196]	8	24	NaOH + CH_4N_2S
	Passive hydrogen charging		
Fujita et al. [220]	0	24	NH_4SCN
Uyama et al. [181]	0	24	NH_4SCN
Evans et al. [199]	0	48	NH_4SCN

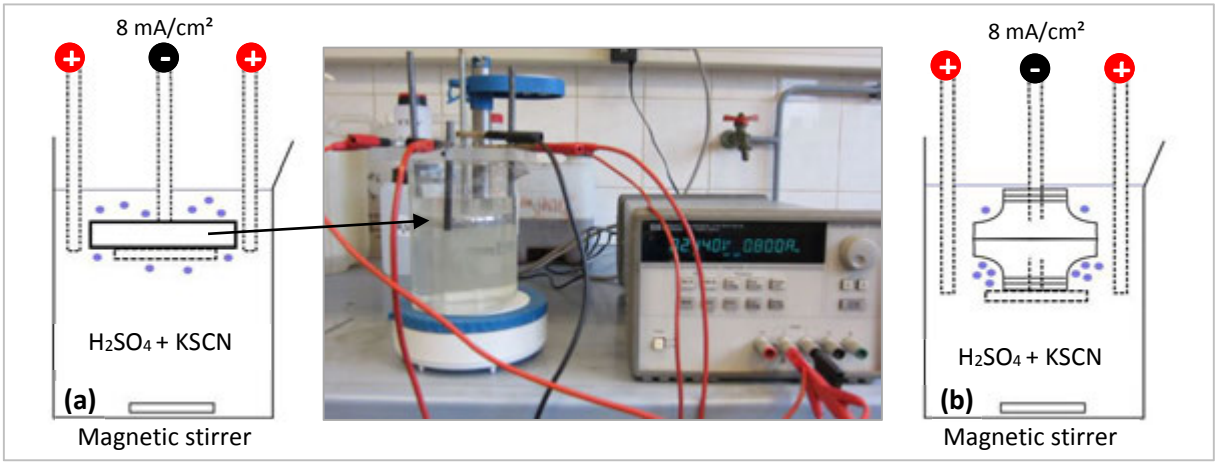

Fig. 3.1: Electrolytic hydrogen charging protocol of TDM specimens (a) and Machine S ACBB IR (b).

3.1.1.2 Diffusible and trapped hydrogen

Hydrogen being the smallest atom, part of it remains highly *diffusible* in steel and the other stays *trapped in the vicinity of defects* such as dislocations (weak traps) and inclusions (strong and durable traps). In this study, the all RCF tests on ACBB IR and TDM (except TDM08_03) were started 48 hours after hydrogenation, leaving sufficient time for most of the diffusible hydrogen to diffuse

out of the steel, as observed by TDA measurements performed in [181,199]. Therefore it is supposed that only a relatively small overall hydrogen concentration remains in the steel prior RCF testing. In consequence, TDA measurements would not be representative of the effective *local hydrogen concentrations*. Indeed, part of the hydrogen seems to concentrate and remain trapped at defects in the matrix. This has been suggested by high resolution TDA in [226–229] and by the drastically reduced RCF life in [215], where hydrogen was not continuously introduced in the steel during RCF testing. In this study, this point has been confirmed by typical brittle transgranular fracture halos displayed around MnS inclusions observed in fractographs performed 96 hours after hydrogen charging, being characteristic of hydrogen embrittlement (**Fig. 3.2**)[230].

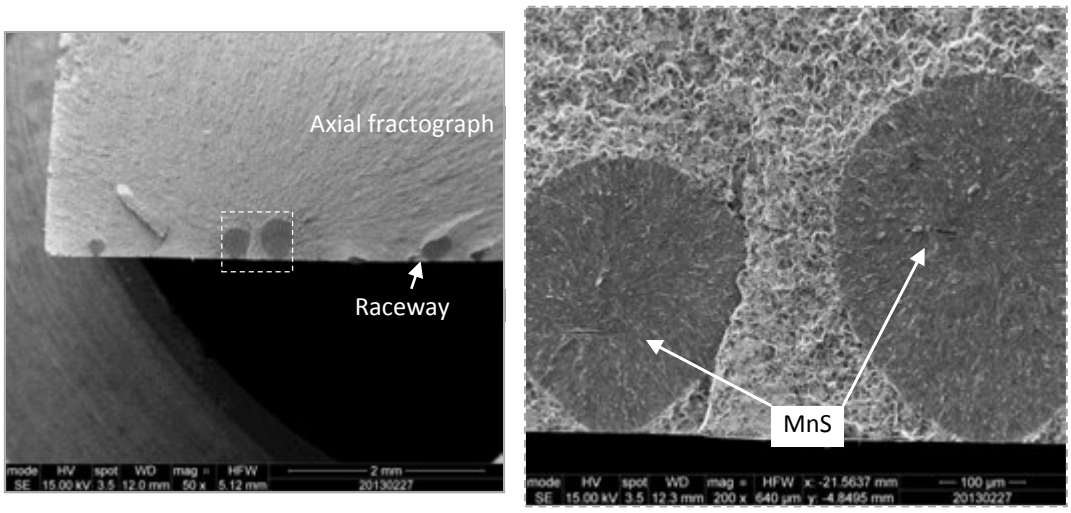

Fig. 3.2: Example of transgranular fracture halos around MnS inclusion on a TDM roller fractograph 96 hours after artificial hydrogen charging.

3.1.2 Operating conditions

In order to better understand the effect of hydrogen on WEC formation mechanisms both *Machine S ACBB* and *TDM RCF* tests have been performed using hydrogen precharged specimens and neutral ones.

3.1.2.1 ACBB RCF tests

Two sets of 10 ACBBs have been tested on the Machine S operating under *load case 1* and standard Machine S operating conditions described in section 2.2.2. The unique difference between the two sets was that the first one was composed of *hydrogen precharged* (H-precharged) turned IRs (#27-36 in Appendix D) while the second one was kept *neutral* (non H-precharged) (#1-10 in Appendix D).

3.1.2.2 TDM RCF tests

A total of 3 TDM tests have been performed with *H-precharged cylindrical rollers* against standard crowned rollers kept neutral (ref TDM08_01, _02; _03 in Appendix H). The contact parameters, such as the Hertzian pressure, the lubricant A and temperature, have been chosen to be most representative of the ACBB tests. However some parameters have been modified in order to evaluate the possible impact of tribological conditions on WEC reproduction in H-precharged specimens, notably the SRR:

- TDM08_01: SRR=30
- TDM08_02: SRR=0
- TDM08_03: identical to TDM08_02 but test launched 4 hours after hydrogen charging

In TDM08_01 the H-precharged roller and neutral one have not lived the same contact conditions and number of cycles (the first one being the driver). In the two other tests, the H-precharged rollers and neutral ones have seen exactly the same contact conditions.

3.1.3 Results: WEC associated premature failures

In both the ACBB and the TDM RCF test, artificial hydrogen charging resulted in *premature failures* of the concerned component associated to *WEC formation*. On the ACBB RCF tests, WEC have been reproduced both on *H-precharged* and *neutral* IR.

3.1.3.1 ACBB RCF results

In ACBB RCF tests, each pair of test bearings, launched 48 hours after artificial hydrogen charging, was stopped after a significant increase of the vibration level, revealing surface damage on one of the bearings. On one hand, most ACBBs with non-H-precharged IRs #1-10 lasted *more than 1000 hours* corresponding to 8.5×10^7 cycles of the most loaded ball/IR contact, which is also confirmed by similarly loaded ACBBs #23-26. ACBB #1 stopped prematurely after 424 hours due to a surface indent initiated spalling of a ball. All other ACBBs #4, 7, and 9 were either stopped due to IR spalling with an axial cracking aspect (**Fig. 3.3** (a)), or suspended. All those ACBB IRs presented incipient axial micro-cracks in the lower border of contact (**Fig. 3.3** (b)). On the other hand, all H-precharged ACBB IRs failed at *~100 hours*, corresponding to 8×10^6 cycles, due to premature IR spalling displaying a similar axial aspect (**Fig. 3.3** (c)).

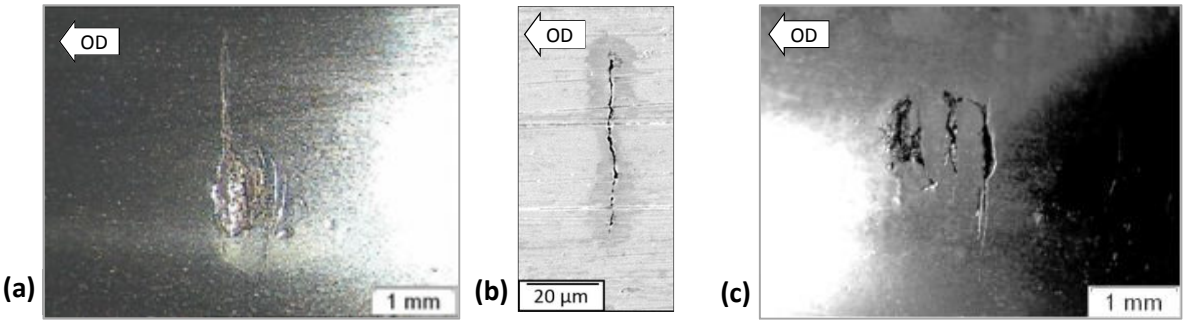

Fig. 3.3: Examples of axial spalls on ACBB IR: (a) neutral #7, (b) neutral unspalled #8, (c) H-precharged #28.

On each neutral or H-precharged IR, with or without apparent surface damage, circumferential and axial LOMs with Nital 2% etching as well as fractographs have revealed large WEC networks with similar propagation aspects (**Fig. 3.4**). Complementary circumferential LOMs of WEC reproduced on the ACBB IRs have been illustrated in **Fig. 1.39**. WEC reproduction on H-precharged ACBBs was expected. Indeed, it had been previously mastered similarly using artificial H-precharged DGBB IR [177] and other various H-precharged RCF specimens [172,174,177,181,204]. Nevertheless, in this study, WEC have been reproduced repeatedly on a radial ball bearing test rig, both *with* and *without H-precharged* IRs running under the same moderate and constant operating conditions.

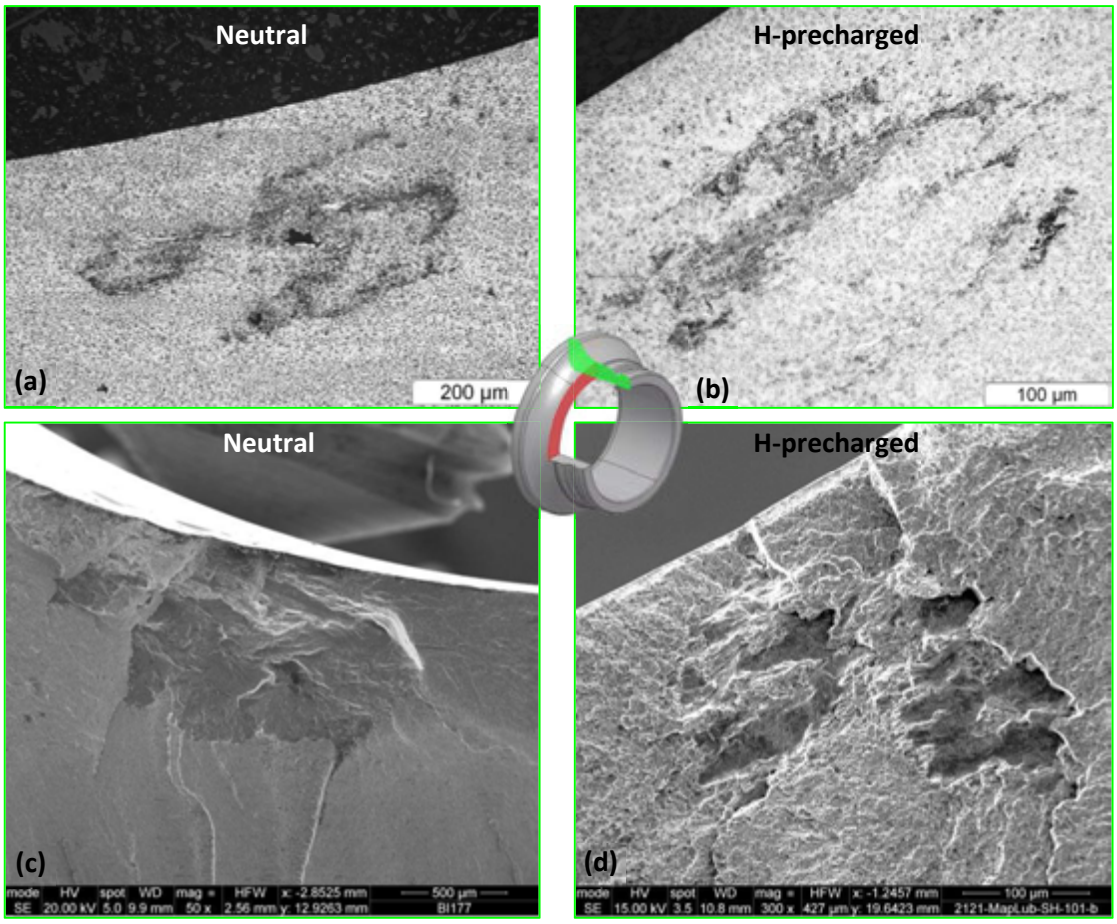

Fig. 3.4: Large WEC networks with similar propagation aspect on neutral ACBB IR #7 and H-precharged IR #28 with respectively: axial LOM Nital etched in (a)-(b) and fractographs in (c)-(d).

3.1.3.2 TDM RCF results

In *TDM RCF tests*, macroscopic premature spalling has led to immediate test arrest in TDM08_01 ($2.5x10^7$ cycles, **Fig. 3.5**) and TDM08_03 ($2.5x10^6$ cycles). TDM08_02 has been intentionally suspended after $2.5x10^7$ cycles to compare it with TDM08_01. In that case, only consequent surface cracks have been observed on the surface. They would have most certainly led to spalling subsequently. TDM08_03, which started *4 hours* after hydrogen charging instead of *48 hours* has failed ten times sooner than TDM08_02 despite the exact same tribological conditions. This tends to confirm that the higher the concentrations of diffusible hydrogen, the more the steel is embrittled.

In addition, no spall or surface brittle cracking has been observed on the respective neutral counter rollers (TDM08_YY) nor on other TDM tests having operated under similar conditions but without hydrogen charging despite the presence of dents (TDM07_YY). Hence, it seems clear that hydrogen remaining trapped in the steel prior to RCF testing has also a detrimental effect on rolling contact fatigue by enhancing WEC formation mechanisms [215]. Indeed, *on the three H-precharged rollers*, dense WEC networks have been revealed by axial and circumferential cross sections as well as fractographs despite different tribological conditions. This is consistent with other findings based on other twin-disc test rigs [198–200,204]. Finally, this may explain why *artificial hydrogen charging* has been widely used to ease WEC reproduction, without having to master the precise tribological conditions responsible for WEC formation in the field.

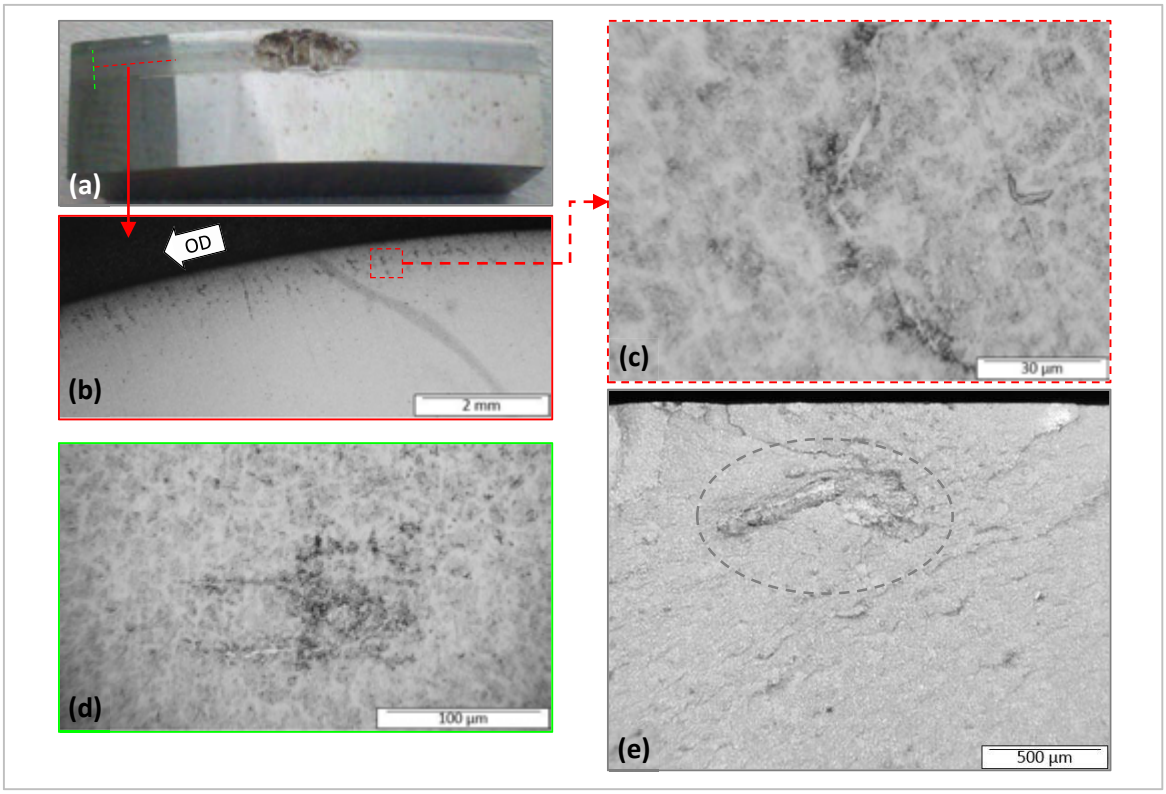

Fig. 3.5: WEC reproduction on the artificial H-precharged TDM roller of TDM08_01: (a) premature spall, (b) circumferential LOM revealing WEC, (c) close-up on a WEC in the depth of maximum shear stress, (d) axial LOM revealing WEC; (e) axial fractograph revealing a brighter WEC network.

Artificial hydrogen charging eases *WEC reproduction* on RCF test rigs quasi-regardless the *conditions*.

3.2 WEC analyses on neutral and hydrogenated specimens

Further analyses have been led on the ACBB IRs and TDM rollers cross sections and WEC fractographs in order to better *characterize* and *understand* WEC formation in case of neutral and H-precharged specimens.

3.2.1 Similar WEC propagation aspects

3.2.1.1 Similar WEC apparent morphology

The WEC networks revealed by cross sections or fractographs of H-precharged and neutral ACBB IR presented similar morphological aspects corresponding to the *WEC definition* and *macroscopic and microstructural characterization* detailed in section 1.4, in agreement with previous observations of WEC networks in H-precharged RCF specimens [177,188,199,201,204] and on H-precharged TDM rollers. In this section, it will be emphasized that, if WEC layouts are similar on neutral and H-precharged specimens, they highly depend on the cross section type and position.

a. Function of the cross section type

First, as illustrated in **Fig. 3.6** and confirmed by all other cross sections performed both on ACBB IRs and TDM rollers, H-precharged or not, WEC *macroscopic layout*s are radically different

from an axial or circumferential point of view. In *axial LOMs*, WECs are commonly parallel and often gathered close to the raceway. In *circumferential LOMs*, WECs tend to present a highly branched and stair-like layout comprising some vertical sections that may extend beyond the Hertzian zone. The direction of propagation in the OD seems to be opposite to conventional RCF. It could be tempting to scheme the depth of maximum shear stress on all LOMs and fractographs but it would be inappropriate. As WECs develop at the contact edges, the maximum shear stress is not the same as at the contact center. However, the axial layout can be interpreted by repositioning the respective axial slice on the circumferential layout as proposed in **Fig. 3.6**. This has been confirmed by the full *3D reconstruction* of WEC networks by serial sectioning of H-precharged rollers [188,200,201] (**Fig. 1.43**).

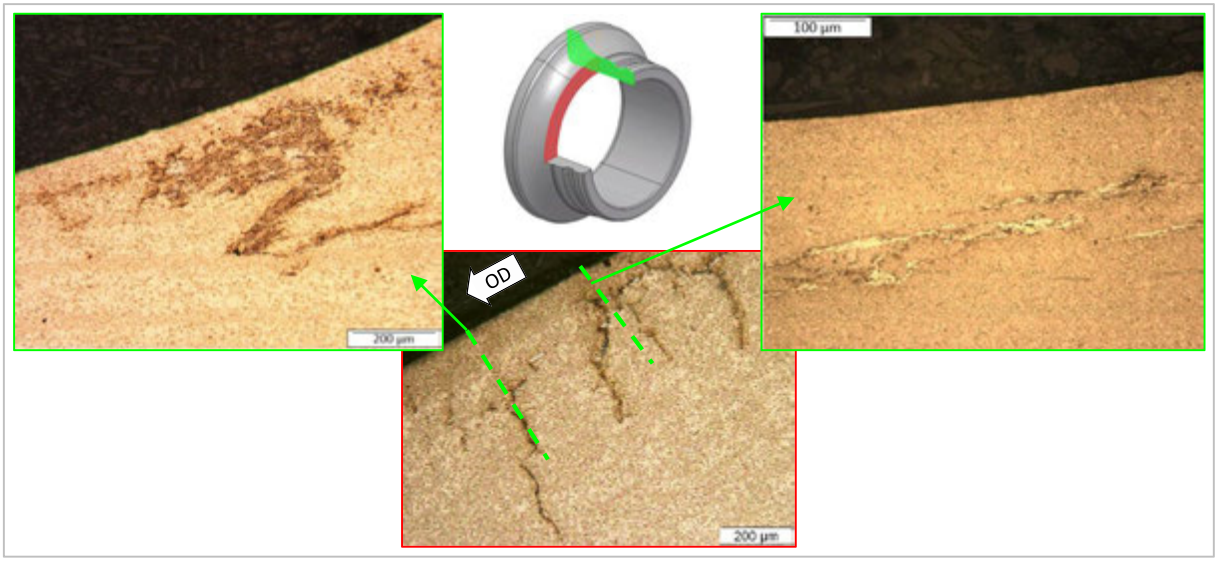

Fig. 3.6: Axial and circumferential LOMs of the neutral IR #7 revealing different morphological layouts of WECs and suggesting a possible interpretation of the different WEC aspects on the two axial LOMs.

b. Function of the cross section position versus the contact area

Moreover, several IRs have been selected and circumferential cross sections were made precisely at the same reference position. Then, by successive polishing, 20 LOMs were made at a regular spacing of approximately 50 µm. As a typical example, four representative circumferential slices from neutral IR #4, z_1, z_2, z_3 and z_4 are detailed in **Fig. 3.7**. Clearly, the respective WEC 2D circumferential *morphology* highly depends on the position of the slice versus the contact area.

Considering first circumferential cross sections of non-H-precharged IR at the edge of the contact area marked by the DER (section 1.3.2.2), corresponding to z_1, WECs often display heavily branched brittle with punctual connections to the surface (**Fig. 3.7** and close-up available **Fig. 1.39** (b)). Then, going progressively from z_1 to z_4, 900 µm further towards the contact center, WECs tend to dive more and more vertically *under the DER* (**Fig. 3.7**). On one hand, this may be explained by the compressive residual stress buildup in the DER (section 1.3.2.1)[29,103,231] that prevents the cracks from entering this area. On the other hand, tensile hoop stress (section 2.2.2.1) promotes the straight propagation towards the bore in through-hardened IRs (**Fig. 3.7**)[31,139,162]. WECs become more and more vertical and disparate as the circumferential slice is positioned towards the center of contact. Therefore, it is understandable that z_3 and z_4 do not intersect with any WEC displayed on the axial LOM provided in **Fig. 3.7**.

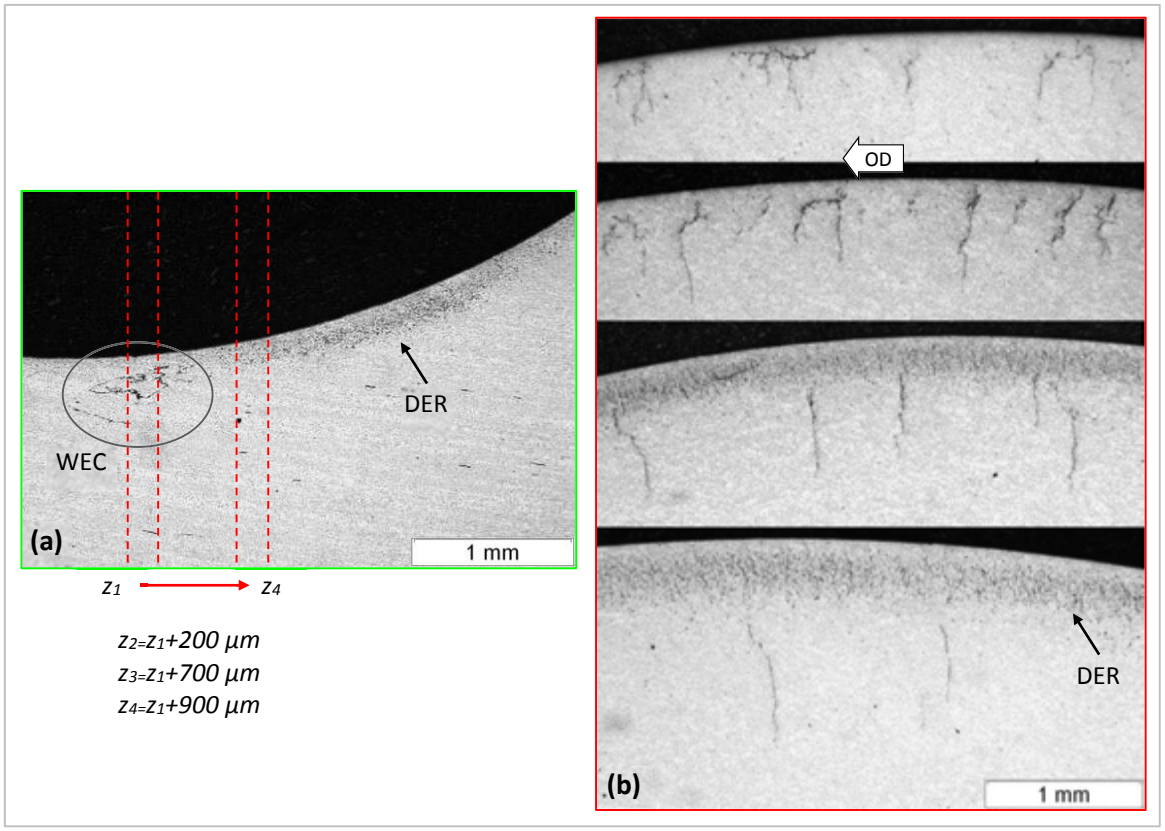

Fig. 3.7: Axial LOM (a) of neutral IR #4 revealing the typical WEC position at the border of the DER and the approximate position of the 4 circumferential slices by successive polishing of the same IR (b).

WEC *apparent 2D morphology* depends on the type and position of cross sections.

3.2.1.2 Similar WEC microstructure

WECs reproduced in neutral and H-precharged specimens present the same microstructure consisting of very *thin cracks* bordered by more or less *white etching microstructure* referred to as WEA (section 1.4.1). This has been confirmed by the previously illustrated LOMs (**Fig. 3.5** (c) and **Fig. 1.39** (d)). It has been nevertheless noticed that for H-precharged specimens, shorter RCF testing often led to less WEA formation at the crack flanks (**Fig. 3.8**). This supports the fact WEA form subsequently due to crack rubbing and enhanced plasticity, similarly to WEA in RCF butterflies or WEL in railway or hard turning applications (section 1.4.2.1).

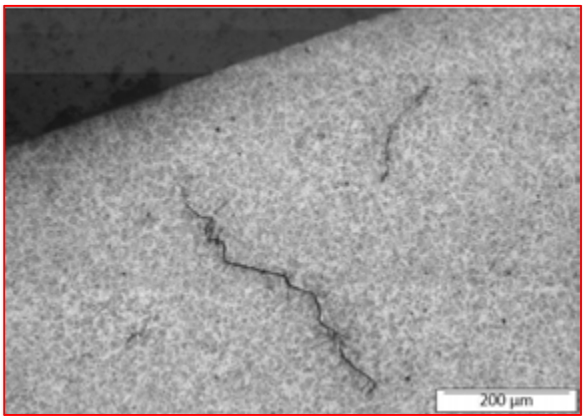

Fig. 3.8: LOM of an H-precharged TDM roller that failed prematurely after 2.5x10^6 cycles (TDM08_03)

On *fractographs*, all preexistent WECs forced open present a brighter aspect than the bulk fracture (**Fig. 2.21** and further **Fig. 3.10**), both on neutral and H-precharged specimens, in agreement with [6,29,162,178]. SEM magnifications reveal smooth transgranular crack flanks lightly striated like similarly to stress-corrosion cracking [29,115,217,225,230] (**Fig. 3.9** (a)). Moreover, in *fractographs,* MnS inclusions have often been observed in the vicinity of WECs without displaying any signs of WEC-like transgranular fracture nor preexistent butterfly crack extension around them (**Fig. 3.9** (b)). This tends to support that WECs and conventional RCF butterflies tend to be mutually independent, especially in non-H-precharged specimens where WEC occur at the border of contact, far from the maximum shear stress zone.

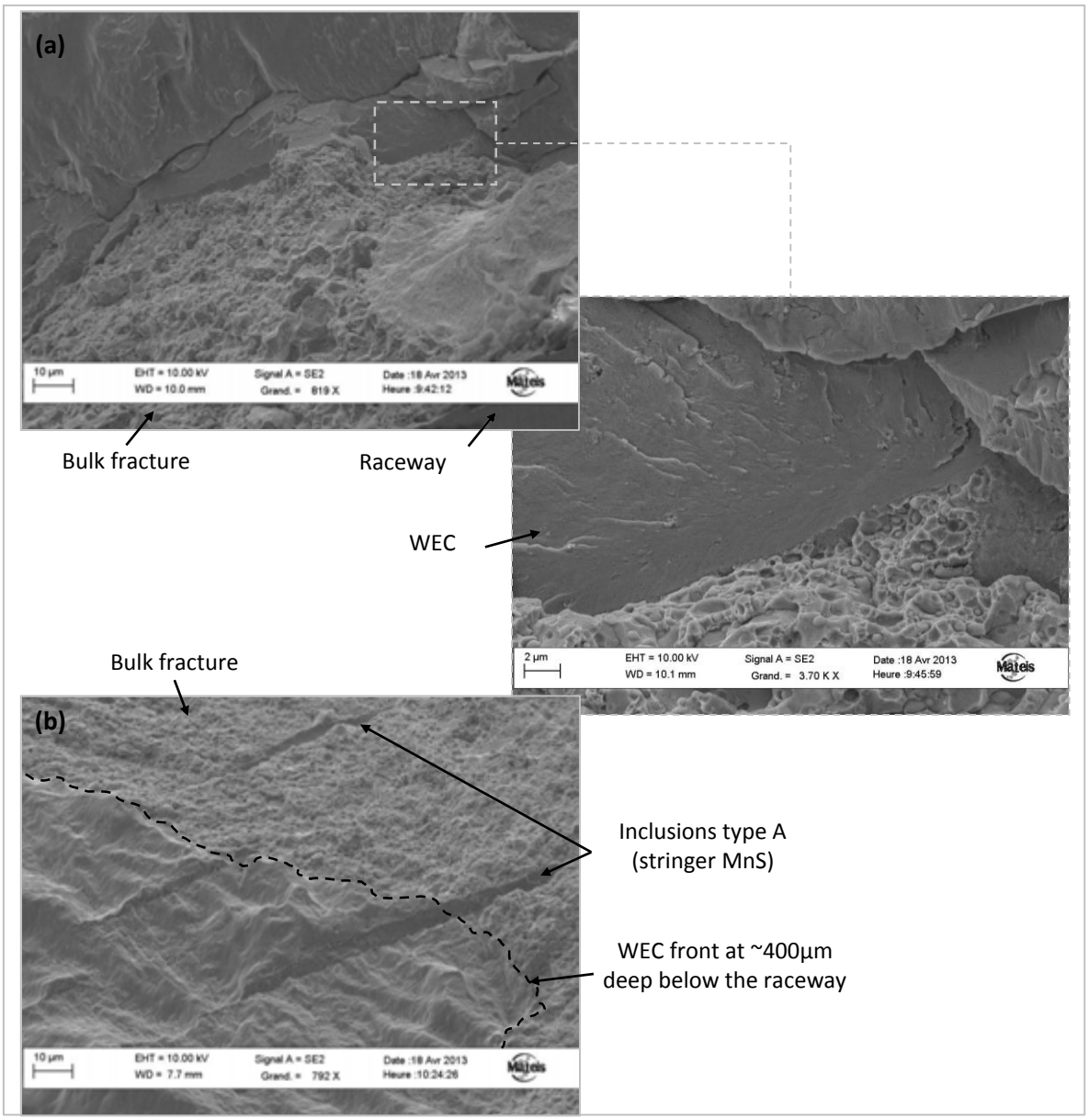

Fig. 3.9: SEM top view imaging of a WEC fractograph at the contact border of neutral IR #7 (SEM SUPRA 55 VP available at MATEIS): (a) close-up on the striated preexistent WEC crack flank near the raceway; (b) close-up on type A MnS inclusions in the vicinity of WEC crack tip far beneath the raceway.

WEC fractographs reveal smooth but striated mainly *transgranular* crack flanks.

3.2.2 Different WEC location versus the contact area

Despite similar WEC macroscopic and microstructural propagation aspects, it has been noticed on axial LOMs and fractographs that WECs in *H-precharged* specimens tend to occur *at the center of contact* contrarily to WECs in *neutral* specimens that develop *at the contact borders* (**Fig. 3.10**).

On one hand, in both H-precharged ACBB IRs #27-36 and TDM rollers TDM08_YY, LOMs and fractographs have revealed WEC networks at the angle of contact (**Fig. 3.10** and **Fig. 3.11** (b)), especially around the depth of maximum shear stress, in agreement with [177,188,199,201]. WECs revealed by fractographs on H-precharged IRs may appear significantly smaller than those on neutral IRs (**Fig. 3.10** (a)). This could be explain either by the lower number of cycles (no DER has been observed in any of the H-precharged specimens) or by the fact that, as the whole IR is subjected to trapped hydrogen embrittlement, fracture occur as soon as the first weaken defect is met by the three-point bending stress field. This is supported by the fact, fracture occurs for much lower loads in case of H-precharged IRs (F<5 kN).

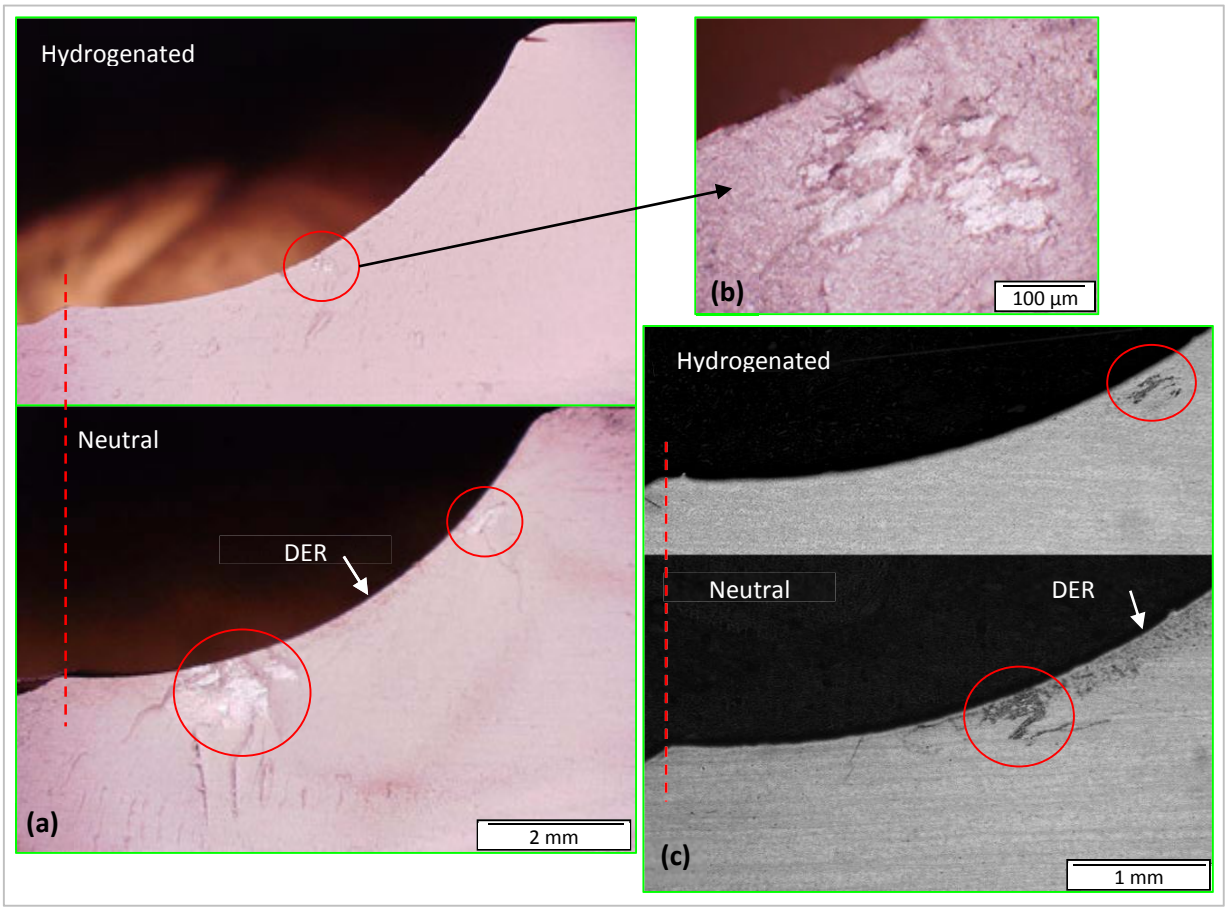

Fig. 3.10: WEC different position versus the contact area: (a) fractographs of the H-precharged IR # 28 aligned with that of the neutral IR #7 (opposite side of **Fig. 2.21** (e)); (b) close-up on the small WEC network of IR #28 at the angle of contact (SEM imaging in **Fig. 3.4** (d)); (c) axial LOM of IR #28 and neutral IR #9 aligned confirming the WEC offset to the border of the DER region in neutral IRs.

On the other hand, as no WEC has been reproduced on TDM rollers without hydrogen charging, only axial LOMs and fractographs of non-H-precharged and H-precharged IRs have been aligned (using the bottom groove) for *comparison*. It reveals that *without artificial hydrogen charging*, WEC only appear at the border of the DER, thus with an offset regards the contact angle (**Fig.**

3.11). This is in agreement with usual *WEC occurrences in application* as well as with **Fig. 3.7** where WEC networks tend to avoid the DER. Computations of the surface energetic criterion $P.\Delta U$ for the ACBB load case 1 (P being the local contact pressure and ΔU being the slip velocity) (section 2.2.2.1) have been performed. Results indicate that WEC development in neutral IR #1-10 corresponds to the location of maximum slippage and of a $P\Delta U$ peak that appears at the border of contact, in agreement with the recent similar finding of Fujita et al. on a DGBB [180]. This point will be further discussed later on.

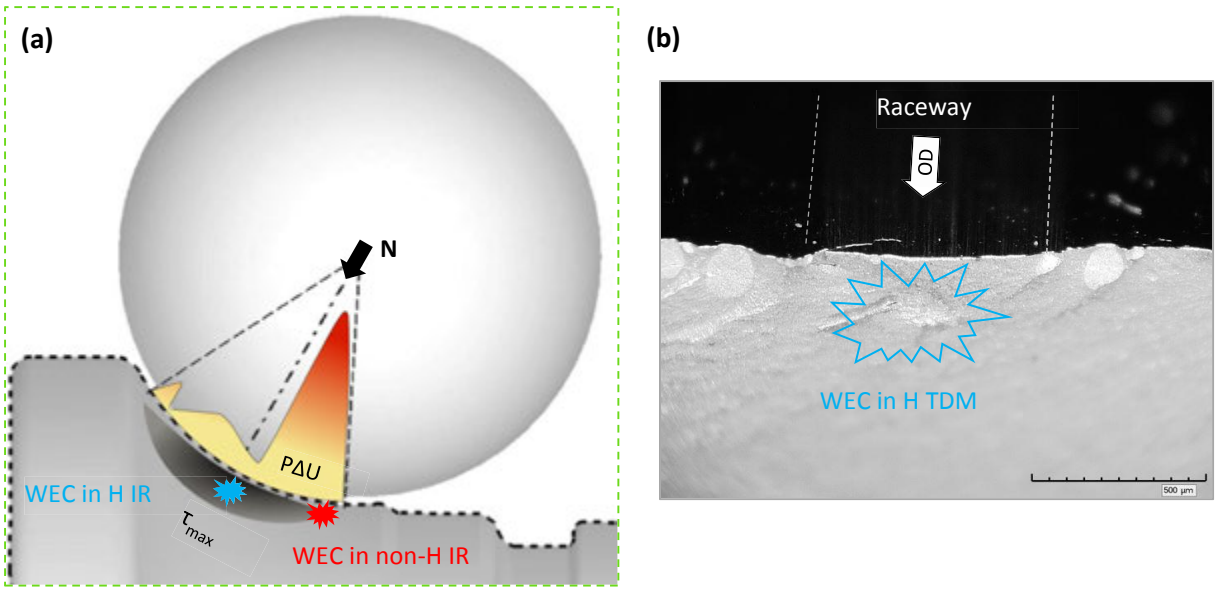

Fig. 3.11: (a) Scheme illustrating the WEC location versus the contact area in non-H-precharged and H-precharged ACBB IR; (b) Three-quarter view of the H-precharged (H) TDM roller fractograph revealing a WEC at the center of contact below the raceway (cf. **Fig. 3.5**).

WECs develop *at different locations* versus the contact *in neutral and H-precharged* specimens.

3.2.3 Different WEC layout versus the raceway

In addition to being located at different positions versus the contact area, WECs in neutral and H-precharged specimens have been analyzed more closely in order to better understand their *interaction with the raceway surface* and *preferential direction for propagation*.

3.2.3.1 Incipient axial microcrack on neutral specimens

It has been demonstrated that only targeted cross sections could actually reveal quasi-punctual WEC network connections to the raceway on the non-H-precharged but WEC-affected ACBB IRs #1-10 (**Fig. 3.7** and **Fig. 1.39** (b)). In case of spalled specimens, it is *relatively* easy to position the cross sections to reveal WECs by spotting the upside edge of the spall (**Fig. 3.3** (a)). However in case of unspalled specimens, *only numerous but almost undetectable incipient axial microcracks* can be observed by thorough SEM analyses at the border of contact to help position the cross section (**Fig. 3.3** (b)). This makes cross section positioning highly delicate if the operator does not know in advance the WEC position versus the contact.

Therefore, under the hypothesis that the weakest plane for fracture does go by the WEC connection to raceway (section 2.4.2.2), WEC fractography actually increases the probability of

revealing such WECs typical 10-100 µm deep axial microcrack connections to the surface as illustrated, for example, in **Fig. 3.12**. Those surface axial cracks have also been associated to WECs in WEC-affected IRs from the field in various NTN-SNR expertise as well as in through-hardened REB from wind turbine and other application [6,29,162,165–167,178,182]. However, in H-precharged ACBB IR or TDM rollers, *no such connection* has been observed neither by metallographic sectioning nor by fractographs, in agreement with similar results from [177,188,199,200]. As also observed by Gegner et al. [29], WEC connection to the surface can be so incipient that they may remain undetectable on the extreme surface even at high SEM magnifications (**Fig. 3.13**). In those cases, it could be supposed that the link takes place quasi-punctually inside the asperity of a grinding mark to gradually widen in the first µm below the raceway (**Fig. 3.13**).

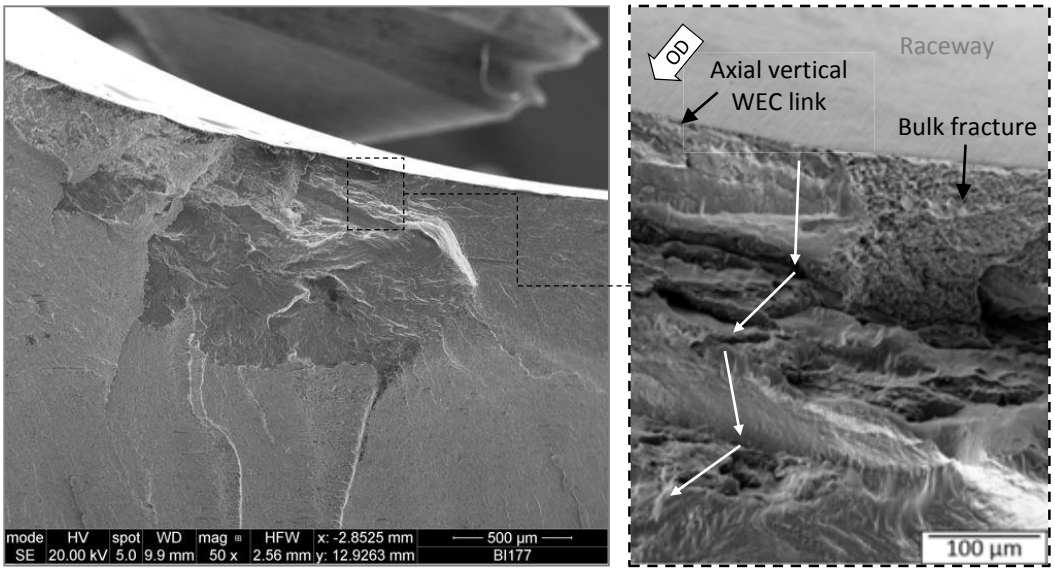

Fig. 3.12: Fractograph SEM close-up on the WEC connection to the surface revealing a smooth vertical preexistent axial crack consistent with those observed in surface analyses (**Fig. 3.3** (b)).
The white arrows suggest a stair-like top down growth in the direction of OD (neutral IR #7).

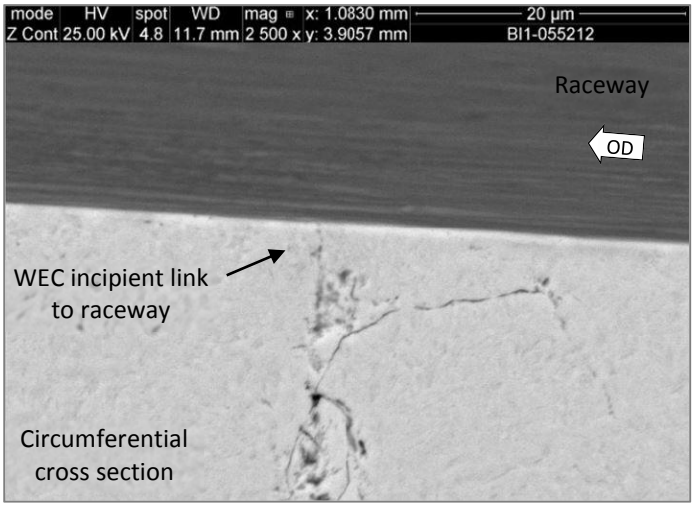

Fig. 3.13: SEM close-up on a three-quarter view of an undamaged raceway despite the presence of a WEC network in its vincinity confirmed by a circumferential unetched cross section (IR #61).

3.2.3.2 Top-down growth towards the core in the over-rolling direction

Both circumferential cross sections (**Fig. 1.39** (a-b), **Fig. 3.6** and **Fig. 3.7**) and fractograph 3D assessment (**Fig. 2.21**(g) and **Fig. 3.12**) suggest that WEC present a preferential direction in their layout versus the raceway, especially in non-H-precharged ACBB IR. All WECs observed on the ACBB IRs, present a typical *stair-like top-down growth in the direction of OD* in agreement with observations made on various REBs from applications [6,29,162,165,167,178,181,190,204]. This preferential layout from the raceway down to the core, opposite to conventional RCF butterfly extension, suggests that WECs in *non-H-precharged* specimens most probably initiate in the surface layer. In case of *H-precharged* ACBB IR or TDM rollers, this preferential layout is less evident.

WECs *in neutral IRs* display a *stair-like top-down growth in the OD with a connection to the raceway.*

3.3 Hydrogen charging effect on WEC initiation

3.3.1 Hydrogen embrittlement theories

Hydrogen embrittlement of steel, also referred to as Hydrogen Induced Delayed Brittle Fracture or Hydrogen Stress Cracking [221], has been widely studied throughout the literature in the past decades. The term *embrittlement* suggests a kind of ductile to brittle transition caused by the mechanical field interacting with hydrogen [224].

In addition to the previous results on the ACBBs and TDM H-precharged RCF tests, numerous experimental studies have proved that the presence of diffusible and/or trapped hydrogen in concentrations above 1-2 wt. ppm can drastically reduce toughness and resistance to both structural fatigue [217,220,222,224,225,230,232] and RCF [174,177,181,199,204,215,216,221]. As hydrogen embrittlement theoretical atomistic mechanisms are still controversial, extensive reviews can be found in [217,222–225]. The main theories for hydrogen embrittlement in high strength bearing steels that do not form hybrids are [224]:

- *Hydrogen enhanced decohesion* (HEDE) [223]: local hydrogen accumulation in hydrostatic tensile regions at crack tip weakens the cohesive bonds between metal atoms and enhancing crack propagation.
- *Hydrogen enhanced localized plasticity* (HELP): local hydrogen favors dislocation mobility which results in localized softening enhancing localized plasticity.

As WECs present similar microstructural morphologies in neutral and H-precharged specimens, WEC formation is most certainly associated to hydrogen embrittlement [6,17,19,29,58,96,164,171,172,174,177,179,180]. Moreover, considering WEC morphology, deep and branched crack propagation beyond contact mechanical stresses may certainly be attributed to HEDE while heavily plasticized adjacent white etching microstructure formation should more correspond to HELP.

3.3.2 WEC initiation conjecture for hydrogen precharged specimens

WECs in H-precharged RCF specimens differ from WECs observed in non-H-precharged ones in the sense that they appear predominantly at the contact center at depths corresponding to the maximum Hertzian shear stress and that they most often do not present any interaction with the raceway. Therefore, it is proposed that, in case of *artificial hydrogen charging* of the specimens prior testing, hydrogen remains trapped at material defects, such as inclusions, drastically lowering the crack initiation thresholds at the interfaces with the steel matrix. As the whole specimen is excessively embrittled, subsurface crack initiation is must probable to occur in the *maximum shear stress zone* (**Fig. 3.11**), similarly to conventional RCF butterflies and microstructural alterations, despite the fact the contact stresses may be lower than the conventional threshold H_1 (sections 1.1.1.3 and 1.3.2). This conjecture is in agreement with other RCF results on H-precharged specimens available in the literature [177,181,199]. It further explains why (1) *WEC reproduction* is so "easily" achieved on H-precharged specimens *quasi-regardless the contact conditions* and why (2) no WEC-raceway interactions have been observed on those specimens despite high resolutions serial sectioning [188,199,200]. WEC morphology on H-precharged specimens mainly depend on the hydrogen concentration artificially introduced in the steel: the more hydrogen is introduced, the more crack propagation is eased by HEDE and the more failure occurs prematurely leaving unsufficient time for adjacent WEA to form by HELP (**Fig. 3.8**).

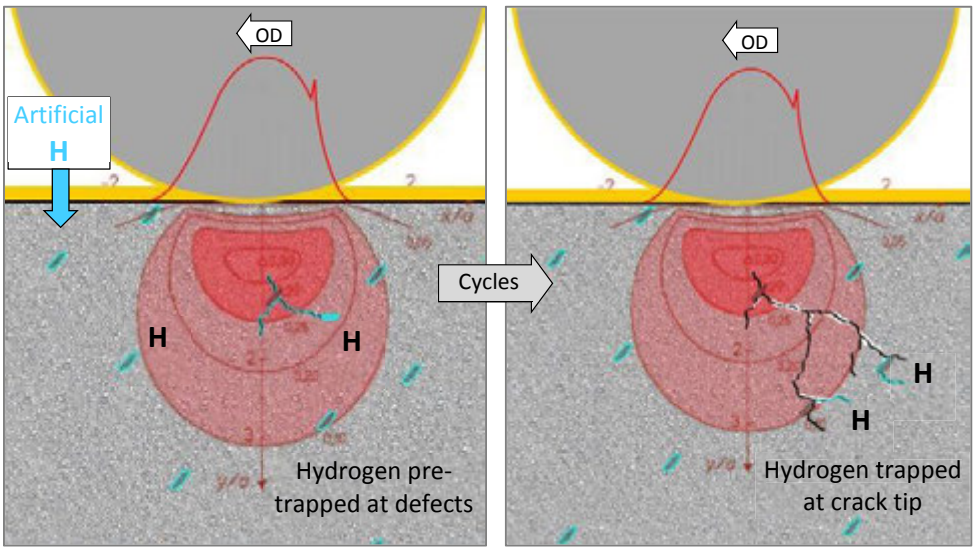

Fig. 3.14: Scheme of WEC formation conjecture in H-precharged specimens where crack initiation occurs in the subsurface maximum shear stress zone due to excessive steel embrittlement

WECs in *H-precharged RCF* specimens *initiate in the subsurface* maximum shear stress zone

3.3.3 WEC initiation different for neutral specimens

As aforementioned, WECs have been reproduced on the ACBB IRs and TDM rollers with similar propagation aspects in both neutral and H-precharged specimens. This highly supports that WECs do propagate at least partially by *local* hydrogen embrittlement *at crack tips* even in non-H-

precharged specimens such as in application, thus explaining the unconventional, premature and brittle propagation beyond the contact mechanical stresses (section 1.5.1).

Nevertheless, natural hydrogen concentrations inherent to bearing steel manufacturing process (~1 wt. ppm) are clearly unsufficient to generate WECs since WECs remain relatively rare in application (even if relatively frequent when considering specific known WEC-affected configurations, e.g. wind turbine gearboxes REBs or the neutral ACBB IRs #1-10). Moreover, no additional hydrogen is introduced artificially in WEC-affected application REB nor in the ACBB IR #1-10 in order to ease crack initiation and WEC development. Therefore, if it seems consistent that hydrogen is inherent to WEC formation, *WEC initiation mechanisms cannot be the same* in hydrogen and non-H-precharged components since *hydrogen first has to enter* the bearing steel. In that sense, the source and the driving vectors for hydrogen penetration are still remaining major unknowns… Therefore, it seems that the real question is more, *how does sufficient hydrogen penetrate* into the steel of WEC-affected non-H-precharged components?

The difference in WEC initiation mechanisms is supported by the fact that, contrarily to H-precharged specimens, in non-H-precharged ACBB IRs (#1-10 and #37, 39, 45, 57, 61), all WEC have always been observed (1) after a significant number of cycles, (2) only at the contact edges bordering the DER region and not in the Hertzian zone, and (3) with a connection to the raceway via incipient axial microcracks. These three experimental observations are most probably related to specific hydrogen penetration mechanisms inherent to WEC formation.

The *first hint* in understanding why WEC initiation is different in non-H-precharged components and why hydrogen penetrates in the steel, is that the typical WEC position at the border of contact area is consistent with the location of *maximum slippage* and a *local peak of surface energetic criterion* $P.\Delta U$ (**Fig. 3.11** (a))[180]. This will thus be further studied later on. The *second hint* is that the incipient axial surface microcracks detected at the raceway borders on non-H-precharged ACBB IR seem to correspond to WEC surface initiation considering the WEC branching top-down propagation. Further analyses have revealed that these incipient surface microcracks actually allow lubricant or *lubricant compound to penetrate deep into the IR* core (**Fig. 3.15**and **Fig. 3.16**), thus being a probable vector for hydrogen penetration into the bearing steel. These observations are in agreement with previous WEC fractograph SEM-EDX analyses in radial REBs [29,95].

Hence, the fact that in non-H-precharged components, hydrogen penetration and thus WEC initiation seem to rely on specific combinations of *tribological parameters,* such as contact kinematics and lubrication, might explain why WECs are so *delicate to reproduce willingly on RCF test rigs without H-precharged* specimens and why they remain *relatively uncommon in application* despite drastic consequences for the wind turbine industry.

WECs in *non-H-precharged* RCF specimens *develop by local hydrogen embrittlement* but *require specific tribological conditions to initiate* as hydrogen first has to penetrate into the steel.

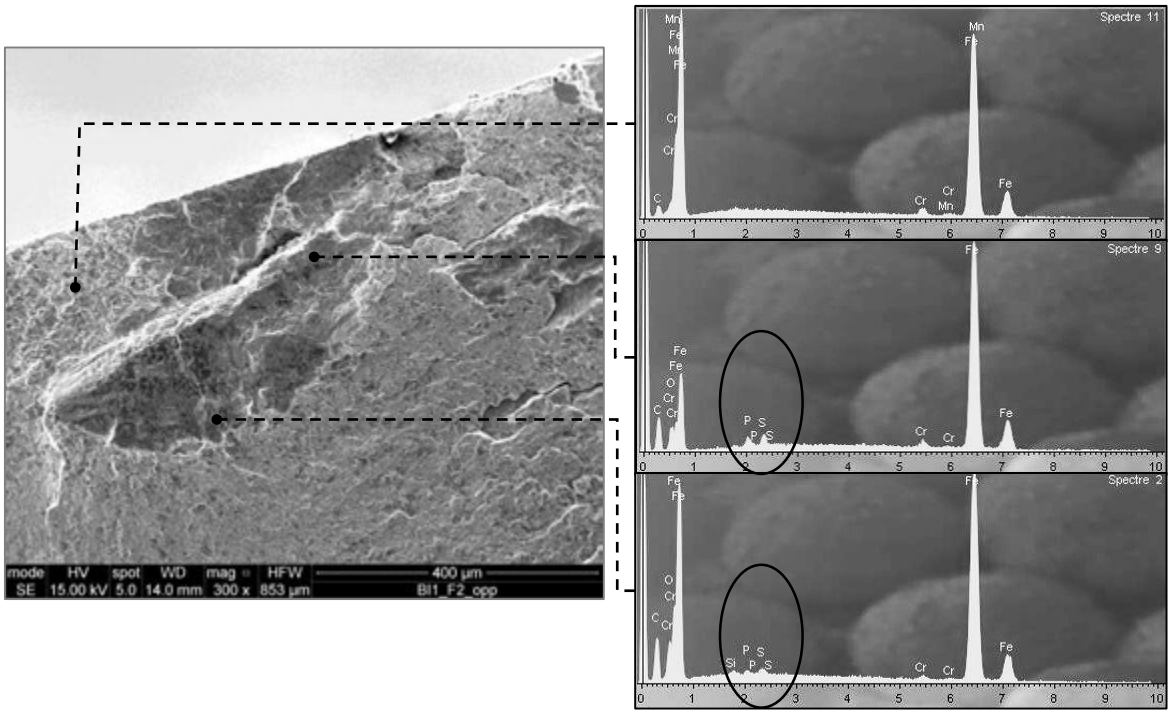

Fig. 3.15: SEM-EDX analysis of a WEC fractograph of neutral IR #61 revealing the presence of lubricant compounds all the way down to the crack tip and a wide vertical connection to the raceway (IR cleaned by ethanol ultrasound bath rinsing and immediately put in SEM chamber after fracture).

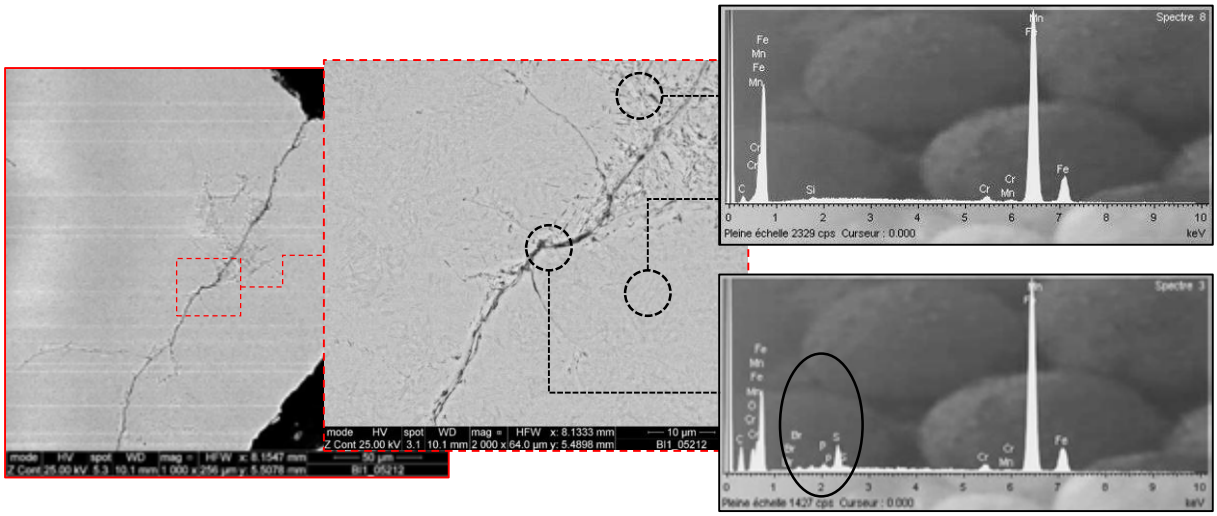

Fig. 3.16: SEM-EDX analysis of a circumferential cross section of neutral IR #61 revealing a WEC network connected to the surface with the presence of lubricant compounds deep into the primary crack but not in the adjacent WEA.

3.4 Closure

As a closure to this third chapter, *for the first time*, WECs have been reproduced on a full radial REB endurance test rig both on artificially H-precharged and neutral IRs operating under exactly the same environmental and tribological conditions. Further analyses have revealed that (1) WECs remain delicate to observe and easy to miss and that (2) artificial hydrogen charging reproduces WEC propagation aspects but seems to alter WEC initiation mechanisms.

3.4.1 WEC delicate observations in unspalled specimens

As a *first important conclusion*, it should be noted that, in addition to their discontinuous and discrete layout on specimen circumferences (**Fig. 3.7**), WECs in non-H-precharged specimens, as in application, tend to develop at an *unconventional and yet isolated axial location* versus the contact area (section 3.2.2). Since, historically, cross sections have been mainly done at the contact center where conventional RCF microstructural changes and spalling usually occur, expertise might have inadvertently concluded REBs were WEC free while the cross sections just did not come across the offset WEC network... In that sense, it seems that *fractography seems more suitable* to detect and/or rapidly confirm the presence of WECs when no signs on the surface can help to pre-locate them (e.g. spalls or axial cracks).

It should further be kept in mind that some expertise, especially in the past decades, could have simply missed numerous WEC occurrences as those could have been masked by the fact that:

- Prevailing gear failures occurred frequently in the past;
- Other REB prevailing failure modes relative to poor steel cleanliness or lubrication contamination issues also occurred frequently in the past;
- Cross sections were not systematically performed and if they were, they were probably done at the center of contact corresponding to conventional RCF and not to locations where WECs apparently develop.

Moreover, as best depicted in section 3.2.1 for all type of RCF specimens in this study, WEC macroscopic 2D layout and morphology, relative to the 3D actual propagation, highly depends on the position of both *circumferential* and *axial cross sections*, thus making WEC experimental observation by cross section quite tricky and possibly misleading. For example, considering solely circumferential cross section z_4 of **Fig. 3.7**, WECs would be interpreted as simple vertical cracks with no connection to the surface and no adjacent WEA, while in fact, this specific WEC network actually connects to the surface and displays a heavily branched layout in cross section z_1 more offset to the contact edge. In that sense, the establishment of a NDT capable of revealing WEC entirety efficiently would definitely help the understanding of WEC formation mechanisms.

3.4.2 Hydrogen charging eases WEC propagation but alters initiation

The second major conclusion is that while artificial hydrogen charging does allow to reproduce WEC macroscopic and microstructural propagation aspects (section 3.2.1), experimental observations on hydrogen and non-H-precharged WEC-affected ACBB IRs from the same test rig have demonstrated that *artificial hydrogen charging alters WEC initiation mechanisms*. Indeed, as in non-H-precharged specimens hydrogen does not initially embrittle the whole specimen, *specific tribological conditions*, which are not necessary for H-precharged specimens, have to be met to drive hydrogen into the steel. This is supported by the fact WECs are reproduced quasi-regardless the contact conditions on all H-precharged RCF specimens (ACBB IR and TDM) but require specific tribological conditions to develop in neutral specimens. Therefore, it could be said that artificial hydrogen charging is *not suitable to test WEC countermeasures* for applications since the latest should mainly be designed to prevent hydrogen penetration itself.

3.4.3 Objectives of the following chapters

Considering these major outcomes, it seems evident that WECs are associated to local hydrogen embrittlement at crack tips and that today the real question is: *how does hydrogen enter the steel* in REB applications such has wind turbines if not artificially precharged? In order to propose a better understanding of hydrogen penetration in REB applications, a comparison of several laboratory WEC reproduction on radically different test rigs *without artificial hydrogen charging* will be proposed in **Chapter 4** thus enabling the formulation of WEC formation mechanisms conjectures. Base on those results, focus will be made in **Chapter 5** on various WEC influent drivers that will finally be transposed on TDM tests without prior artificial hydrogen charging will to qualify their influence on WEC initiation and in attempts of WEC reproduction under an enhanced tribological parameter control.

Tribological analysis of White Etching Crack (WEC) failures in Rolling Element Bearing

Chapter 4:

White Etching Crack reproductions and formation mechanisms

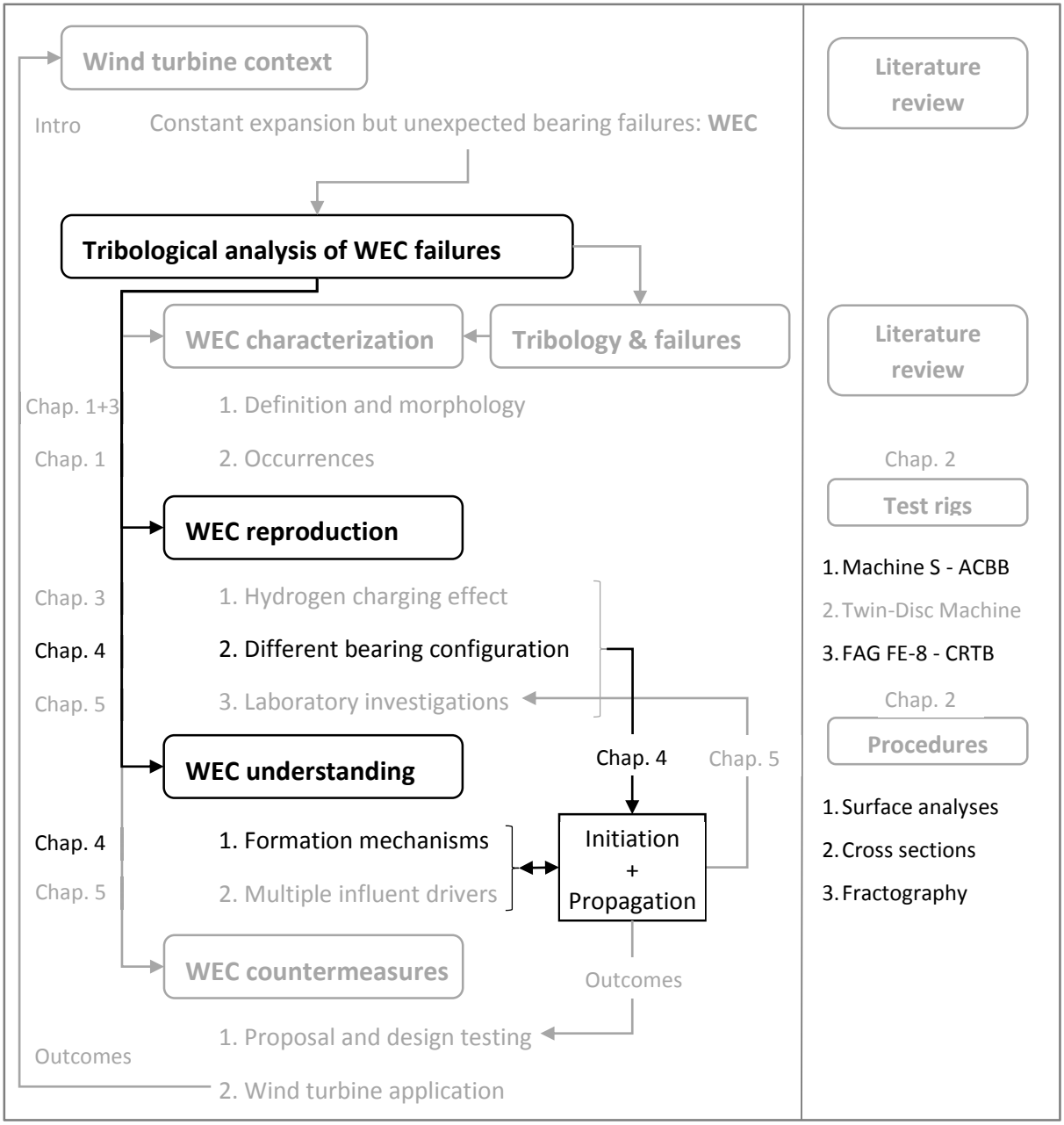

The fourth chapter of this thesis first consists of a thorough tribological comparison of WEC reproductions on two different REB test rigs without artificial hydrogen charging, confirming that WECs tend to be mainly affected by surface tribochemical parameters such as slippage and lubrication. Based on experimental observations, WEC formation mechanisms will be proposed with first, WEC initiation via hydrogen permeation at freshly formed nascent steel surface and second, WEC propagation by local tribochemical hydrogen embrittlement at crack tips. It will thus be emphasized that WEC formation mechanisms and influent parameters might slightly differ from an application to another even though they come down to similar tribological phenomena.

4.1 WEC reproduction without hydrogen charging

It has been demonstrated that WECs can "easily" be reproduced on hydrogen precharged REB components. However, in order to design effective WEC countermeasures, one has to understand *how hydrogen penetrates into the bearing steel* in application. To do so, the analysis of WEC reproductions on *non-hydrogen precharged* bearings in two radically different configurations has been led based on results of (1) *Cylindrical Roller Thrust Bearings* (CRTB) FAG FE-8 RCF tests available in the literature [79,192,198,202], and (2) several *radial Angular Contact Ball Bearings* (ACBB) NTN-SNR Machine S RCF tests under various configurations (Appendix D).

4.1.1 Literature: RCF tests on cylindrical roller thrust bearings

4.1.1.1 Test rig and overall operating conditions

In recent similar studies available in the literature [79,192,198,202], RCF tests have been conducted on CRTBs (universal reference 81212) composed of two washers and 15 rollers and mounted by pairs on FAG FE-8 RCF test rigs without prior hydrogen charging (**Fig. 4.1**). On the basis of moderate and constant rotational speed and contact stresses, the operating conditions appear to be slightly different at tribological scales depending on the study [79,192,198,202] (data available for comparison with the ACBBs in **Table 4-1** page 169).

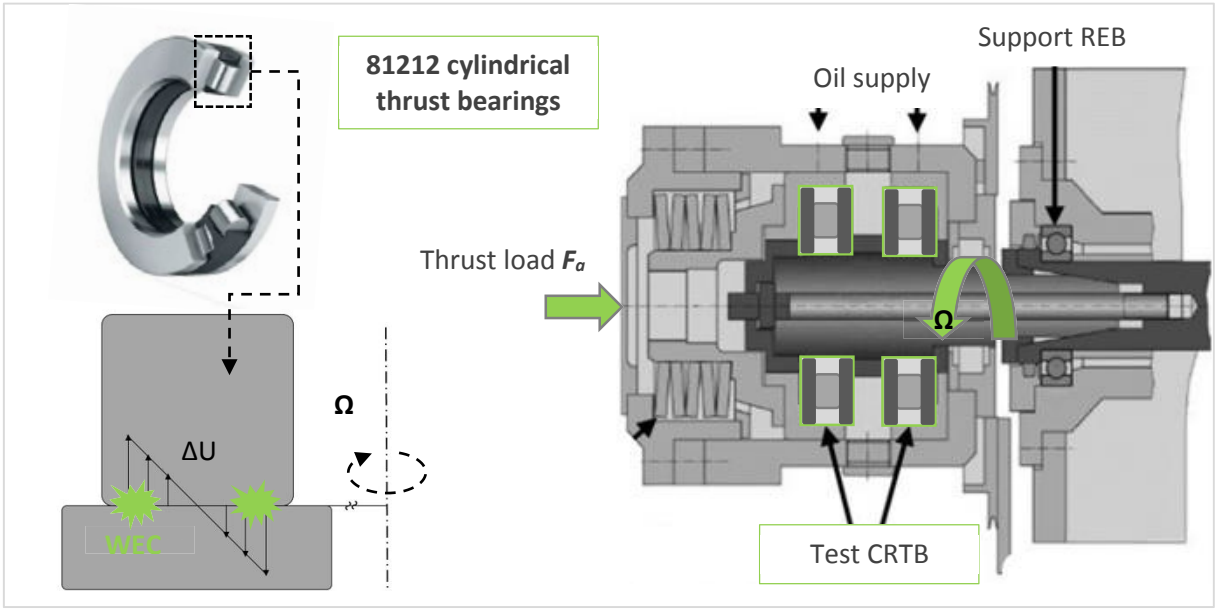

Fig. 4.1: Scheme of the 81212 CRTBs tested on a FAG FE-8 test rig with a focus on the induced slip velocities and WEC locations versus the contact area.

The CRTB specimens were all made of variants of 100Cr6 through hardened bearing steel. For each test, the thrust load induces a constant maximum Hertzian pressure (P_H≈1.9 GPa) along the line of contact. This is relatively low compared to conventional RCF testing and to the bearing steel theoretical endurance limit H_1 (section 1.1.1.3). Moreover, despite a constant and moderate rotational speed, the CRTB design induces naturally a slip velocity gradient along the line of contact which reaches a *maximum slide to roll ratio (SRR) of ~12.5%* at the contact edges (**Fig. 4.1**(a))

(neglecting the possible roller skewing). The CRTBs were jet lubricated at a flow rate Q_{jet} comprised between 0.1 and 1.2 L/min presumably with the same semi-synthetic PAO based automotive gearbox oil at θ=100°C. Indeed, most studies present the same ISO VG64 rheological properties [198,202] and all mention the lubricant as *highly additivated "low reference" oil* [79,192,198,202] apparently known to promote WECs [198].

4.1.1.2 Tribological singularities

Some of these CRTB tests presented some tribological singularities. In [198], the washers presented a significantly low hardness (590 HV) and high surface roughnesses (R_q=0.7 µm) that differed significantly from the ones measured in [202] prior to testing (R_q=0.08 µm). SENSOFAR measurements on similar NTN-SNR CRTBs (universal reference 81110) have been performed revealing that planar grinding and finishing process on washers differs drastically from radial REB rings circumferential grinding. It leaves grinding marks with no-preferential direction versus the over-rolling motion (**Fig. 4.2**). This may be of significant influence in terms of RCF surface distress. Moreover, theoretical central film thicknesses h_c have been re-calculated using the Dowson and Higginson equation for line contacts [233] and lubrication regime indicators λ have been estimated for the two roughness configurations (**Table 4-1**). Except for the first case [198], operating in severe *boundary lubrication* (λ<1) resulting most certainly in significant wear of the softer washers in the aforementioned areas of slippage, the CRTBs ran in *mixed lubrication* (1<λ<3) resulting in low wear rates [202] and apparent tribofilm formation on the washers [79].

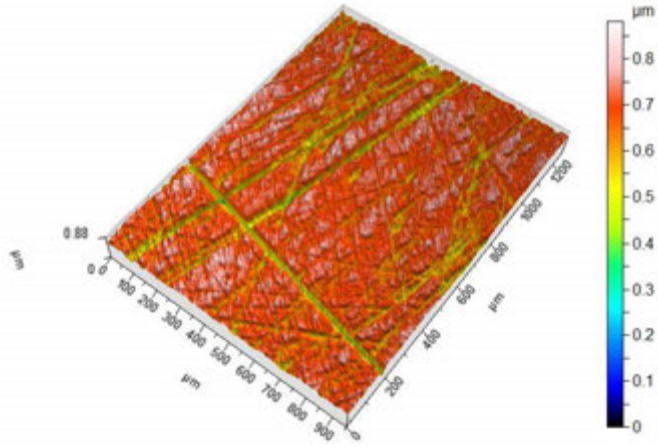

Fig. 4.2: Typical grinding marks on similar NTN-SNR CRTB washers (R_q=0.10 µm)

4.1.1.3 Results: WEC associated failures

Depending on the study the tests were stopped either after a significant increase of the vibrational level due to spalling [192,198,202] or after a predefined number of cycles (**Table 4-1**)[79,202]. All CRTB RCF tests have been stopped before the estimated lifetime L_{10}=1177 hours announced by [79]. As roughly detected by ultrasound probing [79] and/or confirmed by serial sectioning [79,192,198,202], *WECs have been reproduced repeatedly* in each configuration without prior hydrogen charging, thus explaining the premature failures. WECs occurred specifically on the rollers in [198] and only on the washers in [79,192,202]. However they developed only *at contact edges* where slippage is maximum. In two studies, it has also been pointed out that WEC formation was triggered only for *precise CaS detergents and ZnDDP* additive formulations, which had strongly affected tribofilm chemical and structural properties [79,192].

WECs have been reproduced *repeatedly on CRTBs* mostly in washers high slip zones

4.1.2 In-house: RCF test variants on radial angular contact ball bearing

In this study, RCF tests have been performed using ACBBs mounted by pairs on NTN-SNR Machine S endurance test rigs as detailed in **Chapter 2**. A *"reference" ACBB test configuration* reproducing WECs without prior hydrogen charging has been detailed in **Chapter 3** and is summarized in **Table 4-1** comparatively to the CRTB configuration. In this section, several *tribological alternatives* to the *reference configuration* will first be exposed. Then, additional experimental observations will be provided to help understand why the WEC reproducibility rate has been significantly lowered compared to the reference test.

4.1.2.1 Alternative operating conditions

All the ACBB RCF test conditions and results are provided in Appendix D. The main alternatives to the *reference* configuration presented in the previous chapter are the following.

a. Load cases

Five load cases with different ratios of the axial thrust load F_a versus the radial load F_r have been tested on the ACBB mountings in order to qualify the influence of the contact angle and contact kinematics on WEC reproduction. All these load cases and respective theoretical tribological parameters, such as stresses and lubrication indicators, have been previously detailed in **Table 2-2**.

b. Forged and turned IR

ACBB tests have been provided both with turned IRs from a single steel batch and with forged ones from a different steel batch. As the super-finishing process and thus the IR roughness remains unchanged, this is expected to only affect the grain flow and the inclusions ratings and orientations versus the raceway (details have been provided in section 2.2.2.2 and **Fig. 2.5**). Hence, it will thus be possible to evaluate the influence of the machining process on WEC formation mechanisms.

c. Cage

Moreover, throughout the study, the ACBB cage has been modified in reaction to several cage issues. From the *reference* standard design (**Fig. 4.3** (a)), the pocket clearance has first been enhanced with an *oblong* circumferential profile (**Fig. 4.3** (b)). Then, in the *latest design*, in addition to the oblong profile, the cage bridges have been designed *thinner* and less-conforming to the balls (**Fig. 4.3** (a)). As the latest were only available at the end of the study, only four ACBB tests (#65-68) have been performed with that cage design. Even though the influence of the cage on the ball/IR contact tribological behavior is extremely delicate to appreciate, it most certainly affect the *kinematics* respectively at the entrance and exit of the loaded zone (section 1.2.2.4) as well as the lubricant replenishment. Indeed, for example the *standard* pockets (**Fig. 4.4** (a)) (#1-36) and the *oblong* ones at a smaller extent (**Fig. 4.4** (b)) (#37-64), may tend to scrape the lubricant off the balls contrarily to the *thinner* and less-conforming cages (#65-68). This is supposed to enhance local starvation and internal frictions.

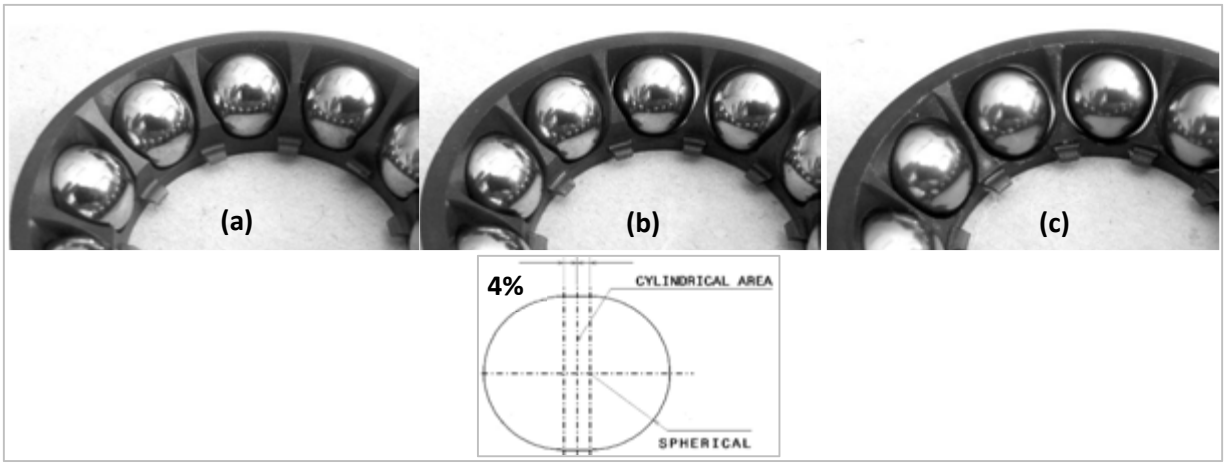

Fig. 4.3: (a) standard cage design with spherical pocket (#1-36); (b) enhanced oblong pocket clearance by a 4% circumferential elongation (#37-64); (c) latest design combining oblong pocket and thinner and less-conforming bridges (#65-68).

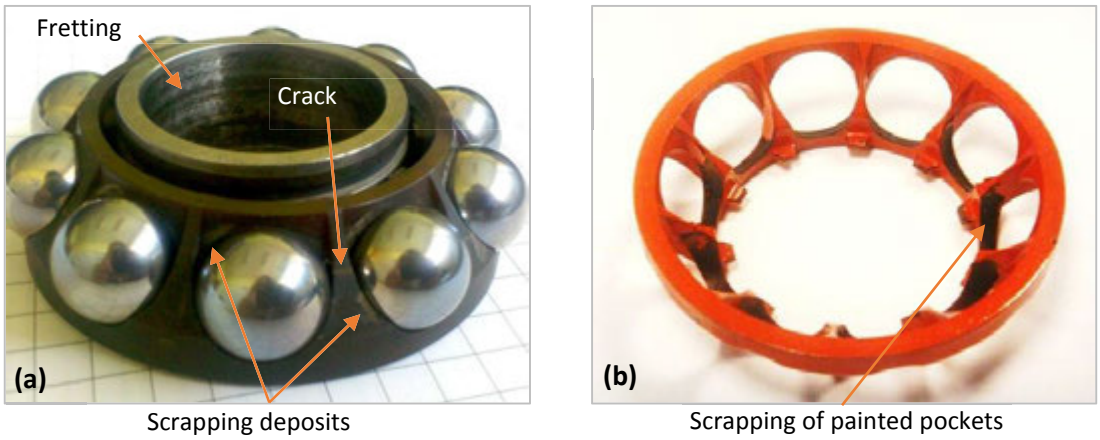

Fig. 4.4: (a) ACBB #40 standard cage after dismounting; (b) Specific ACBB short test under load case 4 with an orange painted oblong cage to locate the friction spots between the ball and the cage pockets.

4.1.2.2 Results and analysis of a lower WEC reproducibility rate

A total of 68 ACBB tests have been performed and the results are detailed in Appendix D. *WECs have been reproduced for multiple ACBB configurations* without prior hydrogen charging in addition to the reference configuration (#1-10). However, WECs have only been reproduced on ACBB IR #37, 39, 45, 58 and 61. So that WECs occur only for combinations of:

- *Forged or turned IRs*
- *Load cases 1 or 2*
- *Standard or oblong cage design*

The WEC-free load cases 3,4 and 5, the latest comprising the latest cage design, suggest that WEC reproduction on the ACBB IRs is very *sensitive to tribological kinematics and lubrication*, which will be discussed and confirmed thereafter. Additional cross sections of WEC-affected and WEC-free ACBBs have been performed on balls and ORs. *WECs exclusively occur at the contact border of the IRs*. Anyhow, all the *alternative configurations* presenting at least one WEC-affected IR have led to a much *lower WEC reproducibility rate* than the reference configuration (Appendix D).

Specifically, WECs have never been detected on ACBBs #23-26 even though they have lived sufficient number of cycles (>1000 hours) *exactly in the same load conditions* as in the *reference configuration*, which has reproduced high density WEC networks (**Fig. 1.39**). Moreover, except for the *reference* configuration tests #1-10, all WEC reproduction have occurred exclusively on the *coupling side*. This lack of repeatability thus questions the symmetry of the Machine S ACBB loading and induced tribological conditions. Therefore, in this section, a thorough experimental analysis of the ACBBs is led in order to grasp the tribological differences between WEC-affected and WEC-free IRs and to better understand drivers triggering WEC formation mechanisms.

WECs have been reproduced in *various ACBB configurations* but with *lower reproducibility rates*.

a. High friction and signs of mixed lubrication

The *first* observation is that all the ACBB tests have been performed under constant and moderate rotational speeds and Hertzian pressure (**Table 2-2**). However, some *broken cage*s (except for the latest design)(**Fig. 4.4** (a)), grey and matt *coloring of the balls* (**Fig. 4.5**) and visible *fretting corrosion* on the IR bore despite a relatively tight fitting (section 2.2.2.1)(**Fig. 4.4** (a))), all support the fact that the ACBBs were subjected to unexpected *high internal frictions*. Unfortunately no resistant torque measurement was available during this study to verify that point.

Fig. 4.5: WEC-affected ACBB #61 balls with a matt grey coloration; WEC-free ACBB #65 and #63 balls with a shiny aspect; WEC-affected ACBB #8 balls with also a shiny aspect.

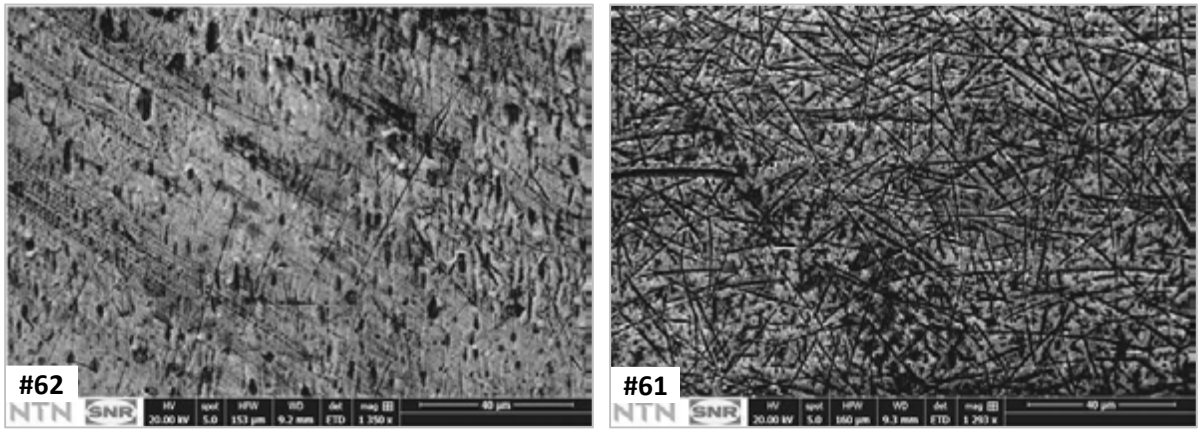

Fig. 4.6: SEM analyses of shiny ball from ACBB #62 and grey and matt ball from ACBB #61.

First, in order to verify that the oil flow rate is the same for all Machine S posts, measurements have been performed, giving ~0.5 L/min. Nevertheless, it is worth mentioning that the *internal oil flow* in the bearing mounting during service is delicate to appreciate and might be partially deviated

from IR contacts for the slightest mispositioning or difference, for example, between the coupling and exterior side of the mounting. This might explain why matt balls have only been observed on the coupling side.

In addition, if IR bore fretting corrosion was somewhat common to all WEC-affected or WEC-free IR (including #65-68 with the latest cage design), broken cages and more particularly *ball coloring have been observed only on WEC-affected IRs*. Further SEM analyses of the balls have revealed that the matt ones present an important abrasive surface distress with numerous scars (**Fig. 4.6**). It suggest that some *severe lubrication* occur at least locally in some part of the contact, even though the bearings are supposedly fully jet lubricated (section 2.2.1). This may be related to the fact that the cage design plays a major role in terms of lubricant replenishment of the contact [234]. In case of the first two cage designs associated to WEC formation on the IRs, considering the tight conformity of the bridges, lubricant scrapping off the balls probably happens, to different extents.

However, if ball coloring may be associated to WEC failures in the *alternative configurations*, it should be noticed that all *WEC-affected ACBB do not display a matt coloring*. In the *reference configuration*, ACBB #1-10 balls remained shiny after RCF testing (**Fig. 4.5** (d)). This suggests that WECs have formed despite sufficient lubrication, probably via the opening of surface microcracks.

b. Unexpected mispositioning and dissymmetry in some ACBB mounting

The *second point* suggesting that all ACBBs have not seen exactly the same operating conditions comes from signs of mispositioning and uneven loadings. As aforementioned, the ACBBs *#19-26* have been tested under the exact *reference configuration* of WEC-affected ACBBs #1-10*:* same turned IRs, same standard cage, same lubricant and same load case. Nevertheless, ACBBs #19-22 have suffered from premature creeping and *no WEC* have been revealed neither by fractographs nor cross sections of ACBBs #23-26.

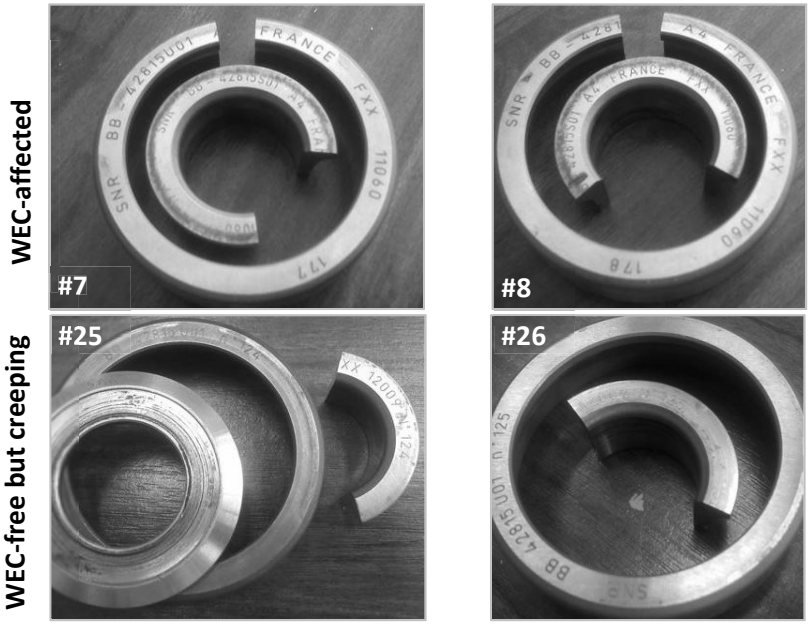

Fig. 4.7: ACBB ring flanges aspect after RCF tests.

A closer look at the overall ACBB aspects after the tests have revealed that, IRs #1-10 all presented a slight fretting halo on the IR outer diameter (**Fig. 4.7** (a-b)). IRs #19-26 have most probably seen a very *different loading* since the IR flanges clearly display a different aspect that is

emphasized in some cases by severe creeping of the spacer (**Fig. 4.7** (c-d)). The reason for such a difference remains unknown but it can be supposed that due to the loose ACBB mounting prior loading (**Fig. 2.2** (b)), some kind of *mispositioning* can occur. This statement is also supported by the fact that axial LOMs of the IRs reveal a significant difference in *DER density* between the coupling side and the exterior side, clearly testifying of an uneven loading (**Fig. 4.8**). In order to avoid the self-entraining spacer creeping, specific spacers have been manufactured in through-hardened steel for the following tests. However, this solution most probably only masks and limits the mispositioning issue, which thus might have also affected the following tests. Therefore, tribological conditions may not have been perfectly symmetric in the alternative ACBB tests, thus being one additional possible reason for the WEC lowered reproducibility rate.

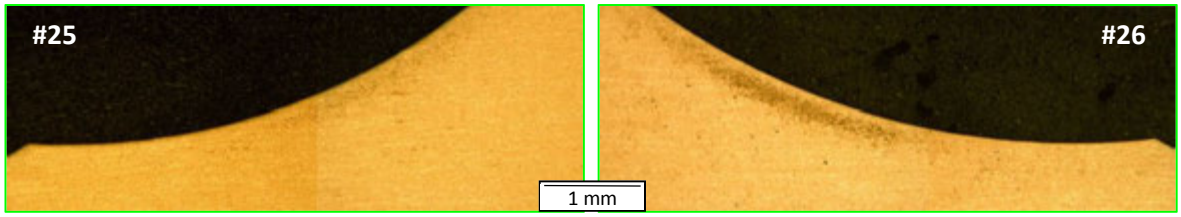

Fig. 4.8: Axial LOM of ACBB IRs from the same shaft revealing a significant variation in DER density.

c. Tribofilm formation

The *last* experimental observation suggesting that all alternative configuration ACBB tests have not seen exactly the same tribological conditions *depending on the cage design* comes from SEM-EDX analyses performed on the IR raceway to qualify the presence or not of tribofilm (procedure detailed in section 2.4.1.2). On WEC-affected IRs with the standard cage, no tribofilm has been formed along the contact major axis (IR #8 in **Fig. 4.9**). Additional assessments have been performed to confirm that IR#8 is representative of all IR #1-10. On the others, with a different cage design, WEC-affected or not, *tribofilm* has been detected at the contact angle for ACBBs with the oblong cage design (IR #61 in **Fig. 4.9** and IR #63 in **Fig. 4.10**) and with the latest cage design (IR #65 in **Fig. 4.11**). In those cases, close-ups have revealed that the closer it is from the contact border, the more the tribofilm presents a *heterogeneous spotted and/or stripped layout* (**Fig. 4.9**). These observations support that the tribological conditions affecting lubrication and thus tribofilm formation may vary from on ACBB test to another, probably depending on the cage design.

Anyhow, *tribofilm formation* is probably one additional reason anticipating the *lowered WEC reproducibility rate*. This is highly supported by the fact that all WECs have always been observed at the border of contact where *no tribofilm is formed* both for the reference (#1-10) and alternative configurations (#37, 39, 45, 58 and 61) (**Fig. 4.9**). However, this observation is apparently unsufficient to explain WEC formation mechanisms on its own. Indeed, similar tribofilm profiles have been detected on WEC-free IR having, supposedly, operated under the same operating conditions (**Fig. 4.10**).

In the ACBB tests, *tribofilm build-up* at the contact center seems to also *prevent WEC formation.*

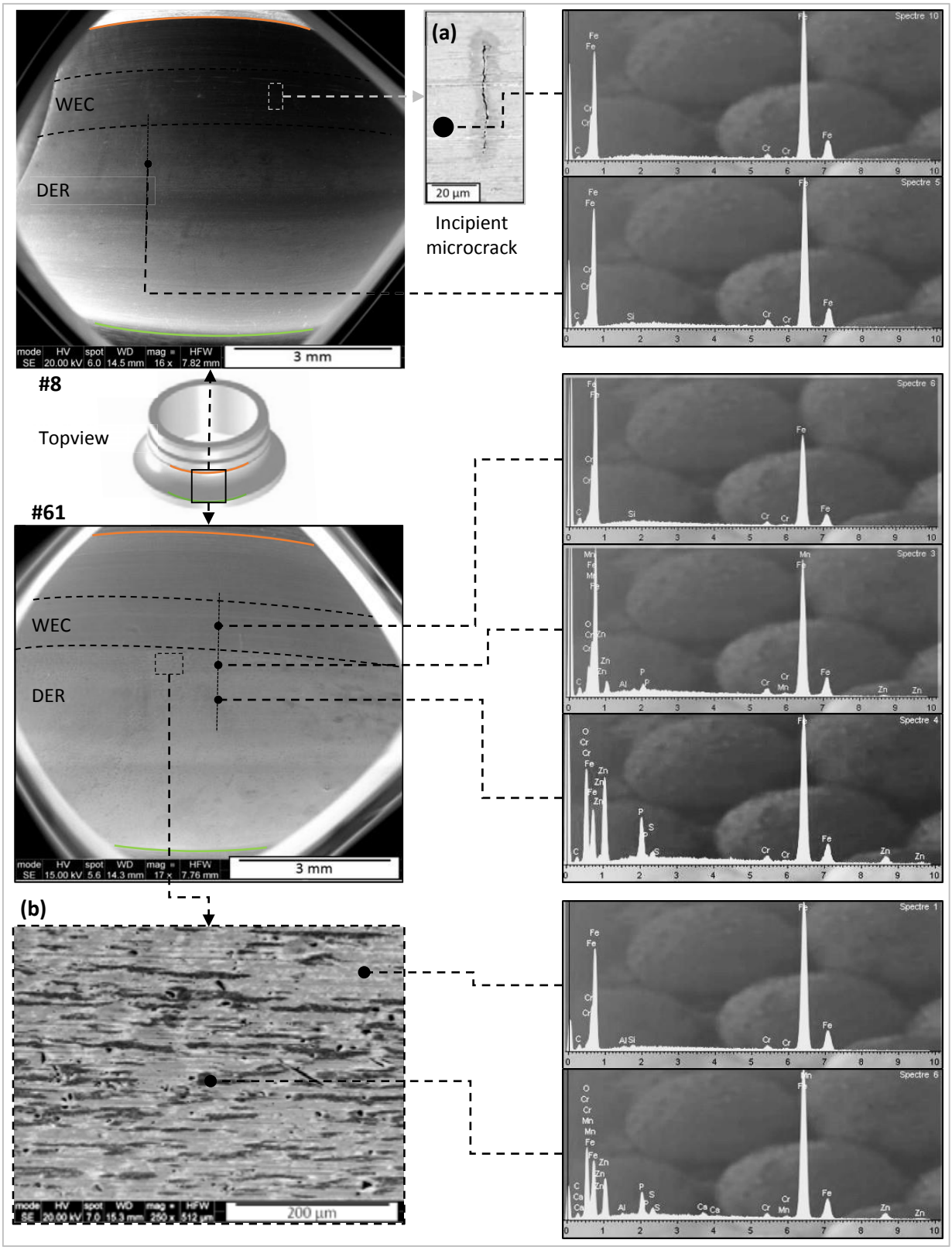

Fig. 4.9: Typical results of SEM EDX linear tribofilm analysis performed on raceway topview of *WEC-affected* IR #8 (standard cage clearance) and #61 (oblong cage clearance) providing close-ups on (a) an axial incipient microcracks positioned at ~2 mm from the groove in the WEC region, and on (b) heterogeneous and stripped tribofilm at the contact border nearby the WEC region (N.B. the size of the EDX spot represented is not scaled but is here as a reminder).

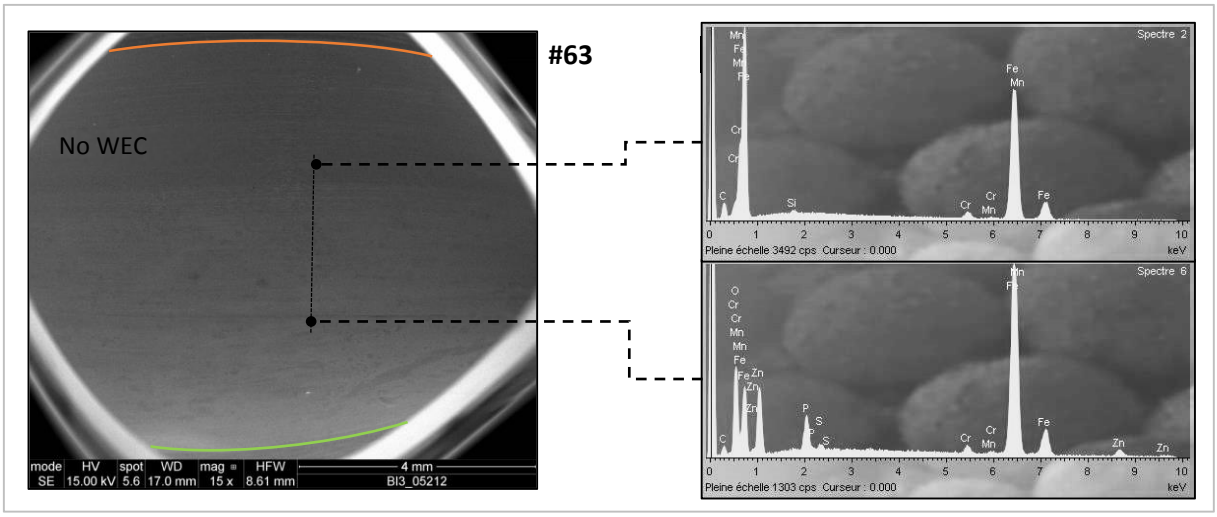

Fig. 4.10: Typical results of SEM EDX linear tribofilm analysis performed on raceway topview of *WEC-free* IR #63 (oblong cage clearance).

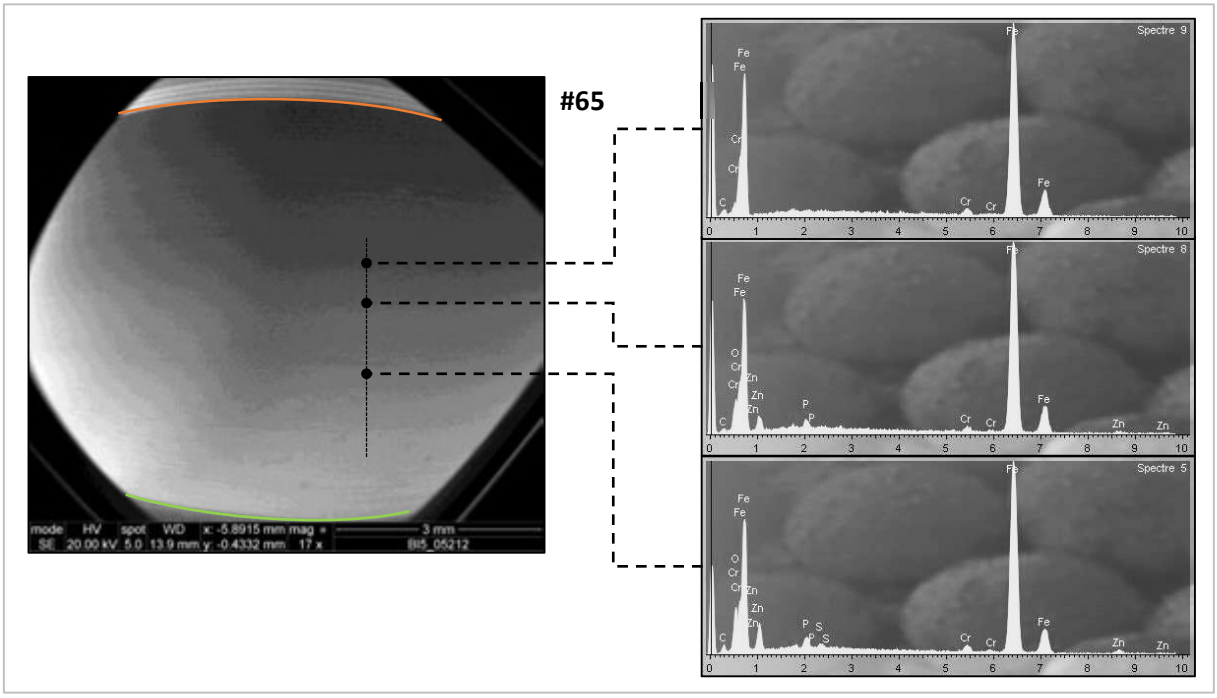

Fig. 4.11: Typical results of SEM EDX linear tribofilm analysis performed on raceway topview of *WEC-free* IR #65 (oblong cage clearance plus less-conforming bridges).

4.2 Analyses and comparison of WEC on both test rigs

In order to better understand WEC formation mechanisms in non-hydrogen precharged specimens, *a tribological comparison* of WEC reproductions on the CRTB and ABB tests have been led. The main factual elements are presented in **Table 4-1**. Contrarily to WEC occurrences in wind turbine bearings [165,166] and previous WEC reproductions [172,200] often associated to dynamic loadings and/or transient speeds, in both the fore-described minimalist tests WECs have been reproduced under *constant loads and rotational speeds* and for approximately the same number of cycles. This indicates that WEC formation may not be solely explained by dynamic loads and transient

speeds as it is often assumed. Hence, this section, focuses on the influence of other drivers such as contact *kinematics*, *lubrication*, and *tribofilm,* on WEC morphology and layout via the comparison of the CRTB and ACBB reproductions.

Table 4-1: WEC reproduction RCF tests without prior hydrogen charging: on CRTBs and on ACBBs (contact conditions given for the most loaded ball).

Data	**CRTB** [79,192,198,202]	**ACBB**
Universal reference	81212	7305 BECBP
Number of REs	15	10
Contact type	Linear	Elliptical (k=10.8)
Thrust load (kN)	60	Load cases 1, 2, 3, 4, 5
Radial load (kN)	0	
Maximum contact stress (MPa)	1890	3400 for WEC load cases 1, 2
Fitting hoop stress (MPa)	0	$90<\sigma_{hoop}<220$
Rotational speed (rpm)	750	2250
Linear speed (m/s)	3.0	2.4
Maximum SRR ratio along contact major axis (%)	12.5	20
Test duration (hrs)	18.5[198] - 40[79,192] - 200[202]	424 - 1436
Number of cycles $x10^6$	12.5[198] - 27[79,192] - 135[202]	35 - 120
Hardness (Hv10) Ring/RE	765/590[198]	800
Lubricant supply (L/min)	0.1[79] - 1.2[202]	0.5
Oil viscosity (mm^2/s)	64 at 40°C 9.5 at 100 °C [198,202]	45 at 40°C 6.9 at 100°C
Oil type	Highly additivated "low ref" semi-synthetic PAO base oil	Lubricant A: mineral base oil
Known additives	CaS [79,192,198] ZnDDP	No CaS ZnDDP
Oil temperature	100°C	ambient
Film thickness h_c (µm)	0.13	0.33
R_q (µm)	Washer ~0.08 [202] – RE ~0.05 Washer ~0.70 – RE ~0.09 [198]	IR ~0.06 RE ~0.02
λ ratio	1.1 for [79,192,202] 0.1 for [198]	4.2
Steel	Hardened martensitic 100Cr6 steel	Top quality hardened martensitic 100Cr6 steel
Fretting-corrosion	Not mentioned	Most IR bore
WEC-affected elements	Washer [79,192,202] – RE [198]	IR only for load case 1*, 2*
WEC location	Contact edge	Contact edge
WEC connection to surface	Not systematic [198]	Systematic

Transient speeds and/or dynamic loadings cannot explain WEC formation in CRTBs and ACBBs.

4.2.1 Different overall bearing configuration

The CRTBs and ACBBs clearly correspond to two very different bearing configurations that most probably influence WEC formation mechanisms. O*n one hand*, from a mechanical point of view, the ACBBs are likely to be *more representative* of radial REBs such as those displayed in wind turbine applications. For example; it also presents transient kinematics relative to the entry – exit of the load zones. Indeed, the large majority of WEC associated failures have occurred on radial REBs of different types (ACBB, DGBB, TRB, SRB, CRB, etc.) presenting many similarities with the ACBB, so that hasty conclusions could be drawn. For example, the ACBB IRs are exposed to significant fitting tensile *hoop stresses* similar to those large-size REBs due to delicate machining and mounting [31]. Thus, hoop stresses may be associated to the vertical WEC layout in through-hardened IR (section 3.2.3)[162]. Eventually, the large majority of the IRs, WEC-affected or WEC-free, presented significant fretting corrosion and relative creeping at the IR bore, thus suggesting these phenomena could be driving WEC formation.

Nevertheless, *on the other hand*, WEC reproduction on CRTBs have demonstrated that hoop stresses, effects of the entry – exit of the load zone, and fretting at the bore are all *not always required* for WEC development as these drivers are not present on CRTBs. This suggests that WEC formation mechanisms might differ slightly between CRTBs and radial REBs.

WECs do not always require *hoop stresses*, *entry – exit of loaded zone* effects nor *fretting* on the bore.

4.2.2 Specific bearing lubrication

4.2.2.1 Different lubricant formulation

Prior to the CRTB and ACBB tests, it had been mentioned that lubricant formulation had a significant impact on WEC formation mechanisms in case of grease lubricated radial REBs [168,172,189]. This has been confirmed by the fact that, on the CRTBs, WECs have only been reproduced with specific *over-based CaS detergents* and *ZnDDP* additive lubricant formulations, predominantly for certain concentrations [79,192]. However, on the ACBBs, WECs have been reproduced *without any CaS additives*. Even though lubricant A is a fully formulated commercial oil for which the author does not have access to the precise formulation, the oil producer has *a minima* confirmed that no metal sulfonates (calcium, magnesium or barium) had been blended in this lubricant. The absence of these additives has then been verified by (1) element infrared mass spectrometry revealing no Ca, Mg or Ba (**Table 2-5**) and (2) additional compound absorption spectrometry assessments revealing no absorption peaks at wavelengths relative to sulfonates (in-between 1180 and 1200 cm^{-1} and/or in-between 1340 and 1365 cm^{-1} [235,236])(**Fig. 4.12**). Therefore, if for the CRTB configuration CaS detergents seem to trigger WEC formation, they were however *unnecessary* for WEC formation in the ACBB configurations.

WEC formation mechanisms may be *in some cases* highly dependent on the *lubricant formulation*.

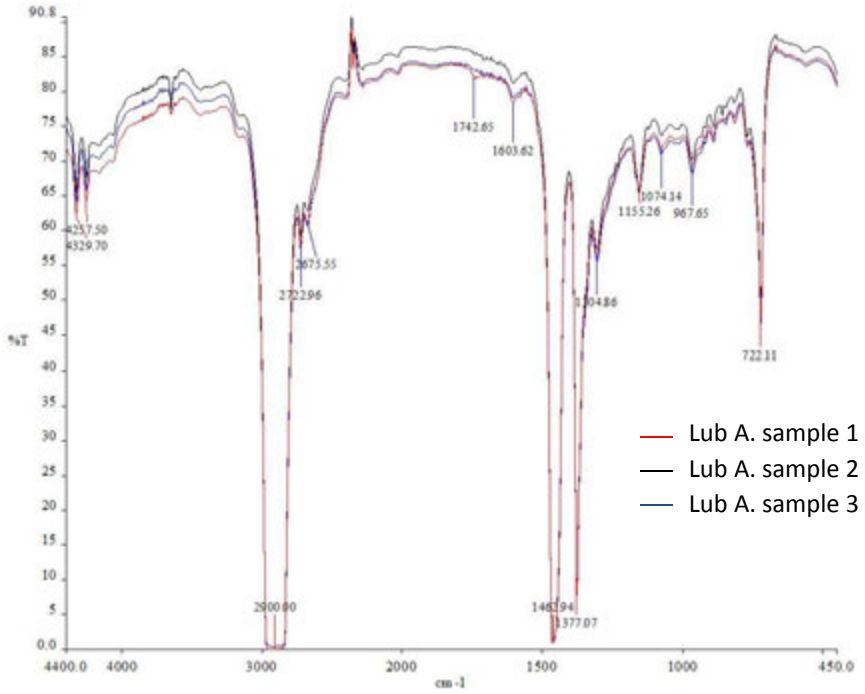

Fig. 4.12: Infrared transmission spectrometry assessment on three different samples of lubricant A

4.2.2.2 Similar local severe lubrication

The importance of lubrication formulation in the CRTBs could have been related to the fact the CTRBs have operated under *boundary to mixed lubrication* ($0.1<\lambda<1.1$) while the ACBBs have operated under, supposedly, fully flooded lubrication ($\lambda>3$) (**Table 4-1**) (section 1.2.3.3). However, the fore-detailed observations suggesting high internal frictions, notably surface distress of some ACBB balls, highly support that mixed lubrication may have also occurred punctually at the ACBB contact edges.

It has indeed been demonstrated experimentally that the minimum film thickness h_{min} actually extends over a significant portion of the *contact edges* in case of *wide spinning elliptical contacts* like in ACBBs [52,237,238]. Therefore, the lubrication parameter λ is most probably significantly reduced locally at the contact edges compared to that computed theoretically with the central film thickeness (**Table 4-1**).

Moreover, *local lubrication starvation* is assumed to occur locally in REB contacts in case of tight cage clearance and/or highly conforming cage bridges that tend to scrape the oil film off the REs [234]. This might therefore explain why the WEC reproducibility rate was much higher for the ACBB tests operating with the *standard cage* design (**Fig. 4.3**) for which scrapping residues have been identified in the pocket recess right above the WEC-affected contact edges (**Fig. 4.4**), even though the balls remain shinny for an undetermined reason (**Fig. 4.5**). Lubricant starvation and its influence on the effective film thicknesses remain however extremely delicate to quantify [205,239,240].

In a wrap-up, both *local minimum film thicknesses* and risk of *local lubricant starvation* are predominant at the ACBB contact edges, which seems consistent with WEC unconventional location versus the contact area (section 3.2.2) and WEC reproduction on severely lubricated CRTBs or grease lubricated REBs [168,172,189]. This local mixed lubrication could possibly

explain the high local surface tensile stresses required to open the numerous incipient axial microcracks observed on the ACBB IR bottom contact edges in relation with WEC networks (**Fig. 3.12**).

WEC formation mechanisms tend to correlate with *local mixed lubrication* in both configurations.

4.2.3 Similar internal slippage kinematics

Despite the two REB configuration, significant slide to roll ratios maxima naturally occur at the contact edges of both the ACBBs (SRR 22%) (**Fig. 2.4**) and CRTBs (SRR 12.5%) (**Fig. 4.1**). This is due to pure geometrical and kinematical considerations (section 1.2.2). The ACBB kinematics have been computed using NTN-SNR SHARCLAB®. Additional computations have then been led to evaluate the surface sliding energetic criteria $P.\measuredangle U$ along the contact major axis transverse to the rolling motion (P being the local pressure and $\measuredangle U$ the slip velocity). The $P.\measuredangle U$ values have been adimensioned versus the maximum $P.\measuredangle U$ obtained for the ACBB load case 1 presenting a high WEC reproducibility. The results have been plotted in **Fig. 4.13** along with the SRR for both the ACBB and the CRTB tests (similar plots are available in Appendix G (a) with scaled contact abscissa). Results show that a significant *$P.\measuredangle U$ peak* occurs along with the *SRR maxima* at the bottom contact edge of ACBB IRs and at both CRTB symmetric contact edges. It is worth to mention that this peak would be more pronounced considering $\mu.P.\measuredangle U$. Indeed, the friction coefficient μ would locally be increased at the contact edges due to local mixed lubrication. However, as friction laws to predict local friction coefficient along the contact remain in development and that the coefficient always remain of the same magnitude, it has been chosen to consider solely $P.\measuredangle U$. Similarly, these results have been obtained neglecting cage effects and possible roller skewing in case of CRTBs. Thus, slippage is most certainly underestimated.

In case of ACBB tests, the $P.\measuredangle U$ criteria has been repositioned along the IR curvature according to the effective contact angle of WEC-affected load case 1. Then the criteria has been superimposed on fractographs and stitched axial LOMs aligned using on the IR flanges and grooves. This demonstrates that the location of *WECs* at the contact edges *always correlates with a $P.\measuredangle U$ peak* (**Fig. 4.14**). Moreover, while the SRR have similar profiles for all ACBB load cases (**Fig. 4.13**), the $P.\measuredangle U$ criteria is significantly higher at the contact edges for WEC-affected load case 1 and 2 than for the others. This supports that the $P.\measuredangle U$ criteria could be representative of a WEC formation threshold, at least for these ACBBs and CRTBs. This is supported by the fact that, in case of the CRTBs, a $P.\measuredangle U$ maximum, equivalent to that of the ACBB WEC-affected load case 1 and 2, occurs at the roller contact edges where serial sectioning have revealed WECs [198] (contrarily to the significantly lower SRR) (**Fig. 4.13**).

As WECs develop specifically at contact edges in both the ACBBs and the CRTBs, it can be concluded that *WEC* formation highly depends on *slippage kinematics,* notably on the *surface energetic criterion $P.\measuredangle U$*. Indeed, high slippage does not only correspond to a local tribological common denominator to the ACBB and CRTB tests, but also to all WEC field occurrences and other laboratory reproduction available in the literature, which will be further discussed thereafter [16,29,79,163,164,167,172,176,178,180,182,189,192,198,241].

WECs develop at the contact edges corresponding to *slide to roll ratios* and *$P.\Delta U$ maxima.*

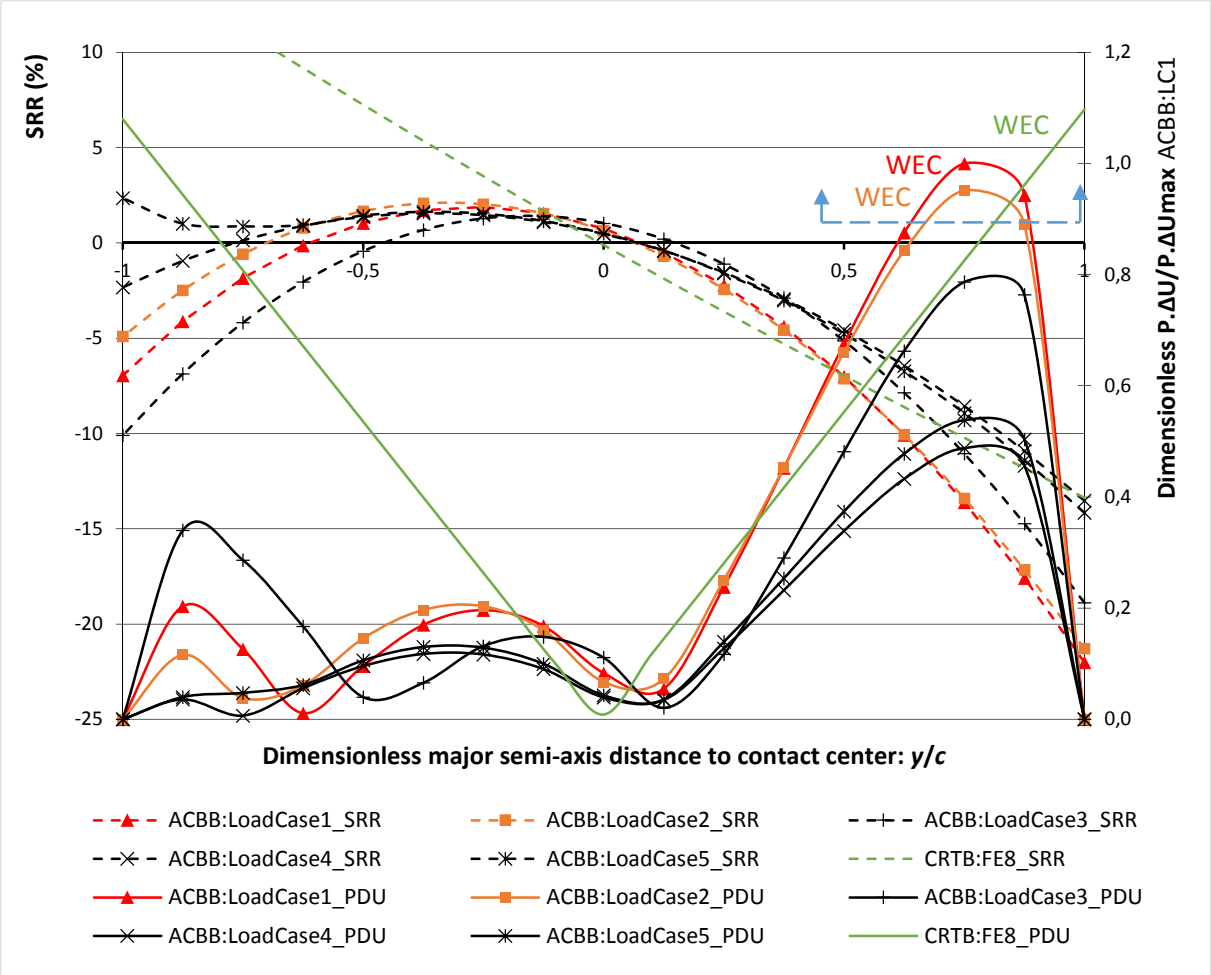

Fig. 4.13: Slide to roll ratio (SRR) and dimensionless sliding energetic criteria P.ΔU along the contact major axis transverse to rolling motion for (1) the CRTB FE8 configuration (green) and for (2) WEC-free (black) and WEC-affected (orange-red) ACBB load cases (**Fig. 2.4** and **Table 2-2**). A suggested P.ΔU threshold for WEC development is represented by the blue dashed lined and arrows. Similar P.ΔU plot accounting for scaled contact major axis available in Appendix G (a).

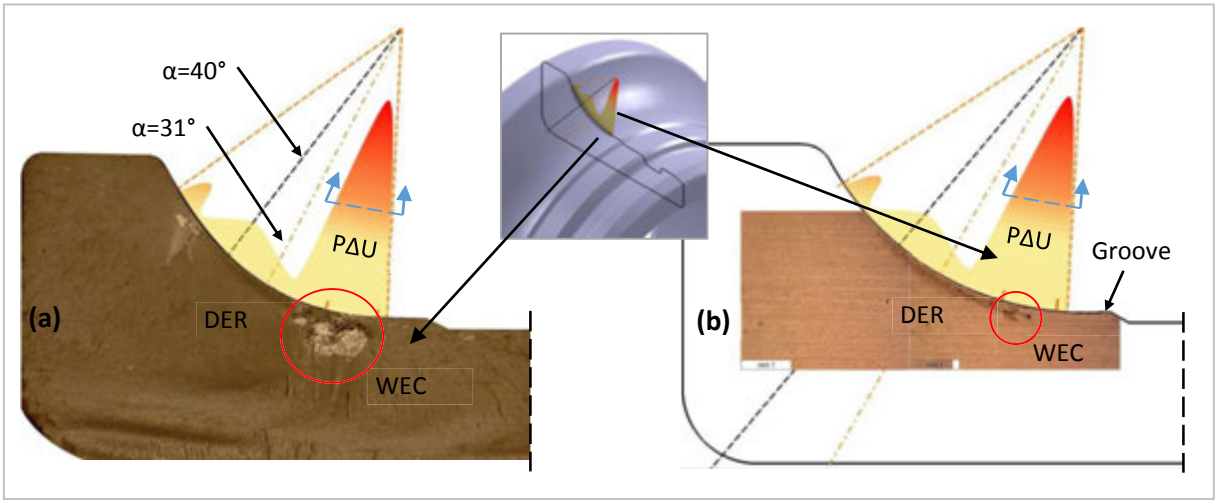

Fig. 4.14: Superposition of the P.ΔU profile along the major axis of the most loaded ball/IR contact (contact angle α=30.7°) for the ACBB tests load case 1: (a) fractographs of IR #9 and (b) stitched axial LOM of IR #7. Repositioning is achieved by aligning the respective grooves and flanges.

4.2.4 Similar incipient wear and poor tribofilm

In relation with mixed lubrication, WEC formation mechanisms seem to be highly influenced by wear and tribofilm formation. As wear is concerned, it should be noted that in one specific case [198], WECs have not formed on the washers but on the rollers. This is most likely associated to the fact that, despite extremely low λ ratio, wear rates on the rollers were probably lower due to the significant hardness difference with the washers (**Table 4-1**). In the other CRTB tests [79,192,202], WECs have developed on the washers where no significant wear has been measured [202]. This is in agreement with the observations of WEC-affected ACBB IRs where grinding marks remain visible, especially at the contact edge, thus supporting that no or only incipient wear has occurred (**Fig. 4.15**). Hence, WEC formation seems to occur only on components with *no or only incipient wear rates*. This counterbalances the fact WECs seem to be triggered by mixed lubrication… It is thought to be that *mixed lubrication has to be sufficient to wear off tribofilms* but *low enough to prevent significant wear* from altering WEC formation mechanisms.

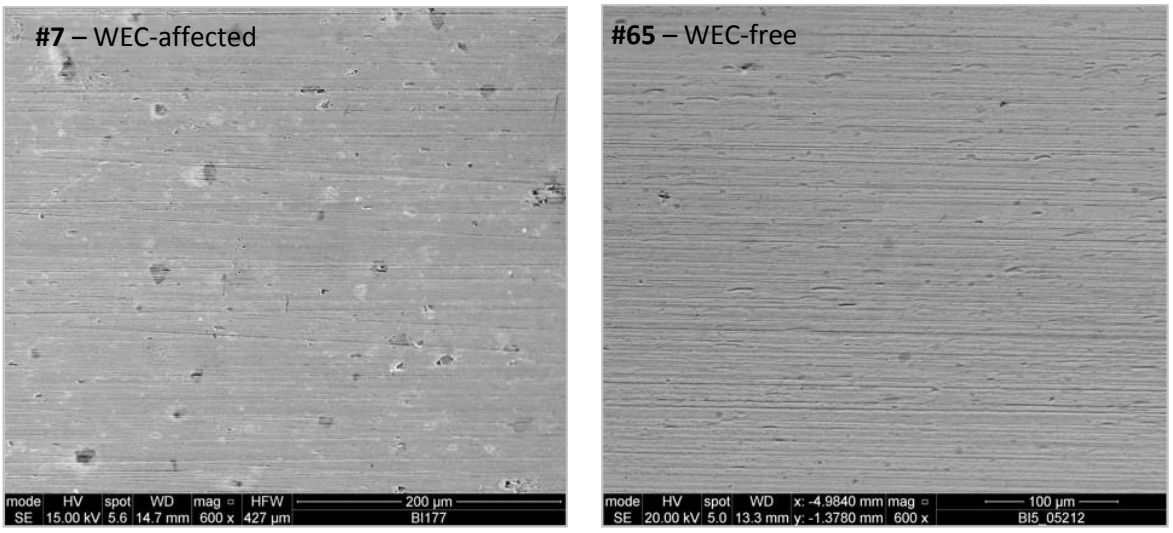

Fig. 4.15: Raceway topview of the contact edges of ACBB IR #7 and #65 where grinding marks remain (dents on IR#7 most probably due to debris from subsequent spalling).

On WEC-affected CRTB washers, FIB, XPS and SNMS analyses have revealed 100 nm thick tribofilm with high calcium content in regions of high slippage above WECs [79]. On all WEC-affected ACBB rings, the fore-detailed SEM-EDX analyses have revealed no traces of tribofilm above WECs (**Fig. 4.9**), which is contradictory. However, it should be recalled that in the CRTBs, the lubricant formulation and more specifically the presence of *CaS detergents*, have been mentioned to trigger WEC reproduction and that these highly polar additives are often employed as detergents (section 1.2.3.2)[235]. Therefore it could be supposed that detergents may actually be in excess in the often mentioned "low reference" oil used in the CRTB. This would partially prevent the formation of tribofilm and at least lead to maybe thick but heterogeneous and patchy tribofilms as described in section 1.2.3.5. Hence, highly reactive nascent surface would be left available at the raceway above WECs. This is in agreement with the fact that on the ACBB tests, all WECs formed at the contact edges where no or only highly disparate tribofilm has been detected by SEM-EDX analysis (**Fig. 4.9**). In a wrap-up, it seems that WEC formation seems to require sufficient *incipient*

wear and/or high detergent concentrations to generate some fresh metal spots in the tribofilm thus available for chemical reaction leading to hydrogen embrittlement.

WEC formation mechanisms seem to rely on a combination of incipient wear and specific lubricant formulation both resulting in *heterogeneous and patchy tribofilm*

4.2.5 Different WEC layout

In both ACBBs and CRTBs, premature spalling have been associated to what has been defined WEC in section 1.4.1. Despite higher Hertzian pressures in the ACBB contacts, WEC have developed at the contact edges where local pressure and slippage are similar to that of the CRTBs. Moreover, in both cases, WEC networks never interacted with any DER where compressive residual stresses build up (supposedly absent in CRTBs due to contact pressures below the 100Cr6 H_1 threshold [198]).

However, on one hand, in the CRTB rollers, 9 of the 13 WECs mapped by high resolution serial sectioning *did not interact with the extreme surface* and apparently presented no preferential orientation versus the over-rolling direction [16,198]. It should yet be noted that the minimum depth of the WEC networks has not been specified so that the possible interactions with the surface layer remain undefined.

On the other hand, on each ACBB IR, all WECs revealed by fractographs exhibited an *axial micro-crack link to the raceway* and a *preferential top-down growth oriented towards the OD* (section 3.2, **Fig. 3.7** and **Fig. 3.12**). All these observations of WEC surface connections are in agreement with previous WEC observations in radial REBs [6,29,162,182,241]. The different WEC layout between the two configurations therefore supports the fact that *WEC formation mechanisms might slightly differ* from REB thrust configurations to the radial REB configurations. In that sense, the ACBB tests would be more representative of WEC occurrences of wind turbine REBs in particular.

WEC *formation mechanisms might differ* as WECs may be *connected to the surface or not*

4.3 WEC formation mechanisms conjectures

The fact that WECs may or may not present a connection to the surface and that a specific low reference oil seems necessary in one configuration and *not* in the other, suggest that slightly *different WEC formation mechansims* and *drivers may actually co-exist*. In that sense, the fore-described ACBB and CRTB tests greatly support the understanding the author has of the WEC formation mechanisms that should be considered in two steps: *initiation* and *propagation*. As discussed in **Chapter 3**, WEC propagation is commonly associated to local hydrogen embrittlement. Considering that hydrogen naturally present in steel is not source of sufficient embrittlement, WEC initiation, in non-hydrogen-precharged components, must correspond to the *surface affected hydrogen permeation* into the steel. As previously anticipated, WEC formation tends to be mainly affected by surface and tribochemical parameters such as lubrication and slippage, and not by bulk material and contact stresses like conventional RCF.

4.3.1 Surface affected initiation through nascent steel

In this section, based on the previous experimental observations, it will be proposed that *WEC initiation* should *first* be triggered by the formation of *highly reactive nascent steel* surfaces on which the lubricant will then be able to react. This can occur either directly at the *raceway* when oxides and tribofilm are gradually removed, or either at freshly opened near-surface *microcracks flanks* in which lubricant can penetrate (**Fig. 4.16**). As discussed hereunder, both phenomena are greatly enhanced by *slippage* and *mixed lubrication* inducing incipient wear and high friction, consistently with reports of WEC field occurrences and various laboratory reproduction. This may also explain why WECs commonly occur at moderate stresses that allow high slippage and incipient wear without risking *smearing* or *scuffing*… This is consistent with the numerous smearing issues also commonly observed in wind turbine gearbox or main shaft bearings when not affected by WECs (section 1.3.4).

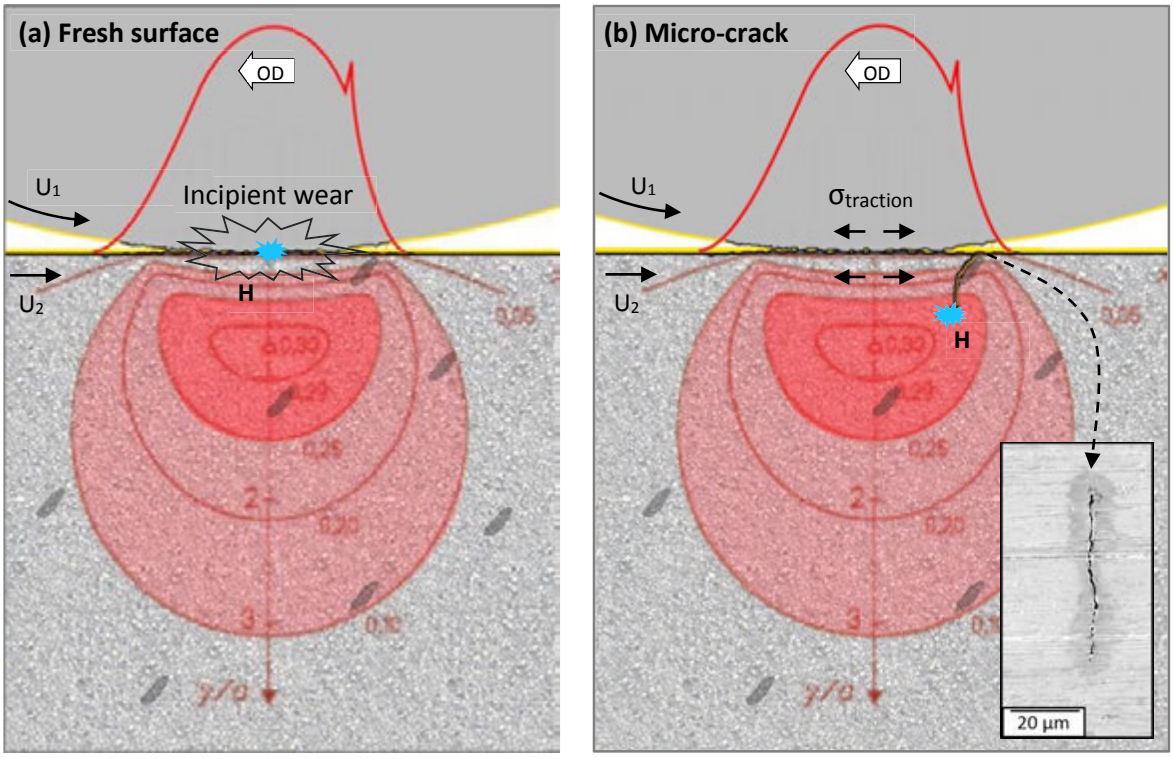

Fig. 4.16: Scheme of WEC initiation mechanisms by formation of nascent steel surfaces either (a) directly at the surface by incipient wear and/or heterogenous and patchy tribofilms, either (b) indirectly by the opening of incipient surface microcracks allowing lubricant contact with nascent flanks.

4.3.1.1 Fresh surface at raceway

In REB contacts, multiple tribological local phenomena can generate fresh metal surface on the raceways, including: wear, tribofilm removal and/or heterogeneous formation, localized corrosion, electrical discharges leading to local remelt, etc. WEC initiation through the formation of nascent surface directly at the raceway (**Fig. 4.16** (a)) has been previously mentioned by different authors [182,189,204] and strongly defended by Evans et al [16,198,201] emphasizing that WEC networks in the CRTB tests present *no interaction with the surface*.

In the previously described CRTBs, combining boundary to mixed lubrication with *considerable slippage*, fresh surface is most probably continuously formed at the raceway borders (**Fig. 4.16** (a)) (section 4.2.4). It could be argued that tribofilm thicknesses have been estimated to 100 nm and 20 nm on washers running with the WEC associated low reference oil and on WEC free washers running with a different lubricant, *respectively* [79]. However, analyses have revealed that tribofilm chemical compositions were significantly different in the two sets of washers. Also, tribofilms, even of the same chemical composition, could have various structural aspects and possible heterogeneous and patchy distributions on the raceway (section 1.2.3.5). Thus, it could be supposed that the 20 nm tribofilm remains dense and homogenous while the 100 nm one may be thick but heterogeneous, hence leaving some nascent metal spots in contact with highly sheared lubricant molecules. This suggestion is fully supported by the fact WEC have only been reproduced with the specific "low reference" oil containing *CaS additives* acting as powerful *detergents* that tend to prevent deposits on contacting surfaces [77,242]. Furthermore, this is in agreement with two previous studies [172,176] having also noticed the high impact of these sulfonate detergents/corrosion inhibitors on WEC occurrences in grease lubricated REBs.

In *thrust REBs,* WECs seem to initiate via *fresh surface formation* directly on the raceway depending on the lubricant formulation and regime.

4.3.1.2 Surface micro-crack flanks and lubricant penetration

The second possibility for lubricant to come in contact with nascent steel is by *lubricant penetration* in freshly opened *surface microcracks* (**Fig. 4.16** (b)), as also proposed by Gegner et al. [29,115,178]. Surface axial micro-cracks are supposed to initiate somewhere in the first ~20 µm below the raceway by combining temporary *local high tensile stresses* and *near surface discontinuities* such as emerging inclusions, machining defects, contamination dents, corrosion pits, local electrical erosion pits, etc. (**Fig. 4.16** (b)). High surface tensile stresses may be achieved by combining hoop stress and local high slide to roll ratio under mixed lubrication, for example at the contact edges of the ACBB IRq. The higher the surface traction, the more the surface micro-cracks are going to propagate vertically in the first µm, under the assumption that excessive wear or smearing does not gradually inhibit the microcracks initiation [116].

Axial micro-cracks are highly susceptible to develop in large size wind turbine REBs due to extended contact areas with high local frictional surface stresses induced by high sliding kinematics and mixed lubrication most often enhanced by considerable hoop stresses due to delicate fitting [31]. Hence, WEC initiation by surface microcracks seems more representative of WEC associated wind turbine bearing failures presenting numerous axial cracks [6,162,165,166]. In the ACBB tests, numerous axial-micro-cracks have also been observed in the WEC region and all WEC fractographs have revealed vertical links to the surface via those micro-cracks (**Fig. 3.12**). The surface microcracks have been found to be more numerous in turned IRs #1-10, all affected by high density WEC networks. This point could be explained by the specific elongated and emerging type A inclusions observed in turned IRs (section 2.2.2.2) that act as weak points in the surface layer (**Fig. 1.4** (b) and **Fig. 4.17**). In forged IRs, the crack connections to the raceway seem to be much more incipient as not eased by emerging inclusions, by yet present (**Fig. 3.13**). The semi-circular stair-like top-down growth propagation aspect of ACBB WEC networks (section 3.2.3.1) suggests that the surface axial micro-cracks do correspond to WEC initiation sites in agreement with other observation in WEC-affected radial REBs [6,29,115,162,165].

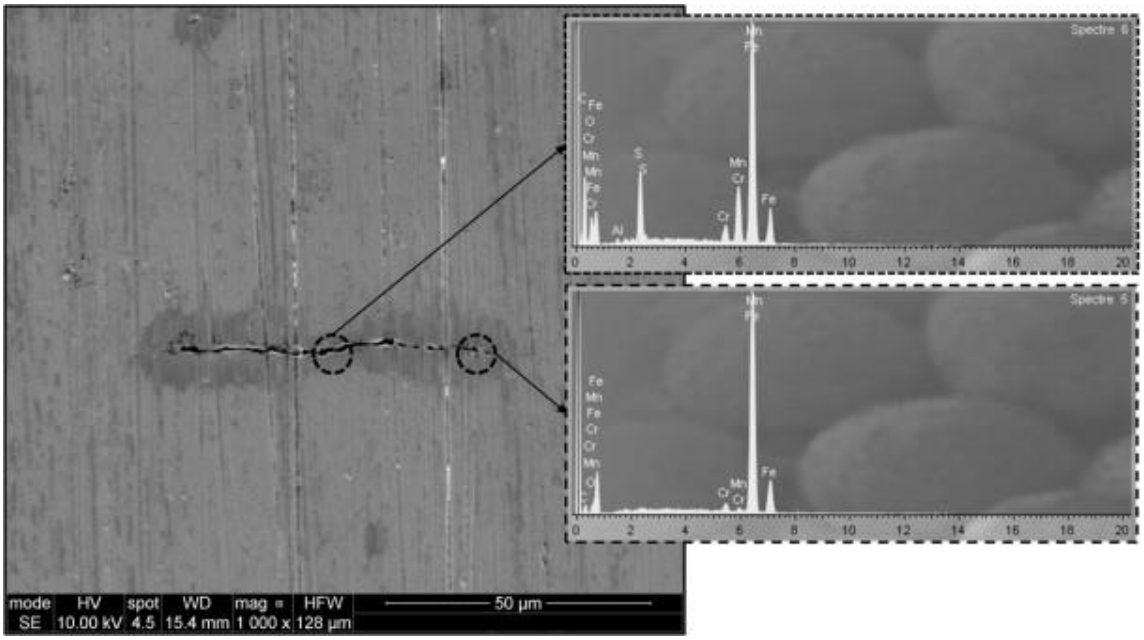

Fig. 4.17: SEM-EDX analysis of an axial microcrack observed in the contact edges of WEC-affected ACBB IR #8 revealing high manganese and sulfur contents in the crack vicinity suggesting the crack has been initiated due to the presence and/or dissolution of a type A inclusion near the surface [29].

As the surface microcracks are opened, lubricant or *lubricant compounds penetrates hundreds of microns deep* into steel despite the thinness of the cracks (**Fig. 3.15** and **Fig. 3.16**), in agreement with observations by [90,115,178]. This allows lubricant compounds to come in contact with highly reactive nascent surfaces repeatedly generated at crack tips most. It is worth mentioning that the thinness and the depth of the cracks clearly suggest tribochemical assisted cracking rather than gradual propagation induced by hydraulic pressure subsequently to oil seepage and entrapment.

In *radial REBs,* WECs seem to initiate via *lubricant penetration* in incipient *surface microcracks*.

4.3.2 Hydrogen permeation at nascent surface

4.3.2.1 Hydrogen chemisorption

Hydrogen permeation through nascent steel surfaces in REB contacts is most certainly the first step in the process leading to hydrogen embrittlement associated to WECs (**Fig. 4.18**). This process is in itself much more complex for lubricant – metal interfaces than for gaz – metal interfaces as it depends on many variables influencing the *electrochemical reactions liberating hydrogen*: the composition and stress state of the metal, the surface tribochemical state, the lubricant chemical reactivity, the presence of catalyzers, the temperature, the pressure, etc. [224]. If it is not clear for the moment whether hydrogen diffuses in the steel matrix in its atomic or ionic form, it is however *theoretically* accepted that hydrogen permeation from an aqueous solution into a metal *M* corresponds to an electrochemical desorption [222,224,243]:

$$H_3O^+ + M + e^- \rightarrow MH_{ads} + H_2O$$: discharge of hydrated protons in acid solutions

$$H_2O + M + e^- \rightarrow MH_{ads} + OH^-$$: electrolysis of water in alkaline solutions

Where MH_{ads} represents hydrogen atoms adsorbed on the nascent metal surface that are then more or less directly absorbed into the metal matrix, represented by MH_{abs}, depending on the surface conditions:

$$MH_{ads} \leftrightarrow MH_{abs}$$

These reactions are susceptible to occur at nascent surfaces in lubricated REB contacts as *H_2O molecules are always present* due to thermal-oxidation of lubricant molecules under high contact pressures and flash temperatures [211–213] and due to external water contamination more or less ingressed into the oil depending on the base oil and additives respective polarities (section 2.3.4.4). Additionally, some unverified electrochemical reactions have been proposed for hydrogen generation by *lubricant base oil molecules chemisorption* at nascent surfaces [244,245], but these reactions seem much more delicate than for water or hydrated protons.

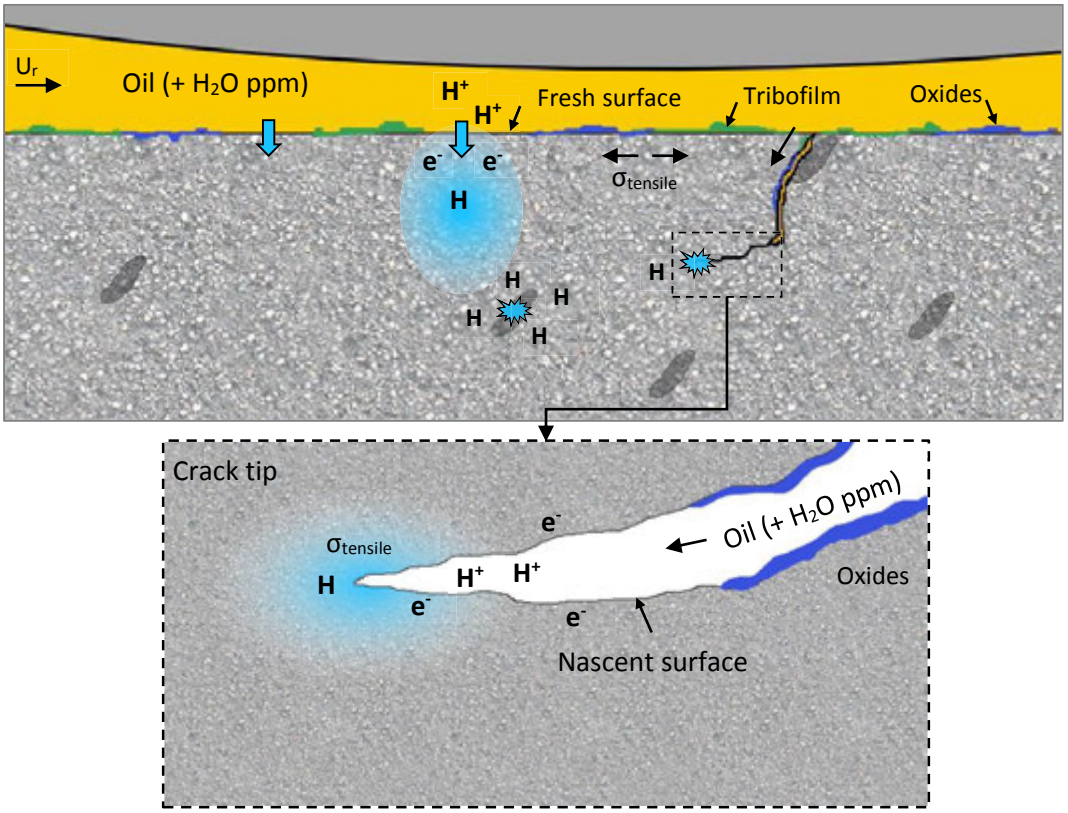

Fig. 4.18: Scheme of hydrogen permeation into the steel: lubricant or water molecules are chemisorpted at tensely stressed nascent metal surfaces at the raceway or at microcrack tips liberating highly diffusible hydrogen that is eventually trapped in the vicinity of defects such as inclusions.

Anyhow, it has been demonstrated *experimentally* by several studies that highly stressed lubricant or degraded lubricant components can chemically decompose at nascent steel surfaces allowing *local hydrogen chemisorption* into the bulk steel [174,184,189,243–246]. Hydrogen generation and/or permeation have indeed been proven to be *enhanced by water contamination* of the lubricant [206,208,214,247] and *by electrical potentials* at lubricant film bounds [29,99,101,168,193], which both highly depend on the lubricant formulation and temperature (sections 1.2.3.2 and 2.3.4.4). It has also been measured by TDA that hydrogen permeation greatly depended on the *lubricant type and additive formulation* [172,174,184,248] supposedly due to (1) the lubricant capacity to form tribofilm for given tribological conditions, and (2) its chemical capacity to promote hydrogen generation.

F*irst*, an homogenous and effective *tribofilm* indeed limits the exposure of reactive nascent steel and restricts hydrogen permeation in the material as hydrogen diffusion coefficient in oxide layers is as low as $1x10^{-18}$ m^2/s [221].

S*econd*, hydrogen absorption into steel is promoted by the presence of certain compounds of elements belonging to the V-A and VI-A periodic groups, even in relatively very low concentrations [224], for example *sulfur* that can be found in lubricant additives or in inclusions (**Fig. 4.17**). Other known *hydrogen poisons*, favoring hydrogen absorption rather than adsorption, are urea (CON_2H_4) and thiouera (CSN_2H_4)[224] which are very commonly employed as thickeners in various greases. This point is consistent with relatively frequent WEC occurrences on polyurea grease lubricated radial REBs [168,172] as well as some NTN-SNR automotive wheel REB WEC associated failures when lubricated with a specific "low reference" polyurea grease.

Finally, it should be noted that that the *mean* amount of hydrogen dissolved in a steel measured by TDA on a volume of specimen is most certainly of orders of magnitude less than that could accumulate *locally* at the crack tip [224] (**Fig. 4.18**), so that TDA measurements would not be representative of the effective concentrations and embrittlement at crack tip.

Hydrogen permeation has be proved to occur nascent steel surfaces in contact with *sheared lubricant – H2O molecules* but TDA is not *representative* of the *local hydrogen concentration* at WEC crack tip.

4.3.2.2 Surface hydrogen embrittlement effect on WEC initiation

To allow hydrogen permeation, the two possible nascent surface formation conjectures previously proposed, i.e. either at directly at the contact or indirectly in surface microcracks, seem to correspond respectively to thrust and radial REB configurations. Yet, it may be supposed that in radial REBs, such as in the fore-described ACBB tests or in wind turbine REBs, a *combination of the two conjectures* could also occur. Indeed, the influent drivers, such as slippage and mixed lubrication, are often similar for both conjectures.

Hydrogen permeation models are yet limited by unknowns such as boundary conditions in case of catalytically generated lubricant chemisorption the raceway [249]. Nevertheless, WEC networks commonly seem to go far beyond theoretical hydrogen diffusion depths of a few microns based on Fick's law and hydrogen diffusion coefficient ($3.8x10^{-11}$ m^2/s [19,204]). Direct hydrogenation at the surface most certainly depends on the contact time ratio over the inter-contact time during which oxidation of the surface may occur [249]. In consequence, hydrogenation most certainly takes place inside the rubbing crack itself, especially for deep cracks.

In ACBBs, WECs occur also in regions of nascent raceway. Therefore, *shallow hydrogen permeation* at the raceway may first accumulates at defects in the top 10 to 20 μm. This would ease the first surface tensile microcracks opening when surface cleavage would not be evident, even considering significant hoop stresses [250]. Anyhow, the fact that the micro-crack conjecture requires both *crack opening and lubricant penetration* may explain why WEC laboratory reproduction on CRTBs seems more common and/or less sensitive than on radial REBs. In the latest, specific conditions such as electrical currents [172,192,193] and/or transient loadings or speeds [16,167,172], are often required even though it was not the case in the present ACBB tests.

Shallow hydrogen permeation may first favor *surface microcrack formation* as both depend on slippage.

4.3.3 Subsurface propagation by local hydrogen embrittlement

After being initiated by near surface local hydrogen permeation through nascent steel surfaces, either directly at the raceway or inside surface microcracks, WECs are commonly agreed to propagate by *local hydrogen embrittlement at crack tips* enhancing both crack ramified propagation and subsequent formation of white etching microstructure. This has been observed in the fore-described ACBB and CRTB WEC reproductions as well as in WEC-affected application such as wind turbine REBs (section 3.2.1) [6,17,19,29,58,96,164,171,172,174,177,179,180].

4.3.3.1 Hydrogen assisted brittle cracking

Once generated, hydrogen tends to stay trapped at tensile crack tips [216,232] and defects in the steel matrix (section 3.1.1.2)[222–225,227]. As best explained in section 3.3.1, hydrogen enhances decohesion between metal atoms (HEDE) and thus allows broad WEC networks to propagate *subsurface* with a brittle aspect *quasi-regardless the contact stresses* beyond the Hertzian zone (**Fig. 4.19**). Transgranular fracture associated to tribochemical embrittlement, as suggested by the smoothly striated WEC fractographs aspects (**Fig. 3.9**) has been confirmed by Electron Backscatter Diffraction (EBSD) and Ion Channeling Contrast Imaging (ICCI) in [14]. WEC tribochemical propagation, as opposed to conventional mechanical crack propagation, is supported by the fact that WEC occurrences are very sensitive to environmental issues and lubricant formulation among other influent drivers [79,172,174,184,189,192,202].

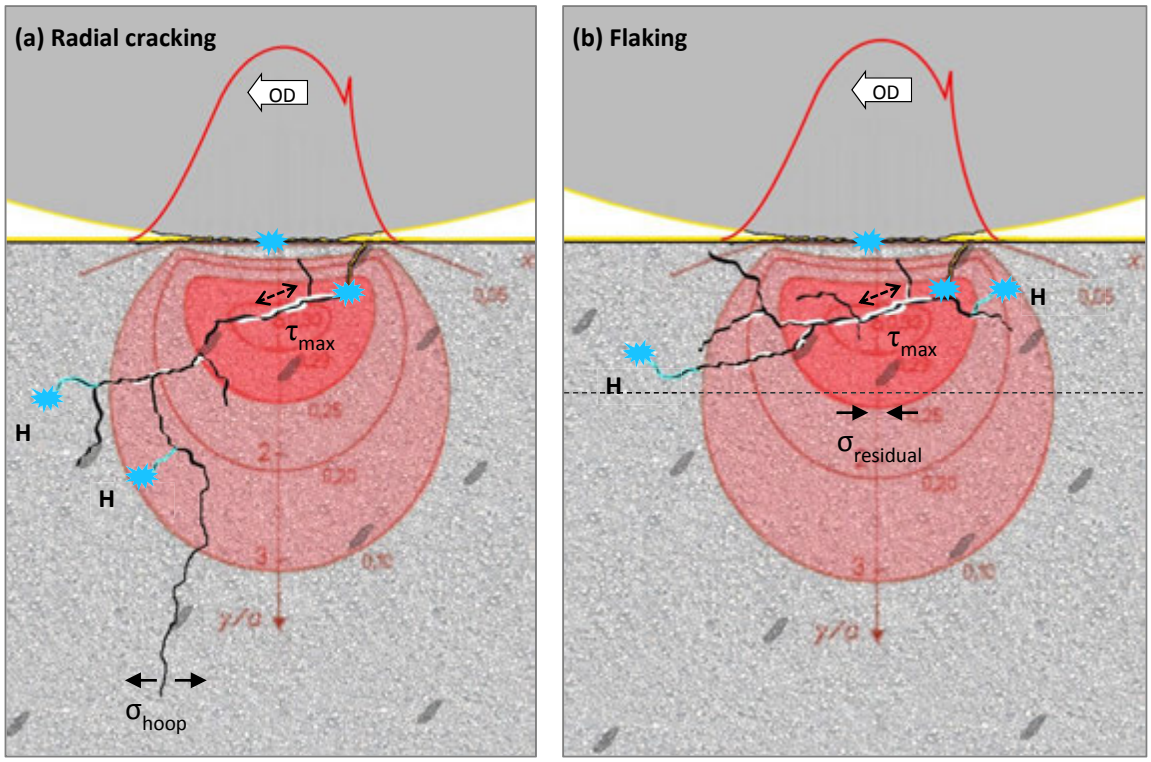

Fig. 4.19: Scheme of WEC propagation due to local hydrogen embrittlement at crack tips: (a) radial cracking in through-hardened bearing subjected to tensile hoop stresses and (b) flaking in components subjected to compressive residual stresses such as case-carburized or significantly loaded components.

Then, depending on structural and residual stresses, WECs will eventually develop into different macroscopic failures in the range of *radial cracking* in through-hardened bearings with

important hoop stresses to *surface flaking* (WSF) in case-carburized or highly stressed components (>2500 MPa) for which compressive residual stresses build up (section 1.3.2.1) (**Fig. 4.19**)[6,162]. Numerous inclusion interactions with WECs observed by Evans et al. [16,198,200,201], may also explain highly ramified and brittle propagation. Indeed, inclusions act both as hydrogen traps and *propagators* where the stress field changes brutally. Nevertheless, WEC formation mechanisms do not seem to rely on inclusions as WEC have developed similarly in turned and forged ACBB IRs despite a significant difference in type A inclusion ratings (section 2.2.2.2). This is also supported by poor interactions observed between inclusions and WECs on fractographs (**Fig. 3.9** (b)).

4.3.3.2 Formation of White Etching Microstructure

As the cracks propagate, *white etching microstructure* (WEA) underlining mainly horizontal cracks flanks in the maximum shear stress zone (**Fig. 4.19**), are supposed to form due to high crack rubbing shear stresses and hydrogen enhanced localized plasticity (HELP)(section 3.3.1) favoring the martensite transformation into nano-grained ferrite (section 1.4.2.1). The fact that WEA seem to form subsequently by crack rubbing and HELP has been discussed previously in sections 1.4.2.1 and 3.2.1.2. It has further been noticed that WEC networks in case-carburized steels tend to display much thicker WEA than in through-hardened steels (**Fig. 1.44**), which may be explained by the higher proportion of horizontal cracks constraint in the maximum shear stress zone and by the often longer service life before macroscopic failure.

Finally, WEC formation conjecture by lubricant penetration in incipient surface microcrack, thus liberating hydrogen and enhancing both brittle cracking and subsequent adjacent WEA formation, is also supported by the observation of an unusual crack network on a specific DGBB IR displaying very similar morphology to WECs (**Fig. 4.20**). *The exceptional crack initiation* down at the IR bore is likely due to excessive fretting corrosion, hoop stresses and IR unconventional thinness. Yet, thick *WEA have developed* aside cracks and heavy branching occurs when entering the contact stressed region. This DGBB IR has operated under highly additivated lubricant B that had been previously associated to WEC formation, thus suggesting *local hydrogen embrittlement* probably occurs. This result confirms that *WEC formation mechanisms, especially adjacent WEA strongly rely on tribochemical* aspects more than on conventional RCF and that they may be initiated by various surface affected initiation mechanisms.

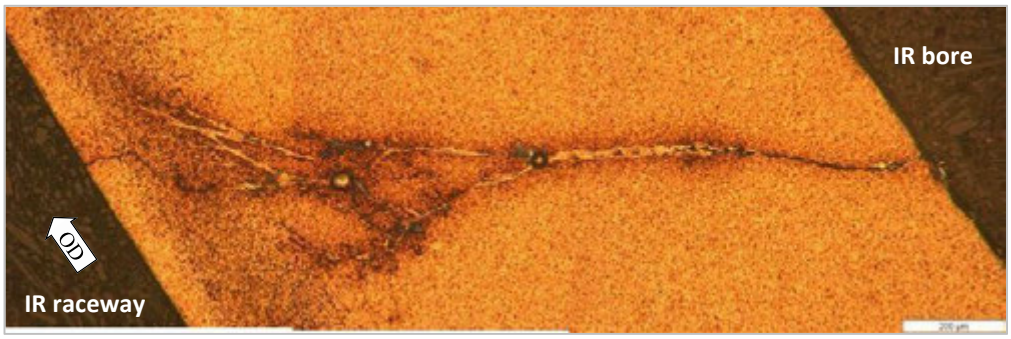

Fig. 4.20: Circumferential LOM of a specific NTN-SNR DGBB IR tested on a Machine S with highly additivated lubricant B: WEA form aside cracks that initiated at the IR bore due to intense fretting.

WEC overall *subsurface* morphology is function of the structural *stress state* of the affected component and the number of cycles before macroscopic failures.

4.4 Closure

As a closure to this fourth chapter, a thorough tribological analysis of two different WEC reproductions, respectively on CRTB tests from the literature and on in-house ACBB tests has been led. Analyses have revealed that (1) WEC correspond to a tribochemical cracking failure mode mainly influenced by lubrication and slippage parameters, and that (2) WEC surface affected initiation via the formation of nascent surface may vary slightly from an application to another, while WEC propagation mechanisms are generally attributed to hydrogen embrittlement.

4.4.1 A surface affected tribochemical cracking failure mode

As anticipated in section 3.3.3 of **Chapter 3**, WEC correspond to *a premature unconventional RCF failure mode* in REB associated to *local hydrogen embrittlement* that does not develop as usual in the subsurface Hertzian zone but most often at contact edges. In this chapter, tribological analysis of WEC reproduction on CRTB and various ACBB tests has confirmed that WEC initiation does not rely on bulk contact stresses and material properties as conventional RCF and that hoop stresses, fretting, transient speeds, and various inclusion ratings are not sufficient to reproduce WECs. This clearly explains why there is no correlation between WEC failures and load cycles on the conventional RCF diagram (**Fig. 1.31** (c)).

Instead, the comparison of the CRTBs and ACBBs fully support that WEC formation relies on *surface tribochemical parameters* that are lubrication and slippage energy associated to the $P.\Delta U$ criterion. Both tend to tribochemically promote hydrogen permeation into the steel by the formation highly reactive nascent steel surfaces. It has been demonstrated that if WECs always develop in regions of high slippage and $P.\Delta U$, on the CRTBs, WEC formation has been triggered by specific detergent additive concentrations that was however unnecessary on the ACBB. This supports that WEC initiation can slightly differ depending on the tribological conditions at asperity scales.

4.4.2 WEC initiation and propagation mechanisms

As hydrogen naturally present in the steel is unsufficient to form WECs, *WEC initiation* must correspond to *hydrogen permeation* into the steel via sheared lubricant and/or ingressed water molecules tribochemical reactions at nascent steel surfaces. Based on experimental observations, lubricant can come in contact of nascent steel by two different means depending on tribological conditions.

Indeed, on the CRTBs, hydrogen seems to penetrate *directly at the raceway* edges due to high slippage, mixed lubrication and the presence of detergents that result in heterogeneous tribofilms leaving some highly reactive fresh metal spots available for hydrogen permeation. On the ACBBs, hydrogen permeation seems to occur via lubricant and/or water molecule penetration into numerous *surface axial microcracks* opened at the contact edges by combining near-surface discontinuities and temporary high surface tensile stress due to high slippage and local mixed lubrication. This seems representative of what has often been observed in wind turbine REBs.

Limited and shallow hydrogen permeation directly from the raceway may also first eases the microcrack opening when surface cleavage is not evident.

Once initiated, in both cases, *WECs propagate* by local hydrogen embrittlement at cracks tips. Indeed hydrogen tends to stay trapped at tensile crack tips physically enhancing metal atoms decohesion (HEDE) so that typical brittle cracking develop quasi-regardless the contact stresses. As the cracks propagate and rub under cycling contact stresses, hydrogen enhances localized plasticity (HELP) leading to local microstructure refinement corresponding to adjacent WEA. Depending on the material properties and structural stress state, the component will be more or less sensible to hydrogen embrittlement and the overall WEC morphology may vary from deep radial cracking to surface flaking with dense WEA. No evident counter-indication to these WEC surface affected initiation and propagation mechanisms has been found in any reports of WEC occurrences available in the literature.

4.4.3 Objectives of the following chapter

Considering the experimental facts and outcomes of this chapter, it may be anticipated that WEC initiation and propagation mechanisms are highly influenced by various *influent mechanical and tribochemical drivers* depending on the test rig or application. For instance, local *P.⊿U* peaks seem to trigger WEC initiation on both of ACBBs and CRTBs, is it the case in other applications? Moreover, lubricant formulation has been proven trigger WEC initiation in the CRTBs, but does it solely affect tribofilm formation? Hence, in order to *generalize the understanding of WEC formation mechanisms* and propose efficient and durable countermeasures regardless the application, WEC influent tribochemical and mechanical interacting drivers will be reviewed in **Chapter 5** from macroscopic scales down to tribological scales and results of specific RCF tests performed on the TDM to qualify the impact of each identified driver will be provided.

Tribological analysis of White Etching Crack (WEC) failures in Rolling Element Bearing

Chapter 5:

White Etching Cracks influent drivers and Twin-Disc Machine investigations

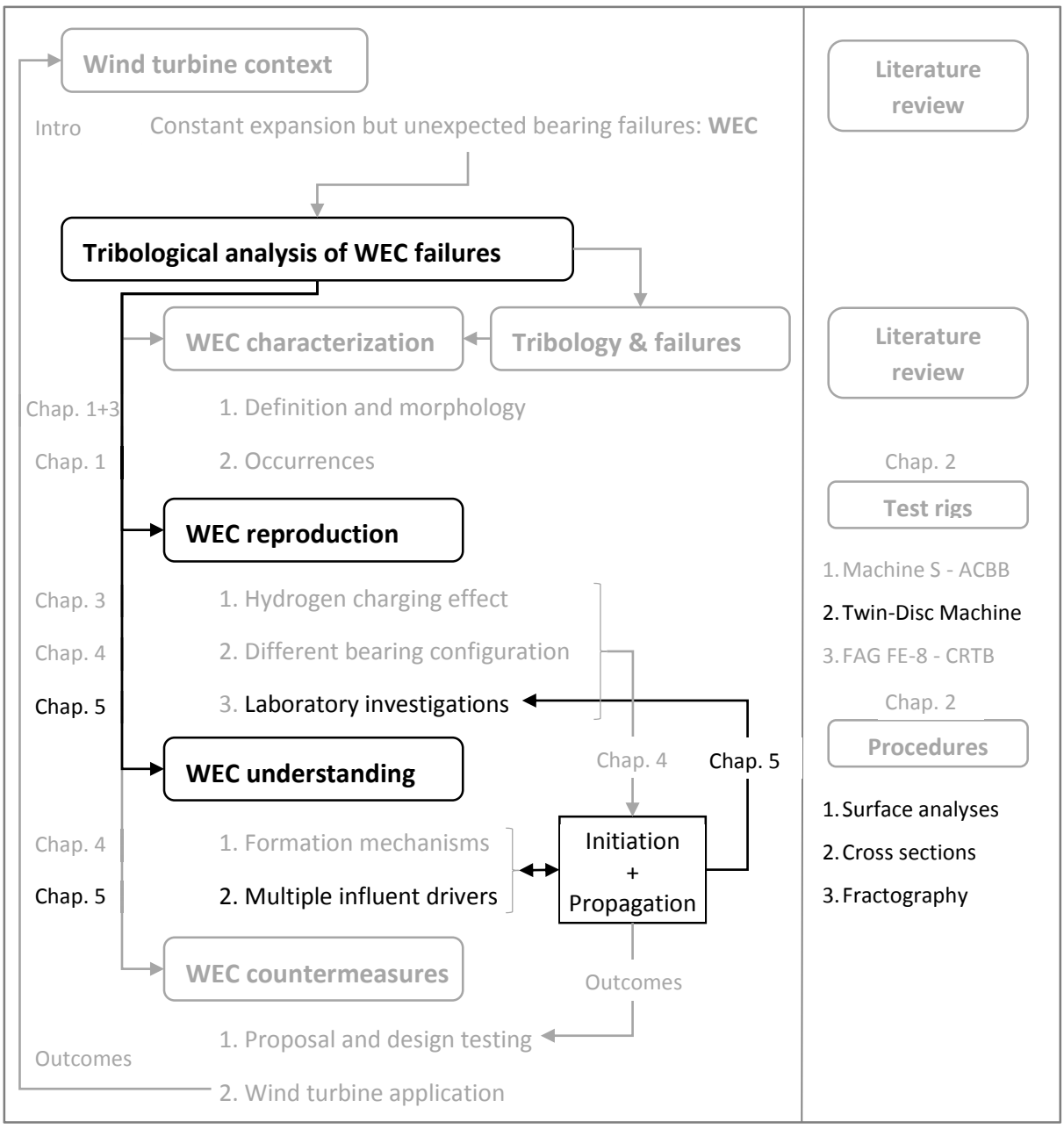

The last chapter of this thesis focuses on the tribochemical and mechanical drivers that affect WEC formation mechanisms based on various experimental observations. At macroscopic scales, multiple combinations of drivers seem to influence WECs depending on the application, but they generally come to down to similar phenomena at tribological scales, all enhancing nascent surface formation and hydrogen chemisorption. In order to clarify the respective influence on WEC initiation and propagation, the identified drivers will subsequently be transposed on the Twin-Disc Machine, revealing that drivers that had once triggered WECs do not seem to be self-sufficient and that WEC formation mechanisms actually rely on a subtle equilibrium between tribo-mechanical, material and tribochemical parameters, which should thus be considered when designing efficient and durable countermeasures.

5.1 WEC drivers manifold and respective tribological influences

Bearing in mind the WEC initiation and propagation conjectures (section 4.3), multiple WEC influent drivers may subsequently be pinpointed based on CRTB and ACBB WEC reproductions and on additional WEC occurrences from the literature or NTN-SNR internal reports. In this section, an *overview of the numerous influent drivers* will first be proposed from macroscopic scales down to tribological scales uncovering various possible combinations and interdependencies. Focus will then be made on specific tribo-mechanical and tribochemical influent drivers affecting WEC formation.

5.1.1 Overview of WEC influent drivers from tribo to macro-scales

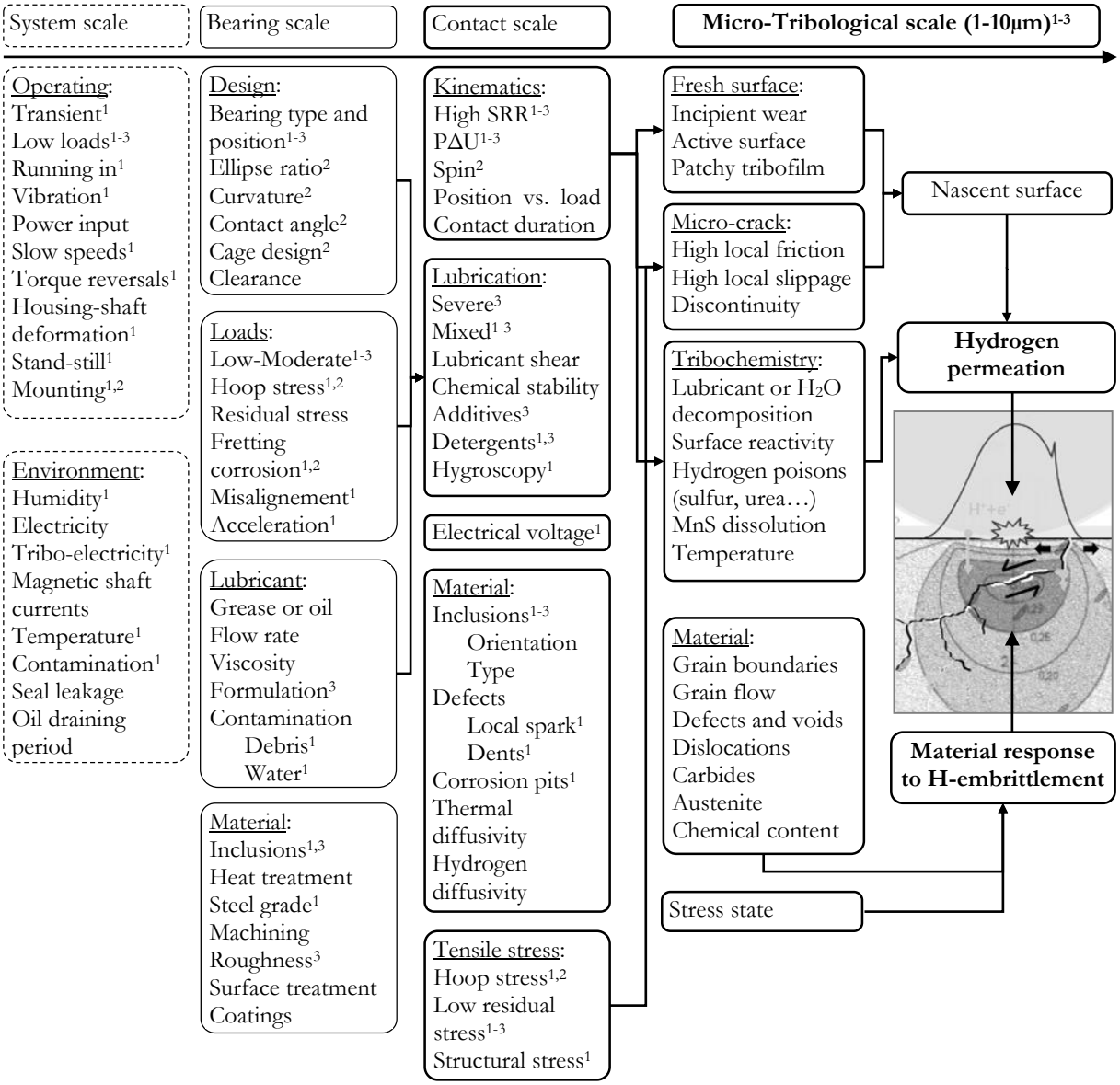

Fig. 5.1: Partial overview of influent drivers on WEC formation from macro to tribo-scales suggested by [1]wind turbine REB, [2]ACBB and [3]CRTB WEC occurrences. Examples of interactions suggested by arrows.

5.1.1.1 WEC root cause analysis from tribo to macro-scales

As anticipated throughout the analyses of WEC reproductions without prior hydrogen charging on the fore-described CRTB and ACBB tests (**Chapter 4**), the root causes and influent drivers of WEC surface affected formation mechanisms are multiple and may vary from an application to another, at least from a *macroscopic* point of view (**Fig. 5.1**). Three specific examples support the latest statement.

First, up to recent years, WECs have mainly been reproduced on REB test rigs comprising *dynamic loadings* and/or *transient speeds* [16,167,172], which have been however unnecessary for both the FE8-CRTB and the NTN-SNR Machine S ACBB WEC reproductions. *Second*, while WEC reproduction on CRTB rely on s*pecific additive concentration,* those additives are unnecessary on the ACBB tests. *Third*, additional Machine S tests performed on DGBBs with fully formulated engine oil at 40°C and 110°C, have reproduced WECs only on IRs operating at 110°C (ref. DGBB-1 in Appendix M), thus suggesting that *high temperatures* tend to favor WEC formation, as confirmed by the FE8-CRTB tests but inconsistent with the NTN-SNR Machine S ACBB tests.

Hence, in this study, a – most probably non-exhaustive – *root cause analysis* has been led to grasp WEC influent driver manifold. Starting from tribo-asperity scales (1-10 μm), *WEC initiation drivers* affecting nascent steel surfaces formation was first considered. Then the main catalyzers for *WEC subsurface propagation* that are hydrogen permeation and the bulk steel resistance to hydrogen embrittlement were considered. Eventually, these local tribological phenomena have gradually been associated to global contact parameters (100-500 μm) such as kinematics and lubrication regimes, to macroscopic drivers at bearing scale (mm-cm) such as loadings and transient speeds, and finally to environmental issues and mechanical behavior of the overall system (cm-m), for example, in case of a wind turbine gearbox (**Fig. 5.2**). The root cause analysis has been built based on drivers identified by analysis of the ACBB and CRTB tests and/or by reports from the literature or NTN-SNR. The root causes drivers identified present no contradictions with previous root cause analyses developed to a smaller extent [163,164,167].

The overview of this root cause analysis has been first wrapped-up into lists (**Fig. 5.1**) and then deployed considering mechanical and tribochemical drivers individually (**Fig. 5.2**). The latest illustrates that WEC formation mechanisms present *no unique common denominator* but rely on various combinations of macro-drivers that all come down to similar phenomena at tribo-scales so that hydrogen permeation occurs by one of the two fore-proposed conjectures. Hence, drivers triggering WEC formation on one test bench are most probably not self-sufficient nor even necessary on different one. WEC drivers seem to differ from one application to another. In **Fig. 5.1** and **Fig. 5.2**, drivers have thus been specifically linked to the respective concerned applications: wind turbine bearings (**Fig. 5.1**[1] and Appendix I), ACBB and CRTB laboratory tests (**Fig. 5.1**[2,3] and Appendix J). It enlightens in particular that wind turbine REB operating conditions seem to overlap with numerous identified drivers. Indeed they combine dynamic loadings with environmental issues with highly hygroscopic and additivated lubricants [97], humidity and electrical potentials or discharges. This might explain why WECs are apparently more frequent in the wind industry than in other applications. Finally, WEC surface initiation mechanisms drivers for the CRTBs and ACBBs appear to be distributed on the predominantly "tribochemical" or on the "mechanical" sides, respectively. This further supports that WEC initiation mechanisms can slightly differ for an application to another (section 4.3.1).

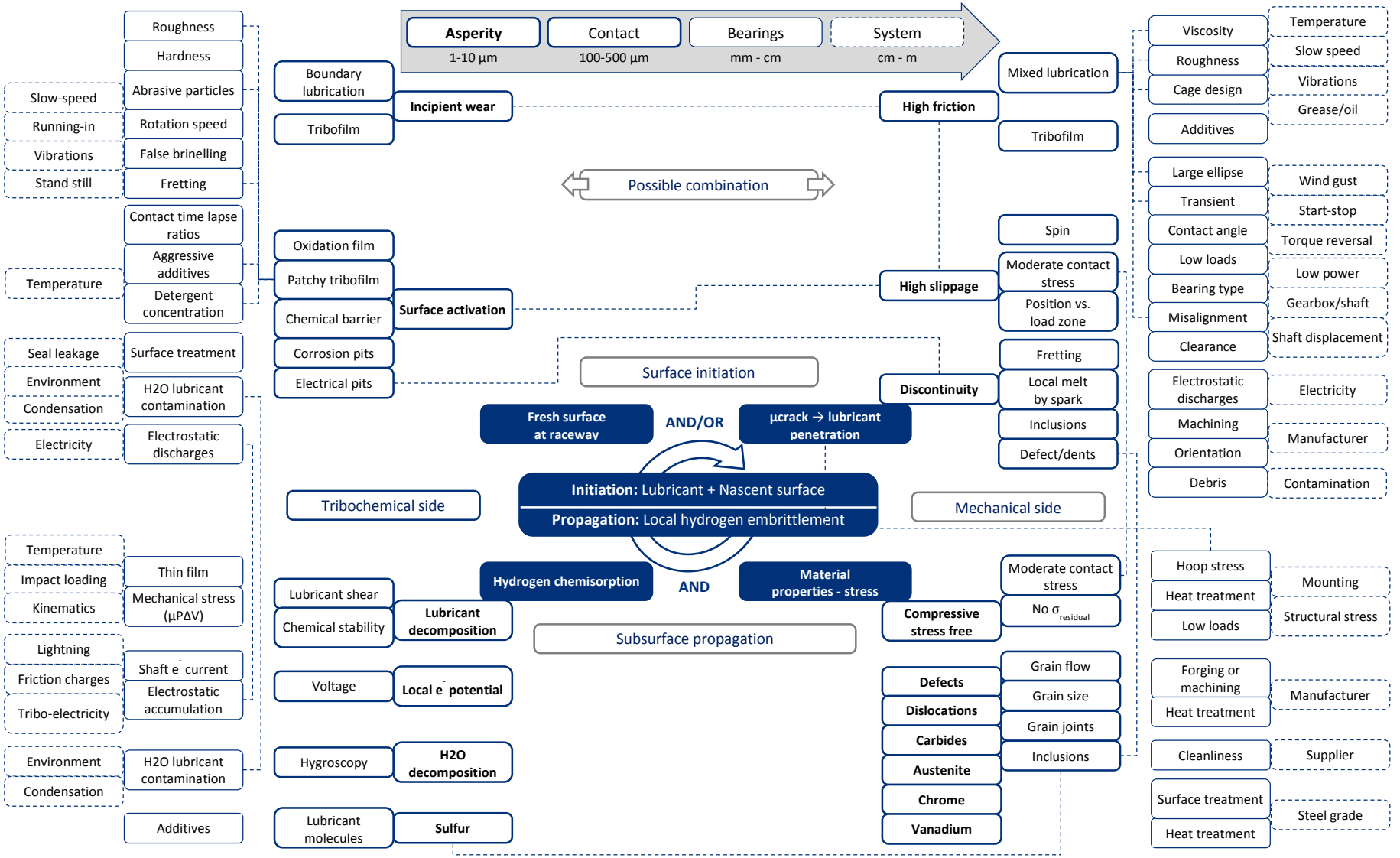

Fig. 5.2: WEC initiation and propagation root cause analysis with some various influences of multiple drivers from tribo to macro-scales (Appendix I, J, K, L).

5.1.1.1 WEC drivers multiple interdependencies

A major complication in qualifying WEC drivers is that they most often interact and influence each other. Few of the numerous possible interactions have been represesented by arrows in **Fig. 5.1** and **Fig. 5.2**. For example, tribochemical drivers such as tribofilm formation may depend on tribomechanical drivers such as heat released by lubricant shear, and *vice-versa.* Interdependencies occur between the two nascent surface formation conjectures, as materialized by the horizontal connections between the top left and right hand corners (**Fig. 5.2**). Alternatives also link drivers between top and bottom corners both vertically or diagonnally (**Fig. 5.2**).

A focus on the three WEC drivers that are slippage, tribofilm properties and temperature is proposed in **Fig. 5.3**. It illustrates that they all influence each other being possible *root causes* and/or *tribo-scale consequences* of one another. For example, local temperatures are higlhy influenced by slippage and reduced film thicknesses, despite the fact that the latest depend on the lubricant viscosity and thus on the bulk temperature itself… In addition, temperature also affects the formation of tribofilm by chemically activating additives, and thus the friction coefficient and friction heat dissipation… Finally, lubricant additives and temperature are not only going to affect tribofilm structural properties but also lubricant hygroscopy and electrical resistivity. Mutiple influences of additives and slippage have been pinpointed in Appendix K and L, respectively.

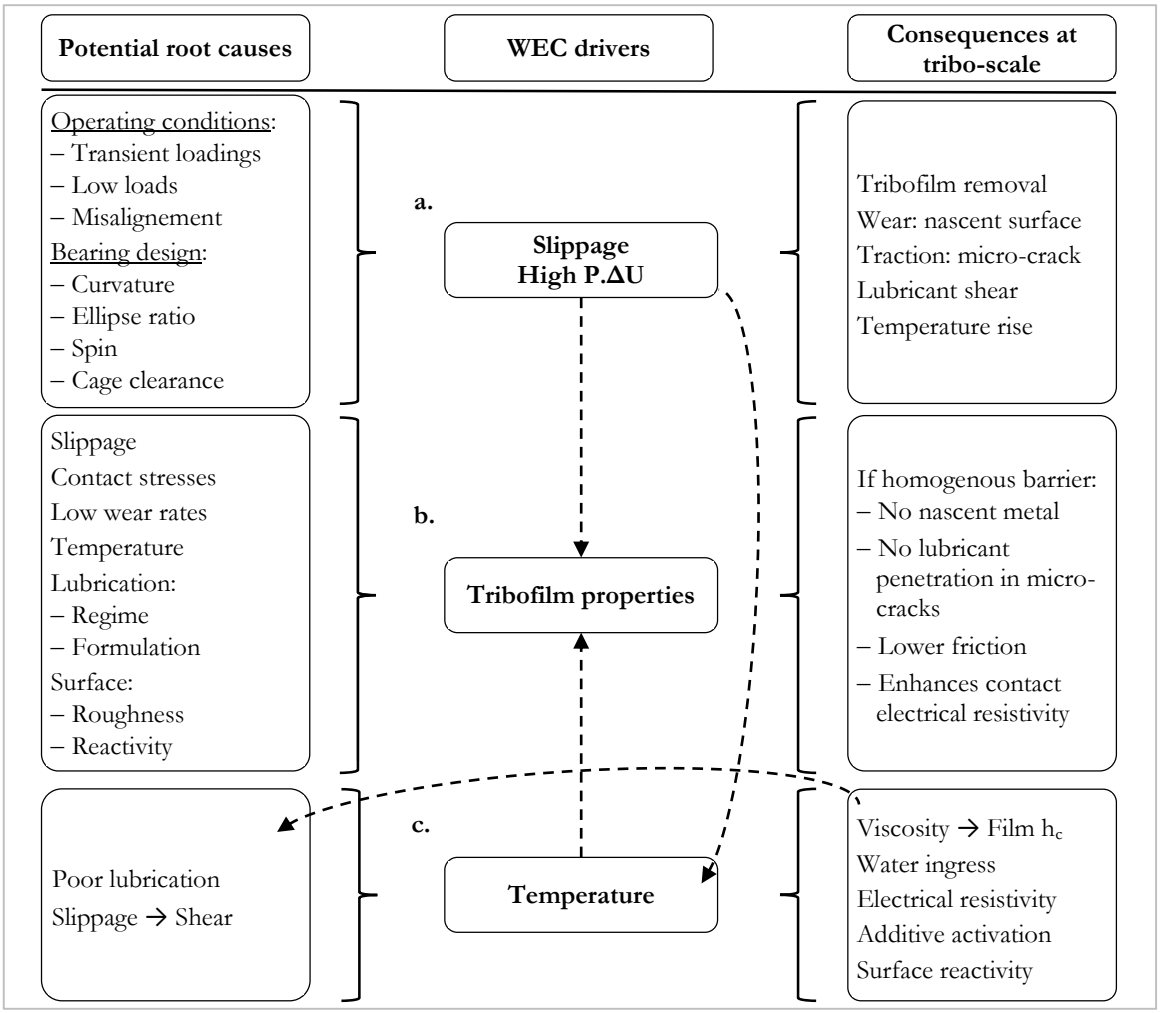

Fig. 5.3: Examples of different root causes leading to similar WEC drivers and multiple consequences at tribo-scales all influencing each other: (a) slippage, (b) tribofilm properties, (c) temperature

Moreover, specific drivers previously identified as detrimental for REBs such as boundary lubrication, water contamination and electrical currents have been all individually been tested in the past decades and most often did not lead to WEC failure modes. Hence, it seems that drivers have different degrees of influence depending on the presence or not of other drivers. Yet, they do not seem to be self-sufficent. Indeed, only combinations of different drivers seem to lead to WEC mechanical and tribochemical formation mechanisms. For example, water contamination and/or electrical potentials will be unsufficient, even though sometimes necessary to form WEC, if no nascent surface is available for tribochemical reactions, and *vice-versa*.

In consequence, the next section will focus on identifying the main tribological influent drivers that will then be tested individually using the LaMCoS TDM in order to limit the possible interdependencies susceptible to occur in application and full REB tests. To sum up this overview, most influent drivers are often *non-self-sufficient*, *affect each other* and, in some cases, rely on *thresholds* that may vary depending on the application. As drivers influence WEC formation mechanisms and other drivers at tribological scales simultanously, WEC reproduction on laboratory test rigs and potential countermeasures are consequently delicate to design.

Depending on the application or test configuration, WEC formation mechanisms rely on:
various combinations of multiple *non-self-sufficient drivers* at macro-scales
that often come down to similar *interacting tribo-mechanical* and *tribo-chemical drivers*

5.1.2 Focus on main WEC tribological drivers

In this section, in order to best qualify the multiple WEC influent drivers, focus will be successively made on main *tribomechanical* and *tribochemical* drivers pinpointed in **Fig. 5.2** *at tribo-scales*. Driver influences will be discussed based on various WEC occurrence reports and eventually confirmed by CRTB and/or ACBB various test results detailed in **Chapter 4**. Also, *complementary NTN-SNR RCF tests results* will be succinctly discussed in order to support some further major statements. Those tests have been conducted to a limited extent compared to the fore-described ACBB (8 REBs) but yet provide additional WEC experiences. Details of these tests are partly provided in Appendix M.

5.1.2.1 Tribo-mechanical influent drivers

a. Component material and stress state

In the literature, the large majority of WEC occurrences have been reported for relatively *low contact pressures* (P_{H} <2 GPa), often below conventional thresholds for RCF [79,188,192,201,202]. This point is first verified by the ACBB Machine S tests (section 4.1.2.2) and by DGBB tests from Fujita et al. [180] in which WECs only develop at the contact borders where local contact pressures and subsurface stresses are significantly lower than at the contact center. Results have even demonstrated that, in case of the latest WEC-affected DGBB IRs, the risk of WEC formation is actually increased when lowering the contact pressures by reducing the osculation [180]. Moreover, axial cross sections have been performed on IRs of endurance tests performed on double-ACBBs composed of two angular contact IRs facing each other (ref D-ACBB in Appendix M). LOMs have revealed WECs exclusively on the interior side IRs where no DER had developed, contrarily to the

exterior side IRs with pronounced DERs, similarly to **Fig. 4.8**. This also supports that WECs tend to develop under moderate loads for which no or few compressive residual stresses buildup.

Indeed, in wind turbine applications, case-carburized REBs tend to be less WEC sensitive than through-hardened REBs thanks to *compressive residual stresses* and enhanced retained austenite contents [162] (section 1.1.1.3). Softer and compressed cores are believed to reduce the sensitivity to hydrogen embrittlement and thus to *delay – but not to fully stop – WEC propagation*, at least in its form of radial cracking (section 4.3.3). In consequence, this point has been accounted for in the root cause analysis (**Fig. 5.1** and **Fig. 5.2**, bottom right hand corner).

WEC sensibility is lowered in case of *compressive residual stresses* and *higher contact pressures.*

b. Inclusion rates and orientations

Considering the WEC initiation conjecture via the opening of surface axial microcracks (section 4.3.1.2), it may be supposed that WEC circumferential density depends on the frequency of discontinuities in the surface vicinity. In that sense, emerging inclusions would be a key parameter for WEC initiation. This would explain why the WEC reproducibility on ACBB tests has been lowered when using ultra-clean forged IRs presenting only small globular MnS inclusions (**Fig. 2.5** and section 4.1.2.2). Nevertheless, as illustrated in **Fig. 5.4**, well targeted circumferential LOMs reveal dense and broad WEC networks on WEC-affected forged IRs similarly to those observed in turned IRs with stringer MnS emerging (**Fig. 1.39** (a)). This suggests that (1) emerging inclusions are clearly not the only driver affecting surface microcracks opening and that (2) WEC formation mechanisms do not rely on inclusions rate and orientation, which does not support the hypothesis of WEC subsurface initiation at inclusions [16,198,201].

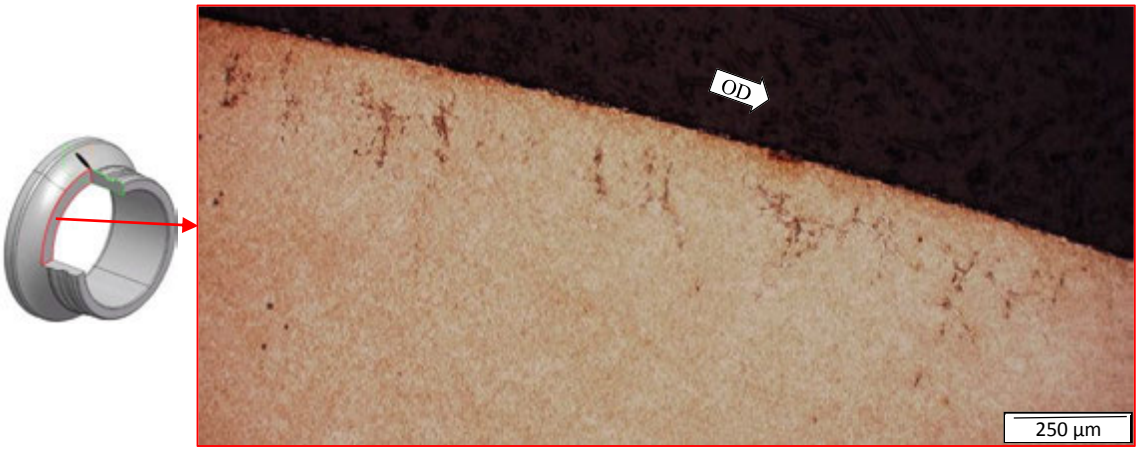

Fig. 5.4: Circumferential LOM of IR#61 with a high WEC density despite at high inclusion cleanliness.

WEC formation mechanisms are *not affected by inclusion rates and orientations* on the ACBB tests.

c. Contact sliding kinematics and possible thresholds for WEC formation

It has been reported, and enlightened in section 4.2.3 (**Fig. 4.13**), that *high sliding kinematics* at contact edges is a common tribomechanical denominator to WEC occurrences in ACBBs and CRTBs. Slippage indeed enhances formation of nascent surface by favoring wear and surface

tensile stresses. Slippage also favors lubricant decomposition at nascent surfaces by increasing lubricant shear and flash temperatures. Therefore, high slippage favors both WEC initiation and propagation mechanisms (specific **Fig. 5.2** in Appendix L). In application, slippage can be associated to different macroscopic drivers: bearing designs, contact ellipse ratios and curvatures, cage clearance, transient moderate loads, etc. (**Fig. 5.2**).

Nevertheless, results of section 4.2.3 tend to support that *sliding energetic criteria based on P.⊿U* are more relevant than simply SRRs in predicting WEC formation (**Fig. 4.13**). To complete the analysis started in section 4.2.3, several *sliding energetic criteria* have been similarly computed for various REB tests known to reproduce or not WECs, either from the literature (DGBB from Fujita et al. [180]) or from NTN-SNR (ref. DGBB 1, DGBB 2, and CRTB in Appendix M). For each configuration, diverse sliding energetic criteria have been plotted along the contact major axis transverse to rolling motion of the most loaded ball/IR contact. All the criteria have intentionally been *adimensioned* by the respective maximum value in case of the most loaded ball/IR contact under load case 1. In doing so, the author would like to insist on the fact that the suggested thresholds for WEC formation require additional testing before being taken for granted, as they are most certainly balanced by other drivers such as tribochemical ones.

First, the *P.⊿U* criterion has been plotted in **Fig. 5.5** considering additional REB configurations. The results are consistent with the observation made from **Fig. 4.13**: all *P.⊿U peaks* above the arbitrary threshold correspond to WEC formation at the contact edges, in agreement with Fujita et al. [180]. Moreover, CRTB tests performed on NTN-SNR FB3 Machines during this study have been considered in **Fig. 5.5**. Indeed, no WEC have been reproduce yet on those CRTBs, which further support the *P.⊿U* criterion as it remains significantly lower than the proposed threshold. This is supposed to be due to a maximum SRR of 5% limited by geometrical considerations of the CRTB design.

Second, the *P.⊿U* criterion has also been considered when designing the planetary REB of a 3MW wind turbine gearbox. The objective was to better qualify the difference between a Double-SRB design and a TRB design (**Fig. 5.6**). Whatever the bearing design and radial load, the *P.⊿U* criterion remains excessively low, so that it would apparently be unsuccessful in predicting WECs.

In consequence, the *N.⊿U sliding energetic criterion* (*N* being the normal contact load) has been plotted for various loads in case of the D-SRB and TRB designs (**Fig. 5.6**), in comparison with the ACBB load case 1 and the FE8 CRTBs. For the TRB design, the *N.⊿U* remains quasi nil whatever the normal load since slippage is close to zero. However, for the D-SRB, when the load is sufficient, the *N.⊿U* criteria exceeds the threshold established based on the ACBB and FE8-CRTB tests. This is in agreement with the fact that SRB designs seem to be more WEC-sensitive than TRB designs (section 1.3.4.1).

Therefore, the *N.⊿U* criteria has also been plotted for other WEC-affected REB tests in **Fig. 5.7**. The criteria seems to be relatively consistent with WEC occurrences even though the WEC-free ACBB load case 3 exceeds the arbitrary threshold and that differences between all REB configurations seem limited, especially regarding the FE8-CRTB.

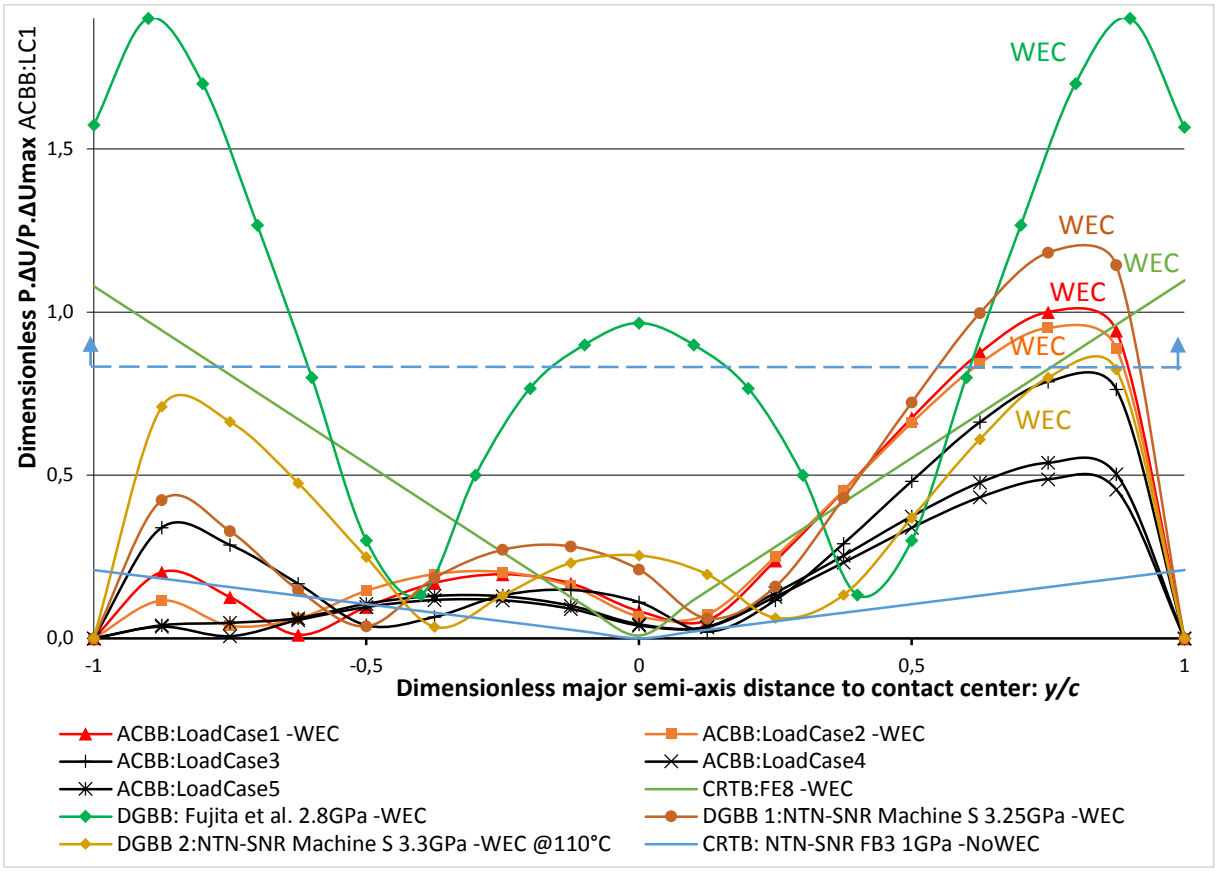

Fig. 5.5: Dimensionless sliding energetic criteria P.ΔU along the contact major axis for various REBs.

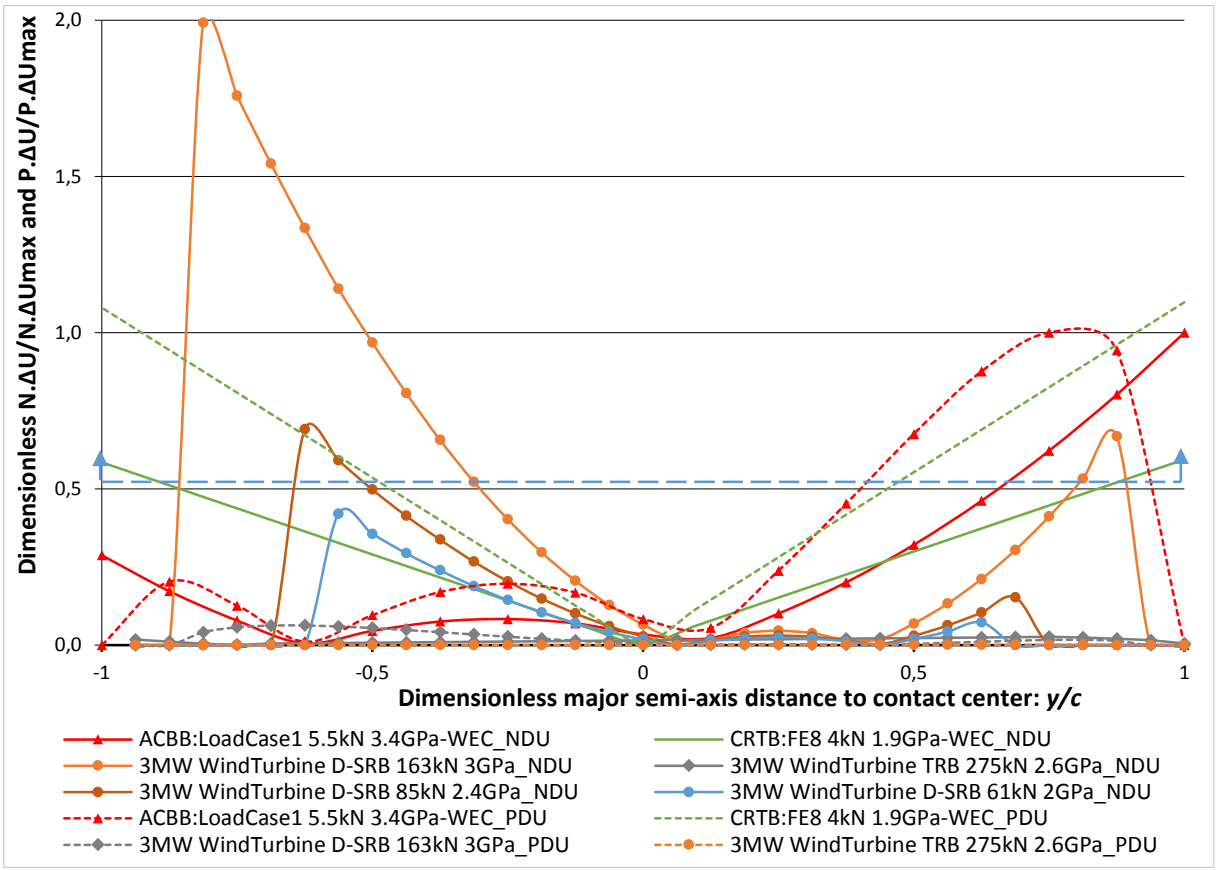

Fig. 5.6: Dimensionless sliding energetic criteria P.ΔU and N.ΔU for wind turbine D-SRB and TRB.

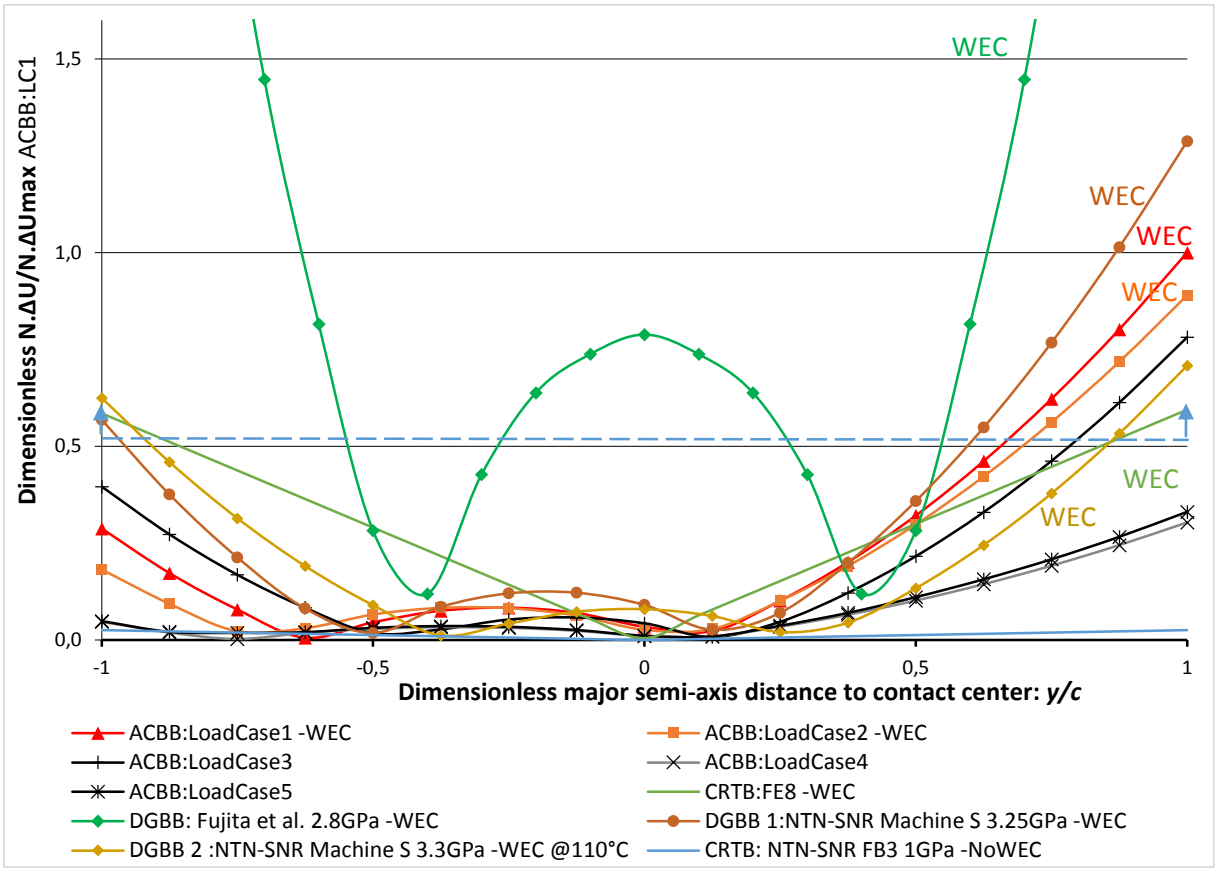

Fig. 5.7: Dimensionless sliding energetic criteria N.ΔU along the contact major axis for various REBs.

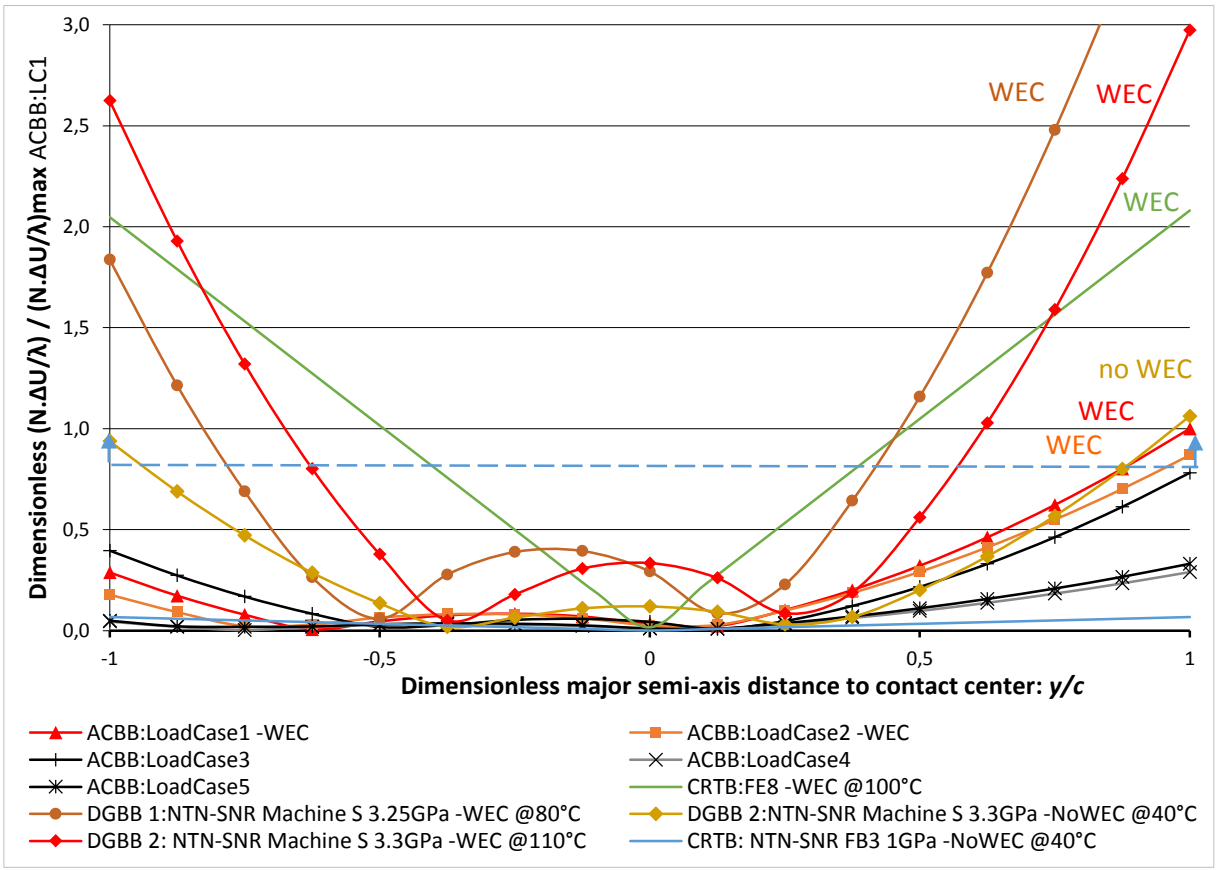

Fig. 5.8: Dimensionless sliding energetic criteria vs. the lubrication parameter N.ΔU/λ for various REBs.

Nevertheless, the $N.\measuredangle U$ criterion apparently underestimates the risk of WEC formation in case of FE8-CRTB tests presenting a high WEC reproducibility. This is most probably because it does not account for the temperature and lubrication regime that have, for instance, triggered WEC formation in case of NTN-SNR DGBB 2 (Appendix M), WEC-free at 40°C and WEC-affected at 110°C. Therefore, the following idea has been to consider the *sliding energetic criteria per film thickness available for shearing*. In consequence, the $N.\measuredangle U/\lambda$ *criterion* (λ being lubrication parameter) has been plotted along the contact major axis for the aforementioned REBs (**Fig. 5.8**). The results indeed show that the $N.\measuredangle U/\lambda$ *criterion arbitrary threshold* appear to be most effective in predicting WECs for most REB configurations. Considering this criterion, it is indeed not a surprise that no WEC has been reproduced on the NTN-SNR CRTBs. Yet, in case of the DGBB test on the Machine S at 40°C exceeding the arbitrary threshold, no WEC have been revealed, contrarily to the same test at 100°C. For those tests, it is supposed that the lubricant formulation could have a significant effect shifting the tribomechanical threshold.

It should be recalled that the kinematics computations fore-proposed do not take into account possible skewing and cage effects that could affect the local sliding velocities $\measuredangle U$ and the lubrication parameter λ. In addition, for sake of readability, the plots have been drawn with adimensioned contact abscissa. However, WEC probability most certainly does not solely depend on exceeding a given sliding energetic threshold. Indeed, the greater the *contact area potentially affected by this high energy dissipation,* the greater the WEC formation risk is supposed to be. For example, the concerned area is significantly larger in the FE8-CRTBs than in the ACBBs, which might explain the reproducibility difference. To support this statement, the previous plots have been re-plotted with scaled contact abscissa in Appendix G. They clearly demonstrate that *larger bearings present a higher WEC-probability*, in consistency with frequent WEC occurrences in wind turbine REBs (section 1.3.4).

To conclude, designing REBs considering the local $N.\measuredangle U/\lambda$ *criterion* and the effective contact area on which it exceeds a predetermined threshold seems to be an effective lead reducing the risk of WEC failure. Indeed, WECs do not seem to develop below a certain threshold of sliding energy per sheared film thickness. This apparent threshold may be explained by the fact sliding energy generates *local flash temperatures* that influence both mixed lubrication and tribochemical reactions at nascent surfaces. This is supported by the fact *high temperatures over 100°C* have often been required for WEC reproduction (FE8-CRTBs [79,192,198,202], DGBB tests of Fujita et al. [180], NTN-SNR DGBB 2 and others [176]), while WEC reproduction rate has been much lower when operating at lower temperatures, like for the NTN-SNR ACBBs.

Nevertheless, further testing has to be led in order to verify the representativeness of these sliding energy criteria as WEC drivers. For sure, surface sliding energy is not self-sufficient to explain WEC formation as WEC occurrences in the FE8-CRTB also require specific additives as tribochemical drivers…

WEC formation seems consistent with the *contact area* for which *sliding energy* exceeds a certain *threshold* but *further testing* has to be led to confirm this *non-self-sufficient tribomechanical driver*.

WEC formation seems to be favored by *significant bulk* and *flash temperatures* (>100°C) induced by surface sliding energy and lubricant shear.

5.1.2.2 Tribo-chemical influent drivers

a. Lubricant formulation and tribofilm affecting hydrogen permeation

By the end of the nineties, Tamada et al. [172,183] had anticipated that *lubricant formulation,* especially regarding corrosion inhibitors had a significant impact on WEC formation mechanisms. They observed that rust preventives keeping the raceway surface "clean", thus preventing deposits, accelerated WEC associated failures while rust preventives passivating the surface inhibited WEC formation [172]. This has further been confirmed by the fact WEC reproduction on the FE8-CRTBs was triggered by the relative concentration of CaS additives even if the sliding energy exceeded the fore-proposed threshold in all tests. As described in section 1.2.3.2, CaS additives are polar additives that act both as corrosion inhibitors and detergents preventing from deposits on the raceways. Several NTN-SNR tests seem to confirm the accelerating effect of CaS additives on WEC formation, notably the NTN-SNR DGBB-1 (Appendix M). As lubricant A used for the NTN-SNR ACBB tests contains no CaS additives, this may further explain why WEC reproducibility rate is somewhat lower on those tests than on the others. However, CaS additives cannot be self-sufficient to reproduce WECs, as all REBs in the field lubricated with those additives are far from being all WEC-affected.

The detrimental effect of excessive detergent concentrations on RCF had previously been pointed out in the literature without being associated to WECs [82,88–90]. It has indeed been observed that the presence of polar detergents and dispersants may tend to inhibit tribofilm formation, leaving heterogeneous spots of fresh metal surface [77], and thus favoring lubricant decomposition at nascent surfaces [184]. The presence of sulfur and/or phosphorus in the tribofilm actually weakens chemical deposits, contrarily to more homogenous oxide layers [82].

Therefore, it is clear that CaS and/or other powerful polar detergent additives are *significant WEC initiation drivers*. First, detergents enhance formation of nascent steel surfaces at the raceway to allow hydrogen permeation (section 4.3.1.1, **Fig. 4.18**). Second, CaS additives tend to form aggregates of relatively small size (~20-100 nm) so they can penetrate into incipient surface microcracks even quasi-undetectable by SEM analysis (**Fig. 3.13**)[64]. Finally, sulfonate additives also indirectly favor hydrogen absorption since they (1) act as hydrogen poison [224] and (2) are polar compounds that enhance oil hygroscopy. The multiple consequences of lubricant formulation has been summarized in Appendix K.

WEC formation is favored by *metal sulfonate additives* that tend to *inhibit tribofilm formation*.

Moreover, not only does tribofilm quality depend on the lubricant tribochemical reactions but it also relies on *tribomechanical thresholds* where incipient wear balances the formation of the chemical deposits. Consequently, tribofilm properties also greatly depend on the lubrication regime and on the nature of the contacting surfaces (grain boundaries, microdents, thermal stress, sliding energy, etc.)[83]. This has been confirmed by the alternative NTN-SNR ACBB tests with the different cage designs affecting local lubricant replenishment at the contact edges where WECs develop (section 4.1.2.2c). While WECs have been reproduced on all IR for the standard cage design, reproducibility rate has been lowered to 50% for the enhanced cage clearance and to zero for the latest cage design (Appendix G). SEM EDX analyses have revealed that no or only highly disparate tribofilm formed

for the standard cage design while heterogeneous and irregularly stripped tribofilm formed for the modified cage designs. If in the latest, WECs still occur at the contact edges where no tribofilm is detected, it is possible that some undetected traces of tribofilm act as local chemical barriers reducing the WEC reproducibility rate. Therefore, even though further testing has to be led to confirm those observations, it clearly confirms that the lubrication regime also affects WEC initiation mechanisms indirectly by influencing tribofilm formation.

This is further supported by the fact several chemically inert coatings such as Ni plating [174], tungsten WC/aC:H [111,192], and various black oxide surface treatments [111,165,166,192] have been mentioned to be beneficial in terms of WEC prevention as long as they do not wear off.

WEC formation is favored by disparate *tribofilm formation* counterbalanced by *incipient wear*.

b. Electrical potentials

Electrical currents have been observed to also trigger WEC formation in several studies [168,192,193]. In addition, electrical currents are indeed most probable in considerable WEC-affected applications such as in wind turbines [99] and automotive alternators [172], both subjected to high-frequency induced electrical currents. Insidious tribological e*lectrical potentials* may also occur due to magnetic shaft currents [98] and tribo-electrical-charging due to local friction of wind turbine blades in air and/or of lubricant molecules in filter cells [101], for example.

Once applied at the lubricant film bonds, electrical potentials are supposed to *favor hydrogen absorption into nascent steel surfaces* as demonstrated by hydrogen charging protocol based on an electrolytic bath as detailed in section 3.1.1. The detrimental effect of electrical currents going through the lubricant molecules has been demonstrated by Tamada et al [172]. DGBB tests reproducing WECs for several grease formulation have been observed to be specifically WEC-free when lubricated with a grease containing oxidized iron powder. This powder has been supposed to conduct directly the electrical current, inhibiting lubricant decomposition into hydrogen. Indeed, complex chemical reactions occur in electrically stressed oil films. Low lubricant electrical resistivity is going to enhance lubricant decomposition, while high lubricant resistivity is going to lead to charge accumulation, electrical discharges and local remelts [98].

This last point could partly explain why WECs often develop for highly additivated oils and why hydrogen permeation increases with oil hygroscopy. Indeed *additives, water content* and *high temperatures* all drastically reduce the lubricant resistivity [98], thus favoring insidious lubricant decomposition rather than brutal discharges. In case of higher lubricant resistivity, the risk of WEC formation may also be increased due to discharges and local remelts. These local melts act both as fresh metal surface and near-surface discontinuities, thus favoring both WEC initiation conjectures (section 4.3). It should be noticed that the overall contact dielectric properties depends on (1) the lubricant resistivity, (2) the electrical potentials and currents (which seem to have a significant influence on the bulk lubricant resistivity (**Fig. 2.12**)[98]), (3) the tribofilm or oxide layer formation and (4) the lubrication regime influencing potential metal to metal contacts (thus on the oil inlet *temperature*).

WEC formation, namely hydrogen generation, are favored in by *electrical potentials* and *currents*.

c. Water ingress

In the large majority of lubricants, water molecules are naturally present at least in incipient concentrations depending on the *lubricant formulation*. Polar blends, in particular (PAG, esters, *CaS detergents*, emulsifiers, etc.) are known to be highly hygroscopic, i.e. capable of ingressing significant amounts of water molecules (section 1.2.3.2) [97,211]. In application, water contents are enhanced by thermal-oxidation under high contact temperatures and pressures [211–213] and by external contamination as condensation, for example in wind turbines [97,211]. For a given lubricant formulation, the higher the *temperature*, the more water molecules tend to dissolve hygroscopically in the lubricant chemistry, up to a given saturation limit (**Table 2-6**).

In the past decades, *water contamination of the lubricant* has often been associated to accelerated RCF [109,195,206–211], even in case of incipient water concentrations as low as tens of ppm. More specifically, it has been demonstrated that water contamination increases the risk of *hydrogen permeation* into nascent steel [184]. Indeed, as previously detailed in section 4.3.2.1, hydrogen generation by cracking water molecules seems more commonly achieved than by decomposing lubricant molecules. In addition to favoring hydrogen generation, water contamination also leads to an increased risk of corrosion pits and tribofilm deterioration [109], both favoring fresh surface formation. Finally, water contamination of the lubricant does seem to be a significant WEC influent driver since out of the seven oils that have been associated to WEC failures at NTN-SNR, four contained over 500 wt.ppm of ingressed water (section 2.3.4.4). The fact that wind turbine oils are often capable of ingressing significant amounts of water (**Table 2-6**)[97,211] may therefore for partly explain why WECs appear to be so frequent in wind turbines.

WEC formation, especially *hydrogen generation*, seem to be significantly enhanced by *oil hygroscopy*.

d. Multiple effects of high temperature

As mentioned previously, *high temperatures over 100°C* have often been required for WEC reproduction. In that sense, it has been underlined that local flash temperatures can be generated in regions of high slippage. This locally affects many other *WEC influent tribochemical drivers*: lubricant film thickness and shear, additive chemical activation, the balance of tribofilm formation and wear, lubricant hygroscopy and dielectrical properties (**Fig. 5.3**). This most certainly explains why temperature can often be an on/off driver for WEC reproduction on the aforementioned test rigs.

The temperature affecting various *tribochemical drivers* appears to be an on/off driver for WECs.

e. Conclusion on WEC tribological influent drivers

Each focus on main tribomechanical and tribochemical WEC influent drivers affecting nascent surface formation and/or hydrogen generation *strongly support the WEC root cause analysis*. At tribo-scales, they indeed pinpoint high slippage energy, lubrication regimes, material stress state and cleanliness, lubricant formulation, water content, electricity, temperature etc. (**Fig. 5.2**). *Various combinations* of them may lead to WEC formation mechanisms since similar tribo-consequences may be induced by various drivers. Depending on the application or test rig, the degree of influence of each tribological driver may be more or less consequent. Therefore, driver interdependencies make *verification of individual drivers* and *WEC reproduction* extremely delicate on full REB test rigs.

5.2 Tribological transposition on the twin-disc machine

In order to test the various identified WEC drivers individually with an enhanced control of the contact parameters, the main tribological conditions reproducing WECs on the ACBBs and CRTBs detailed in **Chapter 4**, have been transposed on the *LaMCoS Twin-Disc Machine (TDM)*. More than 60 tests have been performed resulting in a total of more than 7500 hours of RCF testing in various configurations detailed in Appendix H. The main objective has been to master WEC reproduction on non-hydrogen precharged specimens in order to better qualify the influence of WEC influent driver individually. This would enable to first, to verify WEC initiation and propagation conjectures as exposed in **section 4.3** and second, to establish a test protocol to help design efficient and durable WEC countermeasures. In this section, the experimental approach of the *tribological transposition* will first be described. Then focus will successively be made on tests led to study *WEC initiation* and *WEC propagation* mechanisms.

5.2.1 Experimental approach

To achieve WEC reproduction on the TDM (**Fig. 2.6**), the basic scope was first to transpose tribological parameters identified in the NTN-SNR ACBBs (sections 2.2 and 4.1.2) before testing additional tribochemical drivers (section 5.1). The process may seem simple but in general, tribological transpositions on RCF simulators actually require huge amounts of *compromises* and *simplifications hypotheses*. For example, should the overall or only local WEC-related contact parameters be simulated? Considering the latest, huge amounts of test configurations could be considered to best represent that or that tribological parameter: contact stresses, linear speed, contact time ratios, SRR, driver or follower, temperature, lubricant, roughness, lubrication regime, tribofilm formation, number of cycles, etc. The comparison between the ACBB tribological parameters and the TDM ranges has been wrapped up in **Table 5-1**, underlining that the TDM has been designed to pinpoint specific tribological parameters within a predetermined constant range. Therefore, the TDM cannot simulate spinning, entry-exit of load zone, cage effects, and all other transient effects specific to operating REBs.

Consequently, the *experimental approach* of this study has naturally been to test WEC drivers *incrementally* trying, first, to reproduce *WEC initiation* through the opening of surface microcracks and then, to *propagate these microcracks into WEC-like features* with the help of consistent tribochemical drivers (**Fig. 5.9**). A *typical reference configuration* has been established considering the main ACBB tribological parameters: same lubricant A, same steel batch, similar contact pressure, similar velocities and SRR, and similar contact time ratio (**Table 5-1**). Then tribomechanical and tribochemical drivers have been tested progressively trying to reproduce WEC initiation and/or propagation mechanisms.

First, dents and lubricant starvation protocols have been employed to ease microcrack pre-initiation. Measurements of *surface* residual stresses of typical cylindrical TDM roller raceways, prior to RCF testing, have revealed that they were less compressive than that of ACBB IRs (Appendix E). This should thus favor surface microcrack initiation. Then high SRR and *sliding energy,* combined or not with tribochemical drivers like water contamination, electrical currents and/or structural stresses, have been additionally transposed to help the surface microcracks propagate (**Fig. 5.9**).

Table 5-1: Comparison chart of typical tribological parameters between the ACBB and the TDM tests (TDM ranges are specified excluding specific tests, details in Appendix H).

Data	ACBB	TDM range
Contact type	Elliptical (k=10.8)	Circular or elliptical (k=4.7)
Thrust load (kN)	Load cases 1, 2, 3, 4, 5	0
Radial load (kN)		1000 - 7000 N
Maximum contact stress (MPa)	3400 for load cases 1*, 2*	3500
Fitting hoop stress (MPa)	$90<\sigma_{hoop}<220$	0 or 90
Rotational speed (rpm)	2250	1500 or 3000
Time ratio $^{Inter\text{-}contact}/_{Intra\text{-}contact}$	~570[1]	~440 at 3000 rpm
Linear speed (m/s)	2.4	5.5 or 11
Maximum SRR (%)	20[2]	0, 7, 14, 22, 30, 43 or 63 Driver or follower
Test duration (hrs)	424 - 1436	~10 - 440
Number of cycles x10^6	35 - 120	~0.5 - 45
Hardness (Hv10) Ring/RE	800	800
Lubricant supply (L/min)	0.5	0.13 - 2
Lubricant	Oil A	Oils A, B, C, D
Known additives	Without	With and without CaS
Oil temperature	ambient	50, 80 or 110°C
R_q (µm)	IR ~0.06 RE ~0.02	Commonly ~0.025 Exceptionally ~0.15
λ ratio	4.2	Commonly >10[3] Exceptionally ~2
Steel	Same 100Cr6 batch	Same 100Cr6 batch
Fretting-corrosion	IR bore	Nil
Water content (ppm)	50	20 - 500 (function of oil)
Electrical current (mA)	Unverified	0.5, 10, 50, 100 or 200
Dents	No	Possible
P.ΔU (Pa.m/s)[4]	$7.5x10^8$	Appendix H
P.ΔU/λ (Pa.m/s)[4]	$1.8x10^8$	
N.ΔU (N.m/s)[4]	$2.9x10^3$	
N.ΔU/λ (N.m/s)[4]	$7.0x10^2$	

[1] *Considering 3 balls loaded as in load case 1and the maximum time between the exit and re-entry of load zone*
[2] *Neglecting all transient effects of cage entry-exit of load zone*
[3] *Lubrication parameter unavailable for TDM09 tests under lubricant starvation*
[4] *Maximum value along the contact major axis for the most loaded ball/IR contact in load case 1 (cf. section 5.1.2.1c)*

REB *tribological transposition* to the TDM inherently requires *consequent simplification hypotheses*.

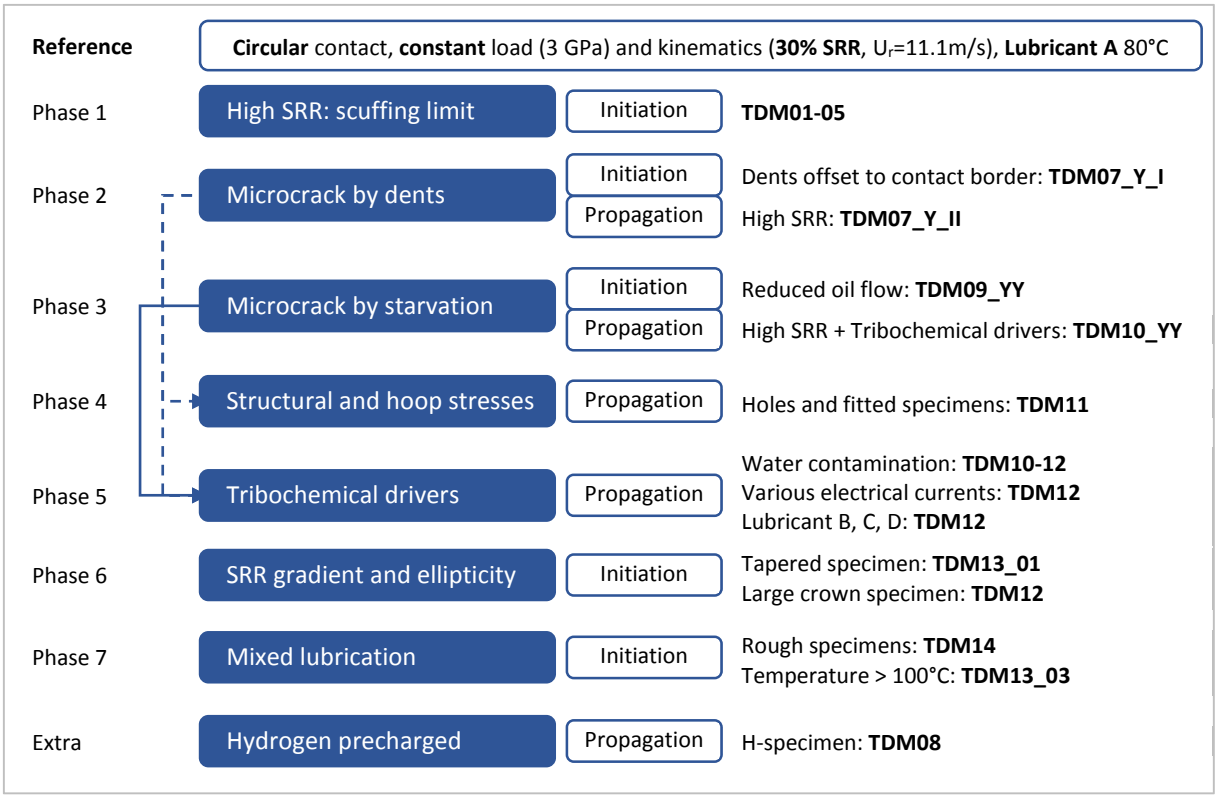

Fig. 5.9: General approach of WEC initiation and propagation on the TDM (details in Appendix H).

As the lubrication parameter and the various surface sliding energy criteria appear to be highly influent WEC drivers, they have been considered in defining the TDM tests in order to be consistent with thresholds identified for WEC failures in REBs (section 5.1.2.1c) (Appendix H). In comparison, the maximum respective values of the criteria have been indicated at the bottom of **Table 5-1** for the WEC-affected NTN-SNR ACBB load case 1 most loaded ball/IR contact (*N.B. these thresholds should not be taken for granted, further testing being required*). For the large majority of TDM tests with a significant SRR, the $P.\sqcup U$ based criteria exceeds the ACBB maximum (sometimes so much that a smearing limit has been established). Nevertheless, some TDM tests present an unsufficient $N.\sqcup U/\lambda$, especially in case of 17.5 mm crowned specimens for which the normal load N is limited in order to maintain reasonable Hertzian pressures. This is also enhanced by the fact most TDM tests have been conducted under high λ due to superfinishing to very low roughnesses.

After each TDM tests, *surface analyses* have first been led to seek for microcracks and to qualify tribofilm formation and wear rates based to protocols presented in section 2.4.1. Then, axial and circumferential *cross section LOM* and *fractographs* have been performed in various areas to reveal subsurface crack propagation, hopefully into WEC-like features (section 2.4.2).

5.2.2 WEC initiation through micro-cracks

It has been observed that Reference and **Phase 1** TDM test conditions were unsufficient to reproduce nor WECs nor surface axial microcracks as those observed at the ACBB contact edges connecting WECs to the raceway. Therefore, TDM tests have been designed to pre-open surface microcracks to increase the probability of lubricant penetration and decomposition into those microcrack as conjectured in section 4.3.1.2, based on (1) dents acting as surface stress raisers

(Phase 2), (2) reduced lubrication enhancing surface tensile stresses (Phase 3), and (3) lubrication with highly additivated oils (part of Phase 5).

5.2.2.1 Dents

TDM tests have been led with artificial dents on one of the specimens so that the slope and shoulders act as stress raisers accelerating *surface crack nucleation* on the counter specimen in less than a couple million cycles. It corresponds to a TDM test protocol developed at the LaMCoS to study surface initiated RCF and discriminate materials or lubricant (section 2.3.4.1)[55,56,90]. Even though dents have not been observed on unspalled WEC-affected ACBB raceways, they remain possible in wind turbine REBs as the filters are intentionally bypassed by thousands of liters during cold starts.

In **Phase 2**, to be more representative of WEC observations in the ACBB and to avoid compressive residual stress buildup below surface microcracks, the microcracks have first been *initiated at the predicted contact border* of the subsequent propagation test. This has been achieved either by offsetting the specimen with aligned dents on its circumference (TDM07), or by regularly spacing the dents in the transverse direction to rolling motion in case of 200 mm crowned specimens (TDM12_04, _06, _07) (**Fig. 2.10** (a)). In each case, microcracks initiate mainly on the follower counter surface in agreement with previous results [25,54–56,94] (**Fig. 2.9** (c)). Once microcracks have been pre-initiated, propagation attempts have performed for over 20 million cycles, under a significant $P.\Delta U$ criterion (**Fig. 5.10**) and eventually adding hoop stresses and/or tribochemical drivers (**Fig. 5.11**). Neither WECs nor consequent enough WEC-like branching subsurface crack networks have been revealed by cross sections despite numerous surface cracks. It should however be noticed that some cracks have propagated despite their location on the *driver* (**Fig. 5.10** and **Fig. 5.11**).

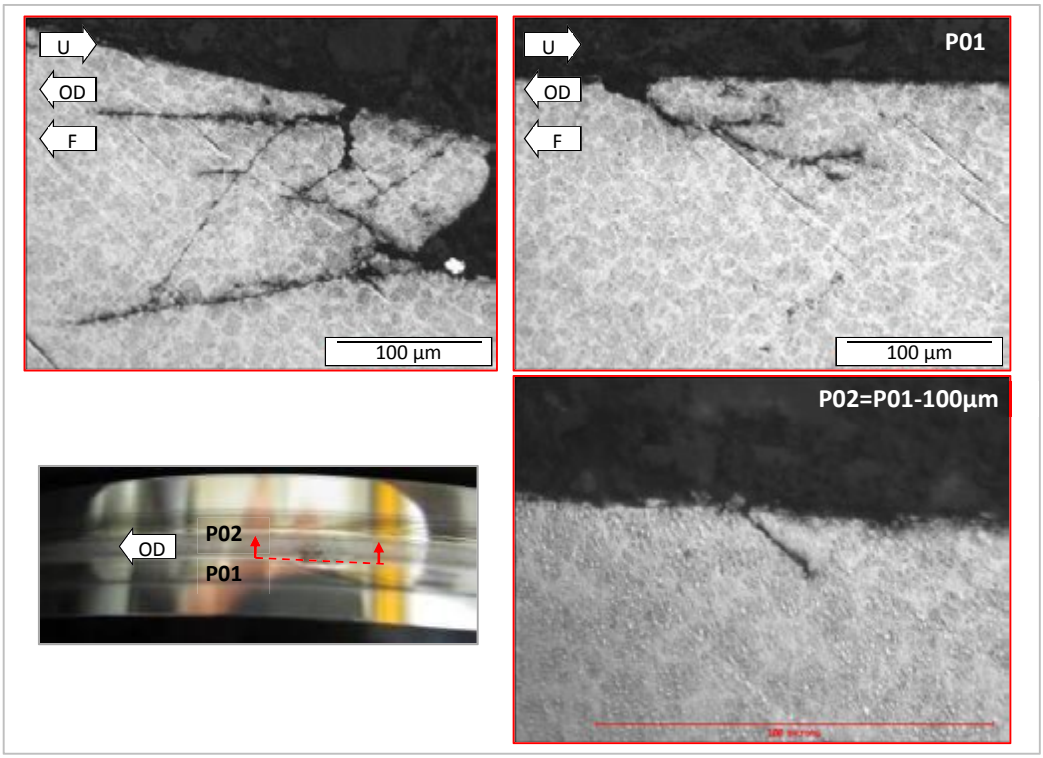

Fig. 5.10: TDM07_01_II cylindrical roller circumferential LOM (propagation phase, 3.0x10^7 cycles, 3.4 GPa, 30% SRR, driver, subsequent to microcrack pre-initiation with a dented counter-roller).

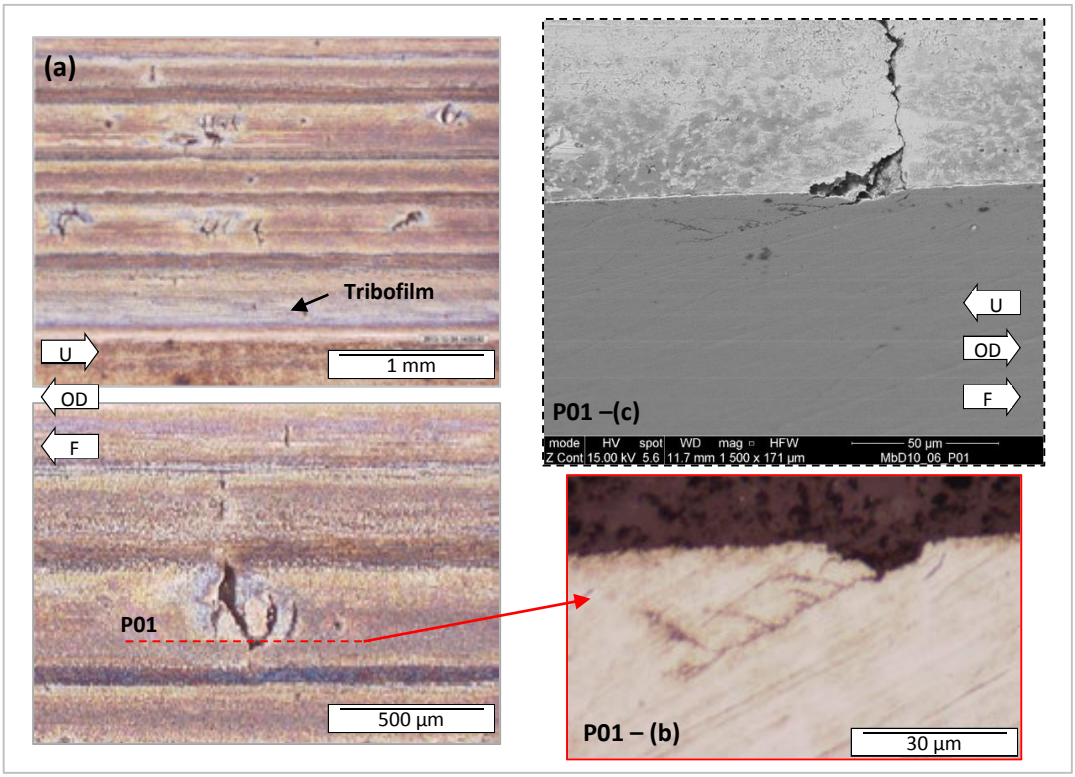

Fig. 5.11: TDM10_06 crowned roller typical raceway topview (a), circumferential LOM (b) and SEM ¾ view of the circumferential cross section and raceway microcrack revealing some crack ramifications opposite to OD without adjacent WEA (propagation phase, 2.9x10^7 cycles, 3 GPa, 30% SRR, driver, 85°C water contamination, and regular EDTA cleaning of the tribofilm, subsequent to microcrack pre-initiation with a dented counter-roller).

Surface cracks have been initiated by using *artificial dents* but have not propagated into WECs.

5.2.2.2 Mixed lubrication

Phase 2 various analyses have led to suppose that tribofilm formation detected throughout the raceway (**Fig. 2.17**) may seal microcracks and prevent lubricant from reaching nascent crack flanks thus inhibiting tribochemical crack propagation. In order to (1) be more representative of the possible local mixed lubrication at the ACBB IR contact edges, believed to significantly enhance near-surface microcrack opening (section 4.3.1.2), and (2) to limit tribofilm formation, specific TDM tests have been performed in **Phase 3**. The oil flow has been reduced to a *minimum threshold of 0.13 L/min* using the experimental procedure described in section 2.3.4.2. In order to favor lubricant starvation still maintaining an overall flow rate sufficient to cool the rollers, the rotational speeds have been inversed (negative values in Appendix H) to be opposite to the oil jet. To be noticed, the λ ratio given in Appendix H is not representative in case of TDM09_YY tests as it does not account for lubricant starvation.

Below the experimentally established threshold of 0.13 L/min, smearing risk is too important for the *given tribological conditions*: 2 GPa, 7 % SRR and lubricant A at 50°C in the jet. These conditions have been chosen to maximize surface tensile stresses while minimizing smearing risk. They have been validated by the results of TDM09_04 where *numerous surface microcracks* have been opened at the contact center despite low contact stresses (**Fig. 5.12**). Microcracks have mainly developed

where no tribofilm remains and where incipient wear occurs. The latest is confirmed by SENSOFAR profile assessments and by the fact no grinding marks remain visible (**Fig. 5.12**). Subsequent identical tests have been conducted to pre-initiate surface microcracks for further propagation investigation, and have confirmed the results of TDM09_04. While adjusting the flow rate on TDM09_08, it has been observed that these surface microcracks open in less than a million cycles. The numerous microcracks may be associated to brittle surface "peeling" suggesting some tribochemical embrittlement occurs but no comparable result has been found in the literature. Nevertheless, despite consequent width, the surface microcracks initiated under mixed lubrication appear excessively thin and shallow on well targeted SEM analyses (**Fig. 5.12** (b-c)).

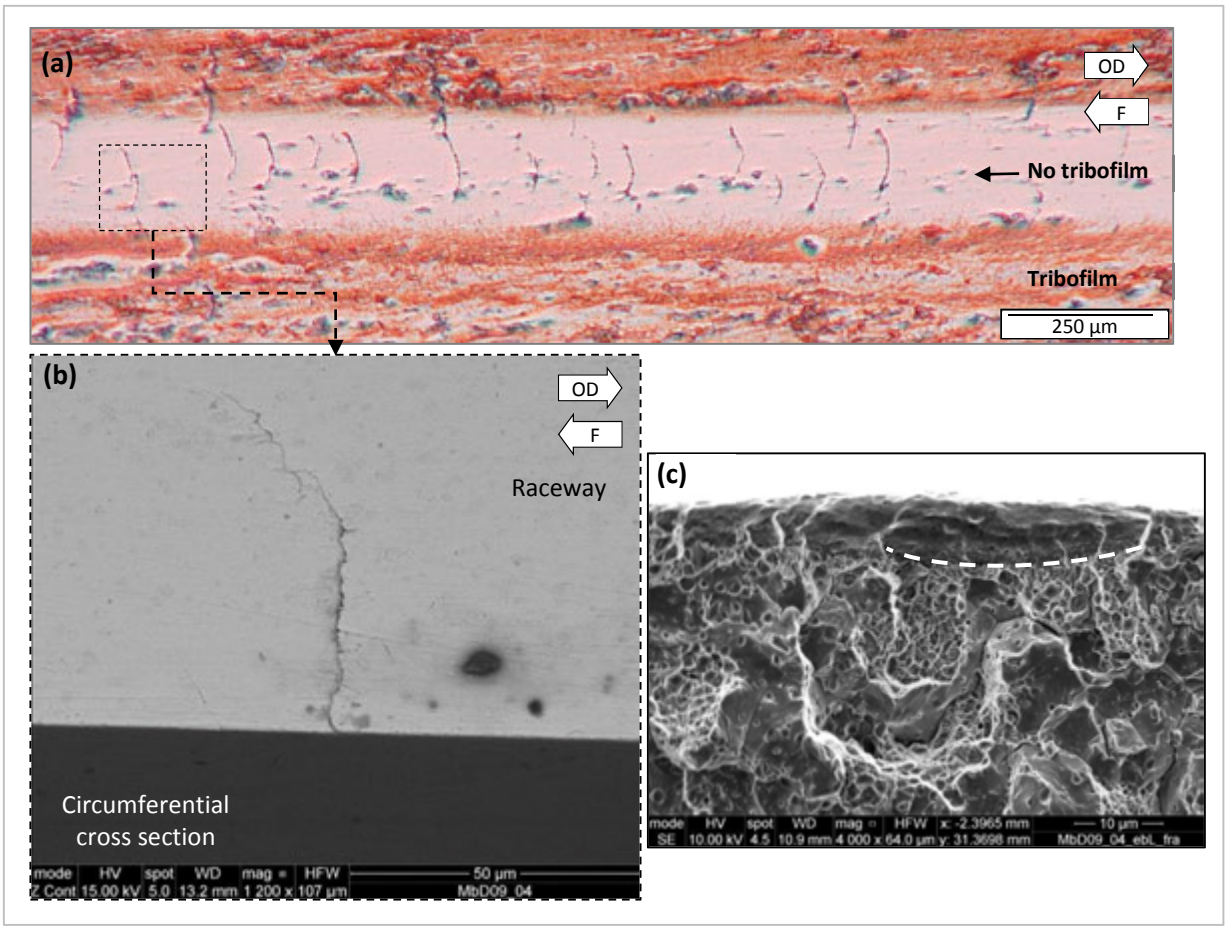

Fig. 5.12: TDM09_04 crowned roller typical raceway center topview (a), SEM ¾ view of a circumferential cross section (b), and SEM analysis of a raceway fractographs opening a shallow surface microcrack (initiation phase; $1.9x10^7$ cycles, 2 GPa, 7% SRR, follower, lubricant A at 50°C).

Incipient surface microcracks initiate on TDM rollers under *moderate stresses* and *starved lubrication.*

5.2.2.3 Highly additivated and sheared lubrication

Finally, considering the possibility of *hydrogen permeation directly at the raceway* via the formation of nascent surface (section 4.3.1.1), part of **Phase 5** tests have been performed using lubricants containing detergents without any surface microcrack pre-initiation prior to testing. The tests were performed using *lubricant B* containing important amounts of calcium and sulfur, among others elements (section 2.3.3, **Table 2-5**). The tests here considered (TDM13_YY) have been conducted

close to the reference configuration (3 GPa, 30% SRR, 85°C (once 110°C)) but with additional drivers as a slight water contamination (~100 ppm) and an insidious 50 Hz electrical current of 50 mA. Despite the "conventional" contact stresses, the absence of dents and the fully flooded lubrication, consequent *surface microcracks* have formed on the follower roller, while irregular and patchy tribofilm has developed on the driver (**Fig. 5.13**). These cracks mainly develop at the contact edges, most probably due to significant tribofilm formation at the contact center. Similar tribological conditions have been tested for *lubricant A* and because slight water contamination and moderate electrical current have also been tested with *lubricant A* (TDM12_01, _02, _03) without opening surface microcracks when no dents or reduced lubrication were employed. Therefore it is supposed that in TDM13_YY tests, the microcracks are due to surface *tribochemical embrittlement* associated to *lubricant B*. Nevertheless, high $P.\angle U$ appears to also be required to "activate" the tribochemical embrittlement since *lubricant B* was unsufficient to generate surface microcracks on the similar TDM12_07 test despite the presence of hoop stresses.

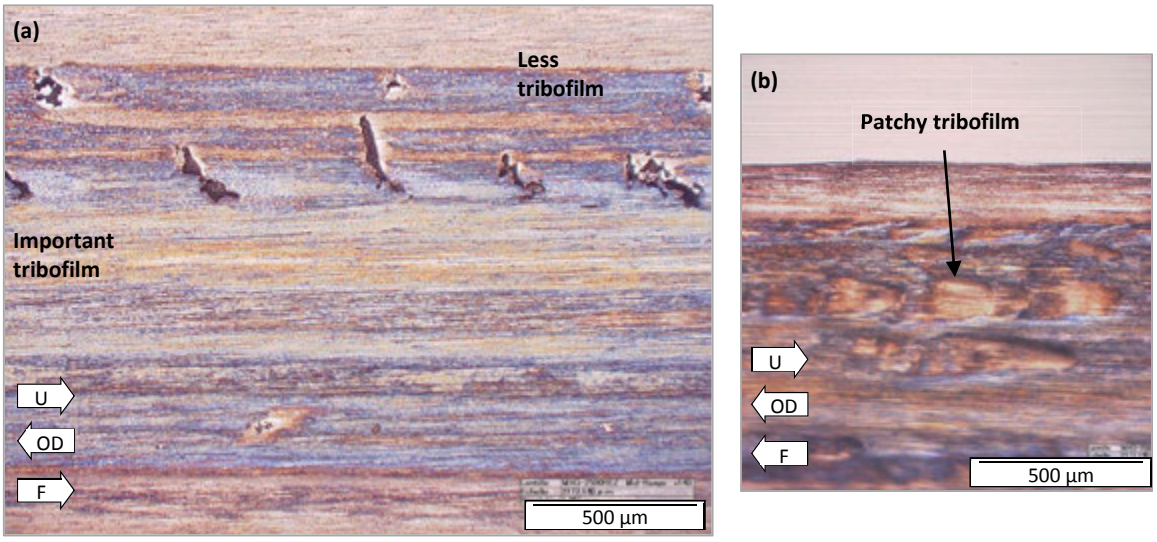

Fig. 5.13: Typical TDM13_02 raceway topview of (a) cylindrical follower roller and (b) crowned driver roller (2.5x 10^7 cycles, 3 GPa, 30% SRR, lubricant B at 85°C, water contamination and 50mA).

Incipient surface microcracks initiate on follower rollers under *highly additivated* and *sheared lubrication*.

5.2.3 WEC propagation attempts with various drivers

The TDM procedures performed in **Phase 2, 3** and **5** have allowed the formation surface microcracks in less than 5 million cycles despite moderate contact pressures. Nevertheless, when prolonging some of these tests beyond 40 million cycles, subsequent fractographs and cross sections have never revealed any WEC-like propagation. In consequence, it may be supposed that even if microcracks are initiated, either the lubricant did not reach the nascent crack flanks, either the tribological conditions were not favorable for lubricant and/or water tribochemical decomposition leading to local hydrogen embrittlement at crack tips (section 4.3.3). Therefore, the other TDM Phases have been designed to test the different WEC influent drivers to help propagate the surface microcracks (section 5.1).

5.2.3.1 Inclusion orientation

Specific rollers have been manufactured horizontally in the steel rod in order to obtain stringer MnS type A inclusions emerging with a continuously varying angle versus the TDM roller raceway. Hence, in those specimens, vertical inclusions emerge at raceway in the two opposite circumferential positions corresponding to the rod principal direction (**Fig. 2.8** (e)). It is supposed that emerging vertical inclusions could enhance surface microcrack propagation towards the subsurface shear stress zone by prolonging the discontinuity [27,29]. The analyses of TDM12_01, _06, _07 reveal that no significant difference has been observed and that no WEC-like propagation has been achieved despite the presence of long and vertical emerging MnS (**Fig. 1.4** (b)). In consequence emerging, and most probably inclusions in general, *do not seem sufficient to explain WEC*.

5.2.3.2 Structural stresses

Additionally, specific rollers have been manufactured to superpose tensile structural stresses to contact stresses near the raceway to help initiate and propagate surface microcracks. The first design was manufactured to artificially introduce ~90 MPa of hoop stresses (TDM06 and TDM12_06, _07) (**Fig. 2.8** (d)). The other design was modified by drilling various holes to introduce partially tensile stresses right ahead and after the "bending bridge" when this section is in the contact (TDM11_00, _01) (**Fig. 2.8** (c)). Apart from TDM11_00, the analyses of these tests have not revealed any significant propagation whatsoever despite the fact in case of TDM12_06, _07, additional WEC drivers have been combined. The superposition of contact and structural stresses are thus *not sufficient to explain WEC*.

In case of TDM11_00, premature failure occurred due to structural fatigue apparently initiated on a machining defect inside one of the largest holes (**Fig. 5.14**). It should however be mentioned that adjacent WEA has been formed similarly to **Fig. 4.20** and WEC layouts, probably due to severe crack flanks rubbing. Indeed, WEA formation cannot be attributed to tribochemical drivers as no additives were present in this test, which was exceptionally lubricated with pure PAO8.

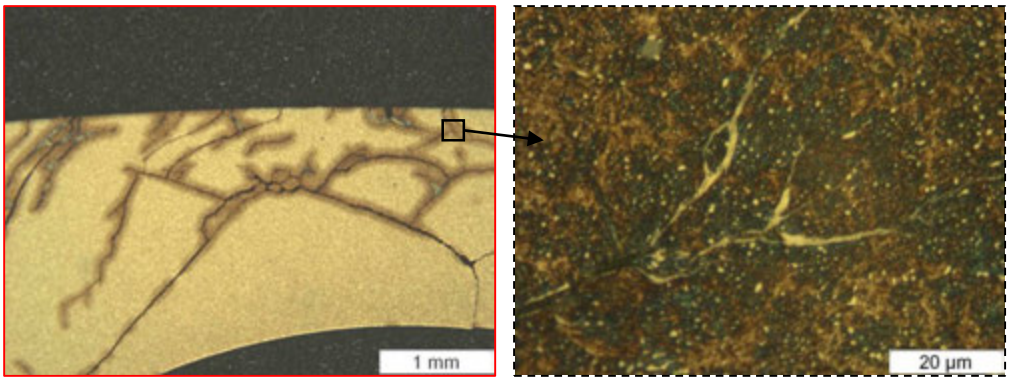

Fig. 5.14: Circumferential LOM of TDM11_00 cylindrical roller with holes inducing additional structural stresses (3.5 GPa, 7% SRR, driver, lubricant PAO8 at 80°C)
(cracks are emphasized due to etchant trap in their vicinity).

5.2.3.3 Hygroscopy

One main hypothesis in explaining why surface microcracks pre-initiated do not propagate has been that the tribological conditions transposed on the TDM are not sufficient to tribochemically decompose lubricant into hydrogen, neither at the surface, nor inside microcracks. As water

contamination has often been associated to WEC-associated failures (section 5.1.2.2c) and water molecules are thought to ease hydrogen generation, various TDM propagation tests have been conducted using *water contaminated lubricants A, B* and *D*. Water contamination has been achieved without mechanical emulsion, in order to avoid the presence of micro-bubbles, which would significantly affect the rheological properties of the lubricant (section 2.3.4.4).

During the **Phase 5** propagation tests (Appendix H), 350 mL was periodically taken from the oil bath and artificially water contaminated by applying the protocol 2.3.4.4 during 2 hours at 98°C so that contamination would be close to saturation level. Oil samples have been made for several tests 1 hour after having added the 350 mL of water contaminated oil. Karl Fisher analysis have been led to quantify the effective water concentration in the oil bath. The mean results are: ~100 wt.ppm for oil A, ~300 wt.ppm for oil B and ~600 wt.ppm for wind turbine oil D. Nevertheless, the analyses of these tests have not revealed any significant propagation whatsoever apart from TDM10_06 (**Fig. 5.11**), so that water contamination *does not seem to be sufficient to explain WEC*.

5.2.3.4 Electrical current

As aforementioned, the pre-initiated surface microcracks have been supposed not to propagate due to the lack of hydrogen generation, even when the lubricant was artificially water contaminated. Yet, electrical currents have also been associated to WEC reproduction on several test rigs from the literature (section 5.1.2.2b) and most certainly trigger electrolytic tribochemical reactions that would decompose water molecules. Therefore the majority of **Phase 5** TDM TDM12_YY and TDM13_YY tests have been performed with an imposed *50Hz electrical current I_e going through the contact* thanks to the protocol defined in section 2.3.4.3 (from 0.5 mA to 200 mA), in order to trigger local hydrogen permeation.

Since TDM12_01 combining I_e=10 mA with water contamination and vertical inclusions, reproduced neither surface nor subsurface cracks after ~40 million cycles, TDM12_02 has then been performed under similar conditions but adding artificial dents and increasing I_e to 200 mA. Surface analyses have revealed strange surface deposit patterns transverse to rolling motion on the crowned roller connected to the positive pole (**Fig. 2.15**). It has been supposed that these artefacts were due to excessive electrical current inducing regular discharges and local remelts. In consequence all further tests of **Phase 5** have been performed at lower currents I_e=50 mA, for which those patterns do not occur even though the current is still sufficient to drastically reduce the contact resistivity (**Fig. 2.12**). Nevertheless, even when combined with various WEC influent drivers such as water contamination and/or additives, no subsurface crack propagation have been observed whatsoever so that electrical currents *do not seem to be sufficient to explain WEC*.

5.2.3.5 Fully formulated WEC related lubricants

The large majority of TDM tests have been performed with lubricant A that had allowed WEC reproduction on the NTN-SNR ACBB tests. As no WEC-like crack propagation has been achieved despite numerous WEC influent drivers and significant amounts of cycles, it has been supposed that the lubricant formulation was not best suited for WEC reproduction on the TDM. Indeed, contrarily to the FE8-CRTB tests, lubricant A was not highly additivated and, in particular, did contain any *metal sulfonate corrosion inhibitor or detergent*. Without detergent inhibiting chemical deposits on the raceway, it is believed that tribofilm formation may tend to seal pre-initiated microcracks and that no hydrogen poisons may be available to favor hydrogen absorption.

In consequence, additional **Phase 5** TDM tests (TDM12_YY and TDM13_YY) have been conducted using fully formulated lubricant B with large amounts of Ca and S, which had been previously associated to WEC on an NTN-SNR test. Also, a wind turbine oil, lubricant D that had been associated to premature failures on the field, has been tested. However, the latest tests were led to a smaller extent as the high viscosity of lubricant D induced too thick lubricant films. Anyhow, those fully formulated and highly additivated oils have *not been sufficient to reproduce WEC* on the TDM, supposedly because the tribofilm formation/wear balance did not generate sufficient nascent surfaces. This could be due to full film lubrication, the lack of transient speeds to wear off tribofilms, and efficient EP/AW additives also present providing an efficient surface protection.

5.2.3.6 Specific additive formulation

In order to better qualify, the influence of specific additives, namely CaS detergents, on RCF surface initiated crack propagation, specific TDM tests have been conducted using *PAO8 base oil with various in-house additive blends*. Those tests have been performed with crowned counter-rollers with 4 artificial dents aligned and centered in order to initiate surface microcracks and allow lubricant penetration (section 2.3.4.1). The standard tribological conditions employed at the LaMCoS were used: standard 100Cr6 rollers, 3.5 GPa, 7% SRR, U_r=11.1m/s, 80°C and none of the aforementioned WEC influent driver. Part of the test results are summarized in **Table 5-2**. For privacy issues, the respective concentrations may not be specified in this manuscript.

Table 5-2: Results of TDM tests performed with specific in-house additive blends in PAO8 based oil.

Oil*	Blend oil	EP/AW	Detergent (Mg.S)	Detergent (Ca.S)	Cycles (x10^6)	Branching cracks
PAO8	0	0	0	0	>20	?
PAO8_1	+	+	+	0	11.0	+
PAO8_2	+	+	0	+	5.1	+
PAO8_3	+	+	+	+	6.4	+

* *In the blends here specified: no dispersant, no rust inhibitors, no foam inhibitors, etc.*
\+ *stands of present*

These tests results fully support the fact that additives, especially *CaS detergents* drastically reduce RCF life in agreement with [82,88–90]. Cross sections of the spalled cylindrical follower rollers have been performed and respective LOMs are illustrated in **Fig. 5.15**. They reveal much deeper and heavily branch crack networks than those observed for previous TDM tests, thus much more WEC-like. The crack networks all present a top-down growth in the direction of OD. A close-up on PAO8_3 LOM at the depth of maximum shear stress reveal a conventional RCF butterfly initiated at an inclusion in the vicinity of the macroscopic crack network, which does not appear to interact the main crack (**Fig. 5.15**). Moreover, it seems that PAO8_2 and _3 LOMs, display the deepest and most ramified crack networks even though they have cycled two times less than PAO8_1. This suggests that CaS detergents do enhance brittle tribochemical cracking beyond the contact stresses, typical of WECs (**Fig. 5.15**).

Nevertheless SEM analysis of the cracks reveal much wider cracks (>5 µm) than those of WEC and no adjacent WEA has been observed. It is therefore supposed that (1) the cracks mainly propagate by oil seepage combined with somewhat of a *tribochemical embrittlement similar or identical to HEDE associated to the presence of detergents* (section 3.3.1) and that (2) cycling was unsufficient de generate WEA by crack flanks rubbing. Hence, if tribochemical HEDE cracking has apparently

been reproduced, the cracks networks do not exactly correspond to the definition of WECs proposed in section 1.4.1.

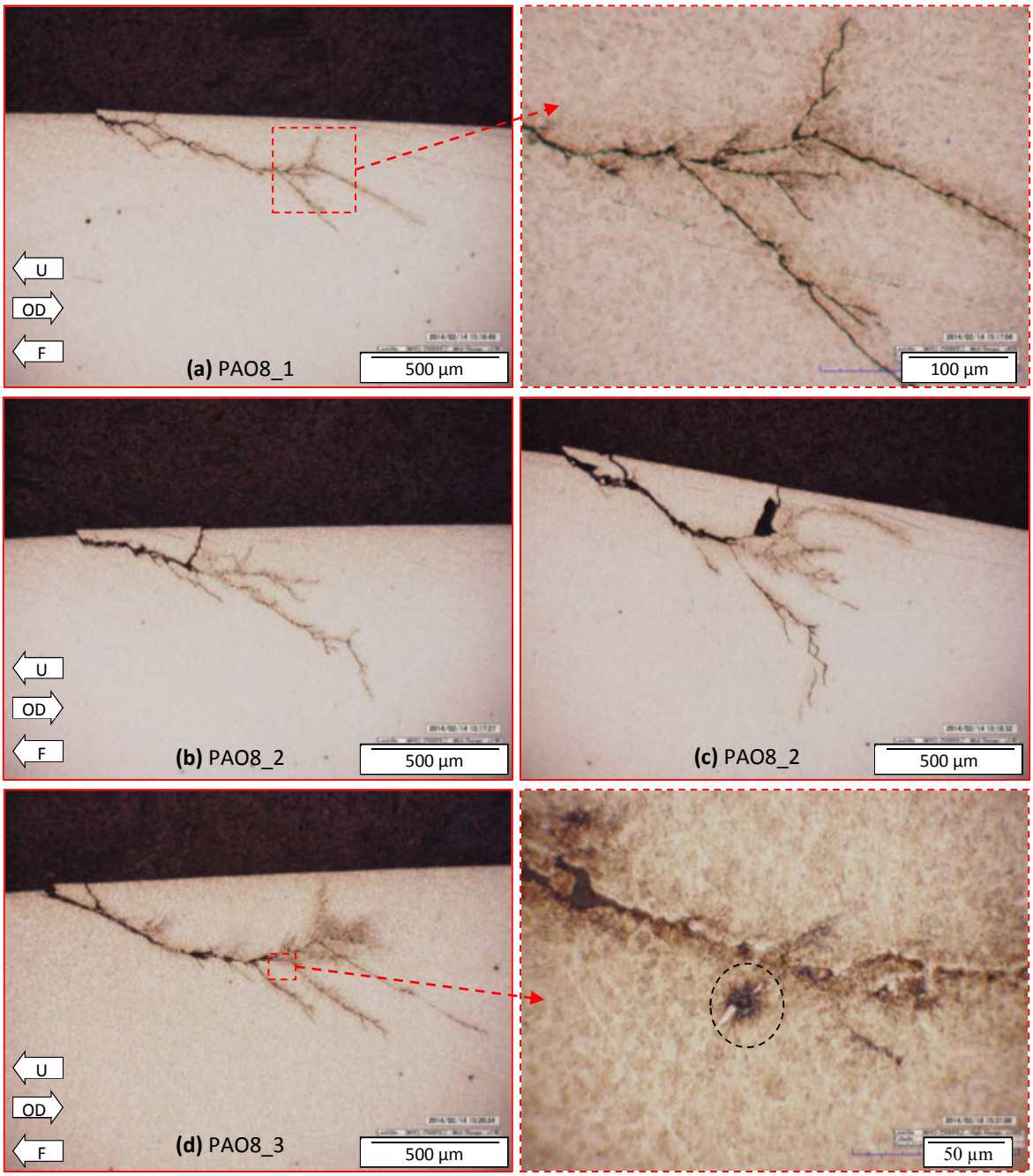

Fig. 5.15: Typical circumferential LOMs of TDM cylindrical follower raceway after RCF testing with various additive blends (**Table 5-2**) targeted to intersect with visible surface cracks.

In order to better understand the tribochemical behavior of the different additive blends on the raceways, SEM-EDX analyses have been performed on the failed cylindrical follower roller (**Fig. 5.16**). It has been first observed that the chemical content is perfectly consistent with the respective additive chemical elements. Then, in case of PAO8_2 and _3 containing CaS detergents, the tribofilm *appears less consequent and with spots of nascent surface* at the raceway center. This observation fully supports the fact that these additives may be most influential on WEC formation mechanisms by favoring nascent surface formation and hydrogen permeation (section 5.1.2.2a).

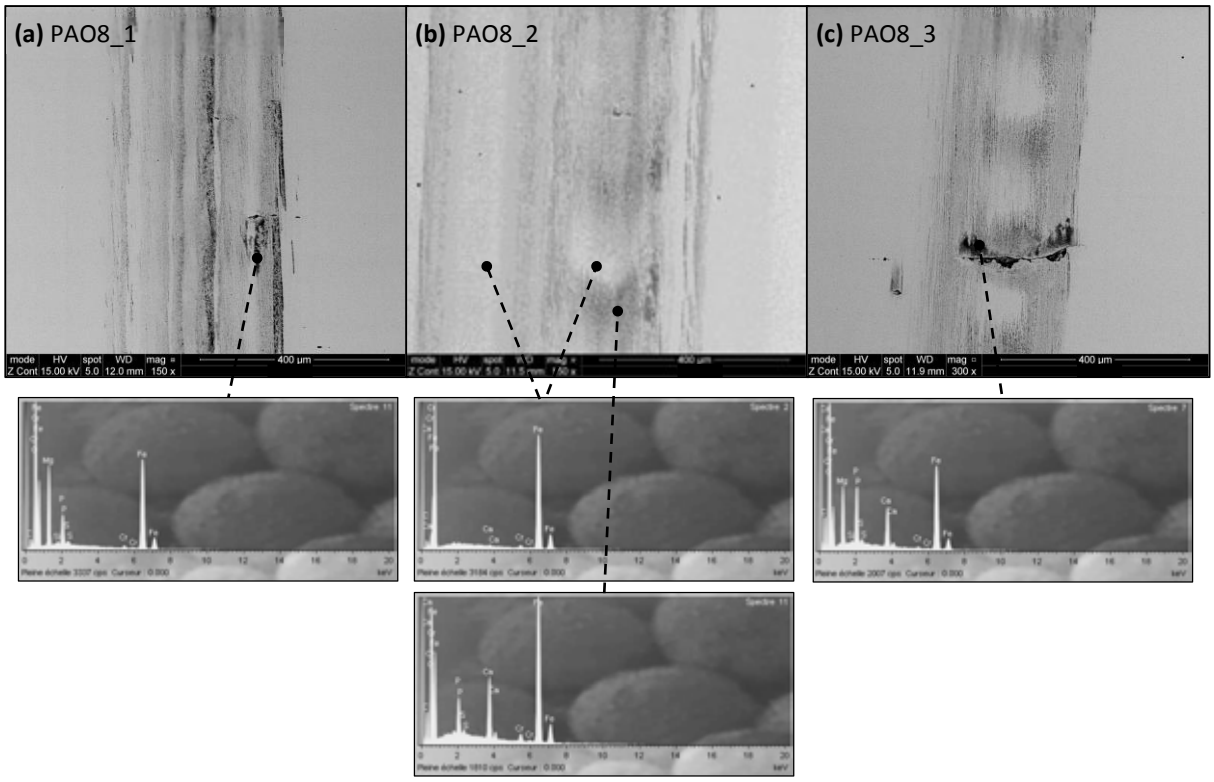

Fig. 5.16: SEM-EDX analysis on TDM raceways after RCF testing with various additive blends (**Table 5-2**) revealing different tribofilm composition.

5.2.3.7 Main outcome of WEC propagation attempts on the TDM

The following statements may summarize the *main outcomes* of WEC driver testing on TDM:

Multiple TDM tests confirm that *high sliding energy, material cleanliness, structural stresses, water contamination, electrical currents, and specific lubricants* are *not self-sufficient* to explain WEC.

TDM tests with in-house additive blends confirm that *detergents* enhance *tribochemical cracking* and *heterogeneous tribofilm formation.*

5.2.4 Results and representativeness of the Twin-Disc machine

As anticipated in section 5.2.1, the transposition of REB tribological conditions on the TDM inherently requires numerous compromises and simplification hypotheses. Hence, the representativeness of the TDM tests should be questioned when analyzing the results. *First*, WEC initiation mechanisms have been partly achieved in reproducing *incipient surface microcracks* in conditions of reduced lubrication, similar to those identified the ACBB IR contact edges. It should however be noticed that the surface cracks do not appear exactly like those observed in the ACBB fractographs with deep vertical cleavages (**Fig. 3.12**). Furthermore, despite all the WEC influent drivers and combinations tested in the 61 tests, *microcracks have not propagated exactly into what has been precisely defined as WEC* (section 1.4.1). These results support the fact that *no driver seems self-sufficient:* WEC formation mechanisms most certainly rely on a precise combination of tribological conditions leading to hydrogen permeation that has not been met yet on the TDM.

These TDM results are *consistent with similar tests* performed on a different twin-disc machine by Evans et al. [201]. Except when using hydrogen precharged specimens, they have not managed either to reproduce WECs even when combining transient loads, acceleration/deceleration and various formulated oils (some containing CaS detergents). It may however be suppose that despite all these drivers certainly affect WEC formation, they may not have yet tested the correct combination. For example they have not tested significant SRR (>10%) with high temperatures and lubrication containing detergents… This could eventually confirm the WEC-like crack propagation reproduced in this study using the TDM with in-house additives blends.

Finally, it should be recalled that the TDM is a fatigue simulator designed to best control the tribological parameters. In that sense, the contact conditions are as constant as possible, so that some transient events occurring in REBs are not transposable on the TDM. Consequently, the conditions may often be too constant on TDM to counterbalance tribofilm formation by incipient wear in case of fully formulated oils, which would inhibit hydrogen permeation and WEC formation.

5.3 Closure

As a closure to this fifth and last chapter, after having proposed WEC initiation and propagation mechanisms in **Chapter 4**, focus has been made on the manifold WEC influent drivers. *First*, a full root cause analysis has been led from macro to tribo-scales considering various WEC occurrences previously reported in this manuscript or in the literature, hence identifying the multiple WEC drivers. *Second,* drivers have been tested more or less individually on the TDM in attempts of WEC reproduction. Consequently, the main outcomes of this chapter are a better apprehension of WEC reproducibility on the TDM and an enhanced tribological understanding of WEC formation mechanisms and influent drivers.

5.3.1 WEC multiple influent drivers at macro-scales

Literature review and analyses of WEC reproductions without prior hydrogen charging reveal that, depending on the application, multiple combinations of drivers seem to influence WEC from a macroscopic point of view, but that they generally come to down to similar phenomena at tribological scales enhancing nascent surface formation and hydrogen chemisorption. The full root cause analysis have been schemed in **Fig. 5.2**.

5.3.2 WEC main drivers at tribo-scales

Thorough analyses of WEC reproduction on the NTN-SNR Machine S ACBB and/or on the FE8-CRTB have confirmed that, at local asperity scales, WEC formation mechanisms do not rely on conventional RCF parameters as inclusions but mainly on several tribomechanical and tribochemical drivers, that are:

- *High sliding energy* exceeding a representative $P.\Delta U$ *or* $N.\Delta U/\lambda$ *threshold* over a significant contact area, as confirmed by several REB WEC occurrences;

- *High bulk and flash temperatures* (>100°C) increasing *tribofilm incipient wear* and *chemical activation of additives*, as confirmed by a REB WEC reproduction and the literature;
- Tribochemical phenomena favoring hydrogen generation at nascent steel surface such as *water contamination* and *electrical potentials* confirmed in the literature;
- Lubricant formulation and namely concentrations of *metal sulfonate additives* or other *detergents* that tend *to inhibit or deprave tribofilm formation,* as confirmed by TDM tests with in-house additive blends and by FE8-CRTB tests.

5.3.3 WEC multiple non-self-sufficient

Additional investigations on the TDM tests have confirmed that high sliding energy, material cleanliness, structural stresses, water contamination, electrical currents, and specific lubricants formulation are all *not self-sufficient* to explain WECs even though most of them have once triggered WEC reproduction on specific test rigs. Therefore, the *main outcome* is that WEC initiation and propagation mechanisms actually rely on a subtle and instable *equilibrium between material, tribo-mechanical, and tribochemical parameters,* as illustrated in **Fig. 5.17**. If parameters are slightly modified, the tribological equilibrium may collapse inhibiting WEC formation. In consequence, f*urther testing* has to yet be led to fully meet this equilibrium on the TDM. Indeed, one main complication comes from the fact the WEC tribological equilibrium appears to vary significantly from one application to another, which should thus be considered in designing efficient and durable countermeasures.

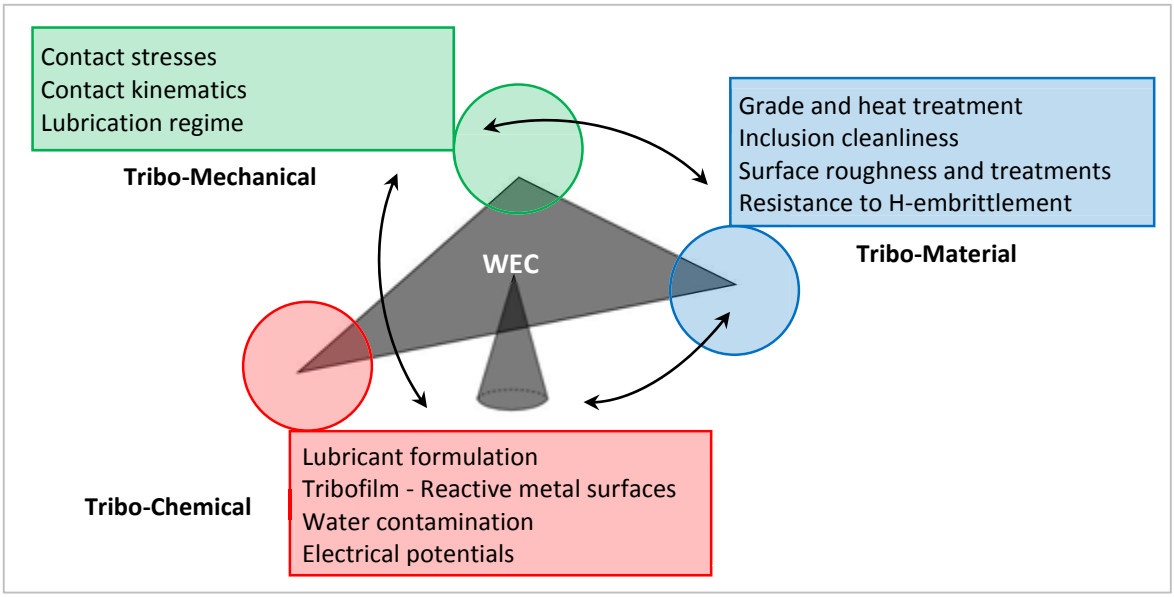

Fig. 5.17: WEC formation seems to require a subtle instable equilibrium between mechanical, material and chemical tribological phenomena all interacting.

Tribological analysis of White Etching Crack (WEC) failures in Rolling Element Bearing

General conclusion

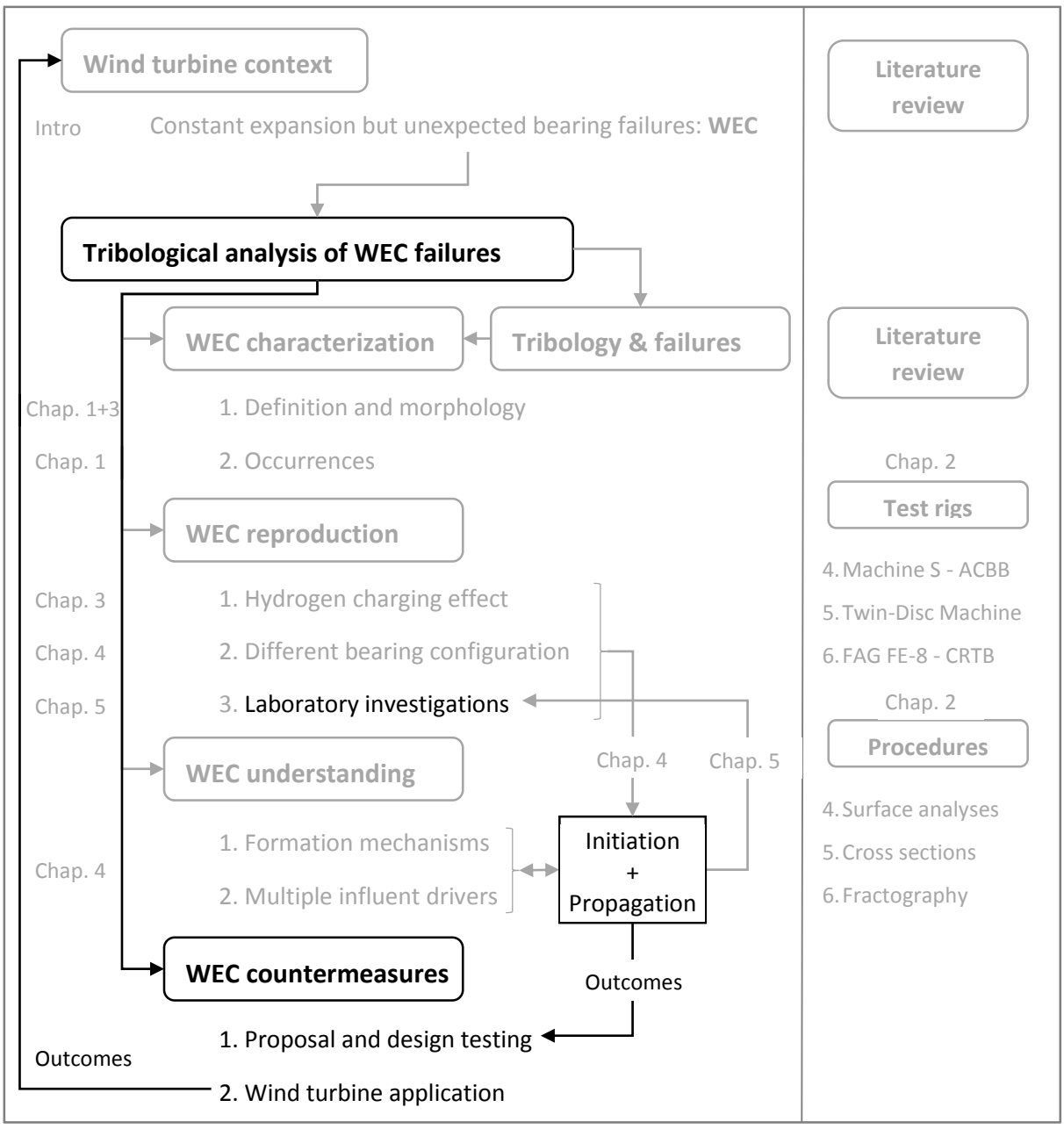

As a closure to this thesis, the main *outcomes* of the WEC tribological analysis led in this study will be first recalled. Then, as illustrated in the thesis flow chart, in order to loop the analysis and comply with its background industrial objective, potential WEC *countermeasures* will be evoked. Finally, several *perspectives* will be suggested to continue on this analysis, which should prompt future discussions and/or confirmations.

A. General outcomes

The wind turbine industry is currently experiencing an outstanding expansion to, hopefully, fulfill the exploding worldwide demand for electricity. However, despite engineering progress to design wind turbines supposed to endure 20 years of service life in complex and fluctuating operating conditions, unexpected and premature Rolling Element Bearing (REB) failures drastically impact the cost of energy. Among prevalent tribological failures, a peculiar and yet prevalent rolling contact fatigue mode has been associated to broad subsurface three-dimensional branching crack networks bordered by white etching microstructure, and thus named White Etching Cracks (WEC).

An initial literature review provided in **Chapter 1**, has first allowed a *tribological characterization of WECs*. It has been emphasized that WECs are independent of conventional rolling contact fatigue microstructural alterations. Generally quite rare but quasi-systematic for each very specific affected REB configurations, WECs have been reported for various industrial applications, REB types, components, lubricants, steel grades and heat treatments. Therefore, no common intuitive denominator seems to explain WEC formation mechanisms. Yet, WECs commonly develop at moderate loads and cycles eventually leading to premature failures that remain unpredictable using fatigue life estimations. Hence, the main presumption has been that WECs correspond to unconventional rolling contact fatigue cracking associated to hydrogen embrittlement.

In order to better understand WEC formation mechanisms, an *experimental methodology* has been established in **Chapter 2** to reproduce and analyze WECs on the NTN-SNR Machine S and LaMCoS Twin-Disc Machine test rigs. Subsequently, tests have been performed in **Chapter 3** with both hydrogen precharged and neutral specimens. Cross sections and fractographs revealing broad WEC networks in hydrogen precharged and neutral ACBB inner rings have demonstrated that artificial hydrogen charging does ease WEC propagation morphologies but tends to alter WEC initiation mechanisms. Indeed, contrarily to WECs in hydrogen precharged specimens, WECs in neutral ones have exclusively formed at the contact edges displaying an incipient connection to the surface. Therefore, one major outcome of this study is that artificial hydrogen charging does not seem to be relevant to design efficient WEC countermeasures for applications.

Moreover, the WEC atypical location at the contact edges in neutral ACBB inner ring has supported that WEC correspond to an unconventional surface-affected failure mode and that expertise led in the past decades could have simply missed those crack networks. Another outcome is that, even targeted cross sections may be misleading as WEC apparent morphologies greatly depend on the type and position of the cross section versus the contact.

Then, a thorough tribological comparison of *WEC reproductions without prior hydrogen charging* has been led in **Chapter 4** considering results of two different test rig configurations: FE8-CRTB results available in the literature and various alternatives of the NTN-SNR Machine S tests. Even though WECs have solely formed at the contact edges where high sliding occurs in both test rigs,

WEC networks did not always connect with the surface in the FE8-CRTBs contrarily to the NTN-SNR ACBBs. In addition, WEC formation has been triggered by specific lubricant additives in the FE8-CRTBs, which were unnecessary on the NTN-SNR ACBBs.

Hence, further analyses have been performed to a better understand *WEC tribological formation mechanisms*. It has been enlightened that initiation mechanisms most certainly slightly differ between the two configurations. WEC initiation is assumed to take place via local lubricant and/or water tribochemical decomposition and hydrogen permeation at nascent steel surfaces. Nascent steel can be formed either directly at the raceway in case of incipient wear and/or heterogeneous tribofilms, either at incipient surface microcrack flanks opened by combining local and temporary high tensile stresses and near surface discontinuities. Hydrogen then tends to stay trapped at tensile crack tips physically enhancing metal atoms decohesion so that typical brittle cracking develops quasi-regardless the contact stresses. As the cracks flanks rub against each other under cycling contact stresses, hydrogen enhances localized plasticity. This leads to local microstructure refinement forming the crack adjacent white etching microstructures. Depending on the material properties and structural stress state, the component will be more or less sensible to hydrogen embrittlement. The overall WEC morphology may then vary from deep radial cracking to surface flaking. Up to now, no counter-indication to the fore-proposed scenarios has been found in the literature.

Considering WEC tribological initiation and propagation, an extensive *tribological root cause analysis* has been detailed in **Chapter 5** in order to identify WEC influent drivers. An overview has first highlighted that from a macroscopic point of view, multiple combinations of drivers seem to lead to WEC formation depending on the application, but that they often come to down to similar phenomena at tribological scales. All enhance nascent surface formation and hydrogen chemisorption. Then, based on additional WEC reports, specific tribomechanical and tribochemical drivers have been identified. It has been demonstrated that WEC formation mechanisms seem to rely on a local sliding energy threshold, which affects local flash temperatures and may be represented by either $P.\Delta U$, $N.\Delta U$ or $N.\Delta U/\lambda$ criteria. Nevertheless this tribomechanical threshold is believed to vary from an application to another, for example depending on the presence of tribochemical drivers. For example, in some tests, it has been revealed that concentrations of detergent additives, water contamination and/or electrical currents could respectively trigger WEC formation mechanisms even though they were all absent in the NTN-SNR ACBB tests. Anyhow, it has been noticed that wind turbine operating conditions significantly overlap with the identified WEC drivers, thus providing a partial explanation as to why WEC are more frequent in wind turbine applications.

In order to better qualify their respective influence on WEC initiation and propagation, the identified drivers have been tribologically transposed on *Twin-Disc Machine investigations*. This includes specific procedures developed to account for lubricant hygroscopy and electrical currents. The presented results tend to confirm that drivers that had once triggered WECs do not seem to be self-sufficient. Therefore, WEC formation mechanisms are presumed to rely on a subtle equilibrium between tribo-mechanical, material and tribochemical parameters, which leads to hydrogen permeation. This equilibrium may explain why WECs are delicate to reproduce on laboratory test rigs without prior-artificial hydrogen charging. It should thus be considered in designing efficient and durable WEC countermeasures. Finally, this surface-affected equilibrium highly supports the unconventional aspect of WEC associated failures, for which life prediction standards seem to be outdated, notably in case of transition to large size REBs.

To conclude, this *thesis* could arguably be best qualified as an empirical and eclectic tribological analysis merely leading to a series of "*hypo"-thesis* to better understand White Etching Cracks tribological formation, which will hopefully be discussed and/or verified in the future.

B. Industrial countermeasures

Even though WEC reproduction may seem very delicate to master without artificial hydrogen charging, the fact formation mechanisms rely on an instable equilibrium between material, tribomechanical and tribochemical drivers, suggests that durable countermeasures can be designed within reasonable industrial costs. Even a slight modification could successfully unbalance the WEC tribological equilibrium, thus inhibiting WEC failures.

Considering the potential *material countermeasures*, the bearing steel resistance to hydrogen embrittlement has first been proved to be enhanced by high chromium and/or vanadium contents. Additionally, wind turbine REBs have been observed to be less sensitive in case of case-carburized or bainitic bearing steels. Those steels indeed provide significant protective compressive residual stresses which increases the steel toughness. In case of through-hardened this could maybe be achieved by ensuring that the REBs operate under sufficient cycles at a given contact pressure to buildup compressive residual stresses. Nevertheless, these material aspects are assumed to only delay macroscopic surface failure as they mainly affect WEC subsurface propagation without fully preventing from WEC initiation.

To do so, *tribochemical countermeasures* limiting hydrogen permeation into the bearing steel seem to be most effective in preventing from WEC-associated failures. The first possibility is to prevent nascent steel surface formation either by providing a durable coating or by favoring tribofilm formation in service. It has for example been reported that bearings with black oxide surface treatments seem to be more resistant to WECs, at least until the surface treatments wear off. More durable surface coatings, for example WC/aC:H tungsten coatings, but also surface compressive protection layer as shot-peening, are still under ongoing research. Therefore, up to now, mastering tribofilm formation, for example by providing best suited lubricant formulation with restricted amounts of detergents, seems to be a major key in preventing nascent surface formation and thus most tribochemical surface initiated failure modes. The other possibility, probably somewhat less efficient, is to anneal lubricant and/or water molecule decomposition at nascent surfaces by limiting water contamination and electrical potentials going through the contacts both favoring tribochemical reactions.

Nevertheless, REB designs have to adapt to complex mechanical systems in which external contamination are hardly controlled and in which lubricants are in priority designed for gears. Therefore, *tribomechanical countermeasures* appear to be most interesting countermeasures to develop. Further testing has yet to be led, but designing REBs to maintain sliding energy criteria $P.\Delta U$, $N.\Delta U$ and/or $N.\Delta U/\lambda$ below a predetermined threshold, seems to be an interesting lead in solving durably WEC formation as demonstrated in **Chapter 5**. This is supported feedbacks form the field suggesting that replacing SRBs by TRBs in wind turbine limits WEC-associated failures.

To conclude, it is worth underlining that the most durable and efficient countermeasures certainly rely on a collaborative design of the mutually dependent rolling element bearings and overall mechanical system in which they operate. In that sense, WEC countermeasures should

probably be designed considering each application and its respective operating conditions, humbly keeping in mind that tribological issues, inherent to all mechanical systems, could consistently arise elsewhere while solving White Etching Cracks.

C. Perspectives

As illustrated by this thesis, achieving WEC reproduction on various full REB test rigs and on tribological simulators as the Twin-Disc Machine would for sure allow to better qualify the various identified drivers and thus to achieve a precise understanding of WEC formation mechanisms. In doing so, WEC could be better predicted and efficient countermeasures could designed and tested to unbalance the specific tribological equilibrium leading to WEC failures in application.

In consequence, further tests seem required to pursue WEC reproduction attempts, notably better considering drivers such as the lubricant formulations, the temperature, the lubrication regime and the sliding energy criteria. Short term perspectives on the full REB would be first to re-conduct tests at higher temperatures and with various lubricant formulation, notably containing high concentrations of calcium sulfonate detergents and/or artificial water contamination. Also, further analyses and tests have to be performed on cylindrical thrust bearings in order to better qualify the sliding energy thresholds and to understand why WECs have not been reproduced yet.

Consequently, mid-term perspectives would be to use the additional data to design and conduct additional Twin-Disc tests to hopefully reproduce WECs. In addition to continue tests with in-house additives blends and specific tribochemical protocols, the possibility of performing tests under transient slide to roll ratio may also be considered. Nevertheless, the main goal on the Twin-Disc Machine should be more to reproduce WEC-like tribochemical crack propagation and to qualify the influence of optimized driver combinations, rather than to aim the exact WEC Indeed, WEC morphology may differ significantly depending on the application, especially on the Twin-Disc Machine that has been designed to simulate specific tribological conditions and not that of a full REB.

Finally, supposing WEC reproduction has been mastered, long-term perspectives are numerous. First, countermeasures could be best designed and tested according to each application specificities. In case of wind turbine REBs this step is for sure mandatory prior to full scale testing. For example, focus could be made on the accurate tribochemical mechanisms leading to hydrogen permeation and embrittlement. This would enable to overcome the variability of WEC influent drivers and to implement numerical models to help understand and design efficient countermeasures. Also, mastered WEC reproduction could contribute to the development of nondestructive techniques to detect WECs prior to macroscopic failure in order to monitor WEC formation *in-situ* and wisely stop endurance tests and/or plan field maintenance. This would significantly accelerate research to design WEC countermeasures.

To conclude, at first, WECs have naturally been addressed as an unsolved rolling contact fatigue failure mode, thus supposedly demanding material and mechanical expertise. Nevertheless, it has been revealed that tribochemistry has a major impact on WEC formation mechanisms. Therefore, the last overall recommendation would be to continue on always fully considering the complex and interdisciplinary definition of *tribology,* which comprises multi-scale material, mechanical and chemical phenomena, all highly interdependent.

References

[1] EIA, 2014, "U.S. Energy Administration Information" [Online]. Available: www.eia.gov.

[2] The Harris Poll, 2010, "Large Majorities in U.S. and Five Largest European Countries Favor More Wind Farms and Subsidies for Bio-fuels, but Opinion is Split on Nuclear Power," Harris Interact. [Online]. Available: http://www.harrisinteractive.com.

[3] AREVA, 2014, "Areva Wind - M5000 -Technical data" [Online]. Available: www.areva.com.

[4] Global Wind Eenrgy Council GEWEC, 2013, Global Wind Statistics. Available: http://www.gwec.net/wp-content/uploads/2014/02/GWEC-PRstats-2013_EN.pdf

[5] Goch, G., Knapp, W., and Härtig, F., 2012, "Precision engineering for wind energy systems," CIRP Ann. - Manuf. Technol., **61**(2), pp. 611–634.

[6] Greco, A., Sheng, S., Keller, J., and Erdemir, A., 2013, "Material wear and fatigue in wind turbine Systems," Wear, **302**(1-2), pp. 1583–1591.

[7] Kotzalas, M. N., and Doll, G. L., 2010, "Tribological advancements for reliable wind turbine performance.," Philos. Trans. A. Math. Phys. Eng. Sci., **368**(1929), pp. 4829–50.

[8] Rensselar, J. V., 2010, "The elephant in the wind turbine," Tribol. Lubr. Technol., **June**, pp. 38–50.

[9] Rosinski, J., and Smurthwaite, D., 2010, "Troubleshooting wind gearbox problems," Gear Solut., **February**, pp. 22–33.

[10] Terrell, E. J., Needelman, W. M., and Kyle, J. P., 2012, Wind Turbine Tribology. In: "Green Tribology", Nosonovsky, M. and Bhushan, B., Springer, Berlin Heidelberg, pp. 483-525. ISBN: 9783642236808.

[11] Jonsson, T., 2006, "Gearbox Repair Experiences," Sandia National Laboratories Wind Turbine Gearbox Reliability Workshop, October 3-4 2006, Albuquerque, NM, U.S.A, 13 pages.
Available: http://windpower.sandia.gov/2006reliability/tuesday/12-thomasjonsson.pdf.

[12] McNiff, B., 2006, "Wind Turbine Gearbox Reliability," Sandia National Laboratories Wind Turbine Gearbox Reliability Workshop, October 3-4 2006, Albuquerque, NM, U.S.A, 18 pages.
Available: http://windpower.sandia.gov/2006reliability/tuesday/14-brianmcniff.pdf.

[13] Sheng, S., Mcdade, M., and Errichello, R., 2011, "Wind Turbine Gearbox Failure Modes – A Brief," NREL - Gearbox Reliability Collaborative, February 10-12, 2011, Golden, CO, U.S.A., 26 pages.
Available: http://www.nrel.gov/wind/grc/meeting_grc.html

[14] West, O. H. E., Diederichs, A. M., Alimadadi, H., Dahl, K. V, and Somers, M. A. J., 2013, "Application of Complementary Techniques for Advanced Characterization of White Etching Cracks," Pract. Metallogr., **50**(6), pp. 410–431.

[15] Grabulov, a., Petrov, R., and Zandbergen, H. W., 2010, "EBSD investigation of the crack initiation and TEM/FIB analyses of the microstructural changes around the cracks formed under Rolling Contact Fatigue (RCF)," Int. J. Fatigue, **32**(3), pp. 576–583.

[16] Evans, M.-H., Wang, L., and Wood, R., 2014, "Formation mechanisms of white etching cracks and white etching area under rolling contact fatigue," Proc. Inst. Mech. Eng. Part J J. Eng. Tribol., **228**(10), pp. 1047–1062.

[17] Harris, T., and Kotzalas, M. N., 2006, Essential Concepts of Bearing Technology, Fifth Edition, CRC Press, 392 pages. ISBN: 9781420006599.

[18] Harris, T. A., and Kotzalas, M. N., 2006, Advanced Concepts of Bearing Technology,: Rolling Bearing Analysis, Fifth Edition, CRC Press, 368 pages. ISBN: 9780849371820

[19] Bhadeshia, H. K. D. H., 2012, "Steels for bearings," Prog. Mater. Sci., **57**(2), pp. 268–435.

[20] Zaretsky, E. V, 2012, "Rolling bearing steels – a technical and historical perspective," Mater. Sci. Technol., **28**(1), pp. 58–69.

[21] Amey, C. M., Huang, H., and Rivera-Díaz-del-Castillo, P. E. J., 2012, "Distortion in 100Cr6 and nanostructured bainite," Mater. Des., **35**(October), pp. 66–71.

[22] Perez, M., Sidoroff, C., Vincent, A., and Esnouf, C., 2009, "Microstructural evolution of martensitic 100Cr6 bearing steel during tempering: From thermoelectric power measurements to the prediction of dimensional changes," Acta Mater., **57**(11), pp. 3170–3181.

[23] Girodin, D., Dudragne, G., Courbon, J., and Vincent, A., 2007, "Statistical analysis of non metallic inclusions for the estimation of rolling contact fatigue range and quality control of bearing steel," ASTM Bear. Steel Technol., **STP1465**, pp. 85–100.

[24] Beswick, J. M., 2011, Bearing Steel Technologies - 8th Volume: Developments on Rolling Bearing Steels and Testing, ASTM Bear. Steel Technol, **STP1524**, 252 pages. ISBN: 9780203186316.

[25] Tonicello, E., 2012, "Etude et modélisation de la fatigue de contact en présence d'indentation dans le cas de roulements tout acier et hybrides," PhD Thesis, Laboratoire Matértiaux Ingénierie et Sciences, INSA de Lyon, 139 pages.

[26] Girodin, D., 2008, "Deep Nitrided 32CrMoV13 Steel," NTN Tech. Rev., **76**, pp. 24–31.

[27] Lamagnere, P., Fougeres, R., Lormand, G., Vincent, A., Girodin, D., Dudragne, G., and Vergne, F., 1998, "A Physically Based Model for Endurance Limit of Bearing Steels," J. Tribol., **120**(3), p. 421.

[28] Vincent, A., Elghazal, H., Lormand, G., Hamel, A., and Girodin, D., 2002, "Local Elasto-Plastic Properties of Bearing Steels determined by Nano-Indentation Measurements," ASTM Bear. Steel Technol., **STP1419,** pp. 427–442.

[29] Gegner, J., 2011, "Tribological Aspects of Rolling Bearing Failures," Tribology - Lubricants and Lubrication, C.-H. Kuo, ed., InTech, Rijeka, Croatia, pp. 34–94.

[30] Lund, T. B., Beswick, J., and Dean, S. W., 2010, "Sub-Surface Initiated Rolling Contact Fatigue—Influence of Non-Metallic Inclusions, Processing History, and Operating Conditions," J. ASTM Int., **7**(5), p. 102559.

[31] Kim, T. H., Olver, A. V., and Pearson, P. K., 2001, "Fatigue and Fracture Mechanisms in Large Rolling Element Bearings," Tribol. Trans., **44**(4), pp. 583–590.

[32] "Wind Turbine Panel Discussion," STLE 69th Annual Meeting & Exhibition, May 18-22, 2014, Lake Buena Vista, FL, USA.

[33] Errichello, R., Sheng, S., Keller, J., and Greco, A., 2011, "Wind Turbine Tribology Seminar - A recap," Presented November 15-17 2011, Broomfield, CO, USA, 55p pages. Available: http://www.nrel.gov/docs/fy12osti/53754.pdf

[34] Greco, A., 2014, "Bearing Reliability- White Etching Cracks (WEC)," NREL - Gearbox Reliability Collaborative, February 10-12, 2014, Golden, CO, USA, 28 slides. Available: http://www.nrel.gov/wind/grc/meeting_grc.html

[35] Tichy, J., 2014, "Limits of Lubrication: films, how thin? Surfaces, how soft? Lubricants, how wet?," First African Congress on Tribology, Plenary session, April 27-30, 2014, Marrakesh, Morocco.

[36] Dowson, D., 1998, History of tribology, 2nd Edition, Wiley, London, 768 pages. ISBN: 978-1860580703.

[37] Frêne, J., and Zaïdi, H., 2011, "Introduction à la tribologie," Tech. l'Ingenieur, **Tribologie**(TRI100), 15 pages.

[38] Johnson, K. L., 1985, Contact Mechanics, Cambridge University Press, Cambridge, 468 pages. ISBN: 978-0521347969.

[39] Hertz, H., 1896, "On the contact of rigid elastic solids and on hardness," MacMillan, London, **1**(Miscellaneous Papers), pp. 163–183.

[40] Voskamp, A. P., 1998, "Fatigue and Material Response in Rolling Contact," ASTM Bear. Steel Technol., **STP1327**, pp. 153–166.

[41] Williams, J. A., 2005, "The influence of repeated loading, residual stresses and shakedown on the behaviour of tribological contacts," Tribol. Int., **38**(9), pp. 786–797.

[42] Gentile, A. J., Jordan, E. F., and Martin, A. D., 1964, "Phase transformations in High-Carbon, High-Hardness steels under Contact Loads," Trans. Metall. Soc. AIME, **233**(1085-1093), pp. 1085–1093.

[43] Williams, J. A., and Dwyer-Joyce, R. S., 2001, "Contact Between Solid Surfaces," Modern Tribology Handbook, CRC Press, 1760 pages. ISBN: 9780849384035.

[44] Hamrock, B. J., and Anderson, W. J., 1983, "Rolling-Element Bearings," NASA Ref. Publ., **1105**(June), pp. 1–63.

[45] Flamand, L., 1993, "Fatigue des surfaces," Tech. l'Ingenieur, **Tribology**(B5055), 19 pages.

[46] Lubrecht, A. A., 2009, "An introduction to elastohydrodynamic lubrication," Mechanical Engineering and Development Master Degree Course, INSA de Lyon, 117 pages.

[47] Chaise, T., and Nélias, D., 2011, "Contact Pressure and Residual Strain in 3D Elasto-Plastic Rolling Contact for a Circular or Elliptical Point Contact," J. Tribol., **133**(4), p. 041402.

[48] Brandao, J., 2013, "Gear tooth flank damage prediction using high cycle fatigue and wear models," PhD Thesis, Departamento de Engenharia Mecanica e Gestao Industrial, Universidade do Porto, 226 pages.

[49] Qiao, H., Evans, H. P., and Snidle, R. W., 2008, "Comparison of fatigue model results for rough surface elastohydrodynamic lubrication," Proc. Inst. Mech. Eng. Part J J. Eng. Tribol., **222**(3), pp. 381–393.

[50] Labiau, A., Ville, F., Sainsot, P., Querlioz, E., and Lubrecht, T., 2008, "Effect of sinusoidal surface roughness under starved conditions on rolling contact fatigue," Proc. Inst. Mech. Eng. Part J J. Eng. Tribol., **222**(3), pp. 193–200.

[51] Kaneta, M., Sakai, T., and Nishikawa, H., 1993, "Effects of Surface Roughness on Point Contact EHL," Tribol. Trans., **36**(4), pp. 605–612.

[52] Lugt, P. M., and Morales-Espejel, G. E., 2011, "A Review of Elasto-Hydrodynamic Lubrication Theory," Tribol. Trans., **54**(3), pp. 470–496.

[53] Dwyer-Joyce, R. S., 2005, "The life cycle of a debris particle," Tribol. Interface Eng. Ser., **48**(Life Cycle Tribology - Proceedings of the 31st Leeds-Lyon Symposium on Tribology), pp. 681–690.

[54] Ville, F., 1998, "Pollution solide des lubrifiants indentation et fatigue des surfaces," PhD Thesis, Laboratoire Mécanique des Contacts, INSA de Lyon, 163 pages.

[55] Diab, Y., Coulon, S., Ville, F., and Flamand, L., 2003, "Experimental investigations on rolling contact fatigue of dented surfaces using artifical, defects: subsurface analyses," Tribol. Ser., **41**(Proceedings of the 29th Leeds-Lyon Symposium on Tribology), pp. 359–366.

[56] Coulon, S., Ville, F., and Lubrecht, T., 2005, "Experimental investigations on Rolling Contact Fatigue for dented surfaces using artificial defects," Tribol. Interface Eng. Ser., **48**(Life Cycle Tribology — Proceedings of the 31st Leeds-Lyon Symposium on Tribology), pp. 691–702.

[57] Nélias, D., and Ville, F., 2000, "Detrimental Effects of Debris Dents on Rolling Contact Fatigue," J. Tribol., **122**(1), p. 55.

[58] Tallian, T. E., 1999, Failure atlas for Hertz contact machine elements, ASME Press, 496 pages. ISBN: 9780791800843.

[59] Heathcote, H. L., 1921, "The ball bearing: in the making, under test and in service," Proc. Intitute Automob. Eng., **15**, pp. 569–702.

[60] Ayel, J., 1997, "Lubrifiants - Constitution," Tech. l'Ingénieur, **BM5341**(Tribologie), 17 pages.

[61] Cousseau, T., Björling, M., Graça, B., Campos, a., Seabra, J., and Larsson, R., 2012, "Film thickness in a ball-on-disc contact lubricated with greases, bleed oils and base oils," Tribol. Int., **53**, pp. 53–60.

[62] Hamrock, B., Schmid, S., and Jacobson, B., 2004, Fundamentals of Fluid Film Lubrication, CRC Press, 768 pages. ISBN: 9780824753719.

[63] Ayel, J., 2001, "Lubrifiants: additifs à action chimique," Tech. l'Ingenieur, **B5433**(Tribologie), 18 pages.

[64] Ayel, J., 2002, "Lubrifiants: additifs à action physique ou physiologique," Tech. l'Ingenieur, **BM5344**(Tribologie), 18 pages.

[65] Morina, A., Neville, A., Priest, M., and Green, J. H., 2006, "ZDDP and MoDTC interactions in boundary lubrication—The effect of temperature and ZDDP/MoDTC ratio," Tribol. Int., **39**(12), pp. 1545–1557.

[66] Dowson, D., 1995, "Elastohydrodynamic and micro-elastohydrodynamic lubrication," Wear, **190**(2), pp. 125–138.

[67] Halme, J., and Andersson, P., 2010, "Rolling contact fatigue and wear fundamentals for rolling bearing diagnostics – state of the art," Proc. Inst. Mech. Eng. Part J J. Eng. Tribol., **224**(4), pp. 377–393.

[68] Dowson, D., and Ehret, P., 1999, "Past, present and future studies in elastohydrodynamics," Proc. Inst. Mech. Eng. Part J J. Eng. Tribol., **213**(5), pp. 317–333.

[69] Hamrock, B. J., and Dowson, D., 1976, "Isothermal Elastohydrodynamic Lubrication of Point Contacts: Part 1—Theoretical Formulation," J. Lubr. Technol., **98**(2), p. 223.

[70] Hamrock, B. J., and Dowson, D., 1976, "Isothermal Elastohydrodynamic Lubrication of Point Contacts: Part II—Ellipticity Parameter Results," J. Lubr. Technol., **98**(3), p. 375.

[71] Hamrock, B. J., and Dowson, D., 1977, "Isothermal Elastohydrodynamic Lubrication of Point Contacts: Part IV—Starvation Results," J. Lubr. Technol., **99**(1), p. 15.

[72] Hamrock, B. J., and Dowson, D., 1977, "Isothermal Elastohydrodynamic Lubrication of Point Contacts: Part III—Fully Flooded Results," J. Lubr. Technol., **99**(2), p. 264.

[73] Sakamoto, T., Uetz, H., Föhl, J., and Khosrawi, M. A., 1982, "The reaction layer formed on steel by additives based on sulphur and phosphorus compounds under conditions of boundary lubrication," Wear, **77**(2), pp. 139–157.

[74] Hsu, S. M., and Gates, R. S., 2006, "Effect of materials on tribochemical reactions between hydrocarbons and surfaces," J. Phys. D. Appl. Phys., **39**(15), pp. 3128–3137.

[75] Hsu, S. M., Munro, R., and Shen, M. C., 2002, "Wear in boundary lubrication," Proc. Inst. Mech. Eng. Part J J. Eng. Tribol., **216**(6), pp. 427–441.

[76] Minfray, C., Martin, J.-M., Lubrecht, T., Belin, M., and Le Mogne, T., 2003, "A novel experimental analysis of the rheology of ZDDP tribofilms," Tribol. Ser., **41**(Proceedings of the 29th Leeds-Lyon Symposium on Tribology), pp. 807–817.

[77] Zhang, J., Yamaguchi, E., and Spikes, H., 2014, "The Antagonism between Succinimide Dispersants and a Secondary Zinc Dialkyl Dithiophosphate," Tribol. Lubr. Technol, **June**, pp. 60–70.

[78] Aktary, M., McDermott, M. T., and Torkelson, J., 2001, "Morphological evolution of films formed from thermooxidative decomposition of ZDDP," Wear, **247**(2), pp. 172–179.

[79] Franke, J., Holweger, W., Surborg, H., Blass, T., Fahl, J., Elfrath, T., and Merk, D., 2014, "Influence of Tribolayer on Rolling Bearing Fatigue Performed on a FE8 Test Rig," TAE 19th International Colloquium Tribology, January 21-23, 2014, Ostfildern, Germany, 13 slides.

[80] Topolovec-Miklozic, K., Forbus, T. R., and Spikes, H. a., 2007, "Film thickness and roughness of ZDDP antiwear films," Tribol. Lett., **26**(2), pp. 161–171.

[81] Taylor, L. J., and Spikes, H. a., 2003, "Friction-Enhancing Properties of ZDDP Antiwear Additive: Part I—Friction and Morphology of ZDDP Reaction Films," Tribol. Trans., **46**(3), pp. 303–309.

[82] Pasaribu, H. R., and Lugt, P. M., 2012, "The Composition of Reaction Layers on Rolling Bearings Lubricated with Gear Oils and Its Correlation with Rolling Bearing Performance," Tribol. Trans., **55**(3), pp. 351–356.

[83] Evans, R. D., Doll, G. L., Hager, C. H., and Howe, J. Y., 2010, "Influence of Steel Type on the Propensity for Tribochemical Wear in Boundary Lubrication with a Wind Turbine Gear Oil," Tribol. Lett., **38**(1), pp. 25–32.

[84] Brandão, J. a., Meheux, M., Ville, F., Seabra, J. H. O., and Castro, J., 2012, "Comparative overview of five gear oils in mixed and boundary film lubrication," Tribol. Int., **47**, pp. 50–61.

[85] Minfray, C., 2004, "Reactions tribochimiques avec le dithiophosphate de zinc," PhD Thesis, Laboratoire de Tribologie et Dynamique des Systèmes, Ecole Centrale de Lyon

[86] Aktary, M., Mcdermott, T., and Mcalpine, G. A., 2002, "Morphology and nanomechanical properties of ZDDP antiwear films as a function of tribological contact time," Tribol. Lett., **12**(3), pp. 155–162.

[87] Nixon, H. P., and Zantopulos, H., 1995, "Observations of the Impact of Lubricant Additives on the Fatigue Life Performance of Tapered Roller Bearings," SAE Technical Paper Series, **952124**, 7 pages.

[88] Nixon, H. P., and Zantopulos, H., 1995, "Lubricant additives, friend or foe: What the equipment design engineer needs to know," STLE Lubr. Eng., **51**(10), pp. 815–822.

[89] Nixon, H. P., 2006, "The Impact of Some Gear Lubricants on the Surface Durability of Rolling Element Bearings," SAE Technical Paper Series, **2006-01-0357**, 7 pages

[90] Meheux, M., Minfray, C., Ville, F., Mogne, T. L., Lubrecht, a a, Martin, J. M., Lieurade, H. P., and Thoquenne, G., 2010, "Effect of lubricant additives in rolling contact fatigue," Proc. Inst. Mech. Eng. Part J J. Eng. Tribol., **224**(9), pp. 947–955.

[91] Booser, E. R., 1988, Handbook of Lubrication (Theory and Practice of Tribology), Volume 2, CRC Press, 704 pages. ISBN: 9781420050448.

[92] Diab, Y., Ville, F., and Velex, P., 2006, "Prediction of Power Losses Due to Tooth Friction in Gears," Tribol. Trans., **49**(2), pp. 260–270.

[93] Poll, G., and Wang, D., 2012, "Fluid rheology, traction/creep relationships and friction in machine elements with rolling contacts," Proc. Inst. Mech. Eng. Part J J. Eng. Tribol., **226**(6), pp. 481–500.

[94] Ville, F., Nélias, D., Tourlonias, G., Flamand, L., and Sainsot, P., 2001, "On The Two-Disc Machine : A Polyvalent and Powerful Tool to Study Fundamental and Industrial Problems Related to Elastohydrodynamic Lubrication," Tribol. Ser., **39**(Proceedings of the 27th Leeds-Lyon Symposium on Tribology), pp. 393–402.

[95] Graca, B., Castro, J., Martins, R., Fernandes, C., and Seabra, J., 2013, "Failure and oil analysis in wind turbine gearboxes," BallTrib 2013, November 14-15, 2013, Kaunas, Lithuania, 6 pages.

[96] Tallian, T. E., 2006, "Failure Atlas for Rolling Bearings in Wind Turbines," Subcontract Report for the National Renewable Energy Laboratory, NREL/SR-500-52524, 98 pages.Available: www.osti.gov/scitech/

[97] Vasiliw, T., 2011, "Extending Gear Oil Performance," Wind Systems, **September**, pp. 38–45. Available: www.windsystemsmag.com/article/detail/286/extendinggear-oil-performance

[98] Prashad, H., 2006, "Tribology in Electrical Environments", Trib. Int. Eng. Ser., **49** Elsevier, 494 pages. ISBN: 9780444518804.

[99] Whittle, M., Trevelyan, J., and Tavner, P. J., 2013, "Bearing currents in wind turbine generators," J. Renew. Sustain. Energy, **5**(5), p. 053128.

[100] Vance, J. M., Palazzolo, A. B., and Zeidan, F. Y., 1987, "Electric shaft currents in turbomachinery," Proceedings of the 16th turbomachinery symposium, The Laboratory, pp. 51–63.

[101] Harvey, T. ., Wood, R. J. ., Denuault, G., and Powrie, H. E. ., 2002, "Investigation of electrostatic charging mechanisms in oil lubricated tribo-contacts," Tribol. Int., **35**(9), pp. 605–614.

[102] Sadeghi, F., Jalalahmadi, B., Slack, T. S., Raje, N., and Arakere, N. K., 2009, "A Review of Rolling Contact Fatigue," J. Tribol., **131**(4), p. 041403.

[103] Olver, A. V., 2005, "The Mechanism of Rolling Contact Fatigue: An Update," Proc. Inst. Mech. Eng. Part J J. Eng. Tribol., **219**(5), pp. 313–330.

[104] Williams, J. A., 2005, "Wear and wear particles - some fundamentals," Tribol. Int., **30**, pp. 863–870.

[105] Dwyer-Joyce, R. S., and Heymcr, J., 1996, "The Entrainment of Solid Particles into Rolling Elastohydrodynamic Contacts," Tribol. Ser., **31**, pp. 135–140.

[106] Nikas, G. K., and Sayles, R. S., 1998, "Effects of debris particles in sliding / rolling elastohydrodynamic contacts," Proc. Inst. Mech. Eng. Part J J. Eng. Tribol., **212**(5), pp. 333–343.

[107] Nikas, G. K., 2010, "A state-of-the-art review on the effects of particulate contamination and related topics in machine-element contacts," Proc. Inst. Mech. Eng. Part J J. Eng. Tribol., **224**(5), pp. 453–479.

[108] Zika, T., Gebeshuber, I. C., Buschbeck, F., Preisinger, G., and Gröschl, M., 2009, "Surface analysis on rolling bearings after exposure to defined electric stress," Proc. Inst. Mech. Eng. Part J J. Eng. Tribol., **223**(5), pp. 787–797.

[109] Nedelcu, I., Piras, E., Rossi, a., and Pasaribu, H. R., 2012, "XPS analysis on the influence of water on the evolution of zinc dialkyldithiophosphate-derived reaction layer in lubricated rolling contacts," Surf. Interface Anal., **44**(8), pp. 1219–1224.

[110] Bormetti, E., Donzella, G., and Mazzù, A., 2002, "Surface and Subsurface Cracks in Rolling Contact Fatigue of Hardened Components," Tribol. Trans., **45**(3), pp. 274–283.

[111] Evans, R. D., Barr, T. a., Houpert, L., and Boyd, S. V., 2013, "Prevention of Smearing Damage in Cylindrical Roller Bearings," Tribol. Trans., **56**(5), pp. 703–716.

[112] Errichello, R., 2004, "Another perspective: false brinelling and fretting corrosion," Tribol. Lubr. Technol., **60**(4), pp. 34–36.

[113] Pierres, E., Baietto, M. C., Gravouil, A., and Morales-Espejel, G., 2010, "3D two scale X-FEM crack model with interfacial frictional contact: Application to fretting fatigue," Tribol. Int., **43**(10), pp. 1831–1841.

[114] Nelias, D., Dumont, M. L., Champiot, F., Vincent, A., Girodin, D., Fougères, R., and Flamand, L., 1999, "Role of inclusions, surface roughness and operating conditions on rolling contact fatigue," Trans. ASME, **121**(2), pp. 240–251.

[115] Gegner, J., and Nierlich, W., 2011, "Mechanical and Tribochemical Mechanisms of Mixed Friction Induced Surface Failures of Rolling Bearings and Modeling of Competing Shear

and Tensile Stress Controlled Damage Initiation," Tribol. und Schmierungstechnik, **58**(1), pp. 10–21.

[116] Kaneta, M., Suetsugu, M., and Murakami, Y., 1986, "Mechanism of Surface Crack Growth in Lubricated Rolling/Sliding Spherical Contact," J. Appl. Mech., **53**(2), p. 354.

[117] Rabaso, P., Gauthier, T., Diaby, M., and Ville, F., 2013, "Rolling Contact Fatigue: Experimental Study of the Influence of Sliding, Load, and Material Properties on the Resistance to Micropitting of Steel Discs," Tribol. Trans., **56**(2), pp. 203–214.

[118] Warhadpande, A., Sadeghi, F., and Evans, R. D., 2013, "Microstructural Alterations in Bearing Steels under Rolling Contact Fatigue Part 1—Historical Overview," Tribol. Trans., **56**(3), pp. 349–358.

[119] Gegner, J., and Nierlich, W., 2012, "Comparison of the Microstructural Changes and X-ray Diffraction Peak Width Decrease during Rolling Contact Fatigue in Martensitic Microstructures," ASTM Bear. Steel Technol., **STP1548**, pp. 303–328.

[120] Gegner, J., Nierlich, W., and Brückner, M., 2007, "Possibilities and extension of XRD material response analysis in failure research for the advanced evaluation of the damage level of Hertzian loaded components," Materwiss. Werksttech., **38**(8), pp. 613–623.

[121] Schlicht, H., Schreiber, E., and Zwirlein, O., 1988, "Effects of Material Properties on Bearing Steel Fatigue Strength," ASTM Bear. Steel Technol., **STP987**, pp. 81–101.

[122] Zwirlein, O., and Shlicht, H., 1982, "Rolling Contact Fatigue Mechanisms - Accelerated Testing versus Field performance," ASTM Bear. Steel Technol., **771**, pp. 358–379.

[123] Warhadpande, A., Sadeghi, F., Kotzalas, M. N., and Doll, G., 2012, "Effects of plasticity on subsurface initiated spalling in rolling contact fatigue," Int. J. Fatigue, **36**(1), pp. 80–95.

[124] Grabulov, A., 2010, "Fundamentals of Rolling Contact Fatigue," PhD Thesis, Metallurgy and Metal Materials Technology, Delft University of Technology.

[125] Tricot, R., 1975, "Influence des paramètres métallurgiques sur les phénomènes de fatigue de contact en roulement-glissements des roulements et engrenages," Rev. Metall., pp. 385–411.

[126] Martin, J. A., Borgese, S. F., and Eberhardt, A. D., 1966, "Microstructural Alterations of Rolling—Bearing Steel Undergoing Cyclic Stressing," J. Basic Eng., **88**(3), p. 555.

[127] Polonsky, I., and Keer, L. M., 1995, "On white etching band formation in rolling bearings," J. Mech. Phys. Solids, **43**(4), pp. 637–669.

[128] Carroll, R. I., and Beynon, J. H., 2007, "Rolling contact fatigue of white etching layer: Part 1," Wear, **262**(9-10), pp. 1253–1266.

[129] Simon, S., Saulot, a., Dayot, C., Quost, X., and Berthier, Y., 2013, "Tribological characterization of rail squat defects," Wear, **297**(1-2), pp. 926–942.

[130] Baumann, G., Fecht, H. J., and Liebelt, S., 1996, "Formation of white-etching layers on rail treads," Wear, **191**(1-2), pp. 133–140.

[131] Ramesh, a., Melkote, S. N., Allard, L. F., Riester, L., and Watkins, T. R., 2005, "Analysis of white layers formed in hard turning of AISI 52100 steel," Mater. Sci. Eng. A, **390**(1-2), pp. 88–97.

[132] Schwach, D., and Guo, Y., 2006, "A fundamental study on the impact of surface integrity by hard turning on rolling contact fatigue," Int. J. Fatigue, **28**(12), pp. 1838–1844.

[133] Grabulov, a., Ziese, U., and Zandbergen, H. W., 2007, "TEM/SEM investigation of microstructural changes within the white etching area under rolling contact fatigue and 3-D crack reconstruction by focused ion beam," Scr. Mater., **57**(7), pp. 635–638.

[134] Evans, M.-H., Walker, J. C., Ma, C., Wang, L., and Wood, R. J. K., 2013, "A FIB/TEM study of butterfly crack formation and white etching area (WEA) microstructural changes under rolling contact fatigue in 100Cr6 bearing steel," Mater. Sci. Eng. A, **570**, pp. 127–134.

[135] Lamagnere, P., Girodin, D., Meynaud, P., Vergne, F., and Vincent, A., 1996, "Study of elasto-plastic properties of microheterogeneities by means of nano-indentation measurements: Application to bearing steels," Mater. Sci. Eng. A, **215**(1-2), pp. 134–142.

[136] Branch, N. a., Arakere, N. K., Svendsen, V., Forster, N. H., Beswick, J., and Dean, S. W., 2010, "Stress Field Evolution in a Ball Bearing Raceway Fatigue Spall," J. ASTM Int., **7**(2), p. 102529.

[137] Lundberg, G., and Palmgren, A., 1947, "Dynamic Capacity of Rolling Bearings," Acta Polytech. Mech. Eng. Ser., **1**(3).

[138] Ioannides, E., and Harris, T. A., 1985, "A New Fatigue Life Model for Rolling Bearings," J. Tribol., **107**(3), p. 367.

[139] Harris, T. A., Ragen, M. A., and Spitzer, R. F., 1992, "The effects of hoop and material residual stresses on the fatigue life of high speed, rolling bearings," Tribol. Trans., **35**(1), pp. 194–198.

[140] Zaretsky, E. V, Poplawski, J. V, and Peters, S. M., 1995, "Comparison of life theories for rolling-element bearings," NASA Tech. Memo, **106585**.

[141] Zaretsky, E. V., Poplawski, J. V., and Miler, C. R., 2000, "Rolling Bearing Life Prediction _ Past, Present, and Future," NASA Tech. Memo, **4159847**.

[142] Zaretsky, E. V., August, R., and H.H., C., 1997, "Effect of hoop stress on ball bearing life prediction," Tribol. Trans., **40**(1), pp. 91–101.

[143] Oswald, F. B., Zaretskty, E. V., and Poplawski, J. V., 2010, "Interference-Fit Life Factors for Ball Bearings," Tribol. Trans., **54**(1), pp. 1–20.

[144] Gabelli, A., Lai, J., Lund, T., Rydén, K., Strandell, I., and Morales-Espejel, G. E., 2012, "The fatigue limit of bearing steels – Part II: Characterization for life rating standards," Int. J. Fatigue, **38**, pp. 169–180.

[145] Lai, J., Lund, T., Rydén, K., Gabelli, A., and Strandell, I., 2012, "The fatigue limit of bearing steels – Part I: A pragmatic approach to predict very high cycle fatigue strength," Int. J. Fatigue, **38**, pp. 155–168.

[146] Sidoroff, C., Girodin, D., Dierickx, P., and Dudragne, G., 2012, "Rolling Contact Fatigue Evaluation of Materials Using the NTN-SNR FB2 Test Rig—A Useful Piece of Equipment for the Qualification of Steels and Steelmakers and for Research," ASTM Bear. Steel Technol., **STP1548**, pp. 1–33.

[147] Bower, A. F., 1988, "The Influence of Crack Face Friction and Trapped Fluid on Surface Initiated Rolling Contact Fatigue Cracks," J. Tribol., **110**(4), p. 704.

[148] Balcombe, R., Fowell, M. T., Olver, A. V., Ioannides, S., and Dini, D., 2011, "A coupled approach for rolling contact fatigue cracks in the hydrodynamic lubrication regime: The importance of fluid/solid interactions," Wear, **271**(5-6), pp. 720–733.

[149] Fletcher, D. I., Hyde, P., and Kapoor, a., 2008, "Modelling and full-scale trials to investigate fluid pressurisation of rolling contact fatigue cracks," Wear, **265**(9-10), pp. 1317–1324.

[150] Donzella, G., Mazzù, A., and Petrogalli, C., 2013, "Failure assessment of subsurface rolling contact fatigue in surface hardened components," Eng. Fract. Mech., **103**, pp. 26–38.

[151] Murakami, Y., Takahashi, K., and Kusumoto, R., 2003, "Threshold and growth mechanism of fatigue cracks under mode II and III loadings," Fatigue Fract. Eng. Mater. Struct., **26**(6), pp. 523–531.

[152] Kudish, I. I., 2000, "Fracture mechanics and modeling of contact fatigue," Encycl. Life Support Syst, 12 pages. Available: www.eolss.net/sample-chapters/c05/e6-167-16.pdf

[153] Kudish, I. I., 2000, "A New Statistical Model of Contact Fatigue," Tribol. Trans., **43**(4), pp. 711–721.

[154] Kudish, I. I., 1991, "Numerical study of a model of fatigue wear and fracture," J. Appl. Mech. Tech. Phys., **32**(3), pp. 427–433.

[155] Murakami, Y., and Beretta, S., 1999, "Small Defects and Inhomogeneities in Fatigue Strength : Experiments , Models and Statistical Implications," Extremes, **2**(2), pp. 123–147.

[156] Gravouil, A., Moes, N., and Belytschko, T., 2002, "Non-planar 3D crack growth by the extended finite element and level sets?Part II: Level set update," Int. J. Numer. Methods Eng., **53**(11), pp. 2569–2586.

[157] Moes, N., Gravouil, A., and Belytschko, T., 2002, "Non-planar 3D crack growth by the extended finite element and level sets?Part I: Mechanical model," Int. J. Numer. Methods Eng., **53**(11), pp. 2549–2568.

[158] Ribeaucourt, R., Baietto-Dubourg, M.-C., and Gravouil, A., 2007, "A new fatigue frictional contact crack propagation model with the coupled X-FEM/LATIN method," Comput. Methods Appl. Mech. Eng., **196**(33-34), pp. 3230–3247.

[159] Raje, N., Sadeghi, F., Rateick, R. G., and Hoeprich, M. R., 2008, "A Numerical Model for Life Scatter in Rolling Element Bearings," J. Tribol., **130**(1), p. 011011.

[160] Jalalahmadi, B., and Sadeghi, F., 2010, "A Voronoi FE Fatigue Damage Model for Life Scatter in Rolling Contacts," J. Tribol., **132**(2), p. 021404.

[161] Noyel, J. P., Ville, F., and Jacquet, P., 2014, "Development of a granular cohesive model for rolling contact fatigue analysis: investigations on material loading," STLE 69th Annual Meeting & Exhibition, May 18-22, 2014, Lake Buena Vista, FL, USA, extended abstract,3 pages.

[162] Errichello, R., Budny, R., and Eckert, R., 2013, "Investigations of Bearing Failures Associated with White Etching Areas (WEAs) in Wind Turbine Gearboxes," Tribol. Trans., **56**(6), pp. 1069–1076.

[163] Evans, M.-H., 2012, "White structure flaking (WSF) in wind turbine gearbox bearings: effects of 'butterflies' and white etching cracks (WECs)," Mater. Sci. Technol., **28**(1), pp. 22–3.

[164] Stadler, K., and Studenrauch, A., 2013, "Premature bearing failures in wind gearboxes and white etching cracks (WEC)," SKF Evol., **March**, 7 pages.
Available: evolution.skf.com/premature-bearing-failures-in-wind-gearboxes-and-white-etching-cracks-wec/

[165] Luyckx, J., 2011, "Hammering Wear Impact Fatigue Hypothesis WEC/irWEA failure mode on roller bearings," NREL - Gearbox Reliability Collaborative, February 10-12, 2011, Argonne, IL, USA, 86 slides.

[166] Luyckx, J., 2011, "WEC failure mode on roller bearings From observation via analysis to understanding and an industrial solution," VDI Wissenforum, October 12-13, 2011, Baden-Baden, Germany, 28 slides.

[167] Holweger, W., 2011, "Influence on bearing life by new material phenomena," NREL - Wind Turbine Tribology Seminar, November 15-17, 2011, Broomfield, CO, USA, 38 slides. Available: http://www.nrel.gov/wind/pdfs/day2_sessioniv_4_schaeffler_holweger.

[168] Mikami, H., and Kawamura, T., 2007, "Influence of Electrical Current on Bearing Flaking Life," SAE Technical Paper Series, **2007-01-0113**, 7 pages.

[169] Standard ISO 281:2007, Rolling beargins - Dynamic load ratings and rating life.

[170] Becker, P. C., 1981, "Microstructural changes around non-metallic inclusions caused by rolling-contact fatigue of ball-bearing steels," Met. Technol., **8**(1), pp. 234–243.

[171] Tsushima, N., 1993, "Rolling contact fatigue and fracture toughness of roling element bearing materials," JSME Int. journal. Ser. 3, Vib. Control Eng. Eng. Ind., **36**, pp. 1–8.

[172] Tamada, K., and Tanaka, H., 1996, "Occurrence of brittle flaking on bearings used for automotive electrical instruments and auxiliary devices," Wear, **199**(2), pp. 245–252.

[173] Hiraoka, K., Nagao, M., and Isomoto, T., 2007, "Study on Flaking Process in Bearings by White Etching Area Generation," ASTM Bear. Steel Technol., **STP1465**, pp. 234–243.

[174] Kino, N., 2003, "The influence of hydrogen on rolling contact fatigue life and its improvement," JSAE Rev., **24**(3), pp. 289–294.

[175] Hirai, E., Okuhata, M., Kino, N., Otani, K., and Furukawa, T., 2003, "Rolling bearing," United States Patent, **US 2003/0165279** A1, September, 2003, 28 pages.

[176] Harada, H., Mikami, T., Shibata, M., Sokai, D., Yamamoto, A., and Tsubakino, H., 2005, "Microstructural Changes and Crack Initiation with White Etching Area Formation under Rolling/Sliding Contact in Bearing Steel," ISIJ Int., **45**(12), pp. 1897–1902.

[177] Vegter, R. H., Slycke, J. T., Beswick, J., and Dean, S. W., 2010, "The Role of Hydrogen on Rolling Contact Fatigue Response of Rolling Element Bearings," J. ASTM Int., **7**(2), p. 102543.

[178] Gegner, J., 2011, "The Bearing Axial Cracks Root Cause Hypothesis of Frictional Surface Crack Initiation and Corrosion Fatigue Driven Crack Growth," NREL - Wind Turbine Tribology Seminar, November 15-17, 2011, Broomfield, CO, USA, 110 slides. Available: http://www.nrel.gov/wind/pdfs/day2_sessioniv_2_skf_gegner.pdf

[179] Gegner, J., and Nierlich, W., 2011, "Hydrogen Accelerated Classical Rolling Contact Fatigue and Evaluation of the Residual Stress Response," Mater. Sci. Forum, **681**, pp. 249–254.

[180] Fujita, S., Mitamura, N., and Murakami, Y., 2005, "Research of New Factors Affecting Rolling Contact Fatigue Life," World Tribology Congress III, Volume 2, ASME, pp. 73–74.

[181] Uyama, H., Yamada, H., Hidaka, H., and Mitamura, N., 2011, "The Effects of Hydrogen on Microstructural Change and Surface Originated Flaking in Rolling Contact Fatigue," Tribol. Online, **6**(2), pp. 123–132.

[182] H. Uyama, 2011, "The Mechanism of White Structure Flaking In Rolling Bearings," NREL - Wind Turbine Tribology Seminar, November 15-17, 2011, Broomfield, CO, USA, 37 slides.
Available: http://www.nrel.gov/wind/pdfs/day2_sessioniv_1_nsk_uyama.pdf

[183] Tamada, K., Tanaka, H., and Tsushima, N., 1998, "A New Type of Flaking Failure in Bearings for Electrical Instruments of Automotive Engines," ASTM Bear. Steel Technol., **STP1327**, pp. 167–185.

[184] Kohara, M., Kawamura, T., and Egami, M., 2006, "Study on Mechanism of Hydrogen Generation from Lubricants," Tribol. Trans., **49**(1), pp. 53–60.

[185] Umeda, A., Tsutomu, T., and Ihata, K., 2009, "Rolling bearing incorporated in auxiliary device for internal combustion engine," United States Patent, **US 7.618.193 B2**, November 2009 22 pages.

[186] Ruellan, A., Ville, F., Kleber, X., Burnet, C., Liatard, B., and Cavoret, J., 2014, "Understanding White Etching Cracks in Rolling Element Bearings: Reproduction and Influent Tribochemical Drivers," STLE 69th Annual Meeting & Exhibition, May 18-22, 2014, Lake Buena Vista, FL, USA, 12 slides.

[187] "Wind Turbine Panel Discussion," STLE 68th Annual Meeting & Exhibition, May 5-9, 2013, Detroit, MI, USA.

[188] Evans, M.-H., Wang, L., Jones, H., and Wood, R. J. K., 2013, "White etching crack (WEC) investigation by serial sectioning, focused ion beam and 3-D crack modelling," Tribol. Int., **65**(2), pp. 146–160.

[189] Iso, K., Yokouchi, A., and Takemura, H., 2005, "Research Work for Clarifying the Mechanism of White Structure Flaking and Extending the Life of Bearings," SAE Tech. Pap., **2005-01-18**, pp. 1–12.

[190] Stadler, K., 2014, "Premature wind gearbox bearing failures \& (not by) white etching cracks," NREL - Gearbox Reliability Collaborative, February 10-12, 2014, Golden, CO, USA, 22 slides. Available: http://www.nrel.gov/wind/grc/meeting_grc.html

[191] Liu, W., 2014, "The failure analysis of the repeat geartooth breakage in a 40MW steam turbine load gearbox and the butterfly in the carburized case," Eng. Fail. Anal, **46**, pp. 9-17.

[192] Holweger, W., 2014, "Progresses in solving White etching crack phenoma," NREL - Gearbox Reliability Collaborative, February 10-12, 2014, Golden, CO, USA, 45 slides. Available: http://www.nrel.gov/wind/grc/meeting_grc.html

[193] Pohrer, B., Holweger, W., Korth, Y., Wolf, M., and Goss, M., 2013, "In situ IR-Spektroskopie an elektrisch beanspruchten Wälzlagern für White Etching Crack-Untersuchungen," GfT - Gesellsschaft fur Tribologie - Tribologie-Fachtagung, pp. 1–10.

[194] Imai, Y., Endo, T., Daming, D., and Yamamoto, Y., 2010, "Study on Rolling Contact Fatigue in Hydrogen Environment at a Contact Pressure below Basic Static Load Capacity," Tribol. Trans., **53**(5), pp. 764–770.

[195] Matsumoto, Y., Murakami, Y., and Oohori, M., 2002, "Rolling Contact Fatigue Under Water-Infiltrated Lubrication," ASTM Bear. Steel Technol., **STP1419**, pp. 226–243.

[196] Szost, B. a., Vegter, R. H., and Rivera-Díaz-del-Castillo, P. E. J., 2013, "Developing bearing steels combining hydrogen resistance and improved hardness," Mater. Des., **43**, pp. 499–506.

[197] Uyama, H., and Yamada, H., 2013, White Structure Flaking in Rolling Bearings for Wind Turbine Gearboxes, AGMA Technical Paper, **13FTM15**, 12 pages.

[198] Evans, M.-H., Richardson, A. D., Wang, L., Wood, R. J. K., and Anderson, W. B., 2014, "Confirming subsurface initiation at non-metallic inclusions as one mechanism for white etching crack (WEC) formation," Tribol. Int., **75**, pp. 87–97.

[199] Evans, M.-H., Richardson, A. D., Wang, L., and Wood, R. J. K., 2013, "Effect of hydrogen on butterfly and white etching crack (WEC) formation under rolling contact fatigue (RCF)," Wear, **306**(1-2), pp. 226–241.

[200] Evans, M.-H., Richardson, A. D., Wang, L., and Wood, R. J. K., 2013, "Serial sectioning investigation of butterfly and white etching crack (WEC) formation in wind turbine gearbox bearings," Wear, **302**(1-2), pp. 1573–1582.

[201] Evans, M. H., 2013, "White Structure Flaking Failure in Bearings under Rolling Contact Fatigue," PhD Thesis, nCATS, University of Southampton, 234 pages.

[202] Bader, N., Wittek, E. C., and Poll, P. G., 2014, "Tribological Properties of Fuel Economy Gearbox Oils," STLE 69th Annual Meeting & Exhibition, May 18-22, 2014, Lake Buena Vista, FL, USA, 29 slides.

[203] Roffey, P., and Davies, E. H., 2014, "The generation of corrosion under insulation and stress corrosion cracking due to sulphide stress cracking in an austenitic stainless steel hydrocarbon gas pipeline," Eng. Fail. Anal., **44**, pp. 148–157.

[204] Hamada, H., and Matsubara, Y., 2006, "The Influence of Hydrogen on Tension-Compression and Rolling Contact Fatigue Properties of Bearing Steel," NTN Tech. Rev., **74**, pp. 54–61.

[205] Querlioz, E., Ville, F., Lenon, H., and Lubrecht, T., 2007, "Experimental investigations on the contact fatigue life under starved conditions," Tribol. Int., **40**(10-12), pp. 1619–1626.

[206] Cantley, R. E., 1977, "The Effect of Water in Lubricating Oil on Bearing Fatigue Life," A S L E Trans., **20**(3), pp. 244–248.

[207] Schatzberg, P., and Felsen, I. M., 1968, "Effects of water and oxygen during rolling contact lubrication," Wear, **12**(5), pp. 331–342.

[208] Schatzberg, P., 1971, "Inhibition of Water-Accelerated Rolling-Contact Fatigue," J. Lubr. Technol., **93**(2), p. 231.

[209] Magalhaes, J. F., Ventsel, L., and Macdonald, D. D., 1999, "Environmental effects on pitting corrosion of AISI 440C ball bearing steels : Experimental results," STLE Lubr. Eng., **55**(6), pp. 36–41.

[210] Sullivan, J. L., and Middleton, M. R., 1985, "The Pitting and Cracking of SAE 52100 Steel in Rolling/Sliding Contact in the Presence of an Aqueous Lubricant," A S L E Trans., **28**(4), pp. 431–438.

[211] Barnes, M., 2011, "Mixing Oil and Water : A Recipe for Downtime !," Reliabilityweb.com, p. 3. Available: http://reliabilityweb.com/index.php/articles/mixing_oil_and_water/

[212] Ramasamy, K., 200, "Hydrogen Production From Used Lubricating Oils", Catalysis Today, **129**(3-4), pp. 365-371.

[213] Lea-langton, A., Giannakeas, N., Rickett, G. L., Dupont, V., and Twigg, M. V, 2010, "Waste lubricating oil as a source of hydrogen fuel using chemical looping steam reforming," SAE Int. J. Fuels Lubr., **3**(2), pp. 810–818.

[214] Schatzberg, P., and Felsen, I. M., 1969, "Influence of Water on Fatigue-Failure Location and Surface Alteration During Rolling-Contact Lubrication," J. Lubr. Technol., **91**(2), p. 301.

[215] Ciruna, J. A., and Szieleit, H. J., 1973, "The effect of hydrogen on the rolling contact fatigue life of AISI 52100 and 440C steel balls," Wear, **24**(1), pp. 107–118.

[216] Kanezaki, T., Narazaki, C., Mine, Y., Matsuoka, S., and Murakami, Y., 2008, "Effects of hydrogen on fatigue crack growth behavior of austenitic stainless steels," Int. J. Hydrogen Energy, **33**(10), pp. 2604–2619.

[217] Fontana, M. G., and Staehle, R. W., 1975, Stress-Corrosion Cracking of Metallic Materials. Part III. Hydrogen Entry and Embrittlement in Steel, NTIS Report, **ADA010 265**, 191 pages. Available: oai.dtic.mil/oai/oai?verb=getRecord&metadataPrefix=html&identifier=ADA010265

[218] Lunarska, E., and Samatowicz, D., 2000, "The hydrogen-induced modification of the properties of the metal surface coated with oil and lubricant," Tribol. Int., **33**(7), pp. 491–499.

[219] Ray, D., Vincent, L., Coquillet, B., Guirandenq, P., Chene, J., and Aucouturier, M., 1980, "Hydrogen embrittlement of a stainless ball bearing steel," Wear, **65**(1), pp. 103–111.

[220] Fujita, S., Matsuoka, S., Murakami, Y., and Marquis, G., 2010, "Effect of hydrogen on Mode II fatigue crack behavior of tempered bearing steel and microstructural changes," Int. J. Fatigue, **32**(6), pp. 943–951.

[221] Walton, H. W., 2000, "Ubiquitous Hydrogen," ASM, Heat Treating: Porceedings of the 19th Society Conference, pp. 558–564.

[222] Coudreuse, L., Brass, A. M., and Chêne, J., 2000, "Fragilisation des aciers par l ' hydrogène : mécanismes," Tech. l'ingénieur, **M175**, 12 pages.

[223] Oriani, R. A., 1987, "Hydrogen—The Versatile Embrittler," Corrosion, **43**(7), pp. 390–397.

[224] Barnoush, A., 2011, "Hydrogen embrittlement," Thesis, Saarland University, 61 pages.

[225] Desjardins, D., and Oltra, R., 1992, Corrosion sous contrainte: phénomenologie et mécanismes, Bombannes, Les Editions de Physique, 870 pages. ISBN: 9782868831551.

[226] Ruo, P., and Olver, A. V, 2007, "Hydrogen in lubricated contact," Proceedings of the First PhD Conference 19-23 February 2007, Ostravice, Czech republic, 7 pages.

[227] Otsuka, T., Hanada, H., Nakashima, H., Sakamoto, K., Hayakawa, M., Hashizume, K., and Sugisaki, M., 2005, "Observation of hydrogen distribution around non-metallic inclusions in steels with tritium microautoradiography," Fusion Sci. Technol., **48**(1), pp. 708–711.

[228] Otsu, T., Tanaka, H., Ohnishi, K., and Sugimura, J., 2011, "Simple Experiment on Permeation of Hydrogen into Steel in Cyclic Contact," Tribol. Online, **6**(7), pp. 311–316.

[229] Tanimoto, H., Tanaka, H., and Sugimura, J., 2011, "Observation of Hydrogen Permeation into Fresh Bearing Steel Surface by Thermal Desorption Spectroscopy," Tribol. Online, **6**(7), pp. 291–296.

[230] Coudreuse, L., Chêne, J., and Brass, A. M., 2000, "Fragilisation des aciers par l ' hydrogène : étude et prévention," Tech. l'ingénieur, **M175**, pp. 1–24.

[231] Dommarco, R. C., Kozaczek, K. J., Bastias, P. C., Hahn, G. T., and Rubin, C. a., 2004, "Residual stresses and retained austenite evolution in SAE 52100 steel under non-ideal rolling contact loading," Wear, **257**(11), pp. 1081–1088.

[232] Murakami, Y., and Matsuoka, S., 2010, "Effect of hydrogen on fatigue crack growth of metals," Eng. Fract. Mech., **77**(11), pp. 1926–1940.

[233] Dowson, D., and Higginson, G. R., 1977, Elasto-hydrodynamic lubrication, Pergamon Press, 235 pages.

[234] Damiens, B., Lubrecht, a. a., and Cann, P. M., 2004, "Influence of Cage Clearance on Bearing Lubrication," Tribol. Trans., **47**(1), pp. 2–6.

[235] Ayel, J., 1996, "Lubrifiants: propriétés et caractéristiques," Tech. l'Ingenieur, **B5340**(Tribologie), p. 45.

[236] Coates, J., 2000, "Interpretation of Infrared Spectra , A Practical Approach Interpretation of Infrared Spectra , A Practical Approach," Encycl. Anal. Chem., pp. 10815–10837.

[237] Dowson, D., Taylor, C. M., and Xu, H., 1991, "Elastohydrodynamic lubrication of elliptical contacts with spin and rolling," Proc. Inst. Mech. Eng. Part C - J. Mech. Eng. Sci., **205**(33), pp. 165–174.

[238] Damiens, B., 2003, "Modélisation de la lubrification sous-alimentée dans les contacts élastohydrodynamiques elliptiques," PhD Thesis, Laboratoire de Mécanique des Contacts et des Structures, INSA de Lyon, 145 pages.

[239] Chevalier, F., Lubrecht, A. A., Cann, P. M. E., Colin, F., and Dalmaz, G., 1998, "Film Thickness in Starved EHL Point Contacts," J. Tribol., **120**(1), p. 126.

[240] Ali, F., Křupka, I., and Hartl, M., 2013, "An Approximate Approach to Predict the Degree of Starvation in Ball–Disk Machine Based on the Relative Friction," Tribol. Trans., **56**(4), pp. 681–686.

[241] Uyama, H., and Yamada, H., 2014, "White Structure Flaking in Rolling Bearings for Wind Turbine Gearboxes," Wind System, **May**, pp. 14–25. Available:

http://windsystemsmag.com/article/detail/619/white-structure-flaking-in-rolling-bearings-for-wind-turbine-gearboxes

[242] Meheux, M., 2009, "Influence des additifs de lubrification sur la formation des tribofilms , le coefficient de frottement et la durée de vie en fatigue des roulements." PhD Thesis, Laboratoire de Mécanique des Contacts et des Structures, INSA de Lyon, 156 pages.

[243] Nevshupa, R. a., de Segovia, J. L., and Roman, E., 2005, "Surface-induced reactions of absorbed hydrogen under mutual mechanical forces," Vacuum, **80**(1-3), pp. 241–246.

[244] Newlands, C., Olver, A., and Brandon, N., 2003, "Gaseous evolution of hydrogen from hydrocarbon oil and grease lubricated contacts," Tribol. Res. Des. Eng. Syst., **41**(Proceedings of the 29th Leeds-Lyon Symposium on Tribology), pp. 719–726.

[245] Lu, R., Minami, I., Nanao, H., and Mori, S., 2007, "Investigation of decomposition of hydrocarbon oil on the nascent surface of steel," Tribol. Lett., **27**(1), pp. 25–30.

[246] Swets, D. E., and Franck, R. C., 1961, "Hydrogen from a Hydrocarbon Lubricant Absorbed by Ball Bearings," Trans. Metall. Soc. AIME, **221**, pp. 1082–1083.

[247] Strandell, I., Fajers, C., and Lund, T., 2010, "Corrosion - one root cause for premature bearing failures," 37th Leeds-Lyon Symposium on Tribology, September 7-10, 2010, Leeds, UK, 17 slides.

[248] Lu, R., Nanao, H., Kobayashi, K., Kubo, T., and Mori, S., 2010, "Effect of Lubricant Additives on Tribochemical Decomposition of Hydrocarbon Oil on Nascent Steel Surfaces," J. Japan Pet. Inst., **53**(1), pp. 55–60.

[249] Kadin, Y., 2013, "Modeling of Hydrogen Transport in Rolling Contact Fatigue Conditions," Procedia Eng., **66**, pp. 415–424.

[250] Stadler, K., and Baum, J., 2014, "Premature white etching crack bearing failures in wind gearboxes," STLE 69th Annual Meeting & Exhibition, May 18-22, 2014, Lake Buena Vista, FL, USA, extended abstract, 5 pages.

Appendix

A. Contact theory

Hertz elliptical contact pressure and deformation

Given the equivalent geometry (R'_x, R'_y) and the material properties (E, ν) of two contacting smooth bodies (**Fig. 1.8**) and considering that the strains remain within the elastic limit and that contact area remains small versus the dimensions of the bodies, the maximum contact pressure P_H and maximum deformation δ for a static and dry *elliptical contact* of minor semi-axis *a* and major semi-axis *b* under a static normal load N can be approximated by the following equations. These equations are expressed similarly to [17,38,46] in agreement with [43].

$$P_H = \frac{3N}{2\pi ab} \text{ at x=0 and y=0}$$

$$\delta = F^{\#}\left(\frac{9}{2E^{\#}R^*}\left(\frac{Nb}{2\pi aE^*}\right)^2\right)^{1/3} \text{ at x=0 and y=0}$$

With:

$$\frac{1}{E^*} = \frac{1-\nu_1^2}{E_1} + \frac{1-\nu_2^2}{E_2}$$

$$\frac{1}{R^*} = \frac{1}{R'_x} + \frac{1}{R'_y}$$

$$a = \left(\frac{3E^{\#}NR^*}{\pi kE^*}\right)^{1/3}$$

*k being the ellipse ratio of the contact area (***Fig. 1.9***):*

$$k = \frac{b}{a} \approx \left(\frac{R'_y}{R'_x}\right)^{2/\pi}$$

$E^{\#}$ and F being the elliptical integrals approximated by:

$$E^{\#} \approx 1 + \frac{(\pi/2 - 1)}{R'_y/R'_x}$$

$$F^{\#} \approx \pi/2 + (\pi/2 - 1)\ln(R'_y/R'_x)$$

The pressure at any point (x,y) on the contact area can be expressed as follows, thus giving a parabolic evolution along the contact axis:

$$P(x,y) = P_H\left(1 - \left(\frac{x}{a}\right)^2 - \left(\frac{y}{b}\right)^2\right)^{1/2}$$

Similarly for a *line contact* of width *l* in the y direction and of equivalent radius $R^*=R'_x$:

$$P_H = \frac{2N}{\pi l a} \text{ at x=0}$$

$$\delta = (\frac{1}{4} + \frac{1}{2}\ln 2\,)\frac{a^2}{R^*} \text{ at x=0}$$

With:

$$a = \left(\frac{4NR^*}{\pi l E^*}\right)^{1/2}$$

It should be emphasized that for roller bearings, depending on the roller crown and roller end profiles, some edge effects occur and lead to significant pressure spikes in [17].

Hamrock and Dowson film thickness equations for elliptical contacts

The expressions of the minimum and central film thickness (h_{min} and h_c) developed here according to [62,66,68–72] and considering an isothermal EHL contact under the specific assumptions:

- The contact is fully flooded by lubricant, e.g. not under starvation
- The contact surfaces are perfectly smooth
- The contact stresses remain within the elastic range
- The lubricant film is considered as *thin film,* e.g. the mean film thickness is smaller by several order or magnitudes than the maximum elastic deformation δ of the contacting bodies, so that there are no velocity or pressure gradient other than along the z axis

The following dimensionless parameters were defined to take these into account [62]:

$$H_c^* = \frac{h_c}{R_x} \text{ and } H_{min}^* = \frac{h_{min}}{R_x}$$

$$G^* = 2\alpha^* E^* \text{ and } W^* = \frac{N}{2E^* R^{*2}} \text{ and } U^* = \frac{\eta U_r}{2E^* R^*}$$

The following dimensionless central and minimum film thicknesses can then be derived from these parameters [62]:

$$H_c^* = 2.69 U^{*0.67} G^{*0.53} W^{*-0.067}(1 - 0.61e^{-0.73k})$$

$$H_{min}^* = 3.63 U^{*0.68} G^{*0.49} W^{*-0.073}(1 - e^{-0.68k})$$

B. Type of lubricant and formulation

Base stock oils

Most *base stocks oils* can be divided in three categories [18,60,62]:

- *Vegetable oils* extracted from plants. They are currently extensively studied for their biodegradable properties. They are however not yet used in common machinery because of their low durability for high-temperature applications.
- *Mineral oils* extracted from petroleum based stocks. Depending on the nature of the crude oil, the hydrocarbons contained in the base oil can be either mainly paraffinic, naphthenic or aromatic [62] which affects their Viscosity Index (VI, measures the drop in viscosity when temperature rises from 40 to 100°C: low VIs indicates a very viscous oil at low temperatures and very fluid at high temperatures), resistance to oxidation, pour point, flash point, etc. They are used both as oils and in greases. The far most common mineral oils are paraffinic oil.
- *Synthetic or semi-synthetic oils* composed of hydrocarbon fluids synthetized from chemically modified petroleum or nonpetroleum-based stocks with limited and specifically chosen molecular compounds to provide favorable properties. The most commonly used in gearbox lubrication are polyalfaolefins (PAO), polyglycols (PAG), esters and ethers. In the past decades, PAO have stand out by their chemical structures close to the best hydrocarbons found in mineral oils, by their wide viscosity ranges they can achieve with high VI, and by their resistance to thermo-oxidation. In recent years, polar oils as PAG, esters and ethers gained in interest as more and more additives are blended into oils. Indeed, PAO being apolar, they have a very low solvent power, which is detrimental in terms of additives solubility. This is commonly compensated by blending esters in the PAO oils (3 to 15%).

Additive formulations

- *Boundary lubrication additives.* In the most severe lubrication regimes, when surface separation is near non-existent (section 1.2.3.3), these additives tribochemically react with the surfaces to form what has been called protective *tribofilms* on the steel substrate (section 1.2.3.5). There are different types of boundary lubrication additives, fulfilling different functions: *Friction Reducers (FR) and Modifiers (FM)* such as molybdenum dithio-carbamates (MoDTC) are commonly used, due to their capacity to form excellent friction-reducing molybdenum disulfide (MoS2) films on steel surfaces [64]. Similarly, under the high temperatures generated by severe metal-metal contacts, *Extreme Pressure (EP)* additives form friction-reducing metal sulfide films on the substrate that resist to very high loads and prevent surface adhesion and micro-welding [63] The most common EP additive formulation in transmission oils are based on sulfur-phosphorus compounds. EP additives are a particular type of *Anti-Wear (AW)* additives, which define all the very active chemically surface-protecting compounds. One of the most widespread AW additives are zinc dialkyldithiophosphates (ZnDTP), which are also good oxidation inhibitors. Indeed, because of their tribofilm forming capacity, friction-reducing, Extreme-Pressure, Anti-Wear and other boundary lubrication additives often fulfill several roles at once [63,64].

- *Rust and corrosion inhibitors.* These additives are generally named "rust inhibitors" when destined to reduce the humid corrosion of ferrous metals and "corrosion inhibitors" when fighting the acid or sulfur corrosion of non-ferrous metals such as copper alloys [63]. *Rust inhibitors* are polar compounds that act by forming a waterproof film by physical adsorption (physisorption) onto the surfaces. The surfaces thus change from hydrophilic to hydrophobic and are said to be "passivated". The most common rust inhibitors are organometallic detergents such as over-based calcium or magnesium sulfates [63,64]. *Corrosion inhibitors* may either act chemical adsorption (chemisorption) at the surface, or by deactivating corrosive contaminants in the lubricant through the formation of stable chemical compounds [91].
- *Oxidation inhibitors.* As lubricants often operate above 50-60°C, the presence of oxidation inhibitors in lubricants becomes essential to slow down the oxidation of hydrocarbons and other constituents of the lubricant which can cause lubricant thickening and the formation of sludge and deposits [91]. This can be achieved mainly by either deactivating the free radicals present in the lubricant with radical inhibitors, or by passivating the surfaces to reduce the catalytic action of metals (these additives then also act as corrosion inhibitors) [63]. Zinc dithiophosphates (ZnDTC) are therefore often used in engines both as AW additives and oxidation inhibitors.
- *Detergents and dispersants.* The role of these additives is to ensure the cleanliness of the lubricant and of contacting surfaces. *Detergents* prevent deposits from adhering to the surfaces. The three main types of *detergents* are calcium- or magnesium-based alkylsulfonates (very detergent, especially for *over-based calcium sulfonates*, moderately dispersant and also rust inhibitor), alkyl phenates, and alkyl salicylates [64]. *Detergents* can be used with an over-based formulation to combined detergence and corrosion inhibiting properties *Dispersants* maintain insoluble materials (wear debris, external contaminants…) in suspension to avoid agglomeration before being filtered. *Dispersants* are also vital to preserve sedimentation of additives during long stand-still and start/stop conditions. The most widely used types of *dispersants* are alkenyl succinimides and succinate esters.
- *VI improvers.* The viscosity of oils is very sensitive to changes in temperature and may decreased by several magnitudes between cold start and operating temperature. While sufficient viscosities are generally desirable at high temperatures to ensure sufficient film thicknesses (section 1.2.3.3) and therefore prevent wear, excessive viscosities at low temperatures will generate great power losses. *VI improvers* consist in polymers that are increasingly oil-miscible for higher temperatures. As a result, the polymer macromolecules occupy a small volume fraction of the oil at low temperature, and expand progressively as the temperature increases. The friction between the larger polymers results in a significant increase in viscosity of the oil [64].
- *Emulsifiers and Demulsifiers. Emulsifiers* are used to stabilize oil-in-water or water-in-oil emulsions. These compounds exhibit a structure similar to dispersants, with a polar, hydrophilic group and a lipophilic hydrocarbon chain. For applications where water contamination of the lubricant is an issue, *demulsifiers*, such as high molar mass sulfonates are used to create unstable emulsions and therefore separate oil and water.
- *Others:* foam decomposers, Pour Point Depressants (PPDs), tackiness agents, seal anti-swell agents, dyes, etc.

C. Fitting stress estimations

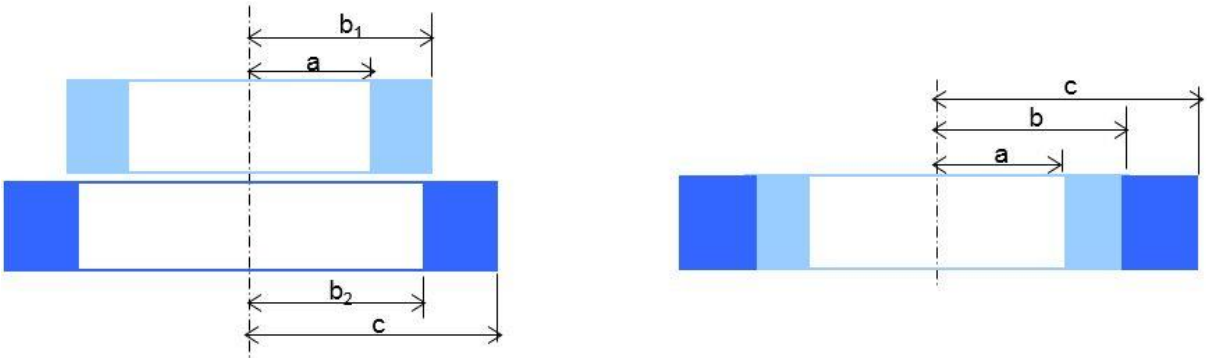

The following equations allow to approximate the stresses induced by fitting a ring on a shaft by the geometry of the above schemes for a given fit value δ=*b1-b2*. The press-fit pressure at the interface P_{fit} is given by:

$$P_{fit} = \frac{\delta}{b\left(\frac{1}{E_2}\left(\frac{b^2+c^2}{c^2-b^2}+\nu_2\right)+\frac{1}{E_1}\left(\frac{a^2+b^2}{b^2-a^2}-\nu_1\right)\right.}$$

Where E and v are the material properties of the respective bodies. In this study, considering a=0, $E_2=E_1=E$ and $v_2=v_1$, P can be expressed:

$$P_{fit} = \frac{\delta E}{b\left(\left(\frac{b^2+c^2}{c^2-b^2}\right)\right)}$$

The circumferential hoop stress σ_{xx} induced inside the ring by the press-fitting pressure at the interface with the shaft decreases as the radius b<r<c of interest increases and can be expressed:

$$\sigma_{xx} = \frac{b^2}{c^2-b^2}\left(1-\frac{c^2}{r^2}\right)P_{fit}$$

These equations have allowed us to estimate the circumferential hoop stresses in the ACBB tests and hoop stress specific TDM specimen in this study, the fit being the measurements of the respective b_1 and b_2 for each case prior to fitting:

RCF test	Fit	Value (µm)	r (mm)	P_{fit} (MPa)	σ_{xx} (MPa)
ACBB	Min	15	16	45	100
	Mean	23	16	70	150
	Max	34	16	105	220
TDM	Measured	60	34.5	95	175

D. ACBB RCF tests

In the following table are provided the details of the 68 ACBB tests deployed during this study.

#	IR	Cage	Load case	Side	Time (h)	Failure	WEC	Comment
1	Turned	Standard	1	Coupling	424	Ball	**yes**	High WEC density
2				Opp	424	Sus	**yes**	
3				Opp	1393	Sus	**yes**	
4				Coupling	1393	IR	**yes**	
5				Coupling	1403	Sus	**yes**	
6				Opp	1403	Sus	**yes**	
7				Coupling	1011	IR	**yes**	
8				Opp	1011	Sus	**yes**	
9				Coupling	1436	IR	**yes**	
10				Opp	1436	Sus	**yes**	
11	Turned	Standard	3	Coupling	340	Sus	no	Radial loading
12				Ext	340	Sus	no	
13				Coupling	340	Sus	no	
14				Ext	340	IR	no	
15	Turned	Standard	4	Coupling	534	Sus	no	Axial loading
16				Ext	534	Sus	no	
17				Coupling	534	Sus	no	
18				Ext	534	Sus	no	
19	Turned	Standard	1	Coupling	20	Creeping	no	Mispositioning
20				Ext	20	Sus	no	
21				Coupling	172	Creeping	no	
22				Ext	172	Sus	no	
23				Coupling	1633	Sus	no	
24				Ext	1633	Sus	no	
25				Ext	1296	Sus	no	
26				Coupling	1296	Sus	no	
27	Turned	Standard	1	Coupling	104	Sus	**yes**	High WEC density **Hydrogen precharged** *section 3.1.1*
28				Ext	104	IR	**yes**	
29				Coupling	156	IR	**yes**	
30				Ext	156	Sus	**yes**	
31				Coupling	110	Sus	**yes**	
32				Ext	110	IR	**yes**	
33				Coupling	123	IR	**yes**	
34				Ext	123	Sus	**yes**	
35				Coupling	168	Sus	**yes**	
36				Ext	168	IR	**yes**	
37	Forged	Oblong	2	Coupling	676	Sus	**yes**	
38				Ext	676	Sus	no	
39				Coupling	749	IR	**yes**	

40				Ext	749	Sus	no	
41				Coupling	225	Sus	no	
42				Ext	225	IR	no	Dent
43				Coupling	582	Sus	no	
44				Ext	582	Cage	no	
45				Coupling	1265	IR	**yes**	
46	Forged	Oblong	1	Ext	1265	Sus	no	
47				Coupling	340	IR	no	Dent
48				Ext	340	Sus	no	
49				Coupling	1540	Sus	no	
50				Ext	1540	Sus	no	
51				Coupling	72	Sus	no	Machining defect
52				Ext	72	Sus	no	
53				Coupling	1500	Sus	no	
54	Forged	Oblong	1	Ext	1500	Sus	no	Aged lubricant A
55				Coupling	1500	Sus	no	
56				Ext	1500	Sus	no	
57				Coupling	1500	Sus	**yes**	
58	Forged	Oblong	1	Ext	1500	Sus	no	New lubricant A
59				Coupling	1500	Sus	no	
60				Ext	1500	Sus	no	
61				Coupling	812	IR	**yes**	High WEC density
62		Oblong		Ext	812	Sus	no	
63				Coupling	1239	IR	no	
64	Forged		2	Ext	1239	Sus	no	
65				Coupling	1435	IR	no	
66		Oblong + Thin bridge		Ext	1435	Sus	no	
67				Coupling	1435	Sus	no	
68				Ext	1435	Sus	no	
		Fig. 4.3	*Table 2-1*	*Fig. 2.2*		*Sus: suspended*		

E. Residual stress assessment

X-Ray difractometer ELPHYSE Set X and dedicated software were used to assess the *surface* residual stresses of ACBB forged and turned IR as well as on a typical disc specimen for the TDM prior to RCF testing.

Specimen	Circumferential position on the raceway					
	0°		120°		240°	
	σ_{res} (MPa)	uncertainty (MPa)	σ_{res} (MPa)	uncertainty (MPa)	σ_{res} (MPa)	uncertainty (MPa)
TDM	-162	31	0	66	-97	43
Turned IR	-504	71	-423	38	-	-
Forged IR	-538	62	-489	62	-	-

F. Steel cleanliness data

Non-metallic inclusion cleanliness rating according to ISO 4967 Method A (worst field for each inclusion type) of the steel rods used to manufacture the forged and turned ACBB .IR

Type	**A**		**B**		**C**		**D**		**DS**
Aspect	**Fine**	**Thick**	**Fine**	**Thick**	**Fine**	**Thick**	**Fine**	**Thick**	**Fine**
Forge	1.0	0	0.5	0	0	0	0.5	0	0
Turned	1.5	0.5	0	0	0	0	0.5	0	0

Group A (sulfide type), group B (aluminate type), group C (silicate type), group D (globular type, usually oxide), group DS (single globular type with D>13 μm)

Details of the length of the type A inclusions numbered in **Fig. 2.5**.

(a) Forged IR			(b) Turned IR		
Number	**Length (μm)**	**Depth (μm)**	**Number**	**Length (μm)**	**Depth (μm)**
1	11.4	262.6	1	2.2	236.8
2	9.7	116.1	2	1.5	110
3	11.1	263.6	3	3.2	153.8
4	14.7	230.7	4	3.1	214.6
5	5.9	268.2	5	1.3	78.7
6	10	258.3	6	1.6	53.9
7	6	147.9	7	1.5	13.6
8	16.5	159	8	2.9	109.6
9	12.7	184.9	9	1.3	83.4
10	15.4	263.6	10	4.6	~80
11	38.3	12.6			
12	32.4	42.7			
13	7.5	6.8			
14	7.1	24.9			
15	7.3	141			

G. Contact kinematics and criteria

a. Dimensionless *P.ΔU* along the contact major axis in mm for various WEC-affected and WEC-free tests from NTN-SNR or the literature

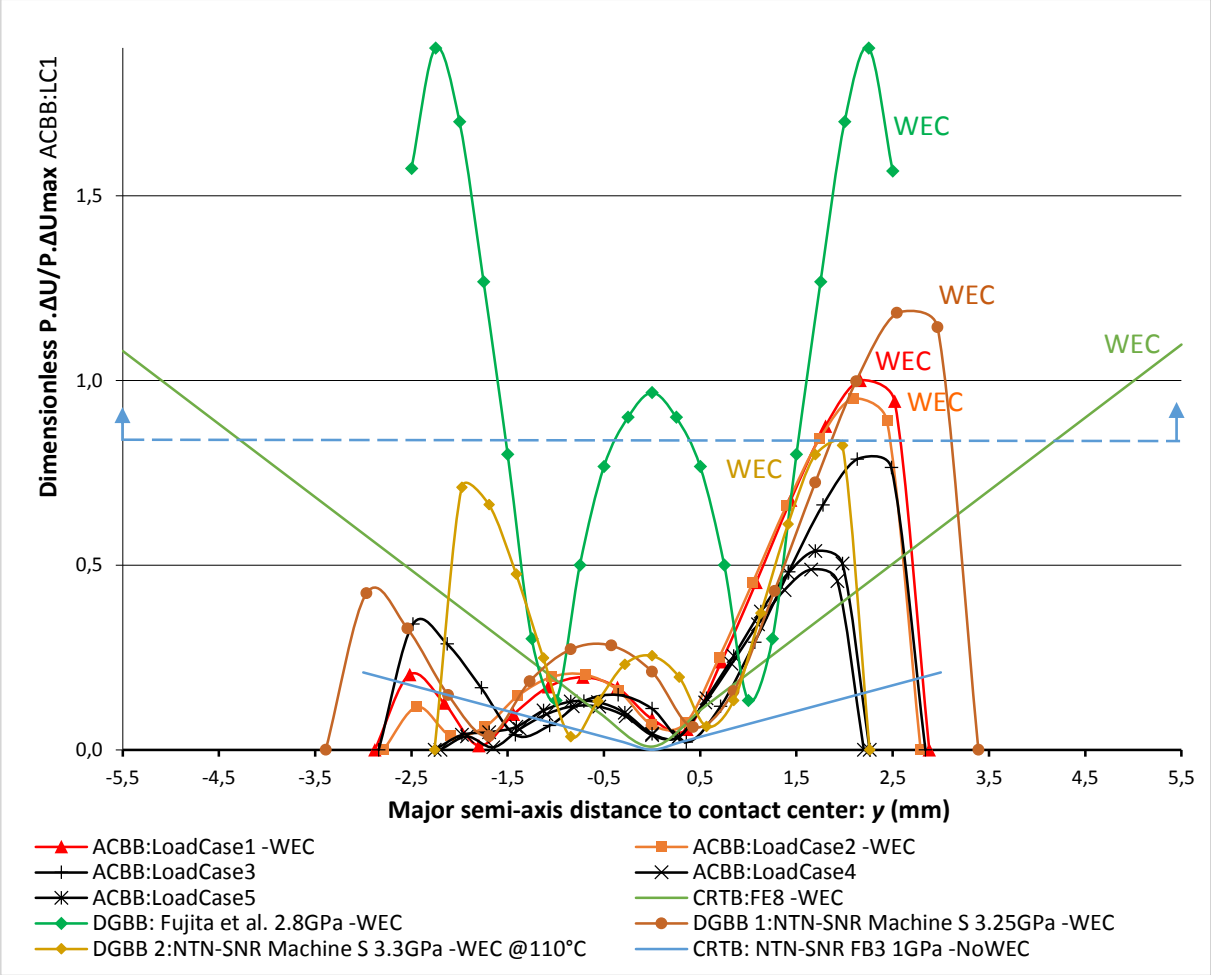

P being the local contact pressure and ⊿U the local slip velocity.
The dashed blue line represents a possible threshold for WEC formation.

a. Dimensionless *P.ΔU* and N.*ΔU* along the contact major axis in mm for various WEC-affected and WEC-free tests and computations for a 3MW wind turbine gearbox planetary Double-SRB or TRB

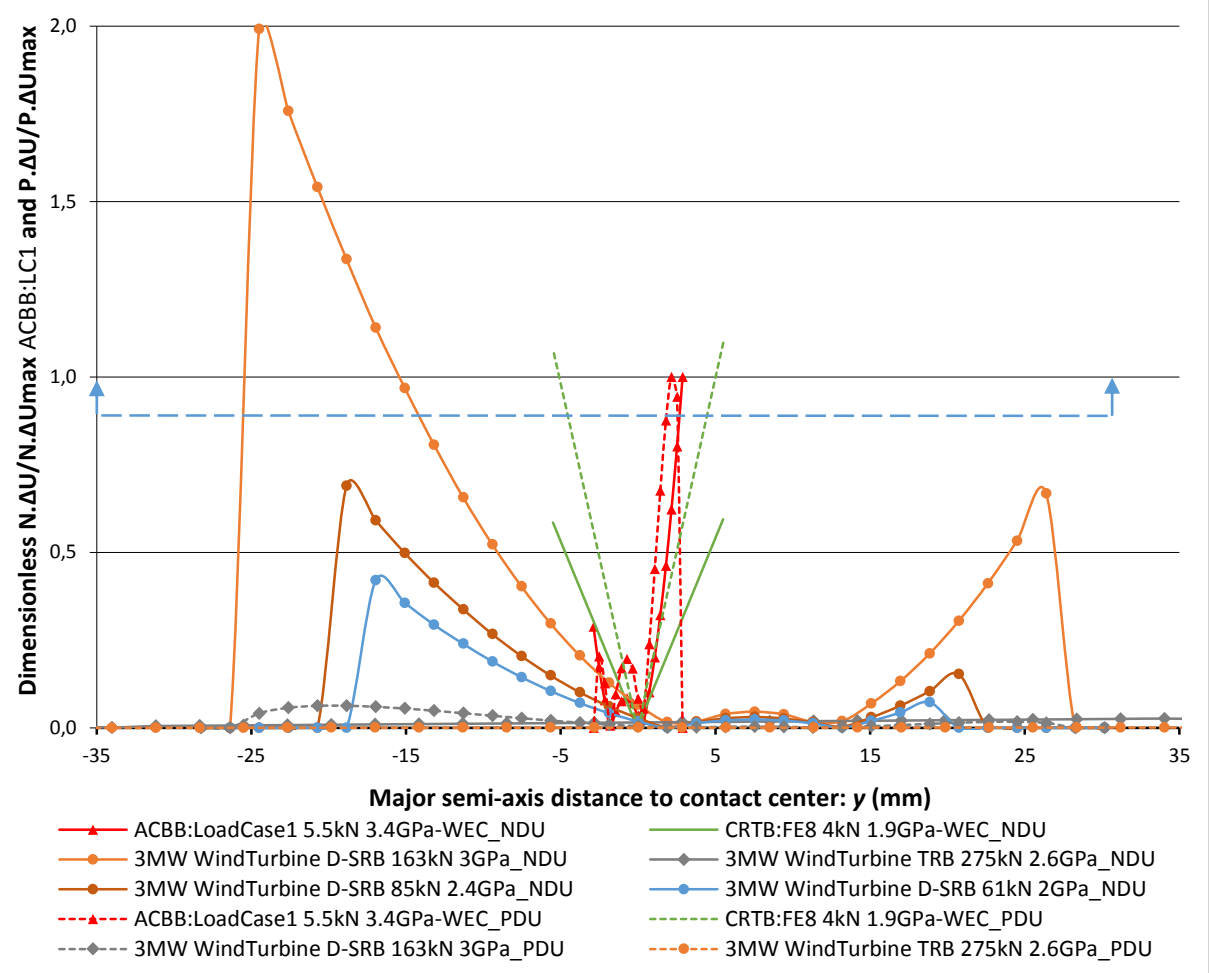

P being the local contact pressure, N the global contact load and ⊿U the local slip velocity.
The dashed blue line represents a possible threshold for WEC formation.
The P⊿U have not been plotted for the additional load conditions of the Double-SRB as the criteria remains low.
The criteria have not been plotted for other Wind Turbine TRB as quasi-no sliding occurs in stationary conditions.

b. Dimensionless *N.ΔU* along the contact major axis in mm for various WEC-affected and WEC-free tests from NTN-SNR or the literature

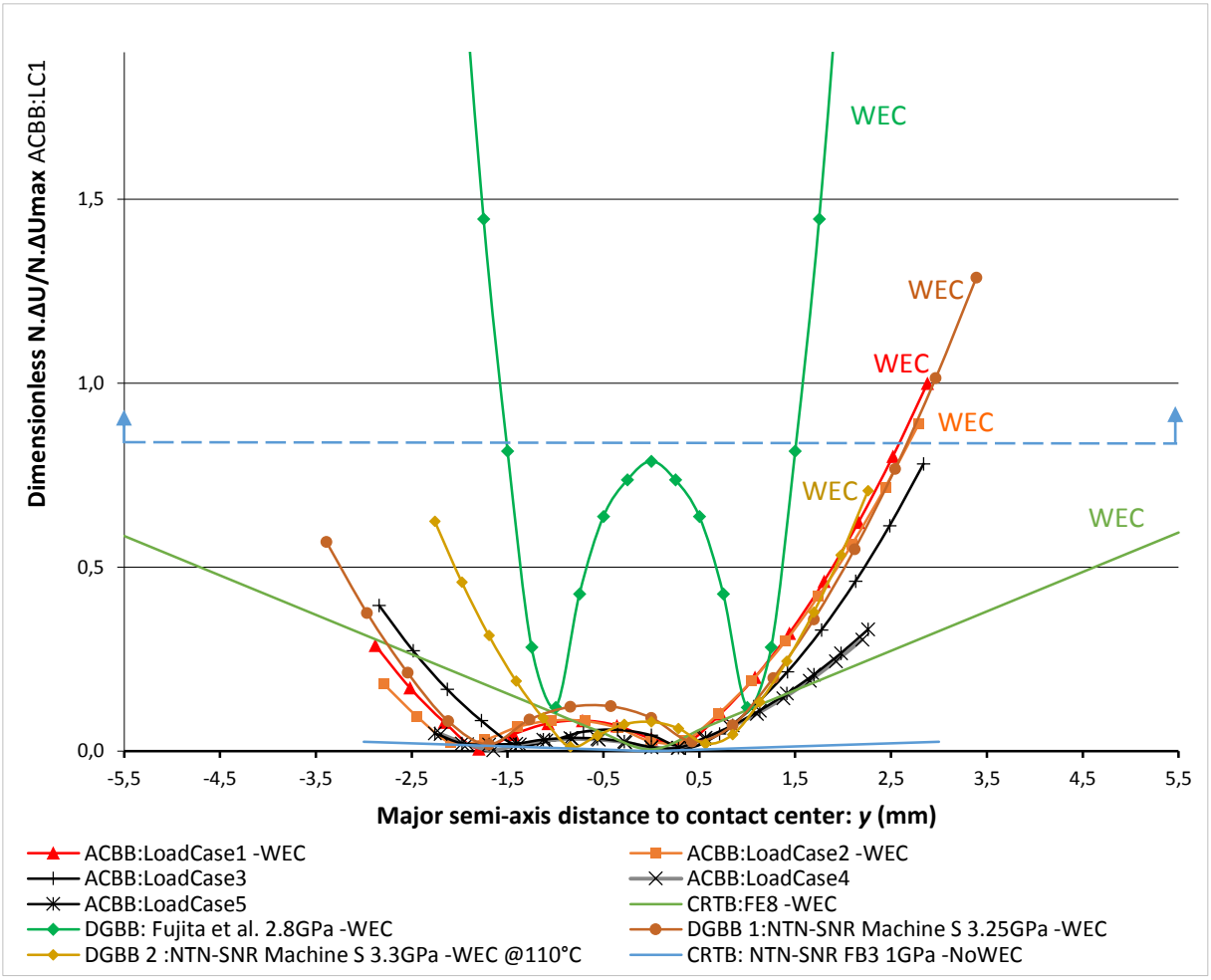

N being the global contact load and ⊿U the local slip velocity.
The dashed blue line represents a possible threshold for WEC formation.

c. Dimensionless $N.\Delta U/\lambda$ along the contact major axis in mm for various WEC-affected and WEC-free tests from NTN-SNR or the literature

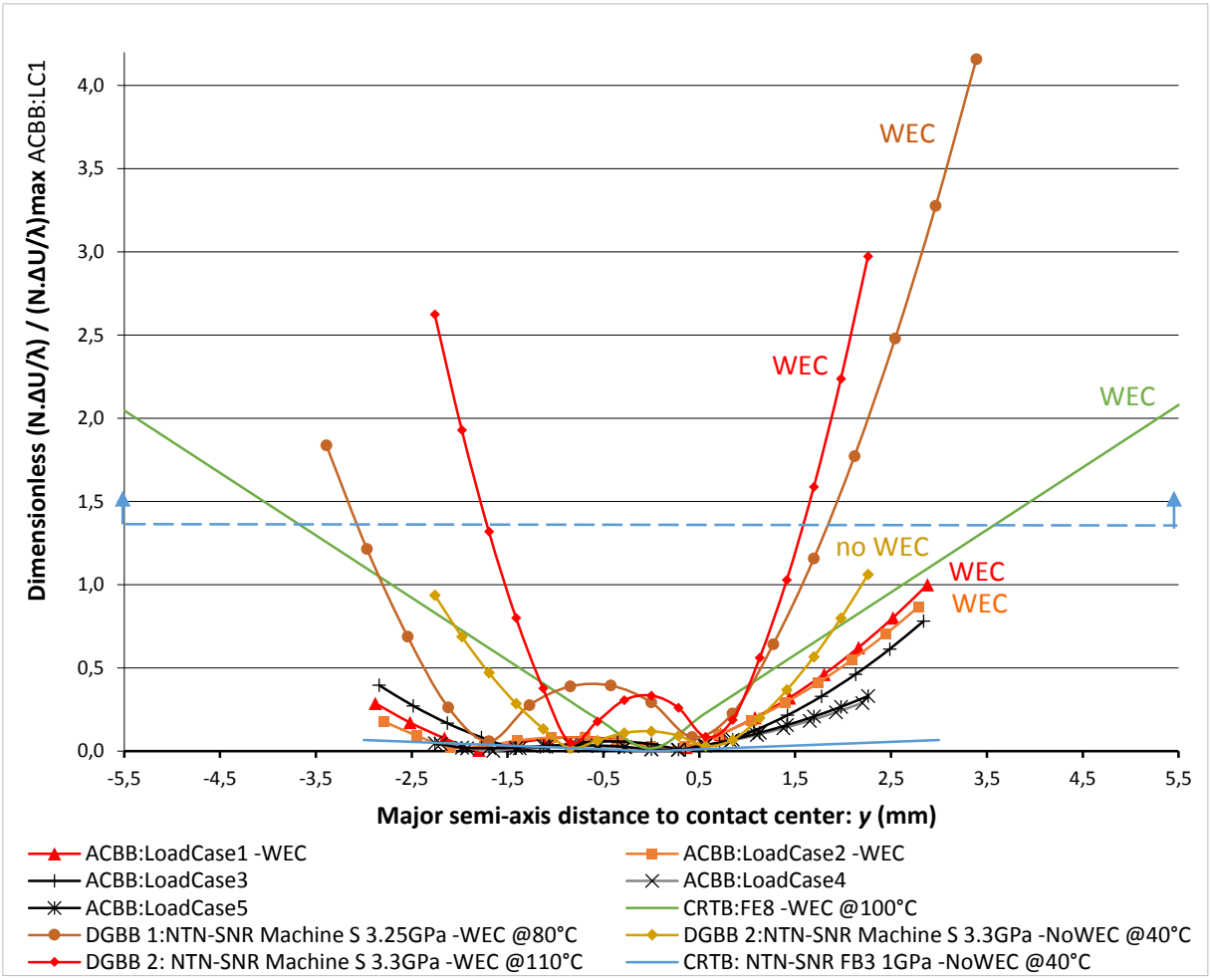

λ being the global contact lubrication parameter, thus accounting for the temperature among others.
Lubrication data is not provided for DGBB of Fujita et al [180].
The dashed blue line represents a possible threshold for WEC formation.

H. TDM RCF tests

The TDM RCF specifications and results are referenced in the following pages.

Ref.	Objective	Ds	Hrs	Cycles	Contact Conditions									Lubrication				Specimen		Results			
					P (GPa)	SRR	Ur (m/s)	hc (m)	λ	PΔU	NΔU	PΔU/λ	NΔU/λ	Oil	θ (°C)	Status	L/h	Type	SRR	Tribofilm	µµcrack	WEC	Wear
TDM01	WEC	High SRR	648	1,2E+08	2	63%	11,6	6,1E-07	17	1,5E+10	6,9E+03	8,4E+08	4,0E+02	A	80	new	Full	Std_R17.5	D	Y	N	N	Y
																		Std_Cyl	F		N	N	N
TDM02	WEC	High SRR	7	1,3E+06	3	63%	11,6	5,6E-07	16	2,2E+10	2,3E+04	1,4E+09	1,5E+03	A	80	aged	Full	Std_Cyl	D	N	N	N	Scuffing
																		Std_R17.5	F		N	N	Scuffing
TDM03	WEC	High SRR	2	2,8E+05	3	43%	11,3	5,6E-07	16	1,4E+10	1,5E+04	9,1E+08	9,7E+02	A	80	aged	Full	Std_Cyl	D	N	N	N	Scuffing
																		Std_R17.5	F		N	N	Scuffing
TDM04	WEC	High SRR	20	3,6E+06	3	30%	11,1	5,6E-07	16	9,9E+09	1,1E+04	6,3E+08	6,7E+02	A	80	aged	Full	Std_Cyl	D	N	N	N	N
																		Std_R17.5	F		N	N	N
TDM05	WEC	High SRR	333	6,1E+07	3	30%	11,1	5,6E-07	16	9,9E+09	1,1E+04	6,3E+08	6,7E+02	A	80	aged	Full	Std_Cyl	D	Y	N	N	N
																		Std_R17.5	F		N	N	N
TDM06	WEC	Hoop stress	167	3,5E+07	3	30%	11,1	5,6E-07	16	9,9E+09	1,1E+04	6,3E+08	6,7E+02	A	80	aged	Full	HoopStress_Cyl	D	Y	N	N	N
																		Std_R17.5	F		N	N	N
TDM07_1_I_a	Microcrack	Dents aligned with offset	17	3,0E+06	3,5	0%	11,0	5,5E-07	15	0,0E+00	0,0E+00	0,0E+00	0,0E+00	A	80	aged	Full	Std_Cyl	-	N	Y	N	N
																		Std_R17.5	-		N	N	N
TDM07_1_I_b	Microcrack	Dents aligned with offset	17	3,1E+06	3,5	7%	11,0	5,5E-07	15	2,5E+09	3,7E+03	1,6E+08	2,4E+02	A	80	aged	Full	Std_Cyl - TDM07_1_I_a	D	Y	Y	N	N
																		Std_R17.5	F		N	N	N
TDM07_1_I_c	Microcrack	Dents aligned with offset	17	2,9E+06	3,5	0%	10,6	5,5E-07	15	0,0E+00	0,0E+00	0,0E+00	0,0E+00	A	80	aged	Full	Std_Cyl - TDM07_1_I_b	-	N	Y	N	N
																		Std_R17.5	-		N	N	N
TDM07_1_II	WEC	High SRR	84	1,7E+07	3,4	30%	11,1	1,0E-06	28	1,1E+10	1,5E+04	4,0E+08	5,4E+02	A	57	aged	Full	Std_Cyl - TDM07_1_I_c	D	Y	Y	N	Y
																		Std_R17.5	F		Y	N	Y
TDM07_2_I_a	Microcrack	Dents aligned with offset	14	2,5E+06	3,5	0%	11,0	5,5E-07	15	0,0E+00	0,0E+00	0,0E+00	0,0E+00	A	80	aged	Full	Std_Cyl	-	N	N	N	N
																		Std_R17.5	-		N	N	N
TDM07_2_I_b	Microcrack	Dents aligned with offset	14	2,4E+06	3,5	7%	11,0	5,5E-07	15	2,5E+09	3,7E+03	1,6E+08	2,4E+02	A	80	aged	Full	Std_Cyl - TDM07_2_I_a	D	N	N	N	N
																		Std_R17.5	F		N	N	N
TDM07_2_II	WEC	High SRR	111	1,7E+07	3,4	30%	11,1	9,0E-07	25	1,1E+10	1,5E+04	4,4E+08	6,0E+02	A	60	aged	Full	Std_Cyl - TDM07_2_I_b	F	Y	N	N	N
																		Std_R17.5	D		Y	N	N
TDM07_3_I_a	Microcrack	Dents aligned with offset	20	3,5E+06	3,5	0%	11,0	5,5E-07	15	0,0E+00	0,0E+00	0,0E+00	0,0E+00	A	80	aged	Full	Std_Cyl	-	N	N	N	N
																		Std_R17.5	-		N	N	N
TDM07_3_I_b	Microcrack	Dents aligned with offset	20	3,4E+06	3,5	7%	11,0	5,5E-07	15	2,5E+09	3,7E+03	1,6E+08	2,4E+02	A	80	aged	Full	Std_Cyl - TDM07_3_I_a	D	N	N	N	N
																		Std_R17.5	F		N	N	N
TDM07_3_II	WEC	High SRR	155	1,2E+07	3,4	30%	5,6	5,7E-07	16	5,6E+09	7,6E+03	3,5E+08	4,7E+02	A	60	aged	Full	Std_Cyl - TDM07_3_I_b	F	Y	N	N	N
																		Std_R17.5	D		Y	N	N
TDM08_01	WEC	Hydrogen precharged	236	2,5E+07	3,4	30%	5,6	5,7E-07	16	5,6E+09	7,6E+03	3,5E+08	4,7E+02	A	60	aged	Full	Std_Cyl_Hydrogen	D	Y	Y	Y	N
																		Std_R17.5	F		N	N	N
TDM08_02	WEC	Hydrogen precharged	230	2,4E+07	3,4	0%	6,4	5,7E-07	16	0,0E+00	0,0E+00	0,0E+00	0,0E+00	A	60	aged	Full	Std_Cyl_Hydrogen	-	N	Y	Y	N
																		Std_R17.5	-		N	N	N
TDM08_03	WEC	Hydrogen precharged	24	2,5E+06	3,4	0%	6,4	5,7E-07	16	0,0E+00	0,0E+00	0,0E+00	0,0E+00	A	60	aged	Full	Std_Cyl_Hydrogen	-	N	Y	Y	N
																		Std_R17.5	-		N	N	N
TDM09_01	Microcrack	Mixed lubrication - traction	134	2,5E+07	2	7%	-11,0	1,3E-06	38	1,4E+09	6,9E+02	3,8E+07	1,8E+01	A	50	aged	Full	Std_Cyl	D	N	N	N	N
																		Std_R17.5	F		N	N	N
TDM09_02	Microcrack	Mixed lubrication - traction	139	2,6E+07	2	7%	-11,0	1,3E-06	38	1,4E+09	6,9E+02	3,8E+07	1,8E+01	A	50	aged	1/4	Std_Cyl	D	N	N	N	N
																		Std_R17.5	F		N	N	N
TDM09_03	Microcrack	Mixed lubrication - traction	5	9,8E+05	2	7%	-11,0	1,3E-06	38	1,4E+09	6,9E+02	3,8E+07	1,8E+01	A	50	new	4	Std_Cyl	D	N	N	N	N
																		Std_R17.5	F		N	N	N
TDM09_04	Microcrack	Mixed lubrication - traction	111	1,9E+07	2	7%	-11,0	1,3E-06	38	1,4E+09	6,9E+02	3,8E+07	1,8E+01	A	50	new	8	Std_Cyl	D	Y	N	N	Y
																		Std_R17.5	F		Y	N	Y
TDM09_05	Microcrack	Mixed lubrication - traction	111	1,9E+07	2	7%	-11,0	1,3E-06	38	1,4E+09	6,9E+02	3,8E+07	1,8E+01	A	50	aged	10	Std_Cyl	D	N	N	N	N
																		Std_R17.5	F		N	N	N
TDM09_06	Microcrack	Mixed lubrication - traction	111	1,9E+07	2	7%	-11,0	1,3E-06	38	1,4E+09	6,9E+02	3,8E+07	1,8E+01	A	50	aged	8,5	Std_Cyl	D	Y	N	N	N
																		Std_R17.5	F		N	N	N
TDM09_07	Microcrack	Mixed lubrication - traction	172	3,0E+07	1,9	7%	-11,0	1,3E-06	38	1,4E+09	6,9E+02	3,6E+07	1,8E+01	A	50	aged	7,9	Std_Cyl	D	Y	N	N	Y
																		Std_R17.5	F		Y	N	Y
TDM09_08	Microcrack	Mixed lubrication - traction	54	9,4E+06	1,95	7%	-11,0	1,3E-06	38	1,4E+09	6,9E+02	3,7E+07	1,8E+01	A	50	aged	7,8	Std_Cyl - TDM09_05	D	Y	N	N	Y
																		Std_R17.5 - TDM09_05	F		Y	N	Y
TDM09_09	Microcrack	Mixed lubrication - traction	11	1,9E+06	1,95	7%	-11,0	1,3E-06	38	1,4E+09	6,9E+02	3,7E+07	1,8E+01	A	50	aged	7,8	Std_Cyl	D	Y	N	N	Y
																		Std_R17.5	F		Y	N	Y
TDM09_10	Microcrack	Mixed lubrication - traction	58	3,0E+06	1,95	7%	-11,0	1,3E-06	38	1,4E+09	6,9E+02	3,7E+07	1,8E+01	A	50	aged	8,1	Std_Cyl	D	Y	N	N	Y
																		Std_R17.5	F		Y	N	Y
TDM09_11	Microcrack	Mixed lubrication - traction	133	7,7E+06	1,95	7%	-11,0	1,3E-06	38	1,4E+09	6,9E+02	3,7E+07	1,8E+01	A	50	aged	7,9	Std_Cyl	D	Y	N	N	Y
																		Std_R17.5	F		Y	N	Y
TDM09_12	Microcrack	Mixed lubrication - traction	3	4,4E+05	1,95	7%	-11,0	1,3E-06	38	1,4E+09	6,9E+02	3,7E+07	1,8E+01	A	50	aged + H2O	7,8	Std_Cyl	D	Y	Y	N	Y
																		Std_R17.5	F		Y	N	Y

Ref.	Objective	Ds	Hrs	Cycles	Contact Conditions									Lubrication				Specimen		Results			
					P (GPa)	SRR	Ur (m/s)	hc (m)	λ	PΔU	NΔU	PΔU/λ	NΔU/λ	Oil	θ (°C)	Status	L/h	Type	SRR	Tribofilm	µµcrack	WEC	Wear
TDM09_12_bis	WEC	Mixed lubrication - traction	366	6,4E+07	1,95	7%	-11,0	1,3E-06	38	1,4E+09	6,9E+02	3,7E+07	1,8E+01	A	50	aged + H2O	7,9	Std_Cyl - TDM09_12	D	Y	N	N	Y
																		Std_R17.5 - TDM09_12	F		Y	N	Y
TDM10_01	WEC	High SRR	96	2,0E+07	2,5	30%	11,1	9,6E-07	27	8,3E+09	6,1E+03	3,0E+08	2,3E+02	A	60	aged	Full	Std_Cyl	F	N	N	N	?
																		Std_R17.5 - TDM09_08	D		Y	N	?
TDM10_02	WEC	High stress	107	2,0E+07	3,4	7%	11,0	9,1E-07	26	2,5E+09	3,3E+03	9,6E+07	1,3E+02	A	60	aged	Full	Std_Cyl	F	?	N	N	?
																		Std_R17.5 - TDM09_07	D		Y	N	?
TDM10_03	WEC	High SRR + H2O	95	2,0E+07	3	30%	11,1	7,2E-07	20	9,9E+09	1,1E+04	4,8E+08	5,2E+02	A	70	aged + H2O	Full	Std_Cyl	F	Y	N	N	?
																		Std_R17.5 - TDM09_09	D		Y	N	?
TDM10_04	WEC	High stress + H2O	108	2,0E+07	3,4	7%	11,0	9,1E-07	26	2,5E+09	3,3E+03	9,6E+07	1,3E+02	A	60	aged + H2O	Full	Std_Cyl	F	?	N	N	?
																		Std_R17.5 - TDM10-01	D		Y	N	?
TDM07_04	Microcrack	Dents spaced with offset	16	2,8E+06	3,5	7%	11,0	5,5E-07	15	2,5E+09	3,7E+03	1,6E+08	2,4E+02	A	80	aged + H2O	0	Std_R17.5	D	Y	Y	N	N
																		Std_Cyl	F		N	N	N
TDM07_05	Microcrack	Dents spaced with offset	16	3,0E+06	Linear contact	7%	11,0	-	-	-	-	-	-	A	80	aged + H2O	0	Std_Cyl - TDM07_04	F	Y	Y	N	N
																		Std_Cyl	D		N	N	N
TDM10_05	WEC	Temperature	182	3,7E+07	2,3	22%	11,1	5,3E-07	15	5,5E+09	3,5E+03	3,7E+08	2,3E+02	A	85	aged + H2O	Full	Std_R17.5 - TDM09_10	F	Y	N	N	N
																		Std_Cyl - TDM09_11	D		Y	N	N
TDM10_06	WEC	Temperature + High stress	222	3,6E+07	3,4	22%	11,1	5,3E-07	15	8,2E+09	1,1E+04	5,5E+08	7,4E+02	A	85	aged + H2O	Full	Std_R17.5 - TDM07_04	D	Y	Y	N	Y
																		Std_Cyl - TDM07_05	F		Y	N	Y
TDM10_06_bis	WEC	Temperature + High SRR	187	2,9E+07	3	30%	11,1	5,0E-07	14	9,9E+09	1,1E+04	7,0E+08	7,5E+02	A	85	aged + H2O	Full	Std_R17.5 - TDM07_04	D	Y-	Y	N	N
																		Std_Cyl - TDM07_05	F		Y	N	N
TDM11_00	WEC	Structural stresses	38	6,6E+06	3,5	7%	11,0	5,5E-07	15	2,5E+09	3,7E+03	1,6E+08	2,4E+02	PAO	80	new	0	Std_R17.5	F	N	N	N	N
																		HoleStress_Cyl	D		Structural	WEA	N
TDM07_07	Verification	Dents spaced with offset	36	6,7E+06	3,5	7%	11,0	5,5E-07	15	2,6E+09	3,8E+03	1,7E+08	2,5E+02	A	80	aged + H2O	Full	Std_R17.5	D	Y	?	N	N
																		Std_Cyl	F		Y	N	N
TDM07_06	Microcrack	Dents spaced with offset	20	3,7E+06	3,5	7%	11,0	5,5E-07	15	2,5E+09	3,7E+03	1,6E+08	2,4E+02	A	80	aged + H2O	Full	Std_R17.5	D	Y	N	N	N
																		HoleStress_Cyl	F		N	N	N
TDM07_06_b	Microcrack	Dents spaced with offset	10	1,9E+06	3,5	7%	11,0	5,5E-07	15	2,6E+09	3,8E+03	1,7E+08	2,5E+02	A	80	aged + H2O	Full	Std_R17.5	F	Y	?	N	N
																		HoleStress_Cyl - TDM07_06	D		Y	N	N
TDM11_01	WEC	Structural stresses	701	7,3E+07	2,5	14%	5,6	3,2E-07	9	2,0E+09	1,5E+03	2,2E+08	1,6E+02	A	85	aged + H2O	Full	Std_R17.5	F	Y	N	N	N
																		HoleStress_Cyl - TDM07_06_b	D		Y	N	N
TDM12_01	WEC	E-current (10mA) + H2O	444	4,1E+07	2	7%	5,5	3,9E-07	11	7,5E+08	3,5E+02	6,8E+07	3,3E+01	A	80	aged + H2O	Full	Inclusion_R17.5	F	N	N	N	N
																		Inclusion_Cyl	D		N	N	N
TDM12_02	WEC	E-current (200mA) + dents offset	70	1,3E+07	2,5	0%	11,4	3,9E-07	11	0,0E+00	0,0E+00	0,0E+00	0,0E+00	A	80	aged	Full	Std_R17.5	-	N	Y	N	N
																		Std_Cyl	-		Y	N	N
TDM12_03	WEC	E-current (100mA) + H2O + dents aligned	186	3,5E+07	2,5	0%	11,4	5,9E-07	17	0,0E+00	0,0E+00	0,0E+00	0,0E+00	A	80	aged + H2O	Full	Std_Cyl	-	N	Y	N	N
																		Std_R17.5	-		Y	N	N
TDM12_04	WEC	E-current (100mA) + dents aligned	261	2,3E+07	2	7%	5,5	3,1E-07	9	7,5E+08	2,5E+03	8,4E+07	2,9E+02	C	80	new	Full	Std_B200	D	Y	N	N	N
																		Std_Cyl	F		N	N	N
TDM12_05	WEC	E-current (0.5mA) + Mixed lubrication	53	9,6E+06	2	7%	-11,0	4,1E-07	3	1,5E+09	7,1E+02	4,5E+08	2,1E+02	C	80	new	12L/h	Std_17.5	D	N	Y	N	N
																		Std_Cyl	F		Y	N	N
TDM12_06	WEC	E-current (50mA) + high SRR + dents aligned	65	5,9E+06	2	30%	-5,6	1,1E-06	32	3,3E+09	1,1E+04	1,0E+08	3,5E+02	D	80	new	Full	Std_R200	D	N	N	N	N
																		HoopStress+Inclusion_Cyl	F		1	N	N
TDM12_06_bis	WEC	E-current (50mA) + H2O + dents aligned	65	5,8E+06	2	7%	5,5	1,1E-06	32	7,5E+08	2,5E+03	2,3E+07	7,9E+01	D	80	H2O	Full	Std_R200	D	N	N	N	N
																		HoopStress+Inclusion_Cyl	F		1	N	N
TDM12_07	WEC	E-current (50mA) + dents aligned	256	2,3E+07	2	7%	5,5	3,6E-07	10	7,5E+08	2,5E+03	7,3E+07	2,5E+02	B	80	new	Full	Std_R200	D	Y	N	N	N
																		HoopStress+Inclusion_Cyl	F		N	N	N
TDM12_07_bis	WEC	E-current (50mA) + H2O + dents aligned + high SRR	238	5,6E+07	1,5	30%	11,1	3,6E-07	10	5,0E+09	9,4E+03	4,9E+08	9,3E+02	B	80	H2O	Full	Std_R200	D	Y	N	N	N
																		HoopStress+Inclusion_Cyl	F		N	N	N
TDM12_07_ter	WEC	E-current (50mA) + H2O + dents aligned + high SRR	80	1,5E+07	2	30%	11,1	3,6E-07	10	6,6E+09	2,2E+04	6,5E+08	2,2E+03	B	80	H2O	Full	Std_R200	D	Y	N	N	N
																		HoopStress+Inclusion_Cyl	F		N	N	N
TDM13_01	WEC	Tapered + e- 50mA + H2O + high SRR	224	4,1E+07	3	30%	11,1	3,6E-07	6	9,9E+09	2,2E+04	1,5E+09	1,5E+03	B	80	H2O	Full	Tpr	F	Y	Y	N	N
																		Std_R17.5	D		N	N	N
TDM13_02	WEC	e- 50mA + H2O + high SRR	135	2,5E+07	3	30%	11,1	3,6E-07	10	9,9E+09	1,1E+04	9,7E+08	1,0E+03	B	80	aged + H2O	Full	Std_Cyl	F	Y	Y	N	N
																		Std_R17.5	D		N	N	N
TDM13_03	WEC	e- 50mA + H2O + high SRR + high temperature	135	2,5E+07	3	30%	11,1	2,5E-07	7,1	9,9E+09	1,1E+04	1,4E+09	1,5E+03	B	110	aged + H2O	Full	Std_Cyl	F	Y	Y	N	N
																		Std_R17.5	D		N	N	N
TDM14_01	WEC	E-current (50mA) + H2O + high SRR + Roughness	206	35E+07	2	30%	11,1	3,6E-07	2	6,6E+09	2,2E+04	3,5E+09	1,2E+04	B	100	new	Full	Rough_R200	F	Y	N	N	?
																		Rough_Cyl	D		N	N	?
TDM14_02	WEC	E-current (50mA) + H2O + high SRR + Roughness	-	-	3	30%	11,1	3,6E-07	2	9,9E+09	1,1E+04	5,2E+09	5,6E+03	B	100	new	Full	Rough_R200	F	?	?	?	?
																		Rough_Cyl	D		?	?	?
		Details section 2.3.4	7657	1,18E+09			*- for inv. rotation*			*Reference value in Table 5-1*				*Details Table 2-4, Table 2-5, Table 2-6*				*Details Fig. 2.8 D: driver and F: follower*		*Y: Yes – N: No WEA: only white etching microstructure*			
			Total																				

I. Probable wind turbine influent drivers

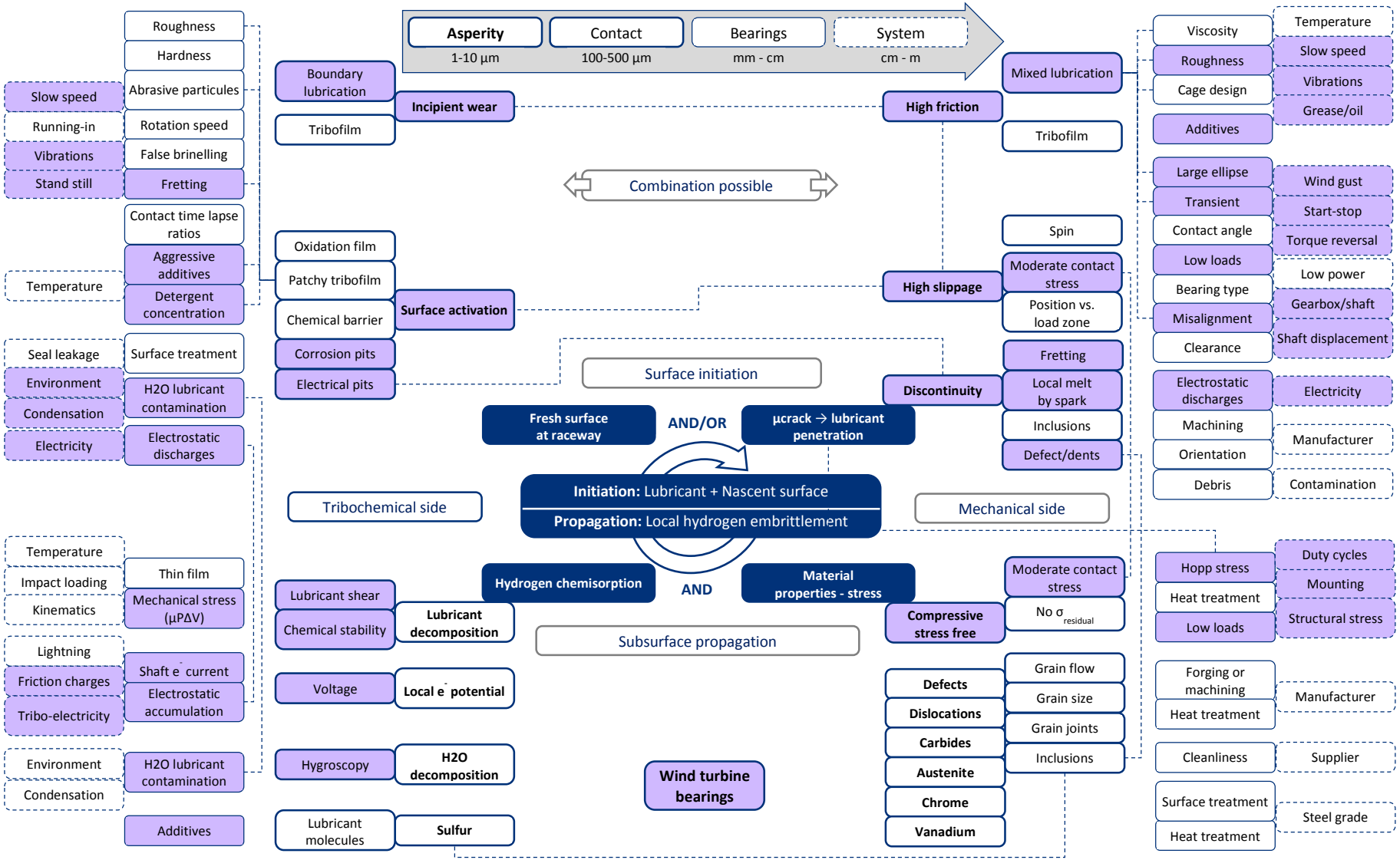

J. Identified ACBB and CRTB influent drivers

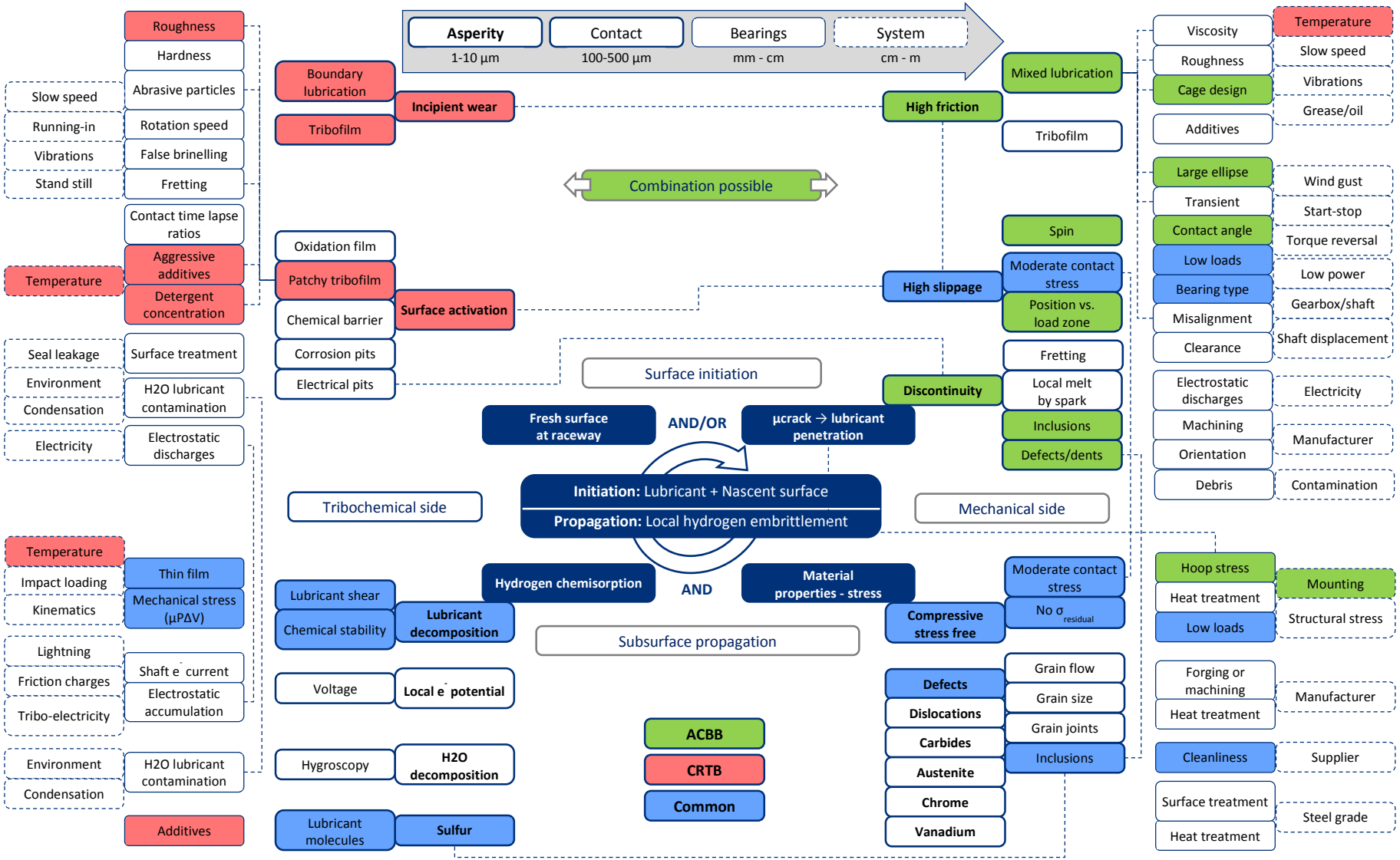

K. Multiple consequences of lubricant additive formulation

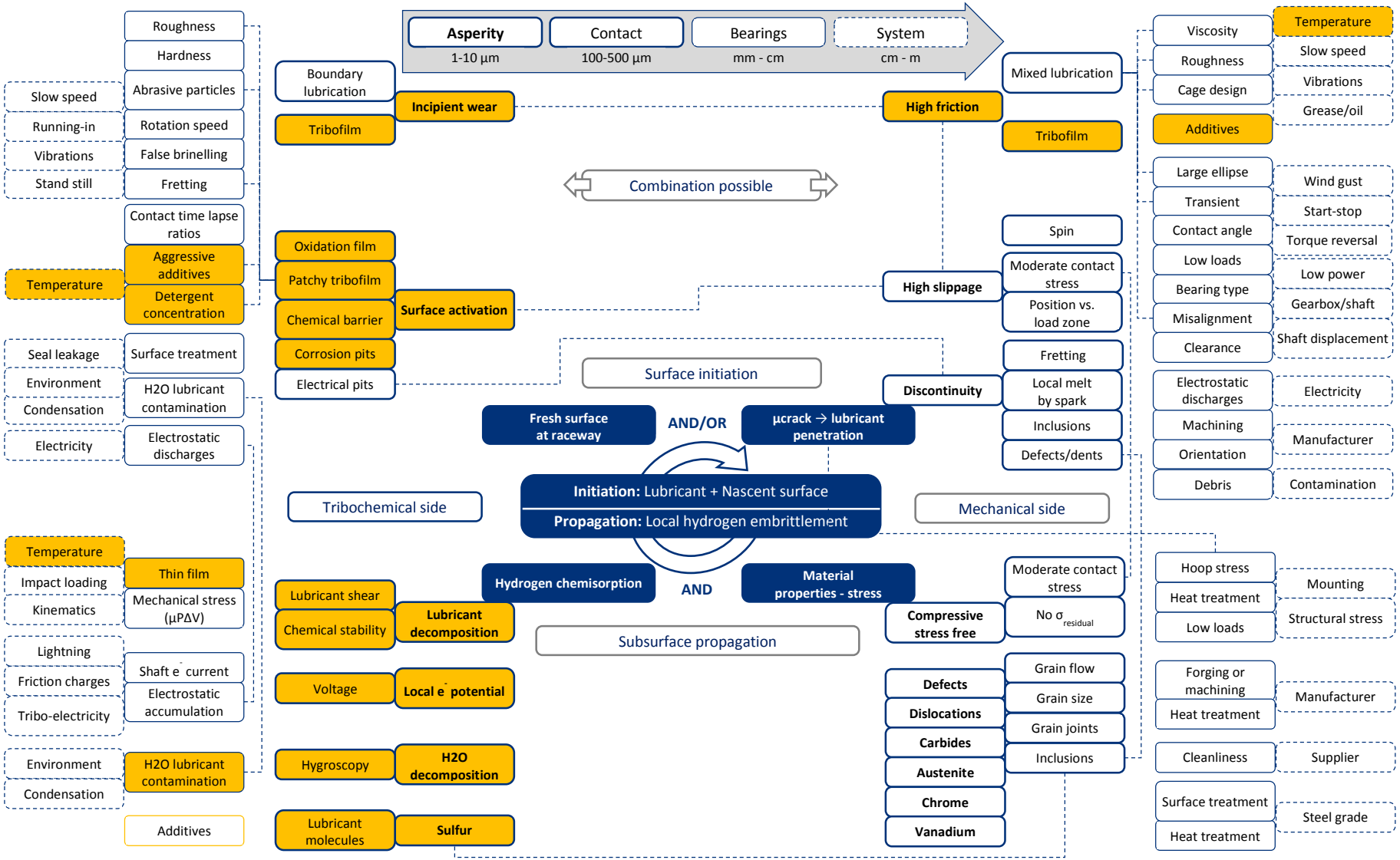

L. Multiple drivers and consequences of sliding kinematics

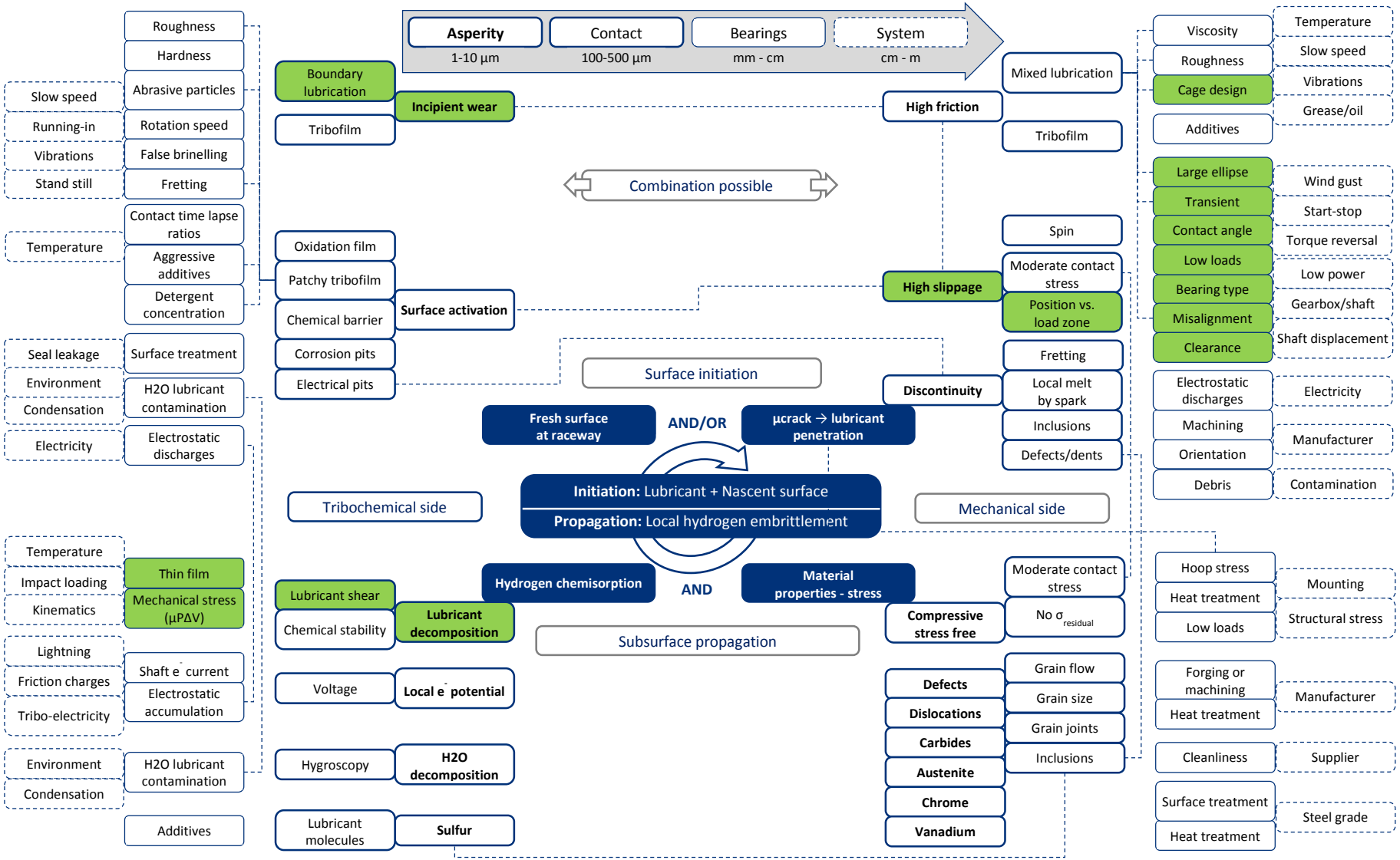

M. Additional NTN-SNR RCF tests with WEC occurrences

Reference	Configuration	F_a/F_r	P_H (GPa)	Ω (rpm)	θ* (°C)	Lubrication	Number of tests	WEC**
D-ACBB[1]	GRB wheel bearing test rig	0.6	-	*	<70	Formulated grease with lithium thickener	8	2 IR strictly on the interiror side[1*]
DGBB-1	Machine S	1.0	3.25	2250	40	Formulated gearbox oil with CaS additives[3]	8	3 REs and 1 IR all of different REB
DGBB-2	Machine S	0.1	3.3	2250	40 110	Formulated engine oil	8 8	No Yes: 2 IR
CRTB[2]	FB3 thrust bearing test rig	Thrust load	1.0	250 500 1000	40	Lubricant A		No

* D*ata not yet available of public domain.*

*** Known WEC occurrences as further analysis are yet to be led on some components, so that no information on reproducibility rate can be advanced*

[1] *D-ACBB for Double as the IR is composed of two ACBB facing each other*

[1*] *Axial LOM reveal a significant difference in DER density so that the loading is believed to be asymmetric and that WEC develop on the less loaded IR*

[2] *NTN-SNR FB3 CRTB tests have been performed on CRTB comprising 21 rollers of diameter and length equal to 6 mm*

[3] *CaS: Calcium Sulfonates*

Résumé étendu en français

Ce manuscrit de thèse ayant été rédigé en anglais, un résumé étendu des travaux et des principaux résultats est proposé en français dans cette annexe. Les références bibliographiques correspondent à celles du manuscrit.

A. Introduction

Motivations industrielles

Dans le but de satisfaire une augmentation quasi-exponentielle de la demande en énergie électrique tout en limitant l'impact sur l'environnement et les ressources naturelles, le marché de l'énergie éolienne a actuellement le vent en poupe, avec une croissance annuelle d'environ 25% (**Figure 1 (a)**). Près de 40GW de puissance nominale, soit l'équivalent de 40 réacteurs nucléaires, sont installés tous les ans. La majorité des éoliennes sont des turbines multi-MW avec un rotor de plus de 100m de diamètre placé à au moins 100m de haut !

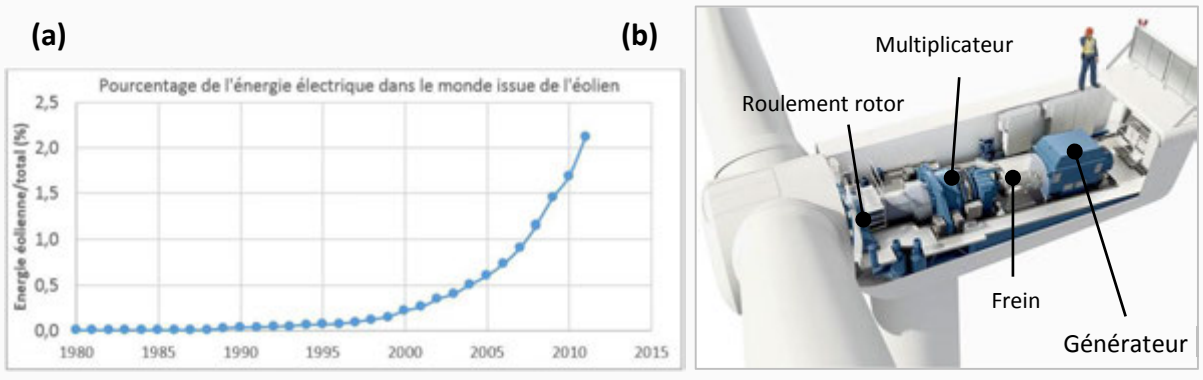

Figure 1 : (a) Pourcentage de l'énergie électrique dans le monde issue de l'éolien (données accessibles [1]); (b) Structure typique de la nacelle d'une éolienne multi-MW (ZF transmission, www.zf.com).

Néanmoins, malgré les progrès technologiques, les éoliennes restent confrontées à des défaillances prématurées de composants mécaniques imposants qui représentent près de 75% du coût de maintenance [5], voire plus dans le cas d'installations offshore. Le multiplicateur, boîte de vitesses mécanique accommodant les faibles vitesses de rotation du rotor aux vitesses nominales de la génératrice située à l'arrière de la nacelle (**Figure 1 (b)**), est actuellement le maillon faible du marché éolien. Plus précisément, 80% de leurs défaillances sont attribuées aux roulements [11]. Parmi les défaillances tribologiques récurrentes au sein des roulements d'éoliennes, un mode de fatigue de contact, atypique et non résolu, a été identifié par l'observation de vastes réseaux de fissures ramifiées avec des phases microstructurales adjacentes d'apparence blanche à l'origine de la dénomination White Etching Cracks (WEC).

Problématique et objectifs de l'étude

Afin de profiter de l'expansion du marché éolien, les roulementiers doivent être en mesure de proposer des roulements performants et robustes sur une durée de vie de 20 ans. Dans cet optique,

une analyse approfondie des défaillances de type WEC a été menée afin de mieux comprendre les mécanismes tribologiques en cause et de proposer des critères de conception pour les éviter. Ceci constitue la problématique générale de l'étude intitulée *Analyse tribologique des défaillances de roulements par fatigue de contact de type White Etching Cracks (WEC)*. Ce titre a été choisi afin de souligner le fait que les travaux conduits n'ont pas pour vocation la caractérisation microstructurale des WEC [14–16], mais plutôt l'analyse expérimentale des mécanismes tribologiques à l'origine des WEC dans leur ensemble, avec des aspects mécaniques, matériaux, chimiques et thermiques. Les objectifs et principaux axes de l'étude sont ainsi spécifiés dans la **Figure 2**.

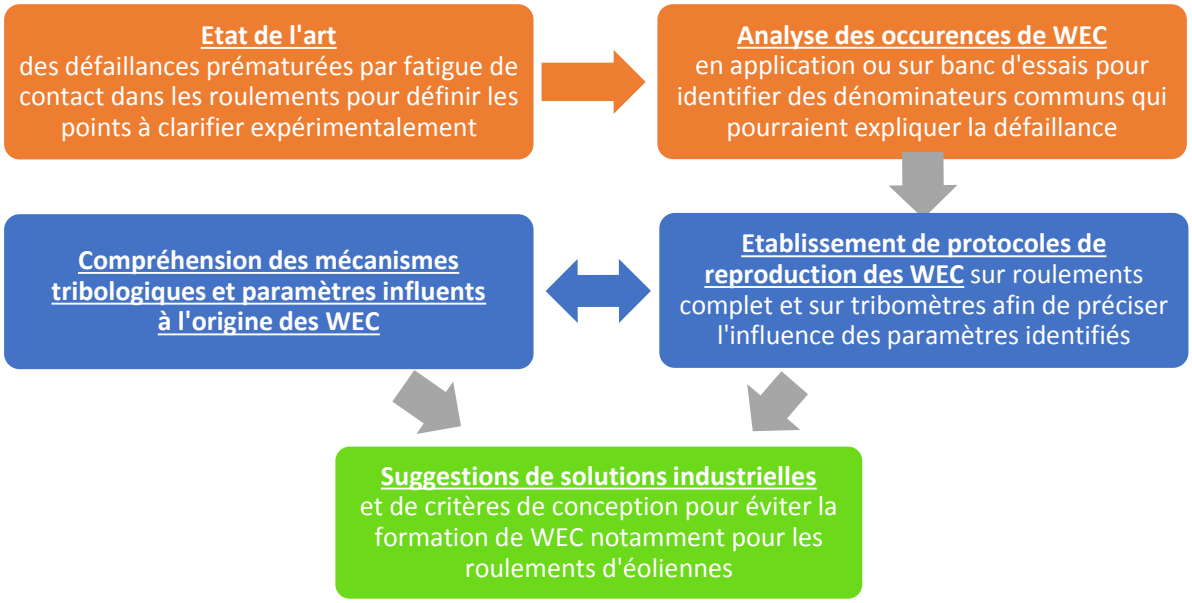

Figure 2 : Problématique et objectifs principaux de l'étude.

Afin de présenter les essais et résultats de l'étude, le manuscrit s'agence de la manière suivante. Le **Chapitre 1** fait tout d'abord état de la tribologie et des défaillances au sein des roulements avant de définir la défaillance par fatigue de contact atypique que sont les WEC. Dans le **Chapitre 2**, la méthodologie et les dispositifs expérimentaux employés lors de cette étude sont présentés, avec en particulier les essais roulements ACBB sur Machine S de NTN-SNR et les essais laboratoires sur tribomètre bi-disques du LaMCoS. L'analyse de reproduction de WEC sur des composants artificiellement chargés ou non en hydrogène est ensuite présentée dans le **Chapitre 3** afin de démontrer que les WEC sont délicates à observer et que le chargement en hydrogène ne semble pas être adéquat pour concevoir et valider des solutions. Fort de ce constat, la comparaison tribologique de deux bancs d'essais reproduisant la défaillance sans chargement en hydrogène est exposée dans le **Chapitre 4**, permettant, dans un second temps, de formuler des scénarii tribologiques à l'origine des WEC. Finalement, un arbre des causes est développé de l'échelle macroscopique à l'échelle tribologique dans le **Chapitre 5**, permettant d'identifier les facteurs tribologiques influents et de les transposer progressivement sur la machine bi-disques afin de reproduire la défaillance.

B. Caractérisation des White Etching Cracks (WEC)

Tribologie du roulement

Elément fondamental de nombreux systèmes mécaniques, le *roulement* est composé de deux bagues, la bague intérieure (BI) et la bague extérieure (BE), séparées par des corps roulants (billes ou rouleaux) eux–mêmes maintenus espacés par une cage. Les roulements permettent d'assurer un mouvement de rotation précis tout transmettant les efforts appliqués et en minimisant les pertes par frottement. L'intégralité de ces efforts, parfois très importants, est transmise très localement via le contact entre les surfaces des différents composants (**Figure 3**). La *tribologie* est la science du frottement, de l'usure et de la lubrification, i.e. du contact entre deux surfaces en mouvement relatif. De par leur conception, la tribologie est inhérente au bon fonctionnement des roulements qui, malgré leur apparente simplicité, sont extrêmement complexes à comprendre d'un point de vue tribologique (**Figure 3**). En effet, de nombreux paramètres interdépendants, tels les contraintes, la cinématique, la thermique et la lubrification des contacts entre bagues et corps roulants, jouent un rôle prédominant sur la durée de vie d'un roulement.

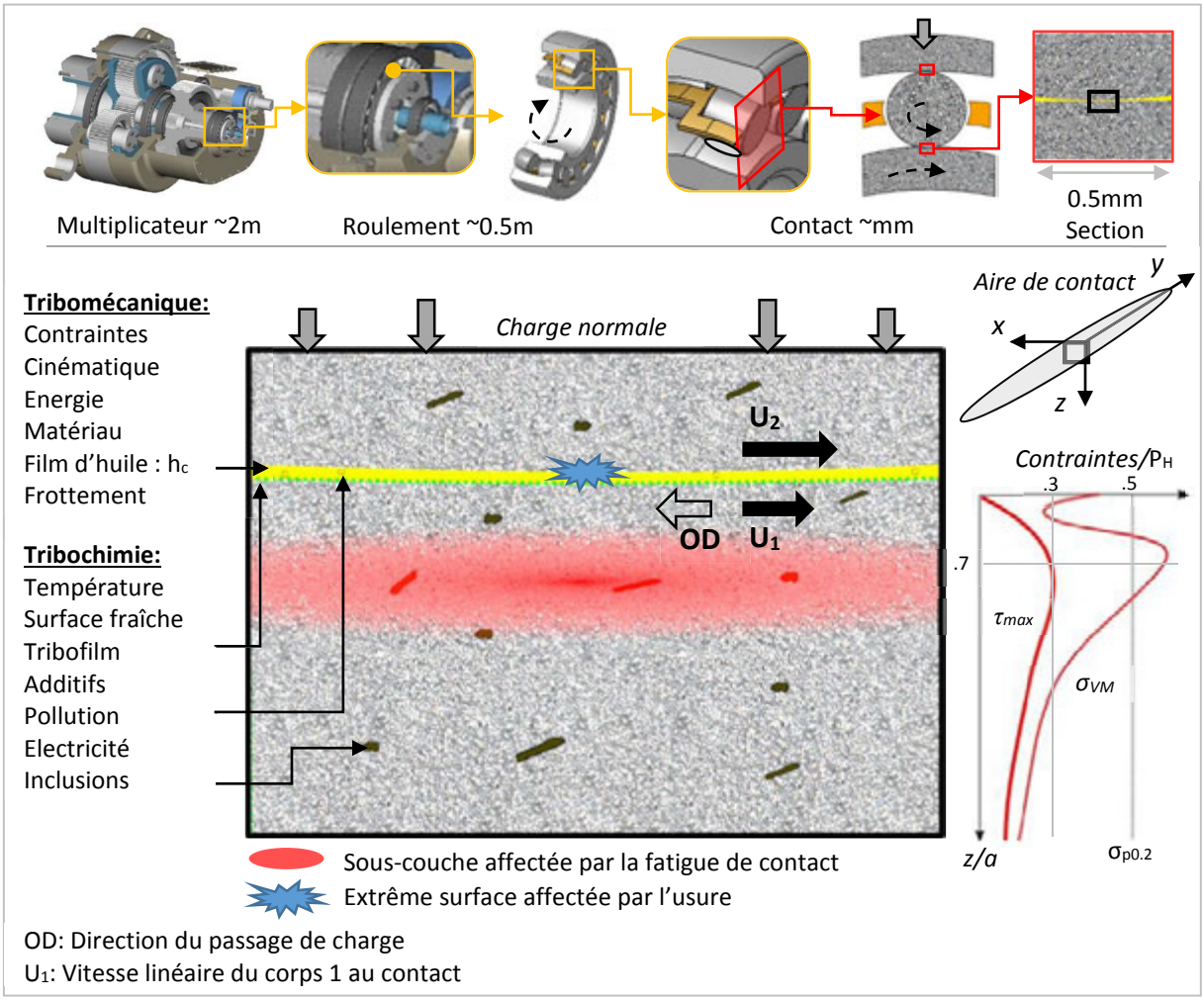

Figure 3 : Schéma général d'un contact tribologique dans un roulement considérant les paramètres tribomécaniques et tribochimiques affectant la durée de vie du contact et donc du roulement.

Défaillance du roulement

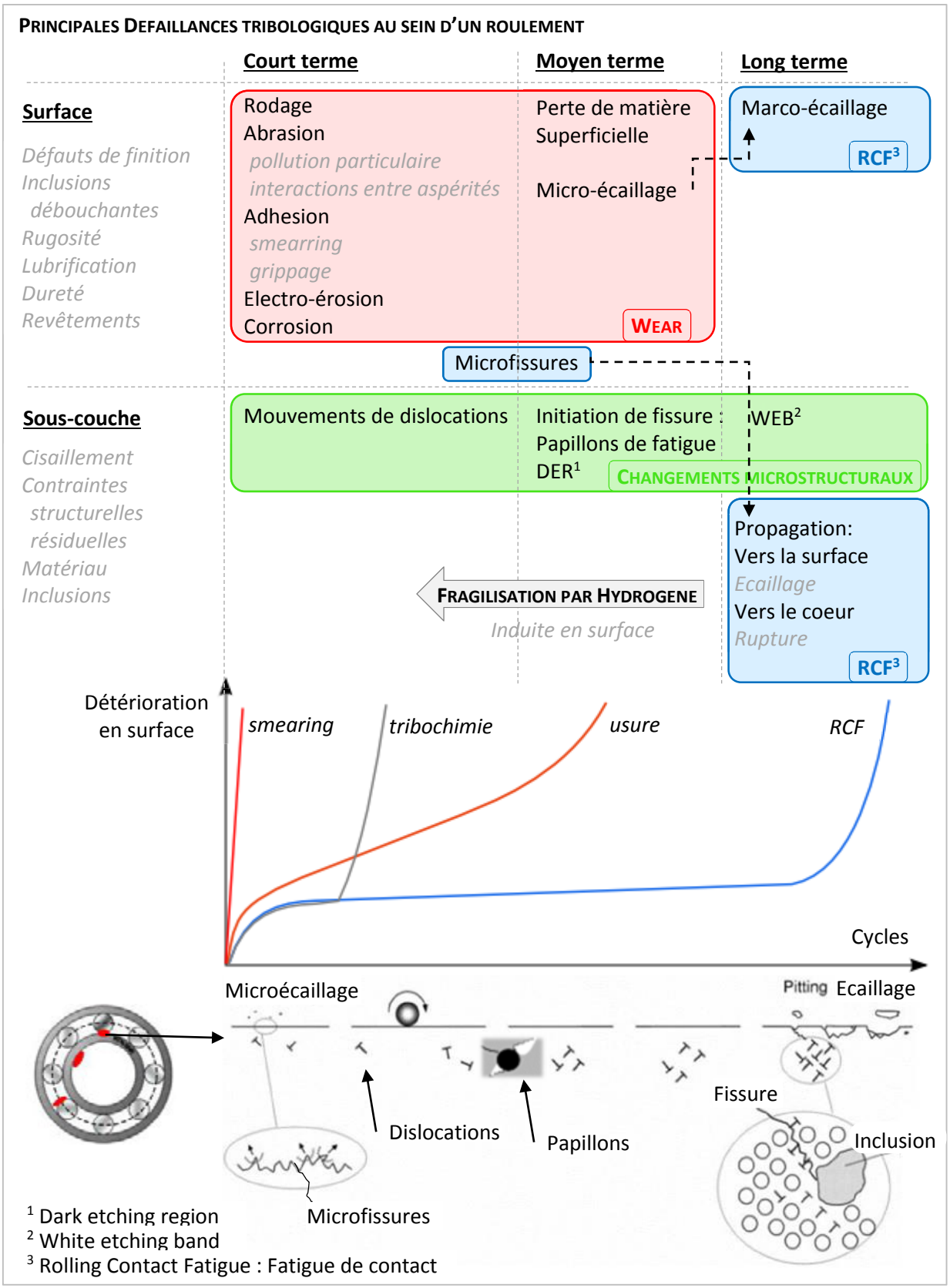

Figure 4 : Aperçu des différents modes de défaillances tribologiques dans les roulements et leur évolution en fonction du nombre de cycles (image du bas [67]).

Une récente étude du CETIM révèle que 80% des défaillances mécaniques s'initient aux interfaces tribologiques [37]. Dans le cas des roulements, la majorité des défaillances répertoriées par Tallian [58] sont effectivement associées aux contacts entre bagues et corps roulants. En fonction des conditions, elles peuvent être de deux types : *usure* ou *fatigue de contact* (**Figure 4**). L'*usure* correspond à une perte de matière superficielle et progressive par abrasion ou adhésion des surfaces. Ce phénomène apparait dès lors que la lubrification et la séparation des surfaces en contact deviennent insuffisantes.

A contrario, la *fatigue de contact* est associée aux contraintes de contact excessives et répétées à chaque passage de charge. Elle se traduit par l'accumulation de changements microstructuraux (**Figure 5 (a-b)**) et l'initiation de microfissures sur des défauts dans le matériau situés dans la zone de cisaillement maximal en sous-couche. Ces derniers constituants sont généralement appelés *papillons de fatigue* (**Figure 5 (d)**). Après une période d'incubation plus ou moins longue en fonction des contraintes de contact (**Figure 5 (c)**), la propagation et la coalescence de fissures initiées en sous-couche convergent vers un arrachement de matière brutal en surface, appelé *écaillage,* synonyme de défaillance irréversible. Les normes actuelles de conception de roulements reposent en grande partie sur des modèles de durée de vie empiriques prenant ainsi en compte les contraintes de contact et les propriétés matériaux. Elles sont donc principalement représentatives des défaillances par *fatigue de contact* classique, et ne permettent donc pas de prémunir des WEC.

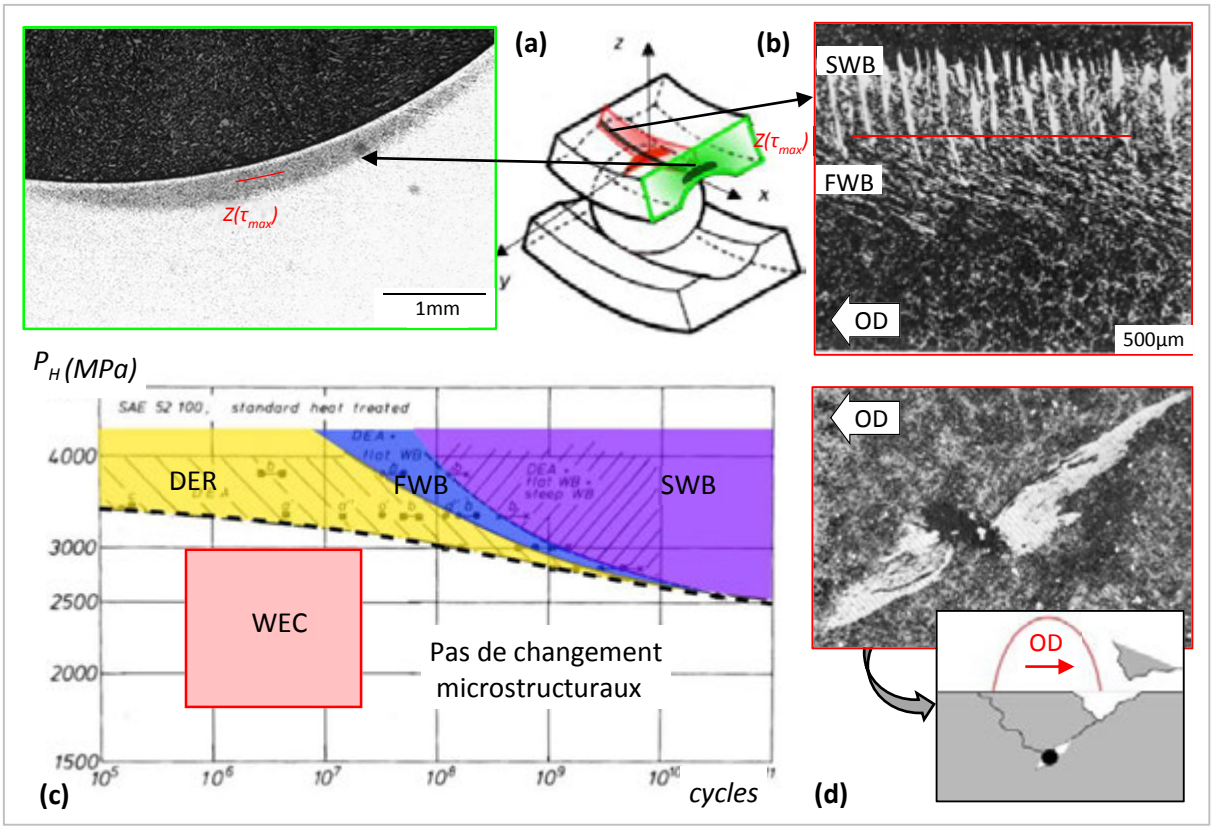

Figure 5 : Changement microstructuraux classique associés à la fatigue de contact :(a) Coupe métallographique axiale d'une BI après 4x10^7 cycles à 3.5 GPa avec attaque Nital révélant des dark etching regions (DER) dans la zone de cisaillement maximal; (b) Coupe métallographique circonférentielle d'une BI révélant des bandes de déformations plastiques (WEB) à la profondeur du cisaillement maximal [122]; (c) Diagramme de Schlicht repositionnant les différents changement microstructuraux en fonction de la pression de contact et du nombre de cycles (adapté de [122]); (d) Développement typique d'un papillon de fatigue autour d'une inclusion menant à un écaillage initié en sous-couche.

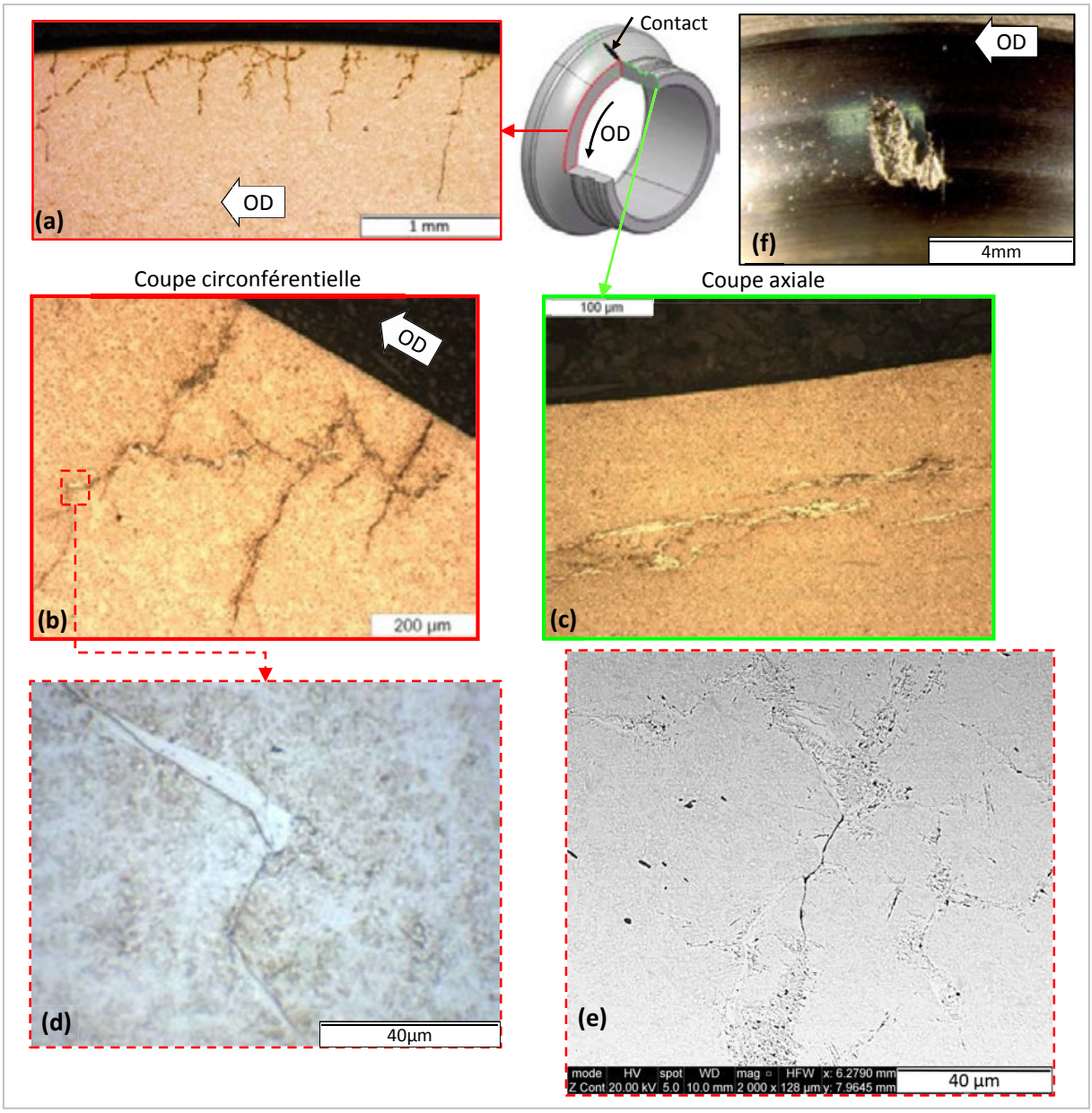

Figure 6 : Coupe métallographiques avec attaque Nital révélant des WEC sur une BI d'un roulement ACBB issue d'un essai Machine S NTN-SNR: (a) Réseaux de WEC discontinus ; (b) Liens verticaux avec la surface et une propagation en escalier de la surface vers l'alésage dans le sens de roulement; (c) Disposition plus parallèle à la surface d'un point de vue axial; (d) Zoom sur les phases blanches adjacentes; (e) Analyse MEB dévoilant de nombreuses fissures secondaires ultrafines; (f) Photographie vue de haut d'un écaillage associé à des WEC et présentant de nombreuses fissures axiales.

*Définition des White Etching Cracks basée sur les observations expérimentales (***Figure 6***):*

- Réseau de fissures atypique et discontinu avec un faciès fragile et largement ramifié,
- Propagation étendue majoritairement en sous-couche avec régulièrement des liens quasi-ponctuels avec la surface,
- Microfissures très fines (<1 µm) délimités par des phases microstructurales adjacentes d'apparence blanche à l'observation après attaque Nital,
- Conduisant à l'écaillage ou la rupture du composant selon les contraintes structurelles.

En effet, contrairement à la fatigue de contact classique, les *White Etching Cracks* (WEC) apparaissent pour un nombre de cycle et des charges relativement faibles (**Figure 5 (c)**) et correspondent donc à une défaillance prématurée du roulement par rapport aux modèles de durée de vie actuels (entre 2 et 20% de la L_{10} [6,162–165]). Observé à plusieurs reprises à la fin des années 1990 dans des roulements d'alternateurs automobile [171,172], ce mode de défaillance prématuré, apparemment peu courant, n'a véritablement fait l'objet de recherche intensive qu'à partir de la fin des années 2000, période où les WEC ont été identifiées comme un enjeu majeur pour l'industrie éolienne [7,12,29,30,115,168,172–185]. La terminologie *White Etching Cracks* a été plus ou moins adoptée en 2013 lors d'une réunion d'experts travaillant sur le sujet au 68ième STLE Annual Meeting and Exhibition [6,162,163,186] .

Comparées aux changements microstructuraux classiques, les WEC présentent une morphologie atypique et discontinue (**Figure 6**). Ce sont des réseaux de microfissures 3D largement ramifiés qui peuvent s'étendre au-delà des contraintes mécaniques induites par le passage de charge. Les fissures sont régulièrement délimitées par des phases blanches correspondant à une microstructure raffinée et composée de nano-grains ferritiques. Les WEC ont été observées chez tous les roulementiers, dans diverses applications industrielles et ce pour différents types de roulements, éléments, lubrifiants, aciers et traitements thermiques. Ce manque de dénominateur commun rend les WEC difficilement reproductibles sur bancs d'essais sans avoir recours au chargement artificiel en hydrogène de l'acier [18,96,163,174,176,182,194,199,204].

Ainsi, pour le moment, les mécanismes de formation des WEC ne font pas l'objet d'un consensus et quoiqu'il en soit, ne semblent pas s'expliquer uniquement en considérant les contraintes de contact et les propriétés du matériau à l'image de la fatigue de contact classique. Par conséquent, à l'aide de différents protocoles expérimentaux, cette étude vise à déterminer l'influence du chargement en hydrogène sur la formation des WEC (**Chapitre 3**) et à qualifier les phénomènes tribologiques à l'origine des WEC (**Chapitre 4 et 5**) afin de proposer des solutions industrielles adaptées.

C. Effet du chargement en hydrogène sur l'initiation des WEC

Reproduction de WEC sur éléments chargés ou non en hydrogène

La majorité de la littérature traitant des WEC mentionne la fragilisation par hydrogène (FPH) comme une des causes principales des WEC [6,17,19,29,58,96,164,171,172,174,177,179,180], s'appuyant notamment sur les nombreuses reproductions de la défaillance sur différents bancs d'essais radicalement différents mais avec des éprouvettes artificiellement chargées en hydrogène. Pour aller plus loin et clarifier l'influence de l'hydrogène, le **Chapitre 3** de ce manuscrit compare des WEC reproduites sur des BI de roulements standards *chargées ou non en hydrogène* ayant opéré dans des conditions d'essai strictement identiques.

Ainsi, pour la première fois, les WEC ont été reproduites sur les BI de roulements à contact oblique (ACBB) montés par paire sur des Machine S de NTN-SNR, dans des conditions tout à fait usuelles (charges et vitesses modérées, pas de transitoire, pas de vibration ou d'impact) et dans un environnement neutre (pas de pollution, pas d'électricité, etc.) (**Figure 7 et 9**). Toutes les WEC révélées sur les BI neutres, écaillées ou suspendues, par des coupes métallographiques circonférentielles ou axiales et/ou par des fractographies, ont été observées au niveau de la bordure

de piste inférieure (**Figure 7 (a)**), i.e. dans une zone où la pression de contact chute mais où le glissement local atteint un maximum de 22% de SRR (taux glissement, cf. notations) (**Figure 8**). De plus, la morphologie apparente des WEC révélée dépend considérablement à la fois du type de coupe métallographique (axiale ou circonférentielle) mais aussi de sa position par rapport au contact (**Figure 7 (b)**). Ainsi, *une expertise précipitée peut nuire à la compréhension de la défaillance*, en particulier vis-à-vis du lien avec la surface, voire même manquer de la révéler puisque les expertises métallographiques sont habituellement réalisées au droit de l'angle de contact, là où les contraintes de cisaillement sont maximales.

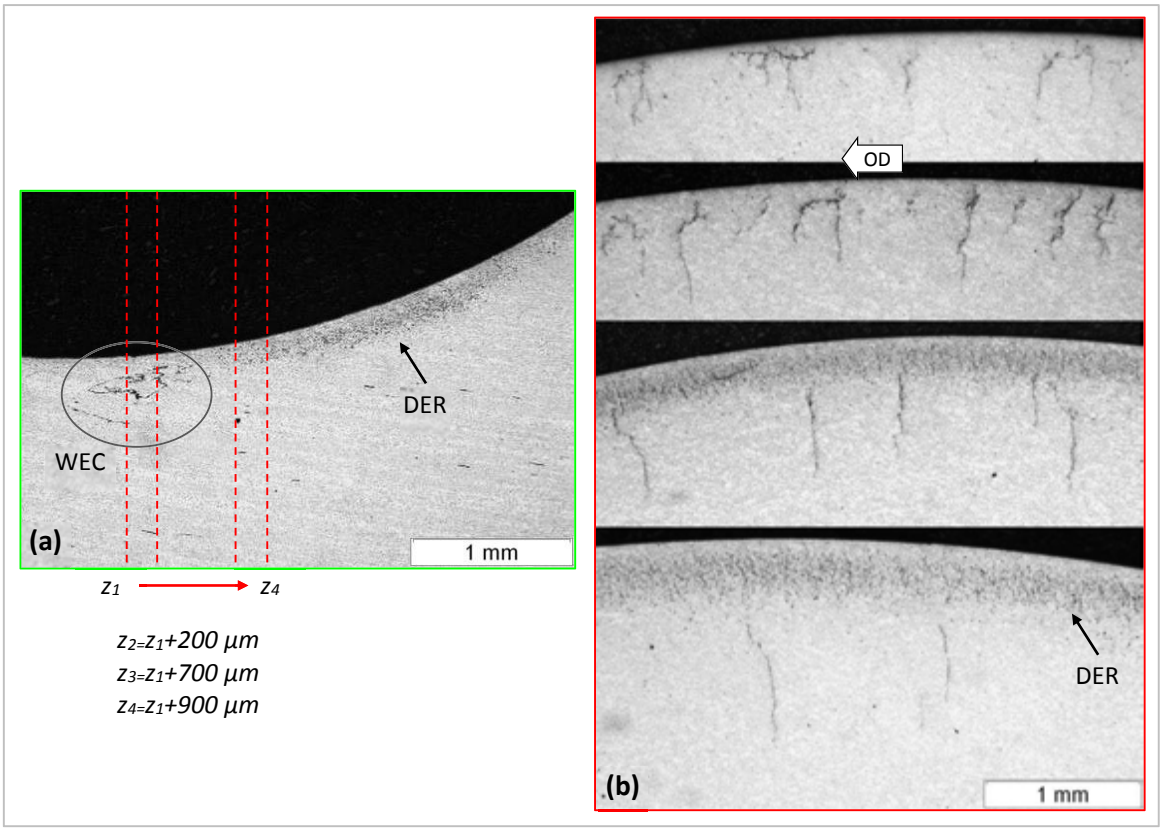

Figure 7 : Coupe axiale d'une BI neutre (a) dévoilant la position typique des WEC à l'extrémité inférieure de la zone de contact (repérée par les DER) et la position approximative des 4 coupes circonférentielles obtenues par polissages successifs de la même BI (b).

Un protocole a ensuite été établi afin de charger artificiellement certaines BI en hydrogène à l'aide d'un bain électrolytique d'acide sulfurique. Des essais Machine S strictement identiques ont alors été conduits avec des BI chargés en hydrogène 48h au préalable (BI-H) et d'autres conservées neutres (BI-nonH). Témoins de la fragilisation par hydrogène (FPH), les BI-H ont écaillé environ 10 fois plus tôt que les BI-nonH. Sur la totalité des BI, H ou nonH, des WEC ont été révélées par fractographie et/ou coupes métallographiques. Les résultats montrent que, dans le cas des BI-H, les WEC apparaissent principalement au centre du contact tandis que dans les BI-nonH elles apparaissent exclusivement en bordure de piste (**Figure 8**). De plus, alors que WEC des BI-H semblent se développer principalement au sein de la zone de Hertz, toutes les WEC ouvertes par fractographie sur les BI-nonH présentent un lien vertical avec la surface (**Figure 9**), ce qui est cohérent avec les observations réalisées sur des coupes circonférentielles bien positionnées (**Figure 6 (b)**).

Le chargement artificiel en hydrogène facilite nettement la reproduction des WEC, notamment en termes de faciès de propagation fragile. C'est pourquoi ce protocole est jusque-là couramment employé pour étudier la défaillance. Néanmoins, au vu des résultats précédents, il semble que *le chargement artificiel en hydrogène modifie les mécanismes initiateurs des WEC*. Il ne serait donc pas adéquat pour mettre au point des solutions efficaces en application. En effet, lorsque l'hydrogène est introduit artificiellement dans l'acier, il réduit drastiquement les seuils de fissuration. Des WEC s'initient alors au moindre défaut sous contraintes, donc principalement dans la zone de Hertz, de manières quasi-indépendantes de la pression de contact. A contrario, dans les BI-nonH et les roulements d'éoliennes par exemple, puisque les WEC se développent, a priori, à cause de la FPH et que l'hydrogène naturellement présent dans l'acier n'est pas suffisant, des *conditions tribologiques spécifiques* semblent être nécessaires pour permettre l'absorption d'hydrogène, expliquant alors le développement des WEC localisé en bordure de piste (**Figure 8**).

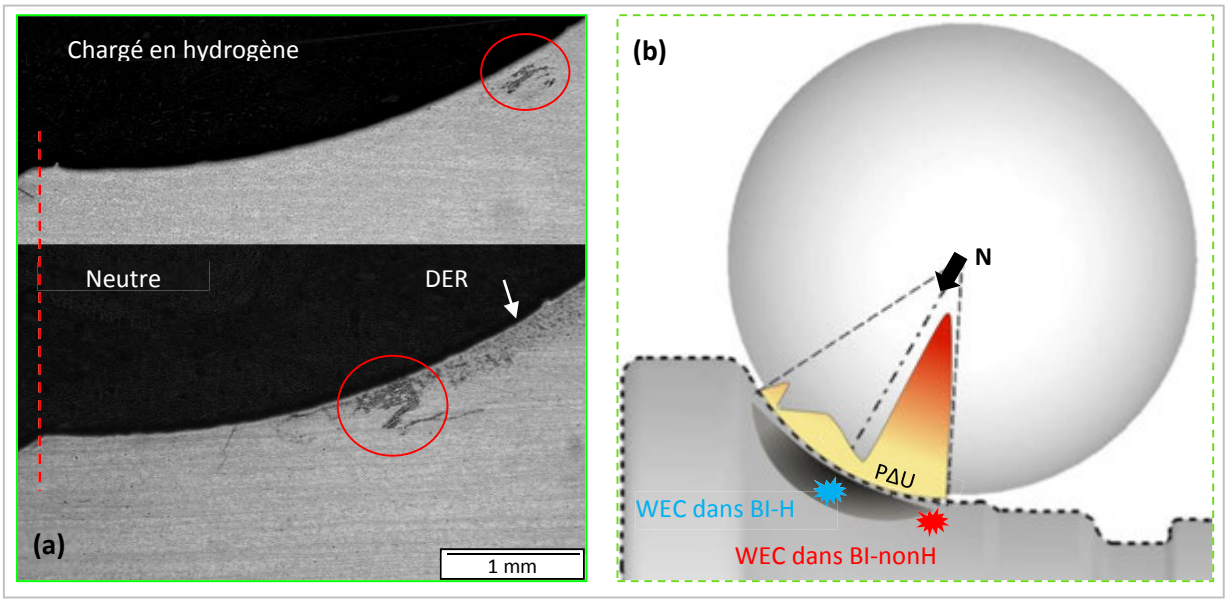

Figure 8: Position différente des WEC sur les BI chargés en hydrogène ou non.

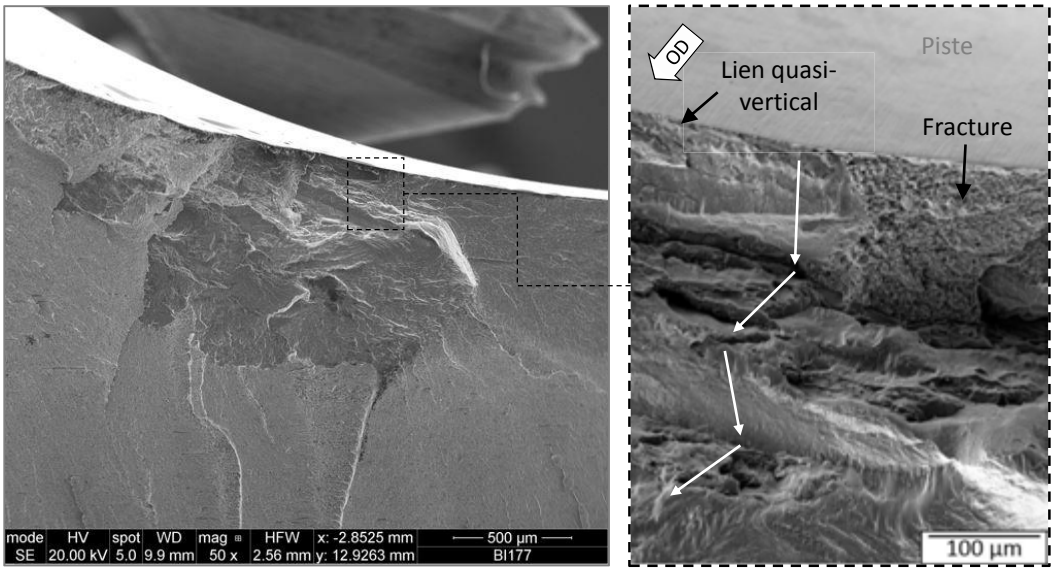

Figure 9 : Fratographie d'une BI avec un grossissement au MEB sur le lien avec la surface dévoilant un faciès de clivage radicalement différent et préxistant par rapport à la fracture globale.

D. Reproductions et mécanismes de formation des WEC

Analyse et comparaison de deux protocoles d'essais reproduisant les WEC

Par conséquent, des reproductions de WEC *sans chargement en hydrogène* et dans des configurations différentes ont été comparées dans le **Chapitre 4** afin d'apporter des éléments complémentaires à la compréhension des phénomènes tribologiques à l'origine des WEC.

D'après des rapports techniques récents issus de la littérature [79,192,198,202], la défaillance a été reproduite à plusieurs reprises sur des roulements de type butée cylindrique (CRTB) montés par paire sur des bancs d'essais FAG FE-8 fonctionnant dans des conditions de lubrification mixte voire sévère. Les WEC ont alors été observées exclusivement en bordure inférieure de contact, où le glissement atteint 15% de SRR et ce, seulement dans le cadre d'essais réalisés avec un lubrifiant spécifique dont la formulation contient de fortes concentrations en additifs de type Sulfonates de Calcium (CaS).

Parallèlement, de nombreuses variantes de l'essai ACBB sur Machine S ont été réalisées modifiant les cas de charge, l'usinage et le lot d'acier des BI, ainsi que la conception de la cage. De manières similaires, les fractographies et coupes métallographiques ont révélé des WEC en bordure de pistes dans diverses configurations (pour des BI forgées ou décolletées, pour deux cas de charge différents et pour les deux types de cage susceptibles de sous-alimenter le contact en lubrifiant) mais avec un taux de reproductibilité plus faible que précédemment. Quoiqu'il en soit, les ACBB étaient lubrifiés abondamment par jet avec une huile faiblement additivée ne contenant pas de CaS.

Les résultats des essais CRTB montrent tout d'abord que les contraintes de traction circonférentielle, le fretting à l'alésage ou encore les phénomènes tribologiques transitoires dus à l'entrée-sortie de la zone de charge dans les roulements radiaux, ne sont pas suffisants pour expliquer la formation des WEC. De plus, tandis que les résultats des essais CRTB suggèrent qu'une certaine concentration de CaS soit à l'origine des WEC sur les butées [79,192,198,202], ceux des essais ACBB démontrent que ces additifs ne sont pourtant pas toujours nécessaires. Enfin, contrairement aux liens verticaux avec la surface révélés sur l'intégralité des WEC des BI d'ACBB par fractographie (**Figure 9**), 9 des 13 WEC reconstruites en 3D par polissage successif dans les CRTB ne présenteraient pas de lien avec l'extrême surface [16,198].

Cependant, malgré leurs configurations radicalement différentes, les deux essais présentent des similitudes tribologiques importantes dans la zone de développement des WEC. D'abord, dans les deux cas, les WEC apparaissent en bordure de piste où sont atteints les maxima de glissement et de critère P.ΔU (P étant la pression locale et ΔU la vitesse de glissement locale le long de l'axe du contact transverse au passage de charge) (**Figure 8 (b)**). De plus, les analyses MEB-EDX des surfaces des BI révèlent qu'au droit de la zone de WEC, le tribofilm est soit absent soit extrêmement irrégulier et poreux, en accord avec les observations FIB et XPS réalisées sur les butées défaillantes [79]. Ces dernières sont cohérentes avec influence des additifs CaS principalement utilisés pour leurs propriétés de détergence affectant largement l'équilibre entre formation de tribofilm et usure.

Ainsi, l'analyse menée confirme que les WEC ne correspondent pas à de la fatigue de contact classique et que les mécanismes initiateurs dépendent de paramètres tribologiques tels que la

cinématique du contact et la qualité du tribofilm qui sont susceptibles de varier légèrement d'une configuration à une autre ; expliquant alors le lien ou non avec l'extrême surface.

Mécanismes tribologiques impliqués dans la formation des WEC

Au vu des analyses tribologiques précédentes, la formation des WEC peut être considérée en deux étapes : *initiation* et *propagation*. Les données issues de la littérature et les observations du **Chapitre 3** démontrent que la propagation des WEC résulte de la FPH de l'acier. L'initiation doit alors correspondre aux phénomènes tribologiques à l'origine de l'absorption de l'hydrogène dans l'acier via les surfaces métalliques fraîches et réactives.

La formation de *surface fraîche* dans un contact peut avoir lieu directement sur la piste de roulement ou au niveau des flancs de microfissures superficielles au sein desquelles le lubrifiant peut pénétrer (**Figure 10**). Dans le premier cas, la surface fraîche peut être créée lorsque la formation de *tribofilm est entravée* par une usure modérée et/ou la présence excessive de détergents dans le lubrifiant. Dans le deuxième, les *microfissures peuvent s'initier* au sein des vingt premiers µm sous la surface lorsque de fortes contraintes superficielles de traction coïncident avec la présence de discontinuités dans la matière comme des inclusions débouchantes, des défauts d'usinage, des indents, des piqures d'électro-corrosion, etc. Les deux scénarii de formation de surface fraîche sont nettement favorisés par les cinématiques de fort glissement et une lubrification insuffisante, du moins localement au sein de l'aire de contact.

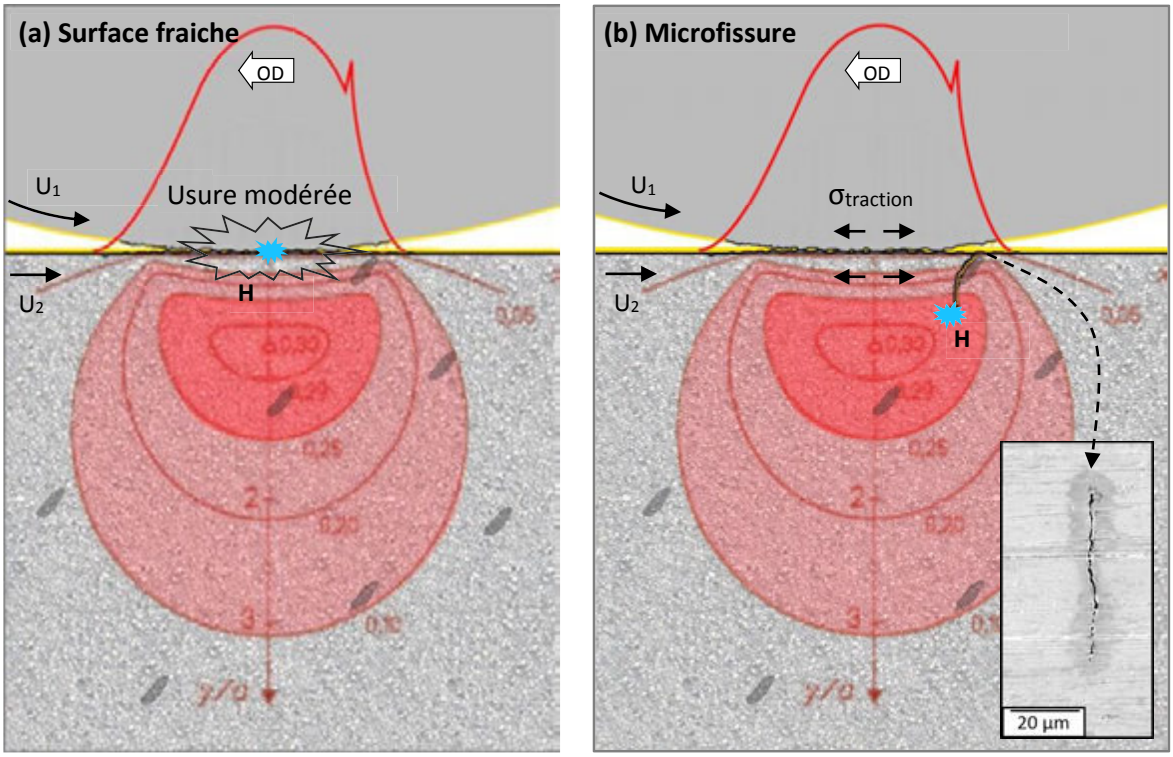

Figure 10: Schéma des mécanismes d'initiation des WEC par la formation de surface fraîche soit (a) directement au niveau de la piste en extême surface en cas d'usure modérée et/ou de tribofilm hétérogène, soit (b) via l'ouverture d'une microfissure permettant au lubrifiant d'atteindre les flancs de fissure.

Tandis que la première conjecture est en adéquation avec l'absence de lien entre les WEC et l'extrême surface dans les essais CRTB et, par conséquent, largement défendue dans la littérature [16,198,201], la deuxième semble plus concorder avec les nombreuses microfissures superficielles correspondant aux liens verticaux des WEC observés en bordure de contact sur BI des ACBB et

sur les roulements d'éoliennes [29,115,178]. Dans ces bagues, les analyses MEB-EDX des fractographes de WEC ont révélé la présence de composants de lubrifiant, notamment soufrés et phosphorés, sur les flancs de fissure près de 500µm sous la surface. Ainsi que ce soit directement en surface pour les essais butées ou au sein de microfissures dans les roulements radiaux, le lubrifiant atteint des surfaces métalliques fraiches et hautement réactives.

L'absorption d'hydrogène via les surfaces fraiches peut alors avoir lieu via une série de réactions électrochimiques décomposant les molécules du lubrifiant ou d'eau contenues au sein du fluide (**Figure 11**) [174,184,189,243–246]. La génération d'hydrogène et sa pénétration dans l'acier sont en effet catalysées par la présence de molécules d'eau dans l'huile [206,208,214,247] et par les éventuels potentiels électriques aux bornes du contact [29,99,101,168,193], qui dépendent tous deux de la température et de la formulation du lubrifiant. Des mesures par désorption thermique ont effectivement démontré que la concentration d'hydrogène ingérée par un composant tribologique variait considérablement selon la formulation du lubrifiant [172,174,184,248]. Ceci peut s'expliquer par leur influence à la fois sur la formation de tribofilm agissant comme une barrière à la pénétration d'hydrogène et sur la capacité chimique du lubrifiant à générer de l'hydrogène. A contrario, sa pénétration via les surfaces fraiches est fortement catalysée par la présence de poisons à hydrogène tels que le soufre [224].

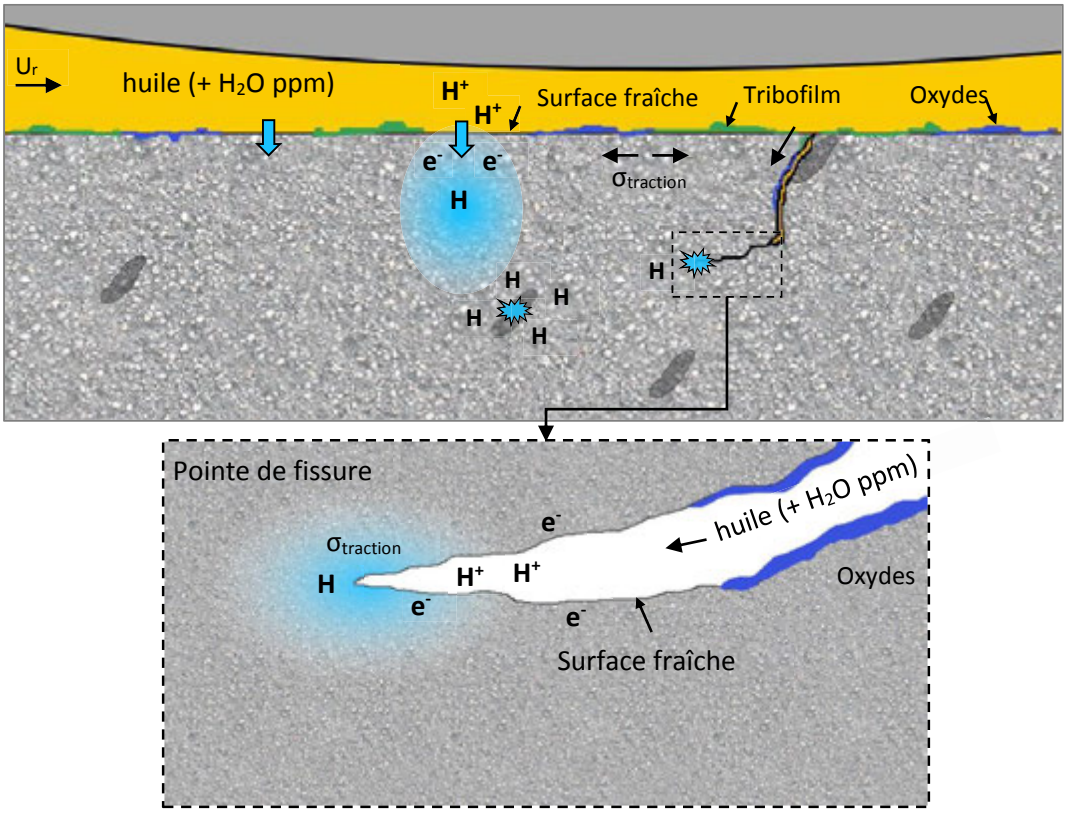

Figure 11: Schéma de l'absorption d'hydrogène dans l'acier: le lubrifiant et/ou les molécules d'eau présentes se décomposent electrochimiquement au contact de surface fraîche métallique en extrême surface ou en pointe de microfissures, libérant ainsi le l'hydrogène hautement diffusible qui est en partie piégé dans les interstices et défauts comme les inclusions.

En appliquant la loi de Fick et le coefficient de diffusion de l'hydrogène dans l'acier, il semblerait que les réseaux de WEC propagent au-delà des profondeurs théoriques atteintes par l'hydrogène généré en surface. Cela suggère que l'hydrogène est généré continuellement en pointe

de fissure au sein des WEC. Cela dit, dans le cas des reproductions sur ACBB, tout comme en application, une combinaison des deux conjectures reste probable puisqu'elles sont toutes deux favorisées par de forts glissements et une lubrification mixte. Une pénétration localisée et peu profonde d'hydrogène dans les vingt premiers µm sous la surface peut d'abord avoir lieu, facilitant ensuite l'ouverture des microfissures là où les conditions tribomécaniques seules ne suffisent pas à expliquer un tel clivage.

Une fois généré, l'hydrogène tend à rester concentré aux pointes de fissure principalement soumises à un champ de contraintes de traction [222–225,227] (**Figure 12**), ce qui favorise la décohésion entre les atomes (*Hydrogen Enhanced Localized Plasticity -HEDE*). L'acier est alors nettement fragilisé, entrainant une propagation à la fois très ramifiée et quasi-indépendante des contraintes de contact. L'aspect transgranulaire des flancs de WEC observés par fractographie souligne par ailleurs l'action de la FPH en accord avec les observations EBSD disponibles dans la littérature [14].

La *propagation* se poursuit ensuite en fonction de l'état de contraintes du composant et des défauts ponctuels dans la matière comme les inclusions. Les contraintes de traction circonférentielle favorisent une propagation quasi-verticale et profonde pouvant mener à la *rupture brutale* du composant, notamment dans le cadre de bagues en acier trempé type 100Cr6 (**Figure 12 (a)**). A l'inverse, des contraintes résiduelles compressives, formées dans les aciers cémentés ou suite à l'accumulation de fatigue de contact classique, tendent à limiter la propagation des WEC en profondeur au-dessus de la zone d'Hertz. Ceci mène alors à un écaillage étendu aussi appelé « *flaking* » (**Figure 12 (b)**).

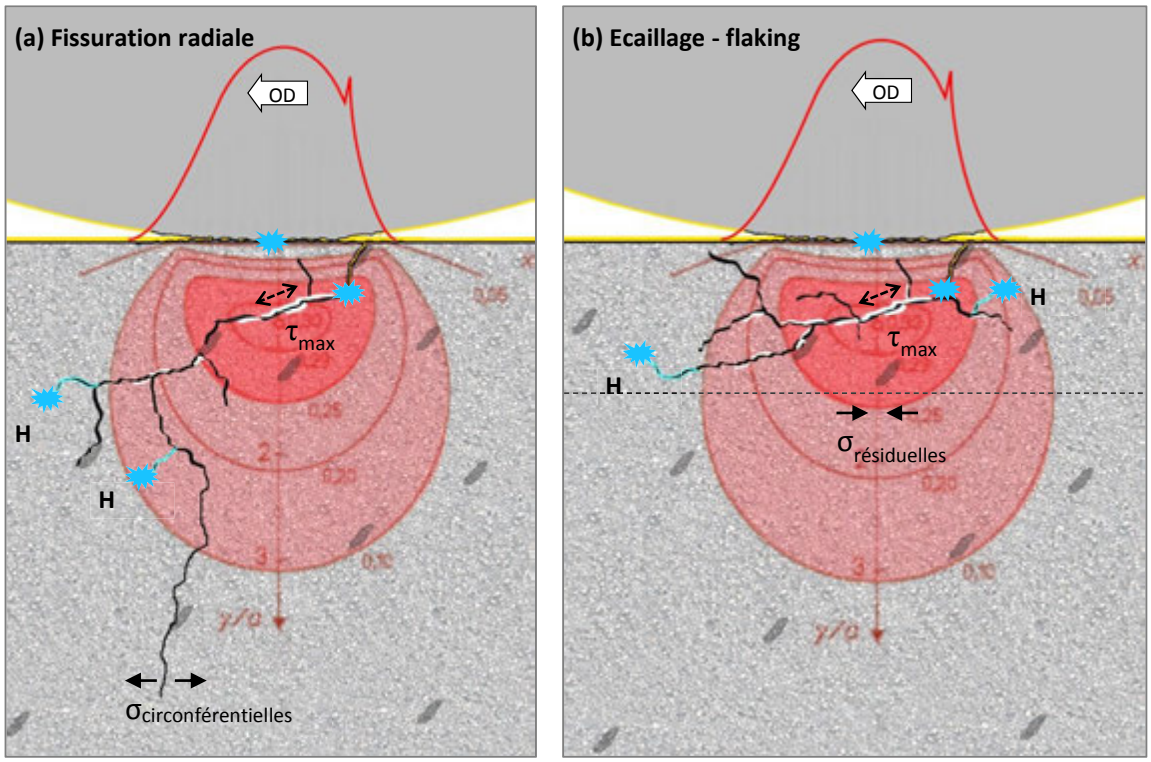

Figure 12: Schéma de la propagation des WEC due à la fragilisation par hydrogène localisée en pointe de fissures : (a) fissuration et rupture radiale des composants trempés et sujet à des contraintes circonférentielles de traction, (b) écaillage (ou flaking) des composants sujet à des contraintes résiduelles compressives, par exemple en cas de cémentation, qui contraignent les WEC proche de la surface.

Au cours de la propagation, notamment dans la sous-couche fortement cisaillée, les flancs de fissures frottent continuellement l'un sur l'autre. La présence d'hydrogène favorise alors la plastification locale (*Hydrogen Enhanced Localized Plasticity - HELP*) via le raffinement de la martensite en nano-grains ferritique associé à une dissolution du carbone. Ceci est à l'origine des *phases blanches* adjacentes observées sur les coupes métallographiques.

Ainsi, les mécanismes à l'origine des WEC reposent principalement sur des phénomènes à la fois *tribomécaniques et tribochimiques*, contrairement à la fatigue de contact classique. Les conjectures proposées à l'issue de cette étude ne trouvent pas de contre-indication dans la littérature et sont cohérentes avec le fait que la formation des WEC reste très sensible aux cinématiques du contact, à la formulation du lubrifiant et aux conditions environnantes [79,172,174,184,189,192,202].

E. Facteurs influents et investigations sur machine bi-disque

Nombreux facteurs influents : de l'échelle macroscopique à tribologique

Afin de généraliser la compréhension des phénomènes tribologiques à l'origine des WEC et d'en concevoir des solutions en adéquation avec les différentes applications, et en particulier pour l'industrie éolienne, une *analyse tribologique étendue*, principalement basée sur les expériences de WEC en interne et dans la littérature, a permis de construire étape par étape *un arbre des causes* partant de l'échelle du roulement voire du système complet et en allant vers l'échelle des aspérités au sein des contacts (**Figure 13**). Il illustre clairement que les WEC peuvent être associées à de multiples combinaisons de conditions opératoires qui semblent toutes conduire à des phénomènes tribologiques similaires avec notamment (1) d'importantes cinématiques de glissement, (2) des réactions tribochimiques spécifiques en fonction de la formulation du lubrifiant et (3) des catalyseurs comme la présence d'eau et/ou d'électricité.

La complexité de l'analyse menée provient du fait que les facteurs identifiées interagissent fortement et ce, à différentes échelles. Par exemple, la *température* au contact est considérablement affectée par les cinématiques de glissement et par le régime de lubrification. Ce dernier dépend lui-même de la viscosité du lubrifiant et donc de la température indirectement… La température agit enfin sur l'activation de certains additifs et la formation de tribofilm qui influencent à leur tour significativement la tribologie du contact.

En ce sens, une attention particulière a été portée sur les facteurs tribomécaniques et tribochimiques identifiés comme clés dans la formation des WEC. En particulier, un certain nombre de critères représentatifs de la puissance dissipée localement au sein du contact due au glissement ont été calculés le long de l'axe du contact transverse au passage de charge puis comparés par rapport à la présence et à la position des WEC. Alors que le simple taux de glissement SRR ne permet pas de différencier les cas avec et sans WEC, les critères de puissances dissipée $P.\Delta U$ et $N.\Delta U$ (N étant la charge normale) présentent à chaque fois des maxima au-delà d'un seuil arbitraire dans la zone de WEC en bordure d'ellipse (**Figure 8**) [180]. Afin de pouvoir prendre en compte aussi la température et le régime de lubrification, les critères ont été ramenés à l'épaisseur de film d'huile. Le critère, dont la différentiation et le seuil semblent les plus pertinents pour évaluer le risque de WEC, correspond à $N.\Delta U/\lambda$ (λ étant le ratio de l'épaisseur de film d'huile sur la hauteur des rugosités) (**Figure 14**).

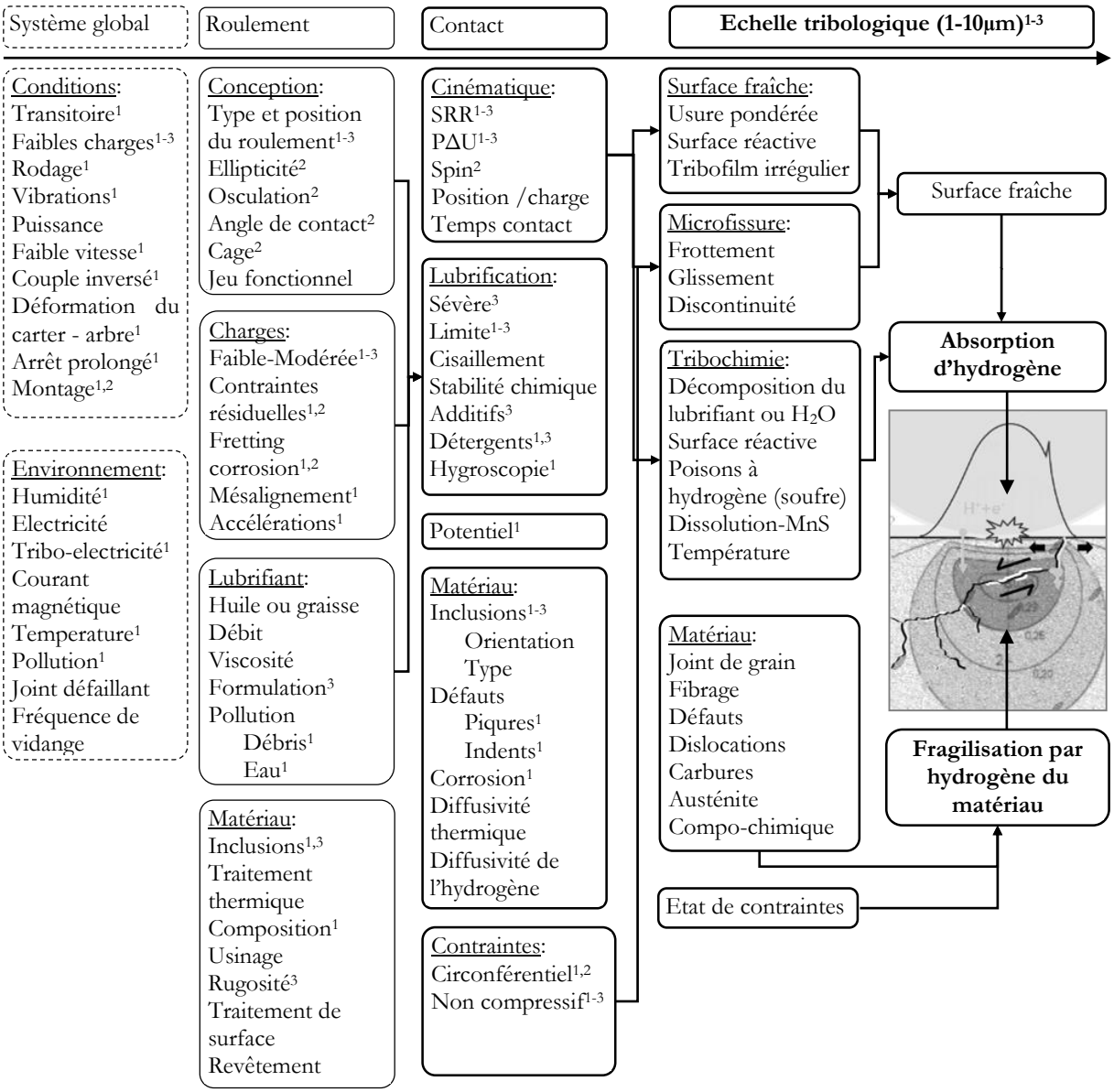

Figure 13: Aperçu global des paramètres influents sur la formation des WEC de l'échelle macroscopique à l'échelle tribologique basé sur l'occurrence de WEC dans: [1] les roulements d'éoliennes, [2]ACBB et [3]CRTB.

Certains paramètres *tribochimiques* ont été étudiés plus spécifiquement. En effet, sur les essais CRTB, malgré un critère local $N.\Delta V/\lambda$ bien plus important que pour les essais ACBB, la reproduction des WEC reste déclenchée par des concentrations spécifiques de détergents à base de CaS, en adéquation avec d'autres essais sur des roulements graissés [172,183]. Non seulement les détergents tendent à *entraver la formation de tribofilm*, laissant alors un taux important de surface fraîche, mais ils augmentent aussi la capacité du lubrifiant à ingérer de l'eau, appelée *hygroscopie*. La contamination en eau du lubrifiant, souvent importante dans le milieu éolien, tend à favoriser la génération d'hydrogène au sein du contact puisque le craquage de la molécule H_2O est plus facile que celui des chaînes hydrocarbonées. Enfin, les *courants électriques*, aussi notables dans les roulements éoliens, ont déclenché la formation de WEC sur différents essais dans la littérature [168,192,193]. Ils favorisent en effet l'absorption d'hydrogène dans l'acier par électrolyse et peuvent conduire aussi à des décharges brutales à l'origine de refonte locale.

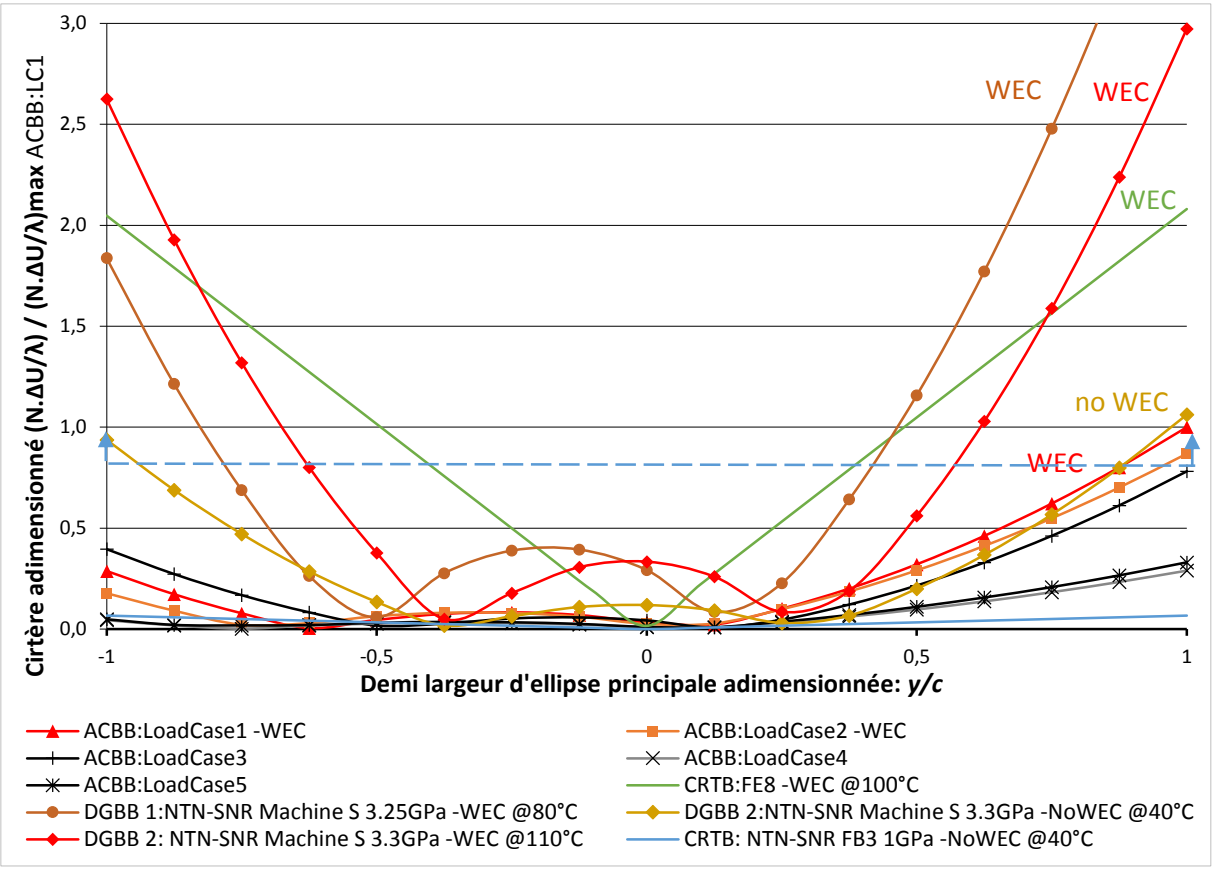

Figure 14: Ratio du critère énergétique par le paramètre de lubrification N.ΔU/λ pour différents roulements.

Au vu du nombre d'interactions et de conséquences tribologiques des paramètres identifiés, leur validation sur banc d'essai roulement complet est extrêmement délicate et justifie la difficulté de la reproduction de la défaillance.

Transposition sur la machine bi-disque

Par conséquent, une vaste campagne d'essai a alors été conduite sur un *tribomètre bi-disques* afin de simuler la fatigue de contact tout en garantissant un contrôle optimum des paramètres tribologiques au détriment d'hypothèses successives de modélisation. L'*ensemble des facteurs influents* préalablement identifiés ont ainsi été testés progressivement afin de reproduire la défaillance. Après chaque essai, les disques sont analysés en surface pour qualifier l'usure et la formation de tribofilm. Ensuite, des coupes métallographiques et fractographies sont réalisées aux endroits stratégiques pour révéler d'éventuelles propagations de fissures et/ou tous types de composants microstructuraux associés à de la fatigue de contact.

En adéquation avec l'observation des microfissures au droit des WEC dans les BI d'ACBB sur Machine S (**Figure 10**), certains protocoles d'essai ont tout d'abord été mis au point pour *initier des fissures superficielles*, soit (1) en réalisant des indents artificiels sur un des disques, soit (2) en réduisant le débit de lubrifiant pour opérer en lubrification mixte voir sévère, soit (3) en utilisant un lubrifiant plus additivé avec une forte teneur en détergents et à plus haute température (110°C). Les trois méthodes reproduisent avec succès les microfissures superficielles après un nombre de cycle relativement faible mais ces dernières ne propagent pas et sont contenues dans les premiers µm de la surface.

Par la suite, de nombreux facteurs influents ont été expérimentés individuellement ou simultanément afin de faire propager ces microfissures : (1) l'orientation des *inclusions* avec des disques spécifiques, (2) l'ajout de *contraintes structurelles* notamment de traction, (3) la *contamination en eau* des lubrifiants à base d'un protocole sans émulsion mécanique pour limiter la formation de microbulles pouvant altérer le film d'huile, (4) l'application d'un courant électrique d'intensité variant de 0.5 à 200mA au bornes du contact, et le tout avec différents lubrifiants totalement formulés et préalablement associés à des WEC sur roulements complets... Aucun de ces paramètres n'a été auto-suffisant pour déclencher la reproduction de WEC ou d'une propagation un tant soit peu ramifiée avec des phases blanches adjacentes.

Enfin, afin de mieux qualifier l'influence des additifs, et notamment des *détergents*, des essais avec indents ont été réalisés avec des lubrifiants spécifiques. Partant du constat que les conditions stationnaires du tribomètre pouvaient favoriser la formation de tribofilm avec les lubrifiants totalement formulés, des mélanges d'additifs ont été réalisées spécifiquement pour accentuer l'impact des détergents. Tandis que l'essai avec l'huile de base (PAO8) a été suspendu à plus de 20 millions de cycles, l'ensemble des essais avec des détergents à base de CaS ont écaillés prématurément à environ 5 millions de cycles. Les coupes circonférentielles au droit des fissures ont alors révélés des vastes réseaux de fissures ramifiés témoin d'une *fragilisation tribochimique* (**Figure 15**). Néanmoins, aucune phase blanche adjacente n'a été observée, potentiellement dû au nombre de cycle trop faible et à des ouvertures de fissure trop importantes dû au piégeage de l'huile.

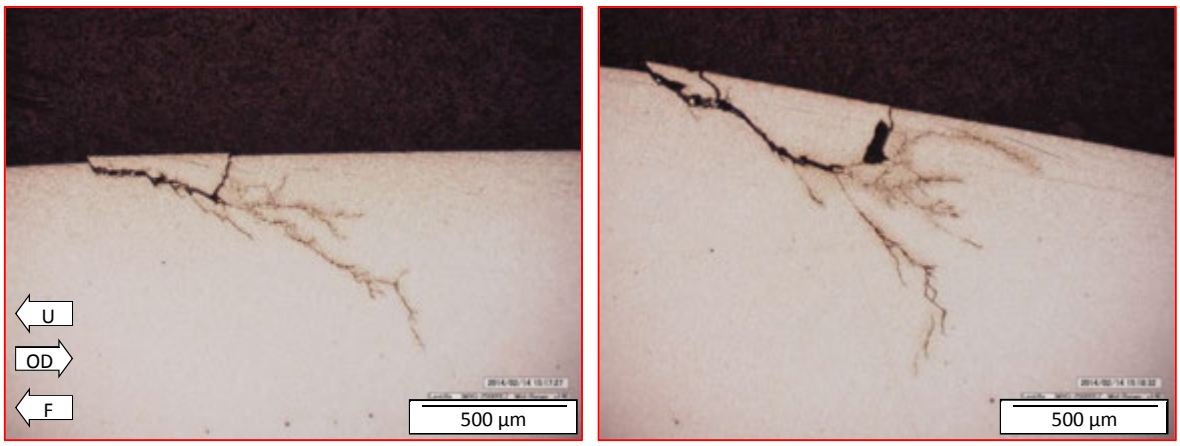

Figure 15: Coupes circonférentielles du disque cylindrique lent après essai avec un lubrifiant dont la formulation contient des détergents de type Sulfonate de Calcium.

Ainsi, malgré la grandes diversité des essais, les microfissures superficielles initiées n'ont pas propagé en ce qui correspond précisément à la définition des WEC, en accord avec d'autres résultats d'essai bi-disques dans la littérature [201]. Cela dit, la machine bi-disques est par nature un tribomètre où les conditions tribologiques sont le plus constantes possibles, de sorte que l'ensemble des phénomènes transitoires présents dans les roulements pouvant par exemple altérer le tribofilm, ne sont pas transposables. En ce sens, la perspective doit être de reproduire, non pas le faciès exact des WEC, mais plutôt la propagation de fissures superficielles assistée tribochimiquement afin de qualifier l'influence des divers facteurs identifiés. Quoiqu'il en soit, les résultats de cette étude confirment que les facteurs influents identifiés ne sont pas *auto-suffisants* : la formation des WEC repose sur un équilibre instable entre aspects matériaux, mécaniques et tribochimiques, à maîtriser pour concevoir des solutions industrielles efficaces et durables (**Figure 16**).

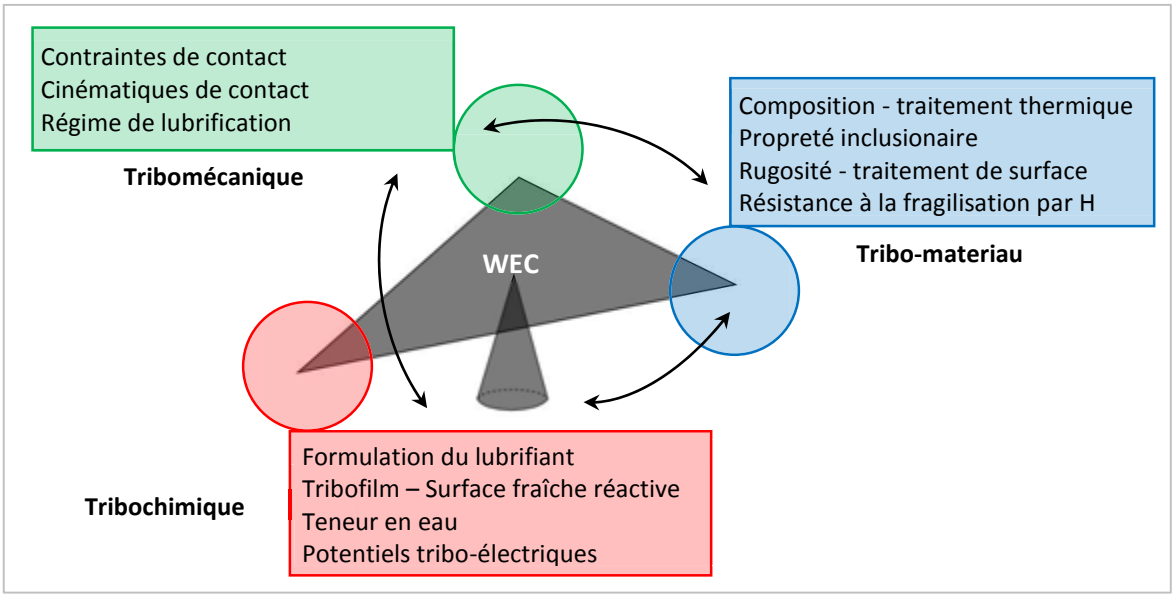

Figure 16: Le mécanisme tribologique à l'origine des WEC nécessite un subtil équilibre instable entre les paramètres mécaniques, matériau et tribochimique qui interagissent fortement.

F. Conclusions et perspectives

Afin de satisfaire à une attente majeure du marché éolien, une analyse approfondie des défaillances de roulements associées aux *White Etching Cracks* (WEC) a été proposée dans ce manuscrit afin de mieux comprendre les mécanismes tribologiques en cause et de proposer des critères de conception afin de les éviter.

Dans un premier temps, les fondamentaux de la tribologie des roulements ont été présentés. Ceci a permis de constater que les WEC correspondent à un mode de *fatigue prématuré et atypique* comparé à la fatigue de contact classique sur laquelle sont basés les modèles de durée de vie actuels. L'état de l'art bibliographique ainsi que des premiers essais sur roulements et tribomètre bi-disques ont démontré que les WEC peuvent être associées à de la *fragilisation par hydrogène* (FPH) *locale* de l'acier mais que le chargement en hydrogène artificiel en modifie les mécanismes initiateurs, rendant ce protocole inadapté à la validation de solutions industrielles.

Fort de ce constat, la *comparaison tribologique* d'essais sur butées cylindriques et sur roulement radiaux reproduisant tous deux la défaillance sans chargement en hydrogène a permis de formuler des scénarii tribologiques à l'origine des WEC. Les résultats suggèrent que l'initiation est principalement déclenchée par des phénomènes de surfaces avec *l'absorption tribochimique d'hydrogène* au niveau des surfaces métalliques fraîches sur la piste de roulement ou au niveau des flancs de microfissures superficielles. La propagation des fissures avec la formation de phases blanches adjacentes est ensuite assistée chimiquement par l'hydrogène concentré en pointe de fissure.

Un arbre des causes étendu a alors été construit progressivement et a illustré le fait que les WEC peuvent être associées à de multiples combinaisons de conditions opératoires qui semblent toutes conduire à des paramètres tribologiques similaires avec notamment : (1) d'importantes cinématiques de glissement, (2) des réactions tribochimiques spécifiques fonction de la formulation du lubrifiant et de la température, et (3) des catalyseurs comme la présence d'eau et/ou d'électricité. Certains paramètres tribomécaniques et tribochimiques ont été étudiés de manière plus

approfondie, avec l'établissement de critères de puissance dissipée avec des seuils empiriques permettant d'évaluer dans un premier temps le risque de WEC en application. Puis, une vaste campagne d'essai a été conduite sur un tribomètre bi-disques. Les résultats confirment que les facteurs influents identifiés ne sont pas pour autant auto-suffisants et que la formation des WEC repose sur un équilibre instable entre aspects matériaux, mécaniques et tribochimiques.

La difficulté à mettre en place un essai reproduisant la défaillance ainsi que sa rareté relative en application suggère que la moindre modification d'un des paramètres peut alors perturber l'équilibre tribologique à l'origine des WEC. De ce fait, les *solutions industrielles les plus optimales* sont certainement à concevoir en identifiant pour chaque cas d'applications l'ensemble des facteurs influents impliqués afin d'éviter l'absorption d'hydrogène dans l'acier. Tandis que certains paramètres tels que le grade de l'acier et les contraintes résiduelles compressives peuvent limiter la sensibilité du composant à la FPH, ce type de solutions a surtout pour vocation de ralentir et limiter la propagation des WEC. Afin d'inhiber l'initiation des WEC, il faut éviter la formation de surface fraîche et les catalyseurs favorisant la pénétration d'hydrogène. La conception de la solution doit alors tenir compte du système complet dans lequel fonctionne le roulement afin de limiter soit (1) les excès de puissance dissipée dus au glissement local, soit (2) toute formulation de lubrifiant trop riche en détergent, ainsi que (3) toute contamination électrique ou en eau. Néanmoins, toute solution doit être mise en place en n'oubliant pas qu'elle peut avoir des conséquences non-négligeable sur le reste du système mécanique, notamment sur les autres contacts.

In fine, l'étude menée lors de cette *thèse* peut être qualifiée d'analyse expérimentale d'une défaillance atypique proposant un scénario d'endommagement tribologique avec une série d'*hypothèses* qui seront, *j'espère*, amenées à être contester et/ou valider par la suite. La poursuite de la mise au point d'un protocole expérimental reproduisant la défaillance sur tribomètre permettrait de valider la plage d'influence de chaque paramètre tribologique. Les critères de conception développés pourraient alors être testés en fonction des spécificités de chaque application. Le dénouement de cette étude encourage à poursuivre étape par étape, gardant toujours en tête que la *tribologie* est intrinsèquement multi-échelle et interdisciplinaire avec des aspects matériaux, tribomécaniques et tribochimiques, tous interdépendants.

Scientific contributions

The work presented in this document has lead so far to several international journal papers and has been presented in different conferences listed below:

Journal publications

- Ruellan, A., Ville, F., Kleber, X., Arnaudon, A., and Girodin, D., 2014, "Understanding white etching cracks in rolling element bearings: The effect of hydrogen charging on the formation mechanisms," Proc. Inst. Mech. Eng. Part J J. Eng. Tribol.. DOI: 10.1177/1350650114522452
- Ruellan, A., Kleber, X., Ville, F., Cavoret J., Liatard B., 2014, "Understanding white etching cracks in rolling element bearings: Formation Mechanisms and Influent Tribochemical Drivers," Proc. Inst. Mech. Eng. Part J J. Eng. Tribol.. DOI: 10.1177/1350650114557710
  *Awarded the *Dowson Prize* at the 41st Leeds-Lyon Symposium on Tribology for the best student journal paper and presentation.*
- Ruellan, A., Ville, F., Kleber, X., Burnet, C., Liatard, B., 2014, 'White Etching Cracks (WEC) in rolling element bearings: influent drivers from wind turbines to laboratory reproduction", 2014, November 2014, Tribol. & Lubrication Tech. (TLT)

Conferences and awards

- Poster presented at the 39th Leeds Lyon Symposium on Tribology, Leeds, UK, September 4-7, 2012, "Rolling Contact Fatigue in Rolling Element Bearings for Wind Turbines: a focus on white etching cracks and flaking" (Ruellan, A., Ville, F., Kleber, X.).
  Awarded the best poster prize sponsored by Exxon Mobil.
- Oral presentation and expert panel discussion at the 68th STLE Annual Meeting & Exhibition, Detroit, MI, USA, Mai 5-9, **2013**, "Rolling Contact Fatigue in Rolling Element Bearings for Wind Turbines: a focus on white etching cracks and flaking" (Ruellan, A., Ville, F., Kleber, X.)
- Poster presented at the 68th STLE Annual Meeting & Exhibition, Detroit, MI, USA, May 5-9, **2013**, "Rolling Contact Fatigue in Rolling Element Bearings for Wind Turbines: characterizing white etching cracks (WEC)" (Ruellan, A., Ville, F., Kleber, X., Arnaudon, A., Liatard, B.)
- Oral presentation at the Porto-Lyon Tribology Workshop I, Porto, Portugal, July 22-23, **2013**, "Rolling Contact Fatigue in Rolling Element Bearings for Wind Turbines: reproducing and understanding white etching cracks" (Ruellan, A., Ville, F., Kleber, X., Arnaudon, A., Liatard, B.)
- Oral presentation at the TriboLyon 2014 for the 40th Leeds-Lyon Symposium on Tribology, Lyon, France, September 4-6, 2013, "Understanding White Etching Cracks

in rolling element bearings: the effect of hydrogen charging on the formation mechanisms" (Ruellan, A., Ville, F., Kleber, X., Arnaudon, A., and Girodin, D.)

- Oral presentation at the TAE 19th International Colloquium Tribology, Esslingen, Germany, January 21-23, **2014**, "Understanding the tribochemical formation of White Etching Cracks in lubricated rolling element bearings" (Ruellan, A., Ville, F., Kleber, X., Burnet, C., Liatard, B.)
- Oral presentation at the First African Congress in Tribology ACT2014, Marrakesh, Morocco, April 27-30, **2014**, "White Etching Cracks (WEC) in wind turbine rolling element bearings: reproduction on neutral and hydrogenated specimens" (Ruellan, A., Ville, F., Kleber, X., Burnet, C., Liatard, B.)
- Oral presentation at the 69th STLE Annual Meeting & Exhibition, Orlando, FL, USA, May 19-22, **2014**, "Understanding White Etching Cracks in Rolling Element Bearings: Reproduction and Influent Tribochemical Drivers" (Ruellan, A., Ville, F., Kleber, X., Burnet, C., Liatard, B., Cavoret, J.)
- Poster presented at the 69th STLE Annual Meeting & Exhibition, Orlando, FL, USA, May 19-22, **2014**, "Understanding White Etching Cracks in Rolling Element Bearings: Influent Drivers from Wind Turbine to Laboratory" (Ruellan, A., Ville, F., Kleber, X., Burnet, C., Liatard, B.)
  * Awarded the *Silver Prize* attributed to posters.*
- Oral presentation for plenary session at the 41st Leeds-Lyon Symposium on Tribology, Lyon, France, September 2-5, **2014**, "Tribochemical formation drivers and mechanisms of White Etching Cracks in Rolling Element Bearings for laboratory reproduction" (Ruellan, A., Ville, F., Kleber, X., Burnet, C., Liatard, B.). Awarded by the *Dowson Prize* at the 41st Leeds-Lyon Symposium on Tribology attributed to the best student journal paper and presentation.
- Oral presentation for NTN-SNR at the WindEnergy Exposition, Hamburg, Germany, September 23-26, **2014** "Premature rolling contact failure modes in wind turbine bearings: Understanding White Etching Cracks (WEC)"
- Oral presentation at the STLE Tribology Frontiers Conference, Chicago, IL, USA, October 26-28, **2014**, "Understanding White Etching Cracks in Rolling Element Bearings: Wind Turbine Tribochemical Drivers and Potential Countermeasures" (Ruellan, A., Ville, F., Kleber, X., Cavoret, J.)
- Oral presentation for plenary session at the NREL Wind Turbine Tribology Seminar, Argonne National Laboratory, U.S. Dept. of Energy, Argonne, IL, USA, October 29-31, **2014**, "Tribological Analysis of White Etching Cracks (WEC) failures in Rolling Element Bearings" (Ruellan, A., Ville, F., Kleber, X.)

FOLIO ADMINISTRATIF

THESE SOUTENUE DEVANT L'INSTITUT NATIONAL DES SCIENCES APPLIQUEES DE LYON

NOM : RUELLAN DU CREHU DATE de SOUTENANCE : 05 Décembre 2014

Prénoms : Arnaud

TITRE :

TRIBOLOGICAL ANALYSIS OF WHITE ETCHING CRACK (WEC) FAILURES IN ROLLING ELEMENT BEARINGS.

NATURE : Doctorat Numéro d'ordre : 2014ISAL0116

Ecole doctorale : MEGA

Spécialité : Mécanique

RESUME :

Despite constant expansion and engineering progress, wind turbines still present unexpected failures of heavy duty mechanical components drastically affecting the cost of energy. Among the most prevalent tribological failures in wind turbine rolling element bearings, a peculiar rolling contact fatigue mode has been associated to broad subsurface three-dimensional branching crack networks bordered by white etching microstructure, and thus named White Etching Cracks (WEC).

Compared to conventional microstructural alterations, WECs tend to develop at moderate loads and cycles eventually leading to premature failures that remain unpredictable using fatigue life estimations. Far from being generic to specific manufacturers, WECs occur in various industrial applications, for various bearing types, components, lubricants, steels grades and heat treatments. As WEC occurrences present no common evident denominator, they remain delicate to reproduce on laboratory test rigs without prior artificial hydrogen charging, so that no consensus on WEC formation mechanisms have been confirmed yet.

In this study, a thorough tribological analysis of WEC formation mechanisms has been led. Expertise protocols have been established to best reveal and observe WECs that commonly develop at unconventional locations versus the contact area. First analysis of WEC reproductions on standard rolling element bearings either hydrogen precharged or kept neutral have signified that artificial hydrogen charging, commonly employed to apprehend the failure mode, results in similar WEC morphologies but tends to alter WEC tribological initiation.

In consequence, WEC reproductions in remarkably different configurations but without hydrogen charging have been compared in order to propose a better understanding of WEC surface-affected formation mechanisms: first, initiation via tribochemical hydrogen permeation at nascent steel surfaces formed either directly at the raceway or at surface microcracks flanks and second, propagation by local hydrogen embrittlement at crack tips function of the stress state.

An extensive root cause analysis have then been led suggesting that WEC may be associated to various combinations of macroscopic operating conditions that often interact and come down to similar tribological parameters including high sliding energy thresholds, specific lubricant formulations and tribochemical drivers such as water contamination and/or electrical potentials. Further investigations on a minimalist twin-disc fatigue tribometer have provided additional evidence that WEC influent drivers are non-self-sufficient, supporting that WEC formation mechanisms rely on a subtle equilibrium between tribo-material, tribo-mechanical and tribo-chemical drivers that all should be mastered to design efficient and durable countermeasures.

MOTS-CLES :

Eolienne, Roulements, Fatigue de contact, White Etching Cracks, Analyse de défaillance,
Tribochimie, Fragilisation par hydrogène, Machine Bi-Disques

Wind turbine, Rolling Element Bearings, Rolling Contact Fatigue, White Etching Cracks,
Tribochemical drivers, Root cause analysis, Hydrogen embrittlement, Twin-Disc Machine

Laboratoires de recherche :

Laboratoire de Mécanique et des Structures (LaMCoS), INSA de Lyon
MATEriaux : Ingénierie et Science (MATEIS), INSA de Lyon

Directeurs de thèse :

Professeurs Fabrice VILLE et Xavier KLEBER

Président de jury :

Professeur Michel FILLON

Composition du jury :

Michel FILLON, Motohiro KANETA, Xavier KLEBER,
Bernard LIATARD, Gerhard POLL, Jorge SEABRA, Fabrice VILLE,